

**(12) LEVEL III**

AD-A068541

**DNA 4501F**

**AD A068541**

# **PHYSICS OF HIGH-ALTITUDE NUCLEAR BURST EFFECTS**

Mission Research  
P.O. Box 719  
Santa Barbara, California 93102

December 1977

**DDC FILE COPY**

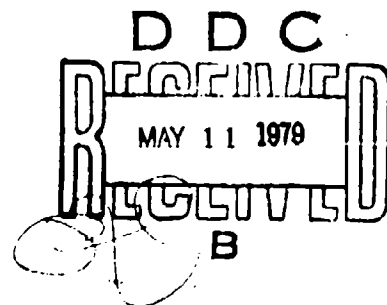
Final Report for Period January 1972—December 1977

**CONTRACT No. DNA 001-73-C-0102**

**APPROVED FOR PUBLIC RELEASE;  
DISTRIBUTION UNLIMITED.**

THIS WORK SPONSORED BY THE DEFENSE NUCLEAR AGENCY  
UNDER RDT&E RMSS CODE B322073464 S99OAXHEU4318 H2530D

Prepared for  
Director  
**DEFENSE NUCLEAR AGENCY**  
Washington, D. C. 20305



**BEST**

**AVAILABLE**

**COPY**

Destroy this report when it is no longer  
needed. Do not return to sender.

PLEASE NOTIFY THE DEFENSE NUCLEAR AGENCY,  
ATTN: TISI, WASHINGTON, D.C. 20305, IF  
YOUR ADDRESS IS INCORRECT, IF YOU WISH TO  
BE DELETED FROM THE DISTRIBUTION LIST, OR  
IF THE ADDRESSEE IS NO LONGER EMPLOYED BY  
YOUR ORGANIZATION.

UNCLASSIFIED

SECURITY CLASSIFICATION OF THIS PAGE (When Data Entered)

REPORT DOCUMENTATION PAGE		READ INSTRUCTIONS BEFORE COMPLETING FORM
1. REPORT NUMBER DNA 4501F	2. GOVT ACCESSION NO.	3. RECIPIENT'S CATALOG NUMBER
4. TITLE (and Subtitle) PHYSICS OF HIGH-ALTITUDE NUCLEAR BURST EFFECTS		5. TYPE OF REPORT & PERIOD COVERED Final Report for Period Jan 72-Dec 77
		6. PERFORMING ORG. REPORT NUMBER MRC-R-30
7. AUTHOR(s) Dan H. Holland William C. Hart Douglas H. Archer Roy W. Hendrick, Jr. Benjamin J. Berkowitz Charles Humphrey		8. CONTRACT OR GRANT NUMBER(s) DNA-001-73-C-0102CW
9. PERFORMING ORGANIZATION NAME AND ADDRESS Mission Research Corporation/ P.O. Box 719 Santa Barbara, California 93102		10. PROGRAM ELEMENT, PROJECT, TASK AREA & WORK UNIT NUMBERS NWED Subtask S99QAXHE043-18
11. CONTROLLING OFFICE NAME AND ADDRESS Director Defense Nuclear Agency Washington, D.C. 20305		12. REPORT DATE December 1977
		13. NUMBER OF PAGES 778
14. MONITORING AGENCY NAME & ADDRESS (if different from Controlling Office)		15. SECURITY CLASS. of this report. UNCLASSIFIED
		15a. DECLASSIFICATION/DOWNGRADING SCHEDULE
16. DISTRIBUTION STATEMENT of this Report Approved for public release; distribution unlimited.		
17. DISTRIBUTION STATEMENT for the abstract entered on Block 29, if different from Report		
18. SUPPLEMENTARY NOTES This work sponsored by the Defense Nuclear Agency under RT&E RMSS Code 8322073464 S99QAXHE04318 H2590D.		
19. KEY WORDS (Continue on reverse side if necessary and identify by block number) Radar Systems High Altitude Bursts Analytic Fluid Dynamics Infrared Systems Electron Radiation Numerical Fluid Dynamics Optical Systems Atomic Radiation Plasma Physics Communication Systems Molecular Radiation Striations Nuclear Weapons Beta Patch Electromagnetic Propagation		
20. ABSTRACT (Continue on reverse side if necessary and identify by block number) This compendium presents a reasonably thorough summary of the physics and chemistry that is particularly relevant to the prediction of effects of high-altitude nuclear bursts on radar, optical, infrared, and communication systems. The various chapters have been written by experts on the particular subjects. Most of the presentations are on a fairly advanced level, but a serious attempt has been made to keep in mind the special needs of new workers in this field. It is assumed that the reader has a thorough general background in physics.		

DD FORM 1473

EDITION OF ENTRIES IS OBSOLETE

UNCLASSIFIED

SECURITY CLASSIFICATION OF THIS PAGE (When Data Entered)



UNCLASSIFIED

SECURITY CLASSIFICATION OF THIS PAGE (When Data Entered)

7. AUTHOR(S) (Continued)

John Ise, Jr	Roger Manasse
Thomas H. Johnson	Austin A. O'Dell
Alfred M. Kaufman	Dale S. Sappenfield
Ralph W. Kilb	Murray Scheibe
Conrad L. Longmire	David H. Sowle

UNCLASSIFIED

SECURITY CLASSIFICATION OF THIS PAGE (When Data Entered)

## PREFACE

In undertaking to introduce new workers to the field of high altitude nuclear effects and pursuing research in this field a major source of difficulty has always been the lack of some single source of basic information. During the period 1970-1975 D.H. Holland led an attempt to alleviate this difficulty by convincing experts to interrupt busy schedules to write a chapter on their area of expertise. The purpose of the chapter would be to serve as an introduction to the area for a newcomer and as a reference for a worker in the field. The material presented should not easily become outdated.

The attempt met with partial success. The accompanying material has been circulated informally for a few years and found to be useful for the intended purposes. It is believed that wider distribution in a single volume would increase its utility.

ACCESSION for

NTIS	Write Section	<input checked="" type="checkbox"/>
DOC	Best Section	<input type="checkbox"/>
UNANNOUNCED		<input type="checkbox"/>

JUSTIFICATION: \_\_\_\_\_

BY \_\_\_\_\_

DISTRIBUTION/CLASSIFICATION CODES

Dist.	APRIL 1962	SPECIAL
-------	------------	---------

**A**

## GENERAL TABLE OF CONTENTS

	<u>PAGES</u>
CHAPTER 1    FUNDAMENTALS OF RADAR Roger Manasse	3 - 61
CHAPTER 2    INFRARED OPTICAL SYSTEMS Roy W. Hendrick, Jr.	62-129
CHAPTER 3    NUCLEAR PHYSICS AND NUCLEAR WEAPONS Dan H. Holland, Charles Humphrey	130-179
CHAPTER 4    THE TRANSPORT AND DEPOSITION OF IONIZING RADIATION Dan H. Holland, Alfred M. Kaufman, Austin A. O'Dell	180-231
CHAPTER 5    ATMOSPHERIC DEIONIZATION Benjamin J. Berkowitz, Murray Scheibe, Dan H. Holland	232-291
CHAPTER 6    ELECTRON RADIATION Dale S. Sappenfield	292-312
CHAPTER 7    ATOMIC AND MOLECULAR RADIATION IN AIR Douglas H. Archer	313-386
CHAPTER 8    EQUILIBRIUM COMPOSITION OF AIR William C. Hart, Dan H. Holland	327-396
CHAPTER 9    THE BETA PATCH Dan H. Holland	397-434
CHAPTER 10   ANALYTIC FLUID DYNAMICS David H. Sowle	435-519
CHAPTER 11   NUMERICAL METHODS OF FLUID DYNAMICS David H. Sowle, Thomas H. Johnson	520-568
CHAPTER 12   PLASMA PHYSICS Conrad L. Longmire, Ralph W. Kilb	569-624
CHAPTER 13   STRIATION FORMATION Ralph W. Kilb	625-707
CHAPTER 14   PROPAGATION OF ELECTROMAGNETIC WAVES John Ise, Jr.	708-763

CHAPTER 1  
FUNDAMENTALS OF RADAR

Roger Manasse

March 1975

Independent Consultant  
Santa Barbara, California

## TABLE OF CONTENTS

	<u>PAGE</u>
LIST OF FIGURES	5
LIST OF TABLES	6
1.1. INTRODUCTION	7
1.2. THE RADAR INSTRUMENT	12
1.3. THE RADAR RANGE EQUATION	13
1.3.1. Derivation	13
1.3.2. Other Forms of the Radar Equation	17
1.3.3. Search Radar Equation	18
1.3.4. Radar Range in the Presence of Jamming	19
1.4. ANTENNAS	20
1.5. RADAR CROSS SECTION	28
1.6. THEORY OF RADAR RECEPTION	34
1.6.1. Introduction	34
1.6.2. Detection	34
1.6.3. Parameter Estimation	43
1.7. THE RADAR OPERATING ENVIRONMENT	49
1.8. SOME COMMONLY USED RADAR ACRONYMS	57
REFERENCES	59
FIGURE CREDITS	61

## LIST OF FIGURES

<u>FIGURE</u>	<u>PAGE</u>
1-1. Block diagram of simple radar.	8
1-2. Radio spectrum.	11
1-3. Block diagram of typical pulse radar.	13
1-4. Search radar displays.	14
1-5. Linear-phased array.	27
1-6. Radar cross section of a sphere.	29
1-7. Bistatic radar cross section of a conducting sphere.	33
1-8. The detection problem.	35
1-9. Probability density functions for noise alone and signal plus noise.	36
1-10. $P_D$ vs $P_F$ curves: signal known and signal known except for phase.	40
1-11. Linear filter response.	41
1-12. Monopulse signal outputs.	49
1-13. Radar attenuation for traversal of entire troposphere at various elevation angles.	50
1-14. Theoretical values of attenuation in rain and fog.	52
1-15. Background temperature vs frequency.	53
1-16. Total atmospheric refraction errors.	54
1-17. Ground clutter return vs grazing angle.	56
1-18. Radar reflectivity vs precipitation rate.	56

## LIST OF TABLES

<u>TABLE</u>		<u>PAGE</u>
1-1.	Radiation patterns for various antenna aperture illumination functions.	25
1-2.	Monostatic radar cross section formulas.	30
1-3.	Swerling RCS fluctuation models.	32
1-4.	Approximate radar resolution and accuracy formulas.	48

## CHAPTER 1

### FUNDAMENTALS OF RADAR

#### 1.1 INTRODUCTION\*\*

The development of radar in the first half of this century has provided the greatest advance in sensing of remotely located objects since the invention of the telescope. In contrast to the use of passive optics, radar provides an active electromagnetic means for probing and sensing the environment. The type of electromagnetic radiation employed (e.g., frequency, waveform, etc.) affects the type and quality of information received about the environment. Most important, radar provides an all-weather, day-night capability not enjoyed by ground-based optics, a consideration that is critical for many civilian and military applications.

The word RADAR is an acronym which is derived from "Radio Detection And Ranging." The development of radar was strongly motivated by a need to detect and locate hostile enemy aircraft, and it was instrumental in winning the battle of Britain in World War II.\* The name radar reflects early emphasis on its use for ranging and measurement of the direction of targets. In modern radar the measurements of range and angle, while still important, represent only two of many significant functions which it can perform. Some of these functions will be discussed below.

Radar in its simplest form is illustrated in Fig. 1-1. The transmitter emits electromagnetic radiation which is beamed by the antenna toward the

---

\* See Ref. 1-1.

\*\* A brief history of radar is contained in Ref. 1-2.



target. A portion of this radiation is intercepted by the target and is reradiated (scattered) in all directions. A portion of this reradiated energy is collected by the receiver where it is processed to detect the presence of a target and to estimate target parameters. The distance to the target is determined from the amount of time required for the radiated signal to travel out to the target and back. The angle or direction of the target may be determined from the angle-of-arrival of the wavefront at the receiver or simply by knowing that the target lies within a narrow antenna beam. If the target is moving, its radial motion can be sensed by measuring the doppler shift of the carrier (i.e., center) frequency of the reflected signal. Radial motion can also be sensed (though not always as accurately) by measuring the time rate of change of range.

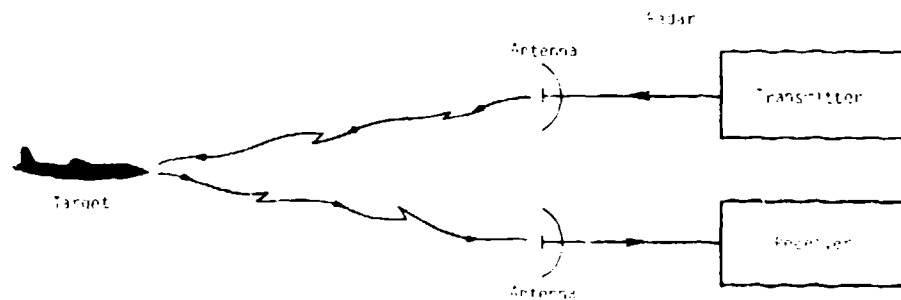


Figure 1-1. Block diagram of simple radar.

The very simple radar shown in Fig. 1-1 employs separate antennas for transmission and reception. Most often these are one and the same antenna, and a switching scheme is employed to prevent the transmitter

from overloading or saturating the receiver. In some applications the problem of protecting the receiver from the transmitter is so difficult that it is more economical to use separate antennas, even though these may be side-by-side. If a single antenna is employed, or the transmit and receive antennas are colocated, the radar is termed "monostatic." If the transmitter and receiver are separated by a substantial distance, the radar is termed "bistatic." The term "multistatic" implies one or more transmitters operating together with one or more receivers. Since the vast majority of radars operating today are monostatic, the discussion of the next few sections is confined primarily to the monostatic case. It is anticipated that multistatic radars will in the future become increasingly popular for certain applications, however.

As noted above, modern radar is called upon to perform a variety of different functions, though a given radar may be called upon to perform only one or a few of these functions. The relative importance of these functions depends on the particular problem. The more significant functions are discussed below.

Detection: To determine whether a target is present or absent; more specifically, to determine whether a target is present in a given region of space or in a given radar resolution cell. Detection is required for warning.

Resolution: The ability to separate two targets in one or more radar coordinates; e.g., range, angle, radial velocity. Resolution becomes important when many targets are close together. Resolution is usually a prerequisite to the measurement of target parameters.

Measurement: For example, the measurement of range, angle, velocity, and derivatives of these quantities. The quality of measurement is termed accuracy.

Discrimination: The ability to recognize the difference between different classes of objects; for example, to distinguish between satellites, missiles, and aircraft. The most famous is to distinguish between missile warheads and decoys.

Signature Analysis: The extraction of information from a target (e.g., translational and rotational motion, size, shape, mass, moments of inertia, etc.), which can be used to deduce its identification, mission or character. An example is the application of signature analysis to space object identification (SOI).

Tracking: The ability to maintain observations on a previously detected object and to use these measurements to predict its future location and velocity. Tracking is essential for guidance of interceptors to a target.

Imaging: Certain types of radars are able to construct two-dimensional images of targets. Side-looking ground mapping radar and range-doppler mapping of planets are both good examples. Imaging has also been performed on satellite vehicles. Imaging is a form of signature analysis and it can be employed for identification and mission analysis.

The ability to perform a particular function generally depends on the operating frequency of the radar. Therefore, radars are designed to operate at frequencies that depend on the functions to be performed. The nomenclature used to denote the various operating bands in the radio/radar spectrum is given in Fig. 1-2.

The performance of most of these functions would be rather straightforward were it not for the presence of noise, which leads to statistical uncertainties in the measurements. In addition to receiver noise, noise can arise from antenna and line losses, solar radiation, natural

and man-made interference, the galactic (*i.e.*, stellar) background, and thermal radiation from the earth and planets. In certain problems intentional jamming can be the predominant consideration. Noise may also arise due to unwanted returns from clutter, such as ground clutter, sea clutter, meteor returns, aurorae, radar chaff, and unwanted targets. The propagation medium can further complicate the situation by distorting the radar signal. Examples include radar multipath, atmospherically induced amplitude and phase scintillation, ionospherically induced bending, signal dispersion and polarization rotation, *etc.* It is the presence of these disturbing influences that makes the radar problem really challenging.

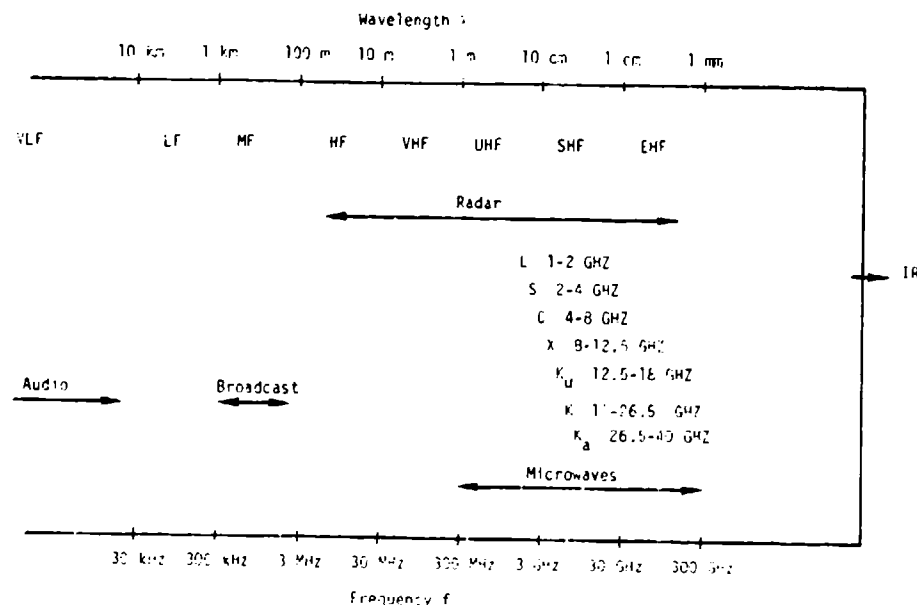


Figure 1-2. Radio spectrum.

Though many of the basic considerations of microwave radar apply also to laser radar, no attempt will be made to cover that subject in this chapter. Conventional radars can be described in terms of purely

classical physics because they operate in regimes where the number of photons involved in the processes of interest is very large, so that classical field theory is applicable; the same is not generally true of laser systems, where only a small number of photons may be detected in the returned signal and quantum effects must be taken into account.

## 1.2 THE RADAR INSTRUMENT

A block diagram of a typical pulse radar is shown in Fig. 1-3. In order to maintain accurate timing and phase coherence, all timing pulses and local oscillator (LO) signals are derived from a stable master oscillator. The master oscillator drives a waveform generator, the output of which is usually at some intermediate frequency (IF) such as 30 MHz. The waveform may consist of a simple sinusoidal pulse, a uniform train of such pulses, or some more complicated waveform. The signal is then frequency translated (i.e., mixed) up to some radio frequency (RF) such as 3000 MHz, where it is amplified and passed by a transmit-receive (TR) switch to the radar antenna. The antenna helps beam the transmitted radiation toward the target and exclude unwanted returns from objects outside the beam. Some reflected energy from the target, usually with both time delay and doppler shift, is intercepted by the antenna and passed by the TR switch to a low-noise preamplifier such as a parametric amplifier (Ref. 1-2). The amplified signal is mixed from RF down to IF, amplified and processed by a matched filter (or approximate equivalent). The matched filter usually takes the form of a linear filter network which has been optimized to maximize signal-to-noise ratio and to facilitate the extraction of target parameters. The output of the matched filter still usually contains carrier phase information which is conveniently removed in an envelope detector. More integration may take place at the output of the envelope detector, termed post-detection or non-coherent integration, to provide a further increase in signal-to-noise ratio. After video (i.e., low frequency) amplification the processed signal

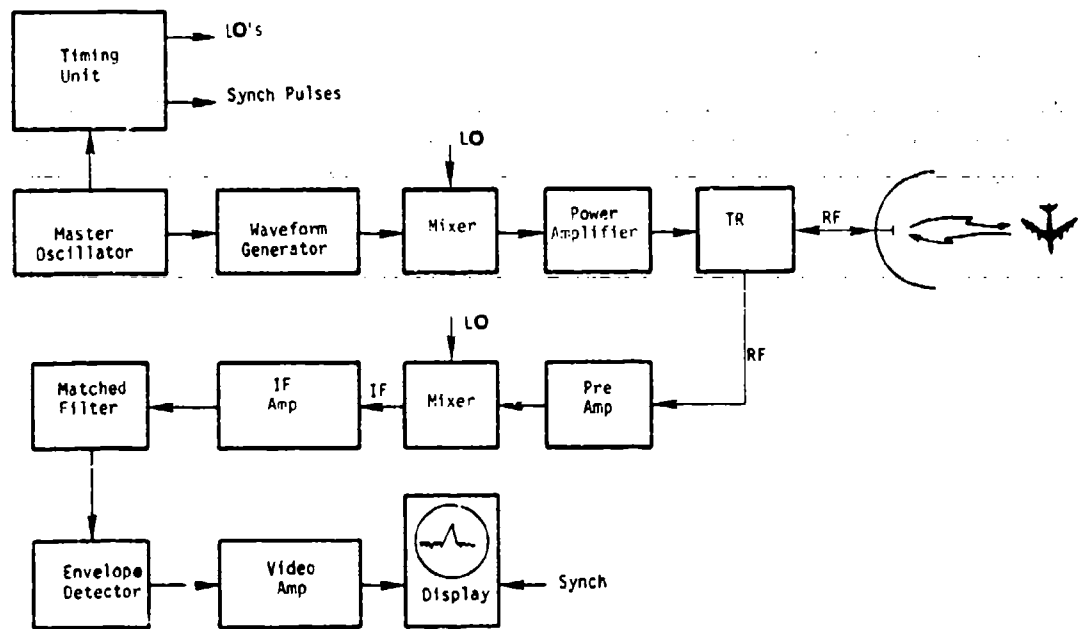


Figure 1-3. Block diagram of typical pulse radar.

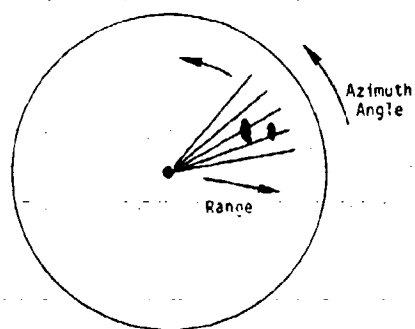
is fed into some type of visual display such as a cathode ray tube (CRT) or automatic detection and processing equipment. The trend in recent years has been to rely more and more heavily on completely automated detection and processing equipment. Some typical search radar displays are shown in Fig. 1-4.\* The most popular of these is the PPI (plan position indicator).

### 1.3 THE RADAR RANGE EQUATION

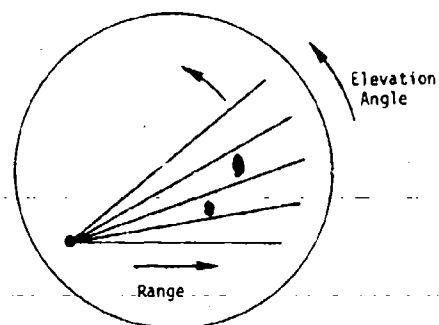
#### 1.3.1 DERIVATION

The radar range equation, usually called simply the radar equation, is the basic relation for determining the detectability of a target in terms of its cross section, range and the known characteristics of the radar. Detectability is usually expressed in terms of signal-to-noise ratio,  $S/N$ , which can be determined as a function of target range from

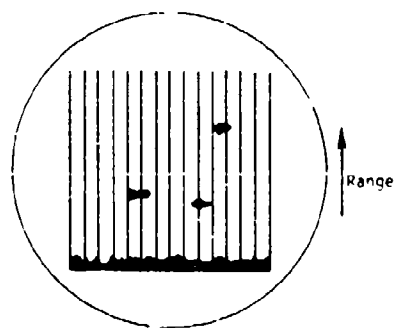
\* See, for example, Fig. 1-4(a) of Ref. 1-3.



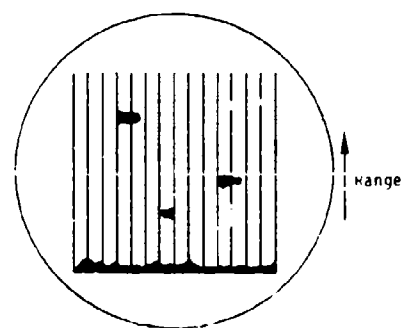
PPI-scope  
(Plan position indicator)



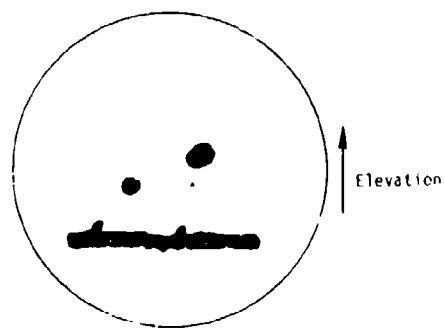
RHI-scope  
(Range-height indicator)



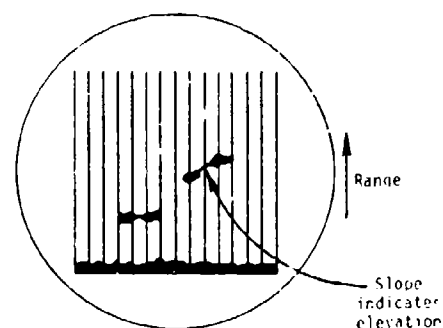
Bearing (azimuth)  
R-scope



Elevation  
E-scope



Azimuth  
E-scope (no range data)



Azimuth  
H-scope

Figure 1-4. Search radar displays.

the radar equation. Various forms of this well known equation are derived below.

Consider a transmitter that radiates power  $P$  isotropically, so that the power radiated is uniformly distributed over a sphere centered at the transmitter. The power density (i.e., power per unit area) at a range  $R$  is then  $P/4\pi R^2$ . If the transmitter is now connected to a directional lossless antenna, the effect is to increase the power radiated in some directions and to decrease that radiated in others in such a way that the total power radiated remains constant. The distribution in angle of the radiated power is called the antenna gain pattern. The antenna pattern can be characterized by an angular function  $G(\theta, \phi)$ , the gain function, such that the power density at the point with polar coordinates  $R, \theta, \phi$ , is  $PG(\theta, \phi)/4\pi R^2$ . From its definition, it follows that for an isotropic radiator  $G(\theta, \phi) = 1$  for all angles, and that for an arbitrary lossless antenna the integral over solid angle is  $\int G(\theta, \phi) d\Omega = 4\pi$ . Thus, speaking crudely,  $G$  is determined by the ratio of the total solid angle,  $4\pi$ , to the solid angle,  $\Omega_B$ , of the beam into which power is radiated, i.e.,  $G \approx 4\pi/\Omega_B$ . If the antenna is diffraction limited, the angular width,  $\phi_B$ , of the beam is approximately  $\phi_B \approx \lambda/D$ , where  $D$  is the diameter of the antenna. Therefore, for a roughly circular antenna

$$G \approx 4\pi/(\phi_B)^2 \approx 4\pi D^2/\lambda^2 = 4\pi A/\lambda^2, \quad (1-1)$$

where  $A$  is the area of the antenna. Antenna theory shows (Ref. 1-5) that this relation is approximately correct for areas of arbitrary shape. If, as we shall assume, this aperture is employed for reception, theory also shows that the effective receiving aperture is given by  $A = G\lambda^2/4\pi$ .

The radar cross section (RCS), denoted  $\sigma$ , of an object is defined as the cross sectional area of an equivalent isotropic reflector which, if located at the same position, would give the same echo strength as the object. Since a sphere large compared with a wavelength is an isotropic



scatterer,  $\sigma$  can be thought of as the cross sectional area of an equivalent sphere. Thus, to obtain the power density at the receiver, one must multiply the power density at the target by a factor  $\sigma/4\pi R^2$ , which yields

$$\text{reflected power density at the receiver} \left\{ \frac{PG\sigma}{(4\pi R^2)^2} \right. \quad (1-2)$$

$\sigma$ , for a given target, is not a simple number, but is a function of the aspect at which the target is viewed.

The total power captured by the receiving antenna is found by multiplying this power density by the effective receiving aperture  $A$ . The received signal power  $S$  is then given by

$$S = \left( \frac{PG}{4\pi R^2} \right) \left( \frac{\sigma}{4\pi R^2} \right) (A) = \frac{PG^2\lambda^2\sigma}{(4\pi)^3 R^4} \quad (1-3)$$

As noted earlier, the actual performance of a radar depends not only on the strength of the returned signal and the sensitivity of the receiver, but also on the extent to which noise interferes with interpretation of the echo. Noise can arise from a variety of sources. Usually the noise spectrum is approximately flat over the receiver bandwidth. The total noise power  $N$  in this band that competes with the signal is defined in terms of the dimensionless operating noise factor  $\overline{NF}_O$  (sometimes called system noise factor or operating noise figure);\*

$$N = kT_O B \overline{NF}_O \quad (1-4)$$

where  $k$  is Boltzmann's constant ( $1.38 \times 10^{-23}$  w/cps  $^\circ K$ ),  $T_O = 290^\circ K$ , and  $B$  is the effective receiver bandwidth in Hertz. The system noise temperature  $T_S$  is defined  $T_S = T_O \overline{NF}_O$ , and  $N$  is sometimes written

$$N = kT_S B$$

The advent of low noise receivers such as parametric amplifiers and masers has permitted very low values of  $T_S$  to be attained. With proper attention to choice of frequency, operating environment, reduction of

\* See, for example, Section 4.1 of Ref. 1-3.

antenna and line losses, etc., system noise temperatures well below 100°K can be achieved.

Combining Eqs. 1-3 and 1-4 yields for S/N

$$\frac{S}{N} = \frac{PG^2\lambda^2\sigma}{(4\pi)^3 R^4 k T_0 \overline{NF}_0 L} \quad (1-5)$$

where a factor L has been included to account for system losses which can arise from many sources. A well designed and maintained radar has losses that typically range from 8-12 dB. Note that S/N is the signal power to noise power ratio at a time when the signal has reached its peak, and at a point in the receiver where the return has been restricted to a bandwidth B which is not less than the radiated signal bandwidth.

### 1.3.2 OTHER FORMS OF THE RADAR EQUATION

The above form of the radar equation is usually derived for the case where the transmitted waveform is a simple sinusoidal pulse (of duration  $\tau$ ) and the receiver bandwidth B is chosen to be matched to this pulse ( $B \approx 1/\tau$ ). P is then replaced by  $\hat{P}$ , the radar peak power. The equation can be put in a more general form with the substitutions

$E \equiv$  received signal energy =  $S\tau$

$N_0 \equiv$  noise power per Hertz =  $N/B$

$B \equiv 1/\tau$  (the matched filter condition)

Then

$$\frac{E}{N_0} = \frac{\hat{P}\tau G^2\lambda^2\sigma}{(4\pi)^3 R^4 k T_0 \overline{NF}_0 L} \quad (1-6)$$

The quantity  $E/N_0$ , the signal energy-to-noise power per Hertz, is a dimensionless ratio that characterizes signal detectability (Ref. 1-4). The significance of this quantity will be discussed further in Sec. 1.6.

In situations where a number of pulses are integrated,  $\hat{P}\tau$  in Eq. 1-6 is replaced by  $PT_I$  where P is the average power and  $T_I$  is the coherent integration interval. In that case, Eq. 1-6 is replaced by

$$\frac{E}{N_o} = \frac{P T_I G^2 \lambda^2 \sigma}{(4\pi)^3 R^4 k T_o \overline{NF}_o L} \quad (1-7)$$

when separate antennas are employed for transmit and receive; e.g., in a bistatic radar, Eq. 1-7 is generalized to

$$\frac{E}{N_o} = \frac{P T_I G_T G_R \lambda^2 \sigma}{(4\pi)^3 R_T^2 R_R^2 k T_o \overline{NF}_o L_T L_R} \quad (1-8)$$

where  $G_T$  and  $G_R$  are the transmit and receive antenna gains,  $R_T$  and  $R_R$  are the target ranges from the transmitter and receiver, and  $L_T$  and  $L_R$  are losses appropriate to the transmitter and receiver, respectively (note that for monostatic radar  $L = L_T L_R$ ). One must, of course, employ a value of  $\sigma$  which is appropriate for the geometry and the polarizations of transmitter and receiver.

### 1.3.3 SEARCH RADAR EQUATION

The above forms of the radar equation apply to a situation where one desires to calculate the detectability of a target located in the radar beam. Suppose instead one wishes to determine the requirements on the radar for conducting a search for targets in a solid angle  $\Omega$  during a frame time  $T_F$ . The solid angle of the radar beam  $\Omega_B$  is given approximately by

$$\Omega_B = \frac{4\pi}{G} \quad (1-9)$$

The effective time  $T_I$  spent by the radar in each beam position is then

$$T_I = \frac{\Omega_B T_F}{2\pi} = \frac{4\pi T_F}{2G} \quad (1-10)$$

It is assumed that the energy received in the time  $T_I$  is coherently processed in a phase coherent manner. The energy devoted to searching each beam position is simply  $P T_I$ , where  $P$  is the average radar power. Setting  $G = 4\pi A/\lambda^2$ , and using the above expression for  $T_I$  in Eq. 1-7 yields

$$\frac{E}{N_0} = \frac{P A T_F \sigma}{4 \pi R^4 k T_0 \overline{N F}_0 L}, \quad (1-11)$$

which can be rewritten as

$$\frac{S(E/N_0)}{T_F} = \frac{\sigma P A}{4 \pi R^4 k T_0 \overline{N F}_0 L}. \quad (1-12)$$

The expression on the left is a measurement of the search capability of the radar. Eq. 1-12 expresses the well known results that the search capability of a radar is determined by its power-aperture product and is not explicitly a function of antenna gain or wavelength. If separate antennas had been employed for transmit and receive, the  $A$  entering the above equation would be for the receiving aperture.

#### 1.3.4 RADAR RANGE IN THE PRESENCE OF JAMMING

When radar is operated in the presence of strong external interference such as jamming, the noise level at the receiver may be dominated by the external noise. For certain types of problems the radar must be designed to function in an ECM (electronic countermeasures) environment where intentional jamming noise can be very much larger than receiver noise. The two cases of interest are sidelobe jamming and mainlobe jamming.

##### Sidelobe Jamming

The jammer noise power  $N_j$  at the receiver is given by

$$N_j = \left( \frac{P_j G_j}{4 \pi R_j^2} \right) \left( \frac{G_s \lambda^2}{4 \pi} \right), \quad (1-13)$$

where  $P_j$  is the jammer power,  $R_j$  the jammer range,  $G_j$  is the jammer gain in the direction of the radar, and  $G_s$  is the antenna sidelobe gain pointed in the direction of the jammer.  $P_j G_j$  is often referred to as the effective radiated power (ERP) of the jammer. This equation can be combined with Eq. 1-5 for  $S$  to find the signal-to-noise ratio  $S/N_j$ .

$$\frac{S}{N_j} = \frac{PG_j^2 R_j^2 \sigma}{4\pi P_j G_j G_s R^4} \quad (1-14)$$

The signal energy-to-noise power per cycle ratio is given by

$$\frac{E}{N_{oj}} = \frac{PT_I G_j^2 R_j^2 B_j \sigma}{4\pi P_j G_j G_s R^4} \quad (1-15)$$

where  $N_{oj}$  is the noise power per Hertz of the jammer and  $B_j$  is its radiating bandwidth. Operation in an ECM environment provides one of the principal incentives for designing antennas with low sidelobes.

### Mainlobe Jamming

In certain situations an adversary might find it advantageous to deploy a very large number of small, low-power jammers in order to fill up many or all main beam positions of the radar with jammers. The above equations can be adapted to this case simply by setting  $G_s = G$

$$\frac{S}{N_j} = \frac{PGR_j^2 \sigma}{4\pi P_j G_j R^4} \quad (1-16)$$

and

$$\frac{E}{N_{oj}} = \frac{PT_I GR_j^2 B_j \sigma}{4\pi P_j G_j R^4} \quad (1-17)$$

Although many mainlobe jammers may be required to fill many beam positions, these jammers have two very important advantages over sidelobe jammers:

1) the power required for masking a target is much lower and 2) cancellation techniques are usually not effective.

## 1.4 ANTENNAS\*

There are many different types of radar antennas, but they all basically perform similar functions. The radar antenna acts as a transducer be-

---

\* See Ref. 1-5.

tween the transmitter and free space. It serves to beam the radiated energy in a particular direction and to provide a collecting aperture for reflected energy. The antenna beam also provides a basis for rejecting unwanted signals that emanate from points outside the beam. The energy that arrives at the antenna aperture can, furthermore, be processed to determine the direction of arrival of the incident radiation.

The directivity of an antenna is determined by its gain. An antenna with unity gain is one that radiates its power  $P$  uniformly in all directions, so that the radiated power per unit solid angle is  $P/4\pi$ . An antenna with gain  $G(\theta, \phi)$ , a function of pointing angles  $\theta$  and  $\phi$ , will radiate a power per solid angle of  $PG(\theta, \phi)/4\pi$ .

Note that  $G(\theta, \phi)$  is a dimensionless quantity that represents a ratio of powers and is therefore often referred to as a power gain. For a lossless system the integral of the power per unit solid angle over all angles must equal the input power  $P$ .

$$\frac{1}{4\pi} \int PG(\theta, \phi) d\Omega = P, \quad (1-18)$$

from which it follows that, as previously noted

$$\frac{1}{4\pi} \int G(\theta, \phi) d\Omega = 1. \quad (1-19)$$

For a dissipative system the integral would be less than unity. The equation states that the average gain of a lossless antenna is unity. Since the main beam gain  $G = G(0, 0)$  is generally much greater than unity, it follows that the average antenna gain in the sidelobe region must be less than unity.

If the transmitted power could be radiated uniformly into a beam of solid angle  $\Omega_B$ , then the gain inside this beam would be

$$G = \frac{4\pi}{\Omega_B}. \quad (1-20)$$

In the discussion preceding Eq. 1-1 simple formulas were written for a roughly circular antenna. These are easily generalized to the case of a rectangular antenna as follows. The solid angle  $\Omega_B$  is given approximately by the product of the beamwidths  $\theta_B$  and  $\phi_B$  in two orthogonal planes

$$G = \frac{4\pi A}{\Omega_B} \quad (1-21)$$

Since 1 steradian equals about 40,000 square degrees, an antenna with a one-degree pencil beam has a gain of 40,000 or 46 dB. For a rectangular aperture the beam widths  $\theta_B$  and  $\phi_B$  are related to wavelength  $\lambda$  and aperture dimensions  $D_1$  and  $D_2$  approximately by  $\theta_B = \lambda/D_1$ ,  $\phi_B = \lambda/D_2$ .

Thus,

$$G = \frac{4\pi A}{\lambda^2} \quad (1-22)$$

where  $A = G/A_e$  is the antenna aperture area. Eq. 1-22 is a general one which holds for planar apertures of arbitrary shape. In practice, the effective antenna aperture  $A$  is usually somewhat smaller than the physical aperture due to non-ideal illumination and losses. If the same antenna is employed for reception, basic antenna theory states that the effective receiving and transmitting areas are equal.

In practice not all the transmitted energy can be confined to the main beam because the antenna gain function cannot be made identically zero outside the beam. In other words, the antenna will have sidelobes into which some power will be radiated and via which signals can be received. It is usually desirable to make sidelobe levels very small in order to reduce returns from unwanted signals such as clutter, radio frequency interference and other sources of external noise.

The antenna gain function  $G(\theta, \phi)$  can be calculated from the current (or voltage) excitation (or illumination) function across an aperture area (usually assumed to be planar),  $A$ , the current or voltage excited at various points on the antenna during transmission. The field

created by the antenna at any given point in space is expressible as a linear superposition, with appropriate phase shift to account for path delay, of the effects of the excitation across the aperture. The form of the resulting expression for field intensity depends on whether the point is in the near field or far field region of the antenna. The near field and far field regions are sometimes referred to as the Fresnel and Fraunhofer regions, respectively. The usual criterion for the transition point between these two regions is  $R = 2D^2/\lambda$ . This criterion is based on the requirement that the portion of a spherical wave emanating from a point at range  $R$  which is intercepted by the antenna aperture be planar to within a distance  $\lambda/8$  (a  $45^\circ$  phase error). Most radar antennas are operated well into the far field region, so that the plane wave assumption usually (though not always) prove to be excellent.

Antenna theory states that for the far field region the field strength is a two-dimensional Fourier transform of the aperture illumination function. The gain  $G(\theta, \phi)$  is of course, proportional to the square of the field strength. Maximum gain is obtained when the aperture illumination function is uniform (i.e., constant modulus). For a one-dimensional uniformly illuminated aperture of length  $D$ ,  $G(\theta, \phi)$  has the form

$$G(\theta, \phi) \propto \left| \int_{-D/2}^{D/2} e^{-i2\pi x \frac{\sin\theta}{\lambda}} dx \right|^2$$

$$= \frac{\sin^2\left(\frac{\pi D \sin\theta}{\lambda}\right)}{\left(\frac{\pi \sin\theta}{\lambda}\right)^2} \quad (1-1.5)$$



where it has been assumed that  $\theta$  is small enough so that  $\sin\theta \approx \theta$ . The 3 dB beamwidth for this antenna, which is the width of the angular region where the gain is within a factor of 2 of its peak value, is readily calculated to be  $0.89\lambda/D$  radians. This beamwidth was calculated for a beam position which is perpendicular to the plane of the aperture. The beam can be scanned mechanically by physically rotating the aperture, or electronically by introducing a phase variation into the aperture illumination function which is a linear function of  $x$ . Electronic scanning of the beam will cause the beam to broaden as it is scanned away from the face normal because the effective aperture width (in a direction perpendicular to the beam) is reduced.

The  $(\sin^2 x)/x^2$  gain pattern for a uniformly illuminated aperture has a series of smaller peaks, called sidelobes, surrounding the main peak at  $x = 0$ . The largest of these is adjacent to the main beam and is only 13 dB lower. This sidelobe level is unacceptably high for many applications. At some sacrifice in main beam gain and some beam broadening, one can achieve lower sidelobes by using a "tapered" aperture illumination function (i.e., one which decreases gradually to a small value near the edge of the aperture). Antenna gain patterns are readily derived by taking the two-dimensional Fourier transform of the aperture illumination function. A number of useful antenna functions have been tabulated by Barton, and an extract from these is summarized in Table 1-1.\* The linear aperture functions are given in terms of the linear aperture distance  $x$ , while the aperture functions with circular symmetry are given in terms of the distance  $r$  from the center of the aperture. Relative gain is the antenna gain relative to that of a uniformly illuminated aperture. This quantity, when expressed as a percentage, is often referred to as the aperture efficiency. In order to obtain the 3 dB (i.e., "half-power") beamwidth in radians, one should

---

\* See Ref. 1-6.

Table 1-1. Radiation patterns for various antenna aperture illumination functions.

Aperture Illumination Function	Relative Gain (dB)	Normalized 3 dB Beamwidth (radians)	Ratio of Power in Main Beam to Power in First Sidelobe (dB)
$ x  \leq D/2$			
Uniform: $I(x)=1$	0.0	0.886	13.3
Cosine: $I(x)=\cos^n(\pi x/D)$			
n=1	-0.956	1.189	23
n=2	-1.804	1.441	31.5
n=3	-2.44	1.659	39
n=4	-2.93	1.849	47
Function:			
$I(x)=[1-4(x/D)^2]^n$			
n=1	-0.836	1.179	21.3
n=2	-1.59	1.365	27.5
n=3	-2.17	1.568	34.7
n=4	-2.63	1.731	38.5
Cosine-on-Pedestal			
$I(x)=k+(1-k)\cos(\pi x/D)$			
k=0.5	-0.157	0.996	17.8
k=0.2	-0.516	1.069	21.8
Circular Functions			
$I(r)=[1-(2r/D)^2]^n$			
n = 0 (uniform)	0.0	1.016	17.6
n = 1	-1.34	1.267	24.5
n = 2	-2.64	1.467	30.5
n = 3	-3.68	1.681	35.8
n = 4	-4.52	1.889	40.6

multiply the number in the normalized beamwidth column by  $\lambda/D$ . From the table it is seen that the more heavily tapered the aperture, the lower is the aperture efficiency, the broader is the beamwidth, and the lower is the first sidelobe. It is possible to make sidelobes extremely low with proper choice of illumination function provided good antenna tolerances can be maintained.

There exist several different basic types of antennas: reflectors, lenses, phased arrays, and hybrid antennas which are combinations of these. The basic antenna considerations discussed thus far apply to all of these. Implicit in this discussion has been the assumption that the antennas are operated at a single frequency or over a narrow band of frequencies. Occasionally it is desired to operate an antenna over a wide band of frequencies. The broadband behavior of an antenna can be determined from its narrowband (or single frequency) response in the same sense that the broadband behavior of a linear filter is characterized by its single frequency response at frequency.

Antenna theory is a highly complex subject, but simple types of antennas such as parabolic reflectors and lense antennas are readily understood in a qualitative manner by using geometrical optics approximations. For simple applications where only one or a small number of radar beams is required, and the coverage limitations imposed by mechanical scanning of the antenna does not represent a serious disadvantage, these conventional types of antennas can be quite satisfactory, particularly from a cost standpoint. The electronically scanned phased array antenna which has come into its own during the past 15 years provides certain important and unique capabilities that are not available in conventional antennas. These include rapid beam scanning agility and an ability to form large numbers of simultaneous receiving beams. It is also possible, in principle, to obtain lower sidelobes through improved control of the aperture illumination function.

A simple one-dimensional linear array is illustrated in Fig. 1-5. The array elements which may be dipoles, waveguide horns or any other type of antenna, are uniformly spaced.

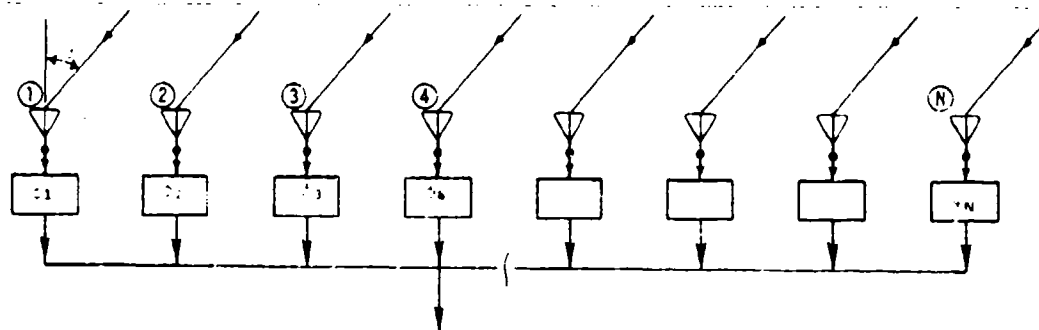


Figure 1-5. Linear-phased array.

Most arrays have an element spacing of about one-half wavelength. The array may be used for transmission or reception or both. The phase shifts  $\phi$  associated with each element increase (or decrease) linearly with element number so as just to compensate for the differential phase shift due to the inclination  $\theta$  of the wavefront. The direction of the beam is determined by controlling these phase shift values. A variety of electronic techniques are used for controlling beam steering by controlling these element phase shifts.

Each array element captures about  $1/N$  of the total signal energy incident on the array face. Proper element phasing and coherent integration will produce a signal to noise ratio at the array output which is  $N$  times larger than the signal-to-noise ratio at each receiving element. It is often desirable to connect an amplifier at

the output of each element prior to addition in order to avoid signal-to-noise degradation from line losses and mismatches. It is then possible to form a large number of receiving beams simultaneously, where each beam is formed by an appropriate summation of the phase shifted outputs of these amplifiers.

The two-dimensional planar array represents a straightforward extension, in principle, of the linear array. Element phase shift values must be chosen in order to accomplish scanning in two angular dimensions. While the beam of a linear array tends to be fan shaped (i.e., very broad in one dimension), one can obtain a pencil beam by using a square or circular planar array. Many other types of arrays are possible, including array elements mounted on the surface of a cylinder or sphere.

### 1.5 RADAR CROSS SECTION\*

The radar cross section (RCS) of an object is defined as the area intercepting that amount of power which, when reradiated isotropically, produces a signal strength at the receiver equal to that from the object. As we have seen in the discussion of the radar equation, a knowledge of radar cross section is necessary to determine radar performance. Unfortunately the problem of determining RCS for objects of complicated shape is not simple, and RCS is only loosely correlated with the physical area of an object. Exact, or nearly exact, solutions of Maxwell's equations to determine RCS has only been obtained for a few canonical shapes. To the extent that targets of interest can be identified with or resolved into a set of reflectors with these shapes, RCS values for these shapes can prove useful.

The RCS of a conducting sphere as a function of sphere radius over wavelength,  $a/\lambda$ , is shown in Fig. 1-6. The RCS has been normalized to

\* See Ref. 1-7.

its frontal area  $\pi a^2$ . In the Rayleigh region where  $2\pi a/\lambda \ll 1$ , RCS varies as  $\lambda^{-4}$ , while at the other extreme,  $2\pi a/\lambda \gg 1$ , the RCS approaches its geometrical optics value of  $\pi a^2$ . The intermediate region is referred to as the resonance or Mie scattering region. It is emphasized that this RCS curve is for the backscatter or monostatic RCS (as opposed to bistatic RCS).

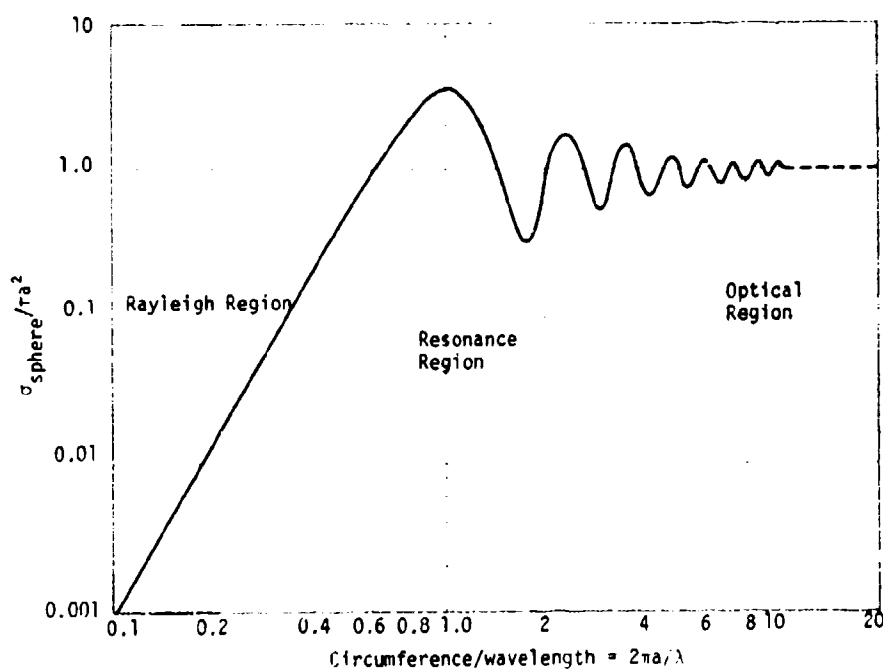


Figure 1-6. Radar cross section of a sphere.  
 $a$  = radius;  $\lambda$  = wavelength.

Monostatic RCS formulas for some typical conducting shapes of interest are summarized in Table 1-2. These formulas are approximate and hold when the characteristic body dimensions are large compared to a wavelength.

Table 1-2. Monostatic radar cross section formulas\*.

SCATTERER	ASPECT	RADAR CROSS SECTION	DEFINITION OF SYMBOLS
Sphere	Arbitrary	$\pi a^2$	$a$ = radius
Convex Surface	N/A	$\pi a_1 a_2$	$a_1, a_2$ = principal radii of curvature
Flat Plate of Arbitrary Shape	Broadside	$\frac{4\pi A^2}{\lambda^2}$	$A$ = cross sectional area
Corner Reflector	Arbitrary	$\frac{4\pi A^2}{\lambda^2}$	$A$ = cross sectional area
Circular Plate	Incidence at Angle $\theta$ to Normal	$\pi a^2 \cot^2 \theta \left\{ \left( \frac{4\pi a}{\lambda} \right) \sin \theta \right\}$	$a$ = radius of plate
Circular Cylinder	Incidence at Angle $\theta$ to Normal	$\frac{a \cos \theta \sin^2(kL \sin \theta)}{k \sin^2 \theta}$	$a$ = radius of cylinder $L$ = cylinder length $k = 2\pi/\lambda$
Circular Cylinder	Normal Incidence	$\frac{2\pi a L^2}{\lambda}$	$a$ = radius of cylinder $L$ = cylinder length
Infinite Cone	Nose-Up	$\frac{\lambda^2 \tan^2 \alpha}{16\pi}$	$\alpha$ = cone half angle
Resonant Dipole ** (length = $\lambda/2$ )	Broadside	$0.88\lambda^2$	-
Resonant Dipole ** (length = $\lambda/2$ )	Randomly Oriented	$0.15\lambda^2$	-

\* These formulas are approximate and assume characteristic dimensions large compared to a wavelength. Cross section values do not depend on polarization except for the broadside-dipole where it is assumed that the E-field is aligned with the dipole.

\*\* See Ref. 1-8.

The RCS for some objects can be derived in the following manner. The intercepted energy corresponds to its cross sectional area  $A$  (the frontal area seen looking along the direction of propagation). The object, with surface currents induced by the incident plane wave, can now be considered as a radiating antenna with a gain  $G$  in the direction of the receiver. The resulting RCS is then  $GA$ . For example, with a flat plate or corner reflector, the object has an effective gain  $4\pi A/\lambda^2$ , from which it follows that

$$\sigma = \frac{4\pi A^2}{\lambda^2} \quad (1-24)$$

In practice a complex scatterer such as an aircraft has an RCS which varies in a complicated manner with both aspect angle and frequency. The rate of variation with aspect angle is proportional to the apparent width of the target in wavelengths, while the rate of variation with frequency is proportional to the length of the target in wavelengths. This wide and often unpredictable variation in RCS creates a problem for the radar designer because he must account for a random distribution of RCS values. To this end, he may employ one of a number of RCS fluctuation models which he feels best approximate his situation. The RCS fluctuation models developed by Swerling are frequently employed and these are summarized in Table 1-3 (Ref. 1-9).

The effect of RCS fluctuations is generally to reduce the probability of detection when the detectability is high, but to increase the probability of detection when detectability is low. A case of particular concern is where RCS fluctuates very slowly so that it is possible for RCS to be near an RCS null for an unacceptably long time period. Pulse-to-pulse or look-to-look frequency jumping is often effective for overcoming this problem.

In the case of bistatic radar one must, of course, use the bistatic RCS. When the bistatic angle  $\epsilon$ , the angle between the transmit and receive lines-of-sight to the target, is small, one can determine RCS



Table 1-3. Swerling RCS fluctuation models (Ref. 1-9).

Swerling Type	RCS Probability Distribution $P(\sigma)$	Remarks
I	$\frac{1}{\bar{\sigma}} e^{-\sigma/\bar{\sigma}}$	Fixed during one sweep of the beam over the target, but independent scan-to-scan.
II	$\frac{1}{\bar{\sigma}} e^{-\sigma/\bar{\sigma}}$	Random from pulse-to-pulse
III	$\frac{4\sigma}{\bar{\sigma}^2} e^{-2\sigma/\bar{\sigma}}$	Fixed during one sweep of the beam over the target, but independent scan-to-scan
IV	$\frac{4\sigma}{\bar{\sigma}^2} e^{-2\sigma/\bar{\sigma}}$	Random from pulse-to-pulse

using the "monostatic-bistatic equivalence theorem" (Ref. 1-10). This theorem states that the bistatic RCS is equal to the monostatic RCS along a direction which is along the bisector of the bistatic angle and at a frequency which is reduced by a factor  $\cos\beta/2$ . This theorem is approximately valid for simple convex shapes at small bistatic angles, but fails seriously at large bistatic angles and for concave shapes such as a corner reflector.

One of the motivations for using bistatic radar is the increase in radar cross section which often occurs as bistatic angle is increased. This phenomenon can be particularly important for objects whose monostatic cross section has been reduced through shaping and/or the use of radar absorbing materials (RAM). This phenomenon is illustrated qualitatively for the case of conducting spheres in Fig. 1-7 where RCS is plotted versus  $\beta$  for two different sphere sizes. As  $\beta$  approaches  $180^\circ$ , RCS approaches a very large value which theory shows is given by

$$\sigma = \frac{4\pi A^2}{\lambda^2}, \quad (1-25)$$

and is independent of polarization.

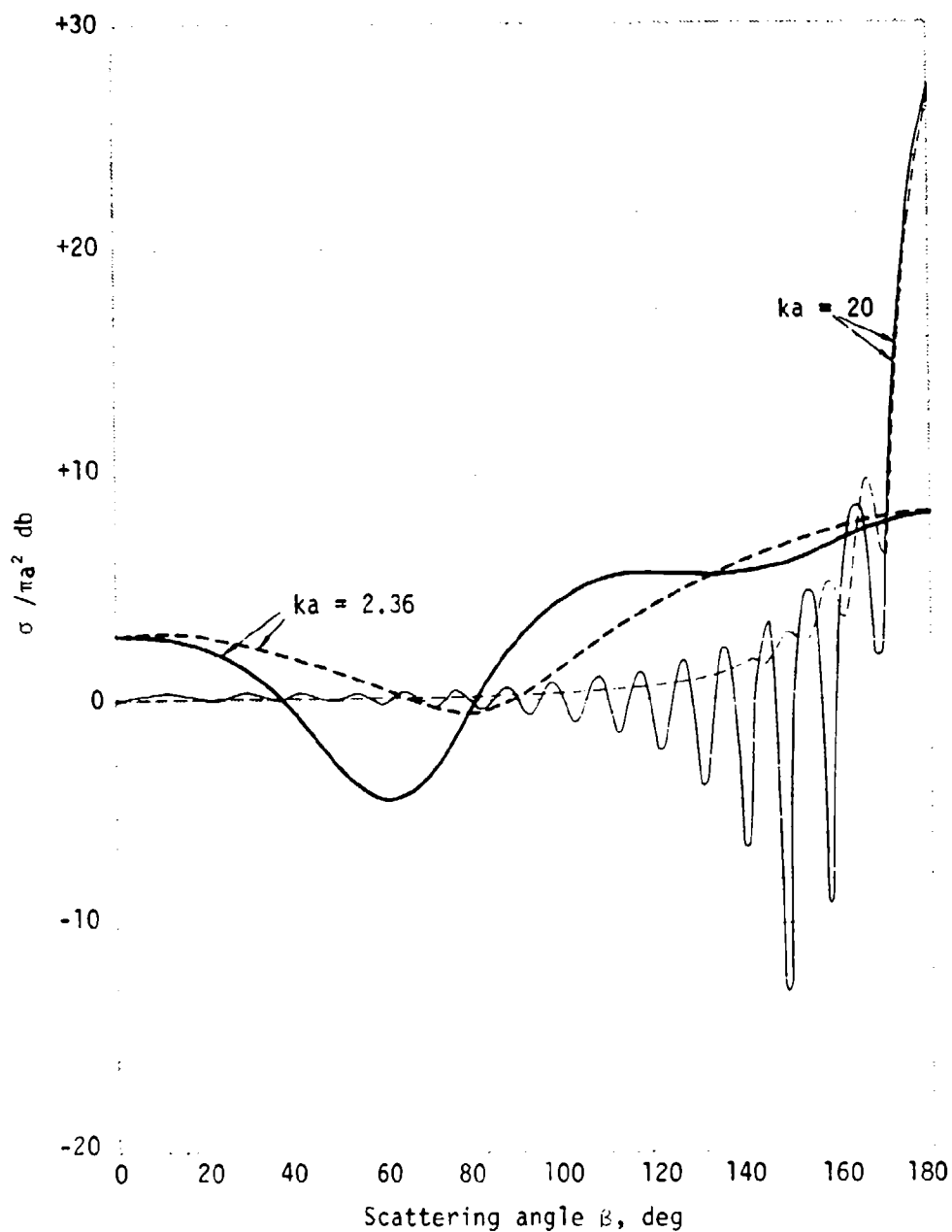


Figure 1-7. Bistatic radar cross section of a conducting sphere [a is the sphere radius and  $k=2\pi/\lambda$ . Solid curves are for the E plane ( $\beta$  measured in the plane of the E vector); dashed curves are for the H plane ( $\beta$  measured in the plane of the H vector, perpendicular to the E vector)].

## 1.6 THEORY OF RADAR RECEPTION\*

### 1.6.1 INTRODUCTION

Radar reception can be thought of as taking place in two steps. The first is to determine if a signal (i.e., target) is present or absent. This first step is termed detection. If the first step reveals the presence of a signal, the second step is to measure the quantities that characterize the signal (e.g., RCS, range, radial velocity, angular direction, etc.). This second step is termed the measurement or parameter estimation problem. The detection problem is complicated by statistical uncertainties due to the presence of noise. This noise may take one of a variety of forms depending on the radar implementation and operating environment. In addition, the form of the signal may not be known exactly in advance, but may be one of a set of signals that occur with specified probabilities.

It should be noted that the theory of detection and parameter estimation exist independently of their application to radar, but the rapid development of the theoretical understanding of these subjects over the past two decades owes its motivation largely to radar.

### 1.6.2 DETECTION

Detection can be considered as a hypothesis test with two alternatives, signal present or signal absent. The problem is illustrated in Fig. 1-8. The received message, denoted  $x$ , is some combination, denoted  $\oplus$ , not necessarily additive, of signal  $s$  and noise  $n$ . The signal may or may not be present.  $s$  and  $n$  are chosen in accordance with certain probability distributions which define the statistics of the problem. The space of all possible messages, denoted by the circle, is divided into two regions, the  $\Gamma$  region in which a yes (signal present) decision

---

\* See Refs. 1-11, 1-12, and 1-13.

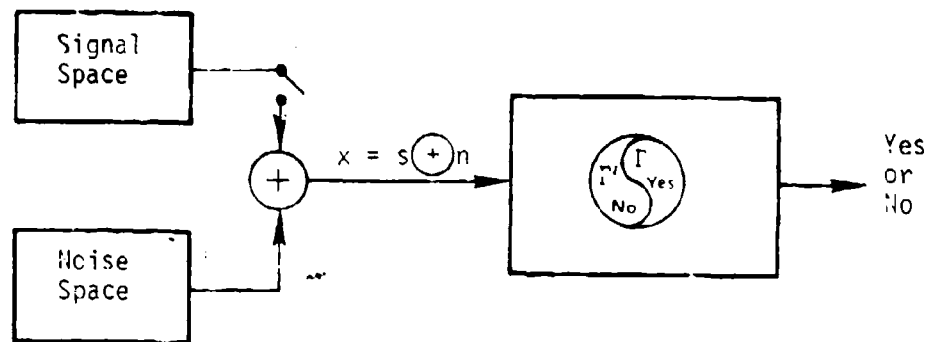


Figure 1-3. The detection problem.

is made, and the  $\Gamma'$  region in which a no (signal absent) decision is made. The manner in which this space is divided between  $\Gamma$  and  $\Gamma'$  is called the "decision rule."

When a decision is made there is always the possibility of error.  $P_D$  is the probability of correctly deciding that a signal is present, while  $(1 - P_D)$  is the probability of incorrectly deciding that a signal is absent (probability of a miss).  $P_F$ , the false alarm probability, is the probability of incorrectly deciding that a signal is present, while  $(1 - P_F)$  is the probability of correctly deciding that no signal is present.

In a simple problem  $x$  might simply be a positive voltage and the decision on whether a signal is present or absent might be based on whether  $x$  exceeds some threshold  $\lambda$ .  $x$  can be considered as a random quantity (i.e., a random variable) with statistical behavior characterized by conditional probability densities  $P(x/S)$  when signal and noise are both present and  $P(x/N)$  when noise only is present. The situation is illustrated schematically in Fig. 1-3. The various probabilities discussed above can be expressed as integrals over these probability functions, in accordance with shaded regions in the figure.

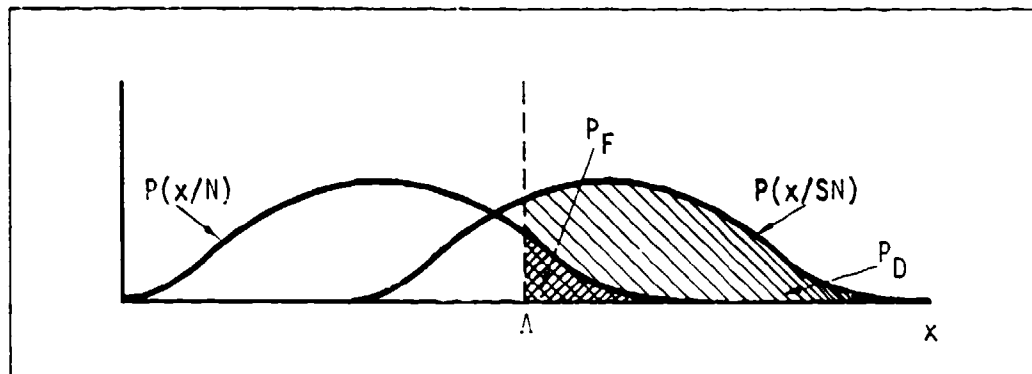


Figure 1-9. Probability density functions for noise alone and signal plus noise.

$$P_D = \int_{\Lambda}^{\infty} P(x/SN) dx \quad (1-26)$$

$$1 - P_D = \int_0^{\Lambda} P(x/SN) dx \quad (1-27)$$

$$P_F = \int_{\Lambda}^{\infty} P(x/N) dx \quad (1-28)$$

$$1 - P_F = \int_0^{\Lambda} P(x/N) dx \quad (1-29)$$

It is seen that  $P_D$  can always be increased by decreasing  $\Lambda$ , but this has the effect of increasing  $P_F$ . The more the two probability functions in Fig. 1-9 tend to overlap, the higher will be  $P_F$  for a given value of  $P_D$ .  $P_F$  can be made low by increasing  $\Lambda$ , but only at the expense of making  $P_D$  low. Thus, detectability cannot be characterized by  $P_D$  or  $P_F$  alone; both must be specified. More generally,  $P_D$  is usually plotted versus  $P_F$  by allowing  $\Lambda$  to vary.

When  $x$  represents a more complicated message, such as a waveform, the decision rule becomes more involved. A number of different criteria exist for optimizing the decision rule. These include such criteria as minimum cost (Bayes decision rule), minimum information loss, Neyman-Pearson and Ideal Observer. The Neyman-Pearson rule maximizes  $P_D$  subject to a specified value of  $P_F$ . The Ideal Observer minimizes the probability of error  $P_E$ .

$$P_E = P(N)P_F + (1 - P_D)P(SN) \quad , \quad (1-30)$$

where  $P(N)$  is the *a priori* probability of noise alone and  $P(SN) = 1 - P(N)$  is the *a priori* probability of both signal and noise being present. Note that the Neyman-Pearson criterion has the advantage of not depending on these *a priori* probabilities.

Fortunately, theory tells us that all of these different criteria lead to exactly the same type of decision rule; namely, one which sets a threshold  $A$  on a quantity called the *likelihood ratio*. The likelihood ratio  $L(x)$  is defined

$$L(x) = \frac{P(x/SN)}{P(x/N)} \quad . \quad (1-31)$$

The only difference between the criteria is the value for  $A$ . The form of the optimum receiver can thus be specified once the statistics of the signal and noise are known.

Most radars are designed to handle the reception of signals in a very specific type of noise called "additive white gaussian" noise.\* Most receiver noise and many other types of noise are of this type. This noise has the properties of being linearly additive to the signal and of having a flat spectrum. Its gaussian character assures that the output of any linear operation on this type of noise, such as linear filtering, will be normally (i.e., gaussian) distributed. The additive

---

\* See, for example, p. 37 of Ref. 1-11.

white gaussian noise assumption also has the advantage of producing mathematically tractable results. Even when this noise assumption is not completely valid, the practical results are often still reasonably good.

Consider the case of a known signal waveform  $s(t)$ , e.g. a voltage vs.  $t$  waveform, in the presence of an additive white gaussian noise waveform  $n(t)$ . Detection theory tells us that the likelihood ratio  $L(x)$  takes the following form

$$L(x) = e^{\chi} \quad (1-32)$$

where

$$\chi = \frac{1}{N_0} \int_{-\infty}^{\infty} x(t)s(t)dt \quad (1-33)$$

$N_0$ , as before, is the noise power per unit bandwidth. Setting a threshold on  $L(x)$  is equivalent to setting a threshold on  $\chi$ , since these are monotonically related. Thus the optimum receiver consists of taking the received message  $x(t)$ , cross correlating it with  $s(t)$ , and setting a threshold on the result. The value of the threshold is usually based on an acceptable false alarm rate. This process is often termed "correlation-reception."

The quantity  $\chi$  is a random variable with mean value zero when the signal is absent (i.e.,  $s(t) = 0$ ), mean  $2E/N_0$  when the signal is present, and variance  $2E/N_0$ . The signal energy  $E$  is defined as the integrated square of  $s(t)$ , which is the energy which would be dissipated in a one-ohm resistor. The effective signal-to-noise ratio is the square of the difference of the mean values of  $\chi$  divided by the variance of  $\chi$ , which yields  $2E/N_0$  as the effective signal-to-noise ratio at the output of the ideal receiver.

On the basis of these considerations, the following formulas for  $P_D$  and  $P_F$  are readily derived.

$$P_D = \frac{1}{\sqrt{2\pi\mathcal{R}}} \int_{\Lambda} e^{-(\chi - \mathcal{R})^2 / 2\mathcal{R}} d\chi \quad (1-34)$$

$$P_F = \frac{1}{\sqrt{2\pi\mathcal{R}}} \int_{\Lambda} e^{-\chi^2 / 2\mathcal{R}} d\chi \quad (1-35)$$

where the abbreviation  $\mathcal{R} = 2E/N_0$  has been employed.  $P_D$  or  $P_F$  curves for various values of  $\mathcal{R}$  based on these formulas are shown as the solid curves in Fig. 1-10. Because probability scales are employed for ordinate and abscissa, these curves are straight lines.

Two significant points are worth emphasizing. The first is that signal detectability, as manifested in the  $P_D$  or  $P_F$  curves, depends only on the signal energy and not the shape of the waveform, provided the signal is exactly known. Thus, modulation of the signal to increase its bandwidth, and hence the required bandwidth of the receiver, does not in principle degrade signal detectability. The second point is that  $P_F$  is a very sensitive function of  $2E/N_0$  for fixed  $P_D$  when  $P_F$  is small. From Fig. 1-10 it is seen, for example, that when  $P_D = 0.9$ , an increase in  $2E/N_0$  from 49 to 64 causes  $P_F$  to decrease from  $5 \times 10^{-9}$  to  $10^{-12}$ .

The introduction of unknown signal parameters can, of course, do nothing but degrade signal detectability. This situation is illustrated in Fig. 1-10 for a signal which is known except for carrier phase which is plotted as the dashed curves. The degradation in detectability below the signal known case becomes less pronounced as  $2E/N_0$  is increased.

Consider now the case where the signal, if it occurs, is one of a set of distinctly different signals, i.e., signals which do not overlap in



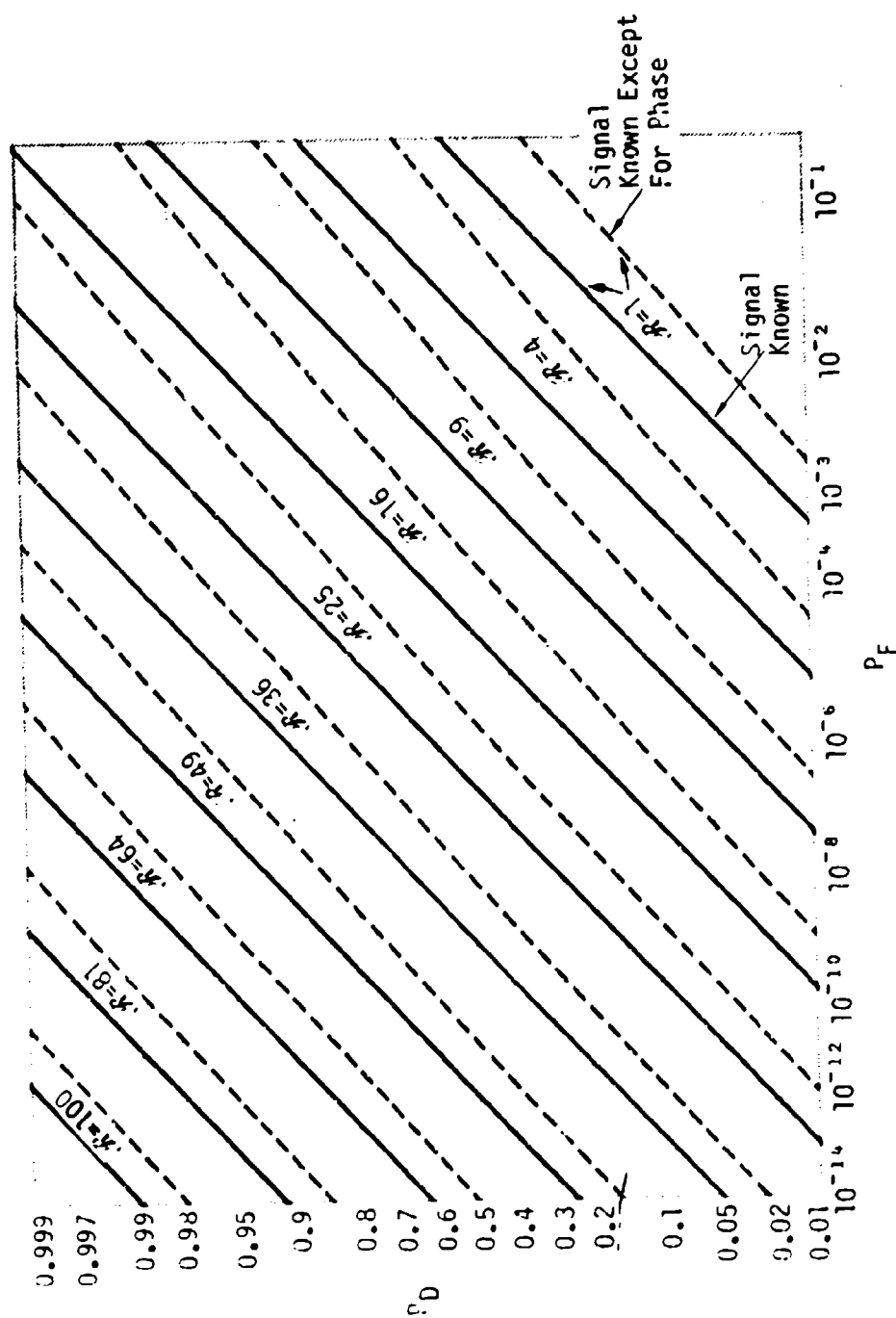


Figure 1-10.  $P_D$  vs.  $P_F$  curves: signal known and signal known except for phase.

time or in frequency) each with signal energy  $E$ . Such might be the case, for example, with a pulse which can occur with one of a set of  $N$  time delays, where the time steps are larger than the pulse length. Theory states that correlation reception must be performed for each distinct resolution cell in which the signal could be located. A threshold can be set on the result of each of these correlation reception operations to obtain a specified  $P_D$ . The probability of false alarm is, however,  $N$  times as large as for the single signal case. Stated generally, if the radar has to look for the presence of a signal in one of  $N$  resolution cells, then  $P_F$  as determined from Fig. 1-10 must be multiplied by  $N$ . Since resolution can exist in several dimensions, such as range, velocity and angle, the number of resolution cells examined by the radar per second can easily be quite large; e.g.,  $10^6$  or larger.

In practice, correlation reception is usually implemented with the aid of a "matched filter." Consider the situation shown in Fig. 1-11.

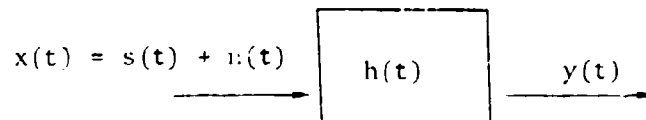


Figure 1-11. Linear filter response.

$x(t)$  is the input to a linear filter which can always be characterized by its impulse response function  $h(t)$ , the response to a delta function at  $t = 0$ . The filter output  $y(t)$  is related to the input by a convolution integral.

$$y(t) = \int_{-\infty}^t x(u)h(t - u)du, \quad (1-36)$$

where  $u$  is a dummy variable. The matched filter condition requires

$$h(t) = s(T - t), \quad (1-37)$$

where  $T$  is sufficiently large to ensure a filter realizability condition  $h(t) = 0$  for  $t < 0$ .  $y(t)$  is then given by

$$y(t) = \int_{-\infty}^{\infty} x(u)s(T - t + u)du. \quad (1-38)$$

The output of the matched filter at time  $T$ ,  $y(T)$ , is seen to be the desired correlation upon which the threshold should be set.

In practice radar signals have time delay as one of their unknown parameters. The matched filter has the great virtue of supplying at its output the cross correlation of the received waveform with all delayed replicas of the expected signal as a time waveform. Detection can then be performed by simply setting a threshold on this time waveform. Signal time delay can be estimated by measuring the time at which the output of the matched filter reaches its peak. It is useful to note that  $y(t)$  can be written

$$y(t) = \int s(u)s(T - t + u)du + \text{noise term}. \quad (1-39)$$

The signal component of the output of the matched filter is seen to be just the time autocorrelation of  $s(t)$ , a fact which will be used in the next section, on parameter estimation.

The signal-to-noise ratio at the output of the matched filter at the instant when the signal reaches its peak is, as we have seen, just  $2E/N_0$ . Usually, however, the matched filter is implemented as a relatively narrowband filter, and the signal out from this filter is therefore narrowband. The time-average signal-to-noise ratio includes the effect of noise both in phase and in quadrature with the signal, thus yielding a time average signal-to-noise ratio of  $E/N_0$ . It is for this reason that the radar equation is usually written to provide  $E/N_0$  rather than  $2E/N_0$ .

An ideal receiver makes use of exact knowledge of signal shape, including phase. In the case of a single pulse, this type of receiver is fairly easy to implement. It is more difficult in the case of a pulse train because the processor must be properly matched in phase for the length of the pulse train. This matching problem can be complicated by unknown doppler shift as well as unknown time delay. As the observation time on the target is increased, other problems such as amplitude and phase scintillation of the target, the existence of radial acceleration and higher derivatives of range, etc., tend to complicate the reception process.

A practical expedient to simplify the reception process in such situations is to envelope detect the signal (thus destroying phase information) and integrate the signal "noncoherently." Such a process is called postdetection integration, as opposed to coherent processing, which is called predetection integration. A loss in signal detectability is incurred, and many curves will be found in the literature which show postdetection integration performance under various situations.\* A good rule of thumb is that postdetection integration is quite efficient when the input signal-to-noise ratio is unity or greater, but it degrades rapidly when the input signal-to-noise ratio falls below unity.

### 1.6.3 PARAMETER ESTIMATION

The parameters of a radar target determine how the transmitted waveform is modified by the target to produce a reflected waveform. During a short time interval the target return can be characterized by RCS, range, radial velocity, and angular position. Over longer periods of time various derivatives of these quantities may also have to be included as unknown parameters. Once the target has been detected, the signal

---

\* See, for example, Sec. 2.6 of Ref. 1-2.

energy received across the aperture can be processed to form an estimate of its signal parameters.

Consider a simple situation where the transmitted waveform is  $s(t)$  and the received waveform has the form  $as(bt + c)$ . The received signal is characterized by the unknown parameters  $a$ ,  $b$ , and  $c$  which are to be estimated. The quantity  $a$  depends on the target RCS and the radar range.  $b$  is determined by the radial velocity of the target and  $c$  depends on the range of the target. If the observation time is short,  $a$ ,  $b$ , and  $c$  can be treated as constants.

It should come as no surprise that the accuracy in determining these quantities is a function of  $s(t)$ . A long sine wave, for example, will yield very good velocity resolution and accuracy but very poor range resolution and accuracy. More complex waveforms can be devised which provide both good range and velocity information.

With the assumption of additive white gaussian receiver noise, parameter estimation theory, based on Bayes' theorem on inverse probability and the *method of maximum likelihood*, specifies how the received signal must be processed to obtain the best estimate of target parameters (Ref. 1-11). Suppose the received signal waveform with energy  $E$  is written  $s(t, \gamma)$  where the parameter  $\gamma$  denotes one or more unknown parameters. Theory shows that one must compute

$$\int x(u)s(u, \gamma)du \quad (1-40)$$

for all possible values of  $\gamma$ . The best estimate of  $\gamma$  is that value which maximizes this expression. In the case where unknown time delay is the only unknown parameter  $s(t, \gamma)$  is replaced by  $s(t - \tau)$  and the integral becomes a crosscorrelation of the received message waveform with delayed replicas of the expected signal. As was seen in the previous section, this function is conveniently calculated with the aid of

a matched filter, and the best estimate of  $\tau$  is obtained by looking for the time at which the output of this filter is a maximum. If the correct value of  $\gamma$  is denoted  $\gamma_0$ , the integral can be written

$$\int x(u)s(u,\gamma) du = \int \overbrace{s(u,\gamma_0) s(u,\gamma)}^{\phi(\gamma_0,\gamma)} du + \text{noise} . \quad (1-41)$$

It is the presence of the noise term which causes the estimate of  $\gamma$  to deviate from its true value, since  $\phi(\gamma_0,\gamma)$  is a maximum when  $\gamma = \gamma_0$ . The more sharply peaked is  $\phi(\gamma_0,\gamma)$ , the less will be the perturbing influence of the noise on the estimate of  $\gamma$ , and the better will be the accuracy in determining  $\gamma$ .

Should the character of  $\phi(\gamma_0,\gamma)$  be such that two or more values of  $\gamma$  give the same, or nearly the same, value of  $\phi(\gamma_0,\gamma)$ , it will not be possible to determine with certainty which value of  $\gamma$  is correct. In other words, there will be an ambiguity in estimating  $\gamma$ . The function  $\phi(\gamma_0,\gamma)$  characterizes the nature of these ambiguities. In the literature  $\phi(\gamma_0,\gamma)$  is usually considered for two unknown parameters, time delay, and doppler shift, and it is that function which is usually referred to as the radar ambiguity function. The theoretical properties of the radar ambiguity function have been a subject of considerable interest in the literature (Refs. 1-11, 1-14, 1-15, 1-16).

As an example of how ambiguities can arise, consider the case where the transmitted waveform has the form (ignoring constants of proportionality)  $\sin \omega t$  and the target introduces a time delay  $\tau = 2R/c$ . The received signal then has the form

$$\sin[\omega(t - \tau)] = \sin \left( \omega t - \frac{4\pi R}{\lambda} \right) . \quad (1-42)$$

The phase shift introduced by the target is  $4\pi R/\lambda$ . Since this phase shift can only be measured as an angle between 0 and  $2\pi$ , the determination of  $R$  is highly ambiguous. Stated differently, incrementing  $R$  by

$n\lambda/2$ , where  $n$  is any integer, will change the phase of the received signal by an amount  $2\pi n$  and hence leave the measured value of phase unchanged. This type of range ambiguity is usually of no concern because range accuracy of better than  $\lambda/2$  is almost never required, and range is usually obtained by measuring the delay of the pulse envelope rather than from carrier phase. For an isolated radar pulse this range measurement will be unambiguous.

More generally, it is desired to choose a waveform which will provide both range and velocity information. The most frequently employed waveform is a uniform train of short identical pulses. Denote the time separation of the pulses by  $T_0$ , and the radian frequency of the radar by  $\omega = 2\pi f$ , as before. This waveform can give rise to both range and velocity ambiguities. For example, a target at range  $R$  gives a return which is indistinguishable in form (except for end effects where the pulse train starts and stops) from a return at a range  $R + \frac{c}{2}T_0$ . In other words, range ambiguities occur with a spacing  $R_B = cT_0/2$ . On the other hand, a velocity shift of  $\lambda/2T_0$  produces a change of phase shift between pulses of exactly  $2\pi$  radians and thus produces no measurable change in phase. It follows that the velocity ambiguity spacing is  $V_B = \lambda/2T_0$ . The product  $R_B V_B$  is thus given by

$$R_B V_B = c\lambda/4 \quad (1-13)$$

Thus, when  $\lambda$  is fixed,  $R_B$  can only be made larger at the expense of making  $V_B$  smaller, and vice versa. This equation expresses the well known range-velocity ambiguity dilemma which afflicts radar. This phenomenon, aside from causing measurement ambiguities, can also "fold-in" clutter from other range or velocity regions which will compete with desired signal returns. In many problems where clutter is not serious and the range-velocity spread from targets is not large, radar ambiguities present no problem. In the case of isolated targets, a priori information can often be employed to resolve measurement ambiguities. One well known radar application where the range-velocity

ambiguity problem is quite serious is the use of airborne radar to detect aircraft in the presence of ground clutter.

From Fourier transform theory one can show that resolution in frequency is  $T^{-1}$ , where  $T$  is the time duration of the signal. Conversely, the resolution in the time domain is  $B^{-1}$ , where  $B$  is the signal bandwidth. The time delay  $\tau$  is related to the range  $R$  by the formula  $R = \frac{1}{2}c\tau$ . It follows that the range resolution  $\Delta R$  is given by

$$\Delta R = \frac{1}{2}c\Delta\tau = \frac{c}{2B} \quad (1-44)$$

The doppler shift  $f_D$  is related to the radial velocity  $V$  by  $f_D = 2V/\lambda$ . It follows that the velocity resolution  $\Delta V$  is given by

$$\Delta V = \frac{2\Delta f_D}{2} = \frac{\lambda}{2T} \quad (1-45)$$

These expressions for  $\Delta R$  and  $\Delta V$  are approximate and assume that the bandwidth  $B$  and the time  $T$  are more or less uniformly occupied by signal.

Once a target has been resolved in at least one radar coordinate from other objects, it is usually possible to determine its parameters (e.g., range, velocity, angle) to an accuracy which is a small fraction of the resolution cell width. This accuracy improves with signal-to-noise ratio. Approximate simplified formulas for radar resolution accuracy are given in Table 1-4. The accuracy formulas include a small degradation factor for non-ideal signal processing. A good rule of thumb is that a minimum detectable signal level, approximately 14 dB signal-to-noise ratio, will yield an accuracy which is one-tenth the resolution cell size.

Some restrictions apply to the use of these accuracy formulas: the signal-to-noise ratio must be substantially greater than unity; the radar ambiguity function must have finite derivatives near its origin; the measurements of angle, range and velocity must be "coupled" in



Table 1-4. Approximate radar resolution and accuracy formulas

	<u>Resolution</u>	<u>Accuracy (rms error)</u>
Angle (circular aperture of diameter D)	$\Delta\theta = 1.2 \frac{\lambda}{D}$	$\sigma_{\theta} = \frac{\Delta\theta}{\sqrt{3} \sqrt{S/N}}$
Range	$\Delta R = \frac{c}{2B}$	$\sigma_R = \frac{c}{4B \sqrt{S/N}} = \frac{\Delta R}{2 \sqrt{S/N}}$
Velocity	$\Delta V = \frac{\lambda}{2T}$	$\sigma_V = \frac{\lambda}{4T \sqrt{S/N}} = \frac{\Delta V}{2 \sqrt{S/N}}$

a statistical sense. Generally, one can assume that radar measurements are uncoupled. A notable case where range and velocity is coupled, however, occurs with a linear FM signal waveform. Such waveforms are frequently employed because they provide a convenient means for increasing the time duration and/or the bandwidth of the signal and thereby provide improved resolution and accuracy. In the audio range a linear FM signal sounds like a chirp, and for this reason these waveforms are often referred to as "chirp" signals (see Ref. 1-15).

An example of how one can obtain an accuracy which is a small fraction of a resolution cell will be illustrated with a scheme known as monopulse (or simultaneous lobing). This term is used to signify that an angle measurement is made on a single pulse. In the case of a dish (i.e., reflecting type) antenna, two feed horns can be displaced so as to form beams at slightly different angles, as shown below. The beams can be added to form a sum beam and a difference beam. The sum beam is used to determine the magnitude  $A$  of the return. The difference beam output, which is essentially linear near the origin, produces an output proportional to  $A\Delta\theta$ , where  $\Delta\theta$  is the angular displacement of the target from the midpoint of the two beams. The angle estimate is

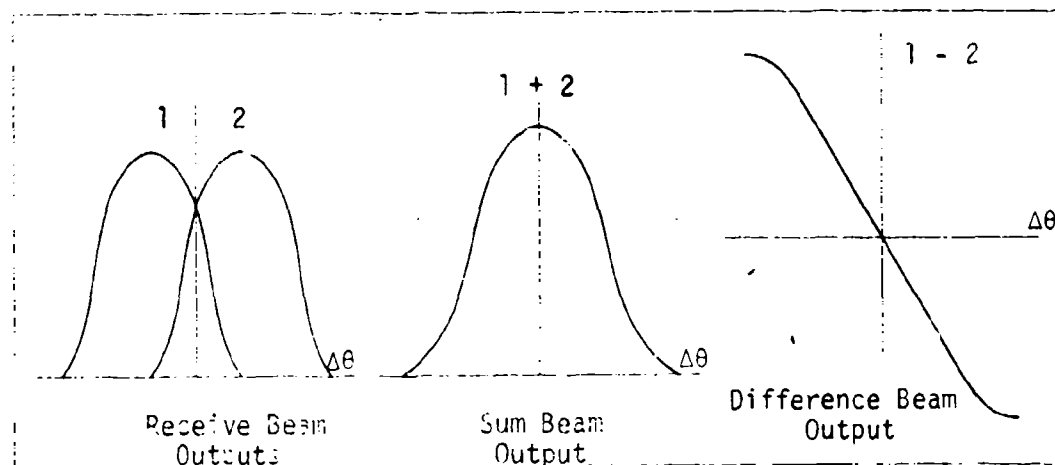


Figure 1-12. Monopulse signal outputs.

obtained by dividing the difference output by the sum output. In a tracking radar the output of the difference channel can be used in a servo loop to drive the antenna so as to keep its boresite pointed approximately at the target. From a theoretical standpoint, the basic approach for measuring range and velocity is similar to that for measuring angle.

#### 1-7. THE RADAR OPERATING ENVIRONMENT

The choice of design parameters for a particular application, and the performance which can be achieved in a radar is often strongly influenced by the environment in which the radar must operate. This environment sets a practical limit on the usable radar frequency band. The high-frequency end of the operating band is limited by atmospheric absorption due to water vapor and oxygen. The low-frequency end of the band is limited by various types of noise and uncertainties in propagation through the ionosphere.

The effect of atmospheric attenuation is shown in Fig. 1-13. The two-way attenuation by the unperturbed atmosphere, in db, is plotted

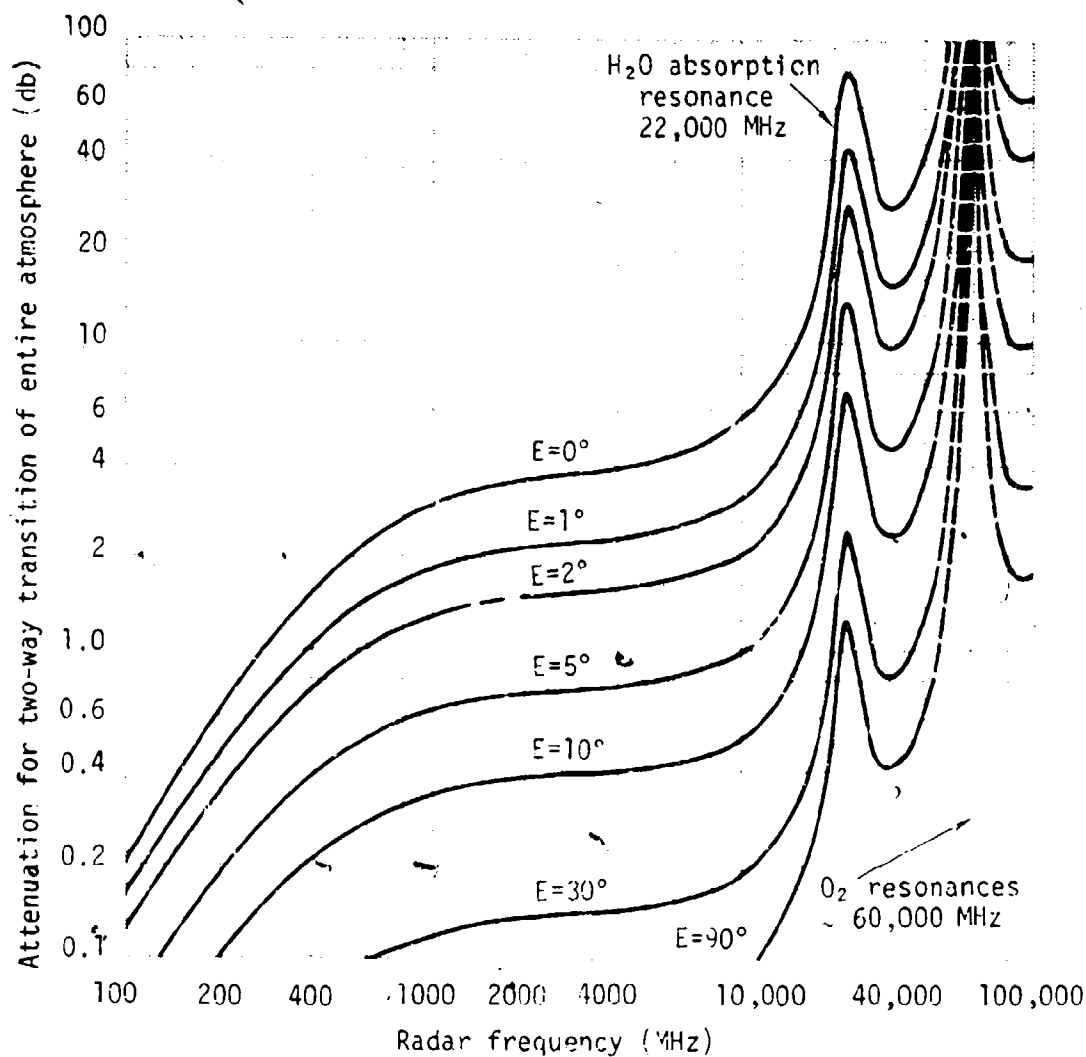


Figure 1-13. Radar attenuation for traversal of entire troposphere at various elevation angles, applicable for targets outside the troposphere. (Does not include ionospheric loss, which may be significant below 500 MHz in daytime.)

os. elevation angle and radar frequency. As noted, the two absorption peaks shown are due to water vapor and oxygen. This absorption can also significantly increase system noise temperature if very low noise receivers are employed. The small "window" between the two absorption peaks is at K<sub>a</sub>-band (26.5-40 GHz). The effect of atmospheric absorption can be mitigated by placing the radar on a high altitude aircraft, or avoided entirely if the radar is located in space.

At the higher frequencies, 3000 MHz and above, precipitation can also cause serious absorption. The two-way attenuation, in dB per mile, in rain and fog, is plotted in Fig. 1-14. Weather attenuation is seen to increase very rapidly with increasing frequency. It is essential to keep the radar frequency low (S-band or lower) in order to achieve an all-weather capability.

Under normal circumstances the earth's ionosphere, which starts at an altitude of about 50 km, has negligible absorption at frequencies above 100 MHz. However, calculations show that a high-altitude nuclear explosion can create attenuations of tens or hundreds of decibels over regions near the blast for periods of minutes, depending on weapon yield, altitude, radar frequency and other factors. This attenuation is caused by collisions between electrons and ionized and neutral atoms and molecules. Ionospheric absorption is not usually of any concern for radars which operate entirely below the ionosphere; i.e., radars for air traffic control. As with atmospheric absorption, ionospheric absorption can increase the noise level in a low-noise radar receiver.

The combined effect of atmospheric absorption and the cosmic noise background is shown in Fig. 1-15. The maximum and minimum cosmic noise correspond to the directions of the galactic center and pole, respectively. The maximum temperature from atmospheric absorption corresponds to an antenna beam pointed at the horizon, while the minimum corresponds to an antenna pointed at the zenith. Other sources

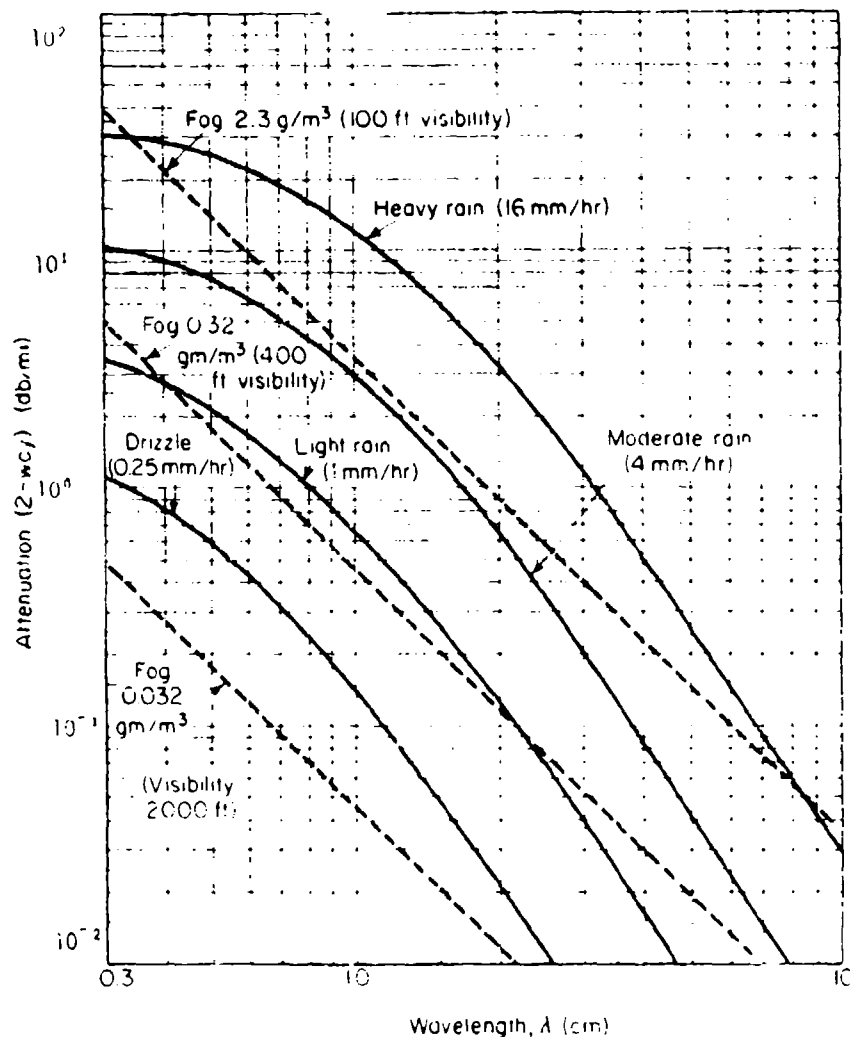


Figure 1-14. Theoretical values of attenuation in rain and fog.

of noise at low frequencies include atmospheric noise (from lightning storms), man-made noise produced by various electrical equipment, solar noise, and radiation from discrete radio stars. All of these tend to decrease with frequency. Atmospheric noise is of little significance above 100 MHz and radio stars are too weak to be a serious problem. Solar noise is potentially a problem, even in the radar sidelobes, at the low end of the radar band during periods of solar outbursts where the radiation can increase as much as 40 dB above its normal value. These outbursts, though not very frequent, can last from minutes to hours.

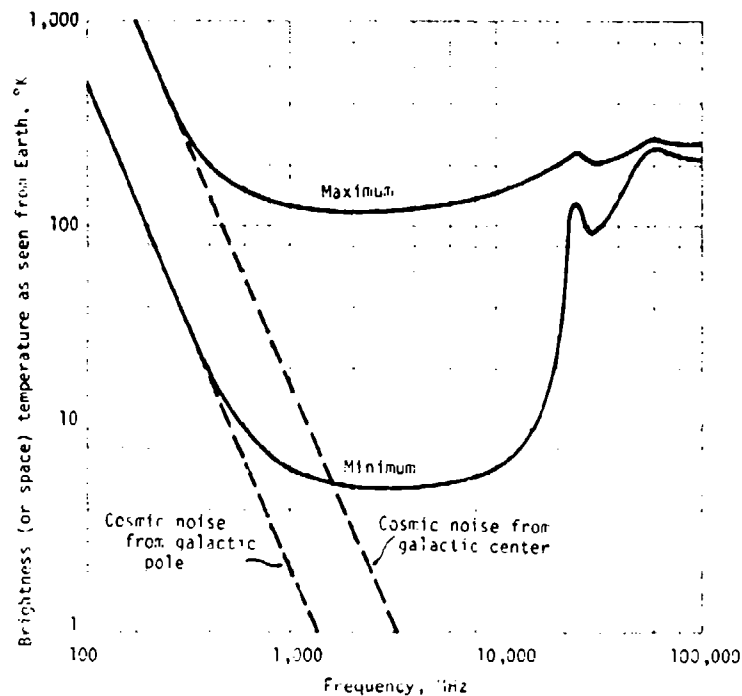


Figure 1-15. Background temperature vs. frequency.

The atmosphere provides a generally favorable environment for propagation of radio waves at frequencies above 100 MHz. For many applications the errors caused by atmospheric bending and path delay can either be ignored or simply corrected. The propagation medium is divided into two regimes which have distinctly different behavior. Refraction errors in the troposphere are essentially frequency independent, while ionospheric refraction, which is caused by the presence of free electrons, scales as the inverse square of frequency. The total angular atmospheric refraction error at 200 MHz versus target altitude and elevation angle is plotted in Fig. 1-16.\* The dashed portion of the curve represents the ionospheric contribution. The tropospheric errors can often be corrected to within a few percent of their residual value with the aid of local index of refraction measurements. The atmosphere will also cause errors in measuring range and radial velocity which can be of

\* See Pt. V, Chapter I of Ref. 1-17.

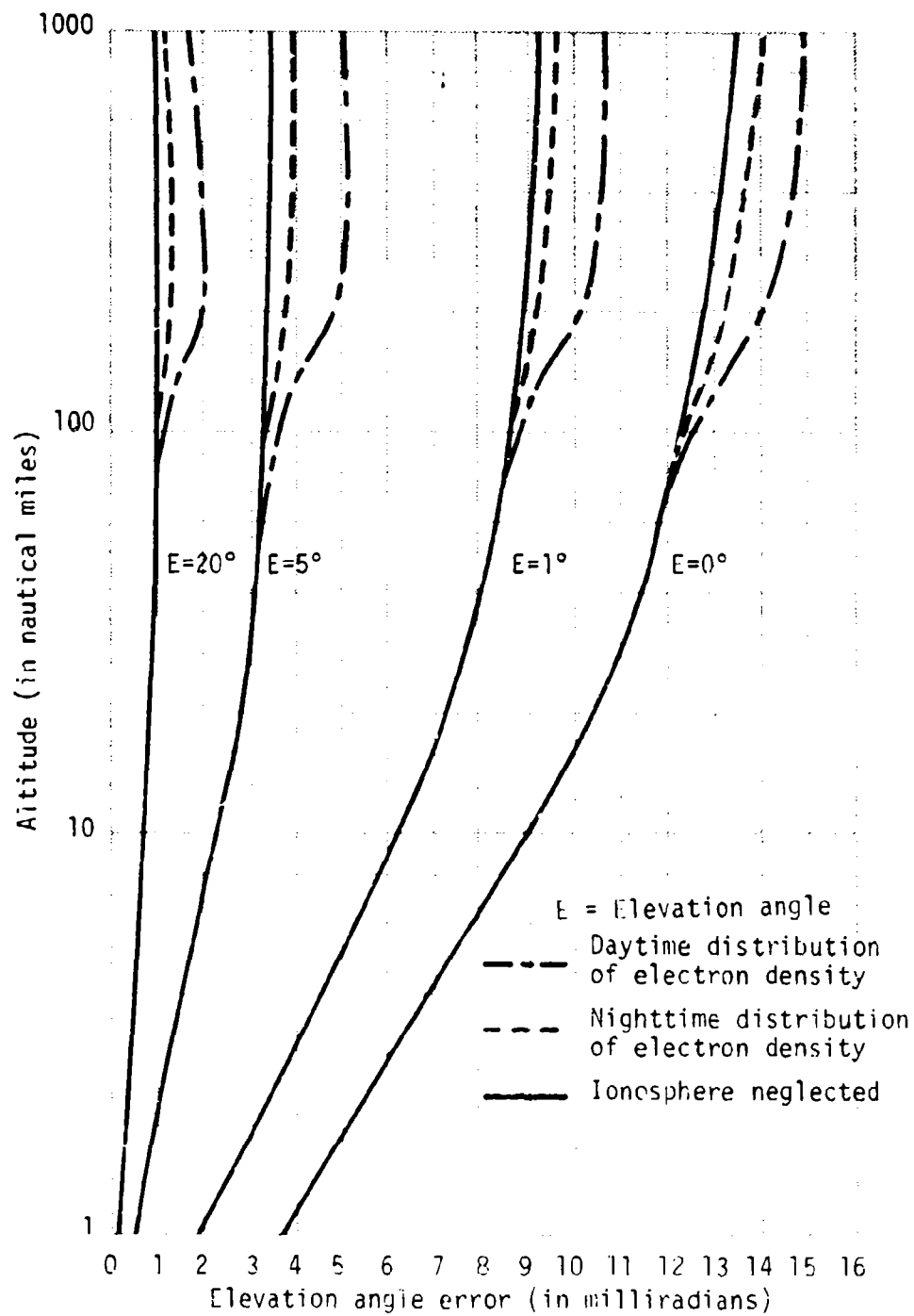


Figure 1-16. Total atmospheric refraction errors at 200 MHz for a standard atmosphere with 100% relative humidity.

concern in some applications where high accuracy is required. (Curves of range and velocity errors, and their dependence on frequency will be found in Chapter I, Part V of Ref. 1-17.)

Radar clutter, which consists of undesired radar returns which interfere with the desired target return, can arise from a wide variety of sources including precipitation, ground reflections, sea reflections, radar chaff, aurora, and even birds or large insects. In a nuclear environment clutter can also arise from dust clouds and weapon-induced ionization. Clutter can often be much more of a constraint in the choice of radar design parameters than either external noise or propagation effects. In some applications it is not unusual for the clutter to exceed the signal by 30-50 dB or more.

In situations where the main beam of the radar lies adjacent to or is pointed down toward the ground or sea, clutter can be very large because of the large area of the clutter which is illuminated. Ground and sea clutter is characterized by a quantity  $\sigma^0$  which is the cross section per unit area of clutter illuminated.  $\sigma^0$  is related to the terrain scattering coefficient  $\gamma$  by the formula

$$\sigma^0 = \gamma \sin \phi \quad (1-46)$$

where  $\phi$  is the grazing angle (the complement of the incidence angle) on the surface. Clutter behavior is usually characterized by plots of  $\sigma^0$  or  $\gamma$  vs.  $\phi$  for various terrains or sea states. An example of the variations of  $\sigma^0$  with grazing angle for various terrain types is shown in Fig. 1-17. Though  $\sigma^0$  has strong dependence on terrain type, its dependence on frequency is weak. The return with horizontal polarization is somewhat lower at low grazing angles.

Fig. 1-18 provides curves of radar reflectivity, in  $m^2/m^2$ , versus frequency for various rates and types of precipitation. Because reflection from rain and snow is in the Rayleigh scattering regime, precipitation echoes increase as the fourth power of frequency.



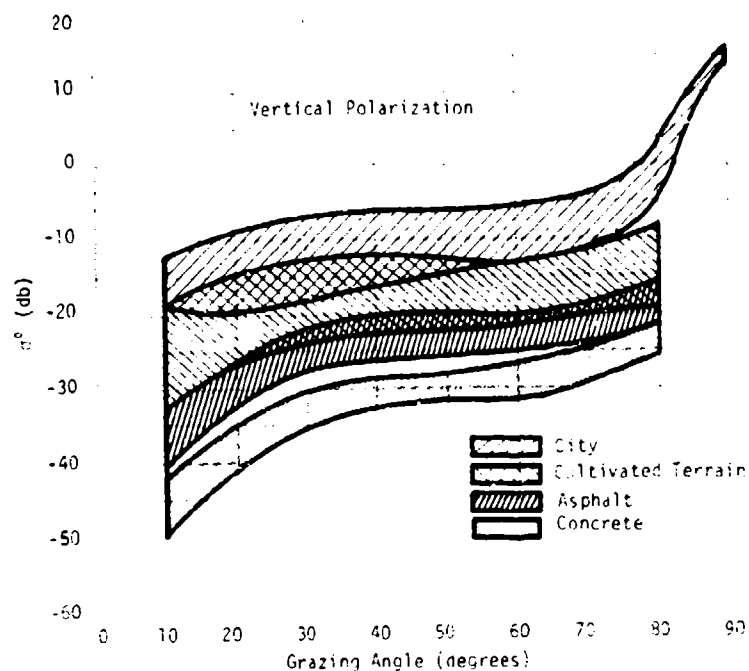


Figure 1-17. Ground clutter return vs. grazing angle.

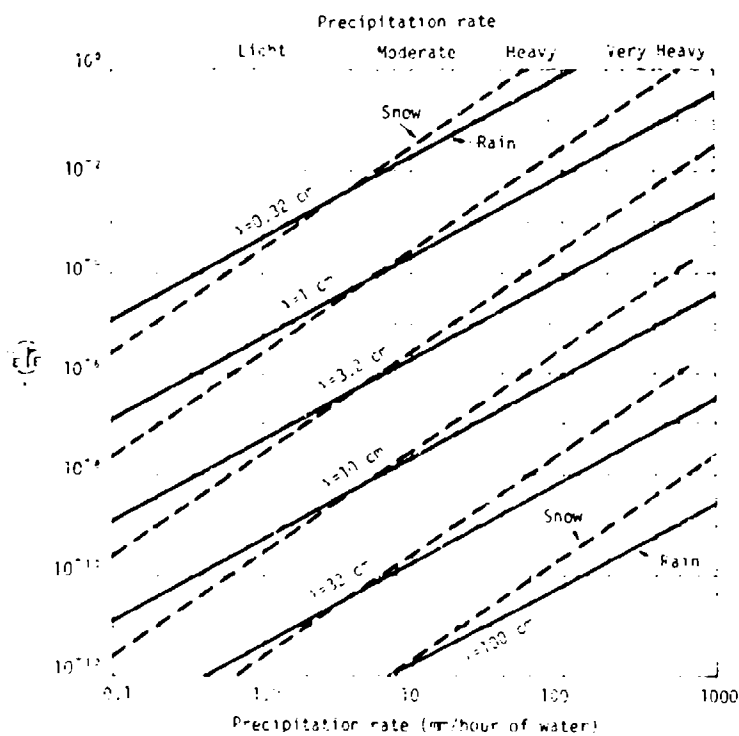


Figure 1-18. Radar reflectivity vs. precipitation rate.

In situations where the clutter return is large and the target cross section is low, a high order of clutter reduction will be necessary to detect the target. The ability of a radar to see targets in clutter is sometimes referred to as *subclutter visibility* (SCV).<sup>\*</sup> The two principal techniques for removing clutter are based on its spatial and velocity behavior. The only clutter which competes with a target is that which is located in the same resolution cell as the target (to the extent, at least, that sidelobes of the resolution cell can be ignored). Since most clutter tends to be distributed over wide areas, signal-to-noise ratio can be increased by increasing radar resolution in angle, range, etc. The second technique makes use of the velocity difference between targets and clutter. For example, the inherent doppler spread from ground clutter may be very small compared to the doppler shift produced by a closing aircraft. This type of clutter rejection is termed MTI (Moving Target Indication). The clutter problem is particularly severe for an airborne radar which must look down into the clutter. When MTI is performed from an aircraft, it is termed AMTI (Airborne MTI). The advent of highly stable microwave components and advanced analog/digital signal processing now permits clutter rejection well in excess of 40 db to be achieved.

#### 1.8 SOME COMMONLY USED RADAR ACRONYMS

AEW	airborne early warning
AMTI	airborne moving target indication
AM	amplitude modulation
AGC	automatic gain control
CRT	cathode ray tube
COHO	coherent oscillator
CFAR	constant false alarm rate
CW	continuous wave

---

\* Definitions of this quantity in the literature are not consistent. Skolnik defines SCV as the gain in signal-to-clutter ratio resulting from the use of MTI (Ref. 1-2).

DPCA	displaced phase center antenna
ERP	effective radiated power
ECM	electronic countermeasures
FFT	fast Fourier transform
FM	frequency modulation
GCA	ground-control approach
IF	intermediate frequency
LO	local oscillator
MTI	moving target indication
PPI	plan position indicator
PRF	pulse repetition frequency
RAM	radar absorbing materials
RCS	radar cross section
RADAR	radio detection and ranging
RF	radio frequency
RFI	radio frequency interference
STC	sensitivity time control
SOI	space object identification
STALO	stable oscillator
SCV	subclutter visibility
TWS	track-while-scan

## REFERENCES

- 1-1. Ridenour, L. N. (ed.), Radar System Engineering, MIT Radiation Laboratory Series, McGraw-Hill, 1947.
- 1-2. Skolnik, M. I., Introduction to Radar Systems, McGraw-Hill, 1962.
- 1-3. Barton, D. K., Radar System Analysis, Prentice-Hall, 1964.
- 1-4. Peterson, W. W., T. G. Birdsall, W. C. Fox, The Theory of Signal Detectability, Trans. IRE PGIT-4, 171-212, Sept. 1954.
- 1-5. Silver, S. (ed.), Microwave Antenna Theory and Design, MIT Radiation Laboratory Series, Vol. 12, McGraw-Hill, 1949.
- 1-6. Barton, D. K. and H. R. Ward, Handbook of Radar Measurements, Prentice-Hall, 1969.
- 1-7. Crispin, J. W. Jr., K. M. Siegel (ed.), Methods of Radar Cross Section Analysis, Academic Press, 1968.
- 1-8. Turpin, R. H., Average Backscattering Radar Cross Section of Wires For Arbitrary Transmitter and Receiver Polarizations, Ohio State Electro Science Laboratory, TR 2409-9, May 1969.
- 1-9. Swerling, P., Probability of Detection of Fluctuating Targets, IRE Trans., Vol. IT-6, pp. 269-308, April 1960.
- 1-10. Zell, R. E., On the Derivation of Bistatic RCS from Monostatic Measurements, Proc. IEEE, Vol. 53, No. 8, August 1965.
- 1-11. Woodward, P. M., Probability and Information Theory with Applications to Radar, McGraw-Hill, 1953.
- 1-12. Helstrom, C. W., Statistical Theory of Signal Detection, Pergamon Press, 1968.
- 1-13. DiFranco, D. V., and W. L. Rubin, Radar Detection, Prentice-Hall, 1963.

#### REFERENCES (Continued)

- 1-14. Rihaczek, A. W., Principles of High Resolution Radar, McGraw-Hill, 1969.
- 1-15. Cook, C. E., M. Bernfeld, Radar Signals--An Introduction to Theory and Application, Academic Press, 1967.
- 1-16. Deley, G. W., The Representation, Estimation and Design of Radar Signals, General Research Corp., TM-69 AD 822609L May, 1967.
- 1-17. Berkowitz, R. S. (ed.), Modern Radar, J. Wiley & Sons, 1965.

#### OTHER REFERENCES

- Berkowitz, R. S. (ed.), Modern Radar, J. Wiley & Sons, 1965.
- Nathanson, F. E., Radar Design Principles, McGraw-Hill, 1969.
- Skolnik, M. I. (ed.), Radar Handbook, McGraw-Hill, 1970.
- Reference Data for Radio Engineers, Chapter 29, Radar Fundamentals, Howard W. Sams Co., March 1970.

## FIGURE CREDITS

- Fig. 1-4      Taken from Fig. 1.4 (a) of Ref. 1-3.
- Fig. 1-6      Taken from p. 41 of Ref. 1-2. (A figure like this appears in many references.)
- Fig. 1-7      Taken from p. 593 of Ref. 1-2.
- Fig. 1-13     Taken from p. 470 of Ref. 1-3.
- Fig. 1-14     Taken from p. 472 of Ref. 1-3.
- Fig. 1-15     Taken from p. 367 of Ref. 1-2.
- Fig. 1-16     Taken from p. 336 of Ref. 1-17.
- Fig. 1-17.    Taken from Chapter 25, p. 26 of Radar Handbook,  
H.I. Skolnik, editor.
- Fig. 1-18.    Taken from p. 106 of Ref. 3.

## CHAPTER 2

### INFRARED OPTICAL SYSTEMS

Roy W. Hendrick Jr

May 1975

Mission Research Corporation

## TABLE OF CONTENTS

	PAGE
LIST OF FIGURES	65
LIST OF TABLES	66
2.1 INTRODUCTION	67
2.2 INFRARED SYSTEM ELEMENTS	67
2.2.1 GENERAL	67
2.2.2 COLLECTOR	69
2.2.3 DETECTORS	73
2.2.4 FILTERS	80
2.2.5 BARREL AND BAFFLES	81
2.2.6 ENCLOSURE	82
2.2.7 SCANNING SYSTEMS	83
2.2.8 AMPLIFIERS	86
2.2.9 SIGNAL PROCESSING	86
2.2.10 RADIATION EFFECTS	90
2.2.11. SIGNAL-TO-NOISE SUMMARY	91
2.3 TARGETS	92
2.3.1 GENERAL	92
2.3.2 THERMAL EMISSIVE TARGETS	92
2.3.2.1 Greybody Radiation	93
2.3.2.2 Emissance and Reflectance	96
2.3.2.3 Emissivity-Area Product	97
2.3.3 GASEOUS RADIATION	97
2.3.4 REFLECTED ILLUMINATION	100
2.3.4.1 Illumination Sources	100
2.3.4.2 Effective Cross Sections	103



## TABLE OF CONTENTS (continued)

	<u>PAGE</u>
2.4 OPTICAL SYSTEM CONSIDERATION	106
2.4.1 ACQUISITION SYSTEMS	106
2.4.2 TRACKING SYSTEMS	109
2.4.3 MEASUREMENT PRECISION	110
2.5. NATURAL INFRARED BACKGROUND	111
2.5.1 GROUND LEVEL SKY BRIGHTNESS	111
2.5.2 AIRGLOW FOR AIRBORNE SENSORS	112
2.5.3 EARTH LIMB	117
2.5.4 AURORAL DISTURBANCES	122
2.5.5 CELESTIAL BACKGROUND	122
2.6. DETECTOR DATA	125
REFERENCES	128
FIGURE CREDITS	129

## LIST OF FIGURES

FIGURE		PAGE
2-1	Characteristic optical systems.	68
2-2	Optical pulse shapes and processed output	88
2-3	Signal-to-noise ratio for processed signals.	89
2-4	Universal blackbody emission function.	94
2-5	Spectral irradiance vs range.	95
2-6	Temperature variation of radiance.	95
2-7	Compiled spectral reflectivities.	97
2-8a	Shapes of idealized targets.	98
2-8b	Projected area as a function of aspect angle.	98
2-9	Sensor irradiance for various target illuminations	101
2-10	The Johnson solar spectral curve	102
2-11	A typical spectral emissive power curve for the thermal radiation leaving the earth.	102
2-12	Geometric factor for planetary thermal radiation incident on sphere versus altitude.	104
2-13	Monostatic cross section of capped cone.	105
2-14	Spectral radiance of the clear daytime sky.	112
2-15	Spectral radiance of a clear zenith sky as a function of sun position.	113
2-16	The spectral radiance of a clear nighttime sky for several angles of elevation above the horizon.	113
2-17	Spectral radiance of overcast skies in winter and summer.	114
2-18	Spectral radiance near 40,000 ft. at 45° elevation.	115
2-19	Filter radiometer transmittance curves.	116
2-20	Typical measured natural background radiances.	116
2-21	Time variation of radiance.	117
2-22	DC background levels.	118

# LIST OF FIGURES (continued)

FIGURE		PAGE
2-23	Limb viewing spectral radiance.	119
2-24	15- $\mu\text{m}$ $\text{CO}_2$ emission data.	121
2-25	9.6- $\mu\text{m}$ $\text{O}_3$ emission data.	121
2-26	All-sky map of sources observed in the 4.2- $\mu\text{m}$ spectral region.	123
2-27	All-sky map of sources observed in the 11- $\mu\text{m}$ spectral region.	123
2-28	All-sky map of sources observed in 19.8- $\mu\text{m}$ spectral region.	124
2-29	Mean source density versus spectral irradiance.	124
2-30	Color temperature distributions.	125
2-31	Spectral detectivities of infrared detectors.	127

# LIST OF TABLES

TABLE		PAGE
2-1	Wavelengths of some common exhaust emission bands longer than 2 microns.	100
2-2	Comparison of computed and measured radiances.	120

## CHAPTER 2

### INFRARED OPTICAL SYSTEMS

#### 2.1. INTRODUCTION

The intent of this chapter is to provide information that will allow the conceptualization and analysis of the capability of infrared optical systems. To provide sufficient information for the detailed design of optical systems is well beyond the scope of this article, and for that purpose, reference should be made to publications such as References 2-1 and 2-2. In view of the intent, emphasis will tend toward definition of parameters in terms of system characteristics.

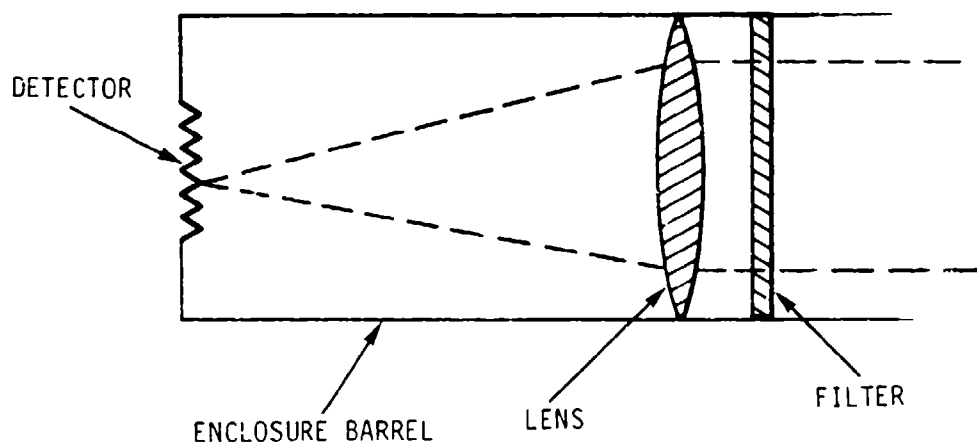
Wavelengths from about 1 to 25 microns ( $\mu$ ) will be of primary concern. The primary type of system will be passive, although the means for extending analysis to laser systems will be covered. The general elements of an optical sensor will be discussed, then optical target characteristics, and finally some typical component characteristics.

#### 2.2. INFRARED SYSTEM ELEMENTS

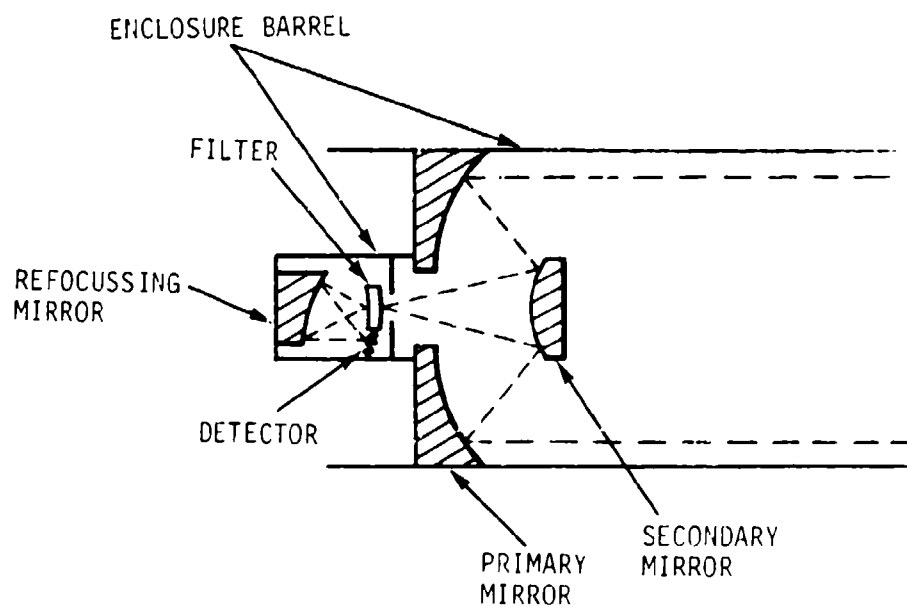
##### 2.2.1. GENERAL

An infrared sensor system utilizes infrared radiation to detect, locate, track or obtain signal characteristics information. The source of the radiation can be self emission such as the radiation from a jet engine or rocket plume, or thermal radiation from a warm object; it can be reflected natural radiation such as sunshine or earthshine; or it can be reflected system generated light such as a laser beam.

An optical sensor comprises four basic elements as schematically shown in Figure 2-1: a system of mirrors or lenses for collecting radiation; one or



REFRACTIVE OPTICS



REFLECTIVE OPTICS

Figure 2-1. Characteristic optical systems.

more detector elements for constraining the field of view and converting the light to an electrical signal; various enclosures, tubes and baffles for rejecting unwanted radiation; and some means for restricting the band of wavelengths which result in output signals. In addition, there are auxiliary elements such as a means for converting the output to an easily amplified ac signal (physically scanning the field of view across the target or chopping the light beam are typical techniques), amplifiers and signal processors, cooling for the detectors and optical elements, a gimbal and control system for pointing the equipment, and possibly shielding if it is to be used in a radiation (nuclear) environment.

### 2.2.2. COLLECTOR

The infrared radiation collection function may be performed by lenses, mirrors or combinations of both. Correction plates may be used to compensate for various aberrations. For collectors larger than about 6 inches diameter and for infrared of wavelengths longer than a few microns, mirrors are used almost exclusively.

The primary descriptors of the collector are the entrance aperture or pupil area  $A_p$ , the effective focal length of the system  $f$  and the optical efficiency  $\epsilon_o$ . The aperture is normally specified by its area in square centimeters or its diameter  $d$  (in centimeters). So long as the target being viewed is small compared to the resolution of the system, the spectral power  $P'_\lambda$  collected is the product of the incident spectral radiant power or irradiance  $H_\lambda$  (watts  $\text{cm}^{-2}\mu^{-1}$ ) and the aperture area.

$$P'_\lambda = A_p H_\lambda. \quad (2-1)$$

Often the optical collecting power of a system is expressed in terms of an f-stop number  $f/\#$  which is the ratio of the focal length to aperture diameter. This is useful when dealing with sources more extensive than

the resolution of the sensor. Such a source produces a flux at the sensor aperture expressed as an irradiance per solid angle (watts steradian<sup>-1</sup>cm<sup>-2</sup>L<sup>-1</sup>, which for writing simplicity is often referred to as a flick or fl). The convenience of this representation is that, in the absence of attenuation, the irradiance per solid angle due to the extended source is invariant along a ray and is equal to the source spectral radiance  $N_\lambda$ . This constancy of radiance (irradiance per solid angle) is maintained throughout the focusing process—the irradiance per solid angle at the detector equals the source radiance.

The detector element is illuminated over a solid angle of convergence determined by the solid angle the pupil subtends as viewed from the detector. If the angle is small enough that the cone angle can be approximated by its tangent, the solid angle of illumination is

$$\Omega_p = A_p / f^2 = \pi / (2 f/\#)^2, \quad (2-2)$$

and the irradiance at the detector is the product  $N_\lambda \Omega_p$ . Consequently, for an extended source, the spectral power collected by a detector element of area  $A_d$  is

$$P'_\lambda = N_\lambda A_p A_d / f^2. \quad (2-3)$$

All of the energy that enters the pupil does not reach the detector. There are losses due to mirrors with less than unity reflectance, lenses or filters having absorption or partial reflection, and obstructions in the optical path. Obstructions can be secondary mirrors and their supports (so called spiders) or baffles designed to improve the rejection of spurious off-axis signals. The various losses can be combined into a single effective optical transmission efficiency  $\epsilon_o$ . To get the true magnitude of optical power incident on the detector, the spectral powers of Equations (2-1) and (2-3) must be reduced by this efficiency. Sometimes the efficiency is combined

with the  $f$  stop number to give an effective  $f$  number, which is an overall measure of its light collecting capability

$$(f/\#)_e = (f/\#)/\sqrt{\epsilon_0} . \quad (2-4)$$

In summary, the spectral power incident on the detector is:

Point Source

$$P_\lambda = \epsilon_0 A_p H_\lambda ; \quad (2-5a)$$

Extended Source

$$P_\lambda = \epsilon_0 N_\lambda A_p A_d / f^2 \quad (2-5b)$$

$$= \pi N_\lambda A_d / [2 (f/\#)_e]^2 . \quad (2-5c)$$

Another property of the light collection system of potential significance is self emission from optical elements that are not 100% efficient. A primary concern for reflective optics systems is thermal emission from the primary and secondary mirrors which necessarily fill the whole optical beam and, hence, illuminate the detector over an angle  $\Omega_p$ . If the radiance of a blackbody, the Planck function (see Section 2.3.2.1), is represented by  $p(T, \lambda)$  and the emissance (the ratio of actual-to-blackbody radiance) is expressed in terms of the mirror reflectance as  $1-r_\lambda$ , the mirror spectral radiance is  $p(T, \lambda) (1-r_\lambda)$  where  $T$  is the temperature of the mirror. The spectral power on a detector element is

$$P_\lambda = \epsilon_0 p(T, \lambda) (1-r_\lambda) A_p A_d / f^2 , \quad (2-6)$$

where each reflective element in the field of view makes a contribution of similar form and  $\epsilon_0$  is the optical efficiency between the radiating element and the detector. In general, elements are cooled sufficiently that their contribution does not significantly degrade system operation.



Transmissive optical elements radiate because they have some emissance. For those elements, Equation (2-6) is simply modified by the replacement of  $(1-\rho_\lambda)$  by the emissance  $\epsilon_\lambda$ .

The collector may also control system resolution. For a transparent circular aperture, diffraction results in the image of a point source being a central disc surrounded by rings, the so called Airy disc. For the target signal to correspond to the power given by Equation (2-5), the major fraction of the energy in the Airy disc must fall on a single detector element. Furthermore, if two targets are to be resolved, their Airy discs must not overlap too much. The classical Rayleigh resolution criterion is that the central point of one Airy disc must be displaced at least as far as the first null in another. All this discussion assumes that optical system aberrations are negligible. The study and elimination of aberrations is an optical element design problem and those who are interested in design should refer to books such as References 2-1 and 2-2.

For a circular aperture, the first diffraction null ring is displaced an angle

$$\theta_0 = 1.22 \lambda/d. \quad (2-7)$$

Thus, a 10 cm diameter aperture system operating at 10 $\mu$  could resolve .122 mrad. Furthermore, 84% of the energy is contained in a circle with a radius corresponding to the angle  $\theta_0$ , which is a physical radius  $\theta_0 f$ . Six percent is diffracted more than 3 times  $\theta_0$ .

If closely spaced objects of greatly different brightness must be resolved, even the small amount of energy diffracted to large angles may be intolerable. However, it can be further suppressed at the expense of broadening the central disc. The situation is identical to side lobe suppression in

radars. Partial absorption of energy around the outer edge of the aperture so the "edge" is not sharp can provide the necessary tapered feed.

### 2.2.3. DETECTORS

A detector is simply a transducer for converting an optical signal into an electrical one. Over the total optical band many different type devices are used; however, at wavelengths greater than a micron, primary concern is with semiconductor diodes which are either photovoltaic or photoconductive. From an overall system standpoint, all detectors can be described in similar terms. Consequently, although the discussion here will be limited to semiconductor detectors, equivalent performance descriptors can be obtained for other detectors, and the system evaluation criteria to be developed used for those other detectors as well.

Some of the parameters characterizing a detector are important for defining overall systems operating capability; some are important primarily for design details (such as impedance match with following amplifier circuits).

Primary system important parameters are the effective area  $A_d(\text{cm}^2)^*$  and  $D^*$  (a measure of detectivity discussed below). Many optical systems utilize a matrix of small detector elements or a linear array of elements in the focal plan to subdivide the total field of view into resolvable elements. For such systems, the detector element area defines the instantaneous single detector field of view  $\omega_d$

$$\omega_d = A_d/f^2. \quad (2-8)$$

---

\* In some of the following discussions the linear dimensions are required separately. The detector width in the direction of a scan will be called  $a$  and its length perpendicular to this will be called  $b$ . The corresponding angular dimensions in terms of field of view are the ratio of the physical dimension to the focal length. Call these  $\alpha$  and  $\beta$ .

It is this solid angle that must be comparable to or larger than the region of the Airy disc containing most of the optical power in order that the analysis being developed here is applicable without inclusion of a degradation factor due to loss of optical power.

Detectors are not noise free. Even in the limit of theoretically perfect detectors, the number of photons and conduction pairs are subject to statistical fluctuations and hence, produce noise. Measures of the noise are expressed in terms of the incident optical signal power necessary to produce a detector output equal to the rms noise. The referenced optical power can be monochromatic, in which case the descriptive parameters are called spectral and subscripted  $\lambda$ , or can be black body, in which case the parameters are called black body and subscripted BB. To have meaning, the reference wavelength or black body temperature must be specified. For detailed system evaluation, the descriptive parameters should be averaged over the optical band pass.

In the following development of useful relationships, the descriptive parameters will not be subscripted, and, depending upon whether a system is to be used in a monochromatic, blackbody or fixed band, the parameter should be interpreted as spectral, blackbody or effective.

The noise-equivalent-power NEP (watt) is the incident optical power necessary to produce a signal equal to the rms noise. Unfortunately, the NEP depends upon the optical chopping frequency (if the signal is chopped to produce an ac output), upon the electrical bandwidth and upon the detector area. Because workers in the field like large numbers to indicate a valuable device, the detectivity  $D$  is often used instead of the noise-equivalent-power.

$$D = 1/\text{NEP (watt}^{-1}\text{)}.$$

(2-9)

Because the detectivity still depends upon the auxiliary parameters of electrical bandwidth  $\Delta f$  and detector area, a normalized detectivity parameter  $D^*$  is usually used. The hope is that this is primarily a property of the detector material because, for a flat noise spectrum, the equivalent optical noise power varies as  $\sqrt{\Delta f}$  and, if the noise is generated by the statistical variation of events in the detector element, it is also proportional to  $\sqrt{A_d}$ .

Thus

$$D^* = \sqrt{A_d \Delta f} D \text{ (cm sec}^{-1/2} \text{ watt}^{-1}\text{)}, \quad (2-10)$$

and

$$\text{NEP} = \sqrt{A_d \Delta f} / D^*. \quad (2-11)$$

It can be seen that the minimum detectable optical signal, which is a few times the noise power, becomes smaller as the detector and bandwidth become smaller, if  $D^*$  is an intrinsic property of the detector material.

A parameter primarily of theoretical interest is the responsivity quantum efficiency RQE which is the ratio of the number of countable output events to the number of incident photons. This depends upon losses due to reflections at the detector surface, incomplete absorption of the radiation in the detector and absorption events which do not result in modifications of the electrical properties of the detector. The RQE is used in deriving theoretical limits on the detector noise descriptors.

For the detectors considered here, the important noise sources are Johnson noise, modulation (or  $1/f$ ), generation-recombination (G-R), or shot. Johnson noise is due to the random motion of charge carriers in resistive

---

\* The electrical noise amplitude varies as  $\sqrt{\Delta f}$ , but the detectors being discussed have an output amplitude that varies linearly with optical power. Hence, the optical noise power varies with  $\sqrt{\Delta f}$ .

elements. If the parallel impedance of the detector and the following amplifier is  $Z$  and the detector and amplifier input are at a common temperature  $T_d$ , the noise voltage at the detector output is

$$V_0 = (4kT_d Z \Delta f)^{1/2} . \quad (2-12)$$

The detector responsivity,  $R'$ , which depends upon detection efficiency and carrier lifetime, is defined as the ratio of the output voltage (for photovoltaic detectors) or output current (for photoconductive detectors) to the incident optical power referred to an infinite or zero load, respectively.

$$R' = \frac{V_{out}}{P_{in}} \text{ or } \frac{I_{out}}{P_{in}} . \quad (2-13)$$

For optimum operation of a detector in a photovoltaic mode, the detector load resistance should be large compared to the detector internal resistance. Thus, the impedance  $Z$  is the detector impedance  $Z_d$  and the Johnson noise limited  $D^*$  is

$$D_J^* = R' \sqrt{A_d / 4kT_d Z_d} . \quad (2-14)$$

If, as is usually the case, the photovoltaic responsivity is inversely proportional to the detector area (that is, the ratio between irradiance and output voltage is independent of detector area),  $D_J^*$  for a photovoltaic detector is nearly independent of detector area as was desired in defining  $D^*$ .

In contrast, detectors operated at extremely low temperatures to achieve large detectivity tend to have very large internal impedances and operate in the photoconductive mode. In this case,  $Z$  is approximately the load impedance  $Z_l$ , and

$$D_J^* = R' \sqrt{\frac{A_d Z_l}{4kT_d}} . \quad (2-15)$$

For photoconductive operation,  $R'$  is independent of detector area, and  $D^*$  becomes proportional to the square root of detector area. Thus, for this mode, detector elements cannot be made ever smaller without degrading  $D^*$ .

Generation-recombination noise is statistical fluctuations in the generation and recombination of carriers in semiconductors. Part of the current is due to thermal excitation of carriers into conductor bands. This is a property of the material and is strongly temperature dependent. If it is suppressed by cooling, the remaining G-R noise is due to current produced by background photons. In that case, the noise is usually referred to as background or photon noise and the resulting  $D^*$  as  $D_{\text{blip}}^*$ .

If the irradiance  $H_b$  due to the background in the optical bandpass (Section 2.2.4) is due to photons of mean energy  $h\nu$ , the variance in the number of detected events is

$$\sigma^2 = \frac{H_b A_d (\text{RQE})}{2\Delta f h\nu} \quad (2-16)$$

and the noise level (in terms of countable events) is the square root of this. In these same terms, the output due to a signal input  $P$  is

$$S = P (\text{RQE}) / 2 \Delta f h\nu \quad (2-17)$$

It follows from the definition of NEP that

$$\frac{(\text{NEP}) (\text{RQE})}{2\Delta f h\nu} = \sqrt{\frac{H_b A_d (\text{RQE})}{2\Delta f h\nu}} \quad (2-18)$$

This expression combined with Equation (16-11) produces

$$D_{\text{blip}}^* = \sqrt{\frac{\text{RQE}}{2 h\nu H_b}} \quad (2-19)$$

If the detector enclosure is sufficiently cold that the significant background is that entering the collector aperture and the detector observes a background of radiance  $N_b$ , the irradiance is

$$H_b = N_b \Omega_p \epsilon_0 \quad (2-20)$$

and

$$D_{\text{blip}}^* = \sqrt{\frac{(RQE)}{2 h \nu \epsilon_0 N_b \Omega_p}} \quad (2-21)$$

$$= \sqrt{\frac{2 (RQE) (f/\#)_e^2}{\pi h \nu N_b}} \quad (2-22)$$

It can be seen that the larger  $(f/\#)_e$ , the greater  $D_{\text{blip}}^*$  for a given background. It is also interesting to note that the only significant property of the detector is the relative quantum efficiency.

The value of  $D_{\text{blip}}^*$  given by Equation (2-22) is strictly applicable to photovoltaic detectors. Photoconductive detectors are sensitive to the population of carriers in the conduction band. This fluctuates due to variations in recombination as well as in generation of carriers. Consequently, the variance in Equation (2-16) is doubled and  $D_{\text{blip}}^*$  is less than given in Equation (2-22) by the factor  $1/\sqrt{2}$ .

Photovoltaic detectors are also subject to shot noise due to the discreteness of the electronic charge in the current flowing through the detector. The noise at the output of the detector is statistical fluctuations in the number of electrons flowing in a resolved time element.

$$V_{\text{shot}} = \sqrt{2q I_{\text{DC}} \Delta f} \quad (2-23)$$

where  $q$  is the electronic charge and  $I_{\text{DC}}$  is the direct current.

Modulation, or 1/f noise is poorly understood. It is observed in some detectors as an output voltage of magnitude

$$V = \bar{R} I_{DC} C \left( \frac{\Delta f}{\lambda_d d} \right)^{1/2} \left( \frac{1}{F} \right)^n \quad (2-24)$$

where  $d$  is the detector thickness,  $C$  is an empirical constant and  $n$  is an empirical exponent which typically lies between 0.8 and 2.

Another detector parameter, which may affect system operation parameters, is the detector time constant. Several definitions used lead to slightly different values. One  $\tau_p$  is the time constant to respond to a step function change in irradiance—specifically, the time to achieve 63% of the steadystate value. The importance of the time constant is that if the time a detector looks at a target is less than  $\tau_p$ , sensitivity is sacrificed and resolution of dim targets near bright ones is compromised.

The time constant can depend upon detector temperature and background radiance. Consequently, it must be known for the design operating parameters. Sensitive detectors operating at very low temperatures have high resistivity and small total current. Consequently, the apparent time constant may be dominated by the electronic circuits (specifically the distributed capacitance) attached to the detector output, and specification of the measurement system is necessary to correctly interpret a measured  $\tau_p$ .

Other parameters important to hardware designers are the detector impedance  $Z$ , supply voltages or currents, spacings of elements in arrays and cross talk, variations in responsivity between elements and at different points on a single element, and operating temperature. Current manufacturing techniques can produce elements smaller than  $10^{-2}$  cm in linear dimension and spacing. On the other extreme, some can be constructed with areas of several square centimeters. Typically, the responsivity of different places



on a single element will vary by at least 30% to 50% and in some cases by factors of 10. Consequently, for precision measurements, it is desirable to have the image of a target cover much of a detector element, to average responsivity variations.

The  $D^*$  of a detector cannot be less than the  $D_{\text{blip}}^*$  corresponding to the radiance of a black body at the temperature of the detector. Therefore, for high sensitivity applications, detectors will be cooled. Depending upon the application, the necessary cooling may be slight, or cryogenic cooling to liquid helium temperature may be necessary. For convenience, many detectors are fabricated directly on heat sinks designed for use with cryogenic systems. In this case, the preamplifiers may also be integral with the detectors so that the Johnson noise temperature is the cryostat temperature.

#### 2.2.4. FILTERS

Optical filters help define the mean operating wavelength  $\lambda$  (microns or  $\mu$ ) and optical bandwidth  $\Delta\lambda$  ( $\mu$ ). Normally, semiconductor detectors require a minimum photon energy to raise a carrier to a conduction band, but any one photon can raise only one carrier. This results in a responsivity that falls rapidly for wavelengths larger than some cutoff wavelength, and maximum  $D^*$  occurs for wavelengths just slightly shorter than the cutoff. Consequently, a filter may be used to limit the short wavelength cutoff of the optical band pass and the detector characteristic used to determine the long wavelength cutoff. In other applications, the filter may determine both limits.

The optical power incident on the detector is just that portion of the spectral power within the band pass,  $P = P_\lambda \Delta\lambda$ . Filters are typically interference filters deposited on substrates of glassy-like substances or pure germanium or silicon. With interference filters, the band center

and bandpass can be arbitrarily chosen. Furthermore, unwanted signals are reflected out of the system or to regions where they can be absorbed without unduly loading the detector cooling system.

Most filter substrates useful for wavelengths longer than a few microns are not perfectly transmissive but are also slightly absorptive. It follows that they are also slightly emissive and, because they fill the detector field-of-view, must be cooled to avoid contributing to the "background" radiation. They may have to be in the detector cryostat. This situation accentuates the necessity for rejecting unwanted radiation by reflection rather than by absorption, which would increase the cryogenic load. In infrared optical system evaluation, the contribution of filters to the background must be considered.

#### 2.2.5. BARREL AND BAFFLES

The optical elements of a sensor are normally supported in a barrel or tube which is the main structural element. In addition to its structural role, the barrel and adjuncts provide rejection of off-axis radiation. For instance, the barrel may shield the primary mirror from direct illumination by the sun for scattering of such a bright source by slight surface imperfections could seriously degrade system sensitivity. A potential application requiring very good off-field rejection is observation of space traffic from a satellite platform such that the earth is near the line-of-sight of the optical system. The required attenuation of earth radiation may be many orders of magnitude just a few degrees outside the system field-of-view.

Baffling typically includes coating the barrel interior with very absorptive material to suppress reflections and scattering, lining the tube with sharp edged rings so that light scattered anywhere but at the ring edge can not impinge on the primary mirror, aperture stops to prevent radiation

diffracted by baffle edges or mirror supports from reaching the detectors, etc. A good treatment of this problem is given in Reference 2-3.

A problem associated with baffling is scattering from the main optical elements. If the bistatic reflectance of mirrors has a significant value at angles other than specular (angle of incidence equal to angle of reflection), radiation from outside the field of view can be scattered into the field-of-view with no chance of further rejection.

Another precaution used in sensitive systems to minimize the effect of scattering from the mirrors is cooling the tube and baffle system to reduce off-axis radiation from the local environment.

#### 2.2.6 ENCLOSURE

The enclosure is the material that immediately surrounds the detector elements. Ideally, it fills all the solid angle around the detector except the converging cone of radiation from the optical elements. Consequently, it subtends nearly  $4\pi$  steradians. To avoid enclosure radiation limiting the sensitivity by background photon noise, the enclosure may need cooling. If the detectors are sensitive only at a few microns, a 300°K enclosure will radiate little in their acceptance band and cooling will probably be unnecessary. On the other hand, if the detectors are sensitive at 10 $\mu$ , they respond to the peak of a 300°K black body spectrum; consequently, considerable enclosure cooling is necessary to assure maximum sensitivity. The enclosure temperature will be called  $T_e$ . A radiance can be obtained for  $T_e$  by data given in the target section (2.5.2.1, Figure 2-4 and used in Equation (2-21) to obtain a  $D_{enc}^+$  by replacing  $\Omega_p$  by  $4\pi - \Omega_p$ .

Even if the enclosure emissivity is low, radiation in the cavity approaches that of a black body at the enclosure temperature because the entrance cone is a small fraction of a sphere. Radiation emitted by the enclosure is

reflected and traverses the cavity many times before it is either re-absorbed or escapes through the cavity entrance. A near equilibrium is established between wall emission and absorption. At equilibrium, the cavity radiation would be exactly the black body radiation at the enclosure wall temperature. Consequently, for the enclosure, little error is produced by using an emissivity of unity.

These factors combine to give an enclosure limited detectivity of

$$D_{\text{enc}}^* = \sqrt{\frac{\text{RQE}}{2 h \nu p(T_e, \lambda) \Delta \lambda (4\pi - \Omega_p)}} \quad (2-25)$$

where  $\Delta \lambda$  is the band over which the detectors are sensitive.

### 2.2.7 SCANNING SYSTEMS

Optical systems of the type discussed generally do not stare in a fixed direction but rather, scan a region. There are several reasons. The field-of-view to be monitored may exceed the instantaneous field-of-view of the detector or detectors, or the number of targets may exceed the number of detector elements. Location of a target against a background is eased if the scene is scanned. The target which appears as an increment superposed on the background can be identified by appropriate filtering and thresholding. Furthermore, locational precision can be finer than detector element size if the target is scanned and the signal-to-noise ratio is large. Finally, scanning converts the target signature from a steady signal to a pulsed signal that can be amplified by ac coupled electronics.

Scans can be generated by moving the image of the scene across the detector array. A circular scan can be generated by including in the optical path a rotating optical element—prism, lens or mirror. If the element is a lens, it is rotated about an axis that is inclined to the optical axis; if it is a mirror, it is rotated about an axis inclined to the mirror normal.

Raster scans can be generated by rotating the optical system on a gimbal system, including an oscillating mirror in the optical system or superposing two equal circular scans rotating in opposite directions.

Raster scans are used for search and acquisition or tracking several targets simultaneously. They may also be used with two detectors in a chevron for terminal tracking. Circular scans or rosettes composed of the superposition of circular scans of different angular extent are used for individual target tracking or homing systems.

The scan determines the time a target image remains on a detector, the dwell time  $\tau_d$ . This is normally defined as the time required for a perfectly focussed point to traverse the detector, or, alternatively, the time the detector output exceeds 50% of the peak value. The dwell time, in conjunction with the electronic amplifying and data processing parameters, contributes to determining the signal-to-noise ratio, target resolution, locational precision and precision in target irradiance estimation.

The maximum possible precision in the estimation of target produced irradiance is limited by statistical fluctuations in the number of detected photons. In the absence of noise sources (i.e., the signal-to-noise ratio is very large), the variance in the number of detected photons very nearly equals the number of detected photons. The standard deviation is

$$\sigma_s = \left( \frac{P \tau_d \text{REQ}}{h\nu} \right)^{1/2} \quad (2-26)$$

which, in terms of a fractional precision, is

$$\sigma_f = (h\nu/P \tau_d \text{REQ})^{1/2} \quad (2-27)$$

The dwell time is directly related to the scan rate  $\dot{\theta}$ .

$$\tau_d = \alpha/\dot{\alpha} = a/f \dot{\alpha}.$$

(2-28)

Alternate scanning techniques are "staring" fields of view and coded recticles. In a staring field, the number of detector elements equals the number of resolution cells, and the scan is produced by the way the data is read from these detectors. A typical example is a television type tube in which data is accumulated on a matrix and periodically read by electron beams. Other configurations for data accumulation and switched readout can be conceived. For such a system, the effective dwell time is the time over which signal photons are accumulated and integrated, and it can be as long as the period between readout times.

A coded reticle system moves a variable transmission reticle across the focal plane in front of one or more extended detectors. The transmission pattern on the reticle is such that the modulation of a signal depends upon its location in the focal plane. Processing the detected output identifies and locates the targets. Normally, processing involves the cross correlation of the received signal with the coding sequence for each point on the focal plane. One of the conceptually simplest arrangements is a rotating circular disc divided into annular rings, each of which contains a different sequence of transparent and opaque regions (corresponding to 1 and 0 in the coding sequence). Cross correlation with the coding sequence is obtained by propagating the detected signal down a delay line tapped at intervals equal to the time for one of the coding bits to pass a target and connecting the output from each tap to a series of summing matrices—one for each annulus. The inputs to a summing matrix are taken positive or negative according to the coding sequence for that annulus. A pulse at a matrix output indicates a target in the corresponding annulus, and its timing indicates the angular position within that annulus.

For a coded reticle scanning system, the dwell time is that for the complete code sequence to traverse a target location, the optical efficiency is

reduced by the fraction of the reticle that is transparent, the detector area is increased to the total area interconnected and the electrical bandwidth is matched to the time for a single element of the code to traverse a spot (rather than to the dwell time).

#### 2.2.8. AMPLIFIERS

The range of possibilities for amplifiers is limited only by the electronic designers ingenuity. Depending upon the impedance of the detector, the amplifier may be either a current or voltage amplifier. Often, for sensitive systems that require cold detectors, the first amplifier stage is integral with the detectors and, hence, is cold. Most optical systems are designed so that the amplifiers can be ac coupled; optical choppers are used with non-scanning systems.

Various parameters may be used to characterize amplifiers. One of the most generally used parameters is the bandwidth  $\Delta f$ . This determines the amount of system amplified noise as given by Equation (2-11). The upper and lower cutoff frequencies may be specified separately or, alternatively, a center frequency may be given. The latter is most common for chopped systems because it is matched to the chopping frequency.

The bandpass shape can affect signal-to-noise ratio some, so the concept of gross bandwidth is useful for crude estimation of system performance, but is inadequate for final, detailed effectiveness evaluation.

#### 2.2.9 SIGNAL PROCESSING

The amplifier is usually an integral part of the signal processor. In as much as optical systems satisfy various functions, the relationship between electrical bandpass, band shape and dwell time are not fixed. For instance, if the function is tracking, the bandpass may be chosen sufficiently wide to follow details of the optical pulse shape; whereas, if the function

is detection of faint objects, a narrower band may be chosen to optimize the signal-to-system noise ratio.

If the noise power is uniformly distributed in frequency, the maximum signal-to-noise ratio is obtained if the amplifier band pass is the same shape as the spectrum of the expected signal. Stated another way, for a flat noise spectrum, maximum signal-to-noise ratio is obtained by cross correlation of the detected signal with the expected noise-free signal envelope.

As examples, consider two alternative pulse shapes: a rectangular pulse (such as is produced if the Airy disk is small compared to a detector) and a single cycle of a cosine on a pedestal.

$$\text{Form 1 } f(t) = \dot{s} \quad 0 < t < \tau_d \quad (2-29)$$

$$\text{Form 2 } f(t) = .5\dot{s} (1 + \cos \pi t/\tau_d) \quad -\tau_d < t < \tau_d \quad (2-30)$$

Figure 2-2 shows these wave forms (free of noise) before and after processing by optimum cross correlators and simple exponentials (in time), which are 6 db/octave high-frequency rolloff filters. These filter outputs are:

Form 1 - cross correlator

$$F(t') = \int_{t'-\tau_d}^{t'} f(t) \tau_d^{-1} dt \quad (2-31)$$

Form 2 - cross correlator

$$F(t') = \frac{1}{2\tau_d} \int_{t'-2\tau_d}^{t'} f(t) [1 + \cos \pi(t'-t+\tau_d)/\tau_d] dt \quad (2-32)$$

Exponential

$$F(t') = \tau^{-1} \int_{-\infty}^{t'} f(t) \exp[-(t'-t)/\tau] dt$$

The noise bandwidth  $\Delta f$  of these three filters are  $1/2\tau_d$ ,  $3/8\tau_d$  and  $1/4\tau$  respectively.



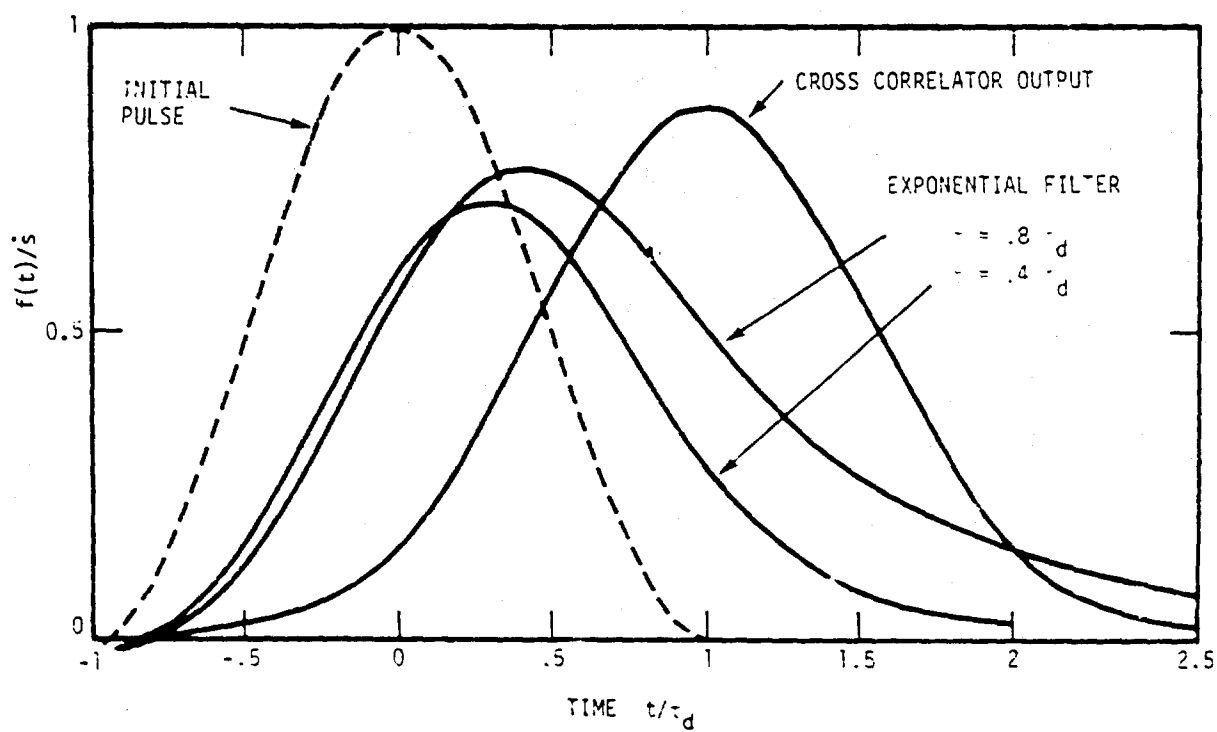
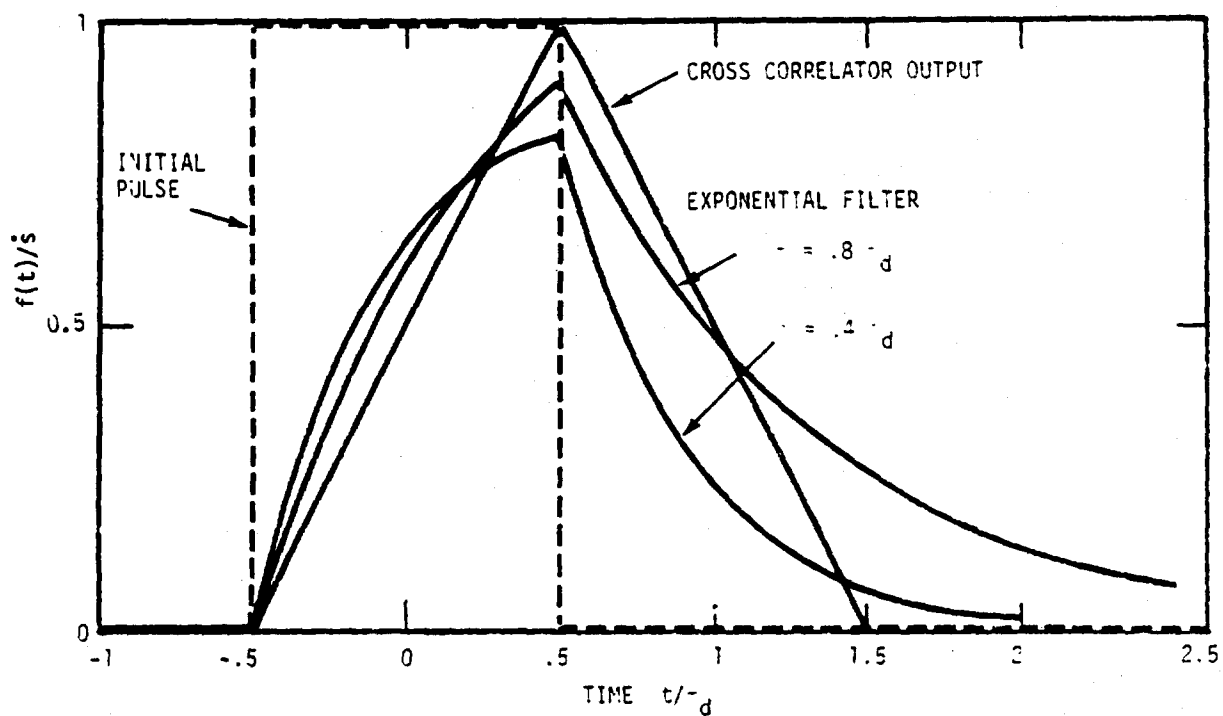


Figure 2-2. Optical pulse shapes and processed output.

The filter gain has been modified in generating the data of Figure 2-2 to keep the noise constant. This requires an additional gain factor inversely proportional to the square root of the bandwidth.

Figure 2-1 shows that the peak amplitude is greatest for the cross correlators and is a function of the ratio of the pulse duration to the exponential roll-off time constant. Also, the shorter time constants lead to narrower output pulses, and, hence, probably better tracking precision (if system noise is not excessive).

Figure 2-3 shows the peak amplitude-to-mean noise ratio as a function of the exponential filter time constant. The data are normalized so the cross correlated output of a rectangular pulse is unity. That pulse and signal processor combination uses fully all photons; consequently, the output signal-to-noise ratio equals the ratio of target power at the detector to NEP. The amplitude factor given in Figure 2-3 can be interpreted as an

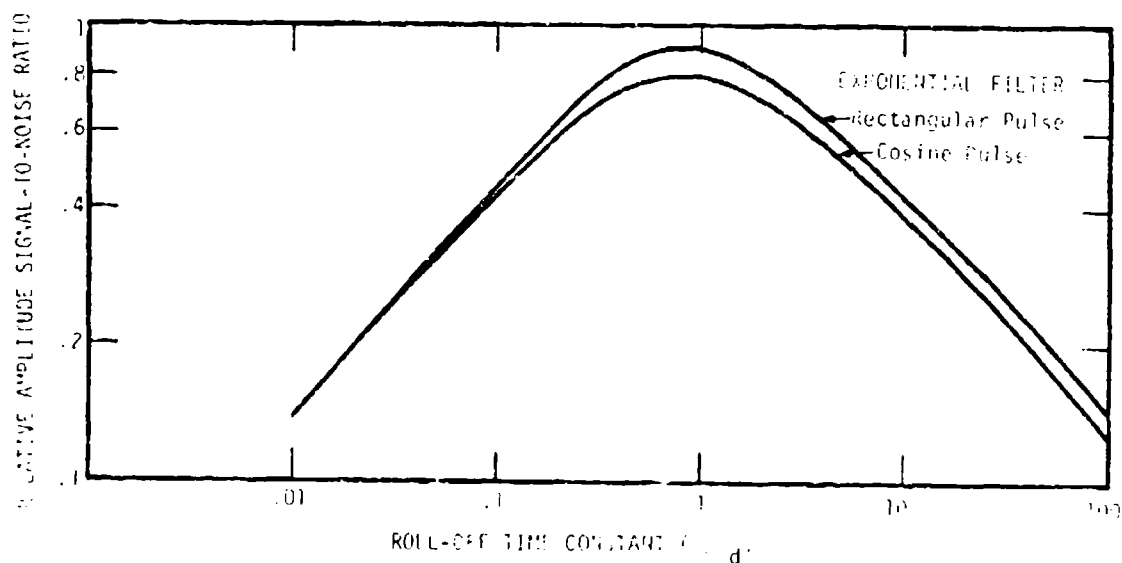


Figure 2.3. Signal-to-noise ratio for processed signals.

electrical efficiency  $\epsilon_e$  that reduces the effective power below the actual input at the detector (Equations 2-5 and 2-25).

Figure 2-2 shows that the maximum efficiency for a cosine wave is 87%. The use of an exponential filter drops the efficiency about 10% if  $\tau/\tau_d$  is 0.8 (the point of minimum loss) or about 18% if  $\tau/\tau_d$  is 0.4 (as might be better for tracking purposes). Thus, the penalty is small for using a simple exponential weighting (which is just a resistor-capacitor high frequency roll-off circuit) instead of using an optimum cross correlator.

If the system objective is target power measurement precision, statistical variations in the number of detected signal photons may be more significant than system noise. A somewhat different efficiency pertains to this process because the variance of the signal involves a convolution of the signal with the square of the filter function. Again the square wave, cross-correlation is 100% efficient. Relative to that, in the limit of negligible system noise, the signal variance is greater by  $\sqrt{10}/3$  or 5% for the cosine wave cross correlator; 6% for the square wave,  $\tau/\tau_d = 0.8$  case; and 21% for the for the square wave,  $\tau/\tau_d = 0.4$  case.

#### 2.2.10. RADIATION EFFECTS

Unfortunately, many semiconductor infrared detectors are also very efficient charged particle detectors. Thus, if they are exposed to beta rays, positrons from nearby neutron activated material, or gamma or beta bremsstrahlung produced Compton electrons, erroneous large-amplitude pulses may be generated. Consequently, if such detectors are to be used in the natural radiation belts or near nuclear detonations, mitigation techniques must be provided.

Shielding can keep beta rays from the detector. About 5 grams/cm<sup>2</sup> will block several MeV beta rays, but most detectors are normally surrounded by this

much material. This shield should be low atomic number material such as aluminum, carbon, organic plastics or beryllium to minimize the bremsstrahlung conversion efficiency.

Attenuation of fission debris gamma rays by a factor of 10 requires about  $50\text{g/cm}^2$  of shield. If the detectors, any associated cooling system and preamplifiers need a 5 cm diameter cavity inside the shield and the shield is  $50\text{g/cm}^2$ , the shield weight will be 50 lb if it is lead. Hundred-fold shielding implies at least a 100 lb shield. Good shielding requires a fold in the optical system so that shielding behind the mirror(s) can block any direct path to the detectors.

For some detectors, the charged-particle-induced current spikes are distinctive and very transitory. Circumvention circuits which identify these spikes and gate them out of the signal are under development. To make use of such techniques requires that the electrical band pass up to the gating circuits must be much broader than the signal spectrum. The expected signal-to-noise ratio is regained by subsequent band-limiting or integration.

## 2.2.11. SIGNAL-TO-NOISE SUMMARY

Several versions of the optical system parameters are interrelated and are hence redundant (e.g., if the three  $A_{\text{eff}}$ ,  $f$ ,  $D$ , or  $\Omega$  are independent, the signal-to-noise ratio can be written in several forms). Often it is convenient to use the detector field of view, not the detector area. One useful version is to explicitly include both the intrinsic system  $\Omega$  and the optical background noise and is given in Table 2.2.11.1. This form is

$$\frac{S}{N} = \frac{\epsilon_e \epsilon_0 A_p H_\lambda \Delta\lambda D_T^*}{\sqrt{A_d \Delta f}} \quad (2-34)$$

$$= \epsilon_e \epsilon_0 H_\lambda \Delta\lambda \sqrt{\frac{A_p \tau_d}{\omega}} \left( \frac{2 (f/\#)^2}{\pi D^{*2}} + \frac{h\nu N_{b,\lambda} \Delta\lambda}{RQE} \right)^{-1/2} \quad (2-35)$$

where the total noise due to  $D_T^*$  has been taken as the root-mean-square of the intrinsic system noise and background noise. Although Equation is more complex than Equation tem requirements in later sections.

## 2.3. TARGETS

### 2.3.1. GENERAL

Infrared optical systems are designed to observe a variety of targets. The specific characteristics of many are classified; however, the general character of most signatures is basic. The source of the infrared radiation falls into three general classes: thermal, "grey body" radiation from solid surfaces; thermally or chemically excited radiation from gases (such as jet engine or rocket exhausts); or reflected radiation. The reflected radiation may be from the sun, the earth and its atmosphere, or a laser illuminator. Except for laser systems, the optical bandwidth is usually relatively wide and target radiances must be integrated across the band.

### 2.3.2. THERMAL EMISSIVE TARGETS

Signal characteristics depend not only upon the type of radiation but also upon target characteristics such as emissivity or reflectance and target shape and orientation. Inasmuch as energy must go somewhere, the sum of absorptance, reflectance and transmittance must be unity:

$$a + r + t = 1$$

$$(2-36)$$

If the material is sufficiently thick to be opaque, transmittance is zero and

$$\alpha + \rho = 1. \quad (2-37)$$

For an opaque surface, it can also be shown<sup>(2-1)</sup> that the absorptance and emittance are equal

$$\alpha = \epsilon, \quad (2-38)$$

where emittance is the ratio of power emitted to that emitted by a black body. This relationship holds either for total hemispherically integrated quantities or any particular angle relative to the surface normal.

### 2.3.2.1. Greybody Radiation

A surface radiates by virtue of its temperature. The spectral radiance normal to the surface is

$$N_{\lambda} = \epsilon_{\lambda} c_1 \lambda^{-5} / (e^{c_2/\lambda T} - 1), \quad (2-39)$$

where  $\epsilon_{\lambda}$  is the spectral emittance,  $c_1 = 2c^2h$  and  $c_2 = ch/k$ .  $c$  is the velocity of light,  $h$  is Planck's constant and  $k$  is Boltzmann's constant. Figure 2-4 is a normalized curve of blackbody emission. By using the scaling given in the figure, the spectral radiance normal to a black surface can be obtained for any temperature and wavelength. This has been used to generate the spectral irradiance at a sensor at various ranges from a square meter of surface emitting at 300°K (Figure 2-5). If the surface is other than 300°K, the irradiance must be multiplied by the factors given in Figure 2-6.

The temperature of a target depends upon many factors. Those flying slowly in the atmosphere tend to adopt the ambient air temperature; those flying

\* Superscripts in parenthesis denote references.

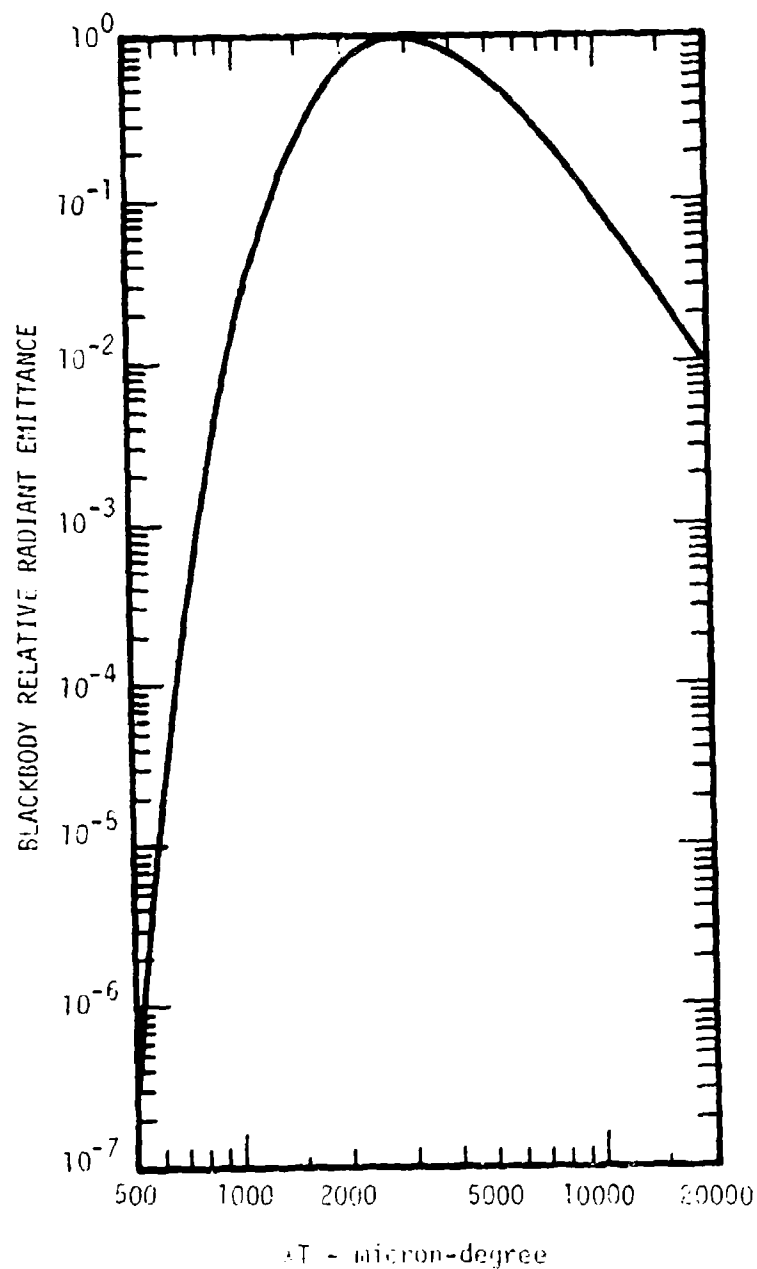


Figure 2.4. Universal blackbody emission function. To obtain radiance in a direction normal to the surface in watts/cm<sup>2</sup> steradian, the ordinate should be multiplied by  $0.411 \cdot (T/1000)^5$ .

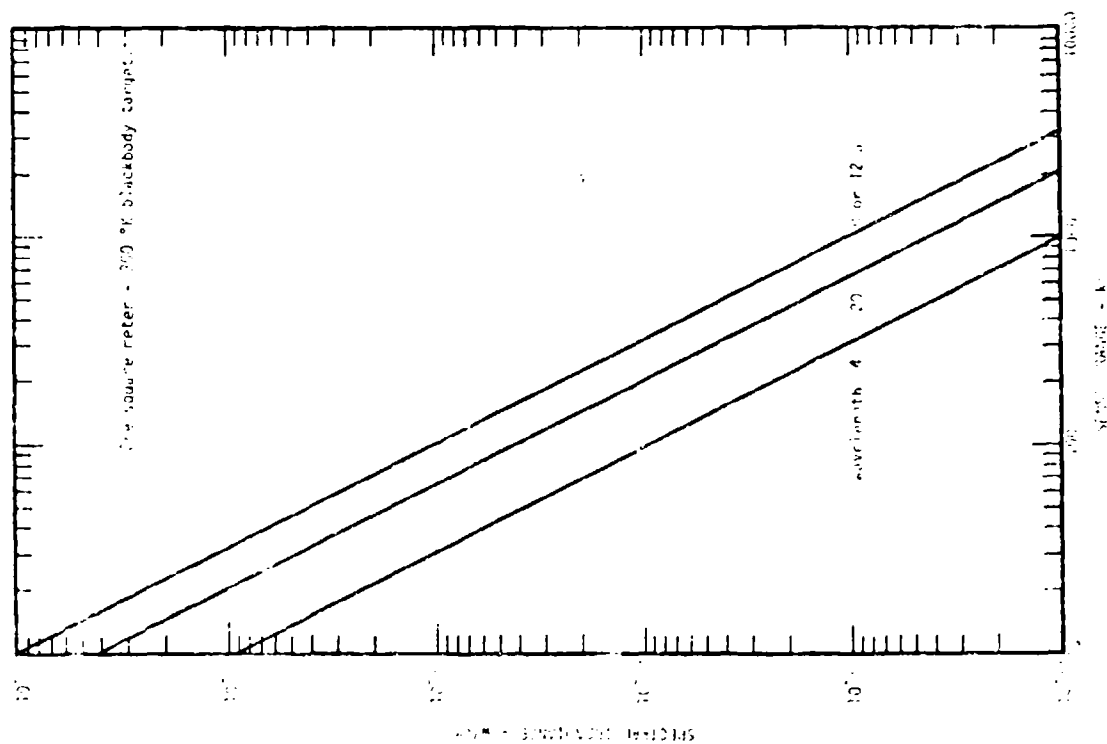


Figure 2-5. Spectral irradiance vs range.

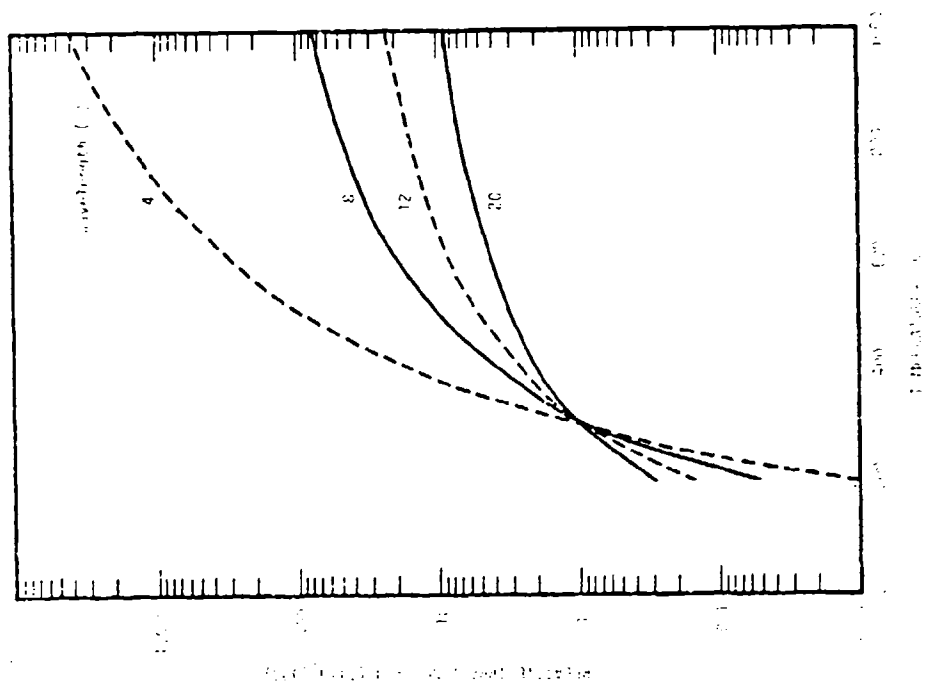


Figure 2-6. Temperature variation of radiance.



fast exhibit ram air heating. Solar illumination of a grey body (i.e., independent of  $\lambda$ ) in space results in a temperature near  $300^\circ\text{K}$ ; earthshine illumination of a grey body nearby results in a temperature near  $200^\circ\text{K}$ . Reentry heating of objects from space may raise the surface temperature to several thousand degrees.

#### 2.3.2.2 Emissance and Reflectance

Material emissivities vary widely so that for detailed computations of signal intensity and spectral content, data for specific surfaces is needed. Much data is now available because thermal radiation balance controls spacecraft temperature. In general, clean metal surfaces have emissances of 0.01 to 0.1 in the LWIR (Figure 2-7) with the emissance somewhat less at the long wavelength end of the band.

Oxidation or anodization of metal surfaces increases the LWIR emissance to more than 50%. Paints tend to have 80% to 90% emissance in the LWIR irrespective of the emissance (or the equivalent, absorptance) in the visible. Most plastics (mylar, teflon, phenolic, etc) have small reflectances and mean absorbing thicknesses of several microns to several millimeters. Thus, thin plastic films may show abrupt changes in emissance such as that in Figure 2-7. Thick layers, however, will have an emissance approaching unity. Some special surfaces, such as Tabor surfaces, have large solar absorptances and small LWIR absorptances.

A Lambertian surface has an emissance that varies as the cosine of the angle from the surface normal. This results in a radiance that is independent of the angle; the surface is equally bright as viewed from all angles. This is not true for all surfaces and, particularly for low conductivity materials, the angular variation of emissance may depend upon the polarization of the emitted radiation. In many cases, an average emissance may be used; in a few cases, detailed integrations over the surface must be performed.

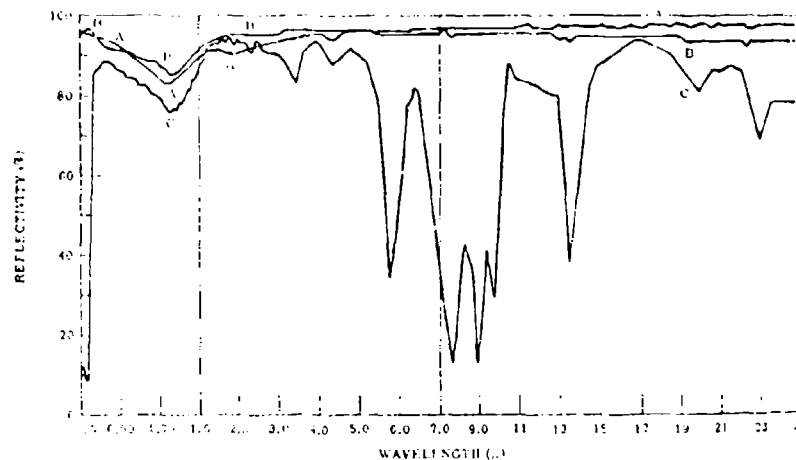


Figure 2-7. Compiled spectral reflectivities. A=evaporated aluminum, 25μin. on polished 6061-T6 aluminum. B=evaporated aluminum (0.2μ), on 1/4-mil Mylar crumpled and stretched, (looking at aluminum). C=evaporated aluminum (0.2μ) on 1/4-mil Mylar crumpled and stretched (looking at Mylar).

### 2.3.2.3 Emissivity-Area Product

The most commonly used parameter for defining thermally emissive targets is the emissivity-area product,  $\epsilon A$ . It is useful by providing adequate information to choose system sensitivity, compute signal-to-noise ratio, etc., without requiring details about target structure.

Many targets for which self emission is the primary source of radiation have an emissance near unity. For these the emissivity-area product is nearly the area of the target as projected on a plane perpendicular to the viewing direction. Figure 2-8 gives the aspect dependent area for some simple shapes.

### 2.3.3 GASEOUS RADIATION

Jet and rocket engines emit large volumes of gas that have just undergone chemical reactions and which may be traveling at a much different speed


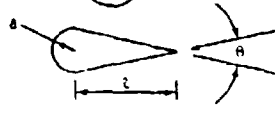
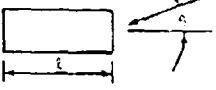
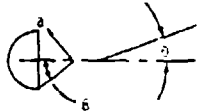
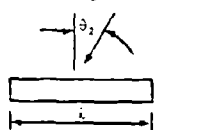
TARGET SHAPE		DESCRIPTION
1. Sphere		
2. Sphere-cone		$l = 2a$
3. Sphere-cone		$l = 5a$
4. Cylinder		$l = 2a$
5. Cylinder		$l = 5a$
6. Sphere segment		$\beta = 45^\circ$
7. Cylinder segment		$h = 2a, \theta = 45^\circ$
8. Cylinder segment		$h = 5a, \theta = 45^\circ$

Figure 2-8a. Shapes of idealized targets.

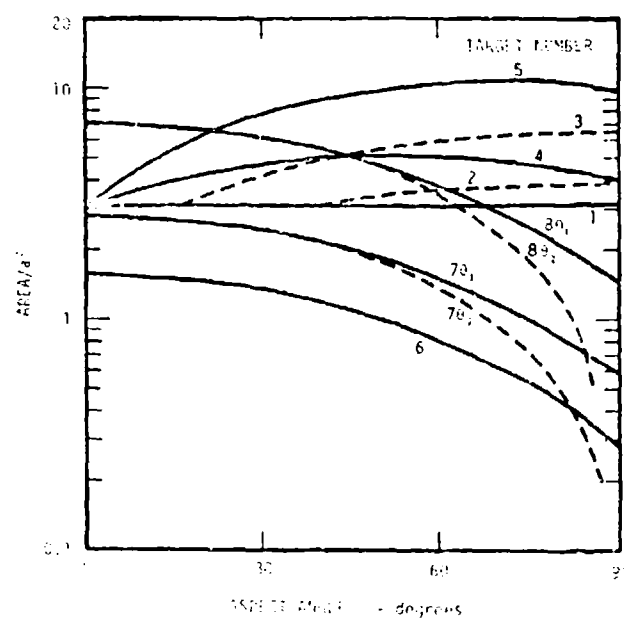


Figure 2-8b. Projected area as a function of aspect angle.

than the ambient air. These conditions may result in the excitation of molecular species and their subsequent radiation. Although the objective of an engine is to transform as much of the chemical energy as possible into translational energy, if only a few percent of the combustion energy is radiated as infrared, the plume radiance is great. To generate a thrust of  $10^5$  kgm (220,000 pounds) with a gas exit velocity of 2 km/sec, which is typical, requires the ejection of 500 kgm/sec of exhaust by virtue of the equality

$$v \frac{dM}{dt} = g T, \quad (2-40)$$

where  $v$  is the exit velocity,  $\frac{dM}{dt}$  is the exhaust mass flow,  $g$  is gravity and  $T$  is the thrust. The energy of this exhaust is 1000 Mw. If only 1% of this is radiated, the power density is about 1 Mw/ster.

There are several excitation mechanisms for the exhaust gas. Vibrational energy may be frozen into the flow as it exits the nozzle or throat. Many engines are operated fuel rich, and unoxidized fuel undergoes "after burning" as it mixes with air. Particularly during final stages of rocket acceleration, exhaust gas is moving fast compared to the ambient air, and collisions with the air may excite the exhaust molecules.

The spectral characteristics of the radiation depend upon the composition of the exhaust gas, which depends in detail upon the fuel composition and combustion environment. Most fuels contain hydrogen and carbon and most oxidizers contain oxygen. Thus, common species in the exhaust are  $H_2O$ ,  $CO$  and  $H_2$ . The centers of some infrared bands for these radiators are given in Table 2-1.

Table 2-1. Wavelengths of some common exhaust emission bands longer than 2 microns.

Gas	Approximate Band Center (microns)
OH :	2.15, 2.80, 2.94, 3.08, 3.25, 3.43, 3.63, 3.87, 4.14, 4.47
H <sub>2</sub> O:	2.66, 2.74, 3.17, 6.27
CO :	2.345, 4.663
CO <sub>2</sub> :	2.01, 2.06, 2.69, 2.77, 4.26, 4.68, 4.78, 4.82, 5.17, 15.0

#### 2.3.4. REFLECTED ILLUMINATION

The power reflected by a target depends upon the illumination, the target reflectivity and the scattering characteristics of the target. As has been discussed in Section 2.3.2.2, target reflectance can range from nearly unity to a few percent. Metals such as are used to build aircraft have large reflectance, most ablation type missile warheads have small reflectance. The reflectance will depend on the angle with respect to the surface normal of both the illumination and viewing vectors. It will include both specular and diffuse reflection and it may be polarization sensitive, particularly for non-conducting materials. Conductors have some polarization sensitivity, but it occurs so close to grazing incidence that it is normally a minor effect when integrated over the whole target.

##### 2.3.4.1. Illumination Sources

For systems utilizing reflected radiance, sources of illumination are sunshine, earthshine and lasers. Sunshine and earthshine can be put in perspective by comparing the irradiance produced by them with that produced by self emission. Figure 2-9 shows the relative magnitude for a target

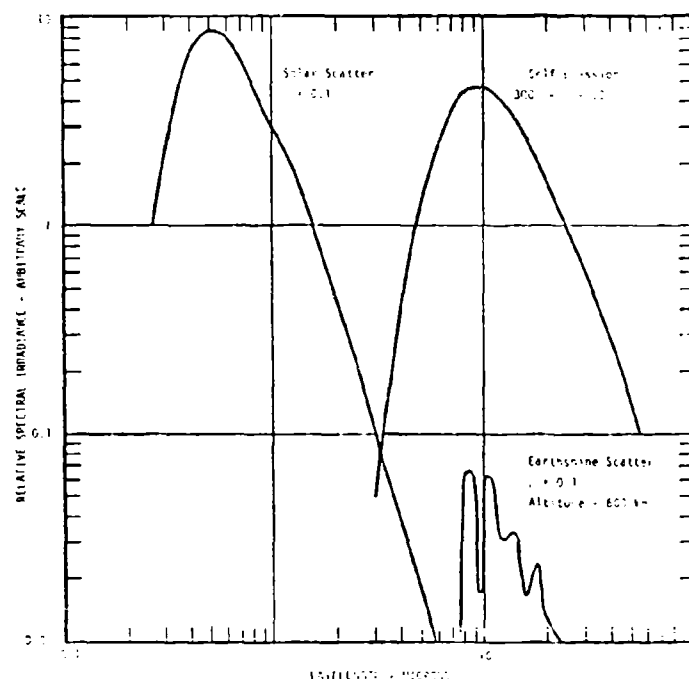


Figure 2-9. Sensor irradiance for various target illuminations.

that scatters the incident radiation isotropically (a nearly spherical body) and has an emissance of 0.9 and reflectance of 0.1. The earthshine is that typical of a clear day. For such an object, solar scatter can predominate at wavelengths less than  $3\mu$ .

The earthshine reflection is minor for absorptive targets. However, for metallic targets the reflectance could be 0.95 and emissance 0.05. This would result in the preponderance of irradiance in the 8 to  $20\mu$  region being due to reflected earthshine.

Figures 2-10 and 2-11 show the irradiance of a flat plate outside the earth's sensible atmosphere due to the sun and earthshine. For overcast conditions with clouds at about 20,000 feet, the irradiance maxima near 9 and  $11\mu$  are reduced by a factor of about 2. For targets at higher

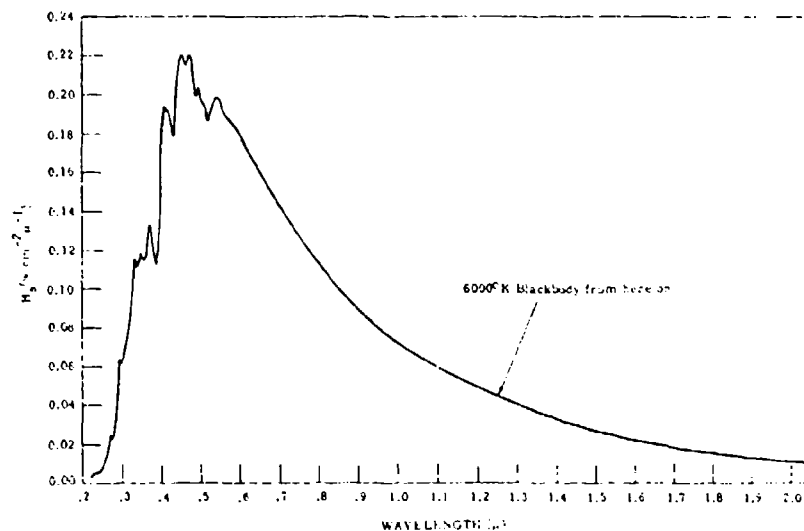


Figure 2-10. The Johnson solar spectral curve.

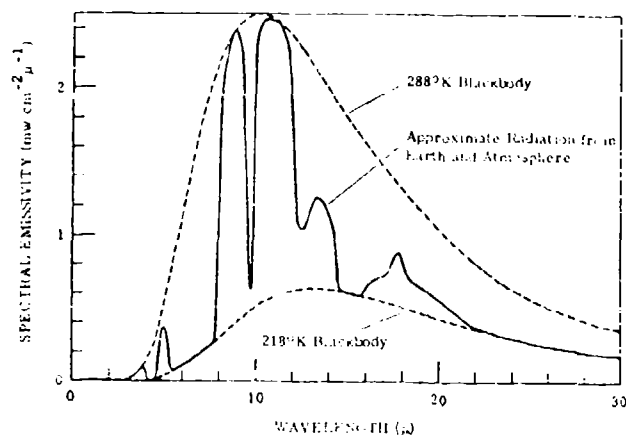


Figure 2-11. A typical spectral emissive power curve for the thermal radiation leaving the earth. (The 288°K blackbody curve approximates the radiation from the earth's surface, and the 218°K blackbody curve approximates the radiation from the atmosphere in those spectral regions where the atmosphere is opaque.)

altitudes, illumination by earthshine is over a smaller solid angle. Figure 2-12 shows the geometric factor to convert the flat plate irradiance of Figure 2-11 into the total radiation reflected by a sphere as a function of altitude.

Irradiance at the sensor (neglecting intervening absorption) is directly related to target irradiance  $H_{\lambda,s}$  and effective scattering cross section  $\sigma^*$ .

$$H_{\lambda} = \frac{H_{\lambda,s} \sigma^*}{4\pi R^2}, \quad (2-41)$$

or if  $\sigma^*$  is in units of meter<sup>2</sup> and  $R$  is in kilometers

$$H_{\lambda} = 8 \times 10^{-9} H_{\lambda,s} \sigma^* / R^2. \quad (2-42)$$

For a laser illuminator, it is better to deal with in-band irradiance, rather than spectral radiance. The target irradiance can be given in terms of the laser power output  $P_{\lambda}$  (watts) and either the area  $A_b$  covered by the illuminator beam or the divergence angle  $\theta_b$  of the beam (taken here to be the full beam divergence). Thus

$$H_s = 10^{-12} P_{\lambda} / A_b = 1.2 \times 10^{-12} P_{\lambda} / R^2 \quad \text{w/cm}^2 \quad (2-43)$$

where  $A_b$  is in units of square kilometers and  $R$  is in kilometers.

#### 2.3.4.2. Effective Cross Sections

Effective cross sections for reflecting and scattering incident radiation are more complex to compute than those for self emission because of the high correlation between the direction of incidence on an elemental area of the target and the direction of the reflected energy.



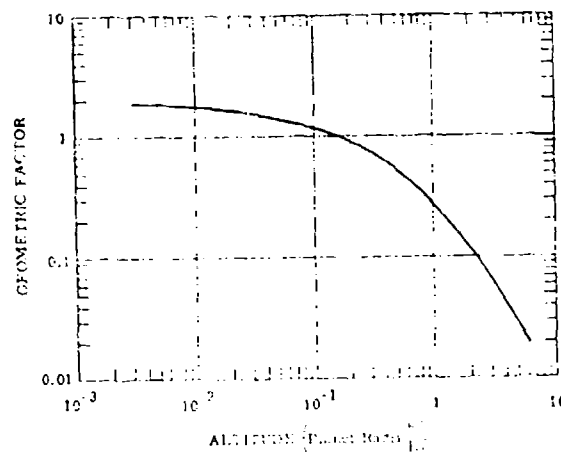


Figure 2-12. Geometric factor for planetary thermal radiation incident on sphere versus altitude.

For laser systems, the monostatic (coincident locations for the illumination source and sensor) cross section is needed. This can be expressed as a two dimensional scattering matrix or, for bodies of revolution, a one dimensional matrix. If the target is primarily a specular reflector, the first order calculation of monostatic cross section consists of finding points where the direction of illumination parallels the surface normal and forming the product of  $\pi$  and the maximum and minimum radii of curvature at that point.

Targets with shapes such that their surfaces are generated partly by straight line segments (cones, cylinders, plates, etc) have directions of high cross section or glint. This results from the "maximum radius of curvature" becoming infinite. Actually, in the glint regions, the power density is limited by diffraction (or by surface irregularities).

The effective monostatic cross section of a sphere of radius  $a$  is just  $\pi a^2$ . The case for a cone capped on each end by a spherical section is shown in Figure 2-12 (assuming a specular reflectivity of 1 and no surface irregularities). The diffraction width of the glint is  $\sqrt{\lambda}$ , and there are additional lower intensity side lobes outside this main lobe.

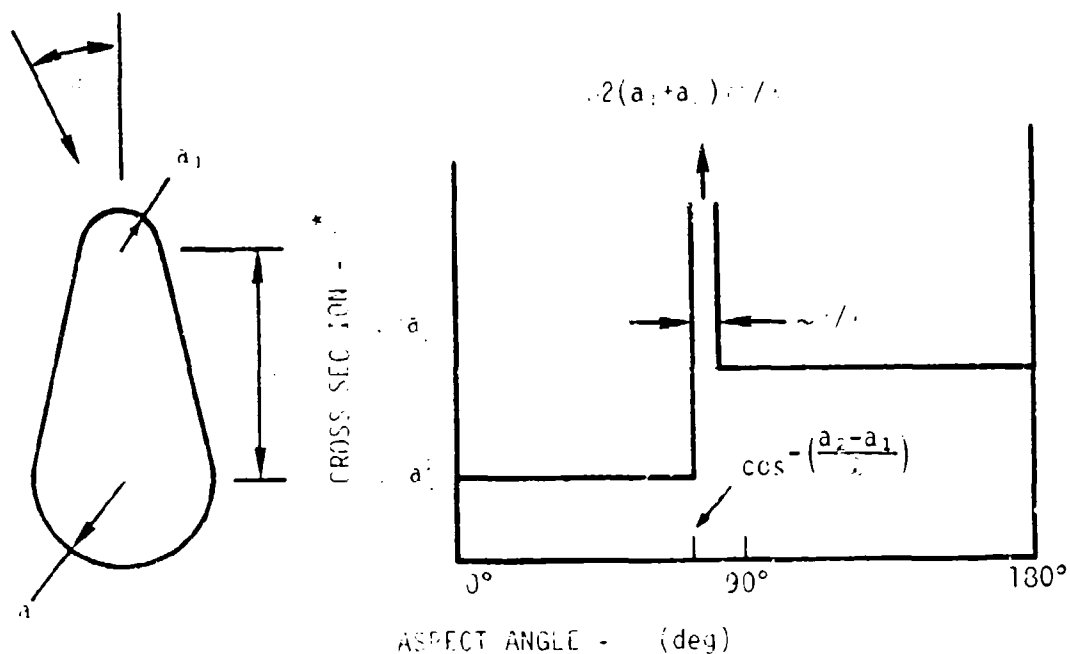


Figure 2-13. Monostatic cross section of capped cone.

Solar reflection will be bistatic, taking place (if specular) where the surface normal bisects the angle from illuminator-to-target-to-sensor. The sun subtends about a degree so the effective cross section is an average over a small solid angle. For arbitrarily shaped targets, the scattering matrix is a function of four angles, two defining the illumination and two the sensor directions. Even for a body of revolution, the matrix is a function of three angles. Usually, the computation of bistatic cross sections is accomplished by approximating the body by a series of simpler surfaces, often flat surfaces, with subsequent smoothing of the calculated data.

Bistatic geometry can emphasize polarization effects because the required scattering angle dictates the angle of incidence of observed radiation—all the radiation comes from regions of constant angle of incidence. It is possible to be incident at "Brewster's" angle so that the signal is com-

pletely polarized. (Most IP detectors are not polarization sensitive and so would not detect this effect.)

Reflection of earthshine involves the illumination of the target over nearly a hemisphere. Thus, the scattering matrix can be averaged over a large solid angle for approximate analysis (assuming the earth is a nearly uniform source of irradiance), or it can be used in detail as with the simple bistatic case and a numerical integration performed over the reflecting surface.

In this application, the surface can be represented by small flat plates, or facets, with little error. The reflection at the edge of one of the facets will come from a slightly different point where the earthshine differs only slightly from that for the central ray through the facet.

## 2.4. OPTICAL SYSTEM CONSIDERATIONS

An optical sensor may fulfill a single or multiple system function such as acquisition, tracking and discrimination. System design may depend upon the functional requirement. Furthermore, design will depend upon whether detector sensitivity is limited by intrinsic detector noise, Johnson amplifier noise or background photon noise. The system signal-to-noise ratio (Equation 2-35) can be re-expressed in various limiting forms to identify critical design parameters for various cases.

### 2.4.1. ACQUISITION SYSTEMS

The system functional description of acquisition systems is in terms of a required field of view and a frame time  $T_f$  to scan the field once. The field of view may be characterized by a solid angle  $\Omega$ , if no information about target location is known, or by an area  $A_t$ , if there is some crude position data available such as from a boost-phase-track system.

The relationships added by these parameters are:

$$\Omega = A_f/R^2 \quad (2-44)$$

and

$$\frac{\Omega}{T_f} = \frac{\omega n f_c}{\tau_d}, \quad (2-45)$$

where  $R$  is the desired acquisition range,  $n$  is the number of detector elements and  $f_c$  is loss due to overlapping detector fields-of-view or non-ideal scanning sequences (some portion of the field being scanned twice, dead time to repoint the array, etc). From an acquisition standpoint  $\Omega/T_f$  is more fundamental than  $\omega/\tau_d$ .

For the condition that the intrinsic  $D^*$  is limiting, the sensitivity equation can be solved for the minimum detectable irradiance

$$I_{z,min} = \frac{2\sqrt{2}}{\pi} \left( S/N \sqrt{\frac{\tau_d}{T_f}} \right) \left( \frac{f/\#}{1.5 d \Omega} \right) \left( \frac{1}{\sqrt{f_c} D^*} \right) \cdot \frac{1}{\tau_d} \quad (2-46)$$

where  $d$  is the aperture diameter.

The three factors in parenthesis pertain to system requirements, optical system design and detector characteristics. For a given system, the system factor is fixed. Usually,  $1/\Omega$  is designed as small as possible and  $\tau_d$  as large and any major variation would be difficult. The optical band pass is also usually not greatly variable and is taken as wide as possible. The sensitivity then depends directly upon the aperture diameter. However, in general, this implies a dependence upon the cube root of sensor volume or approximately cube root of sensor weight. Consequently, there is little freedom there either. Increases in number of detector elements reduce

the detectable radiance as do increases in  $D^*$ . It is only in these factors that there is much hope of advancing system sensitivity greatly.

If this sensitivity is expressed in terms of the power radiated by the target ( $H_\lambda = P_\lambda / 4\pi R^2$ ), Equation (2-46) is transformed to

$$P_{\lambda, \min} = 8\sqrt{2} \left( \frac{S}{N} \sqrt{\frac{\bar{\lambda} f}{T_f}} R \right) \left( \frac{f/\#}{\epsilon_0 d \Delta\lambda} \right) \left( \frac{1}{\sqrt{n} f_c D^*} \right) \frac{1}{\epsilon_c} \quad (2-47)$$

This is the form appropriate to having crude data about target location. Furthermore, under these conditions, the allowable time per frame is nearly proportional to the detection range (i.e., the target must be seen while traversing a given fraction of the range to the sensor). In this limit,  $P_{\lambda, \min} \propto R^{1/2}$  rather than  $R^2$  as is often the case.

One of the interesting deductions is that it makes no difference from a target detection standpoint whether the  $n$  detector elements are large and scan slowly with the large  $\tau_d$  or are small and scan rapidly. On the other hand, this trade-off does affect tracking precision.

Many sensitive optical systems are Johnson noise limited. In this limit, the maximum irradiance is

$$H_{\lambda, \min} = \frac{1}{\sqrt{2}} \left( \frac{S}{N} \right) \left( \frac{1}{\epsilon_0 \lambda_p \Delta\lambda} \right) \left( \sqrt{\frac{4 kT}{\tau_d \tau_f}} - \frac{1}{R^2} \right) \frac{1}{\epsilon_c} \quad (2-48)$$

In this limit, the  $f/\#$  is unimportant as is the number of detector elements, and the only explicit dependence upon scan rate is the dwell time  $\tau_d$ . Once again, however, many detectors may be required to simultaneously achieve precision and a long dwell time.

A final interesting limit is background limited operation. For this,

$$H_{\lambda, \min} = \frac{2}{\sqrt{\pi}} \sqrt{N_{b, \lambda}} \left( S/N \sqrt{\frac{\Omega}{T_f}} \right) \left( \sqrt{\frac{h\nu}{\Delta\lambda}} \frac{1}{RQE} \frac{1}{\epsilon_0 d} \right) \left( \frac{1}{\sqrt{n} f_c} \right) \frac{1}{\epsilon_c} \quad (2-49)$$

Once again, after the system requirements are established, the designer has only limited design choices, primarily  $d$  and  $n$ .

#### 2.4.2. TRACKING SYSTEMS

In general, marginal signal strength is not one of the problems with tracking systems because the target must have been acquired previously. If there is hand over from one sensor to another, the tracker will be designated to a very small field of view. Consequently, within this field of view the required value of  $\Omega/T_f$  is very small and reacquisition is readily achievable. Moreover, in many cases, tracking is merely another mode of operation of the acquisition sensor.

The field-of-view during the tracking mode must be small enough to isolate the particular target being tracked and yet large enough to accommodate any potential target maneuver during signal fades, obscuration, or track-servo response-time.

In most optical tracking applications, a locational precision better than the detector element field-of-view is desired. This results from physical limitations on detector size, use of acquisition sensors that need a relatively large field of view to achieve a reasonable dwell time, etc. With good S/N, measurement precision can be smaller than resolution. Optical detectors are intrinsically square-law, power detectors; the detector output voltage or current is proportional to the signal power. Usually, the dominant noise source—G-R noise, Johnson-noise or background photon

noise—results in a gaussian or near gaussian distribution at the detector output. Consequently, the available  $\alpha'$  is related to the angular subtense of the detector  $\alpha$  by

$$\alpha' = \alpha / (S/N). \quad (2-50)$$

(This contrasts with the radar case. There the noise source is gaussian at the input to the preamplifier, or detector, where the signal is proportional to the wave field-strength. In that case, subdivision of the resolution cell is by only  $\sqrt{S/N}$ .)

In general, for obtaining good tracking precision, the same principles apply as for obtaining good acquisition signal-to-noise, plus a desire for small detector fields-of-view. However, except for the Johnson noise limited case, small detectors are required for good signal-to-noise ratio anyway. It should be noted that after acquisition, the signal-to-noise ratio is probably of the order of 10 or greater before handover to the tracker. If the same sensor is used for tracking, the effective dwell time probably can be increased at least a hundredfold over the acquisition dwell time. Thus, the signal-to-noise ratio should exceed 20 db, and the theoretically achievable precision be smaller than a hundredth of the basic detector resolution. In most cases, this implies adequate precision without switching detector element size.

#### 2.4.3. MEASUREMENT PRECISION

It should be noted that the  $S/N$  discussed so far has been the ratio of the mean-detected-signal to noise-without-signal. This is incomplete for describing the expected fluctuation in measured signal strength. Many proposed sensitive systems operate with few detected signal photons. Consequently, there is a statistical variability in the number of signal photons.

From the standpoint of uncertainties in measured peak amplitude, the signal irradiance behaves like a steady background. Consequently, to obtain a measure of signal-to-rms fluctuation in signal-plus-noise, one can use Equation (2-35) with the replacement of  $N_{b,\lambda}$  by  $N_{b,\lambda} + H_\lambda/\omega$

$$\frac{S}{\sigma_{s+n}} = \epsilon_e \epsilon_0 H_\lambda \Delta\lambda \sqrt{\frac{A_p \tau_d}{\omega}} \left[ \frac{2(f/\#)^2}{\pi D^*{}^2} + \frac{h\nu \Delta\lambda (N_{b,\lambda} + H_\lambda/\omega)}{RQE} \right]^{-1/2} \quad (2-51)$$

## 2.5. NATURAL INFRARED BACKGROUND

The natural infrared background is important because it constrains potential operating wavelength bands and achievable system sensitivity. Background sources to be presented are (1) those seen from near the ground, (2) those seen by an airborne system, (3) the earth limb as seen looking from outside the sensible atmosphere, (4) auroral emissions, and (5) stellar.

### 2.5.1. GROUND LEVEL SKY BRIGHTNESS

The sky brightness as seen from near the ground is dominated by scattering of solar radiation at wavelengths less than  $3\mu$  and by atmospheric emission at longer wavelengths. Figure 2-14 shows the radiance as a function of sight path elevation angle.

The radiance depends upon many factors—solar zenith angle (Figure 2-15), elevation angle, moisture content, cloud cover, atmospheric temperature, etc. A good summary of data is included in Reference 2-1. Figures 2-14 and 2-15 show the effect of water vapor bands at 1.1, 1.4, 1.9 and  $2.7\mu$  as well as of  $CO_2$  at  $2.7\mu$  absorbing the solar scattered radiation. A particular wavelength may seem desirable for a system because the background is dim, but if this dimness is due to absorption, its desirability is questionable. It depends upon the relative ranges to the target and



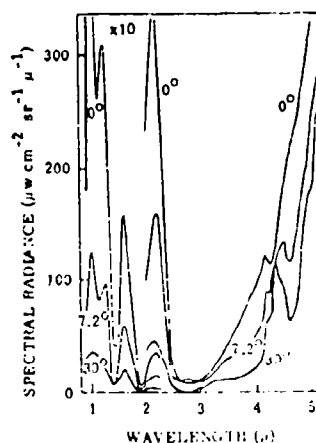


Figure 2-14. Spectral radiance of the clear daytime sky.

the true source of the background. If the target is close enough, its signal may be attenuated only a little and the background a lot.

In the emission region, emission bands are evidenced in peaks in Figure 2-16 at  $6.3\mu(\text{H}_2\text{O})$ ,  $15\mu(\text{CO}_2)$  and  $9.6\mu(\text{O}_3)$ . If the sky is overcast the LWIR is a continuum as seen in Figure 2-17.

### 2.5.2. AIRGLOW FOR AIRBORNE SENSORS

Murcray, et al (2-4) have flown a series of LWIR radiometers and interferometers on balloons in both temperate and arctic locations. Measured spectra, for several flights (Figure 2-18), show a low radiance window between  $10.5\mu$  and  $13\mu$ , bounded at short wavelengths by an ozone band and at long wavelengths by  $\text{CO}_2$ . The peak in the middle of the window is  $\text{HNO}_3$  radiation and it is bounded with narrow lower background regions. Relatively low background slots also occur from 8 to  $9\mu$  and from 5 to  $6\mu$ . Spectra 1 and 6, Figure 2-18, were obtained shortly after sunrise, and others were predawn.

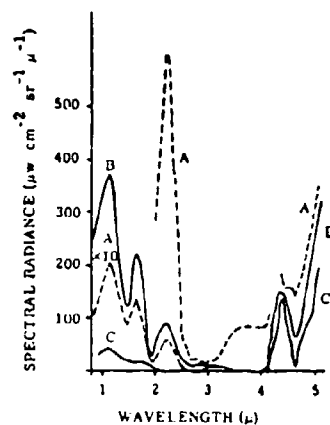


Figure 2-15. Spectral radiance of a clear zenith sky as a function of sun position; A = sun elevation 77°, temperature 30°C; B = sun elevation 41°, temperature 25.5°C; C = sun elevation 15°, temperature 26.5°C.

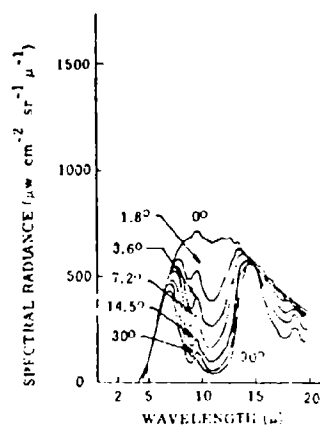


Figure 2-16. The spectral radiance of a clear nighttime sky for several angles of elevation above the horizon (Elk Park Station, Colo.)

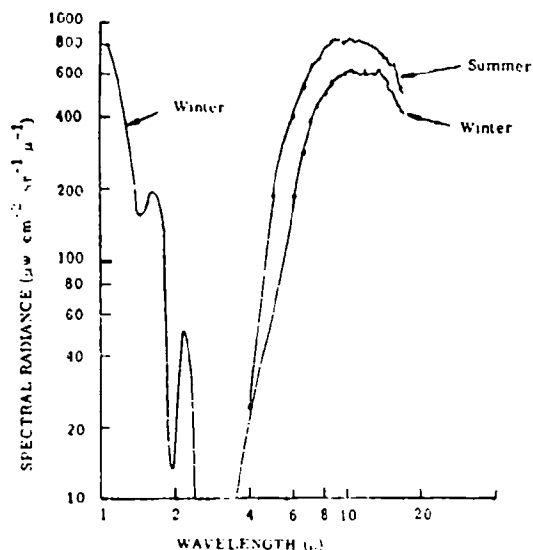


Figure 2-17. Spectral radiance of overcast skies in winter and summer.

Data from a filter radiometer with a 0.039 ster field-of-view at an elevation angle of  $45^\circ$  and with filter bandpasses shown in Figure 2-19 are shown in Figure 2-20. The filters were chosen to explore the 10.5μ to 13μ band in more detail. The radiances shown in Figure 2-20 are typical of those obtained on a number of balloon flights. The abrupt decline above 30,000 ft was due to rising above a thin cloud layer. The general decline in radiance falls off approximately as rapidly as the air density—about a factor of 3 in 20,000 ft.

Data on the time variation of radiance are available only for the highest altitudes where the balloons floated. An example, Figure 2-21, shows fluctuations of a factor of 10 within a few minutes. If the variation were this great at lower altitudes, one would expect to have seen a greater scatter of points about the smooth curve of radiance vs altitude, but even the flight-to-flight scatter of radiance is not that great at 40,000 to 60,000 ft. The large fluctuations may be associated with dawn. In short,

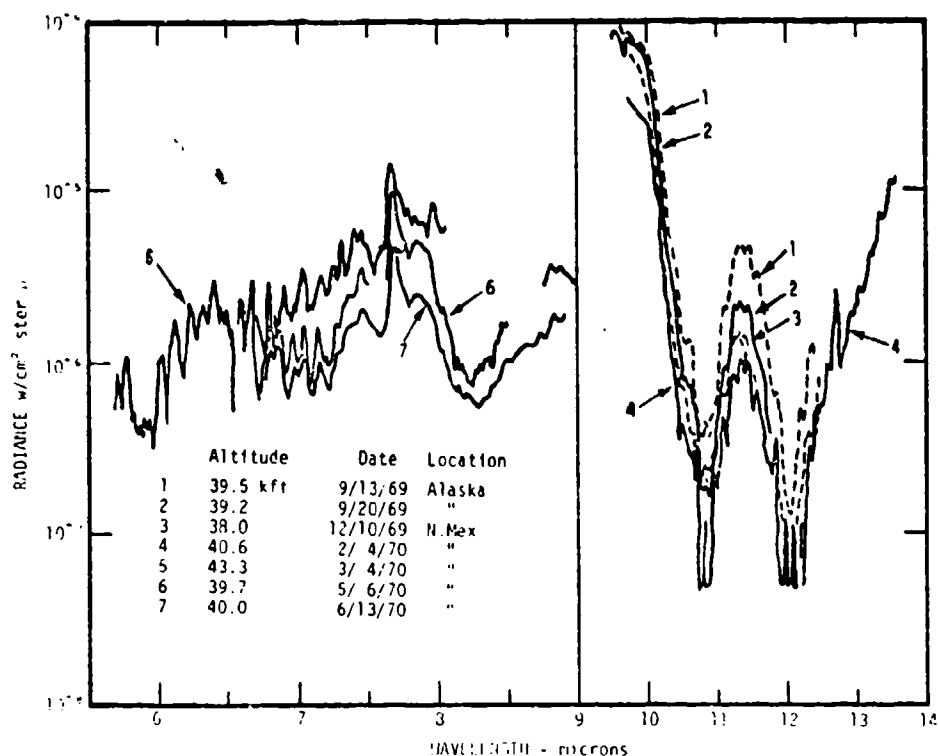


Figure 2-18. Spectral radiance near 40,000 ft. at 45° elevation.

if the radiance profile of Figure 2-19 is used as representative data, it would be prudent to assume that a radiance three times greater would not be unlikely.

In another experiment, Turner<sup>(2-5)</sup> flew a spatially scanning filter radiometer at 92,000 ft. Six filters isolated bands from 9 to 22.7 $\mu$ , and the elevation was changed to view different portions of the sky. Data from a flight made at Holloman AFB (Figure 2-22) shows radiance approximately an order of magnitude greater than reported by Murcray.

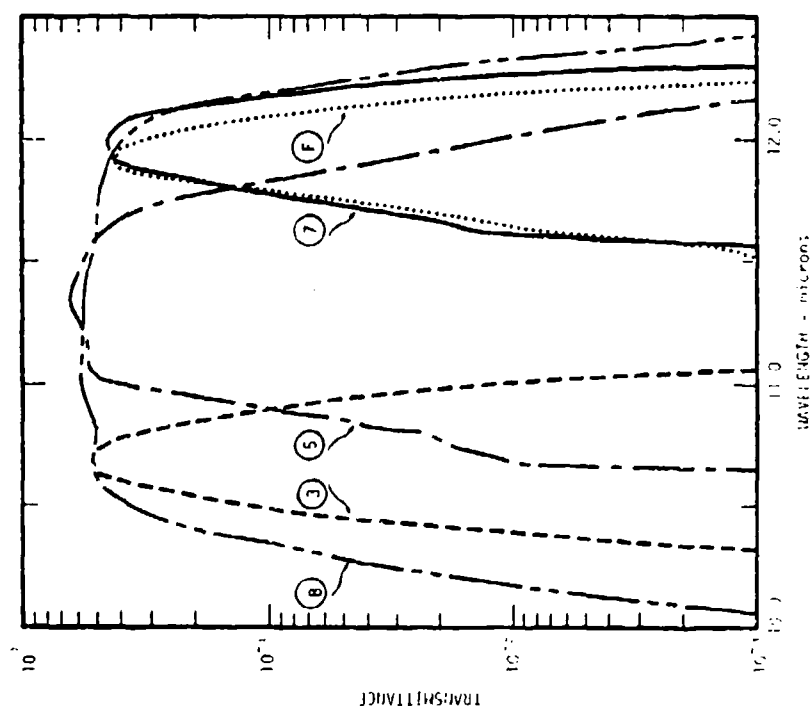


Figure 2-19. Filter radiometer transmittance curves.

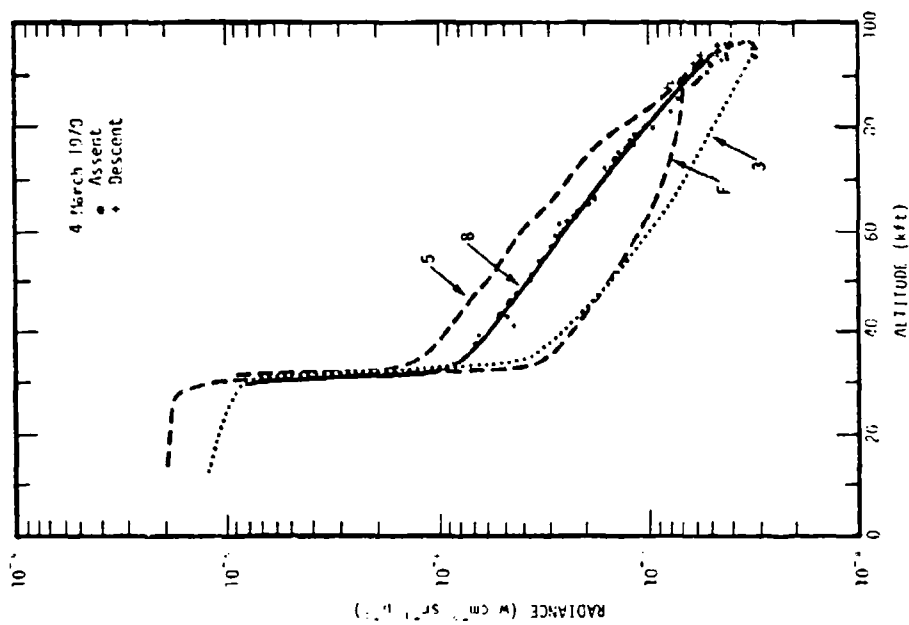


Figure 2-20. Typical measured natural background radiances.

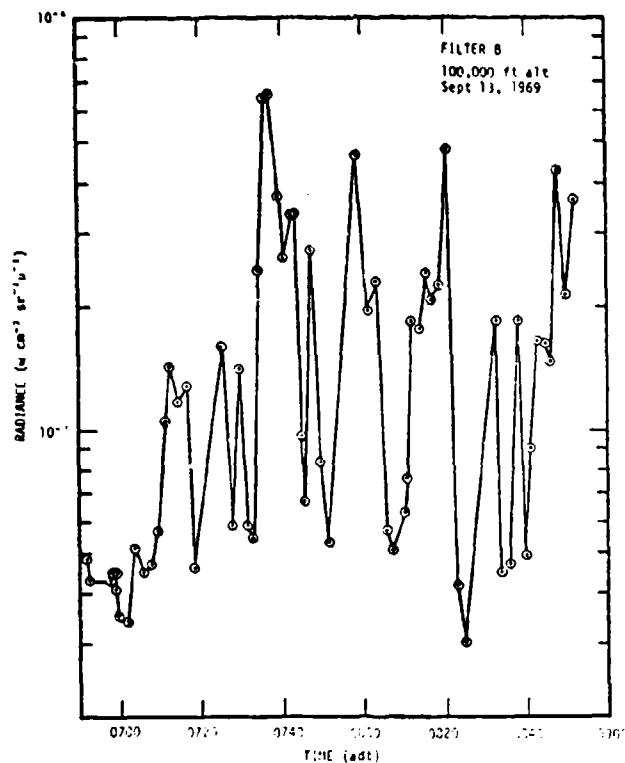


Figure 2-21. Time variation of radiance.

### 2.5.3. EARTH LIMB

Measurements of the earth limb are difficult because the radiance decreases rapidly with increases in tangent height (altitude of the sight path at its point of closest approach to the earth) which necessitates extremely good off-axis rejection. However, there have been several efforts to compute the radiance. This is complex at altitudes above about 70 km because many of the radiators are minor species for which the atmospheric concentration is not well known and excitation is not necessarily through kinetic collisions. Important processes are resonant absorption of earthshine infrared, fluorescence with solar UV or visible, vibrational luminescence with solar or auroral excited major atmospheric species and chemiluminescence. The computation that appears to agree best with the limited experimental data are those of Degges<sup>(2-6)</sup>. Some typical results are shown in Figure 2-23

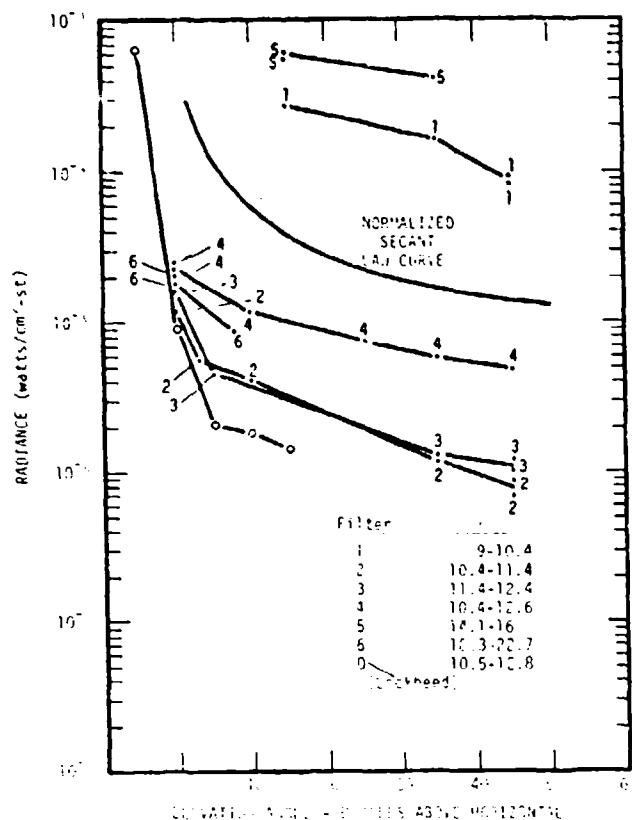


Figure 2-22. DC background levels.

(radiance in  $\text{w/cm}^2 \text{ ster}$  - wave number must be multiplied by  $10^4/\lambda^2(\mu)$  to obtain radiance in  $\text{w/cm}^2 \text{ ster } \mu$ ).

These computations included only minor species  $\text{CO}_2$ ,  $\text{H}_2\text{O}$ ,  $\text{O}_3$  and  $\text{NO}$ . Other computations have indicated there may be significant radiation by  $\text{CH}_4$  at  $6.55\mu$  and  $7.66\mu$ , by  $\text{N}_2\text{O}$  at  $4.5\mu$ ,  $7.78\mu$  and  $16.98\mu$  and by  $\text{NO}^+$  at  $4.27\mu$ , but the computations involving these species have not produced agreement with the experimental data on  $\text{O}_3$  and  $\text{CO}_2$  radiation and can not yet be taken to be quantitatively correct.

The computed data can be compared with data from the flight of a rocket-borne circular-variable-filter spectrometer into an auroral breakup<sup>(2-7)</sup>. The spectrometer was viewing the zenith. The most notable features in the

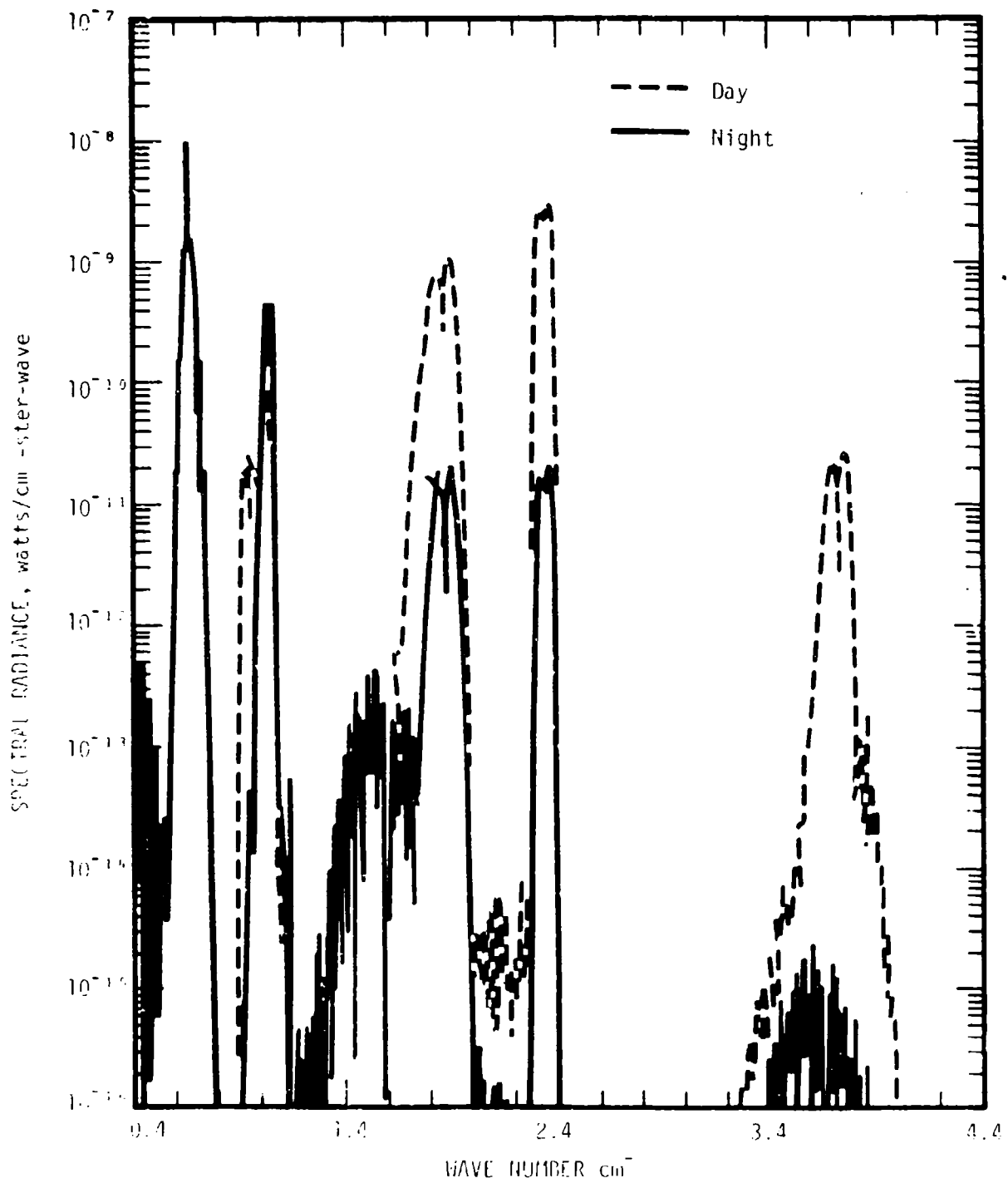


Figure 2-23. Limb viewing spectral radiance, 400 to 4000 cm<sup>-1</sup>, 100 km tangent height.



spectrum up to about 100 km were the  $9.6\mu$   $O_3$  and  $15\mu$   $CO_2$  bands (Figures 2-24 and 2-25). These bands should not be aurorally excited so this data should be representative of quiet conditions also. A comparison of the experimental and computed data are shown in Table 2-2. The agreement for the  $CO_2$  data indicates that the calculational procedures are adequate for that gas. The underestimation of the  $O_3$  data indicates that the concentration or excitation are underestimated. Without a field validation, currently it is probably unwise to ascribe a precision of better than an order of magnitude to such computations.

Data obtained with vertical viewing from a given altitude can be used to estimate limb viewing radiance for that tangent altitude. For an optically thin medium in which the emission can be taken as having a local scale height  $H_s$  (small compared to the geometric radius  $r_e$ ), the ratio of limb viewing to vertical radiance is

$$\frac{N_H}{N_V} = \sqrt{\frac{2\pi r_e}{H_s}} \quad (2-52)$$

( $CO_2$  is not optically thin in the center of the  $CO_2$  band for horizontal viewing unless the tangent height is above about 110 km.)

Table 2-2. Comparison of computed and measured radiances

Altitude km	9.6 $\mu$ - $O_3$ band		15.1 - $CO_2$ band	
	Computed	Measured	Computed	Measured
80	$5 \times 10^{-9}$	$3 \times 10^{-8}$	$2.5 \times 10^{-7}$	$9 \times 10^{-7}$
100	$2 \times 10^{-9}$	$1.3 \times 10^{-9}$	$1.1 \times 10^{-8}$	$4 \times 10^{-9}$
120			$8 \times 10^{-10}$	$4 \times 10^{-9}$
NOTE: Radiances are total band radiance in $w/cm^2$ ster				

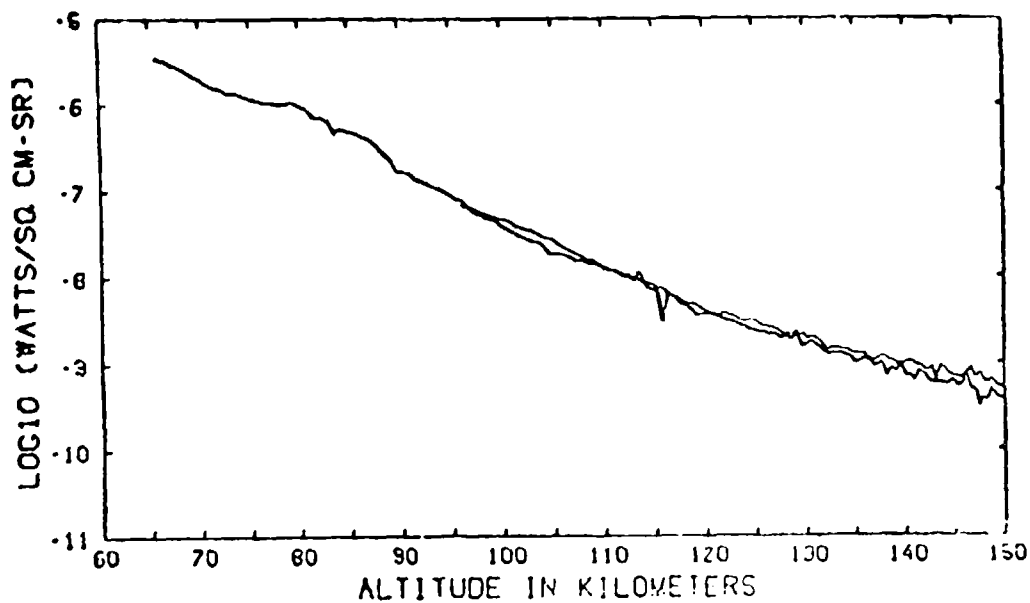


Figure 2-24. 15-μm CO<sub>2</sub> emission data.

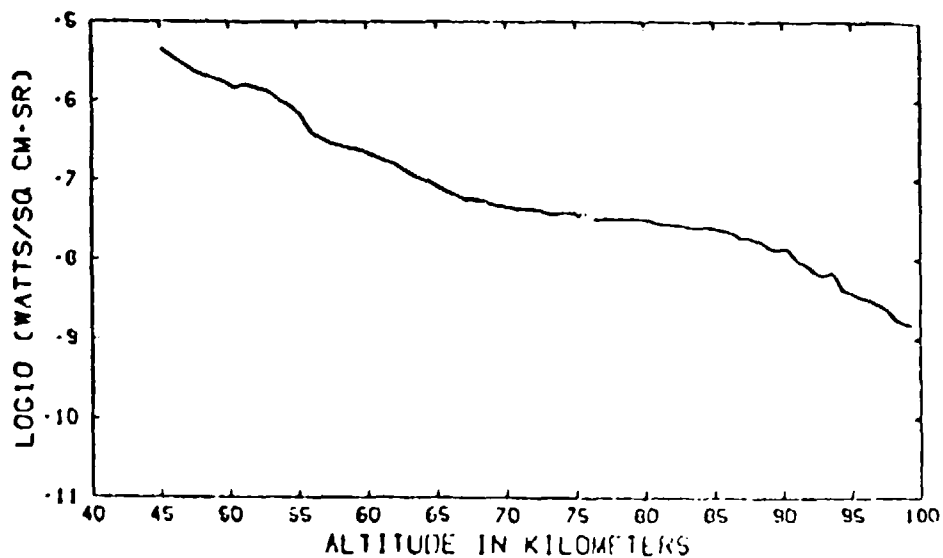


Figure 2-25. 9.6-μm O<sub>3</sub> emission data.

#### 2.5.4. AURORAL DISTURBANCES

There have been studies of possible chemical reactions and excitation mechanisms in aurora <sup>(2-8)</sup>. The only LWIR intensified by the auroral model used were the 10.4 and 13.9 $\mu$  lines of CO<sub>2</sub> excited by vibrational luminescence with electron excited N<sub>2</sub>. For tangent heights above 110 km, the limb viewing radiance in these aurorally excited lines is calculated to be less than 10<sup>-9</sup> w/cm<sup>2</sup> ster for an IBC-III aurora. Thus, it is not significant compared to the normally excited radiation in the LWIR.

Once again, caution must be used in the application of this computed data because the model used is similar to that in OSC which underestimated by orders of magnitude the natural 9.6 $\mu$  O<sub>2</sub> and 15 $\mu$  CO<sub>2</sub> bands.

#### 2.5.5. CELESTIAL BACKGROUND

For completeness the celestial background data of Walker and Price <sup>(2-9)</sup> are included here. All-sky maps of sources observed at about 4, 11 and 20 $\mu$  are shown in Figures 2-26, 2-27, and 2-28. The detector sensitivity was of the order of 10<sup>-15</sup> w/cm<sup>2</sup>  $\mu$  at 4 $\mu$ , 3 $\times 10^{-16}$  w/cm<sup>2</sup>  $\mu$  at 11 $\mu$  and 1.5 $\times 10^{-16}$  w/cm<sup>2</sup>  $\mu$  at 20 $\mu$ . A plot of the cumulative number density of stars as a function of irradiance is shown in Figure 2-29 and the data have been fit with the approximations

$$\begin{aligned} N_4 &= 4.3 \times 10^{-2} I_4^{-1.42} \csc(|b| + 10^\circ) \\ N_{11} &= 2.1 \times 10^{-3} I_{11}^{-1.29} \csc(|b| + 4^\circ) \\ N_{20} &= 6.2 \times 10^{-4} I_{20}^{-1.03} \csc(|b| + 1.5^\circ) \end{aligned} \quad (2-53)$$

where  $N_x$  is the number of sources per square degree at wavelength  $\lambda$ , with irradiances greater than  $I_x$  (in units of 10<sup>-15</sup> w/cm<sup>2</sup>  $\mu$ ) at a galactic latitude  $b$ . As is apparent from the maps the sources are non-uniformly distributed.

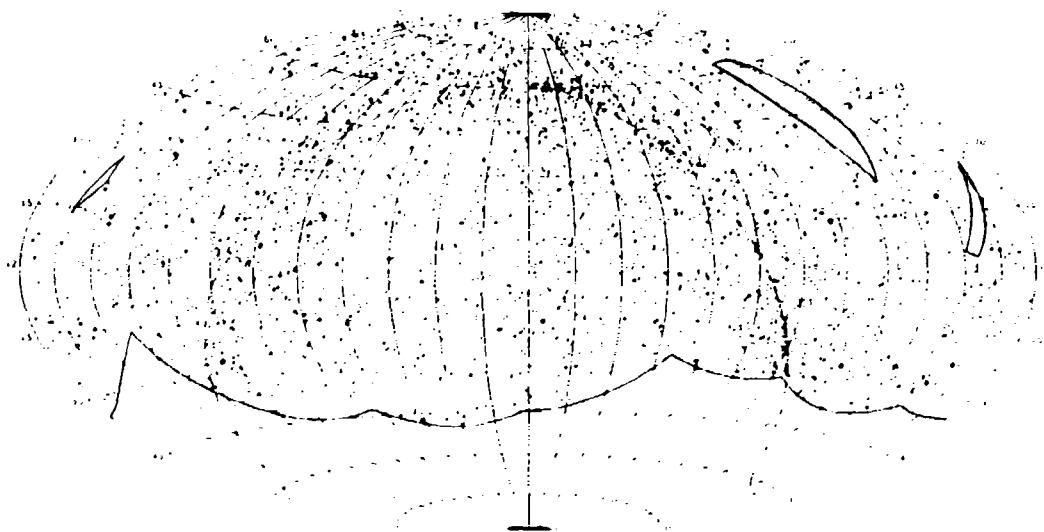


Figure 2-26. All-sky map of sources observed in the 4.2- $\mu$ m spectral region. The coordinates are right ascension in hours and declination in degrees.

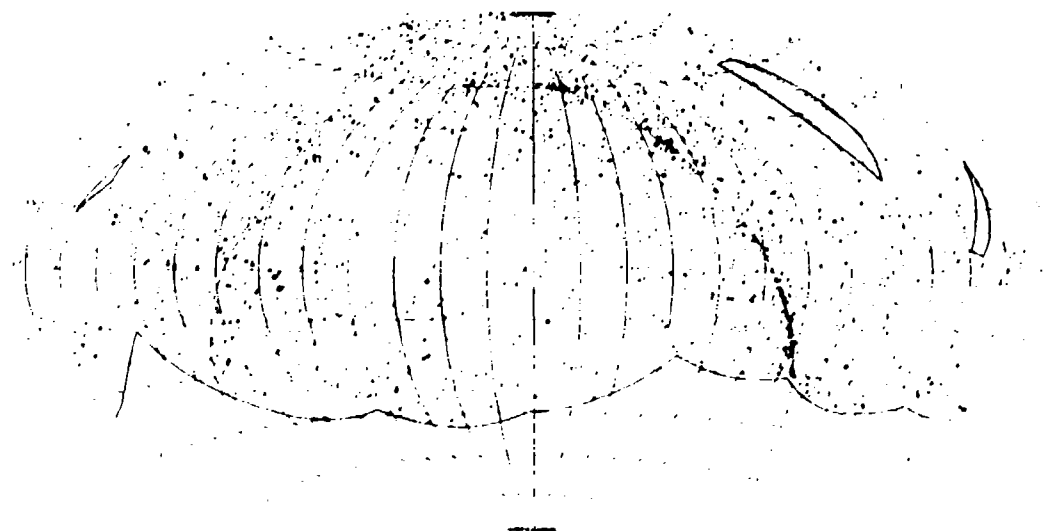


Figure 2-27. All-sky map of sources observed in the 11- $\mu$ m spectral region.

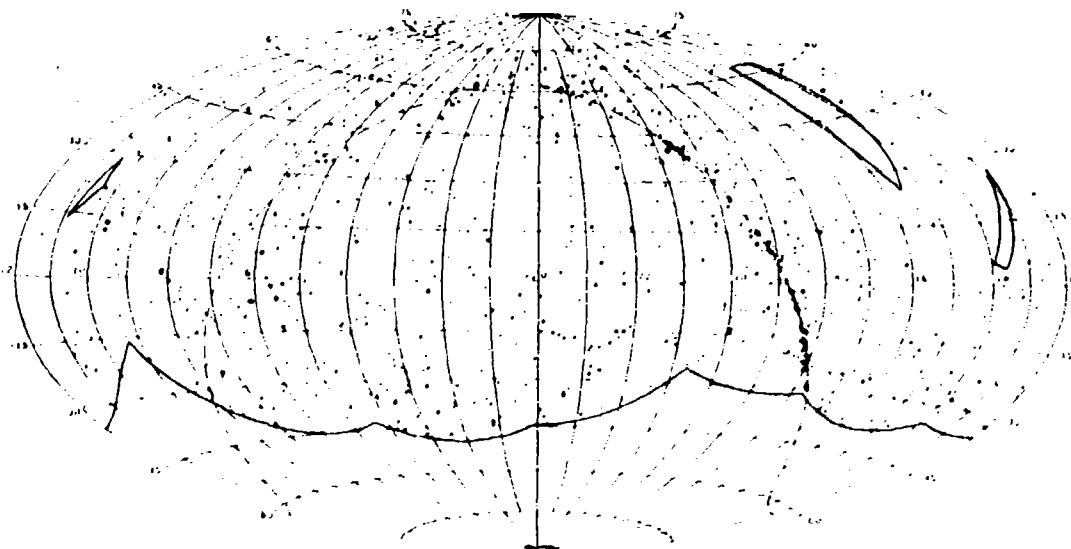


Figure 2-28. All-sky map of sources observed in the 19.3- $\mu$ m spectral region.

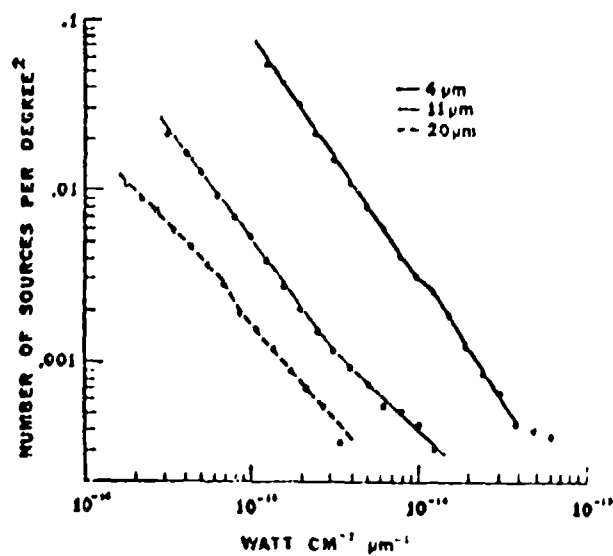


Figure 2-29. Mean source density versus spectral irradiance.

Distribution of the color temperature of objects based upon the irradiance ratio in two bands is shown in Figure 2-30. The dotted histograms are the actual data, the solid histograms are estimates of the actual distributions corrected for observational selection.

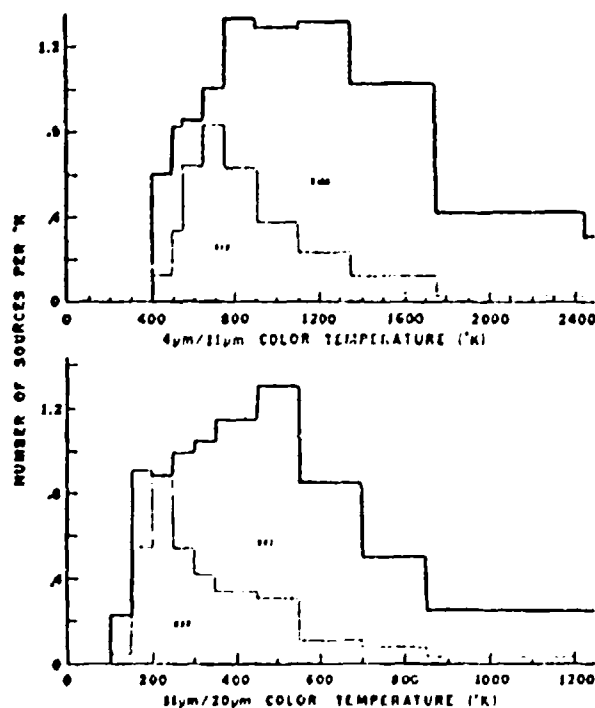


Figure 2-30. Color temperature distributions. The numbers 2188, 512, 902, and 238 are the area (no. of sources) under the appropriate curve.

## 2.6. DETECTOR DATA

There is a continuing advance in the state of the art of sensitive detectors. These advances include increased sensitivity, smaller detectors, larger arrays, and greater uniformity. Consequently, for current information one should contact the manufacturers. Material is given here only as guidance as to what materials are available for operation at various wavelengths and what may be expected with respect to sensitivity.

The characteristics of some infrared detectors are shown in Figure 2-31. It should be added that Si:As detectors are now available that cover about the same spectral range as Ge:Cd and have the added advantage of lower index of refraction (less reflection loss) and greater linear absorption coefficient (detectors can be made thinner and smaller in frontal area).

The data of Figure 2-31 are for operation against a 295°K background. Many cryogenically cooled detectors are operated in the background limited condition. Consequently, if the background were reduced to 100°K, the limit at 10 $\mu$  would be raised by a factor of 100, and that at 20 $\mu$  would be raised 10. For many space applications the background is even less and even greater sensitivities may be achieved.

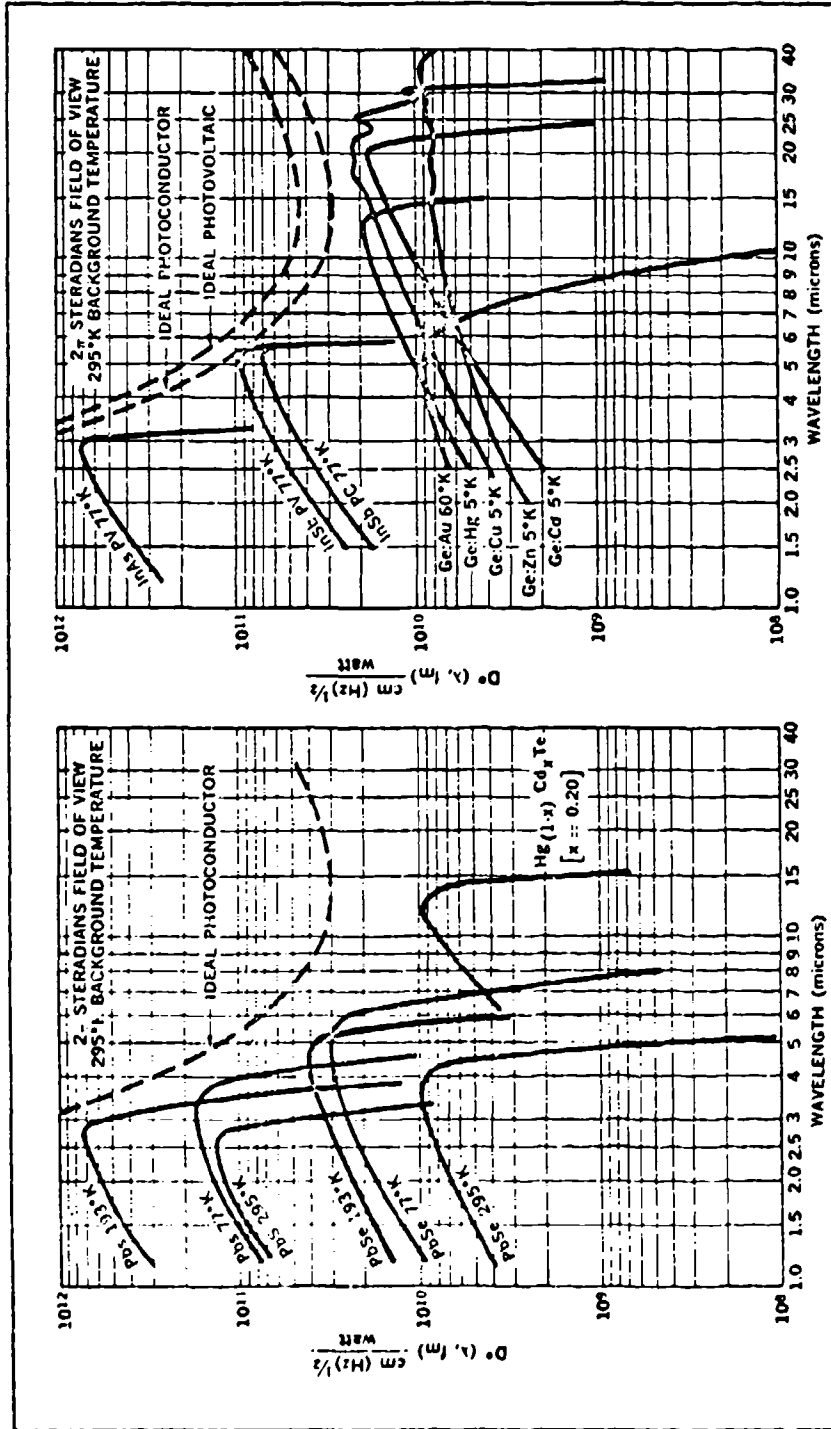


Figure 2-31. Spectral detectivities of infrared detectors. (Courtesy of Santa Barbara Research Center.)



## REFERENCES

- 2-1. Handbook of Military Infrared Technology, Office of Naval Research, W. L. Wolfe, Editor, 1965.
- 2-2. Mauro, J.A., Optical Engineering Handbook, General Electric Company, 1966.
- 2-3. Infrared Sensors and Off-Field Rejection, Volume III, Report No. 1003, The Te Company, January 1973.
- 2-4. Murcay, D.G., W. J. Williams, and J. N. Brooks, Balloon Flight 4 February 1970, University of Denver, May 1970.
- 2-5. Turner, V., Atmospheric Emission Gradients, Long Wavelength Infrared Backgrounds - Measurement Program II. Air Force Cambridge Research Labs, AFCRL-TR-74-0191, April 1974.
- 2-6. Degges, T. C., A High Altitude Infrared Radiance Model, VI-236 Visidyne, Inc., 27 December 1974.
- 2-7. Stair, A. T., Jr. J. C. Ulrick, K. D. Baker, and D. U. Baker, Rocketborne Observations of Atmospheric Infrared Emissions in the Auroral Region, to be published in Atmospheres of the Earth and Planets, ed. B. M. McCormac, D. Reidel (1975).
- 2-8. Bishop, R. H., R. Y. Han, A. W. Shaw and L. R. Megill, Infrared Radiance Model for the Aurorally Disturbed Atmosphere, Utah State University, AFCRL-TR-73-0527, 31 August 1973.
- 2-9. AFCRL Infrared Sky Survey, Volume I. Catalog of Observations at 4, 11, and 20 Microns, AFCRL-TR-75-0373, Air Force Cambridge Research Laboratories, July 1975.

## FIGURE CREDITS

<u>REFERENCE</u>	<u>FIGURE NO.</u>
2-1	7, 10, 11, 12, 14, 15, 16, 17
2-2	4
2-4	18, 19, 20, 21
2-5	22
2-6	23
2-7	24, 25
2-9	26, 27, 28, 29, 30
	31 (Santa Barbara Research Corp.)

## CHAPTER 3

### NUCLEAR PHYSICS AND NUCLEAR WEAPONS

Dan H. Holland\*

Mission Research Corporation

Charles H. Humphrey\*\*

Lockheed Palo Alto Research Laboratory

October 1973

\* Now at New Millennium Associates, Santa Barbara, CA

\*\* Now at Visidyne Inc., Burlington, Mass

## TABLE OF CONTENTS

	<u>PAGE</u>
LIST OF FIGURES	132
LIST OF TABLES	132
3.1 INTRODUCTION	133
3.2 NUCLEAR FORCES AND NUCLEAR STRUCTURE	136
3.3 NUCLEAR FISSION	140
3.4 NUCLEAR FUSION	145
3.5 CONCEPTUAL DESIGN OF NUCLEAR WEAPONS	146
3.5.1 Fission Weapons	146
3.5.2 Fusion Weapons	153
3.6 WEAPON OUTPUTS	156
3.6.1 Prompt Neutrons	157
3.6.2 Prompt Gammas	158
3.6.3 Prompt Alphas	158
3.6.4 Debris Kinetic Energy and Thermal X Rays	161
3.6.5 Delayed Betas	162
3.6.6 Delayed Gammas	170
3.6.7 Delayed Neutrons	177
REFERENCES	178

## LIST OF FIGURES

<u>FIGURE</u>	<u>PAGE</u>
3-1. Nuclear binding energies.	138
3-2. Percentage of fission yield vs mass number for $U^{235}$ .	143
3-3. Maxwell averages for thermonuclear reaction rates.	155
3-4. Prompt gamma energy spectrum from fission of $U^{235}$ .	159
3-5. Gamma energy release rate vs time from fission of $U^{235}$ .	160
3-6. Beta spectrum from fission of $U^{235}$ by a pulse of thermal neutrons.	165
3-7. Rate of beta radiation by fragments of $U^{235}$ from fission induced by thermal neutrons.	167
3-8. Radiated beta power from fission of $U^{235}$ by thermal neutrons.	169
3-9. Gamma energy release rate vs time from fission of $U^{235}$ .	171
3-10. Gamma energy release rate vs time from fission of $U^{235}$ .	172
3-11. Calculated gamma rates compared with measurements of Fisher & Engle.	174
3-12. Average gamma energy from fission of $U^{235}$ .	175
3-13. $U^{235}$ photon spectra at five times after fission.	176

## LIST OF TABLES

<u>TABLE</u>	<u>PAGE</u>
3-1. Beta decay rates from fission of $U^{235}$ by a pulse of thermal neutrons.	166
3-2. Delayed neutron emission.	177

## CHAPTER 3

### NUCLEAR PHYSICS AND NUCLEAR WEAPONS

#### 3.1 INTRODUCTION

The detonation of an explosive, either chemical or nuclear, is characterized by the release of a large quantity of energy into a restricted volume during a short time interval. The quantity of energy released is called the yield of the explosion, and is usually denoted by the symbol  $Y$  or  $W$ . The basic unit of yield used in the discussion of weapon effects is the energy released by the detonation of one ton of TNT. This unit is taken to be  $10^9$  calories, or  $4.18 \times 10^{16}$  ergs.

The yield of nuclear weapons is so much greater than that of chemical explosions involving comparable masses, however, that it is convenient to introduce larger units. The units generally used are the kiloton (KT), the yield of a one-thousand-ton TNT explosion, and the megaton (MT), the yield of a one-million-ton TNT explosion. Thus,  $1 \text{ KT} = 4.18 \times 10^{19} \text{ erg}$  and  $1 \text{ MT} = 4.18 \times 10^{22} \text{ erg}$ . The first nuclear weapons produced by the United States during World War II had yields of about 20 KT. This value is frequently referred to as "a nominal yield". Modern weapons have a very broad range of yields.

The energy in an explosion is liberated as a consequence of reactions that result in the formation of species more stable than those originally present in the bomb materials. In a chemical explosion the reactions are atomic or molecular, and result in the formation of new molecular species with a net release of energy. In nuclear weapons, nuclear reactions occur, both fission and fusion reactions acting to produce energy. Molecular binding energies are typically of the

order of 10 eV, while nuclear binding energies are of the order of 10 MeV, so that one might expect yields from nuclear weapons to be about a million times greater than those from chemical weapons of the same mass, and such is indeed the case.

The energy released in a reaction initially appears as excitation and kinetic energy of the reaction products. Since chemical binding energies are typically of the order of 10 eV, it follows that the excitation energies of the reaction products will also be of this order. Therefore, radiation from excited species produced in chemical reactions will comprise only photon energies of a few eV and thus will lie in the ultraviolet, visible, and infrared portions of the spectrum. Nuclear binding energies are of the order of 10 MeV, however, so the products of nuclear reaction may have excitation energies of this order. It follows that radiation from excited reaction products produced in a nuclear detonation has energies of several MeV. This radiation takes the form of gamma rays, neutrons, beta particles, and neutrinos. The nature and extent of the effects produced by the nuclear radiation are quite different from those produced by the low-energy radiation characteristic of chemical explosions, and give rise to a host of new, and in many cases unexpected, phenomena.

Only a small fraction of the yield from either type of weapon appears as the reaction product radiation discussed above. The bulk of the energy released is rapidly converted to internal energy of the weapon debris. For chemical explosions, the internal energy is about  $10^3$  cal gm<sup>-1</sup>, corresponding to temperatures of a few thousand degrees. The temperature increase is accompanied by a corresponding increase in pressure, and the bomb materials expand violently to produce the explosion. For chemical explosives the expansion velocities are a few kilometers per second, which is the speed of sound for gases at a few thousand degrees and corresponds to conversion of a substantial fraction of the yield to debris kinetic energy. During the expansion some fraction of the yield will also appear as thermal radiation. For chemical

explosions this fraction will be small because of the relatively low temperature, and for the same reason the radiation will lie principally in the visible portion of the spectrum.

In a nuclear explosion the yield is much greater, and the internal energies, pressures, and expansion velocities are correspondingly higher. Similarly a substantial fraction of the yield is emitted as thermal radiation with photon energies of the order of keV. For example, consider the detonation of a 1-MT device with a mass of 1000 kg. Then the internal energy is  $10^9$  cal gm<sup>-1</sup>. For such high energy densities, however, most of the energy is originally stored in the radiation field, rather than in the internal energy of the vaporized bomb materials. If we assume that the dimensions of the device are of the order of a meter, it can easily be shown that the blackbody temperature corresponding to the energy density in the field is of the order of a few keV. Much of this energy, say about half, will be radiated away as keV photons. If most of the remainder of the yield is converted to debris kinetic energy, the corresponding expansion velocity is several thousand kilometers per second.

In addition to the prompt gamma rays and neutrons, the x rays, and the debris kinetic energy, substantial intensities of delayed gammas and betas are radiated at much later times if part of the weapon yield is from fission. The yield in forms other than x rays and debris kinetic energy typically comprises 5 to 10 percent of the total.

In the following sections of this chapter a short discussion of nuclear structure and brief descriptions of the operation of fission and fusion weapons are given, the mechanisms responsible for radiation of the various forms of energy are discussed, and some data pertaining to spectral distribution, intensity, and time dependence of the radiation are presented.



### 3.2 NUCLEAR FORCES AND NUCLEAR STRUCTURE

Atomic nuclei consist of neutrons and protons (generically called nucleons) bound together by nuclear forces to form the nucleus. In spite of the fact that electrons and neutrinos are emitted by nuclei in the process of beta decay, these particles are not present within the nucleus, but are created in the decay process. In this section we give a short qualitative description of those aspects of nuclear forces most important from the standpoint of gaining a superficial understanding of the design and operation of nuclear devices. For detailed quantitative discussions of nuclear forces, the reader is referred to any of the several excellent texts on nuclear physics that cover this subject, e.g., Refs. 3-1, 3-2, 3-3.

Both atomic and nuclear systems are essentially quantum mechanical in nature, and accordingly are characterized by discrete sets of available energy levels and angular momentum states. However, nuclear forces are much stronger and of much shorter range than the coulomb forces primarily responsible for atomic binding. Therefore, nuclei are much smaller than atoms, and are much more tightly bound. We have already noted that nuclear binding energies are about  $10^6$  times greater than atomic binding energies. The ratio of the atomic and nuclear length scales is about  $10^5$ , typical atomic radii being about  $10^{-8}$  cm while typical nuclear dimensions are of the order of  $10^{-13}$  cm.

An important characteristic of the interaction among nucleons is the property of "saturation". The saturation of nuclear forces is discussed in many nuclear physics textbooks, and will not be considered in detail here. For our purposes it is sufficient to note that one consequence of saturation is that the binding energy per nucleon in a nucleus is approximately independent of the total number of nucleons present therein, and has the value of about 8 MeV per nucleon. The failure of the independence to hold exactly is very important, however, and it is just this failure that makes possible the release of large quantities of energy in nuclear explosions.

A nucleus can be characterized by two numbers, which give the number of protons and the total number of nucleons in the nucleus. These are called the atomic number and the mass number or atomic weight, and are denoted by  $Z$  and  $A$ , respectively. Thus for hydrogen  $Z = 1$ ,  $A = 1$ , for helium  $Z = 2$ ,  $A = 4$ , and for the most commonly occurring isotope of uranium  $Z = 92$ ,  $A = 238$ . Isotopes of a particular element are nuclei with the same  $Z$  but different  $A$ . Many elements have several different stable or long-lived unstable isotopes. A frequently used notation to denote a particular nucleus is  ${}_Z^AX$ . So, for example, the previously mentioned isotope of uranium is  ${}_{92}^{238}\text{U}$ , often written simply as  $\text{U}^{238}$ , since inclusion of both the chemical symbol and the atomic number is redundant.

In Fig. 3-1 measurements of binding energies of various nuclei in the range  $2 \leq A \leq 250$  are shown. The actual data points exhibit considerable scatter with respect to this smoothed curve, but the general shape of the curve is qualitatively correct. Although the binding energy per nucleon is slowly varying for intermediate values of  $Z$ , it is much lower than 8 MeV/nucleon for the very light elements, most notably deuterium ( $\text{H}^2$ ), tritium ( $\text{H}^3$ ) and  $\text{He}^3$ . For nuclei with large mass numbers the binding energies fall about an MeV per nucleon below those for intermediate mass number nuclei. It is the fact that the binding energies tend to be low for low and high mass numbers that makes possible the production of vast amounts of energy by the fusion of light nuclei and the fission of heavy nuclei.

That the binding energy curve should display the qualitative features shown in Fig. 3-1 can easily be understood. First we note without elaboration that the observed saturation of nuclear forces is interpreted to imply that a bound nucleon interacts only with its immediate neighbors rather than with all of the other nucleons present in the nucleus. Thus the forces saturate in a sufficiently large nucleus because the addition of more nucleons does not appreciably enhance the binding of the nucleons

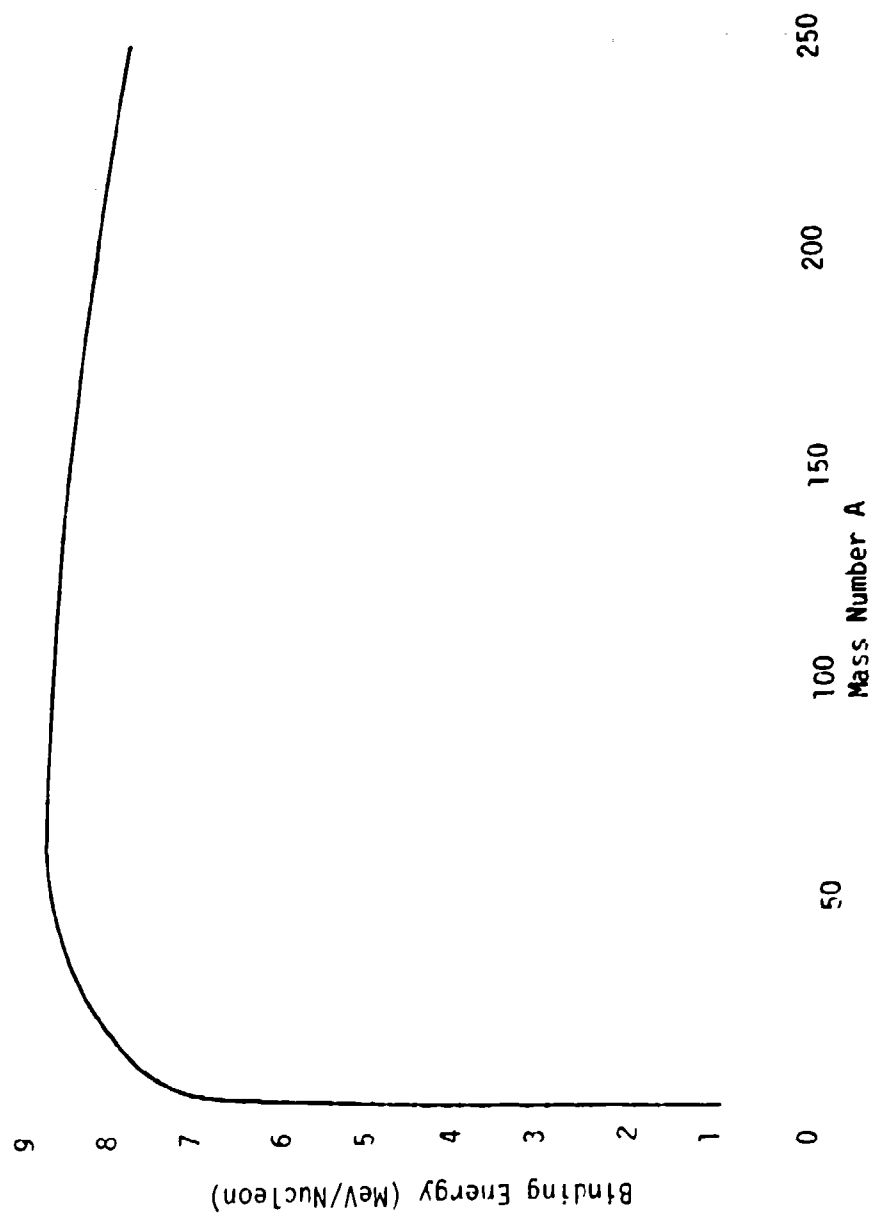


Figure 3-1. Nuclear binding energies.

already present, which have a full complement of neighbors with which to interact. This remark is not valid for nucleons near the nuclear surface, where there is a deficiency of partners with which to interact. The effect is analogous to surface tension at the surface of a body of liquid. The surface correction is of minor importance for large nuclei, but is all-important for very light nuclei, where all of the nucleons are near the surface, and hence are not being subjected to saturated forces. It is this surface effect that accounts for the decrease in average binding energy at low mass numbers.

For heavy nuclei the surface effect is of little importance, and the decrease in binding energy with increasing mass number stems from an entirely different reason. In the preceding discussion we have neglected the effects of the coulomb repulsion among the protons in the nucleus. The nuclear forces as we have used the term refer only to the strong, short-range, saturable forces between nucleons and are related to the coupling between nucleons through the  $\pi$ -meson field. The coulomb forces are of much longer range, but they are also much weaker than the nuclear forces, and play a relatively minor role in determining the structure of light nuclei.

The coulomb forces do not saturate, however. A proton therefore interacts with all the other protons in the nucleus, so the repulsive potential it experiences increases approximately linearly with  $Z$  and the total coulomb energy of all the protons increases roughly as  $Z^2$ . Because of their saturation the nuclear forces produce a total attractive energy that increases approximately only linearly with  $A$ . Hence the relative importance of the coulomb forces increases with increasing  $A$ . The increasingly important role played by coulomb repulsion is responsible for the decrease in average binding energy with increasing  $A$ .

The coulomb forces also lead to the neutron excess observed to occur in heavy nuclei. In light nuclei, where the coulomb forces are negligible,

the number of protons and neutrons present in stable nuclei are observed to be nearly equal. This means that the nature of the nuclear forces is such that when a heavier nucleus is formed by the addition of nucleons to a nucleus, the most stable configuration is attained when the addition is such as to maintain the approximate equality of the number of neutrons and protons.

If a light nucleus is formed with a large disparity between the number of neutrons and protons, the disparity will be reduced either by the emission of nucleons of the type in excess or, in some cases, by the process of beta decay. For heavy nuclei, the effect of the coulomb forces is to render the most stable those configurations that contain an excess of neutrons over protons. The neutron excess increases with increasing  $Z$  as the coulomb effects increase in importance. Thus  $U^{238}$  contains 146 neutrons, but only 92 protons.

### 3.3 NUCLEAR FISSION

Because of their lower binding energies, heavy nuclei are unstable against spontaneous fission into lighter nuclei. Thus referring to Fig. 3-1, we see that the binding energy per nucleon for  $U^{238}$  is about 7.6 MeV, while for  $A = 119$  the corresponding value is about 8.5 MeV/nucleon. Hence, symmetrical fission of  $U^{238}$  should yield about 0.9 MeV/nucleon, or a total of about 215 MeV. In spite of the large amount of energy available for release in the spontaneous fission of  $U^{238}$ , the process is very slow. The lifetime of an isolated  $U^{238}$  nucleus is greater than  $10^9$  years. Even this lifetime is determined by the rate of alpha decay, i.e., the process  ${}_{92}U^{238} \rightarrow {}_{90}Th^{234} + {}_2He^4 + 4.5 \text{ MeV}$ , rather than by the rate of symmetric or near-symmetric fission.

The stability of nuclei against spontaneous fission in spite of the large energy available for the process results from the fact that for fission to occur, a potential barrier must be penetrated. The process is similar to that of alpha decay as described by the well-known theory

of Gamow (Ref. 3-1); indeed, alpha decay of heavy nuclei may be regarded as a case of highly asymmetrical fission. In this section we present a semi-quantitative discussion of the fission process. Anyone interested in details should consult the excellent review article of Wheeler (Ref. 3-4) for more complete information and a more extensive bibliography.

Even though heavy nuclei are so stable with regard to spontaneous fission, i.e., fission in the absence of an external perturbation, the possibility of fast fission still exists and may be realized if the nucleus is perturbed in such a way that it gains enough energy to overcome the potential barrier. One mechanism for providing the required energy is neutron capture, and that is the process of interest in the present context. We have already noted that the mean binding energy per nucleon in a uranium nucleus is of the order of 7.6 MeV. Therefore, we might expect that the addition of another neutron would provide several MeV available to supply the energy required for fast fission. This is indeed the case; neutron-induced fission was first observed by Hahn and Strassmann late in 1938, and is the basis for the design of fission weapons and nuclear reactors.

The addition of a neutron to a  $U^{235}$  nucleus yields about 7 MeV of binding energy. The height of the potential barrier in uranium is about 6 MeV, so fission can be, and is, induced by the capture of slow neutrons. One might expect that this would also be true of  $U^{238}$ , but this is not the case because of a peculiarity of nuclear forces that we have not yet mentioned. When a nucleon interacts with a nucleus, the interaction is stronger if the nucleus contains an odd number of nucleons of the type with which the interaction is occurring. Since  $U^{235}$  contains 143 neutrons (odd) while  $U^{238}$  contains 146 (even), slow neutrons interact more strongly with  $U^{235}$  than with  $U^{238}$ . The excitation energy of the compound nucleus formed by adding a neutron to  $U^{238}$  is only about 5 MeV, or about an MeV below the fission threshold. Therefore  $U^{238}$  does not

undergo fission under bombardment by slow neutrons, but will fission when bombarded with neutrons having kinetic energies of the order of an MeV or higher. In this connection we mention that the mass 239 isotope of plutonium,  ${}_{94}\text{Pu}^{239}$ , also contains an odd number of neutrons, and fissions under bombardment with slow neutrons.  $\text{U}^{235}$ ,  $\text{U}^{238}$ , and  $\text{Pu}^{239}$  are the materials of greatest practical importance from the standpoint of nuclear weapons design.

When a nucleus fissions, it breaks into two lighter nuclei having approximately equal mass numbers. The most probable mode of fission is somewhat asymmetrical, however, and the fission fragment mass distribution curve has the characteristic double-humped form shown in Fig. 3-2, where the distributions for  $\text{U}^{235}$  undergoing fission induced by slow neutrons (thermal) and fast neutrons (14 MeV) are shown. The integral of each of the curves in Fig. 3-2 is 200 percent, a convention adopted to reflect the fact that each fission yields two daughter nuclei.

Since the ratio of neutrons to protons in stable (or metastable) nuclei increases with increasing  $Z$ , the fission products have an overabundance of neutrons. So great is the neutron excess, in fact, that during the fission process several free neutrons are emitted in addition to the heavy fission fragments. The number of neutrons released per fission increases approximately linearly with the kinetic energy of the bombarding neutron. For  $\text{U}^{235}$ , on the average about 2.4 neutrons are released in fission induced by thermal neutrons, whereas the corresponding neutron yield is about 4.5 per fission for reactions induced by 15 MeV primary neutrons. The  $\text{Pu}^{239}$  neutron fission yields for thermal and 15 MeV neutron primaries are about 3 and 5, respectively. For  $\text{U}^{238}$  the number of prompt neutrons per fission is about 2.5 near threshold ( $\sim 1$  MeV) and about 4.5 for 15 MeV primary neutrons. The mean number of prompt neutrons is denoted by  $\nu_p$ ; additional data on this quantity are given in Ref. 3-5. The number of prompt neutrons in a particular event depends on the masses of the fission fragments, as discussed in Ref. 3-6.

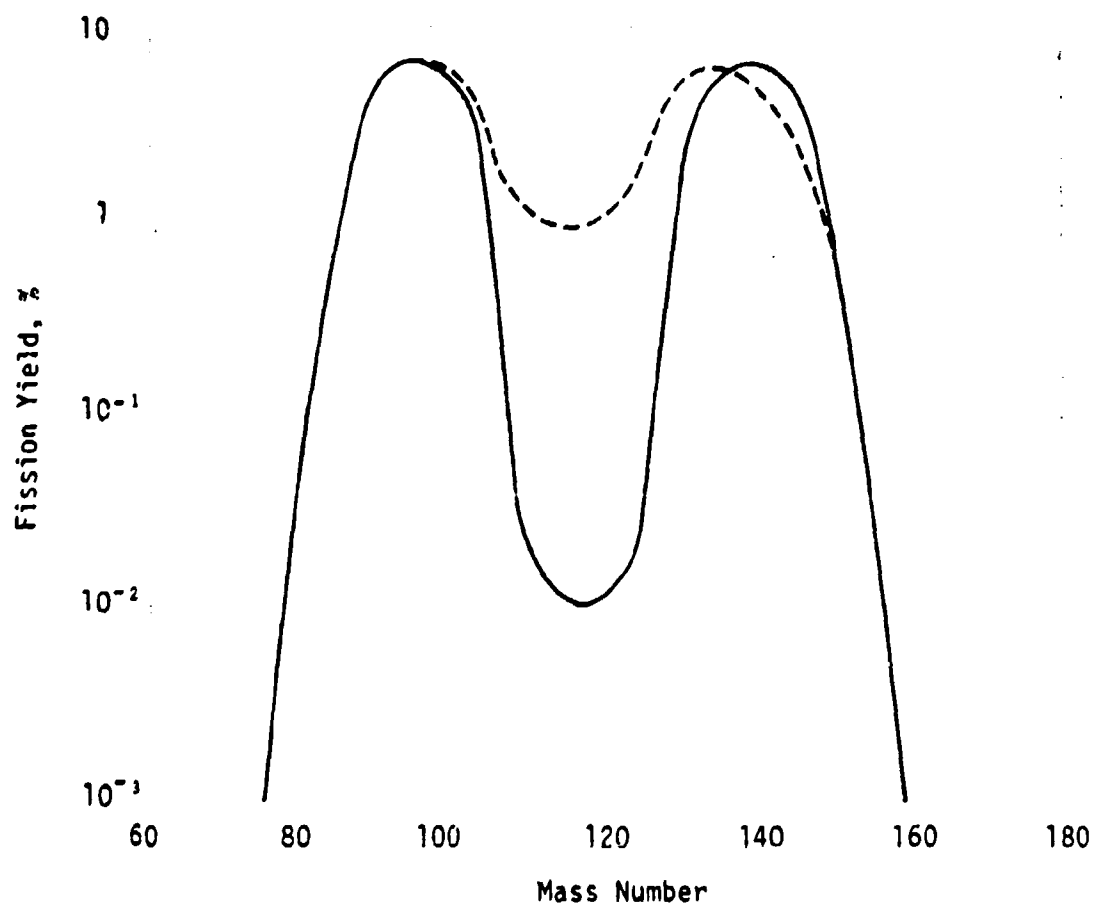


Figure 3-2. Percentage of fission yield vs. mass number for  $U^{235}$ . The solid curve refers to slow neutrons and the dashed curve to 14 MeV neutrons.



The overabundance of neutrons in the fission product nuclei is only partially corrected by the emission of prompt neutrons during the fission process. The daughter nuclei still have a higher ratio of neutrons to protons than stable isotopes of the same atomic weight. After fission and the emission of the prompt neutrons, the subsequent approach to a stable neutron-to-proton ratio is effected primarily through the process of beta decay. (A few cases of delayed neutron emission also occur and are discussed below.) Since the beta-active species are neutron-rich, virtually all of the betas emitted are negative. Thus a single beta decay has the effect of increasing the number of protons by one and decreasing the number of neutrons by one, while leaving the mass number constant. It is these transitions that account for the delayed betas emitted by fission fragments. The probability is high that the daughter nucleus resulting from beta decay is born in an excited state. When this occurs, the excitation energy is radiated away in the form of gamma rays.

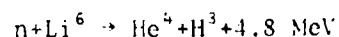
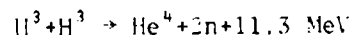
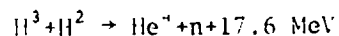
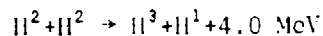
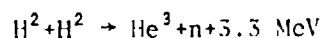
The crude estimates made above gave 215 MeV as the energy yield from a fission reaction. The actual mean yield for fission of  $U^{235}$  by slow neutrons is more nearly 200 MeV. The energy partition, as given by Wheeler (Ref. 5-4) is as follows:

kinetic energy of fission fragments	168 MeV
prompt gammas	~ 5
prompt neutrons	5
delayed gammas	~ 5
delayed betas	6
neutrinos	10
alpha particles	0.04
delayed neutrons	<u>0.008</u>
Total	~ 199 MeV

In addition to the energy released by fission, some gamma rays are also radiated as a result of the  $(n,\gamma)$  reaction discussed above. Details of the time dependence, spectra, etc. of the various radiations are discussed in following sections.

### 3.4 NUCLEAR FUSION

For light nuclei, the possibility of fusion to form heavier nuclei with the release of energy exists. The fusion reactions with which we are concerned here are:



where the yields of the various reactions are those deduced from the nuclear binding energies given by Wapstra (Ref. 5-7). With the exception of the last one, all of these reactions involve two charged particles in the initial state, and therefore a substantial kinetic energy of the reacting particles is required to overcome the coulomb barrier between them. The last reaction cannot be self-sustaining by itself, however, since it does not replace the neutrons consumed in the reaction.

To estimate the height of the coulomb barrier to be overcome, we assume that for separations greater than some value  $a$  the coulomb forces dominate the nuclear forces. Therefore the interacting particles must have sufficient relative kinetic energy to surmount a coulomb potential barrier whose height is of order  $e^2/a$  where  $e$  is the electronic charge. Deuterons are very loosely bound and consequently have a radius considerably larger than the range of the nuclear forces. Although the radius of the deuteron is an ill-defined concept, it is sufficient for our purposes to take it to be  $\sim 5 \times 10^{-13}$  cm, and the value of  $a$  to be twice the radius, or  $10^{-12}$  cm. Then  $e^2/a \sim 150$  keV, and for reactions to occur at their maximum rate, the kinetic energy of the particles must be of this order or greater.

The energy released in a fusion reaction initially appears as kinetic energy of the reaction products, residual excitation of the product

nuclei being negligible for most considerations. The final states of all the reactions listed above have only two particles and therefore the energy yield is divided between these two particles in inverse proportion to their masses, since by momentum conservation both particles have the same momentum. Thus the 17.6 MeV released in the third reaction appears initially as 14.1 MeV of neutron kinetic energy and 3.5 MeV of He kinetic energy. The neutrons released in this and others of the reactions listed may also interact with  $\text{Li}^6$ , if it is present, to produce an additional yield of 4.8 MeV per neutron.

To compare the specific energy yield, i.e., the yield per unit mass of reactants of fusion and fission reactions, we recall that about 200 MeV is released in the fission of  $\text{U}^{235}$ , so the yield is about 0.85 MeV per nucleon. As an example of a fusion device, consider a system consisting of pure deuterium ( $\text{H}^2$ ), and assume that a self-sustaining chain reaction can be made to occur. The branching ratio for formation of  $\text{H}^3$  and  $\text{He}^3$  in the collision of two deuterons is near unity (Ref. 3-8) and therefore the rates of the first two reactions are nearly equal. The concentration of  $\text{H}^3$  is determined by the interplay between the second and third reactions. The concentration of  $\text{H}^3$  will rapidly approach a value such that the production and loss rates are nearly equal. Thereafter the  $\text{H}^3$  concentration follows that of  $\text{H}^2$  as the latter is depleted by further reactions. Of every five deuterons initially present, we expect that two will be consumed in the first reaction, two in the second, and one in the third (by reacting with the  $\text{H}^3$  produced in the second). Thus an initial mass of 10 units produces a yield of about 25 MeV, or 2.5 MeV per nucleon, and the specific yield of deuterium fusion is about three times as large as that estimated above for U or Pu fission.

### 3.5 CONCEPTUAL DESIGN OF NUCLEAR WEAPONS

#### 3.5.1 FISSION WEAPONS

The possibility of a self-sustaining chain of fission reactions among a collection of fissionable nuclei stems from the fact, mentioned above, that for every neutron absorbed to produce fission several additional

neutrons are emitted. Thus there is a multiplication in the number of neutrons available to trigger fission, and one might expect the rate of fission to increase exponentially. On the other hand, several other neutron loss mechanisms compete with fission, and this tends to decrease the multiplication factor. If the multiplication factor falls below unity, the reactions are not self-sustaining, and both the neutron flux and the rate of fission tend exponentially to zero. If the multiplication factor exceeds unity, the neutron flux and fission rate, and thus the rate of release of energy, increase exponentially with time, and an explosion occurs. If the multiplication factor is unity, neutrons are replaced at the same rate they are lost, the neutron flux and fission rate remain constant, and energy is released at a constant rate. The latter situation is that which obtains in a nuclear reactor, where controls are introduced to maintain the neutron multiplication factor at or near unity.

In designing a chain reacting device, either a reactor or a weapon, the various neutron loss mechanisms not leading to fission must be taken into account. The loss mechanisms of interest are:

1. Escape of neutrons through the walls of the device.
2. Neutron capture not resulting in fission.
3. Inelastic scattering, which in the case of isotopes with a non-zero fission energy threshold, e.g.,  $U^{238}$ , may reduce the energy of an initially energetic neutron below the threshold.

The first loss mechanism, escape, implies that there is a critical mass of fissionable material such that if the mass available is less than the critical mass, a chain reaction cannot occur. For example, suppose that the only reaction between neutrons and nuclei is neutron capture leading to fission. If the cross section for this process is  $\sigma_f$  and the nuclear density is  $N$  ( $\text{cm}^{-3}$ ), the fission mean free path is  $\lambda_f = (N\sigma_f)^{-1}$ . If a neutron is produced within a sphere of radius  $R$ ,

on the average it will be absorbed and result in fission if  $R \gg l_f$ , but if  $l_f \gg R$ , most of the neutrons escape and the chain reaction is damped because of the neutron loss. The average kinetic energy of the neutrons released in the fission of  $U^{235}$  is about 2 MeV (Ref. 3-4). For  $U^{235}$   $N \sim 5 \times 10^{22} \text{ cm}^{-3}$ , and the fission cross section for 2 MeV neutrons (Ref. 3-5) is  $\sigma_f = 1.3 \text{ barn}$  (1 barn =  $10^{-24} \text{ cm}^2$ ). Hence  $l_f \sim 15 \text{ cm}$ , so one would expect a sphere of  $U^{235}$  with  $R > 15 \text{ cm}$  to be supercritical.

In the above argument we have neglected the role of elastic scattering in trapping the neutrons. The scattering cross section is greater than the fission cross section, so on the average a neutron is scattered several times before producing fission. The scattering is nearly isotropic, so the neutrons perform a random walk. After  $n$  scatterings they have traveled a total distance  $n l_s$ , but are only displaced a distance  $n^{1/2} l_s$  from their point of origin. The number of scatterings before absorption is  $n = l_f / l_s$ . The neutron will be absorbed before escaping if  $R > n^{1/2} l_s = \sqrt{l_f l_s} = l_f (\sigma_s / \sigma_f)^{-1/2}$ . For 2 MeV neutrons,  $\sigma_s / \sigma_f \sim 2.7$ , so the radius of a barely critical sphere of  $U^{235}$  is reduced to about 9 cm and the critical mass to about 50 kg.

The second neutron loss mechanism, capture not resulting in fission, also effectively decreases the neutron multiplication factor. The capture process of greatest importance is the  $(n, \gamma)$  reaction, i. e., a reaction where a neutron is captured to form an excited nucleus which then radiates its excitation energy away in the form of gamma rays. For example, the cross section for  $U^{235}(n, \gamma)U^{236}$  is about 0.1 barn as compared with the fission cross section of 1.3 barn for 1 MeV neutrons. Thus about ten percent of the neutrons are lost in the  $(n, \gamma)$  reaction.

The third loss mechanism tending to decrease the effective neutron multiplication factor is inelastic scattering. In the case of  $U^{235}$  and  $Pu^{239}$ , inelastic scattering has little effect, for two reasons. First, the inelastic cross sections are small compared to the fission

cross sections, so only a small fraction of the neutrons are degraded in energy by inelastic collisions before being captured in a fission reaction. Second, since the fission threshold energy is zero for these isotopes, even those neutrons that do get degraded can still trigger fission, and will do so unless captured in an  $(n, \gamma)$  reaction.

The effect of inelastic scattering on  $U^{238}$  is quite different from that on  $U^{235}$  and  $Pu^{239}$ . The inelastic cross sections for MeV neutrons on  $U^{238}$  are much larger than the fission cross section, while at the same time  $U^{238}$  has an effective fission threshold energy somewhat above 1 MeV. Thus MeV neutrons introduced into  $U^{238}$  almost certainly fall below threshold before producing a fission, and a self-sustaining chain reaction in pure  $U^{238}$  is impossible regardless of the mass and dimensions of the material. This fact is of the utmost importance, since more than 99 percent of natural uranium occurs in the isotopic form  $U^{238}$ , and  $Pu^{239}$  is so rare in nature that the only practical method of obtaining a sizeable quantity is by neutron bombardment of  $U^{238}$ , which produces  $Pu^{239}$  through the reaction chain  $U^{238}(n, \gamma) U^{239}(\beta^-) Np^{239}(\beta^-) Pu^{239}$ .

Each neutron produces 2.6 additional neutrons when it is captured in a fission reaction, but is lost itself in the process, so the net gain is 1.6 neutrons per fission, and losses by escape and capture lower this still farther, say to about 1.5. If  $\tau$  is the time of flight of a neutron between production and capture, therefore, its average rate of producing neutrons is  $1.5\tau^{-1}$ . Thus, the variation of the neutron density,  $n$ , is governed by the differential equation

$$\frac{dn}{dt} = \lambda n \quad (3-1)$$

For an initial neutron density  $n_0$ , the solution is

$$n = n_0 e^{1.5\tau^{-1}t} = n_0 e^{1.5(t/\tau)} \quad (3-2)$$

The velocity of MeV neutrons is about  $10^9 \text{ cm sec}^{-1}$ . If the density of  $\text{U}^{235}$  nuclei is  $N \sim 6 \times 10^{22} \text{ cm}^{-3}$  and the fission cross section is  $\sigma_f \sim 1.5 \times 10^{-24} \text{ cm}^2$ , the time of flight  $\tau$  is

$$\tau \sim \frac{1}{N\sigma_f v} \sim 10^{-8} \text{ sec} \quad (3-3)$$

Thus the time for the neutron density to increase by a factor of  $e$  is  $\sim 10^{-8} \text{ sec}$ , and the time for complete fission of a supercritical mass of  $\text{U}^{235}$ , assuming only 2 MeV neutrons are present, is of the order of a microsecond. Because of the exponential nature of the energy release, however, most of the energy is triggered by the last few generations of neutrons, i.e., in the last few intervals of length  $\tau$ , so the bulk of the energy is released in a few shakes (1 shake =  $10^{-8} \text{ sec}$ ).

From the foregoing discussion it is clear that a self-sustaining fission chain reaction is possible in principle. Before such a reaction can be attained, however, a number of practical engineering difficulties must be overcome. Substantial quantities of  $\text{U}^{235}$  or  $\text{Pu}^{239}$ , must first be obtained. None of these is readily available in nature.  $\text{U}^{235}$  does occur in considerable abundance, but must be separated from the  $\text{U}^{238}$  with which it occurs. This is a formidable task, since  $\text{U}^{235}$  constitutes only 0.7% of naturally occurring uranium. One of the major accomplishments of the Manhattan Project was devising procedures for separating  $\text{U}^{235}$  from  $\text{U}^{238}$  in sufficient quantity for constructing the first nuclear weapons, and for building reactors in which  $\text{Pu}^{239}$  could be produced by the absorption of fission neutrons by  $\text{U}^{238}$ , as discussed above. At that time the word tuballoy (Tu) was coined for naturally occurring uranium, and oralloy (Oy) was used to denote uranium in which the  $\text{U}^{235}$  content had been enriched. These words still have some currency, particularly in the nuclear weapons community.

Once a critical mass of fissionable material has been acquired, a second practical problem presents itself. The reactions will not be self-sustaining unless a supercritical mass is assembled, but once assembled,

an explosion can be triggered by a stray neutron. Since free neutrons abound in nature and are difficult to shield because of their electrical neutrality, the critical mass cannot be assembled until the actual moment when the explosion is desired.

An important consideration in the problem of accomplishing critical assembly is the fact that the critical mass depends on the density of fissionable nuclei. An increase in the density decreases the critical mass. This follows from the fact that the probability that a neutron escapes from a sample of material having a given mass decreases with increasing density of the material. If  $L$  is a length characterizing the dimensions of a sample of mass  $M$ , the nuclear density varies as  $ML^{-3}$ , so the mean free path varies as  $M^{-1}L^3$ . The distance that the neutron must traverse in escaping increases only linearly with  $L$ , so the escape probability for a given mass decreases with decreasing  $L$ , i.e., with increasing density. It follows that at higher densities the critical mass is lower.

Two methods of accomplishing critical assembly are commonly discussed. In one method, two subcritical masses are brought together to form a critical mass. As soon as the assembly becomes critical, however, the release of energy begins, and the assembly tends to blow itself apart before fission of a large fraction of the nuclei can occur. Therefore, the subcritical pieces must be brought together very rapidly. This is done by explosively firing one of the masses from a device similar to a gun barrel in such a way that it collides with the other mass and the combination becomes supercritical.

The second makes use of the fact that the critical mass decreases with increasing density. Thus a slightly subcritical mass becomes critical when sufficiently compressed. The compression is effected by detonation of a chemical explosive. For example, a spherical shell of high explosive could be placed around a sphere of  $U^{235}$  or  $Pu^{239}$ . By judicious choice of the exact configuration and the manner in which the explosive



is ignited, a strong imploding shock wave can be produced in the fissionable material. The compression produced by the shock can be sufficient to make the system go critical, and a nuclear explosion occurs.

Both methods of accomplishing critical assembly are very simple conceptually, but it is clear that great care and sophistication must be exercised in their actual design if the devices are going to be both safe and efficient. One practical problem was mentioned above, namely the tendency of the fissionable material to expand and become subcritical before much of the energy potentially available is released.

A second problem is prevention of the loss of neutrons from the system. Neutron loss decreases the net multiplication factor  $k$  as discussed above, thus increasing the time required for the nuclear burn to occur and complicating the problem of mitigating the effects of disassembly. Indeed, measurement of  $k$  provides a useful diagnostic tool for determining the efficiency of various devices. The loss of neutrons is minimized by surrounding the fissionable material with a shield to scatter neutrons attempting to escape back into the reaction region. This shield, called the tamper, is frequently made of  $U^{238}$  and may add to the yield of the device by virtue of  $U^{238}$  fission by fast neutrons.

To gain some idea of the efficiencies actually attained in nuclear weapons, we note our previous estimate of critical mass indicated that a barely critical assembly would be about 9 cm in radius. The nuclear density was assumed to be  $5 \times 10^{22}$  cm<sup>-3</sup>, so the critical mass contains a total of about  $10^{26}$  nuclei. If we assume that all of these were to fission with a yield of 200 MeV, the total yield would be about  $3 \times 10^{27}$  erg, or nearly a megaton. It follows that the fission efficiency of a 1 kt weapon is at most of the order of a tenth of a percent, unless the critical mass is reduced substantially below 50 kg by compression upon implosion.

### 3.5.2 FUSION WEAPONS

The possibility of initiating self-sustaining fission reactions hinges on the fact that some isotopes have large fission cross sections for slow neutrons, so the reaction can be triggered with a relatively minor energy input. The large cross section for slow neutrons is in turn dependent upon the fact that neutrons are electrically neutral, so even low-energy neutrons can easily penetrate the nucleus and enter the region where the strong, short-range nuclear forces come into play.

In contrast to the neutron-induced fission reactions, the rate of fusion reactions is impeded by the coulomb barrier discussed in Section 3.4. Because of the coulomb barrier the average energy of the fusion reactants must be high before the rapid release of energy by fusion can occur. A high average energy implies a high effective temperature--hence the term thermonuclear to describe devices that release energy by nuclear reactions only after having been raised to a very high temperature. The temperature required is considerably lower than the 100 keV one might guess from the coulomb barrier argument, both because of the fact that the cross sections fall off rather slowly with decreasing energy and because only a small fraction of the particles in the high energy tail of the energy distribution need be energetic enough to react.

To estimate the temperature required for significant energy release by fusion, we first note that once the reactions have been initiated, they must proceed rapidly enough to overbalance energy loss by the system, since otherwise the temperature will fall, the reaction rate will decrease accordingly, and soon the reactions will effectively cease to occur. The rate  $q$  at which reactions occur is

$$q = \langle \sigma v \rangle N_1 N_2 \quad (\text{cm}^{-3} \text{ sec}^{-1}) \quad (3-1)$$

where  $N_1$  and  $N_2$  are the particle densities of the reactants and  $\langle \sigma v \rangle$

is the mean value of the product of the reaction cross section and the relative velocity taken over an appropriate distribution. If the energy release per fusion is  $Q(\text{keV})$ , the rate of energy generation is

$$\frac{d\epsilon}{dt} = \langle \sigma v \rangle N_1 N_2 Q \quad (\text{keV cm}^{-3} \text{sec}^{-1}) \quad (3-5)$$

where  $\epsilon$  denotes the energy density within the reaction volume.

Next we assume rather arbitrarily that energy losses dictate that  $\epsilon$  be doubled in a time  $\Delta t$  of the order of a shake. The criterion for reaction of a large fraction of the potential reactants is then

$$\frac{d\epsilon}{dt} \Delta t > \epsilon \quad (3-6)$$

or, assuming  $N_1 \sim N_2 \sim N$ , and an equilibrium distribution at temperature  $T$  so that  $\epsilon \sim \frac{3}{2} NkT$ ,

$$\langle \sigma v \rangle N Q \Delta t > 3/2 kT \quad (3-7)$$

As an average energy release per fusion, assume  $Q \sim 10 \text{ MeV} = 10^4 \text{ keV}$ , and take  $N \sim 5 \times 10^{22} \text{ cm}^{-3}$ , corresponding to the density of liquid hydrogen. Then if  $T_k$  denotes the temperature expressed in keV, the criterion is

$$\langle \sigma v \rangle > 3 \times 10^{-19} T_k \quad (3-8)$$

In deriving this expression we have ignored the fact that some of the energy is converted to thermal radiation. A proper accounting of energy would lead to the requirement of somewhat higher temperatures than those inferred from this criterion.

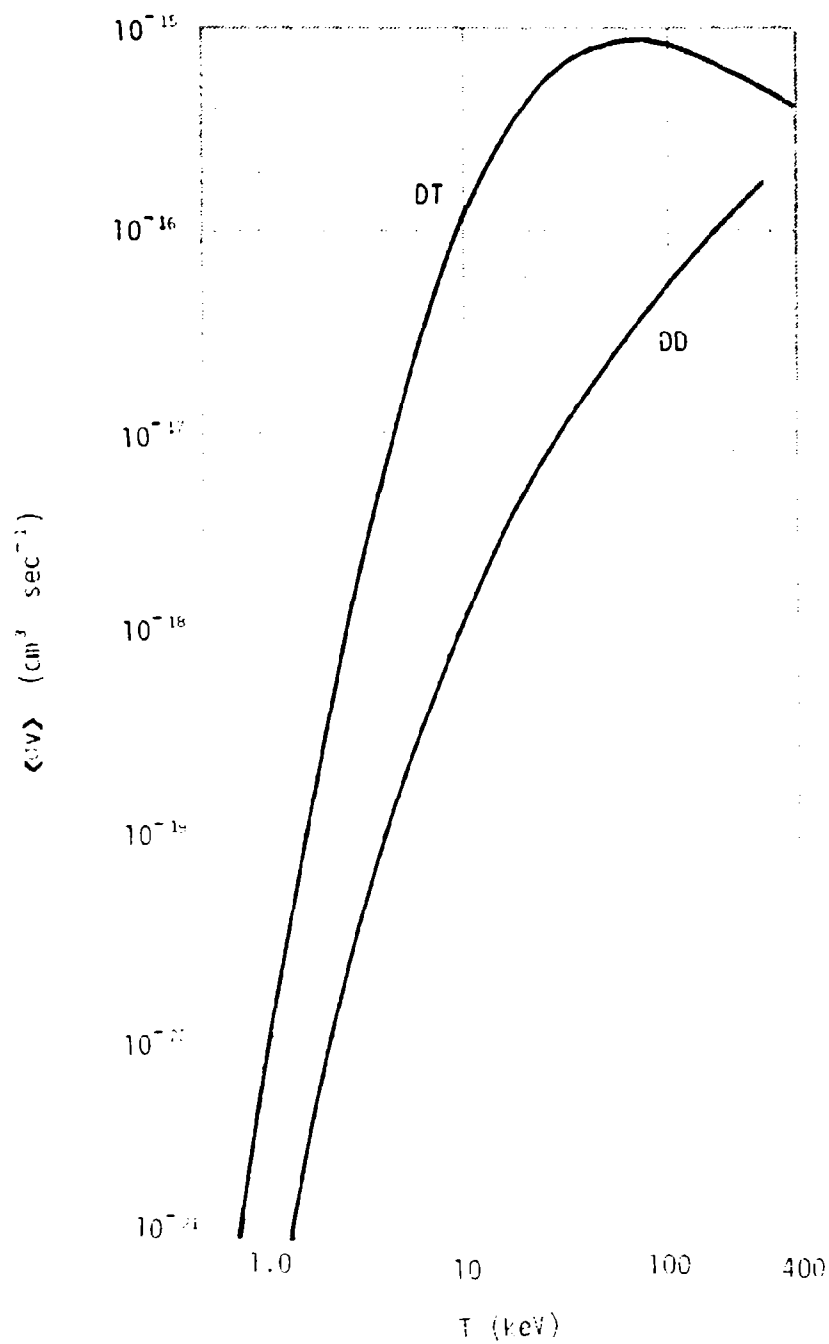


Figure 3-3. Maxwell averages for thermonuclear reaction rates (J.L. Tuck, LASL).

The rate constants  $\langle\sigma v\rangle$  for the fusion of deuterium and tritium (DT) and for two deuterons in pure deuterium (DD) are shown in Figure 3-3 for equilibrium energy distributions. At low temperatures the rate for the DT reaction is nearly two orders of magnitude greater than that for DD because of a resonance in the DT reaction at about 100 keV. According to the previously written criterion, the critical temperatures for initiating self-sustaining reactions are about 2.5 and 25 keV for DT and DD, respectively.

Even temperatures of the order of a keV are not easily attainable. However, as pointed out above, temperatures of this order are achieved in nuclear detonations, which opens the possibility of igniting a thermonuclear device with a fission device. This is the method used in thermonuclear weapons, where a fission device is detonated to heat a mass of light elements to temperatures sufficiently high for a self-sustaining thermonuclear reaction to occur. In some cases, where the presence of fission fragments may be considered unimportant, the entire device may be encased with  $U^{238}$  so additional energy is liberated in the fission of  $U^{238}$  by the fast neutrons produced in the fusion reactions.

### 3.6 WEAPON OUTPUTS

A distinction must be drawn between the form in which the energy from a nuclear detonation is originally released in the various reactions and the form that it has assumed by the time it has escaped the immediate vicinity of the burst point and has begun to interact with the surrounding medium. In both fission and fusion reactions, most of the energy initially appears as kinetic energy of the reaction products. The ranges of the reaction products are so short, however, that they rapidly lose their energy in collisions with other components of the warhead and its associated paraphernalia, and their energy is spent in heating the entire complex.

The details of fission fragment energy distributions, etc., are therefore of little interest in the present context. We note that the energy per nucleon of the fragments is slightly less than an MeV, corresponding to a velocity of  $\sim 10^8$  cm sec<sup>-1</sup>. The initial charge on the fragments is 15 - 20e, but this is rapidly reduced by recombination as the explosion proceeds. Recent data on the properties of fission fragments are contained in Refs. 3-2 and in 3-9 through 3-12.

### 3.6.1 PROMPT NEUTRONS

We have mentioned that the prompt neutrons released in fission have a mean energy of about two MeV. According to Terrell (Reference 3-15), the average kinetic energy  $E_k$  of the prompt neutrons is given by

$$E_k = 0.75 + 0.65(\nu_p + 1) \quad (\text{MeV}) \quad (3-9)$$

where as before  $\nu_p$  is the multiplicity of prompt neutrons from the reaction. For  $U^{235}$  and  $Pu^{239}$ , this formula gives mean kinetic energies of 1.95 and 2.02 MeV, respectively, and a total of about 5 MeV/fission in neutron kinetic energy.

Fusion reactions liberate neutrons with initial energies ranging from somewhat below an MeV to 14.1 MeV. In contrast to fission reactions, a large fraction of the energy is carried by the prompt neutrons. As with the fission neutrons, however, the intensity and spectrum of the neutron flux escaping to great distances depends critically on weapon design. Generally speaking, one would expect the energy distribution to range from low energies to 14 MeV. The energy yield in neutrons could be of the order of a tenth of a percent of the total for fission weapons and a few tenths of the total for fusion weapons. In the former case the neutron energies would be at most a few MeV, and in the latter would extend up to 14 MeV. More precise determinations of the neutron yield for specific devices can be made by field measurements or calculated by elaborate machine codes that contain descriptions of device disassembly and neutron transport.

### 3.6.2 PROMPT GAMMAS

Most of the nuclei produced in fission reactions are left in excited states that radiate prompt gammas. The gammas produced in this way are of little interest, however, since almost all of them are absorbed in the explosion debris and virtually none escape to great distances. The prompt gamma data shown in Figures 3-13 and 3-14 are included here only for completeness.

The prompt gammas that escape the debris are actually those produced by inelastic scattering of neutrons. To escape, the gammas must be produced within about one absorption mean free path, or about one cm, of the debris surface. The cross section for inelastic scattering is of the order of a barn and the debris density is  $\sim 10^{23} \text{ cm}^{-3}$ , so the probability that an escaping neutron produces a gamma within one gamma mean free path of the surface is  $\sim 10^{-1}$ , and the escaping flux of prompt gammas is about one tenth that of the prompt neutrons. The gammas produced have energies of the order of an MeV. Thus, MeV and 10-MeV neutrons convert about ten and one percent of their energy to gammas, respectively. The prompt gamma energy yield inferred from these estimates and those of the preceding section range from hundredths to tenths of a percent of the total yield, the value depending on details of the design of the device. Prompt gammas provide a useful diagnostic tool in field measurements for assessing the performance of nuclear devices, and produce the electromagnetic pulse observed in some high-altitude detonations.

### 3.6.3 PROMPT ALPHAS

When fission of  $\text{U}^{235}$  occurs after capture of a slow neutron, an energetic alpha particle is emitted in about one out of every five hundred events. The energy distribution of the alphas peaks at about 15 MeV, with maximum energies extending as high as 29 MeV. The total energy involved in alpha decay is quite small, and alphas are not extraordinarily penetrating, so they are generally neglected in weapons effects calculations.

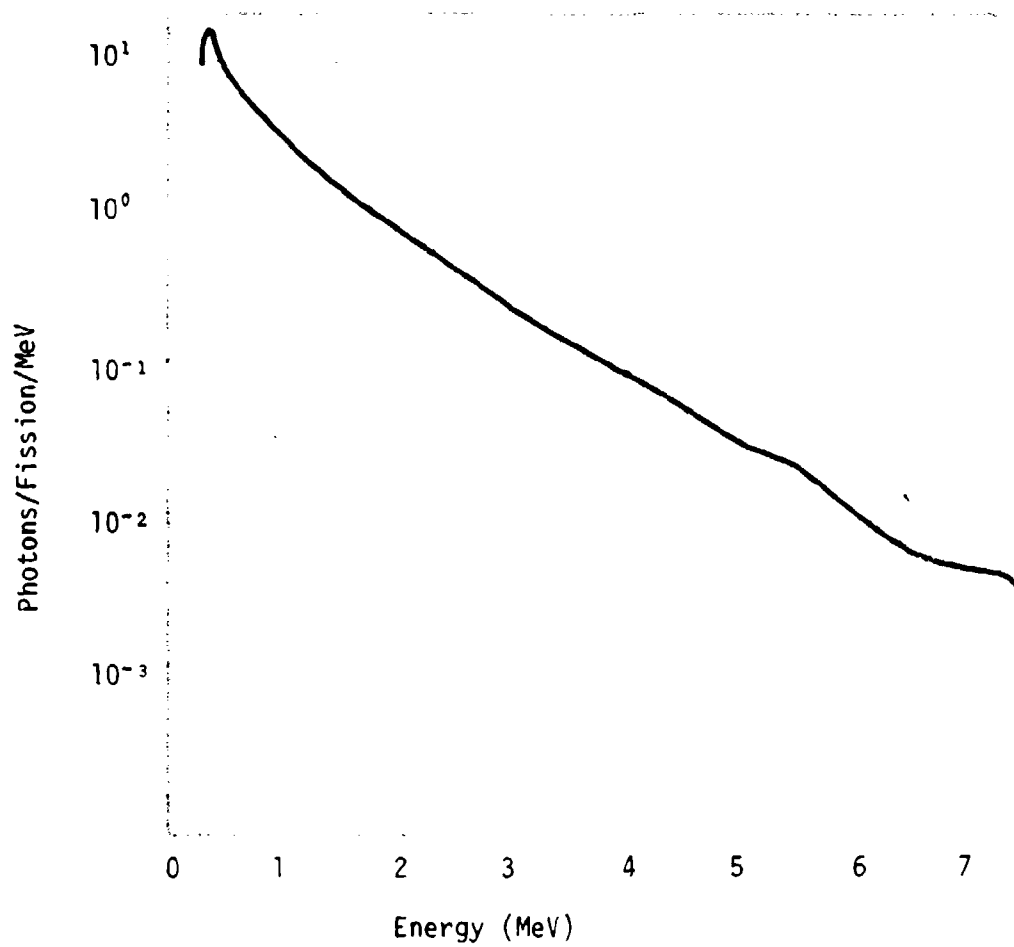


Figure 3-4. Prompt gamma energy spectrum from fission of  $U^{235}$  (Ref. 3-13).



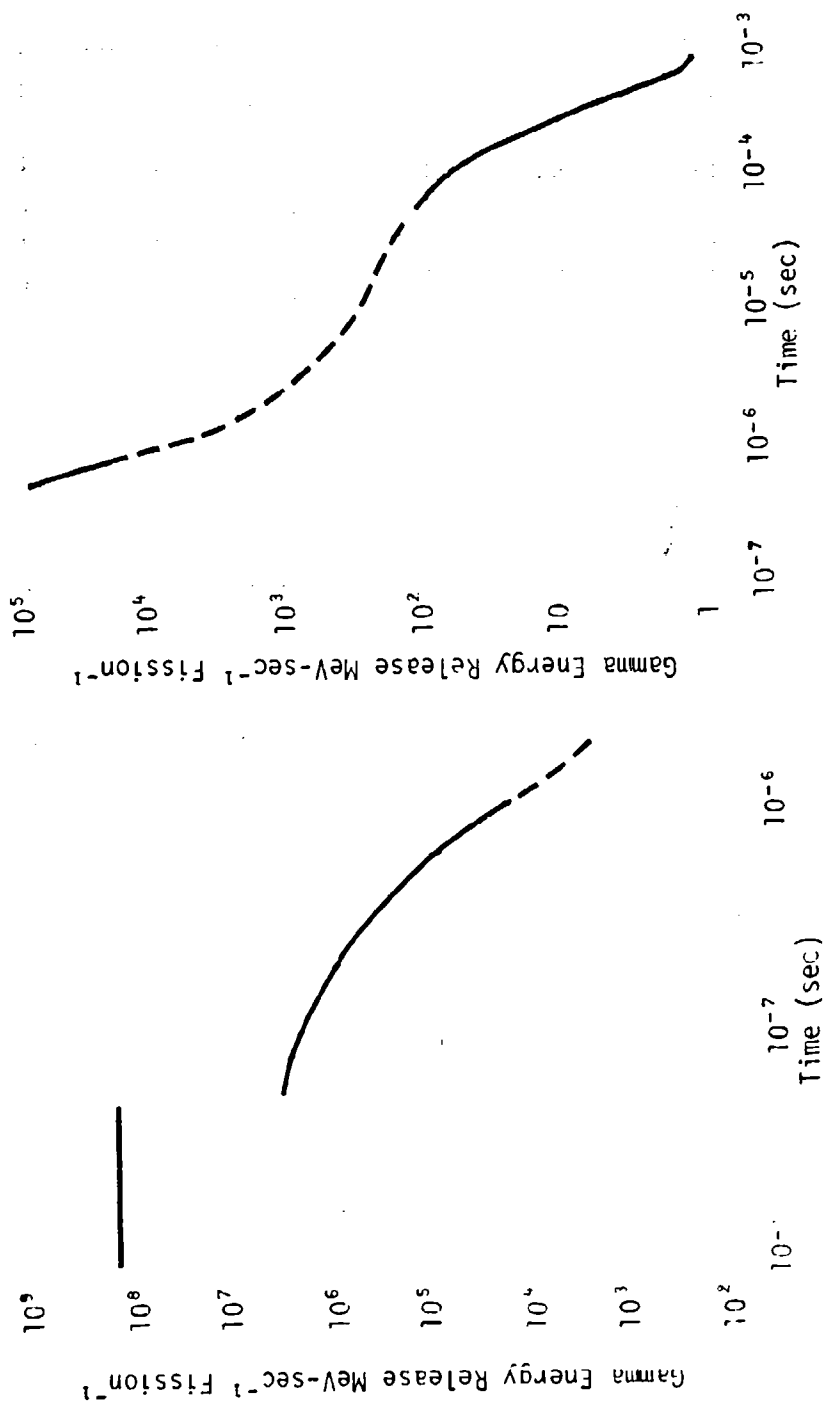


Figure 3-5. Gamma energy release rate vs. time from fission of U<sup>235</sup>. (Ref. 3-14).

### 3.6.4 DEBRIS KINETIC ENERGY AND THERMAL X RAYS

Most of the energy produced in the elementary nuclear reactions discussed above appears initially as kinetic energy of reaction products and is promptly lost in collisions with atoms in the surroundings of the warhead. These include the remains of the chemical explosive used to initiate the nuclear reactions, the associated electronic equipment, the structure of the missile, tower, balloon or other device carrier, and any other material in the immediate vicinity of the burst point at the time of detonation.

The energy is released and deposited in a very short time, say a few shakes. During this interval some of the energy is transferred to the electromagnetic field in the form of thermal radiation. By the time the energetic reaction products have shared their energy with the particles of the surrounding structure the average velocity of all the particles is at most  $\sim 10^8$  cm sec<sup>-1</sup> for typical yields and masses, and is actually considerably less because much of the energy is now in the electromagnetic field in the form of thermal radiation. With these velocities very little motion of the mass of debris can occur in a few shakes. At this stage the radiation is trapped in the interior by the opaque surrounding debris.

After a few shakes the configuration resembles an enclosure filled with a very hot gas in or near equilibrium with the radiation field. The radiation field diffuses through the outer layers of the enclosing material, the radiation front eventually reaching the surface, at which time a sizable fraction of the total yield is radiated away as a pulse of thermal x rays. The time interval occupied by the radiation, the spectral distribution of the x rays, and the total energy radiated away in the pulse all depend on the yield to mass ratio of the weapon and its surroundings, and on other detail of weapon design and configuration.

During the time the radiation field remains trapped by the debris the whole mass of debris experiences an outward acceleration as a result of the pressure being exerted on it, an important component of which is radiation pressure. By the time the x rays have been radiated away, the entire debris cloud is expanding with a velocity of  $10^7$  to  $10^8$  cm sec<sup>-1</sup>, the exact value again depending on weapon design and configuration.

For many purposes it is convenient to have available a model of a typical weapon. We present such a model below, but reiterate that all of the values quoted are subject to wide variation. The model is:

Debris kinetic energy	50%
X-ray yield	45%
Delayed radiation	5%
Debris expansion velocity	$(Y/M)^{1/2} \sim 10^7$ - $10^8$ cm sec <sup>-1</sup>
X-ray radiation time	$<10^{-6}$ sec
X-ray spectrum	1 keV blackbody
Prompt neutrons	$10^{-1}\%$ - $1\%$
Prompt gammas	$10^{-2}\%$ - $10^{-1}\%$

where  $Y$  is the total yield of the weapon and  $M$  is the total mass participating in the expansion. Some results of more detailed estimates for specific cases have been given by Brode (Ref. 3-16).

### 3.6.5 DELAYED BETAS

Fission fragments are excessively rich in neutrons, as noted in Section 3.3. Consequently they are unstable against beta decay, and typically undergo several  $\beta^-$  decays before arriving at a stable configuration. The daughter nuclei produced by  $\beta^-$  decay are seldom formed in their ground states, so associated with each  $\beta^-$  decay is the radiation of one or more  $\gamma$  rays and in a few rare instances, a neutron. This radiation is termed delayed because it persists to very late times after fission.

The persistence of the delayed radiation stems from the weakness of the beta interaction and the correspondingly long lifetimes against  $\beta$  decay. The lifetimes for the emission of gammas and neutrons are so short by comparison that their radiation can be considered to follow the  $\beta$  decay instantaneously. Thus the entire time scale of the delayed radiation is determined by the rate of  $\beta$  decay.

Several betas are radiated by a typical fission fragment before a stable configuration of the product nucleus is reached. Accompanying every beta radiated is a neutrino, which on the average carries somewhat more energy than the beta. Since the interaction of neutrinos with matter is so extremely weak, however, they produce no easily observable effects and are not further considered here.

To characterize completely the  $\beta$  radiation from the entire ensemble of fission fragments, one requires the energy distribution of the betas as a function of time. These spectral-temporal distributions can in principle be determined either experimentally, theoretically, or by some synthetic method based upon a mixture of theory and experimental data. All three procedures have been employed, and all give results that are at least qualitatively consistent with one another.

The earliest attack on the problem was that of Way and Wigner (Ref. 5-18), who assumed a distribution of fission fragments, summed over the various decay chains, and arrived at a determination of both beta and gamma activity. It was in their work that the variation of radiated gamma power as  $t^{-1.2}$  was first observed. A similar, but simpler, calculation was performed by Griffin (Ref. 5-19) who calculated the radiation from a single decay chain with properties chosen to fit experimental data for  $U^{235}$  fission. By appropriate variation of the parameters characterizing the chain, he was then able to perform calculations for other fissionable nuclei. Other synthetic calculations have been performed by a number of workers. Among these frequently quoted are Perkins and King

(Ref. 3-24), Knabe and Putnam (Ref. 3-25), and Heller et al. (Ref. 3-27). Experimental data on beta intensities and spectra have been provided by Seyfarth (Ref. 3-17), West (Ref. 3-20), Alzmann (Ref. 3-21), Armbruster and Meister (Ref. 3-22), Kutcher and Wyman (Ref. 3-23), Löw and Björnerstedt (Ref. 3-26), Carter et al. (Ref. 3-28) and Tsoulfanidis et al. (Ref. 3-29).

As the  $\beta$  decay progresses, the nuclei approach more stable configurations. Consequently the rate of  $\beta$  emission decreases, and the energy of the emitted betas also decreases. These tendencies are shown in Fig. 3-6 (Ref. 3-29). The mean  $\beta$  energy is of the order of an MeV. Initially it is about 2 MeV, falls to somewhat less than an MeV by 1000 sec, and continues to decrease thereafter.

It is frequently useful to have analytical fits to the data. A considerable spread remains among the various determinations of decay rates, however, so such fits cannot be made unambiguously. Furthermore, in practical applications great precision is seldom required because of other uncertainties. Accordingly, it seems that the most important consideration in obtaining fits is that they should be analytically simple, rather than that they provide an extremely accurate fit to one of the several disparate sets of data.

To obtain analytical expressions for the rate of emission of betas for  $U^{235}$ , we have chosen to rely on the results of Tsoulfanidis et al. (Ref. 3-29) and of Seyfarth (Ref. 3-17). According to the former, the total number of betas per fission is  $5.8 \pm 0.5$ , while the latter gives  $6.0 \pm 0.2$  from his experimental data, and quotes a theoretical value of  $6.1 \pm 0.1$ . Seyfarth further asserts that the initial rate of emission is  $6.52 \pm 0.1$  betas/fission/sec and is constant within the interval 0 to 0.2 sec. A comparison of Seyfarth's results with those of other workers is shown in Fig. 3-7. Tsoulfanidis et al. give the data shown in Table 3-1.

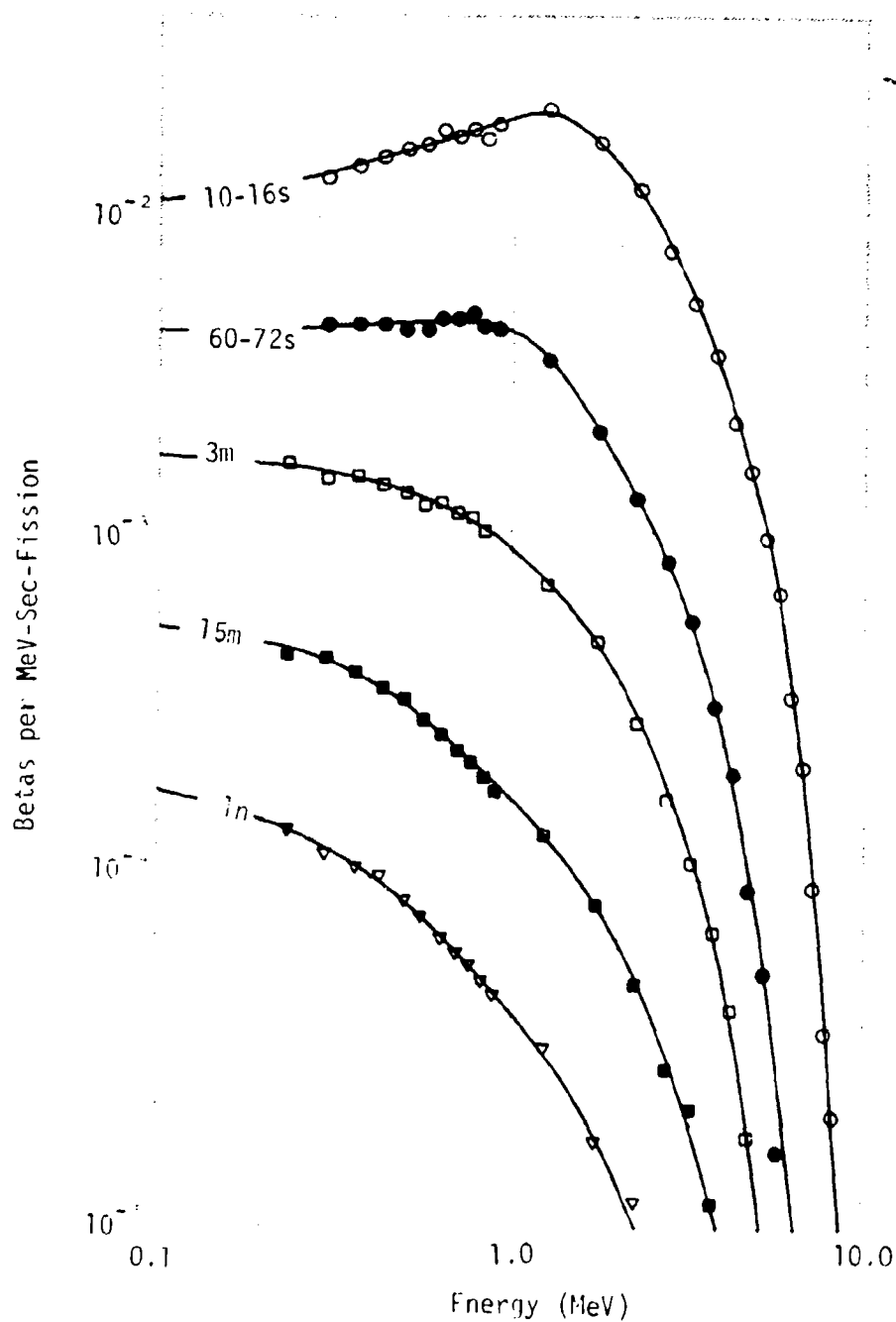


Figure 3-6. Beta spectrum from fission of  $U^{235}$  by a pulse of thermal neutrons (Ref. 3-29).

Time (sec)	$\dot{N}_\beta$ (β/sec/fission)	$\dot{E}_\beta$ (MeV/sec/fission)	$\bar{E}_\beta$ (MeV)
12	$4.2 \times 10^{-2}$	$7.77 \times 10^{-2}$	1.85
66	$8.15 \times 10^{-3}$	$1.06 \times 10^{-2}$	1.30
204	$2.28 \times 10^{-3}$	$2.52 \times 10^{-2}$	1.10
960	$5.11 \times 10^{-4}$	$4.66 \times 10^{-4}$	0.91
3750	$1.35 \times 10^{-4}$	$9.80 \times 10^{-6}$	0.73

Table 3-1. Beta decay rates from fission of  $U^{235}$  by a pulse of thermal neutrons as measured by Tsoulfanidis et al. (Ref. 3-29).

The data for  $\dot{N}_\beta$  in Table 3-1 can be fit to an accuracy of better than ten percent by the expression  $\dot{N}_\beta = 0.5(1+t)^{-1}$ . This also provides a good representation of Seyfarth's data during the interval 1-10<sup>3</sup> sec. As an approximate fit of sufficient accuracy for our purposes, we shall assume for fission of  $U^{235}$

$$\dot{N}_\beta = \begin{cases} 0.33 & t < 0.5 \text{ sec} \\ 0.5(1+t)^{-1} & 0.5 < t < 10^3 \\ 2t^{-1.2} & t > 10^3 \end{cases} \text{ betas/fission/sec } (U^{235}) \quad (3-10)$$

The expression for  $t > 10^3$  sec was chosen to agree with Seyfarth's data and because it gives the familiar  $t^{-1.2}$  dependence. The total number of betas obtained by integrating the expression for  $\dot{N}_\beta$  from zero to infinity is 5.9, in good agreement with the results of both Seyfarth and Tsoulfanidis et al. A plot of this expression together with experimental data of Seyfarth and Tsoulfanidis, et al. is shown in Fig. 3-7.

To get a fit to  $\dot{E}_\beta$ , the rate at which energy is carried off by the betas, we use the data of Tsoulfanidis et al. given in Table 3-1. The data in the interval 12-960 sec are fit with about ten percent accuracy by the expression  $\dot{E}_\beta = 1.65(1+t)^{-1.2}$ . In analogy with the fit for  $\dot{N}_\beta$ , we assume this formula remains valid to times as short as 0.5 sec, and that  $\dot{E}_\beta$  is constant in the interval 0-0.5 sec. Continuity then requires that  $\dot{E}_\beta = 1.0$  in this interval.

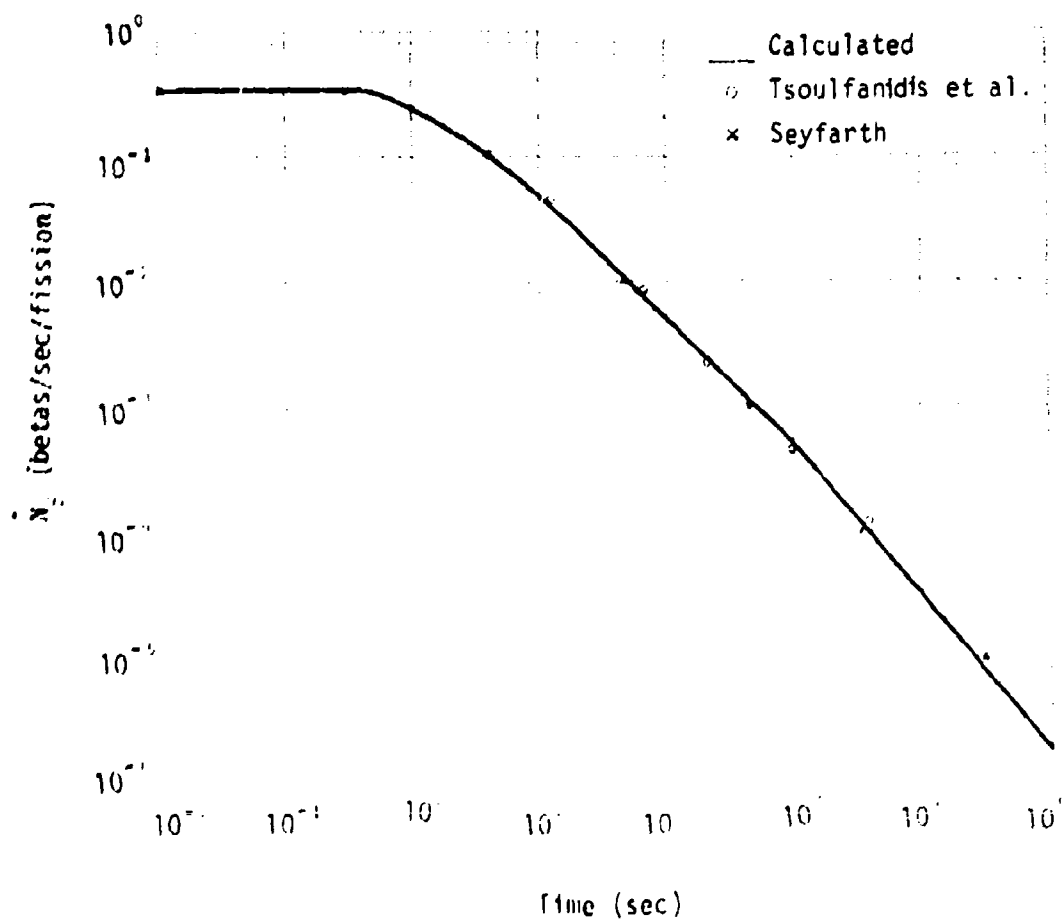


Figure 3-7. Rate of beta radiation by fragments of  $^{137}\text{I}$  from fission induced by thermal neutrons.



To arrive at a formula for  $\dot{E}_\beta$  for times greater than 1000 sec, we assume the form  $\dot{E}_\beta = At^{-(1+\epsilon)}$ . The parameters A and  $\epsilon$  are determined by the requirements that  $\dot{E}_\beta$  be continuous at  $10^3$  sec and that  $\int_0^\infty \dot{E}_\beta dt = 6.9$  MeV the total beta energy quoted by Tsoulfanidis, et al. With these assumptions, we find  $A = 6.3$ ,  $\epsilon = 0.5$ . Accordingly, we adopt as a fit for  $\dot{E}_\beta$  for  $U^{235}$  fission products

$$\dot{E}_\beta = \begin{cases} 1.0 & t < 0.5 \text{ sec} \\ 1.65(1+t)^{-1.2} & 0.5 < t < 10^3 \\ 13.7t^{-1.5} & t > 10^3 \end{cases} \quad \text{MeV/fission/sec } (U^{235}) \quad (5-11)$$

A comparison of the results from these formulas and the data of Tsoulfanidis et al. is shown in Fig. 5-8.

For a description of fission products from other fissionable isotopes, we simply scale the formulas assumed for  $U^{235}$ . In the case of  $Pu^{239}$ , the total number of betas per fission reported by Seyfarth is 5.6, as compared with his corresponding value of 6.0 for  $U^{235}$ , so the ratio of total betas is  $Pu^{239}/U^{235} = 0.93$ . The initial emission rate for  $Pu^{239}$  given by Seyfarth is 0.24, as opposed to 0.52 betas/fission/sec for  $U^{235}$ , for a ratio of 0.8 for the initial activity. Since the first few tenths of a second are of relatively minor importance, we adopt for  $Pu^{239}$

$$\dot{N}_\beta = \begin{cases} 0.5 & t < 0.5 \text{ sec.} \\ 0.45(1+t)^{-1} & 0.5 < t < 10^3 \\ 1.8t^{-1.2} & t > 10^3 \end{cases} \quad \text{betas/fission/sec } (Pu^{239}) \quad (5-12)$$

and

$$\dot{E}_\beta = \begin{cases} 0.9 & t < 0.5 \text{ sec} \\ 1.5(1+t)^{-1.2} & 0.5 < t < 10^3 \\ 1.25t^{-1.5} & t > 10^3 \end{cases} \quad \text{MeV/fission/sec } (Pu^{239}) \quad (5-13)$$

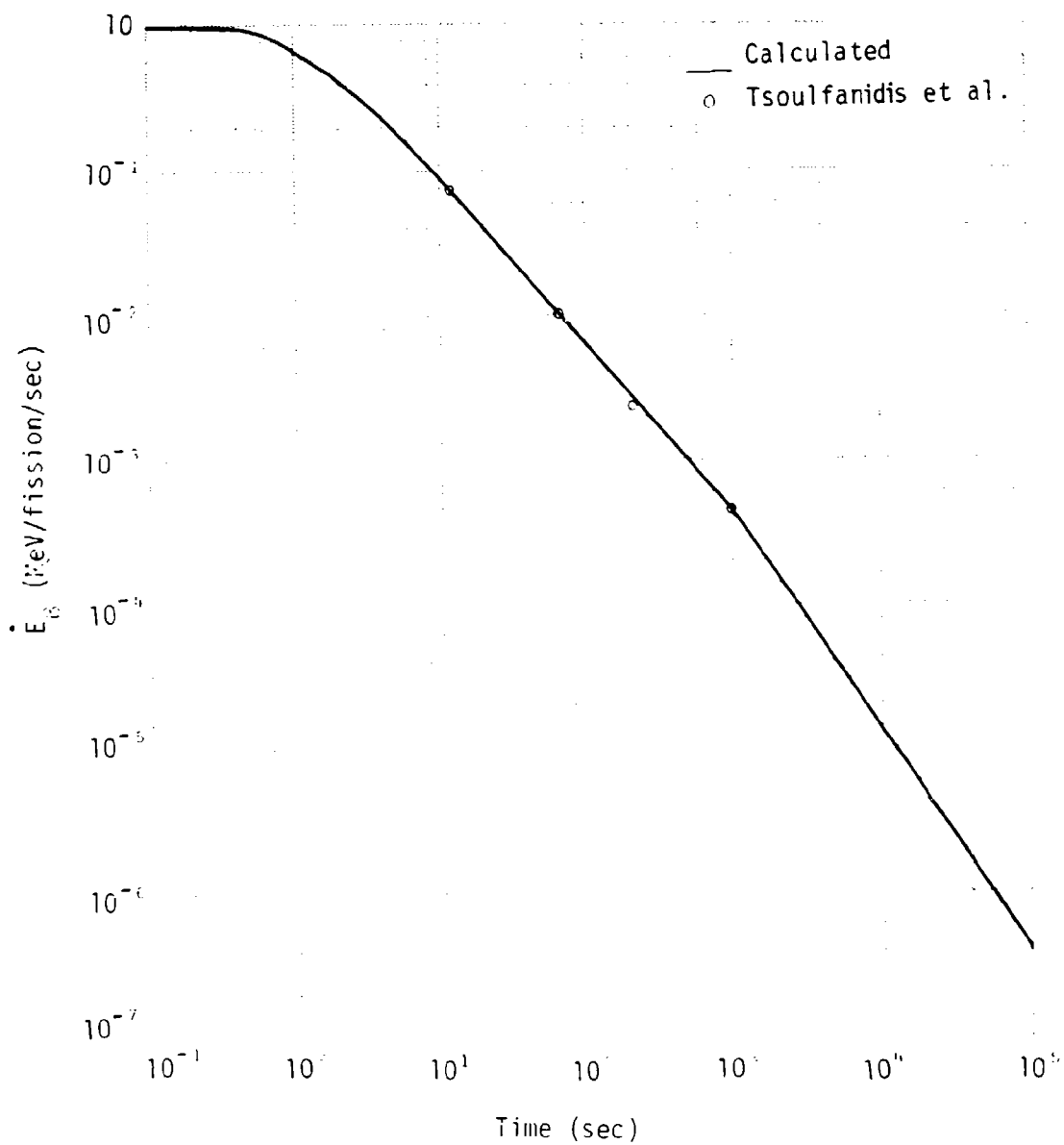


Figure 3-8. Radiated beta power from fission of  $U^{235}$  by thermal neutrons.

For  $U^{238}$  we take the ratio of total activity of  $U^{238}$  and  $U^{235}$  from the work of Griffin as reported by Keith and Shelton (Ref. 3-31). For  $U^{238}$  fission by a Godiva spectrum, (i.e., similar to a fission spectrum), the ratio of  $U^{238}$  to  $U^{235}$  for the total number of betas is 1.15. Scaling the  $U^{235}$  results by this factor, we obtain for  $U^{238}$

$$\dot{N}_\beta = \begin{cases} 0.38 & t < 0.5 \text{ sec} \\ 0.57(1+t)^{-1} & 0.5 < t < 10^3 \\ 2.3t^{-1.2} & t > 10^3 \end{cases} \quad \text{betas/fission/sec } (U^{238}) \quad (3-14)$$

and

$$\dot{E}_\beta = \begin{cases} 1.15 & t < 0.5 \text{ sec} \\ 1.95(1+t)^{-1.2} & 0.5 < t < 10^3 \\ 1.57t^{-1.5} & t > 10^3 \end{cases} \quad \text{MeV/fission/sec } (U^{238}) \quad (3-15)$$

### 3.6.6 DELAYED GAMMAS

Delayed gammas are emitted by the fission fragment nuclei created in any fission reaction. The delayed gammas account for about 5 MeV per fission, or about 2.5 percent of the fission energy yield. Several gammas are radiated by a typical fragment nucleus. The radiation of gammas is a consequence of the beta activity of the fission fragments, and the beta activity in turn results from the large neutron excess of the fragments, as discussed in Section 3.3. Unlike the prompt gammas, the delayed gammas are radiated long after the explosion has occurred, so their intensity and spectrum are those characteristic of the nuclear reactions involved, and are not altered by transport through a dense surrounding medium.

The experimental data for  $U^{235}$  fission by slow neutrons have been reviewed extensively by Holden et al. (Ref. 3-14, an extensive bibliography is contained therein). Data on the rate of radiation from  $10^{-8}$  to  $10^9$  sec are reviewed in this article. In Figs. 3-9 and 3-10 the data for times of  $10^{-3}$  sec to  $10^5$  sec are shown (see Fig. 3-4 for earlier times).

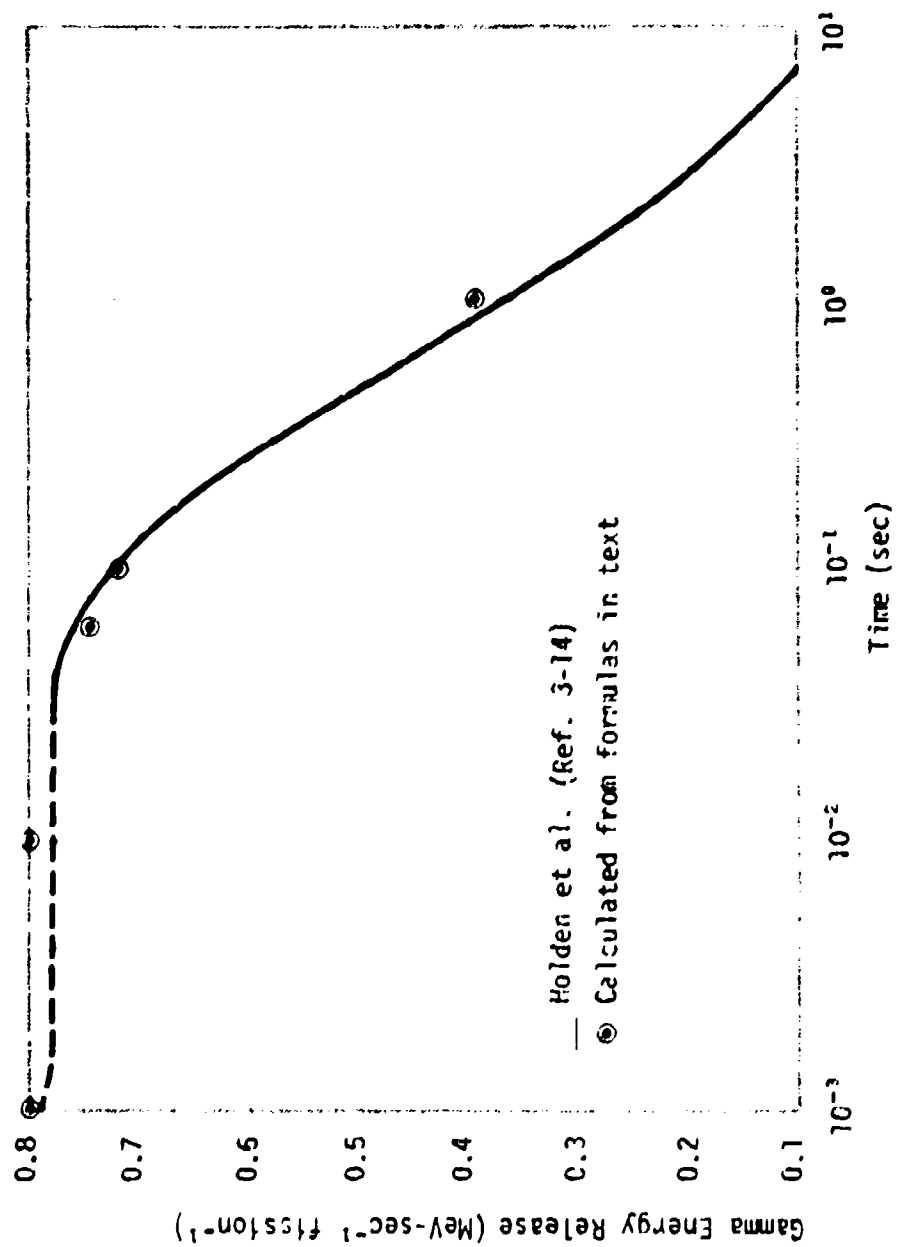


Figure 3-9. Gamma energy release rate vs. time from fission of U<sup>235</sup>.

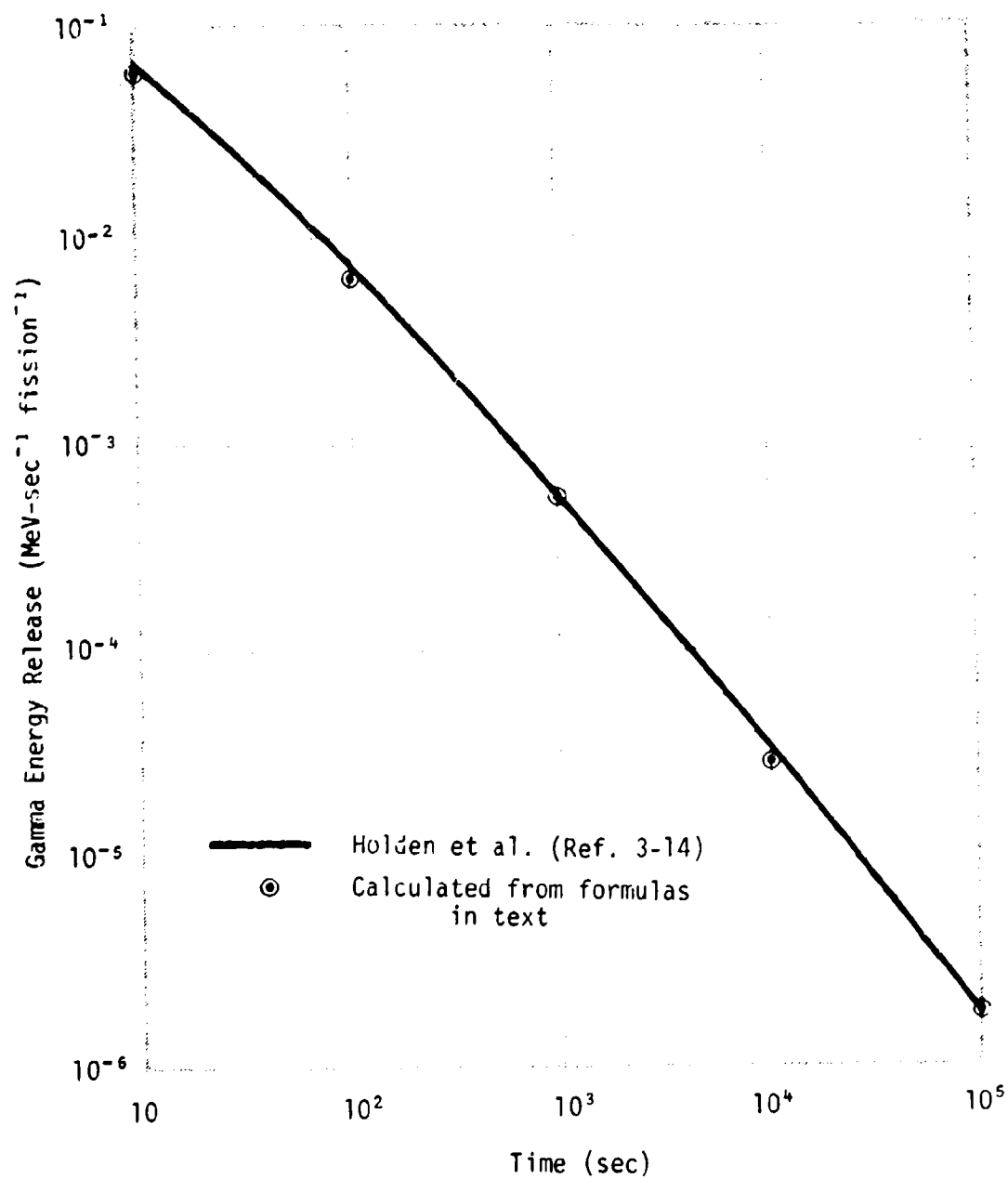


Figure 3-10. Gamma energy release rate vs. time from fission of U<sup>235</sup>.

Griffin's results (Ref. 3-19) for several nuclei are shown in Fig. 3-11, where they are compared with the measurements of Fisher and Engle (Ref. 3-30). Griffin also gives results for  $U^{235}$  that are in substantial agreement with the measurements discussed by Holden.

From Figs. 3-9, 10, 11 it is apparent that  $U^{238}$  radiates considerably more gammas than either  $U^{235}$  or  $Pu^{239}$ . The variation with time of the net rate of radiation by fragments produced in the various reactions is considerably different for the reactions considered. Fits to Griffin's calculations indicate that the gamma energy radiation rate at times greater than one sec varies as  $(1+t)^{-1.05}$ ,  $(1+t)^{-0.89}$ , and  $(1+t)^{-1.31}$  for  $U^{235}$ ,  $Pu^{239}$ , and  $U^{238}$ , respectively.

The mean energy of the gammas emitted is about one MeV, but varies with time and tends to decrease with increasing time, as one might expect. The average gamma energy as reported by several investigators is shown in Fig. 3-12. Since the photon energy varies with time, the emitted photon flux cannot be inferred directly from the variation with time of the energy. However, some measured values are shown in Fig. 3-13.

For simple analytical calculations the  $U^{235}$  data of Holden et al. are fit with sufficient accuracy by the following formulas:

$$\dot{E}_\gamma = \begin{cases} 0.8 & t < 0.1 \text{ sec} \\ 0.8(1+t)^{-1.05} & 10^{-1} < t < 10^2 \text{ sec} \\ 5.2t^{-1.05} & t > 10^3 \text{ sec} \end{cases} \text{ MeV/fission/sec} \quad (3-16)$$

For comparison several calculated points are shown in Figs. 3-9, 10. Integration of these formulas gives 7.2 MeV/fission for the total energy radiated as gammas. From Fig. 3-11 it appears that the gamma ray yield from  $U^{238}$  is somewhat higher, and that from  $Pu^{239}$  somewhat lower, than the  $U^{235}$  value.

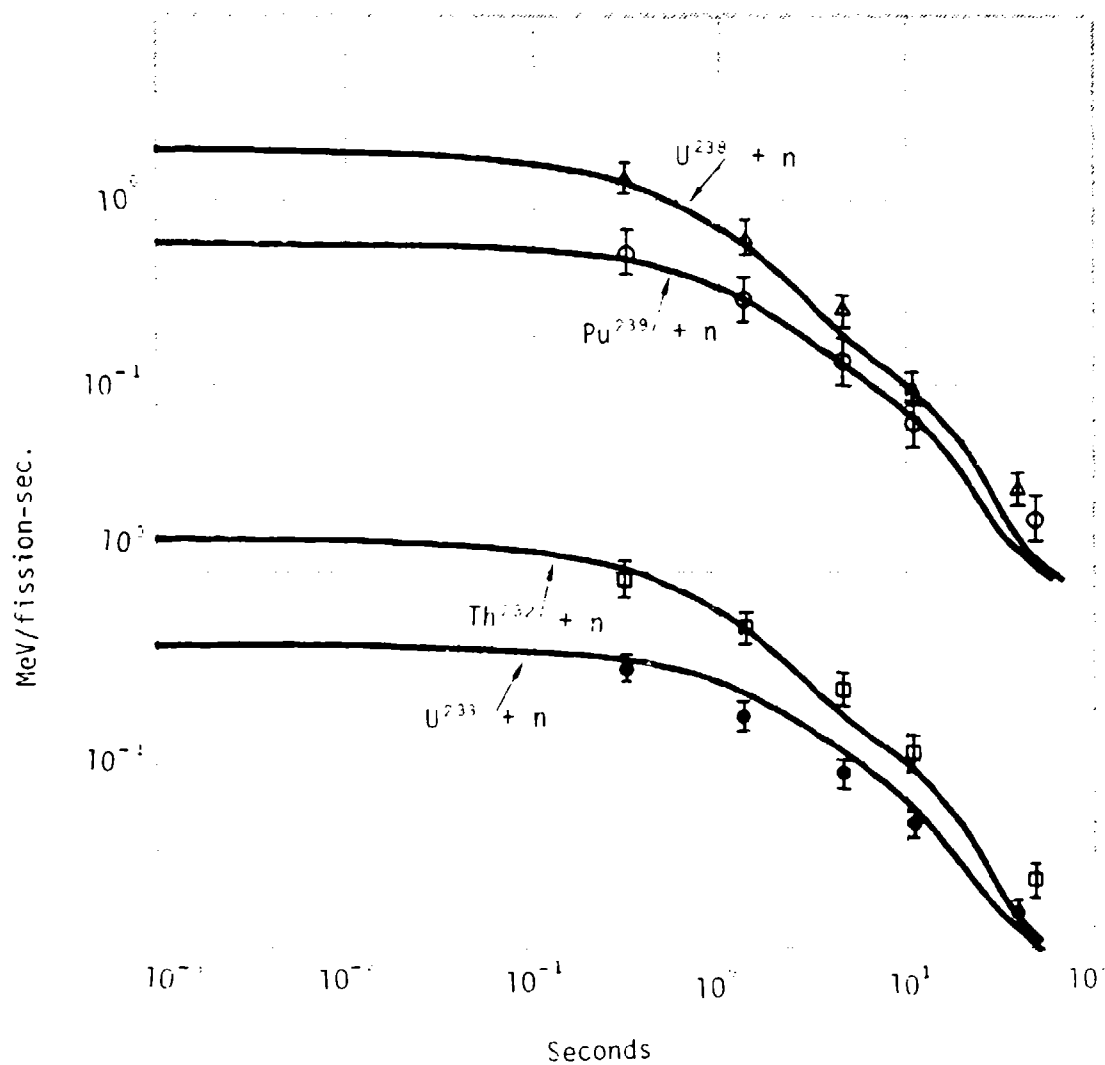


Figure 3-11. Calculated gamma rates (Ref. 3-19) compared with measurements of Fisher & Engle (Ref. 3-30).

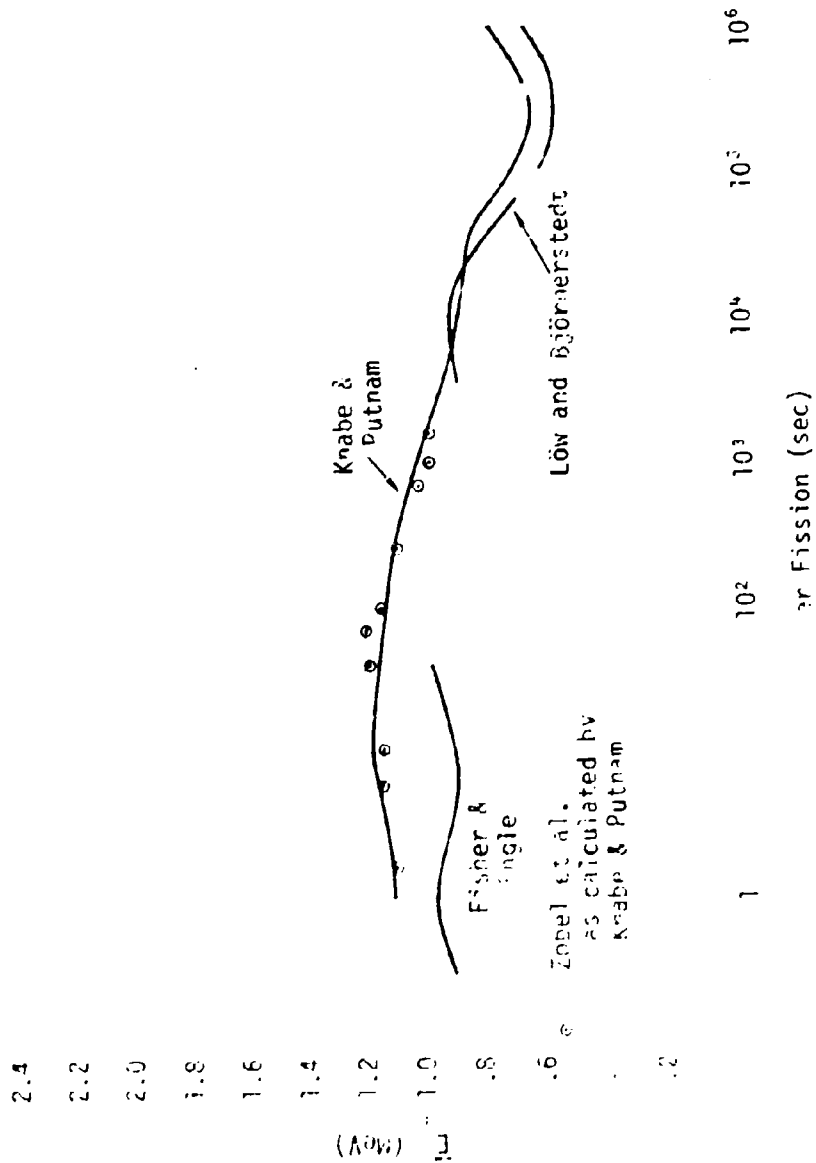


Fig. 1. Average gamma energy from fission of  $U^{235}$ .



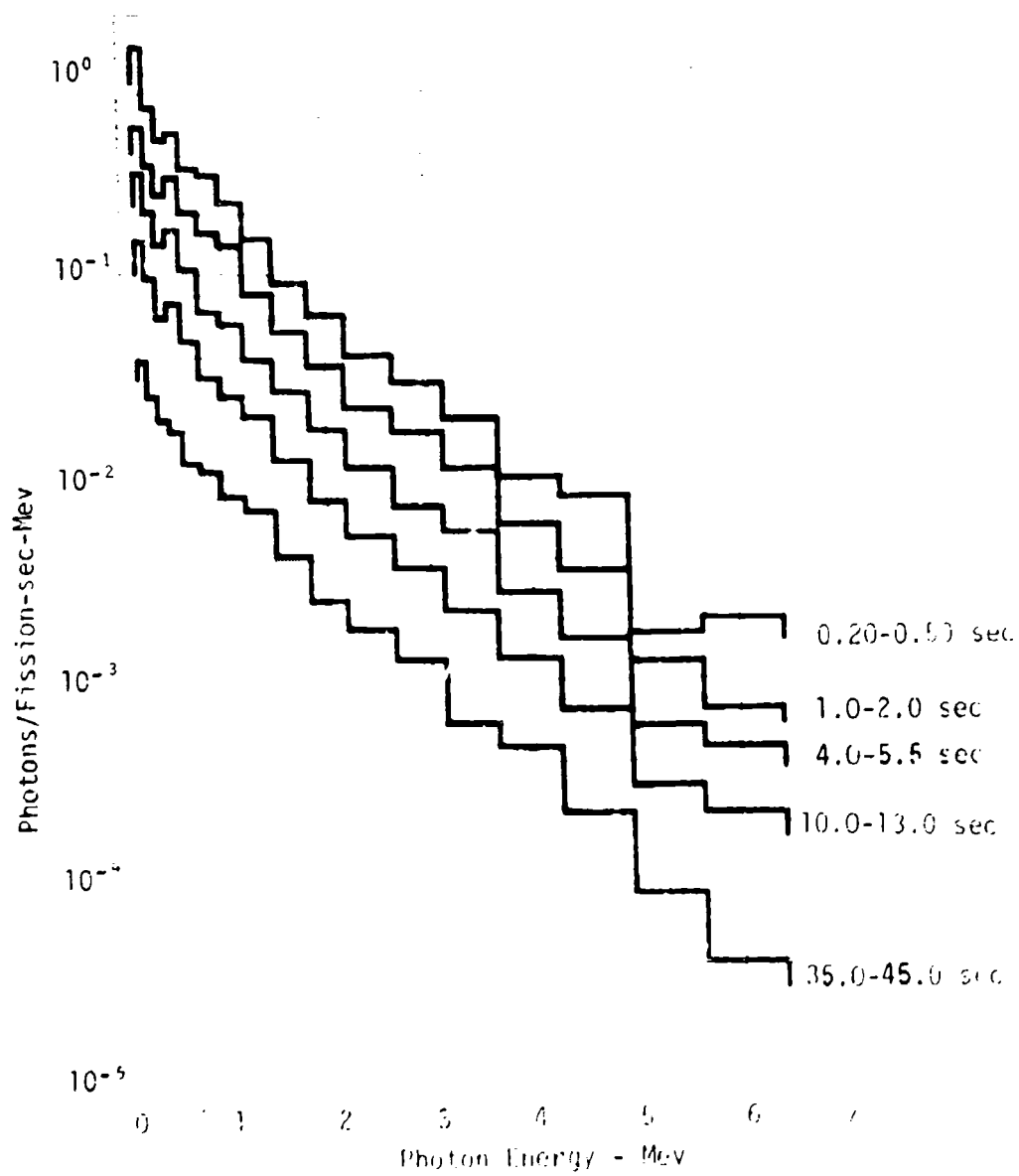


Figure 3-13.  $^{235}\text{U}$  photon spectra at five times after fission (Ref. 3-30).

### 3.6.7 DELAYED NEUTRONS

A small quantity of energy is radiated by the fission fragments in the form of delayed neutrons. Some characteristics of the delayed neutron emission are given in Table 3-2, which is taken from Ref. 3-4.

Emitter	Half life (sec)	$\bar{E}_n$ (kev)	Neutrons per fission	
			$U^{235}$	$Pu^{239}$
Kr <sup>87</sup>	54.5	250	0.06	0.02
Xe <sup>137</sup>	21.8	560	0.35	0.18
Kr	6.0	430	0.31	0.14
	2.23	620	0.67	0.21
	0.50	420	0.21	0.06
			<u>0.04</u>	<u>0.02</u>
			1.65	0.63

Table 3-2. Delayed neutron emission.

It should be noted that the half lives quoted are not the lifetimes against neutron emission of the neutron active emitters. Rather, the half life is determined by the lifetime against beta decay of the emitter's mother nucleus.

## REFERENCES

- 3-1. Blatt, J. M. and V. F. Weisskopf, Theoretical Nuclear Physics, John Wiley & Son, New York 1952.
- 3-2. Fermi, E., Nuclear Physics, Revised Ed., University of Chicago Press, 1950.
- 3-3. Preston, M. A., Physics of the Nucleus, Addison-Wesley Publishing Co., 1962.
- 3-4. Wheeler, J. A., Chapter 11 in Handbook of Physics, E. U. Condon and H. Odishaw ed., McGraw-Hill Book Co., 1958.
- 3-5. Stehn, J. R. et al., Neutron Cross Sections, Vol. III, Z = 88 to 98, Brookhaven National Laboratory, BNL 325, Sec. ed. Supplement No. 2, February 1965.
- 3-6. Obukhov, A. I. and N. A. Perfilov, Sov. Phys. Usp. 10, 559, 1966. General review of all features of nuclear fission.
- 3-7. Wapstra, A. H., "Atomic masses of nuclides," in Handbuch Der Physik, Vol. XXXVIII/1, S. Flugge, ed., Springer-Verlag 1958.
- 3-8. Burcham, W. E., "Nuclear Reactions, Levels and Spectra of Light Nuclei" in Handbuch Der Physik, Vol. XL, S. Flugge, ed., Springer-Verlag 1957.
- 3-9. Terrell, J., Phys. Rev. 113, 527, 1959.
- 3-10. Walton, G. N., Progress in Nuclear Physics, Vol. 6, 1957.
- 3-11. Katcoff, S., J. A. Miskel, and C. W. Stanley, Phys. Rev. 74, 631, 1948.
- 3-12. Munzel, H., M. Hollstein and T. Ishimori, in Proc. of the Symposium on Physics and Chemistry of Fission Held by the International Atomic Energy Agency in Salzburg, 22-26 March 1965, International Atomic Energy Agency, Vienna, Austria.
- 3-13. Maienschien, F. C., R. W. Peele, W. Zobel and T. A. Love, Proc. International Conference on Peaceful Uses of Atomic Energy, Geneva 15, 366, 1959 published by the United Nations, N.Y.

- 3-14. Holden, N. E., M. R. Mendilson, and T. E. Duley, Nuc. Sci. and Engr. 30, 461 (1967).
- 3-15. Terrell, J., Proc. of the Symposium on Physics and Chemistry of Fission Held by the International Atomic Energy Agency in Salzburg, 22-26 March 1965, Intern. Atomic Energy Agency, Vienna, Austria.
- 3-16. Brode, H. L., Am. Rev. Nuc. Sci. 18, 153 (1968).
- 3-17. Seyfarth, H., Nukleonik 10, 193, 1967.
- 3-18. Way, K. and E. P. Wigner, Phys. Rev., 70 1154 (1946) and 73, 1518, (1948).
- 3-19. Griffin, J., Re-evaluation of Optimal Parameters for Post-Fission Beta Decay, LA-2811, Add. II, Los Alamos Scientific Laboratory, Los Alamos, New Mexico, 1964. See also J. Griffin, Phys. Rev. 134, B (1964).
- 3-20. West, H. I. Jr., Trans. Am. Nuc. Soc. 3, 537, (1960).
- 3-21. Alzmann, G., Nukleonik, 3, 295 (1961).
- 3-22. Armbruster, P. and H. Meister, Z. Physik 170, 247 (1963).
- 3-23. Kutcher, J. W. and M. E. Wyman, Nuc. Sci. and Engr. 26, 435, (1966).
- 3-24. Perkins, J. F. and R. W. King, Nuc. Sci. and Eng., 3, 726 (1958).
- 3-25. Knabe, W. E., and G. E. Putnam, The Activity of the Fission Products of U<sup>235</sup>, APEX 448, General Electric, Aircraft Nuclear Propulsion Dept. (1959).
- 3-26. Löw, K. and R. Björnerstedt, Arkiv Fysik, 13, 85-90 (1958).
- 3-27. Heller, R. B., S. Chakravarty, J. Frawley, M. Silver, Nucleonics, 23, 92, 1965.
- 3-28. Carter, R. E., F. Reines, J. J. Wagner, and M. E. Wyman, Phys. Rev. 113, 280, 1959.
- 3-29. Tsoulfanidis, N., B. H. Wehring and M. E. Wyman, Nuc. Sci. and Engr., 43, 42 (1971).
- 3-30. Fisher, P. C. and L. B. Engle, Phys. Rev. 134, 8796 (1964).
- 3-31. Keith, J. R. and F. H. Shelton, Review of Betas and Gamma Emitted by Uranium Fission Products, EN-674-64-11, Fusion Nuclear, Colorado Springs, Colo. (1964).
- 3-32. Thornton, J. P., and W. D. Boughton, J. Appl. Phys., 24, 1377 (1953).

## CHAPTER 4

### THE TRANSPORT AND DEPOSITION OF IONIZING RADIATION

Dan H. Holland\*

Alfred M. Kaufman\*\*

Austin A. O'Dell\*\*

April 1974

Mission Research Corporation

\* Now at New Brunswick, N. J. area.

\*\* Now at Lawrence Livermore Laboratory.

## TABLE OF CONTENTS

	<u>PAGE</u>
LIST OF FIGURES	182
4.1 INTRODUCTION	183
4.2 THE PHOTOELECTRIC EFFECT	184
4.3 THE COMPTON EFFECT	193
4.4 DETAILED NUMERICAL CALCULATIONS OF GAMMA-RAY AND NEUTRON TRANSPORT	196
4.4.1 Point Kernel Methods	198
4.4.2 Discrete Ordinates Methods	199
4.4.3 The Monte Carlo Method	199
4.4.4 The Orders of Scattering Method	200
4.4.5 The Moments Method	200
4.4.6 The Diffusion Approximation	201
4.4.7 Cross Section Data	201
4.5 TRANSPORT AND ENERGY DEPOSITION OF BETAS	202
4.6 TRANSPORT AND ENERGY DEPOSITION OF DEBRIS ATOMS	211
4.6.1 Electronic Stopping Powers	212
4.6.2 Nuclear Elastic Stopping	217
4.6.3 Energy Deposition and Particle Range	218
4.6.4 Partition of Deposited Energy	221
REFERENCES	228

## LIST OF FIGURES

<u>FIGURE</u>		<u>PAGE</u>
4-1.	X-ray photoelectric absorption coefficient $\mu_{\text{ph}}$ in air.	186
4-2.	Universal Planck function $B_{\lambda}$ .	188
4-3.	Specific energy deposition and fractional absorption for several blackbody spectra at small optical depths.	189
4-4.	Specific energy deposition and fractional transmission for several blackbody spectra at large optical depths.	190
4-5.	Compton absorption coefficient.	195
4-6.	Buildup factor, $B(E, m)$ , vs photon energy for several values of attenuation length.	197
4-7.	Energy loss of betas in air.	20*
4-8.	Energy dissipation for an isotropic point source of 1 MeV betas.	208
4-9.	Energy dissipation $(dE/dt)_0$ for a plane isotropic source of 1 MeV betas.	210
4-10.	Diagram for determining $\ln(2/v_m)$ .	214
4-11.	Plot of function $\phi(x)$ .	215
4-12.	Comparison of bound ( $S_{\text{eb}}$ ) and free ( $S_{\text{ef}}$ ) electronic stopping power for Al atoms in air.	216
4-13.	Plots of the nuclear and electronic stopping powers $S_n$ and $S_{\text{eb}}$ for aluminum atoms in air.	219
4-14.	Ranges for various particles in air.	222
4-15.	Partition of deposited energy for aluminum and air atoms in air.	225
4-16.	Fraction of total deposited energy put into direct collisional dissociation and into thermal energy.	227

## CHAPTER 4

### THE TRANSPORT AND DEPOSITION OF IONIZING RADIATION

#### 4.1 Introduction

In Chapter 3 we discussed the ionizing radiation released in a nuclear detonation. In this chapter we discuss the interaction of that radiation with the atmosphere. The radiation to be discussed includes x rays,  $\gamma$  rays, neutrons,  $\beta$  particles and energetic debris particles. The interaction problem comprises two parts:

1. Transport - given a source of ionizing radiation, what is the spectral intensity at some point removed from the source?
2. Deposition - having solved the transport problem for some source to find the spectral intensity at a point, we ask how much energy is deposited in a volume element surrounding that point. Although these are logically distinct questions, they are closely related and are most conveniently treated together, and will be so treated in this chapter.

In discussing this problem we must make a distinction at the outset between absorption and scattering processes. In an absorption process the primary particle or photon is actually absorbed and removed from the beam. Its total energy appears as kinetic and excitation energy of the reaction products. Two absorption processes are of interest - the photoelectric absorption of x rays and the nuclear absorption of neutrons. In a scattering process, however, the primary loses only



part of its energy in the interaction and proceeds with diminished energy (and generally along an altered trajectory) to undergo further interactions, which may be either absorption or additional scattering.

In the remainder of this chapter we discuss the various processes of interest and the corresponding transport and energy deposition. The results of the deposition, i.e., the partition of the energy among the various degrees of freedom of the target gas, are sketched in 4.6.4.

## 4.2 The Photoelectric Effect

Of all the processes occurring, the simplest is the photoelectric absorption of x-ray photons. In this a photon is absorbed by an atom or molecule and the absorption is accompanied by the ejection of an electron. The electron has kinetic energy equal to the energy,  $h\nu$ , of the absorbed photon less the energy required to eject the electron and any additional excitation energy of the target atom or molecule. For photon energies below about 25 keV, photoelectric absorption is the dominant effect. At higher energies Compton scattering, which is discussed in the next section, must be taken into account.

For photon energies above threshold ( $\sim 500$  eV), by far the most probable event is the ejection of one of the innermost (K shell) electrons of an atom. The ejection of the electron leaves a vacancy in the K shell. This will be filled by a transition of one of the outer electrons to the K shell. The transition can be accompanied by the emission of a photon, but a much more common occurrence is the emission of an Auger electron. In air the probability of photon emission is only about one percent, so the photoelectric absorption produces two secondary electrons, one with energy  $E - E_K \sim 200$  eV and the other with energy  $\sim 500$  eV, with the concomitant production of a doubly charged ion.

Photoelectric absorption can be characterized in terms of a cross section, or equivalently, a mass absorption coefficient. For our purposes, the latter is more useful. The absorption coefficient for air as given by a compilation of data by Gilmore (Reference 4-1) is shown in Figure 4-1. An analytical fit valid in the range 1-10 keV has been given by Wright (Reference 4-2).

$$\mu_v = \begin{cases} \frac{4560}{E^3} - \frac{870}{E^4} & (1.0 < E < 3.2 \text{ keV}) \\ \frac{4890}{E^3} - \frac{500}{E^4} & (3.2 < E < 10 \text{ keV}) \end{cases} \text{ cm}^2 \text{ gm}^{-1} \quad (4-1)$$

where  $E = h\nu$  is the photon energy in keV and the discontinuity at 3.2 keV corresponds to the K-edge of Argon. The K-edges of Nitrogen and Oxygen are at 410 and 541 eV, respectively, and are reflected in the discontinuities in  $\mu_v$  at these energies in Figure 4-1.

To calculate the transport and energy deposition of x-ray photons we note that the effect of absorption is simply to attenuate the x rays exponentially. Thus if a point source of spectral intensity  $S_{v0}$  is located at the origin, the intensity at a distance  $R$  from the source is

$$S_v(R) = \frac{S_{v0}}{4\pi R^2} \exp\left[-\int_0^R \mu_v(r) dr\right] \quad (4-2)$$

and the energy deposited per unit mass is

$$\frac{d\epsilon}{dm} = \frac{S_{v0}}{4\pi R^2} \exp\left[-\int_0^R \mu_v(r) dr\right] \quad (4-3)$$

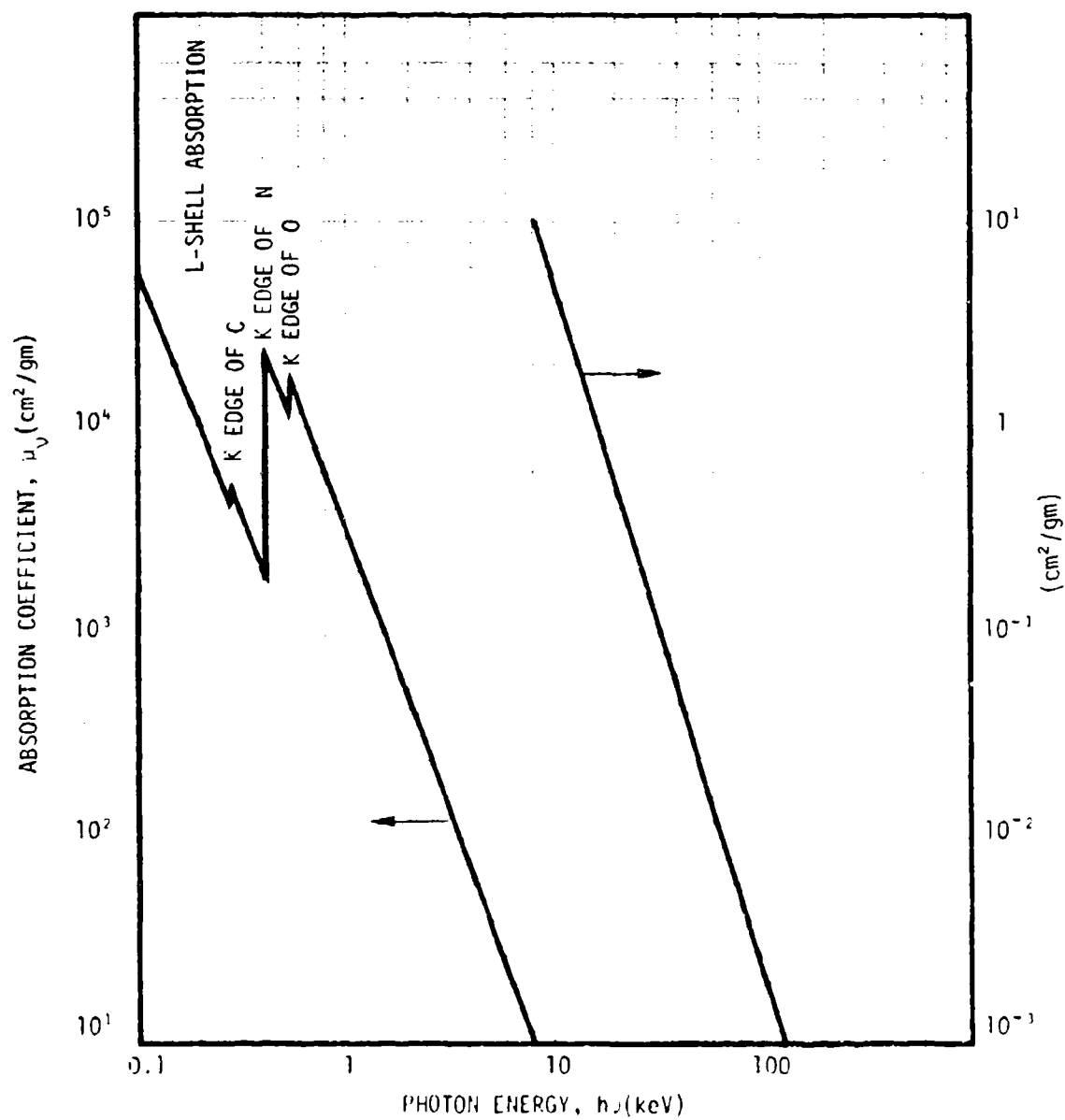


Figure 4-1. X-ray photoelectric absorption coefficient  $\mu_0$  in air.

The total energies and intensities are found by integrating these expressions over  $\nu$ .

Of particular interest is the case where  $S_\nu$  is a blackbody distribution at temperature  $T$ . For this case it is convenient to introduce the dimensionless variable

$$x = \frac{h\nu}{kT} \quad (4-4)$$

in terms of which the blackbody, or Planck spectrum is

$$S_{x_0} = S_0 \frac{15}{\pi^4} \frac{x^3}{e^x - 1} = S_0 B_x \quad (4-5)$$

where  $\int_0^\infty S_{x_0} dx = S_0$ , and  $S_{x_0}$  and  $S_0$  have the dimensions of energy. A plot of the universal Planck function  $B_x$  is shown in Figure 4-2.

Substitution of Equation 4-5 into Equations 4-2 and 4-3 and performance of the required numerical integration over  $x$  yields the results shown in Figure 4-3 and 4-4 for blackbody spectra of 1, 2, 4 and 8 keV. The results shown in these figures also include an approximate treatment of Compton scattering, as discussed in the next section. The abscissa on these graphs is the total mass per unit area of air traversed in arriving at the point  $R$ , i.e.,  $\int_0^R \rho dr$ . The energy deposition per unit mass is obtained by multiplying the left-hand ordinate by  $S_0/4\pi R^2$  where  $R$  is the distance from the source in cm and  $S_0$  is the total energy radiated in the desired units. The energy per unit volume ( $\text{cm}^3$ ) is obtained from this upon multiplication by  $\rho$  ( $\text{gm cm}^{-3}$ ) and the energy per target atom is obtained by multiplying the energy per unit mass by the mass ( $\text{gm}$ ) of an atom.

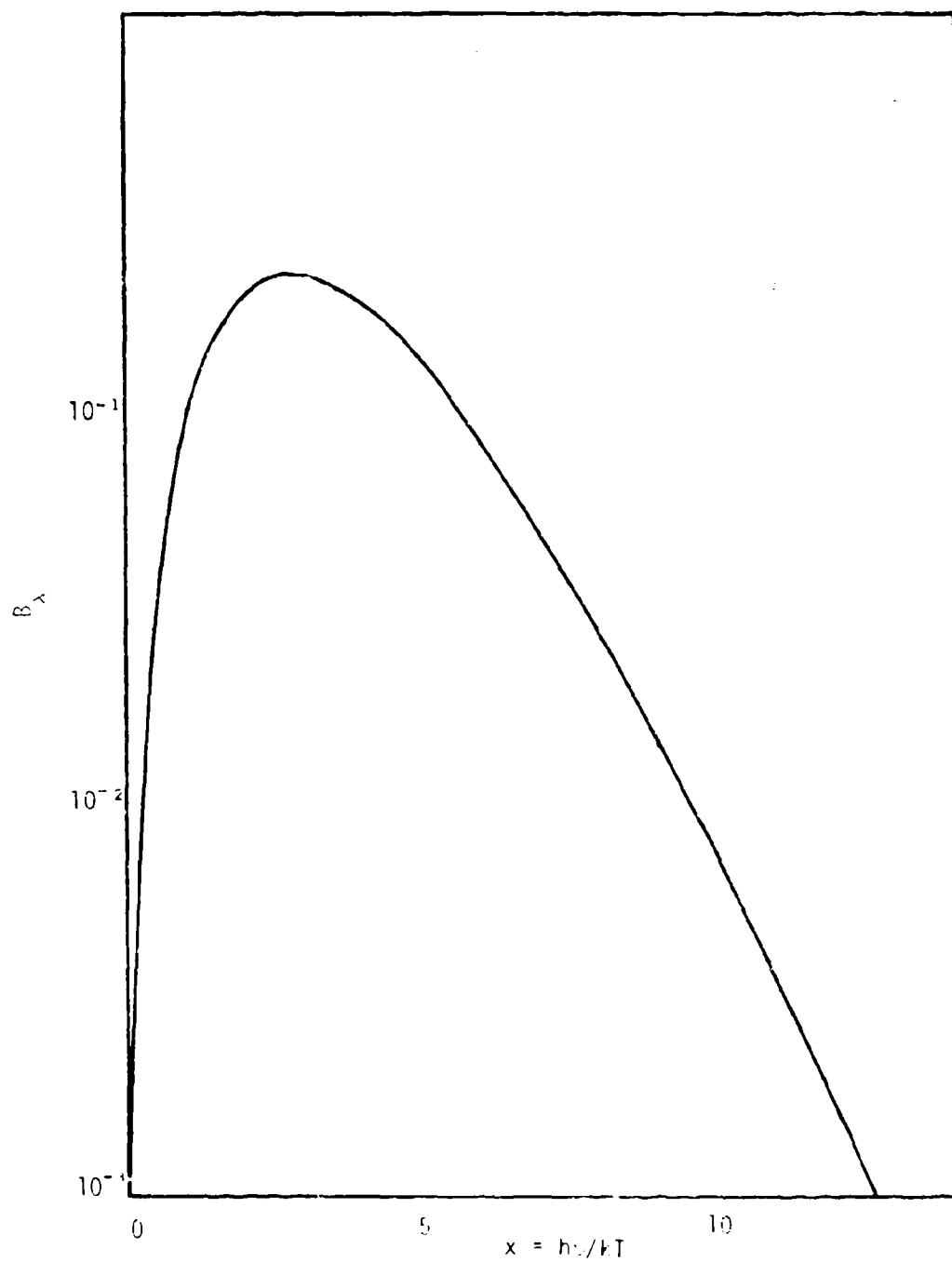


Figure 4-2 Universal Planck function  $B_\lambda$ .

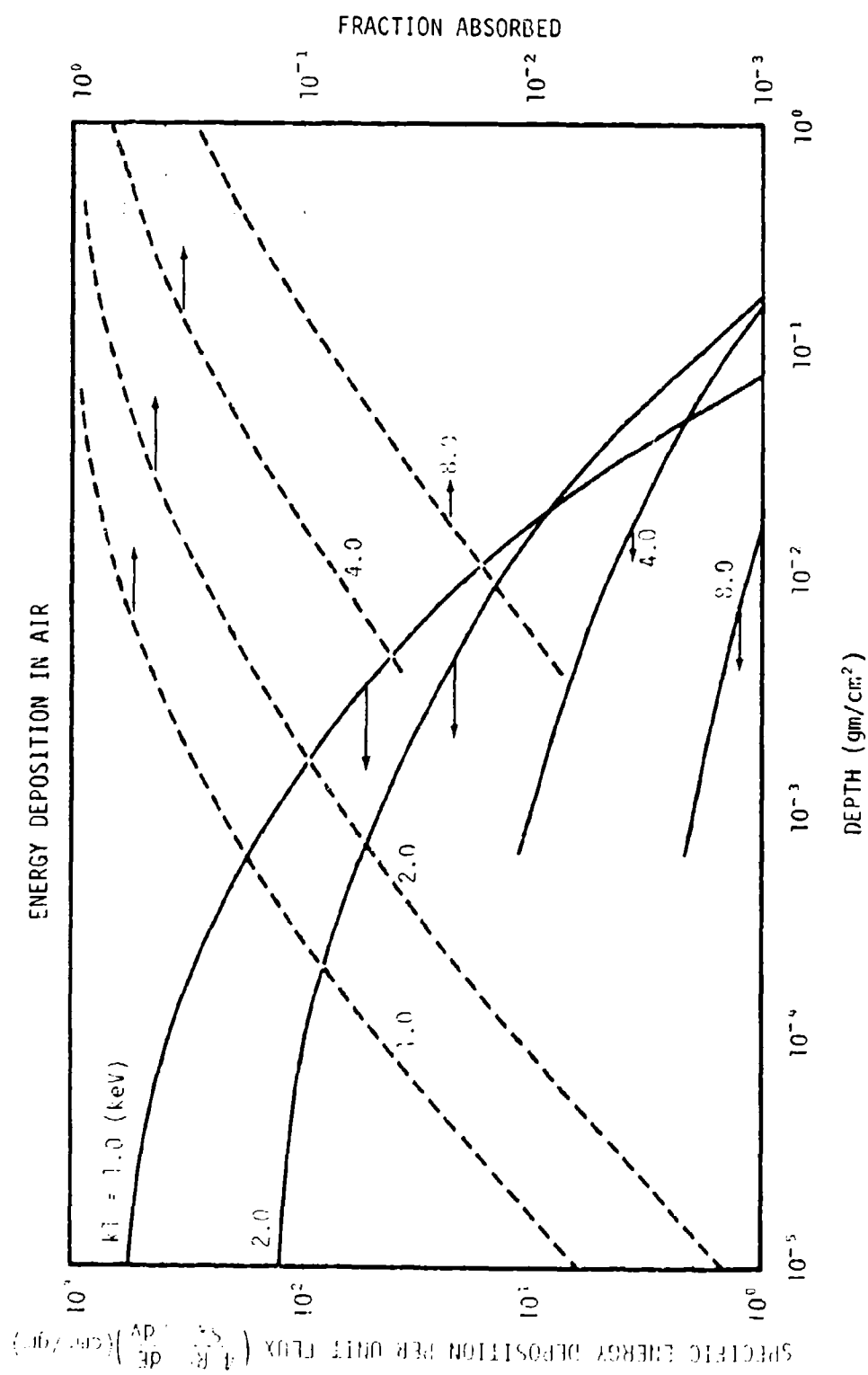


Figure 4-3. Specific energy deposition and fractional absorption for several blackbody spectra at small optical depths.

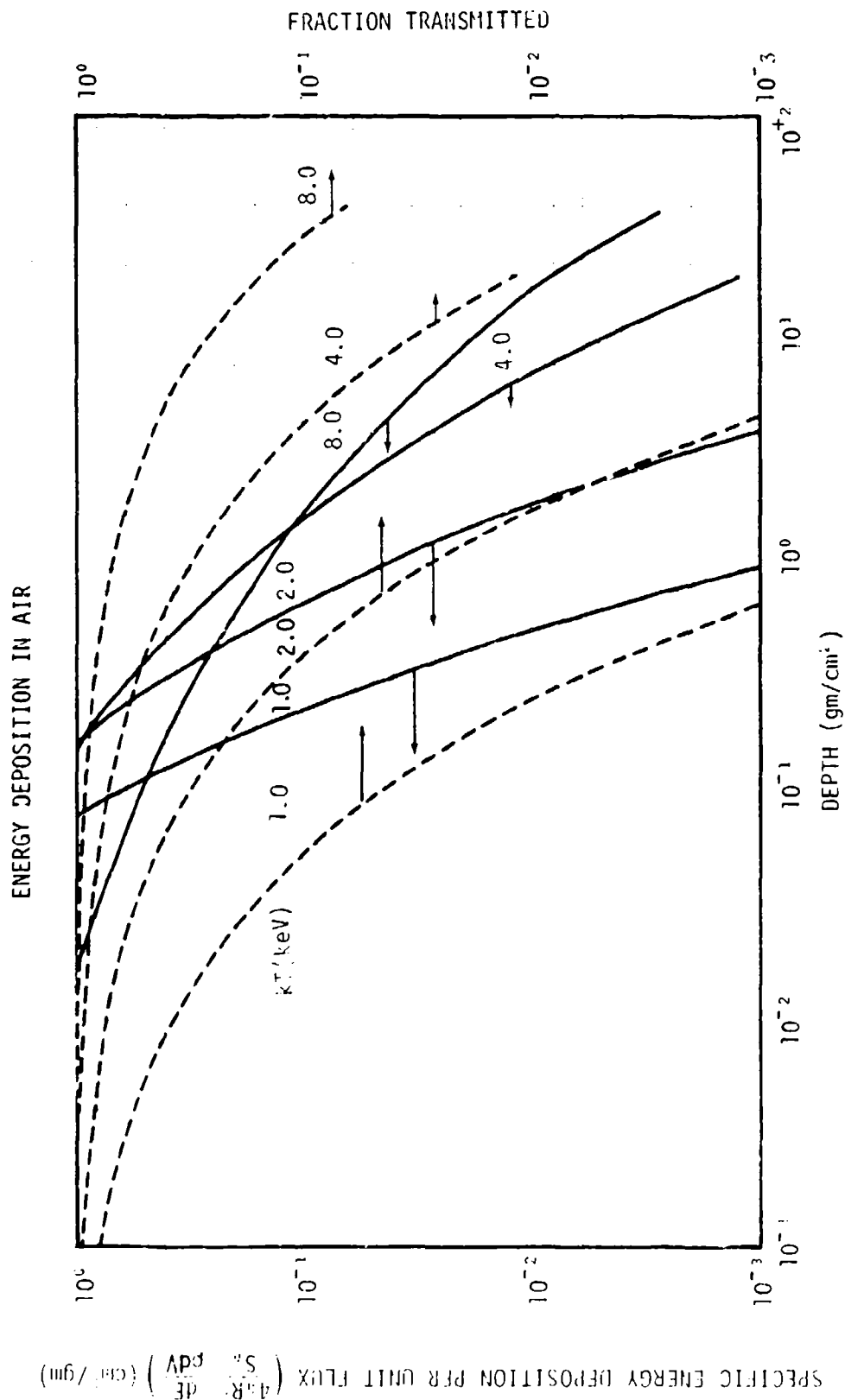


Figure 4-4. Specific energy deposition and fractional transmission for several blackbody spectra at large optical depths.

The crossing of the deposition curves is easily understood from the above equations. Near the source the intensity is unattenuated and the deposition is just proportional to the absorption coefficient, which is larger at the lower photon energies characteristic of the lower temperatures. At greater distances the intensities are attenuated exponentially, the lower energies being more strongly attenuated, so that eventually the larger absorption coefficient is more than compensated by the greater attenuation, and the curves cross. One should note also that because of the energy dependence of the absorption coefficient, the spectrum is harder at increasing distance, since the soft photons are absorbed preferentially.

It is frequently useful to have an approximate analytical expression for the energy deposition. Such an expression has been provided by Bethe (Reference 4-3) for large distances from the source. The general expression for the deposition is

$$\frac{dE}{\rho dV} = \frac{S_0}{4\pi R^2} \int_0^R \mu_{\nu} B_X e^{-\mu_{\nu} r} dr \quad (4-6)$$

For simplicity we assume that

$$\mu_{\nu} = \frac{A}{(h\nu)^3} = \frac{Ax^{-3}}{(kT)^3} \text{ (cm}^2 \text{ gm}^{-1}\text{)} \quad (4-7)$$

and define the mass per unit area  $M$

$$M = \int_0^R \rho dr \text{ (gm cm}^{-2}\text{)} \quad (4-8)$$

and the quantity  $\zeta$



$$\zeta = \frac{AM}{kT^3} \quad (4-9)$$

Clearly  $\zeta$  is the number of mean free paths from the source to the point R for photons with energy  $kT$ .

In terms of these quantities Equation 4-6 becomes

$$\frac{dE}{\rho dV} = \frac{15S_0A}{4\pi^5 R^2 (kT)^3} \int_0^\infty \frac{e^{-\zeta x^{-3}}}{e^x - 1} dx \quad (4-10)$$

At large distances the main contribution is from hard photons for which  $x \gg 1$ , so we can replace  $(e^x - 1)^{-1}$  by  $e^{-x}$  to obtain

$$\frac{dE}{\rho dV} \approx \frac{15S_0A}{4\pi^5 R^2 (kT)^3} \int_0^\infty e^{-(x + \zeta x^{-3})} dx \quad (4-11)$$

The integrand has a sharp maximum at

$$x_0 = (3\zeta)^{1/4} = \left[ \frac{3AM}{(kT)^3} \right]^{1/4} \quad (4-12)$$

The integral can be evaluated approximately by the method of steepest descents. Its value is  $\sqrt{\frac{\pi x_0}{2}} e^{-\left(\frac{4}{5} \frac{AM}{kT^3}\right)}$ , so that Equation 4-11 becomes

$$\frac{dE}{\rho dV} \approx \frac{15S_0A}{4\pi^5 R^2 (kT)^3} \sqrt{\frac{\pi}{2}} \left[ \frac{3AM}{(kT)^3} \right]^{1/4} \exp \left\{ -\frac{4}{5} \left[ \frac{3AM}{(kT)^3} \right]^{1/4} \right\} \quad (4-13)$$

This formula provides a good approximation ( $\sim 10\%$  accuracy) for  $\zeta$  in the range 10-100. At shorter ranges it is in error because of the error

at low photon energies of the approximate form for  $\mu_v$  (Equation 4-7) and at longer ranges because of neglect of the Compton effect.

Finally we mention that at small distances from an intense source the possibility of stripping all of the electrons from an atom must be taken into account. In the preceding discussion we have tacitly assumed that the air was only mildly perturbed by the x-ray deposition. At sufficiently high intensities, however, this approximation breaks down, and stripping may occur. This possibility has been discussed in detail by Landshoff (Reference 4-4).

#### 4.3 The Compton Effect

Compton scattering is the scattering of a photon by an electron. In the case of scattering by free electrons, the interaction can be regarded simply as the elastic scattering of two particles. If the electron is at rest, initially monoenergetic photons scattered at a given angle have a definite energy that is determined by the requirements of energy and momentum conservation.

Scattering can also occur from electrons bound in an atom. In general the fact that the electrons are not free must be taken into account. However, Compton scattering in air plays a negligible role compared with photoelectric absorption at photon energies below 25 keV. At these energies it is not a bad approximation to treat the electrons as free, and the validity of the approximation improves rapidly with increasing energy.

The effect of a Compton scattering is to produce an ejected electron and a photon with lower energy traveling in a direction different from that of the original photon. Clearly an accurate treatment of energetic X-ray or  $\gamma$ -ray transport entails a complicated calculation in which scattering angles, fractional energy losses, etc. are taken into account. In

the next section, methods for performing such detailed calculations are discussed. In the remainder of this section we deal with crude methods of calculating some of the gross features of transport and deposition of  $\gamma$  rays and energetic x rays.

An effective Compton absorption coefficient can be defined as follows: Let  $\mu_c$  ( $\text{cm}^2 \text{ gm}^{-1}$ ) be the total scattering coefficient and suppose the mean energy lost per collision is  $\Delta h\nu$ . Then the fractional energy lost is  $\Delta h\nu/h\nu$ , so we define the effective Compton energy absorption coefficient to be

$$\mu_{\text{CA}} = \frac{\Delta h\nu}{h\nu} \mu_c \quad (4-14)$$

The scattering coefficient and the effective absorption coefficient as calculated in this way by Veigele *et al.* (Reference 4-5) are shown in Figure 4-5, where they are compared with the photoelectric absorption coefficient of Figure 4-1.

The effective absorption coefficient provides a suitable measure of energy deposition for a given local spectral intensity. To obtain the local intensity, however, the transport equations must be solved. The difficulty is that while energy is absorbed, the photons are not. Thus, if one calculates intensities on the basis of an exponential photon absorption, he will underestimate the intensity at large distances from the source.

A useful approximate method of treating this problem is by means of the so-called buildup factor. In this approximation, the intensity is assumed to be attenuated exponentially by scattering, but the intensity calculated from this assumption is multiplied by a correction factor - the buildup factor - to account for the fact that gammas are not

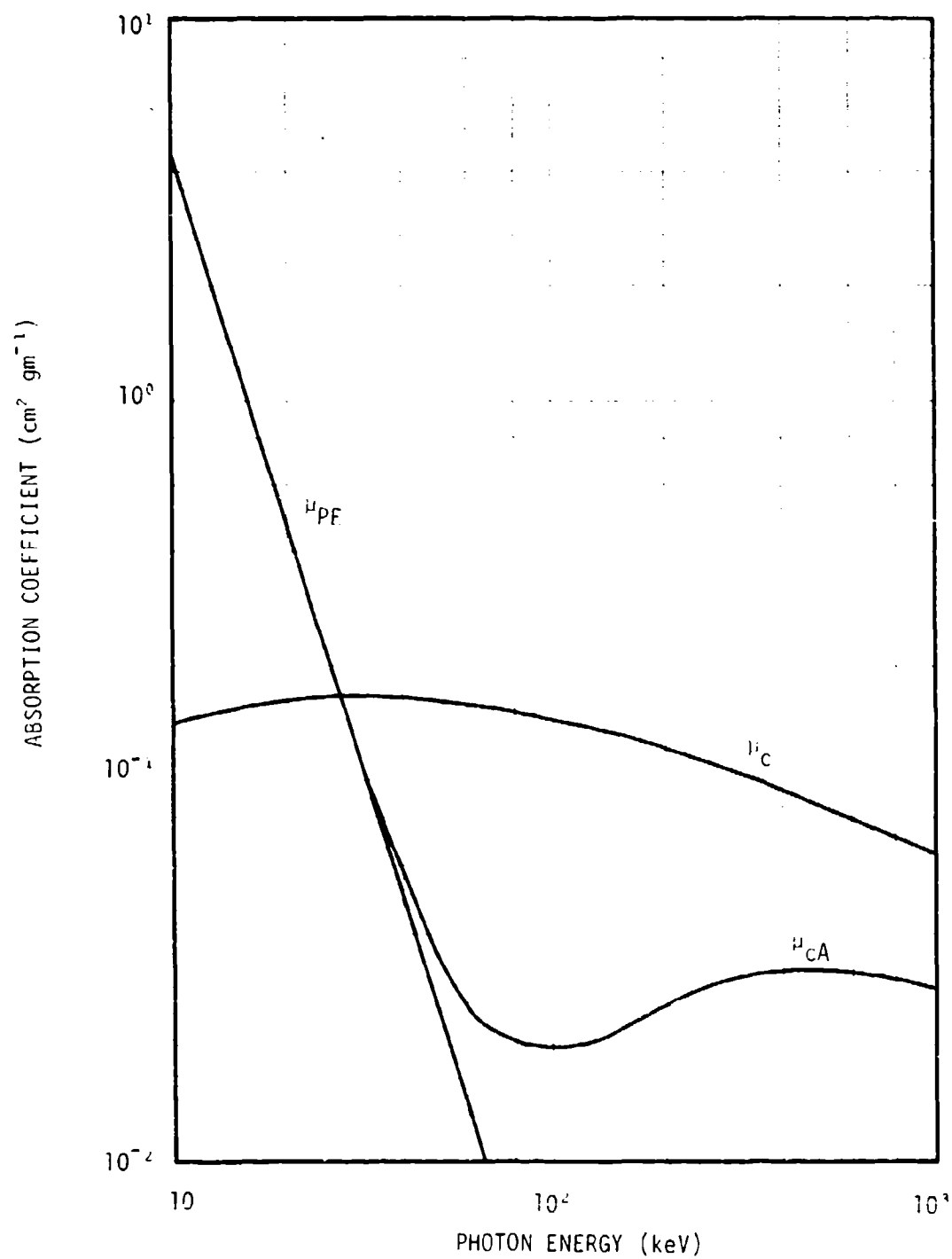


Figure 4-5. Compton absorption coefficient.

destroyed in the scattering process. Thus, if  $N_{E_0}$  is the number of photons emitted per unit energy interval, the number arriving per unit area per unit energy at distance  $R$  is taken to be

$$N(E, R) = \frac{N_{E_0}}{4\pi R^2} B(E, M) e^{-\mu_c(E)M} \quad (4-15)$$

where  $M$  is the mass per unit area traversed in arriving at  $R$  and  $B(E, M)$  is the buildup factor. Values of the buildup factor as calculated by Goldstein and Wilkins (Reference 4-6) and reported by Bennett (Reference 4-7) are shown in Figure 4-6. The number of mean free paths labelling the curves is the number of scattering mean free paths. It is apparent that the buildup is an important factor, particularly at great distances.

#### 4.4 Detailed Numerical Calculations of Gamma-Ray and Neutron Transport

As mentioned in the preceding section, a proper treatment of the transport problem in situations where scattering is occurring requires a detailed numerical calculation. In this section we briefly outline some of the numerical methods that have been developed to handle this problem. No results of such calculations are presented here. The reader is referred to the literature for details of the calculations and the results obtained. A general discussion of the subject is contained in references 4-8, 9, 10, 11.

Calculations of neutron and  $\gamma$ -ray transport have much in common, since they both involve the interplay between absorption and scattering processes. The following discussion is sufficiently general to embrace both types of primaries. The starting point for the discussion of transport is the linearized Boltzmann equation. Let  $\phi(\vec{r}, \vec{\Omega}, E, t)$  denote the flux of particles (either gammas or neutrons) at point  $\vec{r}$

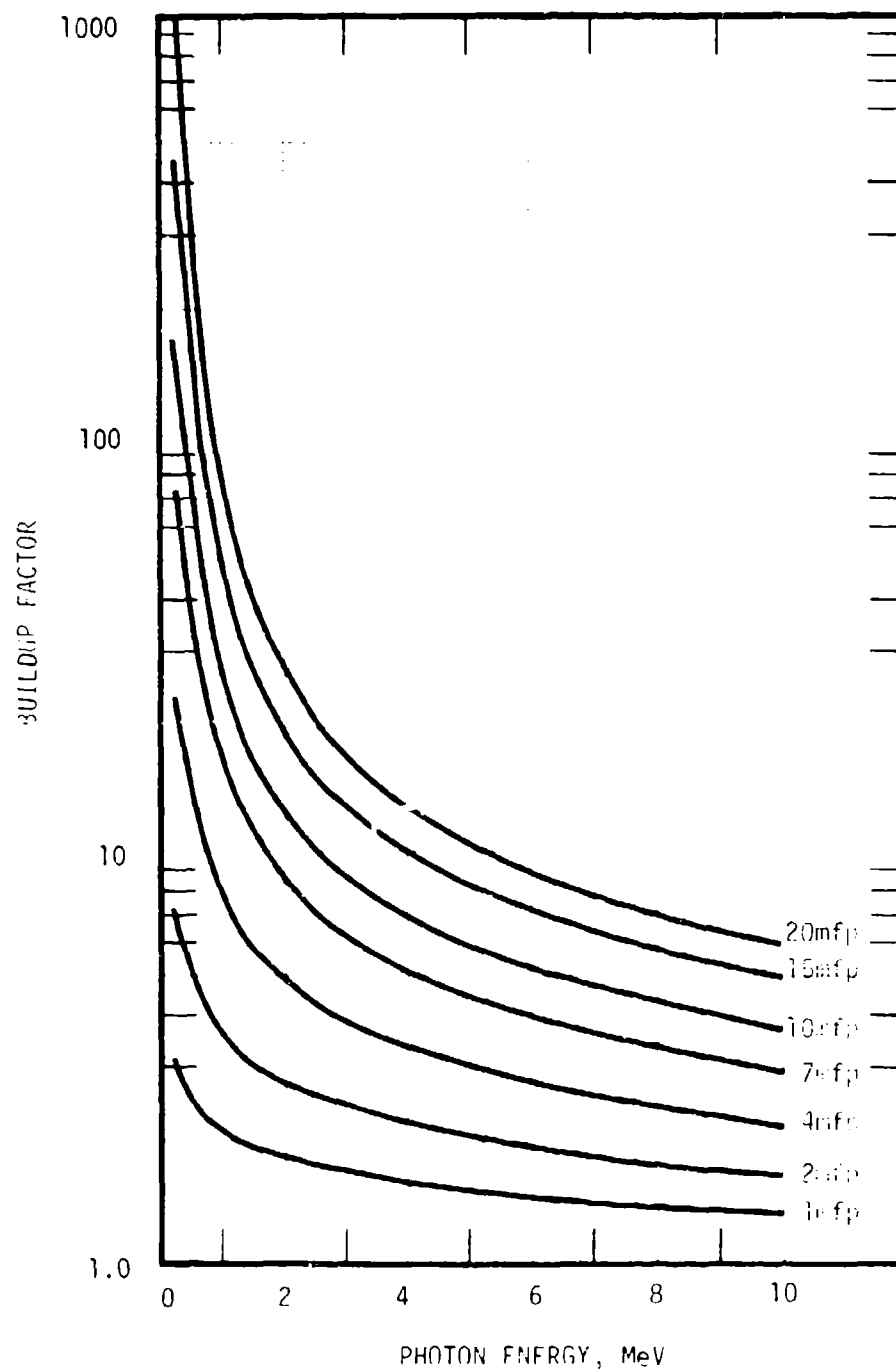


Figure 4-6. Buildup factor,  $B(F,m)$ , versus photon energy for several values of attenuation length.

and time  $t$ . It is to be understood that  $\phi$  is the flux per unit energy interval crossing unit area normal to  $\vec{\Omega}$  in unit time. Thus  $\phi$  is a function of seven variables - three spatial, two angular, energy and time.

The linearized Boltzmann equation that governs the behavior of  $\phi$  is

$$\frac{1}{v} \frac{\partial \phi(\vec{\Omega}, E)}{\partial t} = S + \iint \phi(\vec{\Omega}', E') \sum_s (\vec{\Omega}' \rightarrow \vec{\Omega}, E' \rightarrow E) dE' d\Omega' - \vec{v} \cdot (\vec{\Omega} \phi) - \sum_t \phi \quad (4-16)$$

In this equation  $v$  is the particle velocity corresponding to energy  $E$  (its value is  $c$  in the case of photons), and the arguments  $\vec{r}$  and  $t$  have been suppressed.  $S$  is the source term, the rate of production of particles with  $\vec{\Omega}$ ,  $E$ . The integral gives the scattering into the beam.  $\sum_s$  is the macroscopic scattering cross section, equal to the product of the density of scattering particles and the microscopic differential cross scattering section  $\frac{d^2\sigma}{d\Omega dE}$ . The term  $-\vec{v} \cdot (\vec{\Omega} \phi)$  gives the convective change in the flux, while  $-\phi \sum_t$  is the term that describes absorption and scattering out of the beam, where  $\sum_t$  is the total macroscopic cross section.

Several different numerical procedures have been developed for solution of the transport equation. A brief description of some of these follows.

#### 4.4.1 Point Kernel Methods

Point Kernel, or Green's function methods are discussed in References 4-12, 13, 14. In this approach one first solves the problem for a point impulsive source and then uses this solution in integrating over all

sources. The simplest example of a kernel is the inverse square, exponential attenuation case for which the kernel is  $e^{-\mu M}/4\pi R^2$  as discussed above. Another example is the treatment of scattering by use of a buildup factor, also discussed above, in which case the kernel is  $B(E,M)e^{-\mu M}/4\pi R^2$ .

#### 4.4.2 Discrete Ordinates Methods

The method of discrete ordinates is discussed in References 4-15, 16, 17, 18. This method is completely numerical in nature. Phase space is broken up into finite cells and the particle flow among these cells is balanced by performing a sequence of local integrations over the transport functions. A Gaussian or Gauss-Legendre quadrature scheme is employed in calculating the scattering integral in the transport equation. The method has been successfully applied to one- and two-dimensional steady state problems and to time-dependent one-dimensional problems. The method has the advantage of being relatively straightforward, but great care must be exercised in formulating numerical techniques to assure convergence.

#### 4.4.3 The Monte Carlo Method

Monte Carlo methods for solution of transport problems are discussed in References 4-19, 20, 21, 22, 23. The Monte Carlo method employs random sampling as a means of simulating the statistical aspects of the problem of interest. The range of applicability is large; for example, three-dimensional problems in inhomogeneous media can be treated with this method.

The method may be used to obtain a solution of the transport equation by providing statistical estimates of the quantities appearing in the equation, or by providing a direct simulation of the problem. The latter technique is most frequently employed. In this the probability



of occurrence of a particular event such as absorption or scattering through a particular angle is correlated with the probability of selection of a number chosen at random. Numbers are then chosen from a table of random numbers and used to define the history of a single particle. Many such histories are summed to obtain the final result. The accuracy attained clearly depends upon summing over a large number of histories.

#### 4.4.4 The Orders of Scattering Method

The orders of scattering method is discussed in Section 8 of Reference 4-8. This is an iterative solution of the Boltzmann equation. One first calculates a zero order solution,  $\phi_0$ , that neglects inscattering, substitutes this in the integral to calculate a new approximation  $\phi_1$ , uses this to calculate a new approximation  $\phi_2$ , etc. The solution is presumed to converge after a finite number of iterations, but the rate of convergence of course depends on the accuracy of the numerical procedures employed.

#### 4.4.5 The Moments Method

This method is discussed in Section 12 of Reference 4-8 and in References 4-24, 25. It is a hybrid method employing a combination of numerical and analytical techniques to solve the Boltzmann equation. This approach was originally developed by Spencer and Fano. It is rigorously applicable only to problems involving infinite homogeneous media, but its range of applicability can be extended by various transformations. Good results are obtained for angular distributions and fluxes at distances greater than two mean free paths from boundaries and interfaces. The solution is obtained in the form of a series of Legendre polynomials describing the angular distribution, the coefficients in the expansion being energy dependent.

#### 4.4.6 The Diffusion Approximation

The solution of the transport equation in the diffusion approximation is discussed in References 4-10, 26. In this approximation the flux is assumed to be isotropic and the transport equation is replaced by a diffusion equation. The method is useful because of the ease with which solutions are obtained but is of very limited applicability because of the assumption of isotropy. It is used primarily in neutron transport calculations, where the scattering cross section is nearly isotropic.

#### 4.4.7 Cross Section Data

Finally, we note that the accuracy of all of the calculational methods discussed above depends crucially on the accuracy of the cross section data employed in the calculations. Since a typical particle undergoes a very large number of interactions before it is absorbed, large cumulative errors can result from relatively small errors in the microscopic data.

Over the past ten or so years, many quite flexible and well-proven transport codes have been developed. Each of these codes reads in, stores, and uses the basic data in a slightly different manner. Selected government sponsored centers, mainly the Radiation Shielding Information Center (RSIC) at Oak Ridge National Laboratory and the National Neutron Cross Section Center (NNCSC) at Brookhaven National Laboratory accumulate evaluated nuclear data and provide these data to potential users in an acceptable standardized format. Such a format -- the Evaluated Nuclear Data File/revision B (ENDF/B) -- has been adopted in principle and is beginning to enjoy a much expanded use in current transport calculations. The availability of ready-to-use multigroup cross section sets for discrete ordinates codes and the few multigroup Monte Carlo codes is limited to date, although several peripheral processing codes are

available for converting the ENDF/B data. A new ENDF/D-to-multigroup processing code, AMPX, has been developed and is presently being checked out; when completed this code will facilitate the use of ENDF/B data to a still greater degree.

#### 4.5 Transport and Energy Deposition of Betas

In traversing matter, energetic electrons (*i.e.* those with energies in excess of a few hundred eV) lose energy primarily as a result of ionizing collisions with ambient atoms. Semiclassical theories of the rate of energy loss in this process have been made by Thomson and Bohr (see *e.g.* Reference 4-27, which is an excellent review of this entire subject).

A more accurate quantum mechanical treatment of the problem has been given by Bethe, and an important contribution has been made by Bloch (Refs. 4-27, 28). The results are contained in the Bethe-Bloch formula for the average rate of energy loss per unit length  $z$  measured along the trajectory

$$-\frac{dE}{dz} = \frac{3\sigma_0 N Z E^2 m c^2}{4(E^2 - m^2 c^4)} \left\{ \ln \left[ \frac{(E - m c^2)^2 (E + m c^2)}{2 m c^2 \beta^2} \right] - \frac{m c^2 (2E - m c^2) \ln 2}{E^2} + \frac{m^2 c^4}{E^2} + \frac{(E - m c^2)^2}{2 E^2} \right\} \quad (4-27)$$

where  $N$  is the number density of atoms in the medium being traversed,  $Z$  their mean atomic number,  $c$  the velocity of light, and  $m$  is the mass of the electron.  $E$  denotes the total relativistic energy of the energetic electron

$$E = \frac{m c^2}{(1 - v^2/c^2)^{1/2}} \quad (4-28)$$

so its kinetic energy is

$$T = E - mc^2 \quad (4-29)$$

with  $v$  denoting the velocity of the electron. The quantity  $\sigma_0$  in Equation 4-27 is the Thomson cross section

$$\sigma_0 = \frac{8\pi r_0^2}{3} = 6.57 \times 10^{-25} \text{ (cm}^2\text{)} \quad (4-30)$$

where  $r_0$  is the classical electron radius

$$r_0 = \frac{e^2}{mc^2} = 2.80 \times 10^{-13} \text{ (cm)} \quad (4-31)$$

Finally,  $I$  denotes the mean ionization potential of the target atoms, which we take to be 94 eV for air.  $dE/dz$  as calculated from Equation 4-27 is shown in Figure 4-7. The quantity  $dE/dz$  is frequently called the stopping power of the medium.

For all but very low energies, only the first term in the braces of Equation 4-27 need be retained. Neglect of all the other terms leads to an error of but 5 percent for 5 keV and only about 1 percent at 50 keV. With this approximation, and taking  $Z = 7.2$  for air, we find

$$-\frac{dE}{dz} = 97.5 \frac{\rho}{\rho_0} \frac{E^2}{E^2 - m^2 c^4} \ln \left[ \frac{(E - mc^2)^2 (E + mc^2)}{2mc^2 I^2} \right] (\text{eV cm}^{-1}) \quad (4-32)$$

where  $\rho$  is the density at the point of interest and  $\rho_0$  is the sea level atmospheric density, taken to be  $1.29 \times 10^{-3} \text{ gm cm}^{-3}$ .

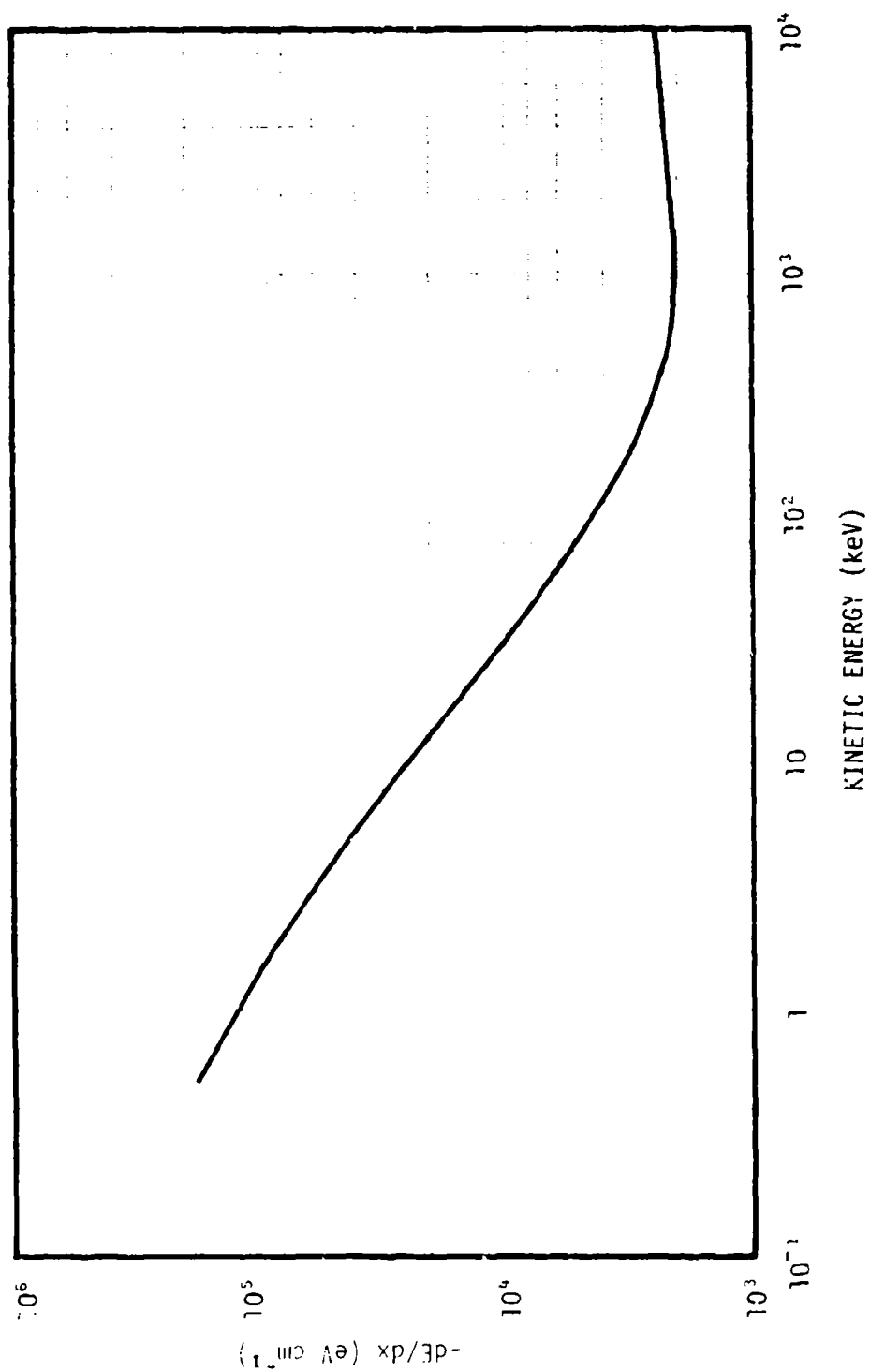


Figure 4-7. Energy Loss of Betas in Sea Level in air ( $1.29 \times 10^{-3} \text{ gm cm}^{-3}$ ).

As a beta progresses through the atmosphere its energy decreases. Because of the variation of atmospheric density with position, it is again convenient to replace the length coordinate with the previously defined mass coordinate  $M$  given by

$$M = \int_{z_0}^z \rho dz' \quad (\text{gm cm}^{-2}) \quad (4-33)$$

We then have

$$\frac{dE}{dM} = \frac{dE}{dz} \frac{dz}{dM} = \frac{1}{\rho} \frac{dE}{dz} \quad (4-34)$$

so that  $dE/dM$  depends only upon the instantaneous energy of the beta, and has no explicit dependence on position or density. The mass traversed and the instantaneous energy  $E$  are related to the initial energy  $E_0$  through the equation

$$M(E_0, E) = \int_E^{E_0} \frac{dE}{-dE/dM} \quad (4-35)$$

Equation (4-35) implicitly gives  $E$  as a function of  $E_0$  and  $M$ . In principle the expression can be inverted to obtain  $E$  as an explicit function of  $E_0$  and  $M$ ; the inversion can in fact be performed numerically. Since  $dE/dM$  depends only on  $E$ , it follows that  $dE/dM$  is completely determined by knowledge of  $E_0$  and  $M$ , and can be regarded as a function of these variables.

The range  $M_0$  is found by setting  $E = mc^2$  in Equation 4-35, so that

$$M_0 = \int_0^E \frac{dE}{mc^2 \frac{-dE}{dM}} \quad (4-36)$$

The range  $R_0$  in units of length can be found from an equation analogous to (4-36) or from knowledge of  $M_0$  and Equation (4-33). It is also useful to define a dimensionless coordinate  $\xi$ ,

$$\xi = \frac{M}{M_0} \quad (4-37)$$

so that  $\xi$  is the fraction of the range traversed, and  $0 \leq \xi \leq 1$ .

The preceding equations can be used to calculate the energy deposition at various points in the neighborhood of a  $\beta$  source. One first calculates the value of  $M$  at the point of interest from Equation 4-33. Next the energy of a particle arriving at this point is determined from Equation 4-35. Finally, this energy is substituted into Equation 4-27 or 4-32 to yield  $dE/dz$ . Note that this procedure assumes that the betas move in straight lines without scattering. All of the energy is deposited within a range  $M_0$  of the source.

The neglect of scattering overlooks the fact that the betas do not actually move in straight lines, but instead follow more complicated trajectories that include many small angle scatterings. This affects the energy deposition in two ways. In moving from the source to a given point, the beta actually travels farther than the geometrical distance, and loses more energy in the process, so that the relationship between energy and range is altered. Indeed, there is no well-defined relationship because many trajectories can lead to the same point, but each trajectory corresponds to a different energy loss. Therefore betas passing

through the neighborhood of a point exhibit a finite energy spread even for the case of a monoenergetic source. The average energy of this distribution is less than that calculated from the assumption of straight-line trajectories. The second effect is that in traversing a given element of volume the beta travels farther than it would in the absence of scattering, and thus deposits more energy in the volume than it otherwise would have.

The effects of scattering have been treated approximately by Spencer in a moments calculation of the energy deposition (Reference 4-29). Spencer defines a dimensionless dissipation function  $J(\xi)$  such that for a monoenergetic source of betas with energy  $E_0$

$$\frac{dE}{dM} = \left( \frac{dE}{dM} \right)_0 J(\xi) \quad (\text{MeV cm}^2 \text{gm}^{-1}) \quad (4-38)$$

where  $(dE/dM)_0$  is the value corresponding to  $E_0$  and  $\xi$  is the dimensionless range variable defined in Equation 4-37.

To illustrate the effects of scattering,  $dE/dM$  for a unit point source of 1 MeV betas, *i.e.*, for one beta per  $4\pi$  steradians, as calculated from Equations 4-27 and 4-38, are shown in Figure 4-8. Also shown is the constant value for the case  $dE/dM = \text{const.} = 2 \text{ MeV cm}^2 \text{gm}^{-1}$  assumed by Latter and Lelevier in Reference 4-30 (for 1 MeV betas,  $(dE/dM)_0$  is  $1.65 \text{ MeV cm}^2 \text{gm}^{-1}$ , see Figure 4-8). The tabulated values of  $J(\xi)$  given by Spencer were used for the scattering calculation, whereas scattering was neglected in the application of Equation 4-27. For this case the energy deposition at a point a geometrical distance  $z$  from the source is found by multiplying  $dE/dM$  of Figure 4-8 by an appropriate factor. The energy deposition per beta per unit mass is

$$\frac{dE}{dm} = \frac{1}{4\pi z^2} \frac{dE}{dM} \quad (\text{MeV gm}^{-1}) \quad (4-39)$$



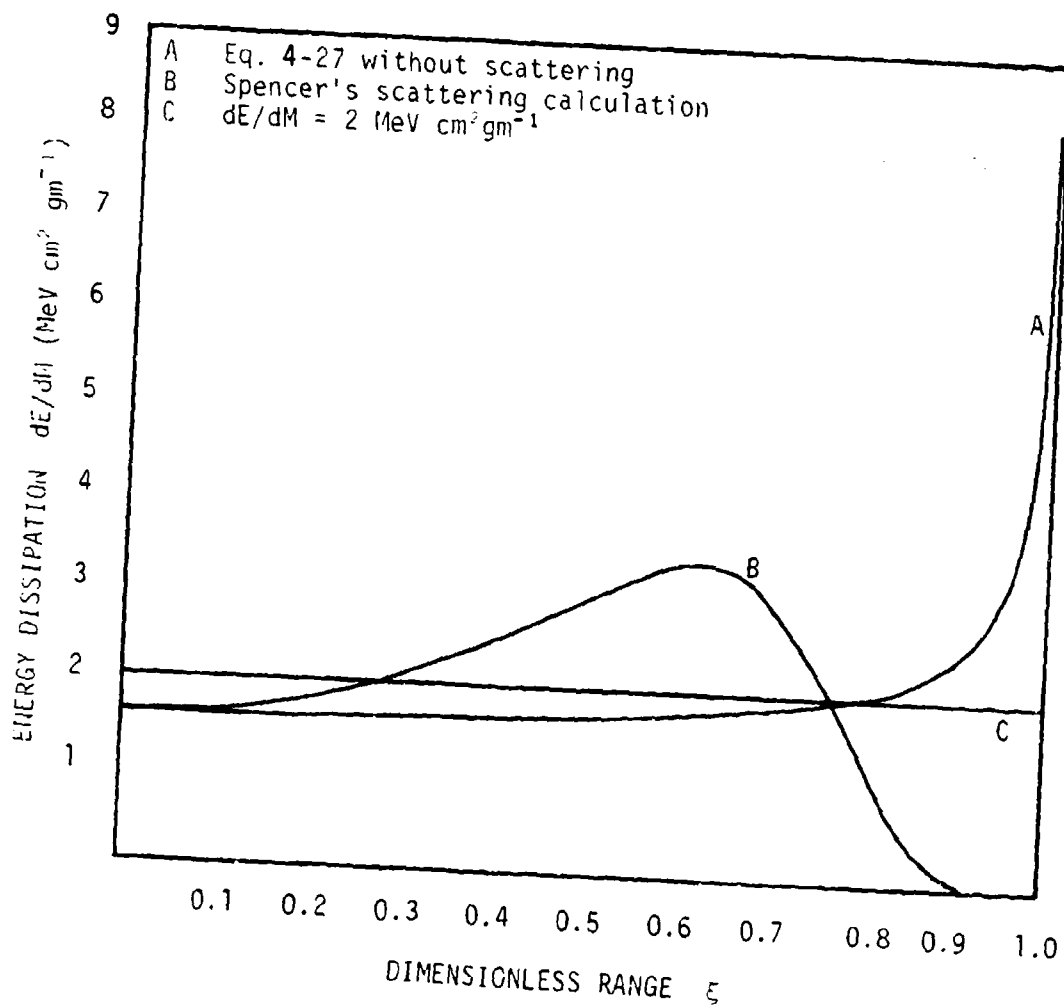


Figure 4-8. Energy dissipation for an isotropic point source of 1 MeV Betas.

and the energy deposition per beta per unit volume  $v$  is

$$\frac{dE}{dV} = \frac{\rho}{4\pi z^2} \frac{dE}{dM} \text{ (MeV cm}^{-3}\text{)} \quad (4-40)$$

where  $dE/dM$  is evaluated at the value of  $\xi$  corresponding to  $z$ .

The results of the two calculations seem to be quite different. They give similar results for short ranges, before the cumulative effects of scattering have become important. These come into play at larger ranges, and result in a higher rate of energy deposition, as is to be expected from the foregoing discussion. At still greater distances, the attenuation of the flux resulting from scattering dominates, and the rate of energy deposition falls below that predicted by the simple theory.

The differences in the calculations are much less marked in the case of a plane isotropic source of betas. Results for a plane isotropic source can be obtained from those for a point isotropic source by integration over a plane. It is easily shown that in this case the scattering calculation gives for the deposition per unit volume

$$\frac{dE}{dV} = \frac{dN_B/dA}{2} \rho (dE/dM)_0 \int_{\xi}^1 \frac{J(\xi') d\xi'}{\xi'} \quad (4-41)$$

where  $dN_B/dA$  is the number of betas emitted per unit area of the source plane and  $\xi$  is the dimensionless coordinate, measured normal to this plane, of the point of interest. A similar result holds for the non-scattering calculation. In both cases the deposition per unit mass is, of course,

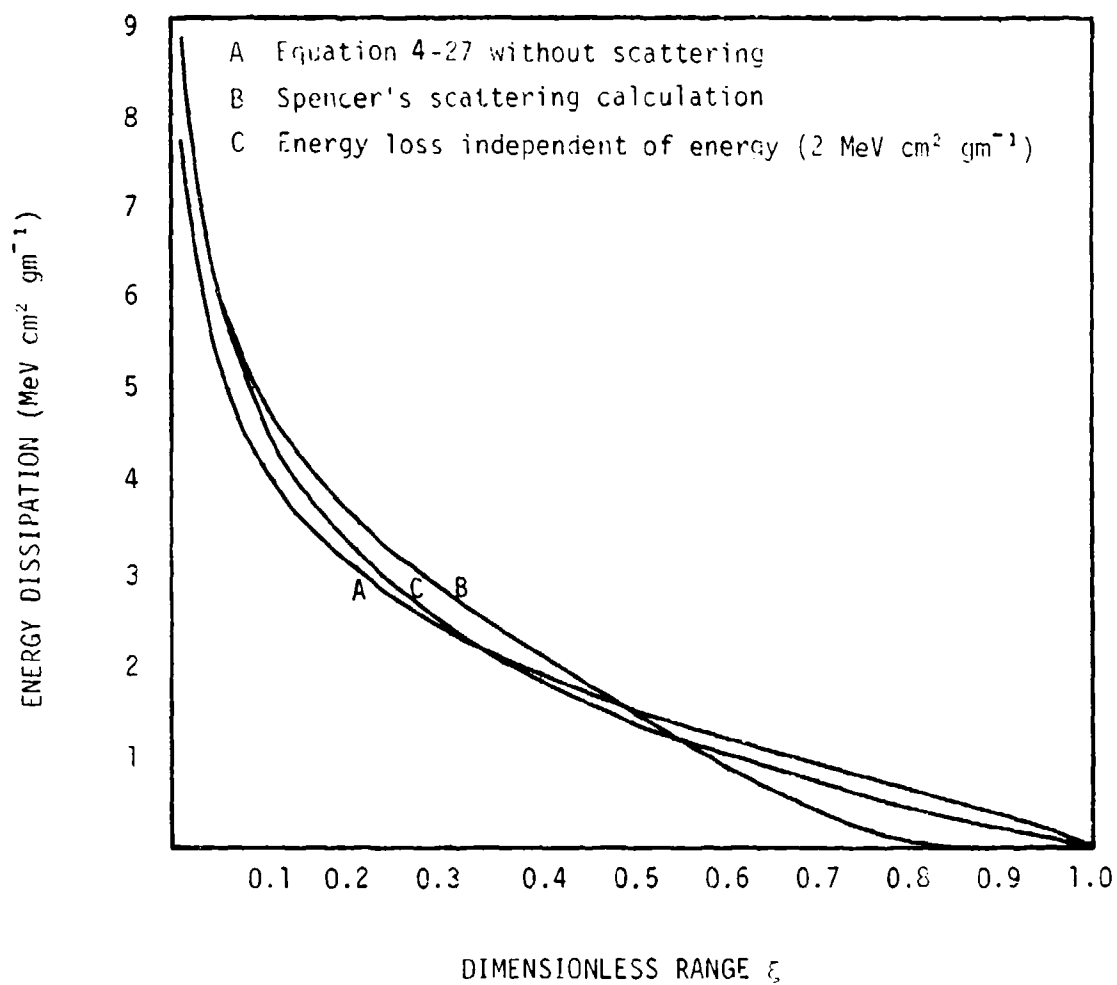


Figure 4-9. Energy dissipation  $(dE/dM)_0 \int_{\xi}^1 \frac{J(\xi') d\xi'}{\xi'}$  for a plane isotropic source of 1 MeV betas.

$$dE/dm = \rho^{-1} (dE/dV) \quad (4-42)$$

The quantity  $(dE/dm)_0 \int_{\xi}^1 \frac{J(\xi') d\xi'}{\xi'}$  for a 1 MeV isotropic plane source

is shown in Figure 4-9, together with the corresponding function for the calculation from Equation 4-2" without scattering. Also shown is the Latter-Lelevier result obtained by taking  $dE/dM$  to have the energy-independent value  $2 \text{ MeV cm}^2 \text{ gm}^{-1}$ . From Figure 4-9 it is apparent, as stated earlier, that the various calculations give quite similar results for the plane isotropic source. This is an important fact, since it makes possible considerable simplification in the calculation of fission beta energy deposition. More detailed results of  $\beta$  energy deposition of calculations can be found in Reference 4-31.

#### 4.6 TRANSPORT AND ENERGY DEPOSITION OF DEBRIS ATOMS

In this section, we shall discuss the transport and energy disposition of debris atoms whose velocities lie within the range of tens to thousands of kilometers per second. At the high side of the velocity range these particles interact and lose energy to the ambient medium primarily by inducing electronic transitions, of which ionization is a frequent result. In this respect, debris atoms are similar to the electrons discussed in the previous section. However, as the velocity of the particles decreases to less than  $4 \times 10^6 \text{ cm/sec}$ , this mode of energy loss changes to one in which nuclear elastic collisions dominate. There is no counterpart in the slowing of electrons because of the difference in masses.

The slowing down of debris atoms is described in terms of the stopping power  $S(E)$  defined by the integral

$$S(E) = \int_0^{E_{\text{max}}} dE' = \frac{dE}{dL} \quad (4-43)$$

where  $\frac{d\sigma(E,T)}{dT}$  is a partial cross section for a particle with incident energy  $E$  to transfer an amount of energy  $T$ .  $T_{\max}$  is the maximum allowed energy transfer.

For fast atoms, the contribution to  $S(E)$  comes primarily from two parts: an electronic stopping power  $S_e(E)$ , which accounts for the effect of electronic excitation; and a nuclear stopping power  $S_n(E)$ , which describes the average energy loss from elastic collisions. In terms of these parts, the total stopping power is

$$S(E) = S_e(E) + S_n(E) \quad (4-44)$$

#### 4.6.1 Electronic Stopping Powers

The electronic stopping power  $S_e(E)$ , of a medium whose fractional ionization is  $f$ , consists of two parts:

$$S_e(E) = S_{eb}(E) + fS_{ef}(E) \quad (4-45)$$

where  $S_{eb}(E)$  and  $S_{ef}(E)$  describe the stopping by bound and free electrons respectively. The magnitudes of  $S_{eb}(E)$  and  $S_{ef}(E)$  are such that free electrons contribute very little to the stopping for  $f \ll 0.01$ . Nevertheless, since conditions under which  $f > 0.01$  can arise, we shall present expressions for both  $S_{eb}(E)$  and  $S_{ef}(E)$ .

In the velocity range  $10^6 \text{ cm/sec} \leq v \leq 10^8 \text{ cm/sec}$ , several simple theories successfully approximate  $S_{eb}(E)$  where it contributes importantly to the overall stopping power. Particular examples of such theories are those of Firsov (Reference 4-32) and Lindhard (Reference 4-33). Both Firsov and Lindhard give electronic stopping powers that vary linearly with projectile velocity. We quote Lindhard's formula below:

$$S_{eb}(E) = 8\pi e^2 \zeta_e a_0 \frac{z_1 z_2}{z_{12}} \left( \frac{v}{v_0} \right) \quad (4-46)$$

where  $z_1$  and  $z_2$  are the nuclear charges of the incoming and target particles respectively,  $a_0 = 0.529 \times 10^{-8}$  cm, the Bohr radius,  $\zeta_e \approx z_1^{1/6}$ ,  $z_{12} = (z_1^{2/3} + z_2^{2/3})^{3/2}$ ,  $v$  is the velocity corresponding to  $E$ , and  $v_0 = e^2/\hbar = 2.19 \times 10^8$  cm/sec, the Bohr orbital velocity. The formula is valid in the range  $v/v_0 \leq z_1^{2/3}$ .

An expression for  $S_{ef}(E)$  is given by Longmire (Reference 4-34).

$$S_{ef}(E) = \frac{8\sqrt{\pi} z_1^2 e^4}{m_1 v^2} \left( \frac{m_1}{m_e} \right) \phi(\alpha) \ln \left( \frac{z_1}{z_m} \right) \quad (4-47)$$

where  $e$  is the electron charge,  $m_e$  the electron mass,  $m_1$  the mass of the incident debris atom, and  $z_1$  the debris atom average charge, which depends on  $v$  but is typically close to unity for metal atoms in air.

The function  $\ln(z_1/z_m)$ , which contains an effective minimum scattering angle  $\theta_m$ , is a function of the electron density  $N_e$  and temperature  $T_e$ .  $\ln(z_1/z_m)$  is plotted as a nomograph in Figure 4-10. Finally for atoms interacting with electrons,  $\phi(\alpha)$  is given by:

$$\phi(\alpha) = -\alpha \exp(-\alpha^2) + \int_0^\alpha dy \exp(-y^2) \quad (4-48)$$

where  $\alpha = \sqrt{\frac{m_e v^2}{2kT_e}}$ .  $\phi(\alpha)$  is plotted in Figure 4-11.

In Figure 4-12 the functions  $S_{eb}$  and  $S_{ef}$  at several electron temperatures have been plotted as a function of  $v$  for aluminum atoms traversing air.  $S_{ef}$  was calculated using  $z_1 = 1$  and  $\ln(z_1/z_m) = 15$ .

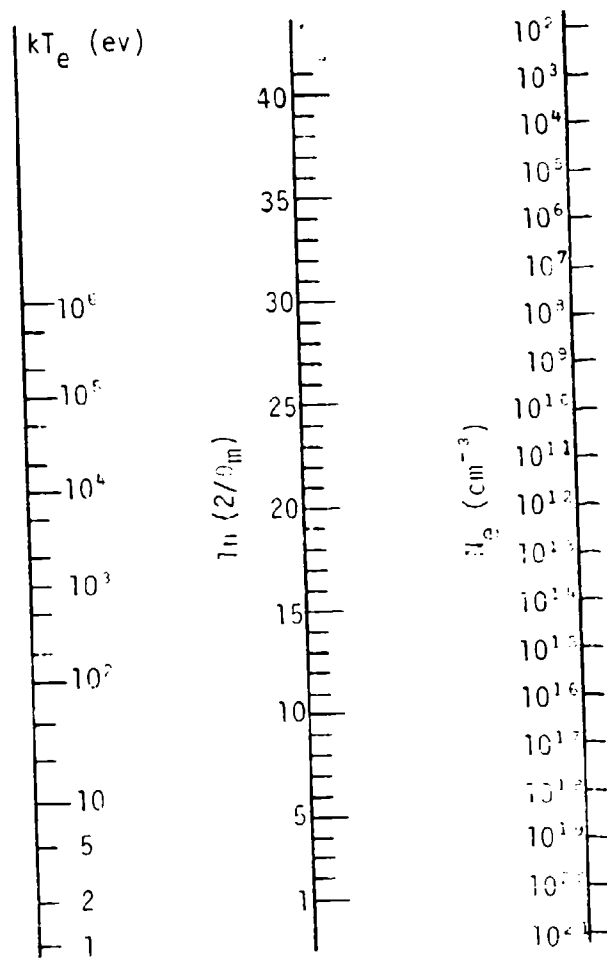


Figure 4-10. Nomograph for determining  $\ln(2/\alpha_m)$ .

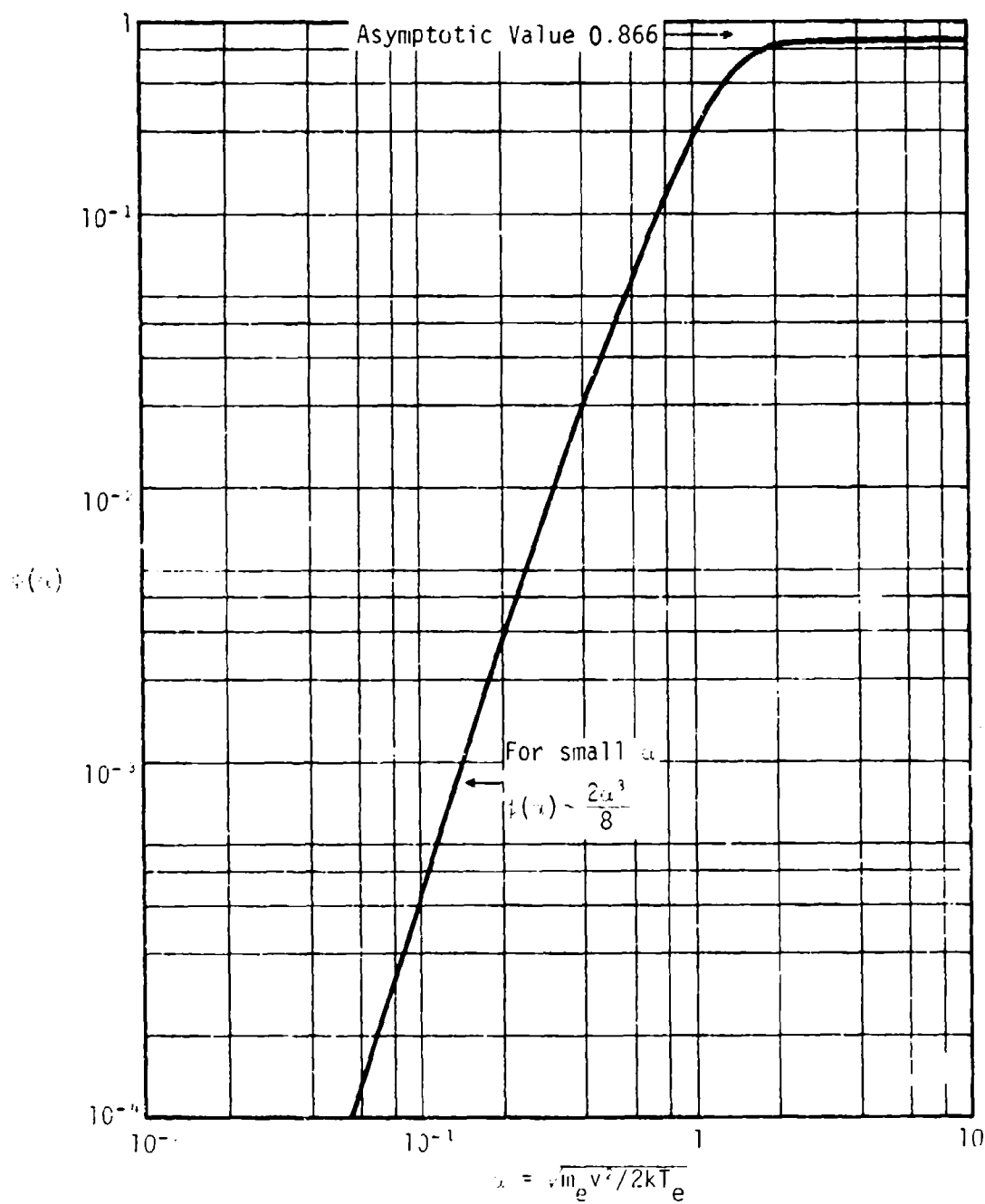


Figure 4-11. Plot of function  $f(x) = -e^{-x^2} + \int_0^x dy e^{-y^2}$



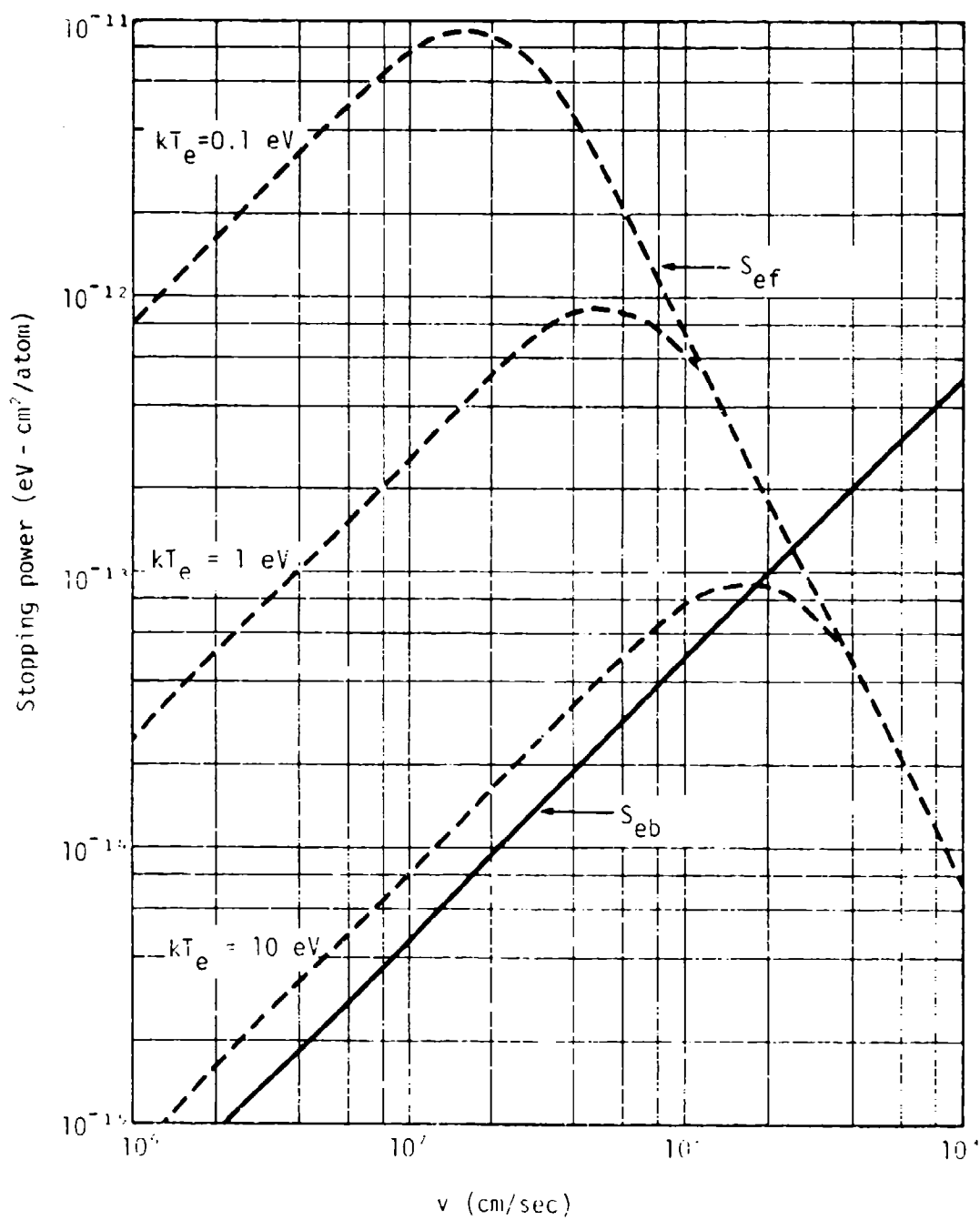


Figure 4-12. Comparison of bound ( $S_{eb}$ ) and free ( $S_{ef}$ ) electronic stopping powers for Al atoms in air.

#### 4.6.2 Nuclear Elastic Stopping

At incident speeds for which nuclear stopping is important, the nuclear collisions that contribute significantly to energy loss can be considered classically. The evaluation of the nuclear elastic stopping power,  $S_n(E)$ , would be relatively straightforward if the interatomic potential could be accurately determined. Early attempts by Bohr (Reference 4-38) and others used various forms of screened Coulomb potentials. Lindhard (Reference 4-36) has made stopping power calculations using various power law potentials or atomic Thomas-Fermi potentials, and recently Kilb (Reference 4-37) has made calculations using a potential obtained by Lee *et al.* (Reference 4-38.)

Lindhard's results are particularly interesting because he presents a universal stopping power that can be scaled according to the masses and nuclear charges of the collision partners.\* His description is in terms of certain dimensionless variables. The incident energy,  $E$ , is measured by  $\epsilon$ , where

$$\epsilon = \frac{a M_2}{z_1 z_2 e^2 (M_1 + M_2)} E \quad (4-49)$$

and where  $a$ , the unit of length is

$$a = 0.8853 a_0 (z_1^{2/3} + z_2^{2/3})^{-1/2} \quad (4-50)$$

where  $a_0 = 0.529 \times 10^{-8}$  cm is the Bohr radius.

The nuclear stopping power  $S_n(E)$  is then given in terms of a dimensionless universal stopping power  $s_n(\epsilon)$  via

\* The incident particle is designated by the subscript 1, the particles of the medium by the subscript 2.

$$S_n(E) = \frac{4\pi a z_1 z_2 e^2 M_1}{(M_1 + M_2)} s_n(\epsilon) \quad (4-51)$$

with

$$s_n(\epsilon) = \frac{9}{8\epsilon} \left\{ \ln \left[ z(\epsilon) + \sqrt{1+z(\epsilon)^2} \right] - z(\epsilon) / \sqrt{1+z(\epsilon)^2} \right\} \quad (4-52)$$

and with  $z(\epsilon)$  defined by:

$$z(\epsilon) = 1.3782 \epsilon^{4/3} \quad (4-53)$$

Plots of  $S_n(E)$  and  $S_{cb}(E)$  for aluminum atoms in air are presented in Figure 4-13. We note that stopping by nuclear elastic collisions and electronic excitation are equally important at  $v = 8 \times 10^7$  cm/sec.

#### 4.6.3 Energy Deposition and Particle Range

For a single fast particle, the energy deposited per unit length of path at position  $x$  in the target medium will be given by:

$$\frac{dE}{dx} = n(x) S(E) \quad (4-54)$$

where  $E$  is the particle energy at  $x$  and  $n(x)$  is the target medium density ( $\text{cm}^{-3}$ ). When a beam of particles having a spread in initial energies,  $E_0$ , is involved in depositing energy, it is necessary to know the local energy spectrum,  $f(E, x)$ . Then the deposition is given by the integral

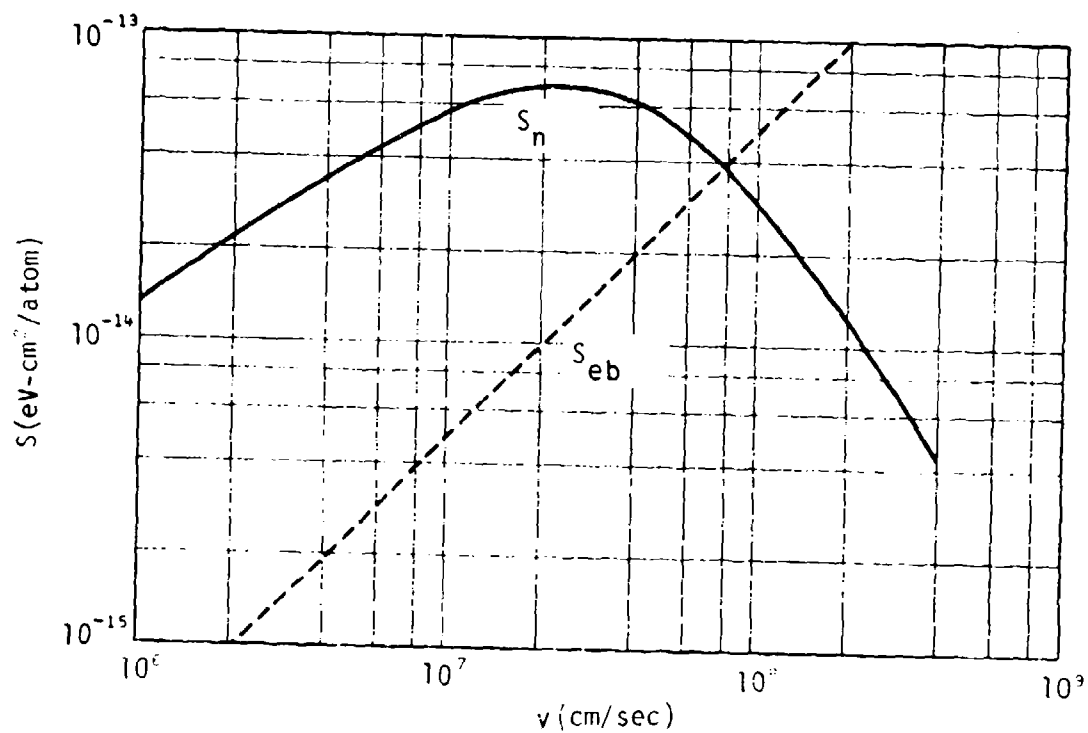


Figure 4-13. Plots of the nuclear and electronic stopping powers  $S_n$  and  $S_{eb}$  for aluminum atoms in air.

$$\frac{dE}{dx} = n(x) \int_0^{E_{\max}} dE f(E,x) S(E) \quad (4-55)$$

Thus, we must relate  $f(E,x)$  to  $f(E_0)$ . Let  $E = g(E_0,x)$  be the kinetic energy of a particle at  $x$ , given that it had energy  $E_0$  at  $x = 0$ .

In terms of  $g(E,x)$  Equation 4-55 can be rewritten as:

$$\frac{dE}{dx} = n(x) \int_0^{E_{\max}} dE_0 f(E_0) S(g(E_0,x)) \quad (4-56)$$

To obtain the function  $g(E_0,x)$ , we first integrate Equation 4-54. Thus

$$\int_0^x dx' n(x') = \int_{E_0}^E \frac{dE'}{S(E')} \quad (4-57)$$

defines a relationship between  $x, E$ , and  $E_0$  that we have already denoted by  $E = g(E_0,x)$ . By setting  $E = 0$ ,  $x$  becomes a function of  $E_0$  alone called the range  $R$ . Usually, it is more convenient to express the range in terms of the column density coordinate  $\xi$ :

$$\xi = \int_0^R dx n(x') \quad (4-58)$$

Then:

$$\xi = \int_0^{E_0} \frac{dE}{S(E)} \quad (4-59)$$

Ranges and electronic stopping powers have been tabulated for a variety of target media and atomic projectiles with velocities above  $1.55 \times 10^8$  cm/sec. These data are found together with an extensive discussion of heavy particle stopping in Reference 4-39. For velocities below  $1.55 \times 10^8$  cm/sec, we have integrated Equation 4-54 using the stopping powers defined in Sections 4.6.1 and 4.6.2 above. Results for the ranges of various particles in air are presented in Figure 4-14. The range units in the figure are  $\text{gm cm}^{-2}$ . The decades on the velocity and energy scales are divided at 1, 2, 5, 10. . .

Included in Figure 4-14 is a nomograph for determining stopping altitudes of charged particles released at infinity. The nomograph allows one to include the effect of magnetic pitch and dip angles on the stopping altitude. The CIRA model 5 hour 8 atmosphere was used in relating stopping altitude to air column density.

A good fit to the range data presented in Figure 4-14 is:

$$\xi = 6600 v_0^{1.79} \quad (4-60)$$

where  $\xi$  is the air column density (# of air-atoms/cm<sup>2</sup>) and  $v_0$  is the incident velocity (cm/sec).

#### 4.6.4 PARTITION OF DEPOSITED ENERGY

A significant fraction of the kinetic energy deposited by a fast debris atom reappears promptly as kinetic energy of secondary particles. These secondary particles themselves interact with the medium and redistribute the primary energy among various more stable energy reservoirs. Examples of such reservoirs are: ionization, excited electronic states, dissociation, molecular vibrational and rotational energy, and thermal kinetic energy. The question of how the energy is partitioned among these reservoirs is of importance for subsequent target medium chemistry.

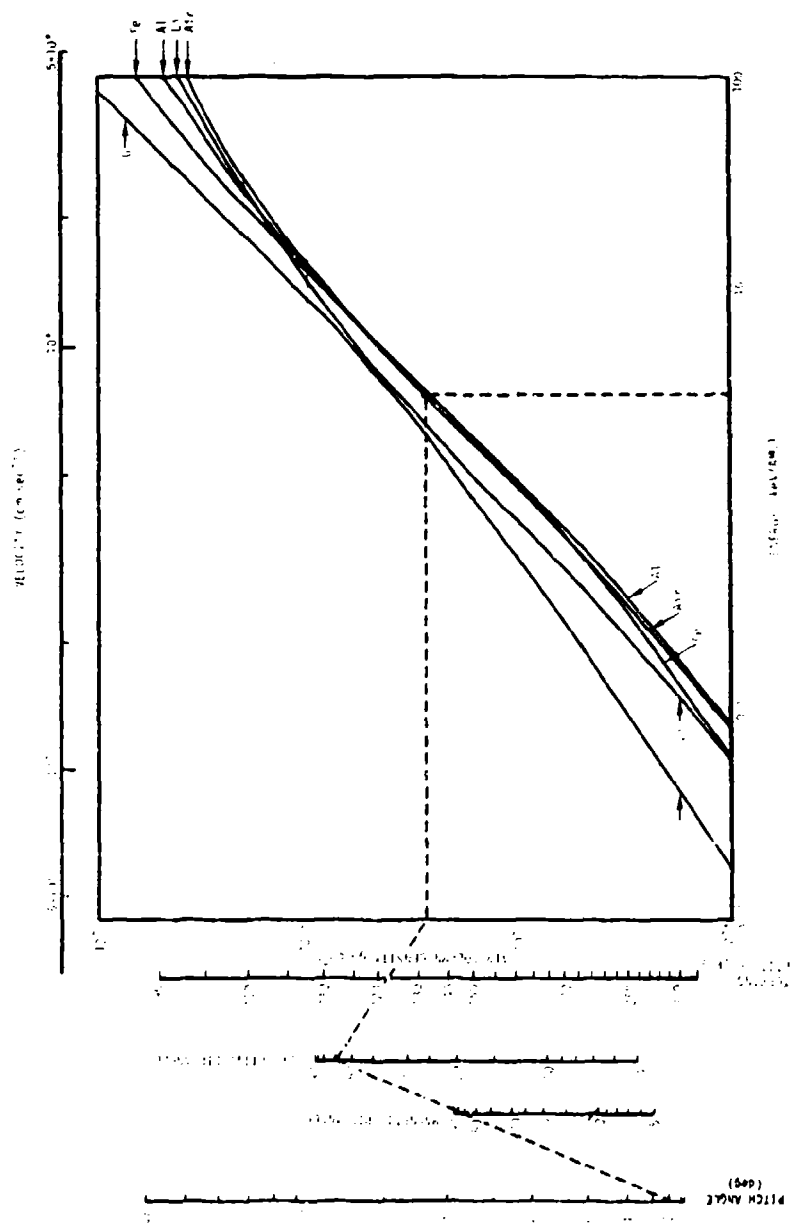


Figure 4.14. Ranges for various particles in air. CIRA Mode 5, Hour 8 atmosphere used to correlate stopping altitude with air column density.

As with the stopping powers, the portion of deposited energy is divided into two rather broad categories: that which results (1) from electronic excitation and (2) from nuclear elastic collisions. These categories each contribute to more specific reservoirs. These are listed in Table 4-1.

Table 4-1. Partition of Heavy Particle Kinetic Energy

- I. Electronic Excitation
  1. Dissociative Ionization
  2. Non-Dissociative Ionization
  3. Dissociation
  4. Non-Dissociative Excitation
  5. Vibrational-Rotational Excitation
- II. Nuclear Elastic Excitation
  1. Dissociation
  2. Vibrational-Rotational Excitation
  3. Kinetic Energy of Secondaries

The partition of deposited energy between electronic and nuclear elastic excitation can be calculated using a formalism of Lindhard (Reference 4-40). For a particle with energy  $E$ , he designates  $\eta(E)$  to be the total electronic excitation and  $\nu(E)$  the total nuclear elastic excitation. Then:

$$\eta(E) + \nu(E) = E \quad (4-61)$$

expresses conservation of energy, and

$$\frac{d\eta(E)}{dE} + \frac{d\nu(E)}{dE} = 1 \quad (4-62)$$



expresses the fractional partition of the energy deposited as the particle loses an amount of energy  $dE$ . The Lindhard formalism tries to account for the effect of succeeding generations of secondary particles in redistributing the energy deposited by the primary. Because of the redistribution of energy by secondaries, the estimate that  $dn/dE$  is given by the ratio of stopping cross sections,  $S_{eb}(v)/(S_{eb}(v) + S_n(v))$ , is not correct.

Figure 4-15 presents  $dn/dE$  obtained from Lindhard's theory. Two curves are plotted; air atoms in air and aluminum atoms in air. We note from the graph that  $\frac{dn}{dE} = 0.5$  at  $v = 4 \times 10^7$  cm/sec. We see the effect of secondaries has been to lower the velocity at which electronic and nuclear elastic excitation are equal.

Application of the partition fraction  $\frac{dn}{dE}$  to estimate the energy in the various reservoirs or partition channels listed in Table 4-1 is still a difficult affair. Nevertheless, a useful approach has been followed by Boring *et al.*, Reference 4-41. In measuring the total ionization produced by a heavy particle in  $N_2$  and  $A$ , they divided the energy per ion pair  $W(E)$  by  $E/n(E)$  to obtain a new number  $W' = W(E)n(E)/E$ .  $W'$  turned out to be insensitive to incident energy. If  $W'$  is taken to be the mean energy to produce an ion pair, and the ionization is assumed to result from electronic processes only, then the number of ion pairs per unit energy loss is given by

$$\frac{dN_c}{dE} = \frac{dn}{dE} \frac{1}{W'} \quad (4-63)$$

where  $W'$  is a property of the target medium ONLY. Boring, *et al.* determined values of  $W'$  for  $N_2$  and  $A$  to be 32 eV/ion pair and 25 eV/ion pair respectively. These numbers are within 10 percent of the 40 keV electron W-values reported for these gases by Valentine

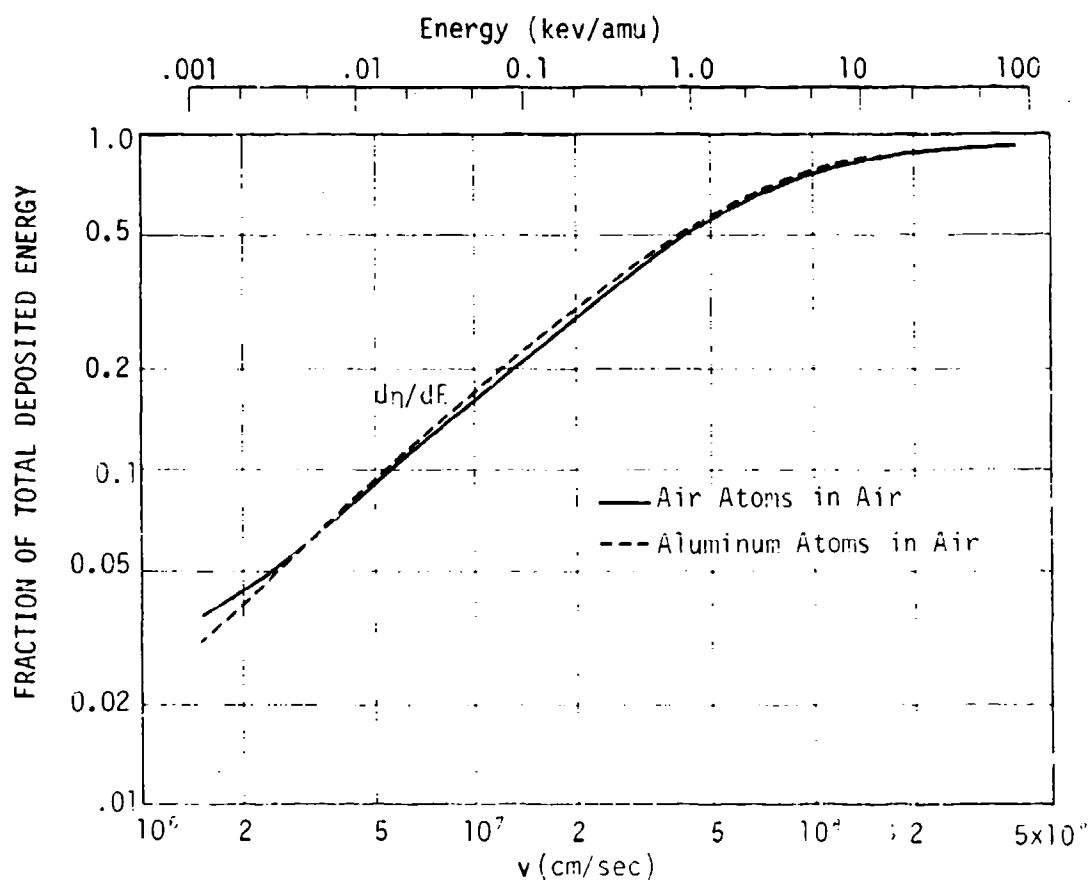


Figure 4-15. Partition of deposited energy for aluminum and air atoms in air. The fraction of total deposited energy put into electronic excitation is  $d\eta/dE$ . The fraction put into nuclear elastic excitation is  $1-d\eta/dE$ .

Reference 4-42. Since partition of electron excitation by electron impact is easier both experimentally and theoretically, a useful estimate of heavy particle electronic excitation partition might be obtained by applying appropriate electron impact results to the electronic energy partition described by  $d\eta/dE$ . An example of such a partition calculation is the work of Stolarski, Reference 4-43.

The partition of nuclear elastic energy is also experimentally and theoretically difficult to obtain. Kaufman, Reference 4-44, has made estimates for aluminum projectiles in air of the fraction of deposited energy going into collisional dissociation of  $N_2$  and  $O_2$ . These estimates are based on an extension of Lindhard's formalism, Reference 4-40, and the dissociation model of Gerasimenko, Reference 4-45. If  $f_{N_2}$  and  $f_{O_2}$  are fractional concentrations per air molecule of  $N_2$  and  $O_2$  respectively, the fraction of total deposited energy,  $\frac{d\Delta}{dE}$ , put into dissociation will be given by

$$\frac{d\Delta}{dE} = f_{N_2} \frac{d\Delta_{N_2}}{dE} + f_{O_2} \frac{d\Delta_{O_2}}{dE} \quad (4-64)$$

the functions  $\frac{d\Delta_{N_2}}{dE}$  and  $\frac{d\Delta_{O_2}}{dE}$  are plotted in Figure 4-16. It should be noted that the dissociation energy stored by the dissociative ionization process is not included in these estimates, but is already included in  $\frac{d\eta}{dE}$ .

The fraction of total deposited energy appearing as thermal energy (vibration, rotation and translation)  $d\Theta/dE$  is given by:

$$\frac{d\Theta}{dE} = \frac{d\psi}{dE} - \frac{d\Delta}{dE} \quad (4-65)$$

This function is also plotted in Figure 4-16.

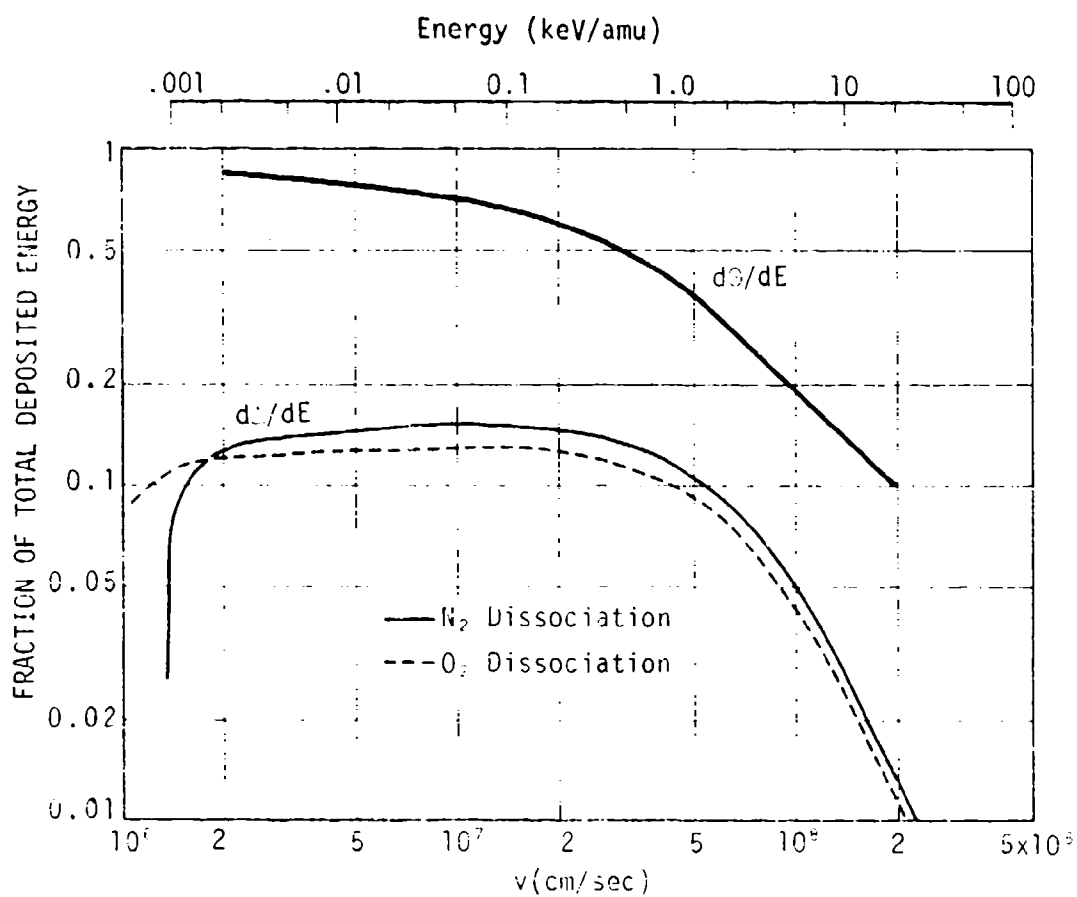


Figure 4-16. Fraction of total deposited energy put into direct collisional dissociation of pure  $N_2$  or pure  $O_2$  ( $d\mathcal{D}/dE$ ), and into thermal energy ( $d\mathcal{Q}/dE$ ).

## REFERENCES

- 4-1. Gilmore, F. R., Graphs of X-Ray Absorption Coefficients for Fourteen Substances, RAND Corp. RM2367-AEC (1959).
- 4-2. Wright, R. S., Aeronutronic Corp., private communication (1957).
- 4-3. Bethe, H. A., Los Alamos Scientific Laboratory, private communication (1957).
- 4-4. Landshoff, R. K. M., Thermal Radiation Phenomena, Vol. 2, Ch. 4, Plenum Press (1969).
- 4-5. Veigele, W.J., E.M. Henry and M.E. Donaldson, X-ray Transport-II (Downed Electron Scattering), Kaman Report KN-65-119(R), 30, March 1965.
- 4-6. Goldstein, H. and J. E. Wilkins, Jr., Calculations of the Penetration of Gamma Rays, AEC Report NYO-3075, Nuclear Development Associates (1954).
- 4-7. Bennett, E. W., Energy Deposition in the Atmosphere by Delayed Gammas from Fission, Los Alamos Report LAMS 3059 (1964).
- 4-8. Fano, U., L. V. Spencer and M. J. Berger, Penetration and Diffusion of X-Rays, Handbuch der Physik, Vol. 38, 660 (1959).
- 4-9. Goldstein, H., Fundamental Aspects of Reactor Shielding, Addison-Wesley (1959).
- 4-10. Weinberg, A. M. and E. P. Wigner, The Physical Theory of Neutron Chain Reactors, University of Chicago Press (1958).
- 4-11. Stevens, P. N. and D. K. Trubey, Weapons Radiation Shielding Handbook, Chapter 3, Defense Nuclear Agency Report DNA-1892-3 (1972).

- 4-12. Hubbell, J. H., A Power-Series Buildup Factor Formulation Application to Rectangular and Off-Axis Disk Source Problems, Journal Research Nat. Bureau Stds. 67C, 291 (1963).
- 4-13. Taylor, J. J., Application of Gamma Ray Buildup Data to Shield Design, Westinghouse Atomic Power Division Report WAPD-RM-217 (1954).
- 4-14. Chilton, A. B., Two-Parameter Formula for Point Source Buildup Factors, Nucleonics 23 (8), 119 (1965).
- 4-15. Carlson, B. G., Solution of the Transport Equation by the  $S_n$  Method, Los Alamos Scientific Laboratory Report LA-1891 (1955).
- 4-16. Mynatt, F. R., A User's Manual for DOT, A Two-Dimensional Discrete Ordinates Transport Code with Anisotropic Scattering, Oak Ridge National Laboratory Report, RSIC CCC-89.
- 4-17. Engle, W. W., A User's Manual for ANISN, Union Carbide Nuclear Division Report K-1693 (1967).
- 4-18. Lathrop, K. D., DTF-IV, A Fortran-IV Program for Solving the Multigroup Transport Equation with Anisotropic Scattering, Los Alamos Scientific Laboratory Report LA-3373 (1965).
- 4-19. Spanier, J. and E. M. Gelbard, Monte Carlo Principles and Neutron Transport Problems, Addison-Wesley (1969).
- 4-20. Irving, D. C., et al., OSR, A General Purpose Monte Carlo Neutron Transport Code, Oak Ridge National Laboratory Report ORNL-3622 (1965).
- 4-21. Cashwell, E. D. and C. J. Everett, A Practical Manual on the Monte Carlo Method for Random Walk Problems, Pergamon Press (1959).
- 4-22. Straker, E. A., et al., The MORSE Code - A Multigroup Neutron and Gamma Ray Monte Carlo Transport Code, Oak Ridge National Laboratory Report ORNL-4585 (1970).
- 4-23. Kimlinger, J., E. F. Plechaty and J. R. Terrall, SORS Monte Carlo Photon Transport for the CDC 6600, Lawrence Livermore Laboratory Report UCRL-50538 (1968).

- 4-24. Goldstein, H. and J. E. Wilkins, Calculations of the Penetration of Gamma Rays, Nuclear Development Associates Report NYO-3075 (1954).
- 4-25. O'Dell, A. A., Moments Method Calculation of the Scattered Angular Energy Flux for Point Isotropic Sources in an Infinite Air Medium, EG&G, Inc. Report EGG 1183-2275 (1971).
- 4-26. Glasstone, S. and M. C. Edlund, The Elements of Nuclear Reactor Theory, Van Nostrand (1952).
- 4-27. Birkhoff, R. D., The Passage of Fast Electrons Through Matter, in Encyclopedia of Physics, Vol. 34, S. Flugge, ed. Springer (1958).
- 4-28. Bethe, H. A. and J. Ashkin in Experimental Nuclear Physics, Vol. 1, E. Segre, ed. Wiley (1953).
- 4-29. Spencer, L. V., Energy Dissipation by Fast Electrons, NBS Monograph 1 (1959).
- 4-30. Latter, R. and R. E. LeLevier, J. Geophys. Res., 68, 1643 (1963).
- 4-31. Lowen, R. W., R. Marriot and D. H. Sowle, Convair, private communication (1964).
- 4-32. Firsov, O. B., A Qualitative Interpretation of the Mean Electron Excitation Energy in Atomic Collisions, JETP 9, 1076 (1959).
- 4-33. Lindhard, J. and M. Scharff, Energy Dissipation by Ions in the keV Region, Phys. Rev. 124, 128 (1961).
- 4-34. Longmire, C. L., Elementary Plasma Physics, Interscience Publishers (1963) p. 202 ff.
- 4-35. Bohr, N., The Penetration of Atomic Particles through Matter, Dan. Mat-fys. Medd. 18, 8 (1948).
- 4-36. Lindhard, J., Approximation Methods in Classical Scattering by Screened Coulombs Fields, Dan. Mat-fys Medd 36, 10 (1968).

- 4-37. Kilb, R. W., Elastic Energy and Momentum Loss in Atom-Atom Collisions Above 50 eV, MRC-R-16, Mission Research Corporation (1972).
- 4-38. Lee, C., *et al*, Thomas-Fermi Calculation of Potential between Atoms, Los Alamos Scientific Laboratory Note (Unpublished).
- 4-39. Northcliffe, L. C. and R. F. Schilling, Range and Stopping Power Tables for Heavy Ions, Nuclear Data, Sect. A7, 233 (1970).
- 4-40. Lindhard, J., *et al*, Integral Equations Governing Radiation Effects, Dan. Mat-fys Medd 33, 14 (1963).
- 4-41. Boring, J. W., G. E. Strohl and T. R. Woods, Total Ionization in Nitrogen by Heavy Ions of Energies 25 to 50 keV, Phys. Rev. 140, A1065 (1965).
- 4-42. Valentine, J. M. and S. C. Curran, Average Energy Expenditure per Ion Pair in Gases and Gas Mixtures.
- 4-43. Stolarski, R. S., Ph.D. Thesis, University of Florida (1966).
- 4-44. Kaufman, A. M., Private Communication (1973).
- 4-45. Gerisamenko, U. I. and Yu. D. Oksyuk, Dissociation of Diatomic Molecules in Fast Collisions, J.E.T.P. 48, 499 (1965).



CHAPTER 5  
ATMOSPHERIC DEIONIZATION

Benjamin J. Berkowitz\*

Murray Scheibe

Dan H. Holland \*\*

March 1974

Mission Research Corporation

\* Now at General Electric-TEMPO  
\*\* Now at New Millennium Associates

## TABLE OF CONTENTS

	LIST OF FIGURES	234
5.1	INTRODUCTION	235
5.2	DEIONIZATION KINETICS: THE THREE-SPECIES MODEL	236
	5.2.1 Model Formulation	236
	5.2.2 Solutions of the Lumped-Parameter Model	241
	5.2.3 Lumped-Parameter Rate Coefficients	253
5.3	ATMOSPHERIC CHEMICAL REACTIONS	256
	5.3.1 Energy Deposition Products	256
	5.3.2 Electron-Ion Recombination and Related Reactions	258
	5.3.3 Attachment, Detachment, and Negative Ion Reactions	268
	5.3.4 Reactions of Neutral Species	274
	5.3.5 Ion-Ion Recombination	281
5.4	THE COURSE OF ATMOSPHERIC DEIONIZATION	284
	5.4.1 Detailed Deionization Models	285
	5.4.2 Deionization Below 100 km	288
	5.4.3 Deionization Above 100 km	289
	REFERENCES	291

## LIST OF FIGURES

<u>FIGURE</u>		<u>PAGE</u>
5-1.	Schematic three-species reaction sequence.	240
5-2A.	Decay of ionization following a nighttime ionization impulse.	246
5-2B.	Decay of ionization following a daytime ionization impulse.	247
5-3.	Approximate quasi-equilibrium solutions.	252
5-4.	Recombination rate coefficients vs altitude.	254
5-5.	Attachment and detachment rates vs altitude.	255
5-6.	Simplified schematic of positive ion evolution.	267
5-7.	Attachment, detachment and negative ion reactions.	273
5-8.	Important neutral chemistry.	282

## CHAPTER 5

### ATMOSPHERIC DEIONIZATION

#### 5.1 INTRODUCTION

The process of atmospheric deionization is the removal of free electrons and ions from the atmosphere following (or during) exposure to a source of ionizing radiation. The time dependence of the electron density is of particular importance in predicting a variety of effects on electromagnetic propagation as discussed in Chapter 14.

Close to an intense perturbing source, high temperatures and radiation densities, hydrodynamic motion, and shock effects are produced. The properties of this violently disturbed region cannot be described in terms of ordinary equilibrium chemical kinetics. Throughout a much larger region of space, however, the source may produce ionization, excitation, and dissociation of the atmosphere such that significant increases in electron density occur without large changes in the gross thermodynamic properties of the air. Under these conditions, the deionization and relaxation processes consist of numerous gas phase reactions by which the energy of the initially formed ions and activated species is degraded and dissipated in thermal motion, radiant emission and the formation of stable reaction products.

This chapter describes the deionization process in mildly to moderately disturbed regions of the atmosphere, that is, in regions where the original fractional ionization does not exceed, say,  $10^{-6}$ . Under these

conditions, the relaxation or deionization process can be described in terms of chemical reactions characterized by rate coefficients that are averaged over near-equilibrium distributions of reactant energies. The deionization kinetic problem, then, consists of describing the composition and properties of a sample field point in the atmosphere before perturbation, the immediate effects of energy deposition at that point due to the source, the rates of the chemical reactions that ensue, and the effect of the continued perturbation of this reacting mixture by both ambient and persistent artificial radiation sources.

In the next section of this chapter, the simplest quantitative model encompassing these elements is presented, the so-called "three-species, lumped-parameter" model. Following this, the important chemical reactions involved in a detailed description of the deionization process are identified and discussed. This leads to a qualitative description of the nature of the deionization process in various altitude regimes, and provides the basis for describing the more complicated quantitative models required for precise specification of atmospheric deionization.

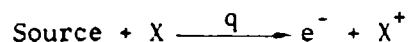
## 5.2 DEIONIZATION KINETICS: THE THREE-SPECIES MODEL

### 5.2.1 MODEL FORMULATION

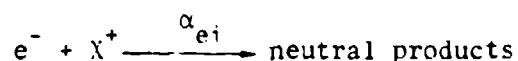
The simplest description of deionization kinetics that preserves the salient features of the actual process is the three-species, lumped-parameter model. The three species represented are free electrons ( $e^-$ ), positive ions of all types ( $X^+$ ), and negative ions of all types ( $X^-$ ). "Neutral air" ( $X$ ), the major atmospheric constituent, is implicitly incorporated into the rate coefficients (since its concentration does not change appreciably during the deionization process); the variation of minor neutral species is ignored. The term "lumped parameter" refers to the fact that the rate coefficients employed may be considered as weighted averages over a number of specific chemical reactions of several

general types. The model is based on five general reactions involving the three species. Written schematically, they are:

(a) Ionization



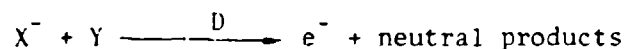
(b) Electron-ion recombination



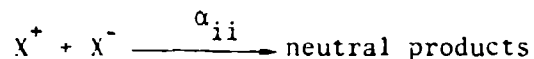
(c) Attachment



(d) Detachment



(e) Ion-ion recombination



In this scheme,  $e^{-}$  represents the free electron while  $X^{+}$  and  $X^{-}$  denote the positive and negative ions, respectively. The chemical entity represented by the symbol "X" is unspecified; it may be atomic or molecular and, in particular, it need not be the same on both sides of the reaction arrow. This underscores the fact that what is important in the three-species model is simply the charge involved, not the chemical composition. Reaction (a) is endothermic, while (b) and (c) are exothermic. The energy released may appear as radiation or as internal or translational energy of the products. No implications

of reaction mechanism are intended in this schematic formulation; specific mechanisms are described in Section 5.3 for each reaction type. However, we note in passing the possibility of a third body in reactions (b), (c) and (e).

The symbol for the lumped-parameter rate coefficient appears above its reaction arrow. It is conventional to use  $\alpha$  to represent recombination coefficients, its subscript indicating the nature of the reactants. (Another commonly encountered notation replaces  $\alpha_{ei}$  by  $\alpha_d$  as discussed in Section 5.3.2, and  $\alpha_{ii}$  by  $\alpha_i$ .)

The kinetics of the species  $e^-$ ,  $X^+$ , and  $X^-$  are governed by the differential equations

$$\frac{dN_e}{dt} = q - \alpha_{ei} N_e N_+ - AN_e + DN_- \quad (5-1)$$

$$\frac{dN_+}{dt} = q - \alpha_{ei} N_e N_+ - \alpha_{ii} N_- N_+ \quad (5-2)$$

$$\frac{dN_-}{dt} = AN_e - DN_- - \alpha_{ii} N_- N_+ \quad (5-3)$$

Additionally, a requirement for local charge conservation is imposed:

$$N_+ = N_e + N_- \quad (5-4)$$

In equations 5-1 - 5-4,

$N_e$  = number density of free electrons ( $\text{cm}^{-3}$ )

$N_+$  = number density of positive ions ( $\text{cm}^{-3}$ )

$N_-$  = number density of negative ions ( $\text{cm}^{-3}$ )

$q$  = continuing source strength ( $\text{cm}^{-3} \text{ sec}^{-1}$ )

$\alpha_{ei}$  = electron-ion recombination rate coefficient ( $\text{cm}^3 \text{ sec}^{-1}$ )

$A$  = electron-neutral attachment rate coefficient ( $\text{sec}^{-1}$ )

$D$  = negative ion detachment rate coefficient ( $\text{sec}^{-1}$ )

$\alpha_{ii}$  = ion-ion recombination rate coefficient ( $\text{cm}^3 \text{ sec}^{-1}$ )

$t$  = time (sec)

Since there are four equations in the three time-dependent variables, ( $N_e$ ,  $N_+$ ,  $N_-$ ) it is conventional to dispense with Equation 5-3 and eliminate  $N_-$  by use of 5-4. This leads to a set of two coupled, ordinary, non-linear differential equations

$$\frac{dN_e(t)}{dt} = q(t) - [A + D + \alpha_{ei}N_+(t)] N_e(t) + DN_+(t) \quad (5-5)$$

$$\frac{dN_+(t)}{dt} = q(t) - (\alpha_{ei} - \alpha_{ii}) N_e(t)N_+(t) - \alpha_{ii}(N_+(t))^2 \quad (5-6)$$

where the time dependence is explicitly indicated. The rate coefficients  $\alpha_{ei}$ ,  $\alpha_{ii}$ ,  $A$ , and  $D$  are parameters whose values depend upon field point altitude (pressure, temperature, and ambient composition), and time of day, which determines the flux of photochemically active solar radiant energy.



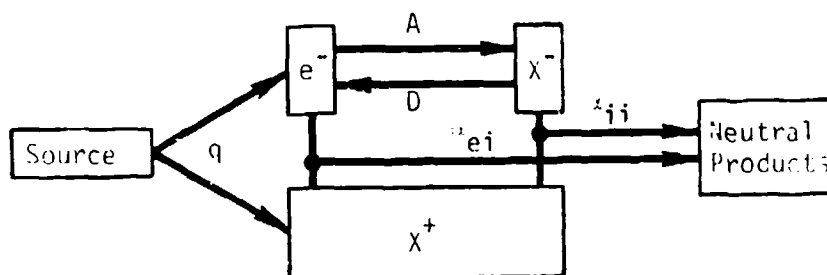


Figure 5-1. Schematic Three-Species Reaction Sequence.

Much of the simplification embodied in the lumped-parameter model stems from the transference to these parameters of the complexities of altitude-dependent atmospheric composition and reaction mechanisms. It is instructive to consider the qualitative implications of the coupled reaction set; the relationship among the species is shown diagrammatically in Figure 5-1.

The atmosphere initially consists primarily of neutral  $X$  and small ambient concentrations of  $e^-$ ,  $X^+$ , and  $X^-$ . An impulsive source gives rise to equal initial concentrations of free electrons,  $N_e(t=0)$ , and positive ions,  $N_+(t=0)$ , while a continuous source produces these

species at rate  $q$ . Under conditions favoring attachment, a significant  $N_-$  value builds up, the bulk of the negative charge in the system eventually appears as  $X^-$  rather than as free electrons, and the net deionization is characterized by the ion-ion recombination path ( $\alpha_{ii}$ ). Conversely, when attachment is small or detachment is large, the negative ion density remains small, the bulk of the negative charge remains as free electrons, and the deionization depends primarily on electron-ion recombination ( $\alpha_{ei}$ ). Stated differently, the initial coefficient for charge disappearance is approximately  $\alpha_{ei}$ , but at later times it approaches a value between  $\alpha_{ei}$  and  $\alpha_{ii}$  depending on the position of the pseudo-equilibrium between  $N_e$  and  $N_-$  dictated by the relative values of  $A$  and  $D$ . Analytic expressions for limiting cases are derived from the approximate solutions of the lumped-parameter equations in the following section.

### 5.2.2 SOLUTIONS OF THE LUMPED-PARAMETER MODEL

A general closed form solution to the coupled equations 5-5 and 5-6 cannot be obtained; numerical integration is required for their solution. However, analytically integrable approximate forms that are useful in special cases can be found. These are not only useful in their domain of validity, but also provide insight into the structure to be expected in solutions of more general applicability.

#### Impulsive Source

We first consider the case of a source that produces finite levels of ionization in an infinitesimal time interval at time zero, and is zero thereafter. Then the  $q$  term in Eqs. 5-5, 6 is zero, and the effect of the source is to provide the initial conditions  $N_e(0) = N_+(0) = N_0$ . To proceed, we first write Eq. 5-6 as

$$\frac{dN_+}{dt} = q - \alpha N_+^2 \quad (5-7)$$

with

$$\alpha = (\alpha_{ei} - \alpha_{ii}) \frac{N_e}{N_+} + \alpha_{ii} = \frac{\alpha_{ei} N_e + \alpha_{ii} N_-}{N_+} \quad (5-8)$$

Now at  $t=0$ ,  $N_e = N_+$  and so  $\alpha = \alpha_{ei}$ . We expect this to be at least approximately true for some time interval after  $t=0$ , so we investigate the nature of the solutions for the case  $\alpha = \alpha_{ei} = \text{const.}$

With  $q = 0$  and  $\alpha = \alpha_{ei}$ , Eq. 5-7 is immediately solved to yield

$$N_+ = \frac{N_0}{1 + \alpha_{ei} N_0 t} \quad (5-9)$$

Substitution of this value for  $N_+$  into Eq. 5-5 yields a linear first order equation for  $N_e$  whose solution is easily shown to be

$$N_e = \frac{N_+}{A + D} \left[ A e^{-(A+D)t} + D \right] \quad (5-10)$$

The assumption upon which this solution is based, that  $\alpha = \alpha_{ei}$ , is valid only if  $N_e \leq N_+$ . This condition is satisfied for  $t \ll (A+D)^{-1}$ , and for all time in the special case  $D \gg A$ .

The physical meaning of these restrictions is clear. If  $D \gg A$ , no significant negative ion density can build up, and hence  $N_e \leq N_+$ . If  $D \leq A$ , then the time for significant attachment to occur is of order  $(A+D)^{-1}$ , we no longer have  $N_e \leq N_+$ , and the solution ceases to be

valid at about this time. Thus we have shown that for an impulsive source

$$N_e \approx N_+ \sim \frac{N_0}{1 + \frac{\alpha}{\epsilon_i} N_0 t} \quad \left\{ \begin{array}{l} \text{for all time if } D \gg A \\ \text{for } t \ll (A+D)^{-1} \text{ otherwise} \end{array} \right\} \quad (5-11)$$

According to the data presented below,  $D$  is always at least ten times as great as  $A$  at altitudes above 90 km, and the condition is satisfied down to about 75 km during the day, when photodetachment is occurring.

Another approximate expression can be found for the case that  $N_+$  is slowly varying, a condition for which a precise definition is given below. In this case we treat  $N_+$  and  $\alpha$  as constants in Eq. 5-5, whose solution is then

$$N_e(t) = \frac{DN_+}{A+D+\alpha N_+} + e^{-(A+D+\alpha N_+)t} \left[ N_e(0) - \frac{DN_+}{A+D+\alpha N_+} \right] \quad (5-12)$$

The second term on the right decays in a time of order  $(A+D+\alpha N_+)^{-1}$ . Thus if  $N_+$  does not change appreciably in time  $(A+D+\alpha N_+)^{-1}$ , the approximation gives

$$N_e \sim \frac{DN_+}{A+D+\alpha N_+} \quad (5-13)$$

the condition for which is that  $\alpha N_+^2 / (A+D+\alpha N_+) \ll N_+$ , or

$$\alpha N_+ \ll A+D \quad (5-14)$$

At  $t = 0$ ,  $N_e = N_{e0}$ , as previously pointed out. Therefore, if

$A+D \gg \alpha_{ei} N_e$ , the quasi-equilibrium ratio (Eq. 5-13) is attained before significant recombination occurs, and we have as before

$$N_+ = \frac{N_0}{1 + \alpha N_0 \tau} \quad (5-15)$$

but now from Eqs. 5-8, 13

$$\alpha = \frac{D \alpha_{ei} + A \alpha_{ii}}{A + D} \quad (5-16)$$

If  $D \gg A$ , we just regain Eq. 5-11, but if  $A \gg D$ ,  $\alpha \approx \alpha_{ii}$  and  $N_e \ll N_+$ .

The physical meaning of the foregoing considerations is clear. If recombination is slow compared with attachment and detachment, the latter two processes come to a quasi-equilibrium such that  $AN_e = DN_+$ , which taken together with Eq. 5-4 implies Eq. 5-15. If  $A \gg D$ , then  $N_+ \gg N_e$ , most of the negative charge resides on ions, and the effective recombination coefficient is  $\alpha_{ii}$ . The condition  $A \gg D$  is satisfied below about 75 km at night and below about 55 km in the daytime.

The preceding analysis makes possible a qualitative description of the ionization history of a parcel of air exposed to an impulsive source. The initial decay of the positive ion density follows Eq. 5-11. At later times the variation of  $N_+$  follows Eq. 5-15 with  $\alpha$  as given by Eq. 5-16. No simple analytical description of the transition between the two regions is possible.

The variation of the electron density is in general qualitatively different from that of the positive ions. Initially the variation is the same as given by Eq. 5-11. At some later time, when  $A \approx \alpha_{ei} N_+$ , the electron density falls below  $N_+$ . This relative decrease continues

until the quasi-equilibrium value of Eq. 5-13 is attained, after which the ratio  $N_e/N_+$  remains constant. The transition cannot be accurately described analytically, but the variation of  $N_e$  is approximately as  $e^{-(A+D)t}$ . Since the transition occurs only if  $A \geq D$ , the variation can be taken to be  $\sim e^{-At}$ .

This qualitative behavior is exhibited by machine calculations of electron density from numerical solution of the lumped-parameter equations. An example of such calculations, kindly supplied by Warren Knapp, is shown in Figure 5-2. These calculations are similar to those described in Ref. 5-2. For several of the higher altitudes, the curves are nearly identical. This is the region where  $D \gg A$  and Eq. 5-11 is valid. At lower altitudes the electron density falls below these curves rapidly at later times, corresponding to the attachment - dominated transition regime. At still later times, the  $N_e$  curves level off and roughly parallel the high-altitude curves, corresponding to the applicability of Eq. 5-13. The absence of strict parallelism stems from the difference between  $\alpha_{ei}$  and the  $\alpha$  of Eq. 5-16, since in these calculations  $\alpha_{ii} < \alpha_{ei}$ . Numerous other approximations useful in special cases and as aids in numerical calculations exist. Discussions of these can be found in Refs. 5-1, 2.

### Constant Source

Next we consider the case where a constant source  $q$  is turned on at  $t = 0$ . The equations cannot be solved in general for this case, but an exact solution is possible if  $\alpha = \alpha_{ei} = \text{const.}$  If  $D \gg A$ , the negative ion concentration remains small compared with  $N_+$ , and the approximations  $\alpha = \alpha_{ei}$ ,  $N_e \approx N_+$  are valid.

The solution for this case is

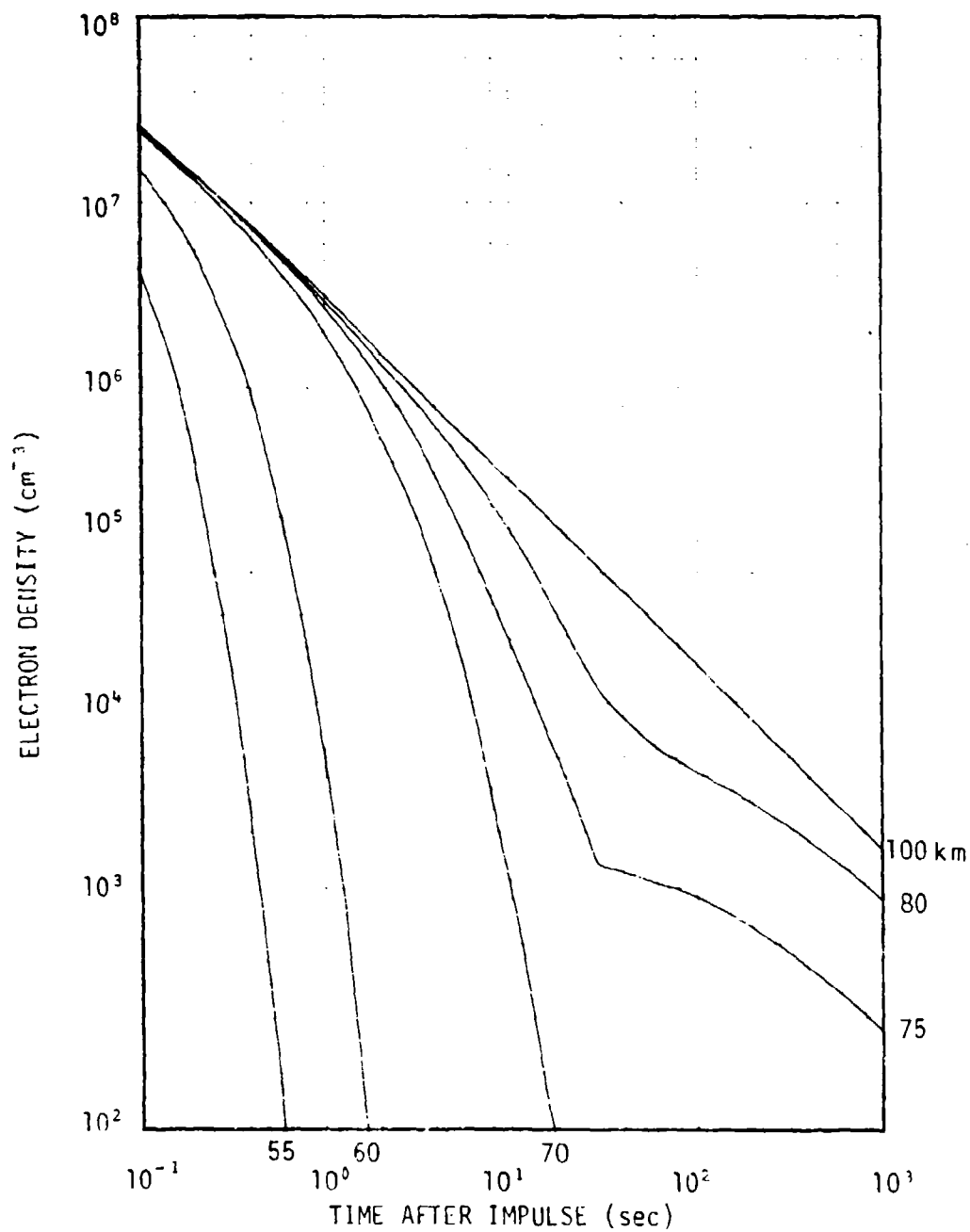


Figure 5-2 A. Decay of ionization following a nighttime ionization impulse of  $10^6$  ion pairs  $\text{cm}^{-3}$  (courtesy of Warren Knapp).

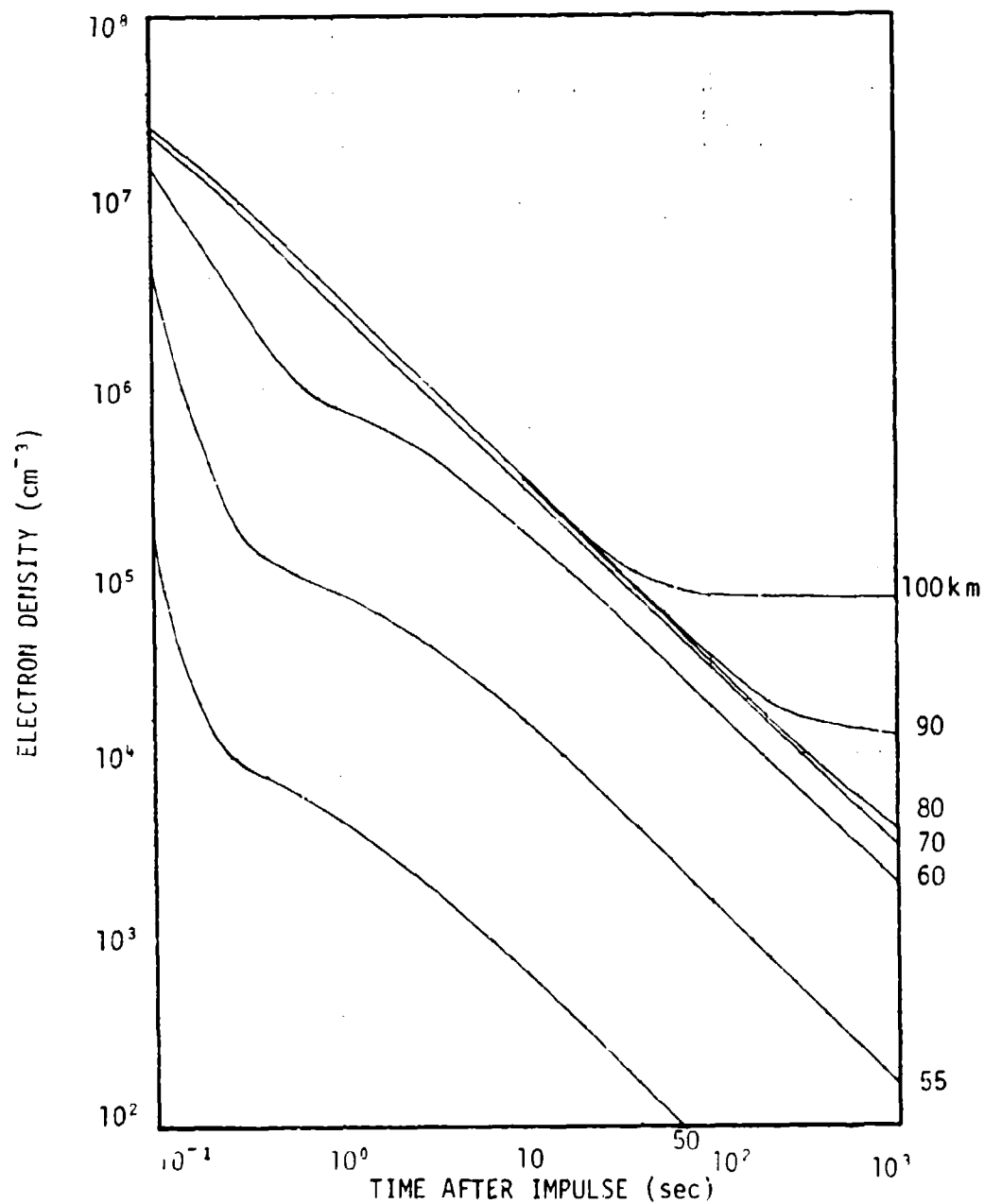


Figure 5-2 3. Decay of ionization following a daytime ionization impulse of  $10^8$  ion pairs  $\text{cm}^{-3}$  (courtesy of Warren Knapp).



$$N_e \approx N_+ \approx \sqrt{\frac{q}{\alpha}} \left[ \frac{N_0 + \sqrt{q/\alpha} \tanh(t\sqrt{\alpha q})}{\sqrt{q/\alpha} + N_0 \tanh(t\sqrt{\alpha q})} \right] \quad (5-17)$$

Since  $\lim_{t \rightarrow \infty} \tanh(t\sqrt{\alpha q}) = 1$ , it follows that for times large compared with  $(\alpha q)^{-1/2}$

$$N_e \approx N_+ \approx \sqrt{\frac{q}{\alpha}} \quad (t \gg (\alpha q)^{-1/2}) \quad (5-18)$$

For  $t \ll (\alpha q)^{-1/2}$ ,  $\tanh(t\sqrt{\alpha q}) \approx t\sqrt{\alpha q}$ , and

$$N_e \approx N_+ \approx \frac{N_0 + qt}{1 + \alpha N_0 t} \quad (t \ll (\alpha q)^{-1/2}) \quad (5-19)$$

For small  $N_0$ ,  $N_e$  and  $N_+$  at first increase linearly with time and approach the late-time value (5-18) asymptotically from below. For large  $N_0$ , the concentrations at first decrease according to the formula derived above for an impulsive source, and approach the late-time value asymptotically from above. In both cases the time required for the approach to the steady state is of order  $(\alpha q)^{-1/2}$ .

Even in cases where the assumption  $\alpha = \alpha_{ei}$  for all time is invalid, the concentrations approach steady-state values for which  $dN/dt = 0$ . From Eqs. 5-5, 7 the steady-state values of  $N_+$  and  $N_e$  are

$$N_+ = \sqrt{q/\alpha} \quad (5-20)$$

$$N_e = \frac{q + DN_+}{A + B + \alpha_{ei} N_+} \quad (5-21)$$

where  $\alpha$  is no longer necessarily equal to  $\alpha_{ei}$ , but is given by Eq. 5-8. Substitution of Eqs. 5-20, 21 into Eq. 5-8 leads to a cubic equation in  $\alpha$ , whose solution then permits calculation of  $N_e$  and  $N_+$ .

Analytical solution of the cubic for  $\alpha$  is quite laborious; solutions are best found numerically or graphically. Nevertheless, several special cases can be distinguished, and it is instructive to consider them.

#### (1) Recombination Dominated

$$D \gg A \quad \text{or} \quad \alpha N_+ \gg A \quad (5-22)$$

In this case the effects of attachment are negligible either because of the large detachment rate or the fact that the rate of electronic recombination is large compared with the attachment rate. In either case we expect that

$$\alpha \approx \alpha_{ei}, \quad N_e \approx N_+ \approx \sqrt{\frac{q}{\alpha_{ei}}} \quad (5-23)$$

That these are self-consistent assumptions can be shown by substitution in Eqs. 5-20, 21, with  $A$  being neglected in the denominator of Eq. 5-21. The second condition above can thus be replaced by  $\sqrt{\alpha_{ei} q} \gg A$ .

#### (2) Attachment Dominated

$$A \gg \alpha_{ei} N_+ \quad (5-24)$$

In this case attachment dominates electronic recombination, and the term  $\alpha_{ei} N_+$  in the denominator of Eq. 5-21 can be neglected.

## (2a) High Detachment Rate

If, in addition  $DN_+ \gg q$ , we have the previously discussed equilibrium between attachment and detachment. The  $q$  term in the numerator of Eq. 5-21 can be neglected, and we find

$$N_+ = \sqrt{\frac{q}{A}}, \quad N_e \approx \frac{D}{A+D} N_+, \quad \alpha \approx \frac{D \alpha_{ei} + A \alpha_{ii}}{A+D} \quad (5-25)$$

The conditions for validity of this result then become

$$A \gg \alpha_{ei} \sqrt{\frac{(A+D) q}{D \alpha_{ei} + A \alpha_{ii}}} \quad \text{and} \quad D \gg \sqrt{\frac{(D \alpha_{ei} + A \alpha_{ii}) q}{A+D}} \quad (5-26)$$

## (2b) Low Detachment Rate

In this case we assume  $DN_+ \ll q$ . It can be shown that this assumption together with the assumption  $A \gg \alpha_{ei} N_+$  leads to negative values of  $N_-$  unless  $A \gg D$ , and that therefore the only physically meaningful solutions are

$$N_e \approx \frac{q}{A}, \quad N_+ = \sqrt{\frac{q}{A}}, \quad \alpha \approx \alpha_{ii} + (\alpha_{ei} - \alpha_{ii}) \frac{\sqrt{\alpha q}}{A} \quad (5-27)$$

In general a quadratic must be solved to determine  $\alpha$ . In the situations of interest, however,  $\alpha_{ii} \leq \alpha_{ei}$ , so that for the case  $\sqrt{\alpha q} \ll A$ ,  $\alpha \approx \alpha_{ii}$ .

## Quasi-Equilibrium Approximation

If the source function  $q$  varies with time, solution of the rate equations become more difficult and no approximations of universal validity for general variations of  $q$  can be found. However, there is a class of problems for which useful approximations exist. If the variation of

$q$  is sufficiently slow, the concentrations have time to assume quasi-equilibrium values consistent with the instantaneous value of  $q$ , and the steady-state solutions discussed above are good approximations.

The condition we wish to impose is that  $dN/dt \approx 0$  and can be neglected, so that the differential equations can be replaced by algebraic equations. If this condition is satisfied, the steady-state solutions discussed above provide a good approximation, although now the  $N$ 's are slowly varying functions of time rather than being constant.

To see the restrictions implied by this condition, first consider the equation for  $N_+$ . With the assumption  $dN_+/dt \approx 0$  we have  $N_+ \approx \sqrt{q/\alpha}$ . The assumption concerning  $dN_+/dt$  is valid provided  $dN_+/dt \ll q$ , which in turn implies

$$\frac{dN_+}{dt} \approx \frac{(\alpha q)^{-1/2}}{2} \frac{dq}{dt} - \frac{N_+}{2\alpha} \frac{d\alpha}{dt} \ll q$$

In the special steady-state cases discussed above,  $\alpha$  is approximately independent of both  $q$  and  $N_+$ . Hence,  $d\alpha/dt \approx 0$  and the condition is that

$$(\alpha q)^{-1/2} \frac{dq}{dt} \ll q$$

i.e. that the fractional change in  $q$  in the characteristic recombination time  $(\alpha q)^{-1/2} \approx (\alpha N_+)^{-1}$  be small.

In case (1) above  $N_e \approx N_+$  and the condition that  $dN_e/dt$  be small implies the same condition on  $dq/dt$  as that inferred above. By arguments similar to those above we find that  $dN_e/dt$  can be neglected in case (2a) provided that

$$(A+B)^{-1} \frac{dq}{dt} \ll q$$

and in case (2b) if

$$A^{-1} \frac{dq}{dt} \ll q$$

i.e., that the fractional change in  $q$  must also be small in the characteristic times for attachment and/or detachment.

When these conditions on the rapidity of variation of  $q$  are satisfied, reactions are proceeding so fast that the species concentrations can adjust to the instantaneous value of  $q$ . The past history of the variation of  $q$  is "forgotten", and the steady-state solutions provide a good approximation, the quasi-equilibrium approximation. Regions of validity for the approximate solutions (1), (2a), and (2b) for daytime ambient atmospheric conditions are shown in Fig. 5-3. The figure was

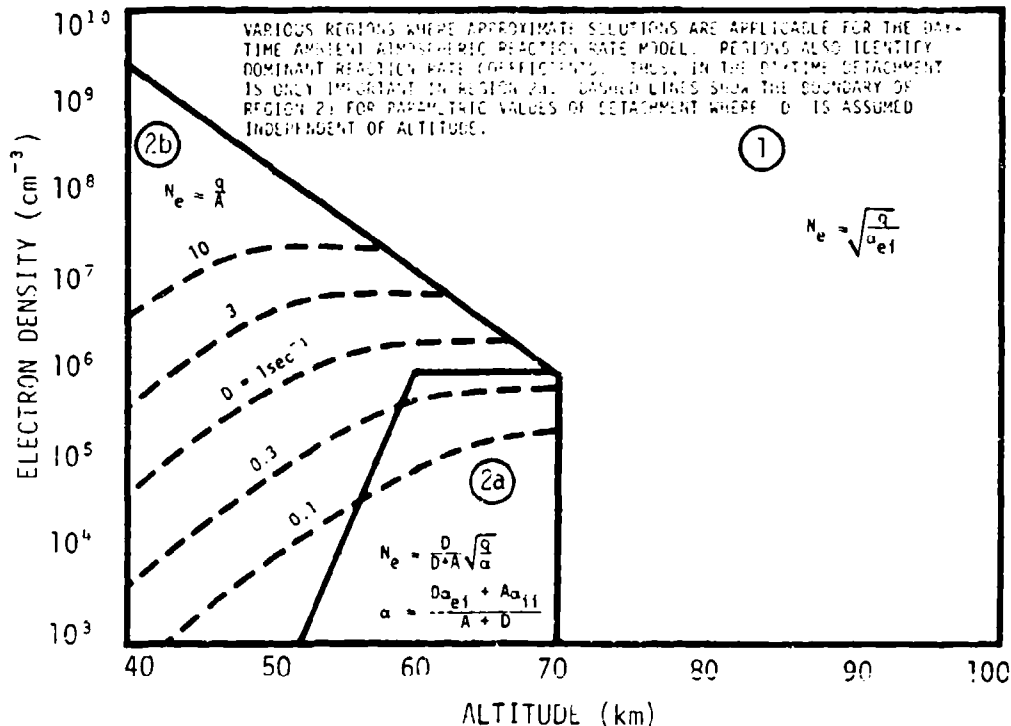


Figure 5-3. Approximate quasi-equilibrium solutions (Reference 5-2).

taken from Ref. 5-2, and corresponds to the lumped-parameter rate coefficients assumed there and discussed below. In general these cases correspond to decreasing altitudes and day to night transition in the order presented.

### 5.2.3 LUMPED-PARAMETER RATE COEFFICIENTS

A set of lumped-parameter values consistent with a limited set of de-ionization data for a moderately perturbed atmosphere below about 120 km is given by the following analytic expressions:

$$\alpha_{ei} = \left\{ \begin{array}{ll} 3 \times 10^{-7} & (T_e \leq 300^\circ\text{K}) \\ \frac{9 \times 10^{-5}}{T_e} & (T_e > 300^\circ\text{K}) \end{array} \right\} \quad (\text{cm}^3 \text{ sec}^{-1}) \quad (5-28)$$

$$\alpha_{ii} = 3 \times 10^{-8} + 6 \times 10^{-6} p T^{-5/2} \quad (\text{cm}^3 \text{ sec}^{-1}) \quad (5-29)$$

$$A = 5.4 \times 10^2 p^2 T^{-5/2} \exp\left[-\frac{540}{T}\right] + 1.3 \times 10^{-15} n(O) + 2.5 \times 10^{-12} n(O_3) \quad (\text{sec}^{-1}) \quad (5-30)$$

$$D(\text{day}) = \left\{ \begin{array}{ll} 0.5 & (60 \leq h) \\ 0.5 \exp[-0.392(60 - h)] & (50 \leq h < 60) \\ 0.01 & (h < 50) \end{array} \right\} \quad (\text{sec}^{-1}) \quad (5-31a)$$

$$D(\text{night}) = 1.5 \times 10^{-13} n(O) \quad (\text{sec}^{-1}) \quad (5-31b)$$

where

$T$  = atmospheric temperature at altitude  $h$ , (K)

$T_e$  = electron temperature at altitude  $h$ , (K)

$p$  = pressure at altitude  $h$ , (dynes  $\text{cm}^{-2}$ )

$h$  = altitude (km)

$n(O)$  and  $n(O_3)$  = number density of atomic oxygen and ozone, respectively, at  $h$ , ( $\text{cm}^{-3}$ ).

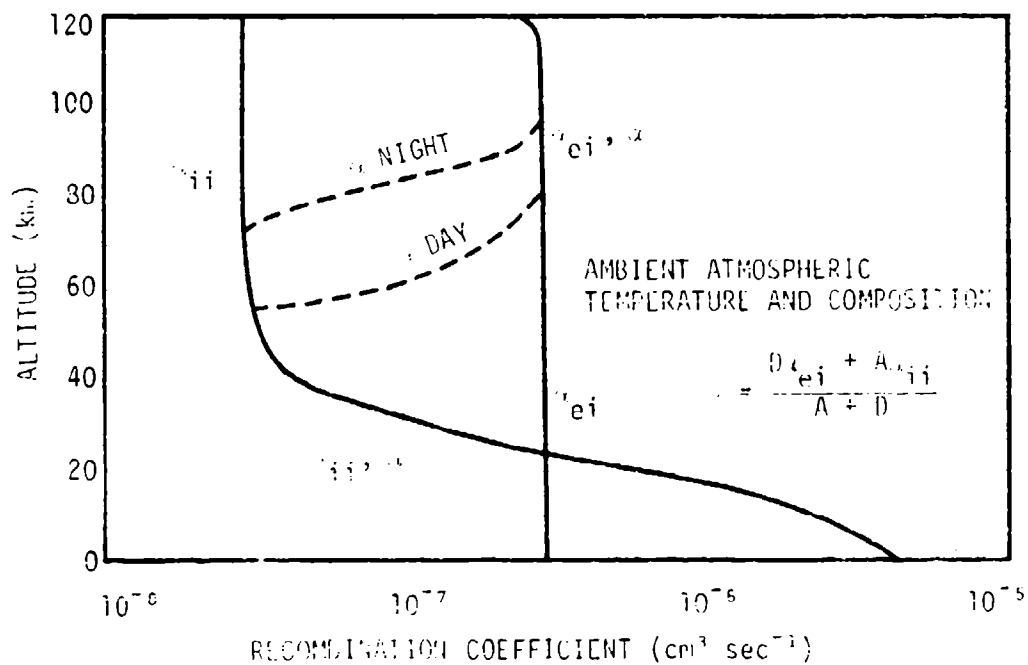


Figure 5-4. Recombination rate coefficients versus altitude (Reference 5-2).

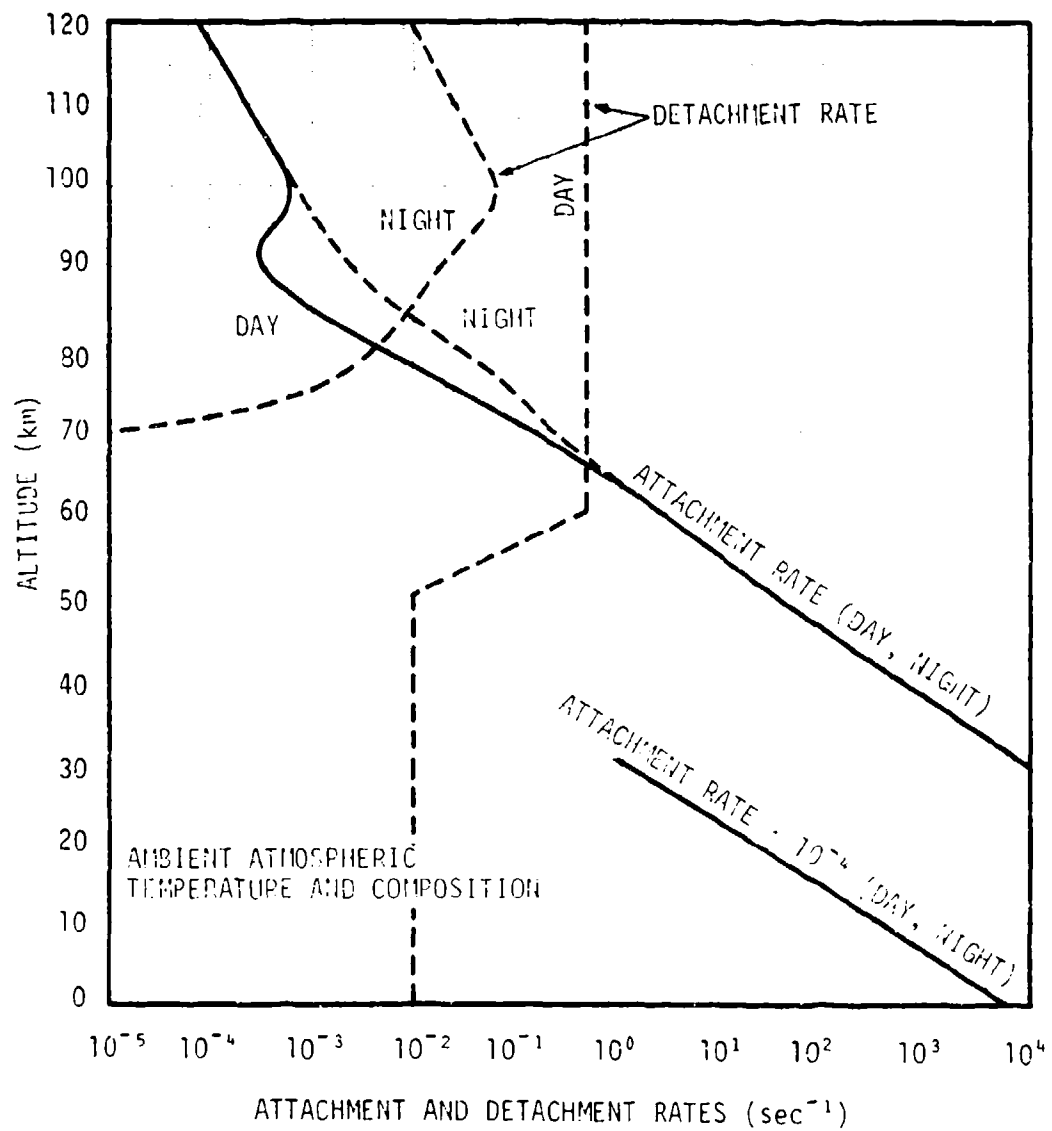


Figure 5-5. Attachment and detachment rates versus altitude (Ref 5-2).



Figures 5-4 and 5-5 show values of the recombination coefficients and the attachment and detachment coefficients as given by Equations 5-28 to 31 from 0 to 120 km altitude. It should be stressed that this is a set of rate coefficients. Used together, they give good agreement with a limited set of experimental data. Great caution should be exercised in making changes in any individual member of the set.

Reactions approximated by lumped-parameter rate coefficients for use under mildly or extensively disturbed conditions below about 100 km are discussed briefly in Section 5.4.1 of this chapter, and the character of deionization at higher altitudes is discussed in Section 5.4.3.

### 5.3 ATMOSPHERIC CHEMICAL REACTIONS

With the exception of the subsection dealing with reactions of neutrals, this section parallels the formulation of the three-species model. Its objectives however, are completely different. For each generic reaction type previously identified in a schematic fashion only, we now consider the chemical species and reaction mechanisms that are important in the deionization process. The discussion here is qualitative in nature; reaction rate coefficients, when cited, are primarily for illustrative purposes. For further details and an extensive list of rate coefficients and related data, the reader is referred to the second edition of the DNA Reaction Rate Handbook, Ref. 5-3.

#### 5.3.1 ENERGY DEPOSITION PRODUCTS

The perturbed atmosphere that constitutes the initial state for the deionization process is established by the deposition of energy from an ionizing source. As before, we confine our attention to regions sufficiently far from the source that the gross thermodynamic properties of the air are essentially unaffected. For example, since the ambient daytime ionization increases with altitude while the total number density decreases exponentially, a maximum fractional ionization of  $10^{-6}$  represents

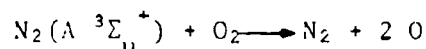
an ionization level  $10^{11}$  times ambient at 55 km,  $10^4$  times ambient at 100 km, and of the same magnitude as ambient as 200 km; thus for the same fractional ionization, the degree of perturbation is much more significant at lower altitudes.

An intense ionizing source gives rise to an initial distribution of products largely determined by the ambient composition at the point of energy deposition. For each 33.9 eV deposited, one ion pair and associated excited products are formed. Although there is some uncertainty regarding the relative amounts of certain of the species formed, the results of Ory and Gilmore (Ref. 5-4) presented in Column 2 of Table 5-1 represent the best current estimate.

Table 5-1. Species produced below 100 km by ionizing radiations.

Species	Initial Particles per Ion Pair	Effective Particles per Ion Pair
$e^-$	1.00	1.00
$N_2^+$	0.75	0.75
$O_2^+$	0.19	0.19
$N^+$	0.04	0.04
$O^+$	0.02	0.02
$N_2(A \ ^3\Sigma_u^+)$	0.6	0.0
$O_2(a \ ^1\Delta_g)$	2.0	2.0
$N(^1D)$	0.3	0.3
$N$	0.2	0.2
$O$	0.3	1.5

Ory and Gilmore indicate that the value for the excited  $N_2$  A-state includes higher electronically excited states of  $N_2$  that rapidly decay radiatively to the A-state. Further, by virtue of the very rapid reaction



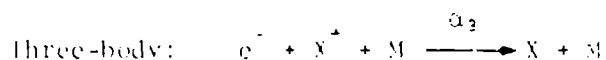
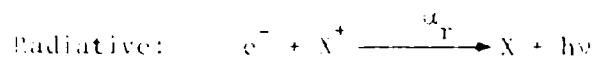
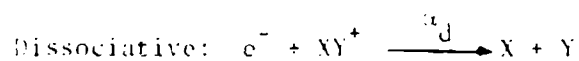
the values in Column 3 effectively define the initial composition for describing the subsequent deionization reactions. The excited and dissociated neutral species are important because of their contribution to key deionization reactions as discussed later.

### 5.3.2 ELECTRON-ION RECOMBINATION AND RELATED REACTIONS

Recombination reactions involving electrons and positive ions afford one of the two charge neutralization paths of the deionization process, the other being ion-ion recombination. As formulated in the lumped-parameter model, electron-ion recombination was characterized by the single rate coefficient  $\alpha_{ei}$ . The present discussion examines the mechanisms of this recombination process, and considers the related set of reactions through which the chemical nature of the ion is changed while conserving the positive charge.

#### Mechanisms of Electron-Ion Recombination

When the requirements of conservation of energy and momentum are taken into account, three distinct recombination mechanisms can be recognized:



$XY^+$  is a molecular ion,  $X^+$  is an atomic or molecular ion, and  $M$  is an otherwise unspecified particle.

### Dissociative Recombination

When positive molecular (diatomic or polyatomic) ions are present, dissociative recombination constitutes the dominant deionization path by virtue of its large rate coefficient, of the order of  $10^{-7}$  to  $10^{-6}$   $\text{cm}^3 \text{sec}^{-1}$ ; the smaller values are characteristic of simple diatomic ions such as  $\text{O}_2^+$ ,  $\text{N}_2^+$ , and  $\text{NO}^+$ , while the larger values apply to the complex and cluster ions described below. The reaction probably proceeds through an intermediate resonance state or molecular complex, which then loses its excess energy by dissociation. Both theoretical considerations and experimental results indicate that dissociative recombination is exothermic, has no activation energy, and shows a temperature dependence between  $T^{-0.5}$  and  $T^{-1}$ . It is the dominance of this dissociative mechanism in the presence of molecular ions that accounts for the frequent use of the symbol  $\alpha_d$  to represent the general electron-ion recombination process, but this deemphasizes the role of the other two mechanisms. It is for this reason that we advocate the use of  $\alpha_{ei}$  as the appropriate symbol.

### Radiative Recombination

The two-body recombination of electrons and positive ions in which excess energy is lost by radiation has a rate coefficient,  $\alpha_r$ , of the order of  $10^{-12}$   $\text{cm}^3 \text{sec}^{-1}$  and a temperature dependence of  $T^{-0.7}$ , making it some five to six orders of magnitude slower than dissociative recombination. The rate coefficient is quite independent of the nature of the positive ion, be it atomic or molecular. It follows that radiative recombination competes with dissociative recombination only if the atomic ion concentration is  $10^5$ - $10^7$  times as large as that of molecular ions. This is the case only under highly ionized conditions.

Under these conditions the electron density and temperature are also high, and three-body recombination with an electron acting as the third body must be taken into account. The three-body and radiative processes are coupled together, and give rise to the so-called collisional-radiative recombination. A wide range of values for the effective rate coefficient for this process has been estimated, depending on temperature and electron density. For temperatures of a few thousand degrees and electron densities less than  $10^{13} \text{ cm}^{-3}$ , the effective rate coefficient is of the order of  $10^{-14}$  or  $10^{-12} \text{ cm}^3 \text{ sec}^{-1}$ . For a discussion of this point and further references, see Ref. 3-3, pp. 16-18, 19.

### Three-Body Recombination

The last mechanism involves the interaction of the electron-positive ion reaction intermediate with a third particle capable of carrying off the excess energy of the reactants. The requirement for an energy-transferring collision during the short lifetime of the intermediate implies that three-body recombination must be limited to regions of high particle density. For this mechanism, with a neutral as the third body, to constitute, say, 10 percent of the deionization, the product of the rate coefficient, which is of the order of  $10^{-26} \text{ cm}^6 \text{ sec}^{-1}$ , and the total particle density must be about 1/10 of the dissociative recombination coefficient, typically  $10^{-7} \text{ cm}^3 \text{ sec}^{-1}$ . Thus, the neutral density required is about  $10^{18} \text{ cm}^{-3}$ , corresponding to an altitude below 25 km.

For a given electron-ion pair, the three-body recombination coefficient varies somewhat with the nature of the neutral third body; polyatomic molecules such as water vapor are more effective in stabilizing the complex than diatomic molecules, which, in turn, are superior to free atoms.

When the third body is an electron, the radiative and collisional recombination must be treated together. See the discussion above under radiative recombination.

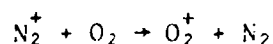
### Positive Charge Conserving Reactions

Reactions that alter the composition of the mix of positive ions from that formed originally are important for understanding atmospheric deionization. The previous section indicated that dissociative recombination necessarily involves molecular ions, and that the rate coefficients tend to increase with increasing complexity of the ion. Consequently, reactions that convert atomic to molecular ions and molecular ions to complexes and clusters create a positive ion mix that increases the dissociative recombination rate. Three classes of positive ion conversion reactions are described in the following subsections.

#### Charge Transfer

Charge transfer reactions provide the route by which initially formed ions of high ionization potential become neutralized by electron capture from species of lower ionization potential. Ranked in order of decreasing ionization potential, the species involved are  $N_2$ ,  $N$ ,  $O$ ,  $O_2$ , and  $NO$ ; each is capable of being ionized by ions of any of the species with higher ionization potential. This yields a set of ten charge transfer reactions whose rate coefficients vary from about  $10^{-12}$  to almost  $10^{-9} \text{ cm}^3 \text{ sec}^{-1}$ . Nitric oxide ( $NO$ ), a minor atmospheric constituent, is enhanced following a disturbance by a series of reactions yet to be considered. Consequently, the result of the charge transfer reactions is the rapid conversion of positive charge to  $O_2^+$  and  $NO^+$  prior to recombination or clustering (discussed later).

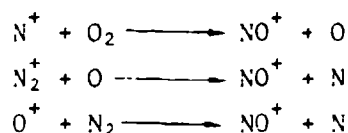
Of particular importance is the reaction



This is usually the only reaction that competes effectively with electron recombination of  $N_2^+$ . When recombination occurs first, two nitrogen atoms are produced (one of which is probably in the  $^2D$  excited state) and the production of NO and  $NO_2$  is enhanced.

### Atom Interchange

These reactions follow the pattern of the charge transfer reactions except that as the name implies, an atom or ion is interchanged rather than an electron. Virtually all the important atom interchange reactions in air lead to production of  $NO^+$  at rates that compete with the charge transfer reactions. Examples are:



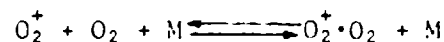
The last reaction is of particular importance in the E- and F-regions. It is not uncommon for large parcels of highly disturbed air to have more  $O^+$  ions than the remaining  $O_2$ . Charge transfer with  $O_2$ , with subsequent dissociative recombination, cannot then provide a path for rapid deionization. Since radiative recombination is slow, the atom interchange reaction of  $O^+$  with  $N_2$  is the rate determining step for deionization. The rate coefficient for the reaction is, in addition to being dependent on the gas kinetic temperature, very dependent on the vibrational state of the  $N_2$  molecule. Since the vibrational populations are not likely to be in thermal equilibrium with the gas kinetic temperature, the deionization calculation becomes somewhat complicated.

In the D-region of the atmosphere the net result of the charge transfer and atom interchange reactions is to convert the initially formed

positive ions to the more stable diatomic ions  $O_2^+$  and  $NO^+$ . This positive ion mix may be thought of as the first phase in the conversion of positive charge to its terminal form.

### Positive Ion-Neutral Association

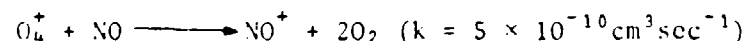
The last two phases of atmospheric positive ion evolution involve reactions with neutral molecules to form simple molecular complexes, which then enter into sequential clustering and rearrangement reactions. The complex formation reactions proceed via three-body association mechanisms that establish transitory equilibria between the complex and its components:



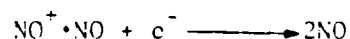
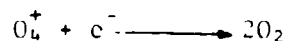
and



The  $O_4^+$  complex is assumed to retain its ability to ionize nitric oxide by the reaction



Both complexes enter into rapid dissociative recombination reactions with electrons:



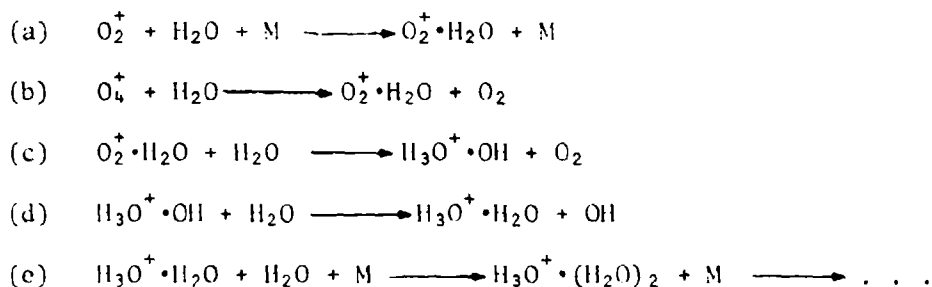
with characteristic rate coefficients  $\alpha_d$  of  $\sim 10^{-6} \text{ cm}^3 \text{ sec}^{-1}$ .

Since the 1965 discovery in the D-region of the hydronium ion,  $H_3O^+$ , and its higher hydrates,  $H_3O^+ \cdot (H_2O)_n$  with  $n$  ranging from 1 to 8



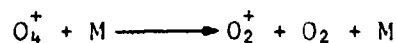
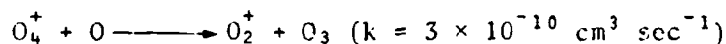
(Ref. 5-5), atmospheric and laboratory experimental efforts have been devoted to elucidating their altitude dependence and the reaction sequences that produce these ions. Two such sequences are now known to be significant in D-region chemistry; one is based on  $O_2^+$  hydration and the other on  $NO^+$  hydration.

The  $O_2^+ - H_2O$  sequence (Ref. 5-6) comprises the reactions:



Reaction (a) is three-body association and (b) is referred to as a switching reaction. Both lead to the same product. Reaction (c) is a charge rearrangement whose product undergoes the switching reaction (d) to generate a hydrated hydronium ion and a hydroxyl radical (OH). Reaction (e) represents the trimolecular clustering mechanism by which further water molecules become electrostatically bonded to the central charge through ion-dipole interactions; the continuation symbol (...) indicates that this three-body process is repeated to form the higher polyhydrates.

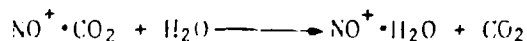
The sequence of hydrate formation involving  $O_4^+$  (reaction (b)) is usually much faster (by several orders of magnitude) than hydration via reaction (a). Any reaction that destroys  $O_4^+$  before it can react with  $H_2O$  will therefore mitigate and retard the formation of the hydronium hydrates. Two such reactions are:



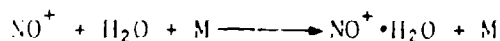
The first of the above reactions prevents the hydronium clusters from becoming the dominant positive ions via the  $O_2^+ - O_4^+$  sequence when atomic oxygen is a significant species constituent. This applies in the E-region of the normal atmosphere and in parts of the D-region in which atomic oxygen has been produced by a strong disturbance such as a PCA event.

The second reaction is the thermal breakup of  $O_4^+$  and is endothermic. However, the binding energy of the  $O_4^+$  cluster is small (<0.5 eV) and only a small change in temperature can have a significant effect on the relative concentrations of  $O_2^+$  and  $O_4^+$ . At 60 km an increase of just 50°K over the ambient temperature decreases the  $O_4^+$  to  $O_2^+$  ratio, when the thermal breakup of  $O_4^+$  is equal to the formation, by about a factor of fifty, and this reverses the dominance of the cluster ions. Thus, clusters formed via the  $O_2^+ - O_4^+$  sequence will be significantly diminished in importance in air that has been only slightly heated by a disturbance.

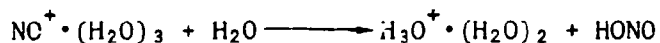
The formation of hydronium hydrates via a sequence of reactions involving  $NO^+$  has also been determined (Ref. 5-7). In addition to the clustering with NO,  $NO^+$  can cluster with  $CO_2$  and possibly  $N_2$  and  $O_2$  via three-body reactions. This is followed by a switching reaction such as



$NO^+$  can also cluster directly with  $H_2O$ :



By whichever mechanism formed, the monohydrate then clusters via three-body associations to the trihydrate,  $\text{NO}^+ \cdot (\text{H}_2\text{O})_3$ , analogous to reaction (e) above. At this point, a unique rearrangement occurs:



and the hydrated hydronium ion then continues to cluster by three-body association (ref. 5-8).

The above sequence does not, however, adequately explain the distribution of hydrated ions in that part of the natural D-region where  $\text{NO}^+$  is the initial ion formed (above 70 km). Another sequence is being sought. However,  $\text{NO}^+$  is not the initial ion formed under most disturbed conditions. The  $\text{O}_2^+$  sequence, about which we know more, is much more important in these cases.

The larger cluster ions provide ideal targets for dissociative recombination with electrons. The coefficients  $\alpha_d$  increase as the number of molecules in the cluster, and hence the possible degrees of freedom for dissipation of the energy, increases. The balance among the various reaction paths for positive ions which have been identified depends on degree of ionization or electron density, and ambient concentrations of  $\text{H}_2\text{O}$  and  $\text{CO}_2$ . As a general rule, higher electron densities and higher altitudes favor recombination with diatomic ions; lower electron densities and lower altitudes that with cluster ions, since time permits their formation.

Figure 5-6 summarizes the salient features of the reactions considered in this section. In general, the species toward the right of the figure form at progressively later times. An important implication of the figure is that the recombination rate coefficients increase as the

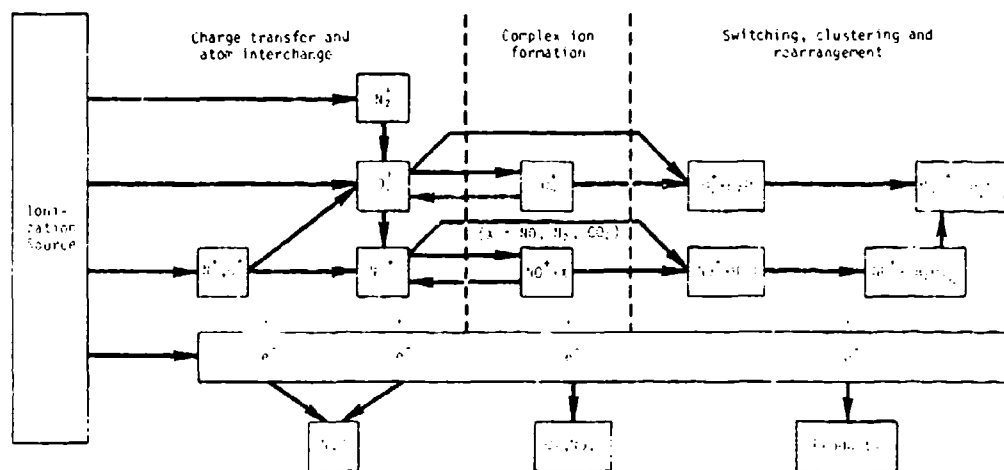


Figure 5-6. Simplified Schematic of Positive Ion Evolution.

positive ion mix changes from diatomic through complex to cluster ion forms at a rate determined by the individual conversion rates of the ions. Thus, lower electron densities (low source strengths) and lower altitudes (higher three-body rates leading to cluster formation) result in characteristically higher effective recombination rate coefficients.

### 5.3.3 ATTACHMENT, DETACHMENT, AND NEGATIVE ION REACTIONS

The negative ions involved in atmospheric deionization processes are formed initially by the attachment of free electrons to neutral species. Once formed, these ions participate not only in a series of charge transfer, atom interchange, and association reactions tending toward the formation of stable, terminal, polyhydrated ions, but also in detachment reactions that regenerate free electrons. At all altitudes, the allotropic forms of oxygen are important species in the early and intermediate phases of the negative ion scheme; other deionization products and minor ambient constituents such as  $\text{CO}_2$ ,  $\text{NO}$  and  $\text{H}_2\text{O}$  play important roles in the late phase, but this develops more slowly than in the case of the positive ions.

#### Electron Attachment

As a measure of their relative tendency to form negative ions by attachment, the electron affinity of typical atmospheric species increases in the order  $\text{NO}$ ,  $\text{O}_2$ ,  $\text{O}$ ,  $\text{O}_3$ ,  $\text{NO}_2$ . Of these,  $\text{O}_2^-$  and  $\text{O}^-$  are usually the initial negative ions formed.

#### Three-Body Attachment

As exemplified by the reaction:



three-body attachment is the dominant mechanism for  $\text{O}_2^-$  formation where  $\text{O}_2$  densities are sufficiently high; it is well established that the rate coefficient of this reaction, approximately  $10^{-30} \text{ cm}^6 \text{ sec}^{-1}$  at  $300^\circ \text{ K}$  when  $\text{M} = \text{O}_2$ , is at least an order of magnitude smaller with  $\text{M} = \text{N}_2$ . Three-body attachment to species other than  $\text{O}_2$  does not play an important role in atmospheric processes except under special circumstances.

### Dissociative Attachment

This mechanism dissipates the excess energy of the electron by dissociating the molecular reactant:



The reaction with  $O_2$  is several eV endothermic, and can be neglected at thermal energies. The reaction with  $O_3$  is slightly exothermic when  $O^-$  is the negative ion produced:



and has a rate coefficient of about  $10^{-11} \text{ cm}^3 \text{ sec}^{-1}$ . Thus, as the ozone concentration builds up, this reaction becomes an important source of  $O^-$ .

### Radiative Attachment

The third attachment mechanism involves the emission of radiation:



The relatively high electron affinity of the free oxygen atom makes this an important process in regions of high  $O$  density, i.e., at high altitude or as a result of high ionization levels. With a rate coefficient of about  $10^{-15} \text{ cm}^3 \text{ sec}^{-1}$ , this reaction is faster than radiative attachment to  $O_2$ , thus favoring the formation of  $O^-$  rather than  $O_2^-$  in low density regions where the three-body formation rate of  $O_2^-$  is small. As a result,  $O^-$  concentrations become significant at altitudes well below that at which the  $O/O_2$  density ratio is near unity (about 120 km).

### Negative Ion Reactions

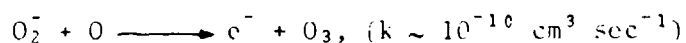
Although detachment reactions are an important class of processes in determining free electron densities, their inclusion under the general heading of negative ion reactions emphasizes the fact that they are competitive with the reactions that form stable (i.e., non-detaching) species and that initiate the reaction chains leading to the terminal negative ions.

#### Detachment Reactions

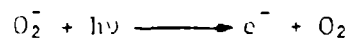
Three of the known detachment reactions are reverses of attachment processes already described. The reverse of three-body attachment is collisional detachment:



The reverse of dissociative attachment is associative detachment:

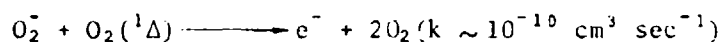


and the reverse of radiative attachment is photodetachment:



Collisional detachment is endothermic and is not of major importance at ambient atmospheric temperatures. It becomes increasingly important at higher temperatures, however, and can easily be the dominant detachment mechanism in disturbed regions that are heated several hundred degrees above ambient.

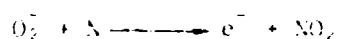
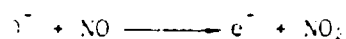
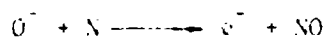
Another type of collisional detachment is by an excited atom or molecule. One such reaction is:



Other reactions of this type may be important but have not as yet been observed.

The high photodetachment rates of  $O^-$  and  $O_2^-$  under the influence of the normal daytime solar flux,  $1.42 \text{ sec}^{-1}$  and  $0.33 \text{ sec}^{-1}$ , respectively, contribute significantly to determining the free electron density; this effect is illustrated by the difference between the overall day and night detachment rates shown in Figure 5-5.

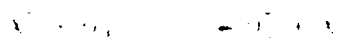
The species  $O^-$  and  $O_2^-$  are by far the most important known detachment reactants in the deionization process. In addition to the detachment reactions above we have:



These reactions have characteristic rate coefficients of the order of  $10^{-12} \text{ cm}^3 \text{ sec}^{-1}$ .

#### Charge Transfer and Atom Interchange Reactions

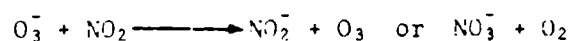
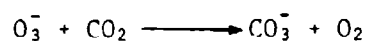
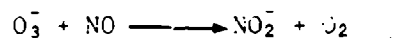
The  $O_2^-$  and  $O^-$  initially formed can undergo charge transfer and atom interchange reactions and, in the presence of the positive ions. Negative charge is transferred, e.g., to  $O_2$  and  $NO_2$  (rate coefficients between  $10^{-13}$  and  $10^{-16} \text{ cm}^3 \text{ sec}^{-1}$ ):



where  $O_2^-$  is either  $O_2(^1\Delta)$  or  $O_2(^3\Sigma)$ .



$O_3^-$  is important in atom interchange reactions because of its ability both to charge transfer and oxidize other molecules:



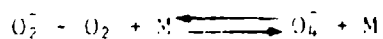
#### Negative Ion-Neutral Association Reactions

The  $O_3^-$  ion involved in the previous reactions is also formed by a three-body association mechanism:

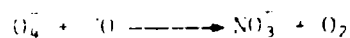


with a rate coefficient of the order of  $10^{-30} \text{ cm}^6 \text{ sec}^{-1}$ .

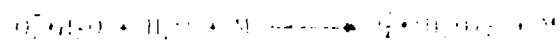
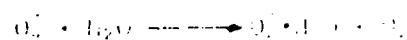
In the lower D-region and below, complex formation by three-body association involving  $O_2^-$  is a key reaction:



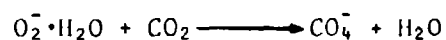
This reaction provides an easily dissociated complex that effectively transforms the  $O_2^-$  ion to other species:



It can also initiate the  $O_4^-$  hydration chain:



but the prevalence of  $\text{CO}_2$  in the D-region favors the faster reaction:



A list of all the possible reaction paths that can occur after the initial negative ion is formed will not be given here, but Figure S-7 summarizes the sequences that are important. In general the trend of these paths is to form the "terminal" ion  $\text{NO}_3^{\cdot-}$ , providing, of

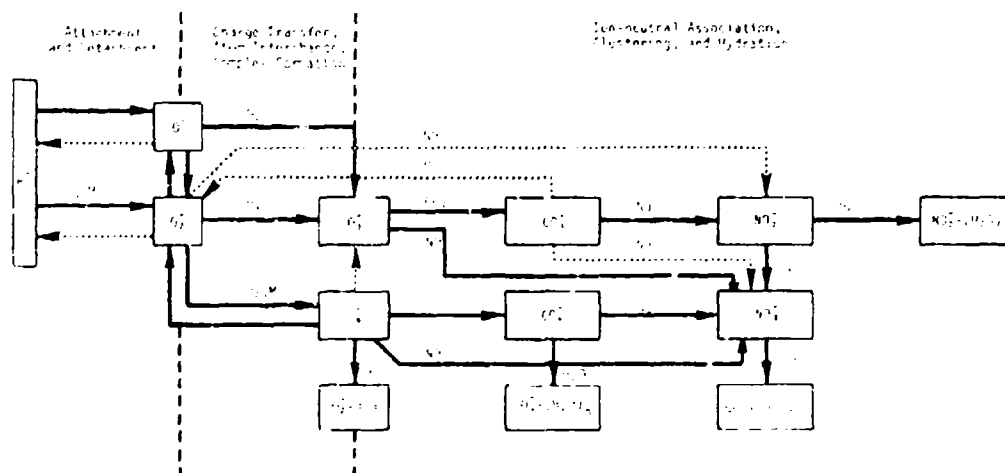


Figure S-7. Attachment, Detachment and Negative Ion Reactions. (Dashed arrows indicate paths most affected by changes in photodetachment conditions.)

course, a detachment or neutralization does not occur along the way. The term "terminal" refers to an ion and its hydrates that will neither undergo detachment nor be converted to another negative ion prior to neutralization. (The  $\text{NO}_3^-$  ion formed from  $\text{O}_4^-$  and  $\text{CO}_4^-$  is believed to be isomerically different from that formed from  $\text{O}^-$ ,  $\text{O}_3^-$ ,  $\text{CO}_3^-$  and  $\text{NO}_2^-$ . The former is probably not a terminal ion as is the latter.)

We have said little about the hydrates of  $\text{CO}_3^-$ ,  $\text{CO}_4^-$ ,  $\text{NO}_2^-$  and  $\text{NO}_3^-$ , although they occur prominently in the natural atmosphere, particularly at low altitudes. This is because they form slowly, much more slowly than the positive ion hydrates, and because there is no evidence yet that they behave significantly differently than the core negative ion

As can be seen from Figure 5-7, the paths to  $\text{NO}_3^-$  are not one-way. The ions  $\text{O}_3^-$ ,  $\text{O}_4^-$ ,  $\text{CO}_3^-$ , and  $\text{CO}_4^-$  can, primarily by reacting with atomic oxygen, be reconverted to  $\text{O}_2^-$ , which is detachable. This is one of the main obstacles in trying to apply a simple lumped-parameter scheme to atmospheric deionization, particularly at altitudes where any atomic oxygen formed by a disturbance persists for many seconds.

Finally, it should be emphasized that the balance among the various paths shown is strongly dependent on altitude, ionization level and the concentrations of minor neutral species such as  $\text{O}$ ,  $\text{O}_3$ ,  $\text{NO}$ ,  $\text{NO}_2$  and  $\text{H}_2\text{O}$ .

#### 5.3.4 REACTIONS OF NEUTRAL SPECIES

A number of reactions significant in atmospheric ionospheric chemistry of neutral particles. In comparison to the ionospheric processes, results are their production or depletion of species that enter into the ionospheric reactions already described.

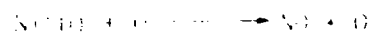
Because of the absence of charge-induced interactions (polarization, ion-dipole effects, etc.), reactions among neutrals are slower and show a greater temperature dependence than those involving ions. This appears in both the pre-exponential and activation energy factors of the rate coefficient. In the cool, mildly disturbed regions considered here, the neutral reactions of importance are, with a single exception, exothermic.

The neutral species, other than  $O_2$  and  $N_2$ , that are of direct or indirect importance are  $N$ ,  $N(^2D)$ ,  $O$ ,  $O_2(^1\Delta)$ ,  $NO$ ,  $O_3$  and  $NO_2$  (when no state is indicated, the ground state is assumed). The last three of these species are not produced initially but evolve, as the initial species decay, relatively slowly after a disturbance. Thus, the variation of these species must be accounted for in the deionization process.

The reactions governing the behavior of these species can be roughly divided into groups that in many situations can be treated independently of each other. The interactions among the groups, however, is not always small, and may sometimes dominate the overall behavior.

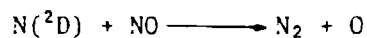
#### $N(^2D)$ and $H$ Decay

The primary depletion mechanism of  $N(^2D)$  is the reaction



$$k_1 = 7.5 \times 10^{-11} \exp(10,000/T) \text{ cm}^3/\text{sec} \quad (1)$$

This reaction also accounts for the main production of atomic oxygen. The  $NO$  produced is ionized, and often loses charge the same way as neutral  $N(^2D)$ , by the reaction



$$k_2 = 7 \times 10^{-11} \text{ cm}^3 \text{ sec}^{-1} (300^\circ\text{K})$$

The saturation value is obtained when the production of NO by the first reaction equals the destruction by the second reaction. This yields

$$[\text{NO}]_{\text{saturation}} = \frac{k_1}{k_2} [\text{O}_2]$$

This value is reached only when the initial  $\text{N}(^2\text{D})$  concentration is very large or when there is a very strong disturbance. For moderate disturbances the NO production will be essentially equal to the  $\text{N}(^2\text{D})$  destroyed.

As can be seen from the two above reactions, atomic oxygen is also produced as the  $\text{N}(^2\text{D})$  is destroyed. The ratio of the O produced to the  $\text{N}(^2\text{D})$  destroyed will be between one and two. The value of two is approached only for very strong disturbances. The atomic oxygen adds to the initially produced oxygen.

The decay of the ground state atomic nitrogen proceeds similarly to that of  $\text{N}(^2\text{D})$ . The controlling reactions are

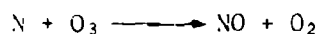


$$k = 4 \times 10^{-12} \text{ cm}^3 \text{ sec}^{-1} (300^\circ\text{K})$$



$$k = 2.2 \times 10^{-11} \text{ cm}^3 \text{ sec}^{-1} (300^\circ\text{K})$$

The value of the first reaction rate is small because of a significant activation energy (  $\sim .35$  eV). Because this reaction is slow, other reactions that deplete the N can be important. If the ambient  $O_3$  and  $NO_2$  concentrations are large enough, one must consider



$$k = 6 \times 10^{-12} \text{ cm}^3 \text{ sec}^{-1} (300^\circ K)$$

and



$$k = 1.8 \times 10^{-11} \text{ cm}^3 \text{ sec}^{-1} (300^\circ K)$$

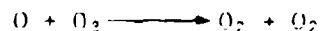
The  $O_3$  produced by the disturbance (discussed in the next section) is often produced rapidly enough to enter into the N decay. Instead of producing atomic oxygen, as in the reaction with  $O_2$ , an ozone molecule is destroyed by the first of the above reactions. This decreases what is called the "odd oxygen" (the sum of  $[O]$  and  $[O_3]$ ), rather than increasing it.

#### Atomic Oxygen and Ozone System

The primary reactions affecting the atomic oxygen and ozone concentrations are:



$$k = 6 \times 10^{-34} \text{ cm}^6 \text{ sec}^{-1} (300^\circ K)$$

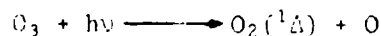


$$k = 1 \times 10^{-14} \text{ cm}^3 \text{ sec}^{-1} (300^\circ K)$$

The second reaction has an activation energy of  $\sim 0.18$  eV, and one of the product oxygen molecules may be excited to the  $^1\Delta$  state.

The atomic oxygen-ozone system behaves very much like the atomic nitrogen-nitric oxide system, in that the ozone formation saturates at a value at which the destruction by the second of the above reactions equals the formation by the first. In the E-region this occurs only for very large initial atomic oxygen concentrations, and therefore only for strongly disturbed regions.

During the daytime the photodissociation reactions



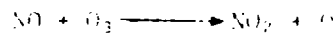
and



must be considered. Sunlight dissociates ozone in times as short as 100 seconds, depending on the altitude and the solar zenith angle. The atomic oxygen produced by the photodissociation of  $O_2$  is the primary source of "odd oxygen" in the natural atmosphere.

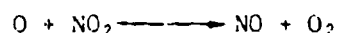
#### NO - NO<sub>2</sub> System

The NO, which is formed during the  $N(^2D)$  and N decay, is converted to NO<sub>2</sub> by the reaction



$$k = 10^{13} \text{ cm}^3 \text{ mole}^{-1} \text{ sec}^{-1} \text{ (NO}_2\text{)}$$

Atomic oxygen reconverts the NO<sub>2</sub> to NO by the reaction



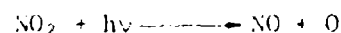
$$k = 6 \times 10^{-12} \text{ cm}^3 \text{ sec}^{-1} (300^\circ\text{K})$$

The first reaction has an activation energy of about 0.1 eV.

Setting the destruction rate of  $NO_2$  equal to the production rate, one finds that the ratio of  $[NO_2]$  to  $[NO]$  can be at most

$$\frac{[NO_2]}{[NO]} \sim 2 \times 10^{-3} \frac{[O_3]}{[O]}$$

at  $300^\circ\text{K}$ . Thus, it takes little atomic oxygen, relative to the ozone, to prevent the conversion of  $NO$  to  $NO_2$ . During the daytime, the natural D-region has appreciable atomic oxygen, and the  $NO_2$  concentration is small compared to the  $NO$  concentration. This ratio is affected in part by the photodissociation of  $NO_2$  during the day, i.e.,



At zero solar zenith angle, the time constant for  $NO_2$  photodissociation is about 100 seconds.

During the night the  $NO$  produced by a disturbance will not be converted to  $NO_2$  until the atomic oxygen concentration has decayed to several orders of magnitude below the ozone concentration.

#### $O(^1D)$ decay

The  $^1D$  state of  $O_2$  has a lifetime against radiation of about 4000 seconds. During the daytime the photodissociation of  $O_2$  is an important production source of  $O(^1D)$ . The collisional quenching is

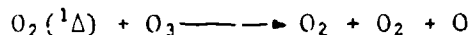


accomplished primarily in the natural atmosphere by  $O_2$ :



$$k = 2.4 \times 10^{-18} \text{ cm}^3 \text{ sec}^{-1}$$

If there is sufficient  $O_3$  present, there is a significant contribution to the decay from the reaction:

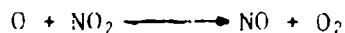


$$k \sim 3 \times 10^{-15} \text{ cm}^3 \text{ sec}^{-1} (300^\circ\text{K})$$

This last reaction is endothermic by about a tenth of an eV, and has an activation energy of about a quarter of an eV.

### Interactions

Although the sets of reactions given as important for each species will usually determine the gross behavior of the species, interactions among the different systems are often important. For instance, if the ambient  $NO_2$  concentration is large compared to the atomic oxygen concentration initially produced by a weak disturbance, the oxygen decay will often be dominated by the reaction



and not by the three-body recombination with  $O_2$  to form  $O_3$ . In addition, the reactions of  $O_2(^1\Delta)$  and  $NO$  with  $O_3$  can affect the ozone concentration significantly.

Figure 5-8 summarizes schematically the neutral species chemistry we have described. A more detailed examination of this subject can be found in Reference 5-11.

#### 5.3.5 ION-ION RECOMBINATION

The mutual neutralization of positive and negative ions does not become important until the negative ion density becomes comparable to the electron density. As a result, ion-ion recombination is characteristic of the latter stages of deionization. At low altitudes, where attachment is large, the negative ion density builds up very rapidly and ion-ion recombination is important very early in the deionization process.

##### Mechanisms and Rate Coefficients

Experimental determinations of ion-ion recombination rate coefficients are quite limited due to the difficulties of preparing specific reactant ion mixtures at the energies of interest. In addition, except for the case of both ions being monatomic, the reaction products are unknown. Nevertheless, experiments have yielded values of the order of  $10^{-7} \text{ cm}^3 \text{ sec}^{-1}$  at thermal energies for positive ions such as  $\text{O}^+$ ,  $\text{O}_2^+$ ,  $\text{N}_2^+$ ,  $\text{NO}^+$  and  $\text{N}^+$  and the negative ions  $\text{O}^-$ ,  $\text{O}_2^-$ ,  $\text{NO}_2^-$  and  $\text{NO}_3^-$ .

There are no experimental data regarding the ion-ion recombination coefficients of hydrated ions. Values have been inferred from atmospheric data that range from  $10^{-8}$  to greater than  $10^{-7} \text{ cm}^3 \text{ sec}^{-1}$ .

In addition to the binary recombination, recombination may be accomplished in a three-body process involving stabilization by a neutral particle. For the reaction

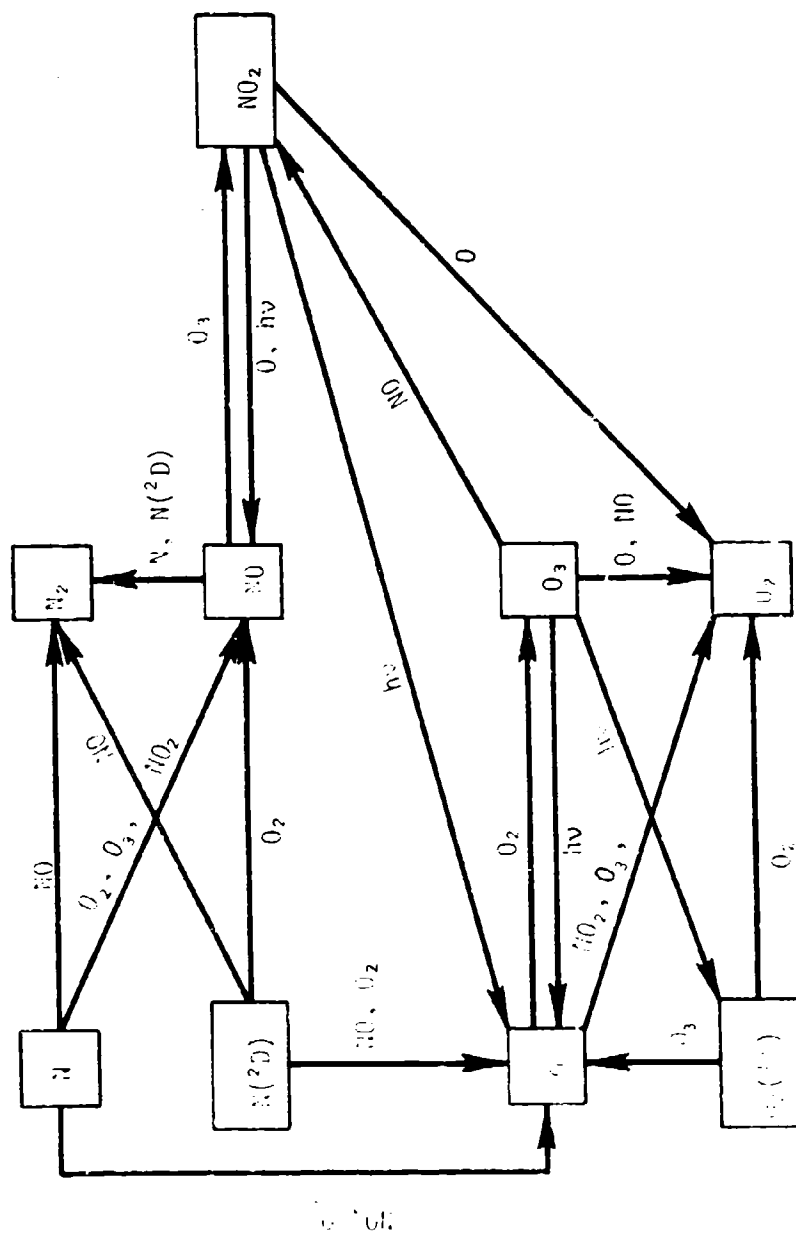
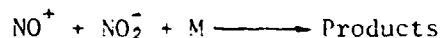


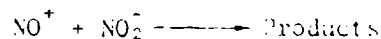
Figure 5-8. Important Neutral Chemistry.



a rate coefficient of  $2 \times 10^{-25} \text{ cm}^3 \text{ sec}^{-1}$  has been measured with  $\text{M} = \text{N}_2$ , and it decreases by an order of magnitude as  $\text{M}$  represents the noble gases in sequence from  $\text{Xe}$  to  $\text{He}$  (Reference 5-9). These results are consistent with theoretical predictions of rate coefficients in the range  $10^{-25}$  to  $10^{-27} \text{ cm}^3 \text{ sec}^{-1}$  for various configurations of the three-body intermediate state. Thus, for three-body recombination to dominate the two-body mechanism, the neutral density must exceed about  $10^{18} \text{ cm}^{-3}$ , corresponding to altitudes below about 25 km. The ions at these altitudes, however, will be strongly hydrated and the rate given above might not apply.

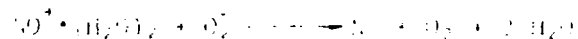
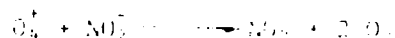
#### Representative Recombination Reactions

For the illustrative reaction



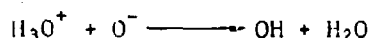
it is not unreasonable to assume the products are  $\text{NO}$  and  $\text{NO}_2$ , particularly when a third body is present to carry away the excess energy. There is enough energy available, however, to produce different products ( $\text{NO} + \text{NO} + \text{O}$ , for instance), and this possibility cannot be discounted.

When small cluster ions are involved, it is reasonable to expect ion-ion recombination to result in the dissociation of the cluster:



Larger clusters, however, demonstrate greater stability in the formation of neutral aerosol particles, as discussed below.

Mutual neutralization reactions involving the hydronium ion or its hydrates can produce free H atoms and hydroxyl and perhydroxyl radicals:



These radicals can play a role in catalyzing the destruction of odd oxygen in the natural atmosphere.

#### Aerosol Formation

There is some evidence to suggest that recombination rate coefficients are a little smaller for the higher hydrates of a given series than for the lower ones. This enhanced stability of larger clusters may be associated with the preliminary stages of aerosol particle formation. At altitudes below about 50 km and in moist air, ions are known to provide effective condensation nuclei for aerosol embryos. The mutual neutralization of such oppositely charged clusters provides a gas to particle conversion mechanism resulting in surfaces for further ion-pair annihilation and continued aerosol growth. The existence of large numbers of small aerosol particles in the lower atmosphere has been repeatedly demonstrated, even if it is not well understood on theoretical grounds. Additionally, minor atmospheric species present at low altitudes ( $\text{NH}_3$ ,  $\text{SO}_2$ ,  $\text{HNO}_3$ ) may prove to be important adjuncts in aerosol formation (Reference 9-10).

#### 5.4 THE COURSE OF ATMOSPHERIC DEIONIZATION

This section identifies the techniques used to obtain detailed, quantitative descriptions of atmospheric deionization, and summarizes the results of their use with emphasis on the main features of the deionization process in the altitude regimes below and above 100 km.

#### 5.4.1 DETAILED DEIONIZATION MODELS

In contrast to the lumped-parameter model described earlier, a detailed model generates the time history of the number density of the individual chemical species at some point in the atmosphere resulting from a given ionizing perturbation. In the general case, as many as sixty significant chemical species are involved, their existence in metastable states may be important, and several hundred different chemical reactions contribute to the overall process, as evidenced by the material of Section 5.3. The problem formulation then consists of a set of coupled, non-linear differential equations, one per chemical species, in which the time derivative of that species density is expressed as the difference between its total rate of formation and its total rate of destruction. These rates, in turn, are expressed as sums of the products of the species densities involved multiplied by the appropriate rate coefficient together with a source term arising directly from the perturbation. For example, if the  $i^{\text{th}}$  species appears as a product in a reaction denoted by  $j$  and as a reactant in the corresponding reverse reaction, the rate equation governing the concentration  $N_i$  is

$$\frac{dN_i}{dt} = q_i + \sum_j n_{ij} \left[ k_{ij} \prod_p N_p^{r_{pj}} - k'_{ij} \prod_p N_p^{r'_{pj}} \right] \quad (5-32)$$

where  $q_i$  is the rate of direct production,  $k_{ij}$  and  $k'_{ij}$  are the rate coefficients for the forward and reverse reactions, respectively, and  $n_{ij}$  is the number of particles of type  $i$  produced in the forward reaction and consumed in the reverse reaction. The  $N_p$  are the densities of the various reacting species, and the product  $\prod$  extends over all reactants. The quantities  $r_{pj}$  and  $r'_{pj}$  denote the number of particles of type  $p$  participating in reaction  $j$  and its inverse, respectively. Clearly we must have  $n_{ij} = r'_{ij} - r_{ij}$ .

The rate coefficients,  $k_{ij}$  and  $k'_{ij}$ , are in general functions of temperature, but the temperature involved may be characteristic of other than the ambient, heavy particle (atom or molecule) translational energy; depending on the reaction, it may be the electron translational temperature or a molecular excitation or vibrational temperature.

Specification of the initial conditions and the environment of the field point under investigation is also necessary; this includes the intensity of the initial ionization, the intensity and time dependence of the continuing source, the effect of any radiative flux present, and the ambient concentrations of major and minor species. In addition to the species rate equations, matter and charge conservation conditions must be satisfied, and if the deionization time scale is long with respect to transport processes or significant changes in the temperatures of interest, these too must be incorporated.

Computer techniques for numerical integration of the multi-species rate equations have been developed to high levels of efficiency in recent years, with the result that detailed solutions to the general problem of deionization are now available. It must be recognized, however, that these are rather large codes requiring considerable running time. It is inappropriate here to discuss the accuracy and adequacy of the numerical methods that underlie these codes; for a review of these matters, the DNA Reaction Rate Handbook (Chapter 22, Reference 5-5) should be consulted.

A second approach to deionization modeling involves the development of analytic expressions for individual species densities as a function of time and the other environmental variables. This work has largely been predicated on the insights gained from the results of the multi-species numerical integration codes. A D-region model developed by Scheibe (Reference 5-11) divided the deionization process into four phases: the initial perturbation; the early recombination, charge exchange,

and atom transfer reactions; the neutral reactions leading to  $O_3$  and  $NO_2$  build-up; and finally the late time deionization by recombination with complex and cluster ions. Although this 39-species analytic solution can hardly be considered simple (the direct evaluation of the equations constituting a moderately complicated computer code), it is much more efficient than a numerical integration solution of the same problem type. Applied to deionization problems in the 40 to 90 km altitude range, it yields good results for high ionization levels and satisfactory results for low ionization cases at the higher altitudes. As might be expected from the number and complexity of the processes involved, low perturbation - low altitude cases produce the greatest discrepancies between the analytic and numerical integration models.

In a somewhat different approach, Knapp has extended the applicability of the lumped-parameter technique by a semi-empirical method based on expressing the parameters as functions of  $q$  as well as altitude, using multi-species code results to provide the data. Two such D-region models have been reported. One is appropriate for the study of mildly disturbed regions ( $N_e(0) \leq 10^8 \text{ cm}^{-3}$ ) in which neutral species are hardly affected and complex and cluster ion formation lead to more rapid decay of the electron density than is predicted by the simple 3-species lumped-parameter model (Reference 5-12). The second model extends the analysis to highly disturbed environments by reducing its dependence on empirical fitting of multi-species code data and analytically incorporating the effect of minor neutral species (Reference 5-13).

Consideration of the factors that have required inclusion in these analytic formulations points up the shortcomings of the simple three-species model described in Section 5.2. The implicit assumptions of that model, even in its mathematically rigorous form, are that the lumped species reaction rate coefficients are truly constant and that deionization is independent of the neutral species. Section 5.3 has shown, however, that the mix of positive and negative ions is not only time-dependent



but that the changing composition and the evolution of neutral species result in significant changes in the overall reaction rates. Consequently, predictions of the three-species model must be looked upon as crude approximations; improved analytic models or multi-species numerical integration codes are resorted to when better results are required.

#### 5.4.2 DEIONIZATION BELOW 100 KM

The purpose of these two final sections is to summarize the main features of atmospheric deionization, emphasizing the factors that determine its course under different environmental conditions. The most important is the altitude of the point in question with its implicit statement of ambient conditions: temperature, density, and composition. The 100 km level is a conventional and useful division, but carries no implication that the deionization process is uniform at all altitudes below or above it.

Below 100 km and increasingly so as the altitude is reduced, the overall process is extremely complicated. In fact, aeronomy today is unable to explain satisfactorily many aspects of the unperturbed, ambient atmosphere. Virtually all the chemical reactions cited in Section 5.3 contribute to the process, and the role of some minor constituents is but poorly understood.

The chief factors contributing to the complexity of atmospheric chemistry below 100 km are the greater density and the presence of the minor species. These factors are crucial to the development of the negative ion sequence initiated by the three-body attachment to  $O_2$ , and to the cluster ion development involving  $H_2O$ . Photodissociation and photoionization by solar radiation act as constant sources of electrons, ions and neutral minor species. Thus, the normal atmosphere is a complex, photochemically driven, quasi steady-state system consisting of free electrons, positive and negative ions, and reactive neutrals.

In its response to a perturbation involving abnormal production levels of ionization, dissociation, and excitation, deionization kinetics following the initial production can be divided into three stages.

The first stage is characterized by electron-ion recombination, charge transfer and neutral and ion reactions leading to the production of NO, O and N. The bulk of the ionization disappears and the remaining positive ions are either  $O_2^+$  or  $NO^+$ . At this point the neutral species chemistry essentially decouples from the charged particle chemistry. The decay of the O, N,  $O_2(^1\Delta)$  and NO and the production of  $O_3$  and  $NO_2$  can be treated separately and this comprises the second stage. The third stage is concurrent with the second and deals with the further electron density decay and the positive and negative ion development.

Primarily because of the production of NO, many of the atmospheric species concentrations will not relax to their previous ambient values after a severe disturbance until transport and long term NO destruction processes can become effective.

#### 5.4.3 DEIONIZATION ABOVE 100 KM

At the higher altitudes, a smaller number of reactions is involved in the deionization process. In particular, the reduced atmospheric density precludes three-body mechanisms with the result that attachment and the subsequent negative ion reactions are insignificant. The absence of water vapor, in addition to the reduced density, prevents cluster ion formation also. Deionization of the normal and mildly disturbed atmosphere is characterized by electron-ion recombination, accompanied by neutral reactions. Low collision frequencies allow metastable species to exist for times comparable with their radiative lifetimes, with the result that radiative processes play a larger role in the overall relaxation.

Between 120 and 250 km, the normal daytime fractional ionization increases from about  $10^{-6}$ , to  $10^{-3}$ , the dominant ionic species being  $O^+$ . Nighttime ionization levels are one or two orders of magnitude lower, primarily in the form of  $NO^+$ . The high  $NO^+$  densities above 100 km are attributed to atom interchange reactions between  $O^+$  and  $N_2$  and between  $N_2^+$  and  $O$ . Although  $O_2^+$  results directly from photoionization of  $O_2$ , the relative abundance of  $O_2^+$  decreases rapidly with altitude in this region. As long as there is sufficient  $N_2$  present, dissociative recombination provides the preferred deionization path.

Because of the low total densities involved, moderate to strong perturbations at high altitudes can result in almost complete ionization or dissociation. Under these conditions, the radiative and radiative-collisional recombination mechanisms afford the main deionization path, but these are relatively slow. Consequently, the free electron density can remain essentially constant for an extended period before electron-atomic ion recombination begins to account significantly for general deionization.

When  $N_2$  is present the reaction with  $O^+$  yielding  $NO^+$  and  $N$  is of considerable importance, and as we mentioned previously this reaction is quite sensitive to the vibrational state of the  $N_2$  molecule. Thus, unlike the D-region and below, one or more energy transfer equations must be added to the chemical rate equations and more than one temperature may be needed to specify the deionization process.

## REFERENCES

- 5-1. Bogusch, R. L., Approximate Series Solutions of the Three-Species Atmospheric Deionization Differential Equations, DASA 1597, Feb., 1965.
- 5-2. Knapp, W. S., and P. G. Fischer, Aids for the Study of Electromagnetic Blackout, DASA 2499, July 1970.
- 5-3. Bortner, M. H., and T. Bauer, eds., DNA Reaction Rate Handbook (2nd edition), DNA 1948H, March 1972.
- 5-4. Ory, H. A., and F. R. Gilmore, The Chemistry of Nitrogen Oxides and Ozone in the Disturbed D-Region, DNA 2835T, September 1971.
- 5-5. Narcisi, R. S., and A. D. Bailey, J. Geophys. Res. **70**, 3687, 1965.
- 5-6. Good, A., D. A. Durdan, and P. Kebarle, J. Chem. Phys. **52**, 222, 1970.
- 5-7. Fehsenfeld, F. C., and E. E. Ferguson, J. Geophys. Res. **74**, 2217, 1969.
- 5-8. E. E. Ferguson, Laboratory Measurements of D-Region Ion-Molecule Reactions in G. Fiocco, ed., "Mesospheric Models and Related Experiments", D. Reidel Publ. Co., Dordrecht, Holland, 1971.
- 5-9. Mahan, B. H., and J. C. Person, J. Chem. Phys. **40**, 3683, 1964.
- 5-10. Mohnen, V. A., Discussion of the Formation of Major Positive and Negative Ions up to the 50 km Level in G. Fiocco, ed., op. cit.
- 5-11. Scheibe, M., An Analytic Model for Nuclear Induced D-Region Chemistry, DNA 2920F, October 1972.
- 5-12. Knapp, W. S., Private communication, April, 1972.
- 5-13. Knapp, W. S., Private communication, March, 1973.

CHAPTER 6

ELECTRON RADIATION

Dale S. Sappenfield

Mission Research Corporation

June 1972

## TABLE OF CONTENTS

	LIST OF FIGURES	294
6.1	INTRODUCTION	295
6.2	QUALITATIVE DESCRIPTION	295
6.2.1	Electron Energy States	295
6.2.2	Free-Free Transitions in the Field of an Ion	296
6.2.3	Free-Free Transitions in the Field of a Neutral Atom	297
6.2.4	Free-Bound Transitions	297
6.2.5	Bound-Bound Transitions	297
6.2.6	Reverse Process	298
6.3	QUANTITATIVE REPRESENTATION	298
6.3.1	General Considerations	298
6.3.2	Free-Free Transitions in the Field of an Ion	301
6.3.3	Free-Free Transitions in the Field of a Neutral Atom	302
6.3.4	Free-Bound Transitions	303
6.3.5	Bound-Bound Transitions	307
6.4	APPLICATIONS IN WEAPON PHENOMENOLOGY	309
	REFERENCES	312

## LIST OF FIGURES

<u>FIGURE</u>		<u>PAGE</u>
6-1.	Schematic representation of electron-photon transitions.	296
6-2.	Schematic representation of free-bound transitions.	304

## CHAPTER 6

### ELECTRON RADIATION

#### 6.1 INTRODUCTION

This chapter describes four processes by which electrons gain or lose energy, with the absorption or emission of a photon. The basic theoretical treatment of each of these processes is given in readily available books and articles, which will be referenced. In this chapter I will describe the processes qualitatively, summarize their quantitative representation, and discuss applications to weapons problems.

#### 6.2 QUALITATIVE DESCRIPTION

##### 6.2.1 ELECTRON ENERGY STATES

Figure 6-1 is an idealized representation of the energy levels available to an electron that is moving in the field of a positive nucleus. The position of the zero on the energy scale is arbitrary; it is usually chosen to be at the ionization threshold. Then negative values of electron energy correspond to bound states, i.e., the electron is associated with a particular nucleus, and does not have enough energy to move to another nucleus. Quantum theory allows only discrete values of energy for bound states. Positive values of electron energy correspond to free states, i.e., the electron is not associated with any particular nucleus, but can move about freely. In contrast with bound states, any and all positive energy values are allowed. In other words, the free electron energy states constitute a continuum.



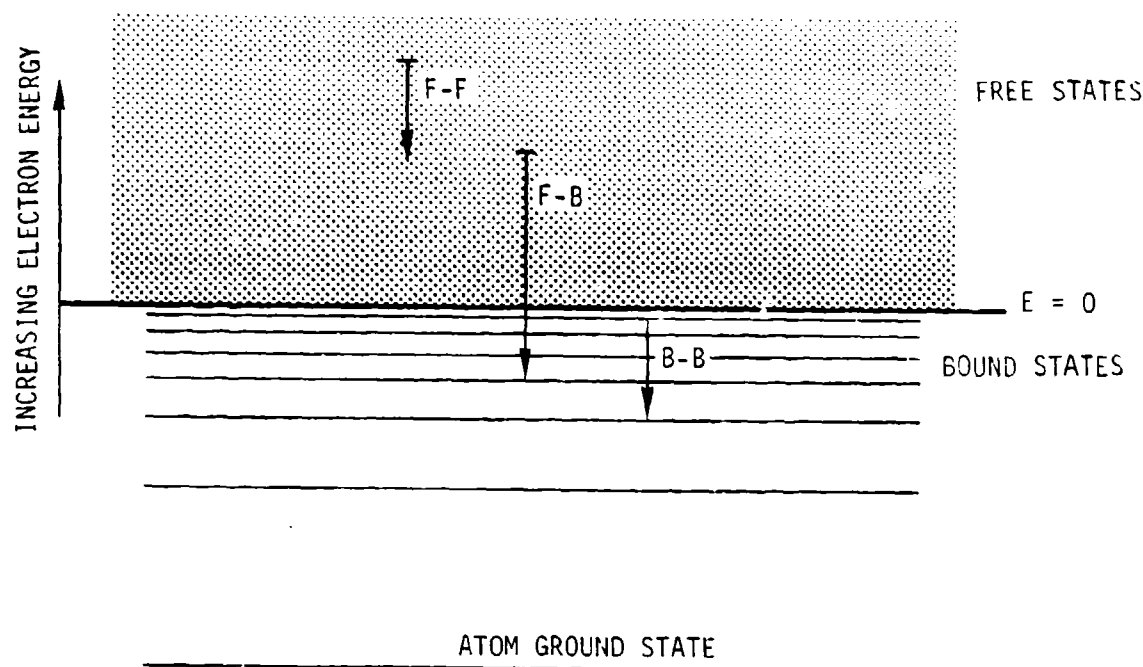


Figure 6-1. Schematic representation of electron-photon transitions.

### 6.2.2 FREE-FREE TRANSITIONS IN THE FIELD OF AN ION

During a collision\* between a free electron and an ion, the electron can lose part of its kinetic energy by radiation. Provided that the final electron energy is still positive, this is called a free-free transition in the field of an ion. Such a transition is labeled "F-F" in Figure 6-1. The participation of the heavy ion is necessary for momentum conservation. The radiation spectrum that results from free-free transitions is a continuum, because any (positive) initial and final values of electron energy are allowed.

\*The word "collision" is not very descriptive. I do not mean to imply something like a head-on traffic accident. In atomic physics, a collision occurs when two or more particles get close enough to affect one another in some well-defined way. To pursue the traffic accident analogy a bit further, an atomic physicist would classify as a collision a "near miss," in which one or more cars had to brake or swerve in order to avoid actual physical contact.

### 6.2.3 FREE-FREE TRANSITIONS IN THE FIELD OF A NEUTRAL ATOM

The same process can occur during a collision between a free electron and a neutral atom. By analogy, this process is called a free-free transition in the field of a neutral atom.

### 6.2.4 FREE-BOUND TRANSITIONS

A free electron may also undergo transitions in which its energy becomes negative. This type of transition is called "free-bound", because the final state of the electron is a bound state. This transition is labeled "F-B" in Fig. 6-1. The term "radiative recombination" is also used to describe this process, inasmuch as a free electron recombines with an ion, accompanied by emission of a photon. Since a continuum of initial, positive electron energy states is available, the photon spectrum is a continuum. However, the continuum has a low energy cutoff at the ionization energy of the final, bound state.

### 6.2.5 BOUND-BOUND TRANSITIONS

A bound electron may spontaneously undergo a transition to a lower energy bound state, with emission of a photon having an energy corresponding to the difference in energy between the initial and final bound states. This type of transition is labeled "B-B" in Fig. 6-1, and is called a bound-bound transition. Because both the initial and final electron states can only have discrete values, bound-bound transitions produce a line spectrum rather than a continuum.

Bound-bound transitions can also be induced by a photon of the same energy as the energy difference between the initial and final electron states. This phenomenon is usually referred to as stimulated emission, because the emission of the photon during the bound-bound transition results from the interaction of the bound electron with another photon

of the same energy. Stimulated emission is the physical process that occurs in lasers, and, as such, could be the subject of several chapters. However, it does not appear to be very important in currently defined weapon problems, and it will be discussed in this chapter only as it causes modifications to mathematical expressions for photon emission or absorption.

### 6.2.6 REVERSE PROCESS

Each of the processes described in Sections 6.2.2 through 6.2.5 is described in terms of a reduction of electron energy and the emission of a photon. For each of these processes, there is a reverse process, in which a photon is absorbed and in which the electron acquires additional energy. Free electrons in the vicinity of an ion or neutral atom can absorb photons of any energy, and acquire more kinetic energy in the process (inverse bremsstrahlung). Bound electrons can absorb any photon having an energy greater than the bound state ionization energy. This process is called "photo-ionization". The final electron state is a free state, and the electron energy is the difference between the photon energy and the ionization energy of the initial, bound state. Photons whose energy corresponds to the energy difference between two bound states may be absorbed by an atom with an electron in the lower state. The electron is excited to the upper, bound state as a result of the photon absorption.

## 6.3 QUANTITATIVE REPRESENTATION

### 6.3.1 GENERAL CONSIDERATIONS

In mathematical models of physical systems, free-free and free-bound transitions are often represented in terms of a spectral emission coefficient,  $\epsilon_v$ , or an absorption coefficient,  $\mu_v$ .

A spectral emission coefficient gives the rate at which radiant energy is created per unit volume, per unit time, and per unit photon frequency

interval. In this chapter, spectral emission coefficients are expressed in the units  $\text{erg cm}^{-3}\text{Hz}^{-1}\text{sec}^{-1}$ . It is sometimes more useful to integrate the spectral emission coefficient over some photon frequency range. For example, visible photon energies range from approximately 1.9 eV (6500 Angstroms) to 3.1 eV (4000 Angstroms). One might integrate the spectral emission coefficient over this interval and express the results as the visible emission coefficient.

The absorption coefficient is proportional to the rate at which radiant energy is converted to other forms of energy as it passes through an absorbing medium. If scattering\* of photons is neglected, the change in intensity† of a light beam per unit length of absorber traversed is proportional to the product of intensity,  $I$ , and the absorption coefficient. In mathematical notation,

$$\frac{\partial I}{\partial x} = -\mu I \quad \text{erg/cm}^3\text{-sec} \quad (6-1)$$

The absorption coefficient has dimensions  $(\text{length})^{-1}$ , and is, in general, a function of photon energy as well as of absorber composition and temperature. The absorption coefficient is defined at a given photon energy, not per unit photon energy.

The effective atomic absorption coefficient must be reduced because of stimulated emission. If a material temperature can be defined, the correction factor is

$$[1 - \exp(-h\nu/ET)]$$

\* Scattering denotes the change of direction of a photon without a change in energy. For example, dust is primarily a light scatterer; smog both scatters and absorbs;  $\text{NO}_2$  absorbs.

† Intensity is defined as the radiant energy that passes per unit time through a unit area in a given direction. If the intensity is also specified per unit photon energy interval, it should be termed "spectral intensity."

in which  $h$  is Planck's constant,  $k$  is Boltzmann's constant,  $\nu$  is the photon frequency, and  $T$  is the material temperature. In this chapter, the correction factor for stimulated emission will be included in expressions for the absorption coefficient. The symbol,  $\mu'$ , will denote an absorption coefficient that contains the correction, i.e.,

$$\mu' = \mu[1 - \exp(-h\nu/kT)] \quad (6-2)$$

The spectral emission coefficient is related to the absorption coefficient by Kirchhoff's law,\*

$$\epsilon_\nu = \frac{8\pi h \nu^3}{c^2} \mu_\nu \exp(-h\nu/kT) \quad (6-3)$$

in which  $c$  is the velocity of light.

Although the concepts of emission coefficient and absorption coefficient are in principle applicable in the quantitative description of bound-bound transitions, they are less commonly used. The spontaneous transition probability for photon emission is generally more useful. This quantity gives the probability that an electron in state  $a$  will spontaneously undergo a transition to a lower energy state  $b$ , with emission of a photon of energy  $E_a - E_b$ . By arguments similar to those used to derive Kirchhoff's law, one can obtain a probability of absorption of a photon of the same energy by an atom with an electron in state  $b$ .

---

\* See Ref. 6-1. pp. 115-120 for derivation and discussion of Kirchhoff's law.

### 6.3.2 FREE-FREE TRANSITIONS IN THE FIELD ON AN ION

Zel'dovich and Raizer (Ref. 6-1) give the spectral emission coefficient for this process as

$$\epsilon_{\nu} = \frac{32\pi}{3} \left( \frac{2\pi}{3mkT} \right)^{1/2} \frac{e^6}{mc^3} N_e \exp(-h\nu/kT) \sum Z_i^2 N_i^+ \quad (\text{erg/cm}^3) \quad (6-4)$$

in which  $m$  is the electron mass,  $e$  is the electron charge,  $N_e$  is the free electron density,  $N_i^+$  is the density of the  $i$ -th ion and  $Z_i$  is its charge. The summation is over all ion species present.

A more exact treatment of the process gives a correction factor for Eq. (6-4), called a Gaunt factor (Ref. 6-2). This factor is very close to unity except when  $h\nu \ll kT$ , a situation not usually of interest in weapons problems. Reference 6-2 gives an expression for the factor.

The absorption coefficient is given by

$$\mu'_{\nu} = \frac{4}{3} \left( \frac{2\pi}{3mkT} \right)^{1/2} \frac{e^6}{hcm\nu^3} N_e \sum (Z_i^2 N_i^+) [1 - \exp(-h\nu/kT)] \quad (\text{cm}^{-1}) \quad (6-5)$$

Three points should be noted about Eqs. (6-4) and (6-5).

1. The emission and absorption coefficients depend on the product of electron and ion density. Therefore the importance of free-free transitions is a strong function of the degree of ionization.
2. The coefficients are inversely proportional to the square root of the temperature.
3. Except where  $h\nu \ll kT$ , the absorption coefficient is inversely proportional to the cube of the photon energy. Therefore, the importance of free-free transitions in absorption is greater at low photon energies.

### 6.3.3 FREE-FREE TRANSITIONS IN THE FIELD OF A NEUTRAL ATOM

The quantitative description of this process is more difficult than the description of free-free transitions in the field of an ion. The dominant interaction between an ion and an electron is via the coulomb field of the ion. Coulomb forces are strong, long range forces, and it is relatively easy to define the strength of an interaction in a coulomb field in terms of the distance between the ion and the electron. This determination is an essential part of the derivation of Eqs. (6-4) and (6-5).

The interaction between an electron and a neutral atom occurs in a much weaker field, and the field itself is a strong function of the distance between the electron and the atom. It is consequently more difficult to define the strength of the interaction, and the resultant expressions for the spectral emission coefficient and the absorption coefficient are less certain. A further consequence of the weaker interaction is that the free-free (neutral) coefficients per atom are smaller than the free-free (ion) coefficients per ion. Therefore, free-free transitions in the field of a neutral atom are important only when the degree of ionization is low.

The treatment of free-free (neutral) transitions by Zel'dovich and Raizer (Ref. 6-1) relates the absorption coefficient to the elastic scattering cross section, and leads to the equation

$$\mu'_v = \{4e^2 \sigma N_a N_e [1 - \exp(-h\nu/kT)] / 2\sqrt{2} h c m^{3/2} v^3\} \int_0^\infty \frac{(E+h\nu)^2}{\sqrt{E}} f(E) dE \quad (6-6)$$

in which  $N_a$  is the atom density,  $\sigma$  is the scattering cross section for the electron-atom collision,  $E$  is the free electron kinetic energy, and  $f(E)$  is the electron kinetic energy distribution function, given by

$$f(E) = 2 \left( \frac{E}{\pi(kT)^3} \right)^{1/2} \exp(-E/kT) \quad (6-7)$$

After integrating, one has

$$\mu'_v = \frac{4e^2\sigma}{3hcv^3} \left( \frac{2}{\pi m^3 kT} \right)^{1/2} [2(kT)^2 + 2hvkT + (hv)^2] [1 - \exp(-hv/kT)] N_a N_e \quad (6-8)$$

The corresponding spectral emission coefficient is

$$\epsilon_v = \frac{32e^2\sigma}{3c^3} \left( \frac{2}{\pi m^3 kT} \right)^{1/2} [2(kT)^2 + 2hvkT + (hv)^2] N_a N_e \exp(-hv/kT) \quad (6-9)$$

Mjolsness and Ruppel (Ref. 6-3) obtain a different temperature and photon energy dependence of the absorption coefficient,

$$\mu'_v \approx v^{-3} (kT)^{-1/2} \left[ (kT)^2 + \frac{1}{2} hvkT \right] [1 - \exp(-hv/kT)] \quad (6-10)$$

based on a different, quantum mechanical representation of the electron-atom collision.

#### 6.3.4 FREE-BOUND TRANSITIONS

The problem of computing the free-bound spectral emission coefficient can be broken down into two parts:

- a) calculation of the spectral emission coefficient for a single free-bound transition,
- b) summing the spectral emission coefficient over all the free-bound transitions that give rise to a photon of the specified energy.

The need for summation is illustrated in Fig. 6-2. Suppose we want the free-bound emission coefficient at a photon energy corresponding to the ionization energy of bound state 1,  $I_1$ . Clearly, if a free



electron with zero kinetic energy recombines to level 1, a photon of energy  $I_1$  will be emitted (transition a). However, a photon of energy  $I_1$  will also be emitted if a free electron with kinetic energy  $I_2 - I_1$  recombines to level 2 (transition b). Similarly, transitions c and d also yield photons of energy  $I_1$ . The general procedure for computing the free-bound spectral emission coefficient is given by Griem (Ref. 6-4).

The photoionization cross section for the  $i$ -th bound state is given by Kramer's formula (Ref. 6-1) as

$$\sigma_i(\nu) = \frac{64\pi^4}{3\sqrt{3}} \frac{e^{10} m Z^4}{h^6 c \nu^3 n_i^5} \quad (\text{cm}^2) \quad (6-11)$$

in which  $n_i$  is the principal quantum number of the  $i$ -th bound state.

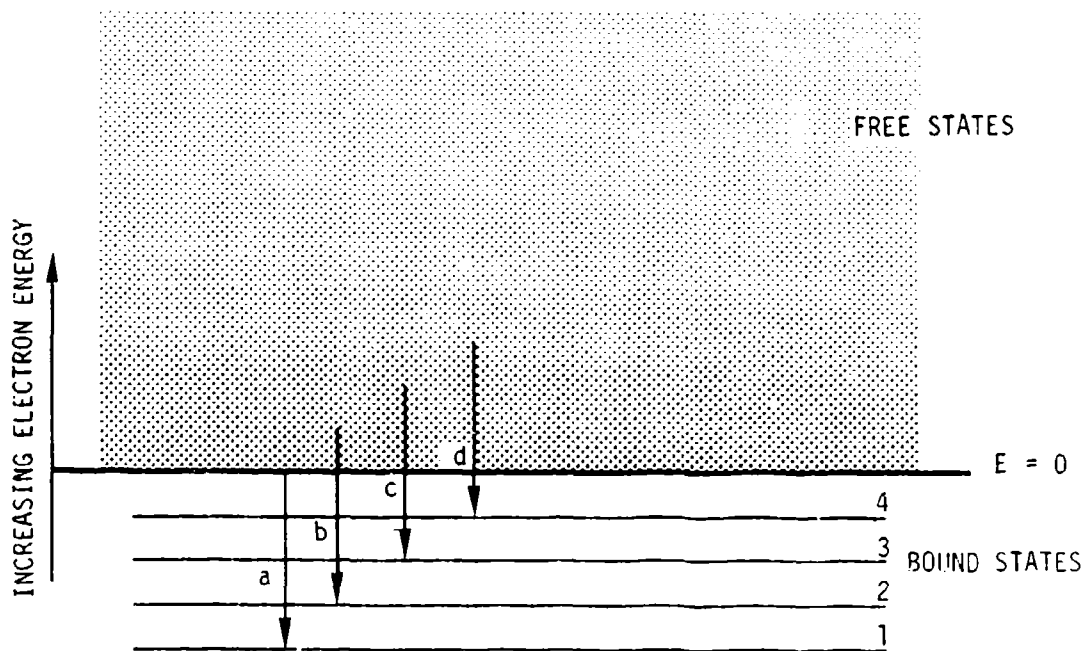


Figure 6-2. Schematic representation of free-bound transitions.

A more rigorous, quantum mechanical derivation leads to a correction factor in Eq. 6-11, which, according to Zel'dovich and Raizer, is very close to unity for most cases of practical interest.

The absorption coefficient is

$$\mu'_v = \sum_i N_i \sigma_i(v) [1 - \exp(-h\nu/kT)] \quad (6-12)$$

in which  $N_i$  is the population of the  $i$ -th state, and the summation is over all bound states with ionization energy less than or equal to  $h\nu$ .

If one assumes that the bound state populations are in equilibrium, and that the population of the ground state is much greater than the sum of the populations of all excited states, then

$$\mu'_v = \frac{64\pi^4}{3\sqrt{3}} \frac{e^{10} m^2 Z^4 N}{h^6 c v^3} [1 - \exp(-h\nu/kT)] \sum_i \frac{\exp(-E_i/kT)}{n_i^3} \quad (6-13)$$

in which  $N$  is the density of absorbers,  $Z$  is the residual charge,\* and  $E_i$  is the excitation energy of the  $i$ -th state.

The spectral emission coefficient is

$$\epsilon_v = \frac{128\pi^{7/2}}{3\sqrt{6m}} \frac{e^{10} N_+ N g_- Z^4}{h^2 c^3 g_+ (kT)^{3/2}} \exp(-h\nu/kT) \sum_i \frac{\exp(I_i/kT)}{n_i^3} \quad (6-14)$$

in which  $I_i$  is the ionization energy of the  $i$ -th bound state, and  $g_-$  and  $g_+$  are the statistical weights of the ground states of the neutral and

---

\* If  $N$  represents density of a neutral species,  $Z = 1$ , and so on.

ionized species, respectively.\* The density,  $N$  is expressed in terms of the product  $N_+ N_e$  by use of the Saha equation,

$$\frac{N_+ N_e}{N} = 2 \left( \frac{2\pi m k T}{h^2} \right)^{3/2} \frac{g_+}{g} \exp(-I_0/kT) \quad (6-15)$$

In which  $I_0$  is the ionization energy of the ground state of species  $N$ . If the neutral species is hydrogen,  $g_+ = 2$ , and Eq. 6-14 is identical to the expression obtained by Holland et al (Ref. 6-5).

For many applications, the sum of the free-free and free-bound spectral emission coefficients (or absorption coefficients) is required. If:

- 1) Only neutral and singly-ionized atoms are present in significant amounts;
- 2) Free-free (neutral) interactions are negligible in comparison with free-free (ion) interactions;
- 3)  $h\nu$  is less than or comparable with  $kT$ ,
- 4) Total excited state populations are small compared with ground state populations;

a simplified expression can be derived.

The procedure, which is outlined by Zel'dovich and Raizer (Ref. 6-1), is to add Eq. (6-4) and (6-13), replacing the summation within Eq. (6-13) with an integral. This is valid if  $h\nu \ll I_0$ , such that the bound states involved are highly excited, closely spaced states that form a near-continuum. The results are

---

\* If  $N$  represents the density of an ion,  $g$  is the statistical weight of that ion ground state, and  $g_+$  is the statistical weight of the ground state of the next, more highly ionized species.

$$\mu_v = \frac{16\pi^2}{3\sqrt{5}} \frac{e^6 kT}{h^4 c v^3} \frac{N}{\exp(-I_2/kT) [\exp(hv/kT) - 1]} \quad (6-16)$$

and

$$n_v = \frac{32\pi^{3/2}}{3\sqrt{6}} \frac{g_-}{g_+} \frac{e^6}{n^{3/2} c^3 v kT} N_A N_e \quad (6-17)$$

### 6.3.5 BOUND-BOUND TRANSITIONS

The spontaneous transition probability for a bound-bound transition, accompanied by the emission of a photon, depends on the wave functions of the initial and final bound states. In particular, the probability depends on the value of the integral

$$\vec{M}_{ij} = \int \psi_i^* \vec{m} \psi_j d\tau \quad (6-18)$$

in which  $\psi_i$  and  $\psi_j$  are the initial and final bound state wave functions, and  $\vec{m}$  is an operator that defines the way in which the photon interacts with the bound electron.

Three interaction mechanisms may be considered in evaluation Eq. (6-18). By far the strongest is the electric dipole interaction, for which the operator is

$$\vec{m} = e \vec{r} \quad (6-19)$$

The spontaneous transition probability is given by

$$A_{ji} = \frac{64\pi^4 v^3}{15hc^3} \frac{1}{g_i} |\vec{M}_{ij}|^2 \text{ sec}^{-1} \quad (6-20)$$

for this interaction. If the value of  $|\vec{M}_{ij}|^2$  is nonzero, with  $\vec{m}$  defined by Eq. (6-19), the transition between bound states  $i$  and  $j$  is "electric

dipole allowed," or more commonly but less correctly, simply "allowed." If, owing to the symmetries of the wave functions, integration of Eq. (6-18) gives identically zero, the transition is said to be "electric dipole forbidden," or, simply, "forbidden."

Electric dipole forbidden transitions may still have nonzero spontaneous transition probabilities due to electric quadrupole or magnetic dipole interactions between the photon and bound electron. Transition probabilities resulting from these interactions are, in general, much lower than nonzero transition probabilities resulting from electric dipole interactions.

The relationship between  $A_{ij}$  and the probabilities for absorption,  $B_{ji}$ , and stimulated emission,  $B_{ij}$ , are given by

$$g_j B_{ji} = g_i B_{ij} = g_i A_{ij} \frac{c^2}{2h\nu^3} \quad (6-21)$$

Tables of  $A_{ij}$ , based on both calculations and experiments, have been published by many authors. Among the most comprehensive are the NBS tables of Wiese, Smith and Glennon (Ref. 6-6), and Corliss and Bozman (Ref. 6-7).

The emission coefficient for a spectral line is given by

$$\epsilon_{ij} = h\nu_{ij} N_i A_{ij} \quad (\text{erg cm}^{-3} \text{sec}^{-1}) \quad (6-22)$$

in which  $N_i$  is the population of the higher energy, bound state. Note that  $\epsilon_{ij}$  is integrated over the emission line shape, and is not a spectral emission coefficient. A discussion of emission line shapes can be found in Ref. 6-4.

#### 6.4 APPLICATIONS IN WEAPON PHENOMENOLOGY

In this section I will mention briefly a few of the areas in weapon phenomenology in which electron-photon interactions are particularly important. Other areas are undoubtedly mentioned in other chapters of the encyclopedia, and still others will occur to each reader.

According to Glasstone (Ref. 6-8), approximately 75 percent of the energy generated in a nuclear explosion leaves the weapon case in the form of photons in the few-keV, or x-ray energy range. Most of the x-ray energy is initially deposited in the surrounding air by photoionization, i.e., bound-free interactions with electrons in nitrogen and oxygen atoms. It is this process, which occurs over dimensions of the order of meters at sea level, and which leads to very high energy density in the air, that produces the initial "fireball" observed in low altitude explosions.

The subsequent growth of fireballs for burst altitudes up to about 100 km occurs by a combination of radiation transport and hydrodynamics. The radiation transport equation contains the absorption coefficient explicitly, and therefore the radiative properties of the fireball depend on the magnitude of the absorption coefficient. At temperatures above 1 eV, at which dissociation of molecules is essentially complete, the absorption coefficient of air is almost entirely due to free-free and bound-free transitions.

For burst altitudes of the order of 100 km and higher, the absorption coefficient, and, by Eq. (6-3), the spectral emission coefficients, are generally very small, due to the low air density. The mean free path ( $1/\mu$ ) for x-ray photons is long,\* a well-defined fireball is not formed, and radiation transport of continuum radiation is not an important process.

\* A typical photon emitted from a 1-keV blackbody source has a 600-km mean-free-path at 100-km altitude.

A significant amount of energy can be transported away from the burst area in line (bound-bound) radiation. Excited bound states are created as a result of collisions between the expanding bomb material and air. The line radiation is emitted as the excited states undergo spontaneous transitions to lower energy states. Since many spontaneous transition probabilities are of the order of  $10^8/\text{sec}$ , the rate of energy loss by this mechanism is generally limited by the rate at which excited states are formed by collision. Such a system has been called "collision-limited." At late times, the radiation from low altitude bursts is primarily due to processes involving molecules, inasmuch as molecules reform rapidly in high density air as soon as fireball temperatures drop to  $1000\text{-}2000^\circ\text{K}$ . This subject is discussed in Chapter 7, and even though some of the radiation emitted involves transitions of bound electrons, this aspect of weapon phenomenology will not be discussed further in this chapter.

At altitudes above 100 km, recombination of ions and electrons can provide a long-lasting source of radiation. The radiation emitted when an ion and an electron undergo radiative recombination is described by Eq. (6-14). In general, the final state in the free-bound transition is an excited state. One or more additional photons may be emitted as the bound electron undergoes transitions to the ground state of the neutral atom. Since the average ionization energy of an air atom is  $\sim 14\text{ eV}$ , there is, in principle, that much energy, plus the energy of the free electron, available to be radiated per recombination event. In practice, some of the transitions may be non-radiative, with the transition energy being converted to free electron kinetic energy.

The general procedure for describing such a system is given by Bates, Kingston, and McWhirter (Ref. 6-9). For each excited state of the neutral atoms, one writes a differential equation describing the rate at which the state is populated and depopulated by all possible mechanisms. The resulting set of equations is solved by assuming that

the excited state populations reach quasi-steady-state values in a time short compared with the time scale of interest. This assumption enables one to reduce the set of differential equations to a set of algebraic equations that can be solved for the quasi-steady-state populations of each excited state. The bound-bound emission can then be computed with Eq. (6-22). Bates and Kingston (Ref. 6-10) have applied this technique to a hydrogen plasma. I have applied the technique to an oxygen plasma (Ref. 6-11).

Estimates of line radiation resulting from transitions between highly excited, bound states during the recombination of electrons and ions can be made simply if the populations of the highly excited states are in equilibrium with the ions and electrons. In this case, the population of an excited state,  $N_j$ , is given by

$$N_j = N_e N_+ (h^2/2\pi m k T)^{3/2} \frac{g_j}{2g_+} \exp(+I_1/kT) \quad (6-23)$$

Determination of the radiation from that state, using Eq. (6-22), is straightforward.

There is no hard-and-fast rule that tells one when  $N_j$  can be determined reliably with Eq. (6-23). The equilibrium population will be approached when the rate of ionization of  $N_1$  is much faster than the rate of any other depopulation mechanism. Since the rate constant for ionization is a function of  $\exp(-I_1/kT)$ , it is clear that the nearer the excited state is to the continuum, the more likely it is to be in equilibrium with the continuum. References 6-5 and 6-10 contain more information on this point.



## REFERENCES

- 6-1. Zel'dovich, Ya. B., and Yu. P. Raizer, Physics of Shock Waves and High Temperature Hydrodynamic Phenomena, English ed., Academic Press, New York 1966.
- 6-2. Spitzer, L., Jr., Physics of Fully Ionized Gases, Interscience Pub., New York, 1962.
- 6-3. Mjolsness, R. C. and H. M. Ruppell, J.Q.S.R.T. 7, 423 (1967).
- 6-4. Griem, H. R., Plasma Spectroscopy, McGraw-Hill Book Co., New York, 1964, p. 113.
- 6-5. Holland, D. H., C. H. Humphrey, G. Gioumoussis, M. Scheibe, D. R. Churchill, and L. M. Tannewald, B2040.
- 6-6. Wiese, W. L., M. W. Smith, and B. M. Glennon, Atomic Transition Probabilities, NSRDS-NBS4, May 1966.
- 6-7. Corliss, C. H. and W. R. Bozman, Experimental Transition Probabilities for Spectral Lines of Seventy Elements, NBS monograph 53, July 1962.
- 6-8. Glasstone, S., The Effects of Nuclear Weapons, USAEC, 1962.
- 6-9. Bates, D. R., A. E. Kingston, and R. W. P. McWhirter, Proc. Roy. Soc. A267, 297 (1962); A270, 155 (1962).
- 6-10. Bates, D. R., and A. E. Kingston, Planet. Space Sci. 11, 1 (1963).
- 6-11. Sappenfield, D. S., B1610, B1955.

CHAPTER 7  
ATOMIC AND MOLECULAR RADIATION IN AIR

Douglas H. Archer

Mission Research Corporation

June 1972

## TABLE OF CONTENTS

	<u>PAGE</u>
LIST OF ILLUSTRATIONS	315
LIST OF TABLES	316
7.1 INTRODUCTION	317
7.2 QUALITATIVE DESCRIPTION OF RADIATION PROCESSES	318
7.2.1 General	318
7.2.2 The Nature of Atomic/Molecular Structure and Radiation	324
7.2.3 Excitation/Deexcitation Mechanisms	328
7.3 ATOMIC/MOLECULAR STRUCTURE AND SPECTRA OF AIR SPECIES	337
7.3.1 Atoms and Atomic Ions	337
7.3.2 Molecules and Molecular Ions	343
7.4 EXCITATION/DEEXCITATION AND EMISSION RATES	365
7.4.1 Atoms and Atomic Ions	365
7.4.2 Molecules and Molecular Ions	368
REFERENCES	383

## LIST OF ILLUSTRATIONS

<u>Figure</u>		<u>Page</u>
7-1	Forbidden transitions among low-lying metastable states of O, O <sup>+</sup> , N, N <sup>+</sup> .	342
7-2	Potential-energy curves for N <sub>2</sub> <sup>-</sup> (unstable), N and N <sub>2</sub> <sup>+</sup> (from Ref. 7-29).	348
7-3	Illustrations of the Franck-Condon principle.	355
7-4	Some prominent electronic band systems of N <sub>2</sub> , N <sub>2</sub> <sup>+</sup> , O <sub>2</sub> , and O <sub>2</sub> <sup>+</sup> .	356
7-5	Pictorial representation of V-R intensity (low resolution).	359
7-6	Structure of some V-R bands of atmospheric interest.	360
7-7	Rate coefficients for electron excitation and deexcitation of metastable states of O, O <sup>+</sup> , and N.	367
7-8	Equivalent temperature of earthshine as a function of wavelength.	373
7-9	Power factor in "collision limited" radiation for the ambient atmosphere.	374
7-10	Lower vibrational level scheme for CO <sub>2</sub> and N <sub>2</sub> molecules.	378

## LIST OF TABLES

<u>Table</u>		<u>Page</u>
7-1	Typical wavelength regions and lifetimes for states involved in molecular band radiation.	328
7-2	Number of collisions required for vibration—translation energy transfer (from Ref. 7-5).	331
7-3	Initial energy partition in air by 1-keV electrons (Ref. 7-8).	332
7-4	Electron configurations and term types for some neutral atoms and ions.	340
7-5	Some allowed transitions for NI, NII, )I, and OII in the visible.	344
7-6	Molecular constants for some diatomic species.	352
7-7	Molecular parameters for some atmospheric triatomic species.	353
7-8	Wavelengths for (0, 0) bands of systems shown in Fig. 7-4.	357
7-9	V-R band wavelengths (fundamentals) and absorption strengths for selected molecules.	365
7-10	Some chemiluminescent reactions of atmospheric interest.	377
7-11	Transition probabilities between some vibrational states of CO <sub>2</sub> .	379
7-12	Photon (IR) emission rate per molecule from solar UV fluorescence.	382

## CHAPTER 7

### ATOMIC AND MOLECULAR RADIATION IN AIR

#### 7.1 INTRODUCTION

The detonation of a nuclear device in the atmosphere results in the emission of radiation that covers the entire electromagnetic spectrum from high-energy gamma rays to low-energy radio waves. This chapter deals only with that spectral portion, emitted by atoms, molecules, and their ions, that extends through the visible and infrared. Indeed, in the following pages considerable emphasis is placed on the infrared vibration-rotation bands of molecular species.

The literature dealing with atomic and molecular radiation is very extensive and no attempt is made here to cover all aspects of it. Rather, it is the purpose of this chapter to outline the basic concepts involved and to present results that are useful for the determination and understanding of optical\* and infrared emissions produced by atmospheric nuclear explosions. References are provided that will enable the reader to pursue the various topics in greater depth or to extend his knowledge into areas not specifically covered here.

Section 7.2 is devoted to a rather qualitative survey of radiation processes. It starts with a brief description of classical concepts, is followed by the modern (quantum mechanical) picture of atomic and molecular structure and radiation, and concludes with a discussion of excitation and deexcitation mechanisms. The remaining sections of the chapter are concerned with more quantitative aspects of the subject and give results, formulas, and tables

---

\* Optical emission refers to radiation in the visible spectral region.

necessary for the actual calculation of radiation rates. Section 7.3 deals with atomic and molecular structure and the spectra of air species. Section 7.4 presents details on excitation/deexcitation and atomic/molecular emission rates, with emphasis on infrared vibration-rotation bands.

## 7.2 QUALITATIVE DESCRIPTION OF RADIATION PROCESSES

### 7.2.1 GENERAL

The simplest classical model capable of radiation is a linear oscillating electric dipole. The electromagnetic waves are radiated at a frequency equal to that at which the electric charge moves back and forth. The intensity of the radiation depends upon the magnitude of the alteration of the dipole moment. In particular, it can easily be shown (Reference 7-1, 7-2) that the energy radiated per second by a point charge  $e$  at the instant when its acceleration is  $a$  is

$$\begin{aligned}\dot{\mathcal{E}} &= \frac{2}{3} \frac{e^2 a^2}{c^3} \\ &= \frac{2}{3} \frac{(\ddot{p})^2}{c^3}\end{aligned}\tag{7-1}$$

where  $c$  is the speed of light and  $p$  is the electric dipole moment. If the oscillator frequency is  $\omega$  and the amplitude of the dipole moment is  $p_0$ , then

$$p = p_0 \sin(2\pi \nu t)\tag{7-2}$$

Equations 7-1 and 7-2 lead to the following simple relation for the time average rate of energy emission:

$$\begin{aligned}\bar{\mathcal{E}} &= \frac{32\pi^4 \nu^4 p_0^2}{3c^3} \\ &= \frac{16\pi^4 \nu^4 p_0^2}{3c^3}\end{aligned}\tag{7-3}$$

where the bars denote time averages. According to classical concepts, the oscillator and its emitted waves can have any frequency  $\nu$ .

The quantum mechanical description of radiation from actual atomic and molecular systems provides a formula for the emission rate that is analogous to Equation 7-3. However, the underlying principles are entirely different and they require that only selected frequencies for the emitted radiation are permitted. Detailed studies of atomic and molecular spectra show, in fact, that only certain energy states  $E_i$  are possible for an atom or molecule. While the system is in one of these discrete (stationary) states no radiation occurs. It is only in a jump from one discrete state of energy  $E_n$  to another one of lower energy  $E_m$  that a photon of frequency  $\nu_{nm} = (E_n - E_m)/h$  can be emitted.\* Similarly, a system in the lower state with energy  $E_m$  can absorb a photon of frequency  $\nu_{nm}$  and be left in the higher state with energy  $E_n$ . Not all transitions among the discrete states, however, are possible. Certain rules, called "selection rules", determine which transitions are allowed. Those that are allowed give rise to the observed spectral lines and bands that appear in emission and absorption spectra.

According to the ideas developed earlier in this century by DeBroglie, Heisenberg, Schroedinger, Dirac and others, an atomic particle (electron, proton, neutron, etc.) has both a corpuscular and a wave nature. Its position in space can be determined with a precision that varies inversely as the precision with which its momentum is known (Heisenberg's uncertainty principle). The positions  $\vec{r}_i$  ( $i = 1, 2, 3, \dots$ ) of particles within an atom can be found only on a probabilistic basis in terms of a complex wave function  $\psi(\vec{r}_1, \vec{r}_2, \dots)$ , the absolute square of which gives the probability of finding the particles at positions  $\vec{r}_1, \vec{r}_2, \dots$ . According to

---

\*  $h$  is a universal constant, called Planck's constant. It has the value  $6.6 \times 10^{-27}$  erg sec.



Schroedinger (Reference 7-3), if  $E$  is the total energy of the system and  $V$  is the potential energy, then  $\psi$  must satisfy the equation

$$\sum_i \frac{1}{m_i} \left( \frac{\partial^2 \psi}{\partial x_i^2} + \frac{\partial^2 \psi}{\partial y_i^2} + \frac{\partial^2 \psi}{\partial z_i^2} \right) + \frac{8\pi^2}{h^2} (E - V)\psi = 0 \quad (7-4)$$

where  $m_i$  is the mass of the  $i^{\text{th}}$  particle whose coordinates are  $x_i, y_i, z_i$ . Equation 7-4, known as the time-independent Schroedinger wave equation, is fundamental to the calculation of atomic and molecular properties including the emission and absorption of radiation.

When it is assumed that  $\psi$  is everywhere single valued, finite, continuous, and vanishes at infinity, then Equation 7-4 is soluble, not for unrestricted values of  $E$ , but only for certain values  $E_n$ , called eigenvalues. The corresponding wave functions  $\psi_n$  are called eigenfunctions. The eigenvalues,  $E_n$ , correspond to the discrete energy values of an atom or molecule observed experimentally in spectral analyses. To each eigenvalue of the Schroedinger equation there belongs, in general, more than one eigenfunction. Each eigenfunction corresponds to a different angular momentum which, like the energy is quantized. The number of such eigenfunctions, for a given energy eigenvalue, is called the "degree of degeneracy" of the state, or its "statistical weight".

As in classical physics, the rate of emission of radiation is related to a change in the dipole moment of the system. In particular, it is found (correspondence principle) that the emission rate due to transitions from an upper state  $n$  to a lower state  $m$  is described by the classical formula (Equation 7-3) provided the following replacement is made:

$$p^2 \rightarrow 2|\vec{p}_{nm}|^2 + \text{magnetic dipole} + \text{electric quadrupole terms} \quad (7-5)$$

Here,  $\vec{p}_{nm}$  is the matrix element of the electric dipole moment between states  $n$  and  $m$ , and is defined as

$$\vec{p}_{nm} = \int \psi_n^* \left( \sum_i e_i \vec{r}_i \right) \psi_m dV \quad (7-6)$$

where the  $e_i$  are the charges on the  $N$  particles with position vectors  $\vec{r}_i$ , and the integral is taken over all space.  $\psi^*$  denotes the complex conjugate of  $\psi$ . When  $\vec{p}_{nm} \neq 0$ , the magnetic dipole and electric quadrupole terms in Equation 7-5 are smaller than the electric dipole term by factors of about  $10^5$  and  $10^8$ , respectively.

The radiative transition probability per second from state  $n$  to state  $m$ , usually referred to as the Einstein A coefficient for spontaneous emission, is determined by making the replacement (7-5) in Equation 7-3 and dividing by the photon energy  $h\nu_{nm}$ . For electric dipole radiation then

$$A_{nm} = \frac{64\pi^3 \nu_{nm}^3}{3hc^3} |\vec{p}_{nm}|^2 \quad (7-7)$$

If  $N_n$  is the concentration of atoms or molecules in state  $n$ , the spontaneous energy emission rate per  $\text{cm}^3$  is given by

$$J_{\text{spont}}^{nm} = h\nu_{nm} N_n A_{nm} \quad (7-8)$$

For spontaneous transitions downward to states  $m$ , the time rate of depletion of the state  $n$  is

$$\dot{N}_n = -\sum_m A_{nm} N_n$$

and so

$$N_n = N_n^0 e^{-\sum_m A_{nm} t} \quad (7-9)$$

After a time  $t = 1/\sum_m A_{nm}$ , the number of atoms in the state  $n$  is  $1/e$  of the initial number. This time is called the mean life, or lifetime, of

state  $n$ . For atomic transitions and those molecular transitions for which a change in the electron configuration occurs (electronic transitions),  $\tau \approx 10^{-8}$  sec provided  $\vec{p}_{nm} \neq 0$ . If  $\vec{p}_{nm} = 0$ , electric dipole radiation does not occur. However, if the matrix elements of the magnetic dipole or the electric quadrupole terms in Equation 7-5 are non zero, radiation can still occur but the mean lifetime of state  $n$  is then much longer. For magnetic dipole transitions it is of the order of  $10^{-3}$  sec; for electric quadrupole transitions, about 1 sec. Such states are called metastable.

In addition to spontaneous transitions downward from state  $n$  to state  $m$ , the presence of a radiation field with frequency components  $\nu_{nm}$  can induce transitions downward ( $n \rightarrow m$ ; induced emission) and upward ( $m \rightarrow n$ ; absorption). Specifically, if  $\rho_{nm}$  is the energy density (per unit frequency interval) of radiation of frequency  $\nu_{nm}$ , then the induced emission rate per  $\text{cm}^3$  is

$$J_{\text{ind.}}^{nm} = \frac{h\nu_{nm} N_n \rho_{nm} B_{nm}}{4\pi} \quad (7-10)$$

where  $B_{nm}$ , the Einstein B coefficient for induced emission, is given in terms of  $A_{nm}$  by the relation

$$B_{nm} = \frac{c^2}{2\pi h \nu_{nm}^3} A_{nm} \quad (7-11)$$

Correspondingly, the absorption of energy of frequency  $\nu_{nm}$  is proportional to  $\rho_{nm} B_{mn}$  where  $B_{mn}$  (equal to  $B_{nm}$  when the states are non-degenerate\*) is the Einstein B coefficient for absorption. In particular, the decrease in the intensity of radiation traversing a thickness  $dx$  is

$$dI_\nu = -k_\nu I_\nu dx \quad (7-12)$$

\* See Section 7.5.1 for the case where degeneracies occur.

where  $k_{\nu nm}$ , the linear absorption coefficient ( $\text{cm}^{-1}$ ), is related to  $B_{mn}$  by\*

$$\int_{\Delta\nu} k_{\nu nm} d\nu = \frac{h\nu_{nm} B_{mn} N_m}{4\pi} \quad (7-13)$$

The integral in Equation 7-13 is taken over the width,  $\Delta\nu$ , of the absorption line.

A useful relationship exists between absorption and emission for systems in thermodynamic equilibrium (for which  $N_n/N_m \propto e^{-h\nu_{nm}/kT}$ ). If  $j_\nu$  is the total emission rate (spontaneous + induced) per unit volume, then for an ensemble of atoms or molecules in thermodynamic equilibrium, the sum of Equations 7-8 and 7-10, together with Equations 7-11 and 7-13, leads to Kirchhoff's law in the form

$$j_\nu = k_\nu B'_\nu \quad (7-14)$$

where  $B'_\nu$ , the blackbody brightness ( $\text{ergs sec}^{-1} \text{cm}^{-2} \text{ster}^{-1} (\Delta\nu)^{-1}$ ), is

$$B'_\nu = \frac{c^0 \nu}{4\pi} = \frac{2h\nu^3}{c^2} \frac{1}{e^{h\nu/kT} - 1} \quad (7-15)$$

Equation 7-14 describes the emission rate from a unit volume. A further useful extension is the determination of the brightness,  $b_\nu$ , of an emitting volume of air as seen along a line of sight, say in the  $x$  direction. By definition,

$$b_\nu = \int_0^x j_\nu(x') e^{-\int_0^x k_\nu(x'') dx''} dx' \quad (7-16)$$

\* When allowance is made for stimulated emission, the right-hand side of Equation 7-13 should be multiplied by  $(1 - e^{-h\nu/kT})$ .

If the temperature is constant along the line of sight so that  $B'_V$  is independent of  $x$ , Equations 7-14 and 7-16 then lead to the result

$$b_V = \epsilon_V B'_V \quad (7-17)$$

where  $\epsilon_V$ , the effective emissivity along the sight path, is

$$\epsilon_V = 1 - e^{-\int_0^x k_V(x) dx} \quad (7-18)$$

The foregoing descriptions and equations are applicable to emission and absorption processes involving both atoms and molecules. However, because molecules, unlike atoms, may undergo internal vibrational and rotational motion, profound differences in the spectra of atoms and molecules can result. The next subsection gives a qualitative description of atomic and molecular structure, particularly as it relates to the origin of these differences.

### 7.2.2 THE NATURE OF ATOMIC/MOLECULAR STRUCTURE AND RADIATION

As described above, quantum mechanics, in conformity with observations, requires that the energy and angular momentum of an atom or molecule be quantized with only certain discrete values possible. The eigenfunctions, as well as the energy and angular momentum eigenvalues, depend on certain integers or half integers called "quantum numbers". For every electron in an atom there are four quantum numbers, designated as  $n, l, m_l, m_s$ . Detailed studies have shown that they can be interpreted approximately as follows. Each electron can be viewed as revolving about the positively charged nucleus in a "cloud-like" orbit at a mean distance from the nucleus determined by  $n$ , an integer (1, 2, 3, ---) called the principal quantum number. The larger the value of  $n$ , the larger the mean radius of the electron orbit. The integer  $l$  is a measure of the angular momentum of the electron due to its orbital motion about the nucleus, while  $m_l$  relates

to its component in a given direction. The quantum number  $m_s$ , which describes the component of the spin angular momentum of the electron in a given direction, can assume the values  $\pm 1/2$ .

In any one atom, no two electrons can have the same set of values for  $n$ ,  $\ell$ ,  $m_\ell$ ,  $m_s$ . This assumption, called the Pauli exclusion principle, is an addition to quantum mechanics that is required for a proper representation of observed spectra. It leads to the concept of electron shells and to the fact that no more than  $2n^2$  electrons can have the same principal quantum number,  $n$ , in a given shell. Electrons having values for  $n$  of 1, 2, 3, ---, are said to be in the  $k$ ,  $l$ ,  $m$ , --- shells, respectively.

The outermost electrons in an atom (those with the largest  $n$  values) are called valence electrons and they determine an atom's chemical properties. They are partially screened from the nucleus by the other electrons and so are more loosely bound by the Coulomb field of the nucleus than are the inner electrons. In fact, for heavy atoms with a large nuclear charge, electrons in the inner shells ( $k$ ,  $l$ , ---) are bound with energies of several keV. Radiative transitions involving these inner-shell electrons then produce photons with energies in the keV range (x rays). Transitions involving the more loosely bound valence electrons, however, correspond to energy differences of several eV and result in the emission of optical and ultraviolet radiation. The radiation that is emitted by an atom appears at discrete frequencies determined by the application of certain selection rules and by Bohr's frequency condition  $\nu_{nm} = (E_n - E_m)/h$ . When observed on a spectrographic plate, the radiation shows up as a series of sharp spectral lines.

If one or more electrons are removed from an atom, the system is left with a net positive charge and is called a positive atomic ion. Like neutral atoms, ions are characterized by discrete energy levels, angular momenta, etc., and the concepts of atomic structure and radiation described above apply equally well to them.

As is the case for atoms, so it is for molecules that the total energy and angular momentum are quantized. However, the energy level structure of molecules is more complicated than that for atoms because, in addition to the energy associated with the electrons, there is also the energy associated with vibrational motion of the nuclei about equilibrium positions and with rotation of the molecule as a whole.

The solution of the Schroedinger wave equation for any but the simplest molecules is a very difficult problem. It turns out, however, that the frequencies of vibration and of rotation are substantially different from one another and also from the (classical) frequency of electron orbital motion. In consequence of this, the wave function for a molecular state is, to a satisfactory approximation, separable into product wave functions

$$\psi = \psi_e(\text{electronic}) \psi_v(\text{vibrational}) \psi_r(\text{rotational}) \quad (7.19)$$

each product function satisfying its own Schroedinger wave equation with its corresponding energy eigenvalues. The total energy,  $E$ , is then expressible as the sum

$$E = E_e + E_v + E_r \quad (7.20)$$

where  $E_e$ ,  $E_v$ , and  $E_r$  are eigenvalues associated with the electronic, vibrational, and rotational motion, respectively.

The picture that then emerges is approximately as follows. For each electronic state of the molecule, corresponding to a given energy  $E_e$  and characterized by a set of electronic angular momentum quantum numbers, there is superimposed a series of vibrational states (quantum numbers  $v = 0, 1, 2, \dots$ ), each representing a different state of vibrational motion with a prescribed energy  $E_v$ . For each of these vibrational states there

is superimposed a series of rotational states (quantum numbers  $J = 0, 1, 2, \dots$ ) with corresponding energy  $E_J$ . The energy separation between adjacent rotational levels is not fixed, but is of the order of  $10^{-2}$  to  $10^{-3}$  eV. The separation between adjacent vibrational levels is typically about 0.1 eV; that between electronic states, as in the case of atoms, is about 1 to 10 eV.

The spectrum that results from transitions between the states of molecules is determined by a set of selection rules derived, as indicated in Section 7.2.1, from consideration of the electric dipole moment matrix elements. In general, the spectrum is much more complicated than that from atoms because of the multitude of vibrational and rotational levels associated with each electronic state. In transitions characterized by a given pair of electronic states and by given values  $v'$  and  $v''$  of the vibrational quantum number, various changes in  $J$ , the rotational quantum number, may occur. The resulting spectral lines form a single band. All of the bands due to transitions between a given pair of electronic states, for all possible values of  $v'$  and  $v''$ , are said to form a band system. Because various electronic jumps are possible, the electronic band spectrum of any molecule consists of many band systems.

Vibrational-rotational (V-R) bands consist of radiative transitions in which the vibrational and rotational (but not the electronic) quantum numbers change. The term "band" is again used to describe the collection of lines arising from a given pair of vibrational states. Radiative transitions are allowed only if they are associated with a changing electric dipole moment. By symmetry, states of molecules with two identical nuclei ( $\text{O}_2$ ,  $\text{N}_2$ ,  $\text{O}_2^+$ ,  $\text{N}_2^+$ ) have no permanent dipole moments and V-R bands for them do not occur.

Pure rotational bands consist of radiative transitions in which only the rotational quantum number changes. Such transitions are allowed only if



the electronic state possesses a permanent electric dipole moment so that, upon rotation, a changing dipole moment results.

The wavelength region into which a band type falls is determined by the energy level spacing involved in production of the band. The intensity of any line is inversely proportional to the mean lifetime of the upper state (see Equation 7-18). Table 7-1 shows the wavelength regions into which the three band types usually fall, together with typical values for the lifetimes of excited electronic, vibrational, and rotational states. The lifetime shown for electronic states assumes that transitions to lower states by electric dipole radiation are allowed. Otherwise, as mentioned earlier in connection with atomic transitions, the states may be metastable and have much longer lifetimes.

Table 7-1. Typical wavelength regions and lifetimes for states involved in molecular band radiation.

TYPE OF TRANSITION/BAND	TYPICAL ENERGY LEVEL SPACING (ev)	SPECTRAL REGION	TYPICAL UPPER STATE LIFETIME (sec)
electronic	1-10	visible/UV	$10^{-8}$
vibration-rotation	0.1	infrared	$10^{-1}$
pure rotation	$10^{-2}$ - $10^{-3}$	far infrared	1

### 7.2.3 EXCITATION/DEEXCITATION MECHANISMS

In order to radiate, an atom or molecule must first be raised to an excited state. It must then remain in the excited state for a time,  $\tau$ , of the order of the natural lifetime of the state, without being deexcited by some other means. As indicated earlier (see Equations 7-8 and 7-10), the emission rate is proportional to the concentration of atoms/molecules in the

upper state involved in the radiative transition. Similar remarks apply to the absorption of radiation where the lower state is involved. The processes of excitation and deexcitation together determine the concentration of species in these states. This subsection gives a qualitative description of the various ways for excitation and deexcitation with special emphasis on vibrational states of molecules.

Excitation and deexcitation may occur by (1) collisions with heavy particles including atoms, molecules, and ions, (2) collisions with electrons, (3) electronic and vibrational energy transfer, (4) chemical reactions, and, (5) interaction with radiation.

In general, all of the above processes go on simultaneously in an assemblage of atoms, molecules and ions. A special case, one that is simplest to treat, is where the gas is in a state of local thermodynamic equilibrium. In this case, the various excitation and deexcitation mechanisms interact to distribute the species among the translational, rotational, vibrational, electronic, and chemical degrees of freedom according to the laws of equilibrium statistical mechanics. A detailed consideration of each excitation process is then not necessary for a complete description of the radiating properties of the gas. In the study of weapon effects in the atmosphere, the assumption of local thermodynamic equilibrium is sometimes a good one, particularly at altitudes below about 20 km. At somewhat higher altitudes (lower densities), all degrees of freedom except the chemical may be in equilibrium. A consideration of chemical reactions and their rates is then necessary to determine the species concentrations. At still higher altitudes the vibrational and electronic degrees of freedom are also out of equilibrium, and a detailed consideration of the rates of production and destruction of specific vibrational and electronic states is further necessary for a description of the radiation. At sufficiently high altitudes (2400 km) the translational and rotational degrees of freedom may also be out of equilibrium. However, since

only a few gas-kinetic collisions are required to establish translational or rotational equilibrium, non-Maxwellian distributions will tend to occur only when the density is so low that radiation processes are not significant.

A brief description of each of the five excitation/deexcitation mechanisms now follows.

### Collisions With Heavy Particles

If the translational energy of relative motion between colliding atoms and molecules is sufficiently large, part of it may be converted to energy of vibrational or electronic excitation. In a gas in translational equilibrium the mean energy of relative motion is about  $kT$ , or  $10^{-4}T(\text{eV})$ , where  $k$  is Boltzmann's constant. Thus, temperatures of the order of  $1000^\circ\text{K}$  are required to produce mean energies comparable with the lowest vibrational states of molecules. Considerably higher temperatures are needed to produce appreciable electronic excitation. In a nuclear environment, however, high speed debris ions are available with ample energy to excite any state and, indeed, to dissociate and ionize the species.

Deexcitation by the transfer of vibrational energy on collision to translational energy has been extensively studied in the laboratory (References 7-4 to 7-6). Theories have also been devised (Reference 7-6) that describe the laboratory results fairly well. Vibrational excitation cross sections, or rates, can often be obtained from these results by applying the principle of detailed balancing (see Ref. 7-50). The results are sometimes expressed in terms of the number of gas-kinetic collisions required to deexcite the first vibrational state of a molecule. Examples for  $\text{N}_2$ ,  $\text{O}_2$ , and  $\text{Cl}_2$  are shown in Table 7-2. It is clear from Table 7-2 that the process of vibration-translation energy transfer is rather inefficient, although the efficiency increases rapidly with a decrease in the vibrational energy to be transferred (i. e., the vibrational energy level spacing) or with an increase in the temperature.

Table 7-2. Number of collisions required for vibration—translation energy transfer (from Reference 7-5).

MOLECULE	VIBRATIONAL ENERGY (ev)	NUMBER OF COLLISIONS	
		(300°K)	(1000°K)
N <sub>2</sub>	0.29	$\sim 10^{10}$	$4 \times 10^6$
O <sub>2</sub>	0.19	$2 \times 10^7$	$5 \times 10^5$
Cl <sub>2</sub>	0.08	$4 \times 10^4$	400

Less information is available on the conversion of translational to electronic energy and vice versa. A few experiments involving shock tubes have given rates for the translation-electronic conversion and some data on the reverse process are available from radiation quenching studies. By and large, however, the available data are inadequate for studies involving electronic states of interest in weapon effects. Theoretical estimates, based on "potential-curve crossing" (Reference 7-7) are usually inadequate also due to uncertainties in the potential-energy curves.

#### Collisions With Electrons

Absorption by the atmosphere of bomb-produced x rays results in the production of fast primary photo and Auger electrons and of slower secondary electrons. In collisions with air species, many of these electrons are effective in producing vibrational and electronic excitation, as well as dissociation and ionization. For example, an estimate of the initial partition of energy resulting from the slowing down of a 1-keV electron in air is shown in Table 7-3.

Table 7-3. Initial energy partition in air by 1-keV electrons  
(Reference 7-8).

MODE OF EXCITATION	ENERGY IN MODE (%)
Prompt ionization and dissociation	51
Allowed electronic states*	26
Metastable states	16
N <sub>2</sub> vibration	7

\* By allowed states is meant states that are not metastable.

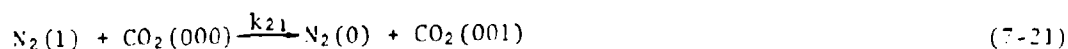
Cross sections for the excitation of vibrational motion by electron impact on molecules of interest such as N<sub>2</sub>, O<sub>2</sub>, CO, CO<sub>2</sub>, have been measured in the laboratory (References 7-9 to 7-11), and theories that account for these measurements are now fairly well established (Reference 7-12). For some molecules, such as H<sub>2</sub>, N<sub>2</sub>, and CO, the cross section for vibrational excitation is very large (due to negative ion resonances) for electron energies near 2 eV (Reference 7-10). As a result, as much as 7 percent of the energy deposited in the atmosphere by bomb x rays is estimated to go directly into vibrational excitation of N<sub>2</sub> (see Table 7-3).

Cross sections for electron excitation of a number of electronic states of air atoms, molecules, and ions have been obtained in laboratory studies (References 7-13, 7-14). Although this work is actively continuing, large gaps still exist, especially with respect to cross sections for excitation of the many allowed states involved in emission processes in a nuclear environment. Quantum mechanical calculations have been carried out for a number of electron-excitation cross sections, especially those involving light atoms (Reference 7-15). Their agreement with experiment ranges from fair to excellent, depending upon the complexity of the atom and the validity of the approximations made.

Electronic excitation, particularly of atoms, may also occur when molecules are dissociated by electron impact. Cross sections for excitation of certain states of N and O atoms by this process have recently been obtained in the laboratory (References 7-16, 7-17).

### Electronic and Vibrational Energy Transfer

An atom or molecule in an excited state may transfer on collision all or part of the energy of excitation and leave the colliding partner in an excited state. This process is particularly significant for the transfer of vibrational energy from a homonuclear molecule ( $N_2$ ,  $O_2$ ,  $N_2^+$ ,  $O_2^+$ , etc.) that cannot radiate this energy, to other molecules, such as  $CO_2$ , that can. The theory of vibrational exchange in molecular collisions (Reference 7-18) usually gives results that agree with experimental data to within a factor of 5 (Reference 7-19). The cross section, or rate for energy transfer depends sensitively on the energy defect,  $E_d$ , (amount by which the energy exchanged is out of resonance), decreasing approximately exponentially as  $E_d^{2/3}$  (Reference 7-20). Except for cases involving large energy defects, deexcitation of vibrational motion by exchange collisions is usually more efficient than the vibration-translation process described above. Deexcitation of  $N_2$  vibrational motion, for example, is particularly effective in the atmosphere through the process



because of the close energy resonance (small energy defect) between the first vibrational state of  $N_2$  and the (001) vibrational state of  $CO_2$ .<sup>\*</sup> The vibrationally excited  $CO_2$  can then proceed to radiate bands at 4.3 $\mu$  and at longer wavelengths as well. Reaction 7-21, in fact, is a good example

---

\* A triatomic molecule has three fundamental modes of vibration. An arbitrary vibrational state is denoted by  $(v_1 v_2 v_3)$ .

of excitation that results in radiation known as vibrational luminescence. It is important in a description of weapon effects because it may produce a long-lasting afterglow in the infrared region. More details are given in Section 7.4.2.

Information on electronic-energy exchange and of vibrational-electronic energy conversion for states of atmospheric interest is largely lacking. Atmospheric and laboratory measurements (References 7-21, 7-22) have led to a considerable amount of data regarding the collisional quenching of electronic states. However, the product states after collision are usually not measured and so the disposition of the electronic energy into electronic, vibrational, and translational motion of the quenching molecule is generally unknown.

### Chemical Reactions

Chemical reactions are often an important source of excited species in nonequilibrium gases. Conversely, chemical reactions can also be the dominant mechanism for deexcitation. An example, illustrative of both of these processes, is the reaction



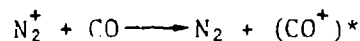
Here  $\text{N}(^2\text{D})$ , a nitrogen atom in the metastable  $^2\text{D}$  state, reacts with molecular oxygen to form  $\text{NO}^\dagger$ , a vibrationally excited NO molecule. Reaction 7-22 is exothermic by 3.77 eV, an energy sufficient to populate vibrational states of NO up to  $v = 18$ . Unless quenched by collisions, the  $\text{NO}^\dagger$  molecules will radiate this energy, or a part thereof, in the fundamental band of NO at  $5.3\mu$  and in shorter-wavelength overtone bands. This radiation is referred to as "chemiluminescence". It may arise from vibrational excitation, as in Reaction 7-22, and lie in the infrared region, or it may arise from electronic excitation of a product

species by some chemical reaction, and lie in the visible or ultraviolet region. In either case, the rate at which photons are emitted is proportional to the rate at which the excited state species is formed. In Reaction 7-22, if  $k_{22}$  is the rate coefficient, then the photon emission rate is proportional to  $k_{22}[N(^2D)][O_2]$ .\*

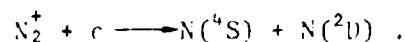
The metastable species  $N(^2D)$  has a lifetime against radiation of about 26 hours. However, at altitudes below about 300 km, the concentration of  $O_2$  in the atmosphere is sufficiently great so that Reaction 7-22 will destroy the  $N(^2D)$  before it has a chance to radiate. Reaction 7-22, therefore, serves to chemically deexcite the  $^2D$  state of atomic nitrogen as well as to form vibrationally excited NO with its subsequent chemiluminescent emission.

Reactions, such as (7-22), that produce vibrational excitation are of considerable importance in the study of weapon effects because they are continuing processes (until the reactants are used up) that emit long-lasting afterglows in the atmosphere.

Other types of chemical reactions that may produce excitation or deexcitation, particularly of electronic states, are those involving charge transfer, for example,\*\*



and dissociative recombination, for example,




---

\* Square brackets around a species symbol denotes "concentration".

\*\* The symbols \* and ‡ are used to denote electronic excitation and vibrational excitation, respectively.



### Absorption of Radiation

An atom or molecule in a given state,  $m$ , can absorb a photon and be excited to a state,  $n$ , of higher energy if the photon energy equals  $E_n - E_m$ , and the transition is a permitted one. If the radiation field is intense enough, the distribution of states may be upset and the radiation properties of the air altered. An example, relating to infrared radiation from species in the atmosphere, is the absorption of earthshine above about 70 km. At altitudes below about 70 km, collisions among the molecules are fast enough to maintain a Boltzmann distribution among vibrational states. As the altitude increases and collisions become more infrequent, however, collisional excitation cannot keep pace with radiative deexcitation and the excited states are depopulated relative to what they would be for a Boltzmann distribution. The (thermal) radiation, which is proportional to the excited state concentrations (Equation 7-8), is then correspondingly less. This phenomenon is referred to as "collision limiting" of the thermal radiation. Tending to offset this effect, however, is the absorption, or scattering, of earthshine which increases the population of excited vibrational states. In fact, at altitudes (70-110 km) where the air temperature is less than the effective radiating temperature of the earth, the infrared thermal emission (including earthshine excitation) can exceed that from a Boltzmann gas (of the same temperature) by factors of up to 100.

Another effect of absorption that may result in significant excitation of infrared radiation is the process of UV fluorescence or, as sometimes called, Franck-Condon pumping. Here, a molecule in its ground electronic and vibrational state may absorb a UV photon and be raised to an excited electronic state. It then drops back to the ground electronic state with the emission of another UV photon. In general, however, the lower state will be one that is vibrationally excited. If the molecule is infrared active, vibrational deexcitation will subsequently occur with emission of the fundamental and overtone bands in the infrared. This mechanism is the principal one for daytime excitation of infrared radiation from certain molecules, particularly metal oxides that may form in the atmosphere.

### 7.3 ATOMIC/MOLECULAR STRUCTURE AND SPECTRA OF AIR SPECIES

This section presents more details on the structure and spectral properties of atoms, molecules, and ions, particularly those encountered in a disturbed atmosphere. Atomic species are considered first, and then molecular species. More details can be found in References 7-23 to 7-26.

#### 7.3.1 ATOMS AND ATOMIC IONS

##### Angular Momenta and Spectroscopic Notation

In quantum (wave) mechanics, as in classical mechanics, the angular momentum of an isolated system is constant. According to quantum mechanics, it can take only discrete values, as can the energy. In the case of one electron, it can have the values  $\sqrt{\ell(\ell+1)}\hbar$  ( $\hbar \equiv h/2\pi$ ), where  $\ell$  is the azimuthal quantum number and relates to the angular momentum due to orbital motion of the electron about the nucleus. For a given value of  $n$ , the principal quantum number,  $\ell$  can take only the values

$$\ell = 0, 1, 2, \dots, n - 1.$$

This orbital motion can be viewed as a ring current with an associated magnetic moment. If a magnetic field is applied to the atom, the angular momentum vector  $\vec{\ell}$  will precess about the field direction so that its component  $\vec{m}_\ell$  along the field is constant. In quantum theory,  $\vec{m}_\ell$  has magnitude  $m_\ell\hbar$  where  $m_\ell$ , called the magnetic quantum number, can have only the  $2\ell + 1$  discrete values

$$m_\ell = \ell, \ell - 1, \ell - 2, \dots, -\ell.$$

Different values of  $m_\ell$  correspond to different orientations of  $\vec{\ell}$ . In the presence of a magnetic field, therefore, states with a given  $\ell$  but

different  $m_l$  will have slightly different energies.\* For zero field, the  $2l + 1$  values of  $m_l$  for a given  $n$  and  $l$  correspond to  $2l + 1$  different modes of motion (eigenfunctions) of the same energy, and the state  $(n, l)$  is  $(2l + 1)$  fold degenerate. Electrons with  $l = 0, 1, 2, 3, \dots$  are called s, p, d, f, --- electrons, respectively.

The angular momentum  $\vec{S}$ , associated with the electron spin, has magnitude  $\sqrt{s(s+1)}\hbar$ , where  $s$ , the spin quantum number, has the value  $1/2$ . In a magnetic field the component of  $\vec{S}$  has the value  $m_s\hbar$  where  $m_s = 1/2$  or  $-1/2$ .

In light atoms containing several electrons, the orbital angular momenta  $\vec{L}_i$  of the individual electrons are strongly coupled among themselves as are also the spin angular momenta  $\vec{S}_i$  among themselves. The  $\vec{L}_i$  add together to form a resultant  $\vec{L}$  of magnitude  $\sqrt{L(L+1)}\hbar$ ; similarly the  $\vec{S}_i$  add together to form a resultant  $\vec{S}$  of magnitude  $\sqrt{S(S+1)}\hbar$ . Since the  $\vec{L}_i$  are integers, the quantum number  $L$  is also an integer. States with  $L = 0, 1, 2, 3, \dots$  are designated as S, P, D, F, --- states, respectively. Since  $s_i = 1/2$ , the quantum number  $S$  is integral for an even number of electrons and half integral for an odd number of electrons.

The resultants  $\vec{L}$  and  $\vec{S}$  are then added together to give the total angular momentum  $\vec{J}$  of the electrons.\*\* Its magnitude is  $\sqrt{J(J+1)}\hbar$  where the quantum number  $J$  can have the  $2S + 1$  values:

$$J = L + S, L + S - 1, \dots, |L - S|.$$

\* Even in the strongest laboratory fields, however, this splitting is less than  $10^{-3}$  eV.

\*\* The coupling assumed above is called Russell-Saunders, or  $(\vec{L}, \vec{S})$  coupling. Alternatively, in heavy atoms, the  $\vec{L}_i$  and  $\vec{S}_i$  couple to form  $\vec{J}_i$  which then combine to form  $\vec{J}$ . This is called  $(\vec{J}, \vec{J})$  coupling.

The component of  $\vec{J}$  in the direction of an applied field is  $M_J \hbar$  where  $M_J$  is quantized with only the  $2J + 1$  values from  $-J$  to  $+J$  permitted. The energies of the states formed in this way depend upon  $L$  and  $S$ . Indeed, states with different  $L$  and  $S$  have very different energies while, on account of the smallness of the coupling between  $\vec{L}$  and  $\vec{S}$ , states with the same  $L$  and  $S$ , but different  $J$ , have only slightly different energies. The latter gives rise to what is called "fine structure splitting" of a state with given  $L$  and  $S$ , and forms a multiplet term which has  $2S + 1$  components (called the "multiplicity").

In spectroscopic notation, the value of  $S$  is denoted by a left superscript whose value is  $2S + 1$ . The value of  $J$  is denoted by a right subscript of value  $J$ . For example, Table 7-4 shows the electron configurations and term types for the ground states of the neutral atoms from hydrogen through argon. Included are also the ions  $N^+$  and  $O^+$ .

As mentioned in the previous section, transitions between states of atoms can give rise to strong emission and absorption lines only if the matrix element of the electric dipole moment between the states is non-zero. For transitions, this leads to two rigorous selection rules that operate to determine the spectrum:

1.  $\Delta J = 0, \pm 1$ , with the restriction  $J = 0 \not\rightarrow J = 0$
2. even terms combine only with odd terms, and vice versa\*

In addition, as long as coupling between  $\vec{L}$  and  $\vec{S}$  is weak, the rules

---

\* The terms (states) of an atom are distinguished as even or odd depending on whether  $\sum_i l_i$ , summed over all the electrons in the atom, is even or odd.

Table 7-4. Electron configurations and term types for some neutral atoms and ions.

ATOM/ION	ATOMIC NUMBER	K 1s	L 2s 2p		3s	M 3p 3d		GROUND TERM
H	1	1						$^2S_{1/2}$
He	2	2						$^1S_0$
Li	3	2	1					$^2S_{1/2}$
Be	4	2	2					$^1S_0$
B	5	2	2	1				$^2P_{1/2}$
C	6	2	2	2				$^3P_0$
N	7	2	2	3				$^4S_{1/2}$
N <sup>+</sup>	7	2	2	2				$^3P_0$
O	8	2	2	4				$^3P_2$
O <sup>+</sup>	8	2	2	3				$^4S_{3/2}$
F	9	2	2	5				$^2P_{3/2}$
Ne	10	2	2	6				$^1S_0$
Na	11	2	2	6	1			$^2S_{1/2}$
Mg	12	2	2	6	2			$^1S_0$
Al	13	2	2	6	2	1		$^2P_{1/2}$
Si	14	2	2	6	2	2		$^3P_0$
P	15	2	2	6	2	3		$^4S_{3/2}$
S	16	2	2	6	2	4		$^3P_2$
Cl	17	2	2	6	2	5		$^2P_{3/2}$
Ar	18	2	2	6	2	6		$^1S_0$

$$\Delta L = 0, \pm 1$$

$$\Delta S = 0$$

hold to a good approximation. (Note, however, that  $\Delta L = 0$  is forbidden for one-electron atoms by Rule 2 above). Finally, in a magnetic or electric field,

$$\Delta M_J = 0, \pm 1.$$

Transitions that may occur weakly (magnetic dipole or electric quadrupole), although violating the above selection rules, are called forbidden transitions. Figure 7-1 (from Reference 7-27) shows the positions and lifetimes of the metastable levels of OI, OII, NI, and NII arising from their ground electron configurations.\* Also shown in this figure are the forbidden transitions and their respective wavelengths. Numbers in parentheses refer to transition probabilities ( $\text{sec}^{-1}$ ).

### Strengths of Spectral Lines

Equation 7-7 gives the transition probability ( $\text{sec}^{-1}$ ) for spontaneous emission. It applies when the states  $n$  and  $m$  are non-degenerate. If degeneracy occurs, Equation 7-7 should be replaced by\*\*

$$A_{nm} = \frac{6.4\pi^4 \nu_{nm}^3}{3hc^3} \frac{\sum_{ij} |\vec{p}_{n_i m_j}|^2}{g_n} \quad (7-25)$$

where the summation is over all possible combinations of the degenerate sub-levels of the upper ( $n$ ) and lower ( $m$ ) state. In addition,

\* The Roman numeral I after an atomic symbol refers to a neutral atom; the Roman numeral II refers to a single ionized atom, etc.

\*\* If  $\sum_{ij} |\vec{p}_{n_i m_j}|^2$  is zero, it can be replaced in Equation 7-25 by its magnetic dipole counterpart. If the latter is also zero, it can then be replaced by its electric quadrupole counterpart.

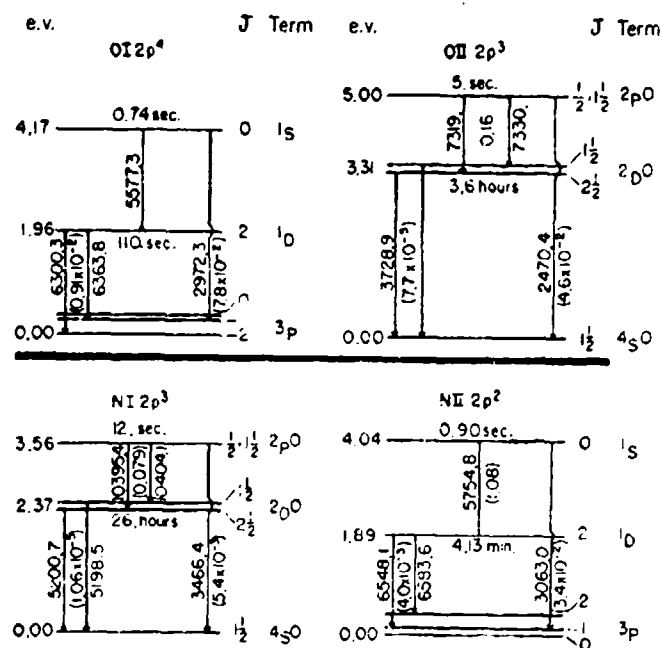


Figure 7-1. Forbidden transitions among low-lying metastable states of O, O<sup>+</sup>, N, N<sup>+</sup>.

$$B_{mn} = \frac{g_n}{g_m} B_{nm}$$

(7-21)

where  $g_n$  and  $g_m$  are the statistical weights of states  $n$  and  $m$ , respectively.

It is sometimes convenient to express  $A_{nm}$  in terms of a dimensionless quantity,  $f_{nm}$ , called the absorption oscillator strength or "f-number". It is defined as

$$f_{nm} = \frac{8\pi^2 m_e}{3c^2 h} \frac{\sum_i f_{ni}^{\rightarrow m}}{g_n}$$

(7-22)

Since  $\nu_{nm} = (E_n - E_m)/h$ , it follows that

$$f_{nm} = - (g_m/g_n) f_{mn} \quad (7-26)$$

where  $f_{nm}$ , the oscillator strength in emission, is negative. For allowed electronic transitions, the quantity  $(\sum_{k < m} f_{mk} + \sum_{n > m} f_{mn})$  is of the order of unity. In terms of  $f_{mn}$ , Equation 7-23 can be written as

$$A_{nm} = \frac{8\pi^2 e^2 \nu_{nm}}{mc^3} \frac{g_m}{g_n} f_{mn} \quad (7-27)$$

Table 7-5 shows some of the prominent allowed transitions in the visible spectra of N, N<sup>+</sup>, O, and O<sup>+</sup>. The fine structure, or multiplet splitting of the energy levels (corresponding to different J values for given L and S) and spectral lines is not shown. The upper and lower energy levels for each transition are shown, along with their statistical weights and the corresponding  $A_{nm}$  and  $f_{mn}$  values. The information contained in Table 7-5 is from Reference 7-28.

### 7.3.2 MOLECULES AND MOLECULAR IONS

#### The States and Their Energy Levels

##### Electronic States

For a given separation of the nuclei, the electrons carry out motion about the nuclei in such a way that only quantized electronic states of the molecule occur. The different electronic states are characterized by certain quantum numbers and symmetry properties of their eigenfunctions. For diatomic and linear polyatomic molecules, the electron orbital angular momentum  $\hat{L}$  about the internuclear axis is defined and has the magnitude  $L\hbar$ , where the quantum number  $L$  can assume only integral values. For  $L = 0, 1, 2, 3$ , the states are designated as  $\Sigma, \Pi, \Delta, \Phi$ , etc. For non linear molecules different types of electronic states arise depending on



Table 7-5. Some allowed transitions for NI, NII, OI, and OII in the visible.

SPECIES	MULTIPLY	$\lambda(\text{\AA})$	$E_m(\text{cm}^{-1})$	$E_n(\text{cm}^{-1})$	$g_m$	$g_n$	$A_{nm}(10^8\text{sec}^{-1})$	$f_{mn}$
NI	$^4P - ^4D^0$	8692	83337	94839	12	20	0.19	0.36
	$^4P - ^4P^0$	8212	83337	95511	12	12	0.23	0.23
	$^4P - ^4S^0$	7452	83337	96752	12	4	0.32	0.09
	$^2P - ^2P^0$	8618	86193	97794	6	6	0.29	0.32
	$^2D - ^2F^0$	9048	99663	110713	10	14	0.27	0.47
	$^2S^0 - ^2P$	9050	93582	104628	2	6	0.26	0.95
NII	$^3P^0 - ^3D$	5679	149013	166616	9	15	0.56	0.45
	$^3P^0 - ^3P$	4623	149013	170637	9	9	1.05	0.34
	$^5P - ^5D^0$	5537	205677	223731	15	25	0.56	0.43
	$^5P - ^5P^0$	5007	205677	225644	15	15	0.77	0.29
	$^3D - ^3F^0$	5005	166616	186593	15	21	1.22	0.64
	$^3S - ^3P^0$	5001	168893	188884	3	9	0.75	0.84
	$^3P - ^3D^0$	5939	170637	187472	9	15	0.57	0.50
	$^5D^0 - ^5F$	5178	223731	243039	25	35	1.02	0.57
	$^5P^0 - ^5D$	5176	225644	244959	15	25	0.83	0.56
	$^3F^0 - ^3D$	6168	186593	202801	21	15	0.36	0.15
	$^3F^0 - ^3G$	4041	186593	211332	21	27	2.64	0.83

Table 7-5 (Continued)

SPECIES	MULTIPLY	$\lambda(\text{\AA})$	$E_m(\text{cm}^{-1})$	$E_n(\text{cm}^{-1})$	$g_m$	$g_n$	$A_{nm}(10^8\text{sec}^{-1})$	$f_{mn}$
OI	$^3D^0 - ^3D$	8227	101143	113295	15	15	0.32	0.33
	$^3D^0 - ^3F$	7949	101143	113719	15	21	0.37	0.50
	$^5S^0 - ^5P$	7773	73768	88629	5	15	0.34	0.92
	$^3P^0 - ^3P$	7477	113916	127286	9	15	0.41	0.57
	$^3P - ^3D^0$	7990	88631	101143	9	15	0.29	0.46
	$^3P - ^5D^0$	9264	86629	97420	15	25	0.42	0.90
OII	$^4P - ^4D^0$	4652	185402	206895	12	20	1.02	0.55
	$^4P - ^4P^0$	4341	185402	208431	12	12	1.05	0.30
	$^2P - ^2D^0$	4418	189008	211636	6	10	1.13	0.55
	$^2D - ^2F^0$	4593	206972	228737	10	14	1.11	0.49
	$^6S^0 - ^6P$	4467	245396	267775	6	18	0.92	3.83
	$^4D^0 - ^4F$	4075	206895	231429	20	28	1.98	0.69
	$^4P^0 - ^4P$	4152	208431	232511	12	12	1.01	0.26
	$^4P^0 - ^4D$	4111	208431	232746	12	20	1.49	0.63
	$^2D^0 - ^2F$	4704	211636	232889	10	14	1.38	0.64
	$^4S^0 - ^4P$	4913	212162	232511	4	12	0.67	0.73
	$^2F^0 - ^3G$	4188	228737	252608	14	18	2.51	0.85
	$^2D^0 - ^2F$	4701	229955	251222	10	14	0.88	0.41
	$^2P^0 - ^2P$	4698	232511	253791	6	6	1.05	0.35
	$^4F - ^4D^0$	6898	231429	245923	28	20	0.33	0.17
	$^4F - ^4G^0$	4094	231429	255850	28	36	2.60	0.84
	$^4P - ^4D^0$	4294	232511	255794	12	20	1.98	0.91
	$^4D - ^4F^0$	4278	232746	256115	20	28	2.12	0.81
	$^4F - ^2G^0$	4342	232889	255915	14	18	2.31	0.84
	$^2D - ^2F^0$	4606	234434	256136	10	14	1.82	0.81

the symmetry properties of the nuclear frame. For example, for molecules with two mutually perpendicular planes of symmetry there are four types of electronic states  $A_1$ ,  $A_2$ ,  $B_1$ , and  $B_2$ .

The electron spins combine to form a total spin angular momentum  $\vec{S}$ . For diatomic and linear polyatomic molecules, the component of  $\vec{S}$  along the internuclear axis is  $\Sigma\hbar$  where

$$\Sigma = S, S - 1, \dots, -S$$

The total electronic angular momentum about the internuclear axis, denoted by  $\vec{\Omega}$ , is obtained by adding  $\vec{\Lambda}$  and  $\vec{S}$ . The associated quantum number,  $\Omega$ , is given by

$$\Omega = |\Lambda + \Sigma|$$

The values of  $S$  and  $\Sigma$  are denoted by using  $(2S+1)$  as a left superscript, and  $(\Lambda+\Sigma)$  as a right subscript. Thus, for example, the state  ${}^3\Delta_2$  implies  $\Lambda = 2$ ,  $S = 1$ ,  $\Sigma = 0$ , and  $\Omega = 2$ .

The electronic energy of a diatomic molecule depends on the internuclear separation  $r$ , and that dependence will be different for different electronic states. When the nuclei move relative to each other, work must be done not only against the Coulomb field of the nuclei themselves, but also in changing the electronic energy. Thus, the sum of the electronic energy,  $E^{el}$  (potential + kinetic energy of the electrons), and the Coulomb potential,  $V_n$ , of the nuclei acts as an effective potential energy under which the nuclei carry out their relative motions (vibrations). Curves representing the variation of this effective potential energy with internuclear separation are called "potential curves". Examples of potential curves (from Reference 7-29) for various electronic states of  $N_2$ ,  $N_2^+$ , and  $N_2^-$  are

shown in Figure 7-2.\* The positions of the vibrational levels associated with many of these states are also shown. Those electronic states whose potential curves have a minimum are stable states of the molecule. If there is no minimum the electronic state is unstable, that is the two atoms repel each other for any value of the internuclear distance. Some of the dashed curves in Figure 7-2 correspond to unstable states of  $N_2$  and  $N_2^+$ .

The electronic energy of a given state is equal to the internal energy of the molecule when it is in its ground vibrational and rotational states. No general formulas for the energies of electronic states of a molecule can be given except for those states (called Rydberg states) in which one electron is excited to orbitals of increasing principal quantum number  $n$ . In this case, to a good approximation,

$$E_e = I - R/(n-a)^2 \quad (7-28)$$

where  $I$  is the ionization potential,  $R$  is the Rydberg constant ( $\approx 13.6$  eV) and  $a$  is the Rydberg correction.

#### Vibrational States

Diatomic Molecules: If the potential curve for an electronic state is approximated by that for a harmonic oscillator (References 7-24, 7-52)

$$V = f(r-r_e)^2 \quad (7-29)$$

\* The letter X denotes the ground state; the letters A, B, C, ..., generally (except for  $N_2$ ) denote excited states (in order of increasing energy) with the same spin,  $S$ , as the ground state; the letters a, b, c, ..., generally denote states (in order of increasing energy) with a different spin,  $S$ , or orbital angular momentum,  $L$ , than the ground state.

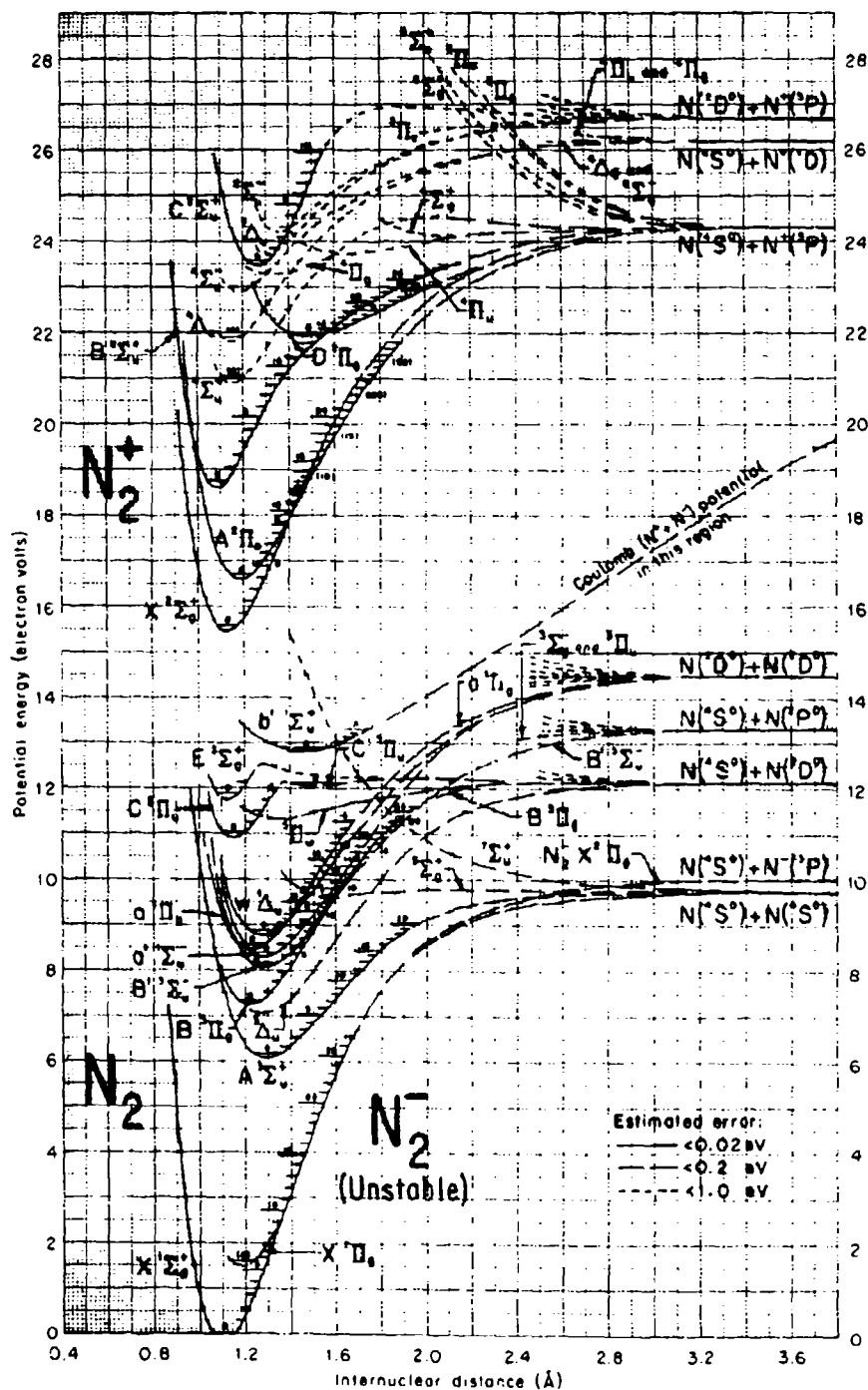


Figure 7-2. Potential-energy curves for  $N_2^-$  (unstable),  $N_2$  and  $N_2^+$  (from Reference 7-29).

the energy eigenvalues,  $E_v$ , that arise from solution of the Schroedinger equation are

$$E_v = h c \omega_e (v + 1/2) ; v = 0, 1, 2, \dots \quad (7-30)$$

Here,  $r_e$  is the nuclear separation corresponding to the minimum of the potential curve, and  $c \omega_e$  is a frequency characteristic of the given electronic state, i.e.,  $\omega_e$  is that frequency expressed in the unit  $\text{cm}^{-1}$ . The vibrational energy levels, represented by Equation 7-30, are thus equally spaced with a separation  $h c \omega_e$ . More generally, if the potential curve is represented by a power series

$$V = f(r-r_e)^2 + g(r-r_e)^3 + \dots \quad (7-31)$$

the vibrational energy levels are then found to be

$$E_v = h c \left\{ \omega_e (v + 1/2) - x_e \omega_e (v + 1/2)^2 + y_e \omega_e (v + 1/2)^3 + \dots \right\} \quad (7-32)$$

where the anharmonicity constants  $x_e$  and  $y_e$  are such that  $x_e \ll 1$ , and  $y_e \ll x_e$ . Equation 7-32 gives a better representation of the vibrational level structure of diatomic molecules than does Equation 7-30 and provides for a diminishing energy level separation with increasing values of  $v$ .

Polyatomic Molecules: If there are  $N$  nuclei in the molecule there will be  $3N-6$  modes of vibration possible. For linear molecules, the number is  $3N-5$ , although some of these may be degenerate. The vibrational energy levels are given by the expression

$$E(v_1, v_2, \dots) = h c \left\{ \sum_i \omega_i (v_i + d_i/2) + \sum_i \sum_{k \geq i} x_{ik} (v_i + d_i/2)(v_k + d_k/2) + \sum_i \sum_{k \geq i} g_{ik} (v_i + d_i/2) + \dots \right\} \quad (7-33)$$

In Equation 7-33,  $d_i$  is the degree of degeneracy,  $\ell_i$  are integral numbers that assume the values  $\ell_i = v_i, v_i - 2, v_i - 4, \dots, 1$  or  $0$ , and the  $g_{ijk}$  are constants of the order of the  $x_{ijk}$ . For triatomic molecules, the principal vibrational quantum numbers are  $v_1, v_2, v_3$ .

### Rotational States

A description of the rotational energy level structure of molecules is simplest for diatomic and linear polyatomic molecules for which the angular momentum about the internuclear axis is zero. Most diatomic molecules of interest (except NO) have a  $\Sigma$  ground electronic state ( $\dots, \Lambda = 0$ ) and so satisfy this requirement. Molecules not satisfying this requirement can be classed as symmetric tops, spherical tops, or asymmetric tops. For them the rotational structure is more complex and will not be described here. Details can be found in references 7-25 and 7-35.

Solution of the Schrodinger equation shows that the angular momentum,  $\vec{J}$ , due to rotation of the nuclei about an axis perpendicular to the internuclear line has magnitude  $\sqrt{J(J+1)}\hbar$  where  $J$ , the rotational quantum number, can take only the integral values  $0, 1, 2, \dots$ . The component of  $\vec{J}$  in a given direction is  $M_J\hbar$  where  $M_J = J, J-1, J-2, \dots, -J$ . The corresponding value for the rotational energy in a state characterized by the quantum numbers  $v$  and  $J$  is found to be

$$E_r(J) = hc \left\{ B_v J(J+1) - D_v J^2(J+1)^2 + \dots \right\} \quad (7-34)$$

Here, the rotational constants  $B_v$  and  $D_v$  are given by the expressions

$$B_v = B_0 - \alpha_0(v+1/2) + \dots \quad (7-35)$$

$$D_v = D_0 + \beta_0(v+1/2) + \dots \quad (7-36)$$

where  $\alpha_e$ ,  $\beta_e$ , and  $B_e$  are characteristic of the electronic state involved, and

$$D_e = 4B_e^3/\omega_e^2 \quad (7-37)$$

It is seen from Equation 7-34 that the separation between rotational energy levels increases with increasing values of  $J$ . Since  $\vec{J}$  has  $2J + 1$  possible orientations in space, the rotational state  $J$  is  $2J + 1$  fold degenerate.

Table 7-6 shows, for selected diatomic molecules of interest, values for the electronic energy,  $T_e$ , dissociation energy\*,  $D_0$ , ionization potential,  $I$ , and other molecular parameters described above. More complete tables can be found in References 7-24 and 7-30.

Table 7-7 shows values of some molecular parameters for selected triatomic molecules of interest in atmospheric studies.

### Selection Rules and Spectra

#### Electronic Bands

Electronic bands consist of transitions in which electronic, vibrational, and rotational quantum numbers change. The selection rules that operate to determine the allowed transitions are complex and are related to changes in the symmetry properties of the wave functions. Briefly, the symmetry properties are:

1. A rotational level is classed as  $+$  or  $-$  if upon reflection at any center the new rotational wave function is identical to the old  $(+)$  or has only its sign changed  $(-)$ .

\* The dissociation energy is the minimum energy required to split apart a molecule in its ground electronic, vibrational, and rotational states.



Table 7-6. Molecular constants for some diatomic species.

SPECIES	STATE	$T_e$ (ev)	$D_0$ (ev)	$I$ (ev)	$\omega_e$ ( $\text{cm}^{-1}$ )	$\omega_e x_e$ ( $\text{cm}^{-1}$ )	$B_e$ ( $\text{cm}^{-1}$ )	$100\alpha_e$ ( $\text{cm}^{-1}$ )	$r_e$ ( $10^{-8}\text{cm}$ )
$\text{O}_2$	$X^3\Sigma_g^-$	0	5.12	12.1	1580.4	12.07	1.45	1.58	1.21
	$a^1\Delta_g$	0.98			1509	12.9	1.43	1.71	1.22
	$b^1\Sigma_g^+$	1.63			1432.7	13.95	1.40	1.82	1.23
$\text{O}_2^+$	$X^2\Pi_g$	12.15	6.67	24.2	1876.4	16.53	1.67	1.98	1.23
	$a^4\Pi_u$	16.11			1035.7	10.39	1.10	1.58	1.38
$\text{N}_2$	$X^1\Sigma_g^+$	0	9.76	15.6	2358.1	14.19	1.99	0.02	1.10
	$A^3\Sigma_u^+$	6.17			1460.4	13.89	1.43	0.01	1.29
$\text{N}_2^+$	$X^2\Sigma_g^+$	15.57	8.71	27.1	2207.2	16.14	1.92	0.02	1.12
	$A^2\Pi_u$	16.69			1902.8	14.91	1.71	0.02	1.18
$^{14}\text{O}$	$X^2\Pi_{1/2}$	0	6.51	9.3	1904.0	13.97	1.70	1.78	1.15
	$^2\Pi_{3/2}$	0.02			1903.7				
$\text{NO}^+$	$X^1\Sigma^+$	9.25	10.86 (N-O <sup>+</sup> )	30.5	2377.1	16.35	2.00		1.07
	$A^1\Pi$				1608.9	23.3	1.59		1.19
$\text{CO}$	$X^1\Sigma^+$	0	11.11	14.0	2170.2	13.46	1.93	1.75	1.13
	$a^3\Pi_r$	6.01			1739.3	14.47	1.68	1.93	1.21
$\text{CO}^+$	$X^2\Sigma^+$	14.21	8.35	27.8	2214	27.93	1.80	3.03	1.17
	$A^2\Pi_i$	16.78			1562	13.53	1.59	1.94	1.24
$\text{AlO}$	$X^2\Sigma^+$	0	5.0 $\pm$ .2	9.5 $\pm$ .5	979.2	6.97	0.64	0.58	
	$A^2\Sigma^+$	2.57	5.1		870.1	3.52	0.60	0.45	
$\text{LiO}$	$X^2\Sigma$	0	3.5	9.0 $\pm$ .2	745	4.84	1.3	1.29	
$\text{BaO}$	$X^1\Sigma$	0	5.75		669.8	2.05	0.31	0.14	
	$A^1\Sigma$	2.08			498.8	1.5	0.26	0.11	
$\text{FeO}$	$X^1\Sigma$	0	4.3 $\pm$ 0.5	8.7 $\pm$ .1	870.8	4.39	0.35	0.29	
$\text{UO}$	$X$	0	7.8 $\pm$ .1	5.7	(776.0)				

Table 7-7. Molecular parameters for some atmospheric triatomic species.

MOLECULE	GROUND STATE	$D_0$ (ev)	$I$ (ev)	VIBRATIONAL INTERVALS (ev)		
				$\nu_1$	$\nu_2$	$\nu_3$
H <sub>2</sub> O	X <sup>1</sup> A <sub>1</sub>	5.12(H-OH)	12.62	0.453	0.198	0.466
CO <sub>2</sub>	X <sup>1</sup> Σ <sub>g</sub> <sup>+</sup>	5.45(CO-O)	13.77	0.172	0.083	0.291
NO <sub>2</sub>	X <sup>2</sup> A <sub>1</sub>	3.12(NO-O)	9.78	0.164	0.093	0.201
N <sub>2</sub> O	X <sup>1</sup> Σ <sup>+</sup>	1.68(N <sub>2</sub> -O)	12.89	0.276	0.073	0.159
O <sub>3</sub>	X <sup>1</sup> A <sub>1</sub>	1.05(O <sub>2</sub> -O)	12.80	0.138	0.087	0.129

- If, upon reflection of all coordinates at some center, the new electronic wave function is identical to the old or has only its sign changed, the state is denoted by a right subscript g, or u. This symmetry is possessed only by molecules with identical nuclei.
- If, upon interchange of nuclei the new wave function is identical to the old or has only its sign changed, the state is denoted by s (for symmetric) or a (for antisymmetric). This symmetry is possessed only by molecules with the same charge on the individual nuclei.
- States with  $\Lambda = 0$  (i.e., Σ states) are divided into Σ<sup>+</sup> and Σ<sup>-</sup> states depending on whether the sign of the electronic wave function changes upon reflection in a plane containing the internuclear axis.

The selection rules are then:

g → g, u → u, g → u

s → s, a → a, s → a

Σ<sup>+</sup> → Σ<sup>+</sup>, Σ<sup>-</sup> → Σ<sup>-</sup>, Σ<sup>+</sup> → Σ<sup>-</sup>

and

$$\Delta S = 0; \Delta \Lambda = 0, \pm 1.$$

The selection rules for the rotational quantum number are:

$$\begin{aligned} \Delta J &= \pm 1 \quad \text{if } \Lambda = 0 \quad \text{for both states} \\ &= 0, \pm 1 \quad \text{if } \Lambda \neq 0 \quad \text{for either state.} \end{aligned}$$

In all cases,  $J = 0 \nrightarrow J = 0$

There are no selection rules for the vibrational quantum numbers in an electronic band, but  $\Delta v$  is limited by the requirements of the Franck-Condon principle. This principle, corroborated by quantum-mechanical calculations, states that an electronic transition in a molecule takes place so rapidly in comparison to the vibrational motion that immediately afterward the nuclei still have very nearly the same relative position and velocity as they did before the transition. An illustration is given in Figure 7-3, in which potential curves for two electronic states are shown. AB is a vibrational level of the upper state and DC and EF are vibrational levels of the lower state. During vibration in the upper state the molecule stays preferentially at the turning points A and B of the vibrational motion, while the intermediate positions are passed through very rapidly. As a result, the electronic transition to the lower state takes place preferentially at the turning points. If it takes place at B, then immediately after the transition, the molecule will be at C, vertically below B, and C forms the right turning point of the new vibrational motion CD. If it takes place at A, the transition is to E, and E forms the left turning point of the new vibrational motion EF. In this example, there would be two vibrational states of the lower electronic state into which the probability of transitions would be a maximum.

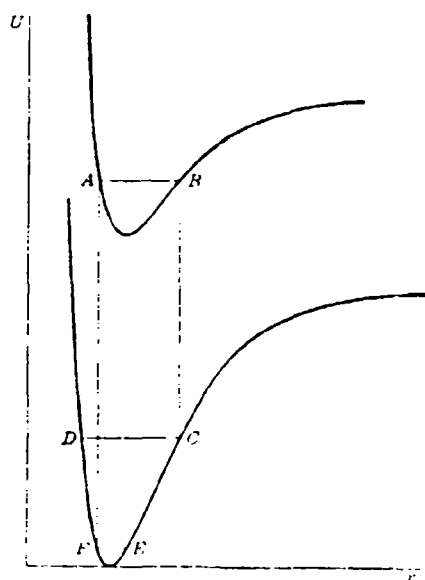


Figure 7-3. Illustration of the Franck-Condon principle.

Mathematically, the principle is described by what are called "Franck-Condon factors" (see Equation 7-41) giving the relative probabilities for different bands of a given electronic band system.

Some prominent electronic band systems of  $N_2$ ,  $N_2^+$ ,  $O_2$ , and  $O_2^+$  are shown in Figure 7-4. Only the states corresponding to  $v = 0$  are shown.

Table 7-8 shows the wavelengths for the  $(0, 0)$  bands of the electronic band systems seen in Figure 7-4.

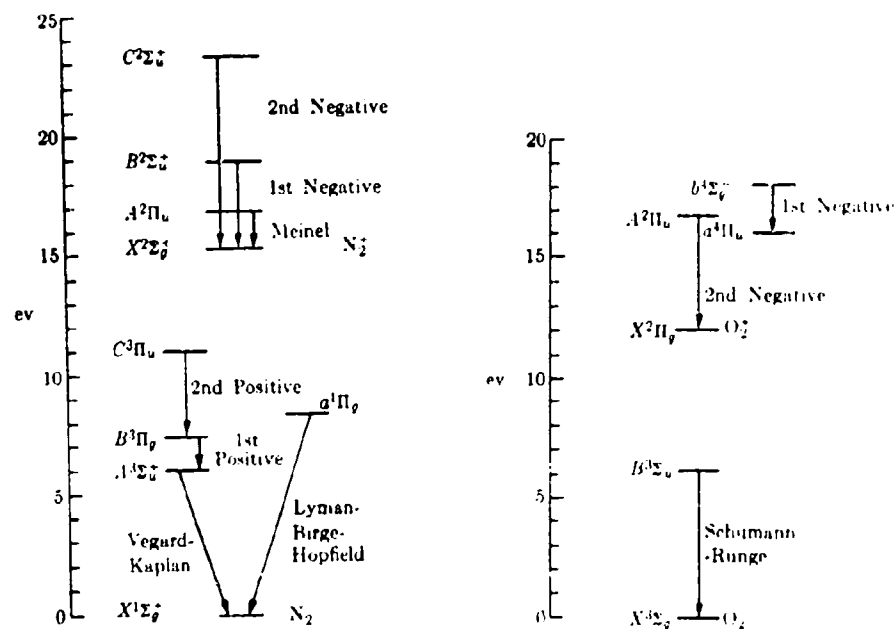


Figure 7-4. Some prominent electronic band systems of  $N_2$ ,  $N_2^+$ ,  $O_2$ , and  $O_2^+$

### Vibration-Rotation Bands

Vibration-Rotation bands result from transitions in which only the vibrational and rotational quantum numbers change. The selection rule governing the vibrational quantum numbers are:

$$\Delta v_1 = \pm 1 \text{ (strongest); } \Delta v_1 = \pm 2 \text{ (weaker); } \Delta v_1 = \pm 3 \text{ (very weak); } \dots$$

Bands that arise from  $\Delta v_1 = \pm 1$  are called "fundamental" bands; those that arise from  $\Delta v_1 = \pm 2$  are called "first overtone" bands; etc. The fundamental is usually stronger than the first overtone by a factor of roughly 100. Transitions may also occur in which several  $v_1$  change. The resulting

Table 7-8. Wavelengths for (0, 0) bands of systems shown in Figure 7-4.

SPECIES	BAND SYSTEM	WAVELENGTH (Å)
$N_2$	Lyman-Birge-Hopfield	1440
	Vegard-Kaplan	2000
	Second Positive	3371
	First Positive	10387
$N_2^+$	Second Negative	1550
	First Negative	3914
	Meinel	11100
$O_2$	Schumann-Runge	2030
$O_2^+$	Second Negative	2610
	First Negative	9150

bands, called "intercombination" bands, are also generally less intense than the fundamentals. For a triatomic molecule, the three modes of vibration that are characterized by the three quantum numbers  $v_1$ ,  $v_2$ , and  $v_3$  are referred to as the  $\nu_1$ ,  $\nu_2$ , and  $\nu_3$  modes, respectively.

As was explained in Section 7.2.2, the ensemble of rotational transitions ( $v'J' \rightarrow v''J''$ ) for fixed  $v'$  and  $v''$  comprise a series of lines called a vibration-rotation (V-R) band. The selection rules on  $J$  are the same as described above for electronic bands. Those transitions in emission for which  $\Delta J = +1$  may give rise to photons with wavelength shorter than the unallowed "null line" ( $J = 0 \rightarrow J = 0$  transition). They form the R branch of the band. Those transitions for which  $\Delta J = -1$  give rise to photons with wavelength longer than the null line and form the P branch. If  $\Delta J = 0$  is permitted, the resulting ensemble of lines forms the Q branch. For a diatomic or linear polyatomic molecule, a Q branch arises

whenever the angular momentum about the internuclear axis is nonzero. Even if the electron angular momentum about this line is zero ( $\Sigma$  states), there may still be an angular momentum due to rotation of one of the nuclei (in a polyatomic molecule) about this line. For example,  $\text{CO}_2$  is a linear symmetrical molecule of the form O-C-O. The  $\nu_2$  mode of vibration, called the bending mode, corresponds to vibration of the carbon atom perpendicular to the internuclear line. The angular momentum that results from simultaneous rotation about this line is described by the quantum number  $\ell$ . A given vibrational state of the molecule is then denoted by the set of quantum numbers  $(\nu_1, \nu_2, \nu_3)$  where, for each value of  $\nu_2$ , the quantum number  $\ell$  can assume the values  $\nu_2, \nu_2-2, \nu_2-4, \dots, 1$  or  $0$ . This represents a special case of the more general case referred to above (Equation 7-33). The vibrational energy levels for the bending mode, specified by given values for  $\nu_2$ , are then split into sub-levels, some of which may be degenerate. The selection rule that governs  $\ell$  is  $\Delta\ell = \pm 1$ . The V-R bands that originate from changes in  $\nu_2$  (called "perpendicular bands") then exhibit a fine structure splitting.

The variation of the intensity of rotational lines in a V-R band, observed with low resolution, would appear qualitatively as in Figure 7-5. Cases where the Q branch is both present and missing are shown. With higher resolution, the individual rotational lines would appear, rather than the smooth envelopes shown in Figure 7-5.

### Pure Rotation Bands

Pure rotation bands consist of radiative transitions in which only the rotational quantum number changes. The selection rule on  $J$  is

$$\Delta J = \pm 1.$$

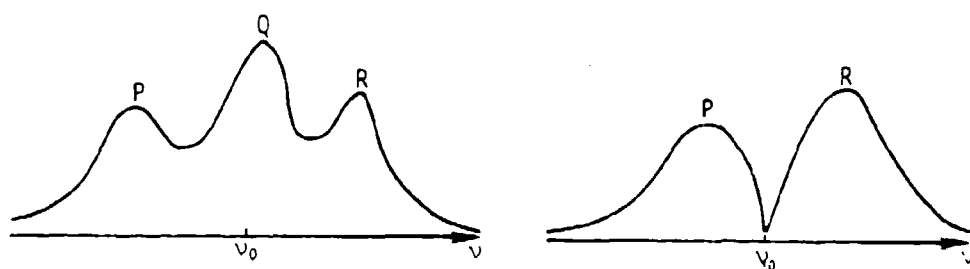


Figure 7-5. Pictorial representation of V-R-band intensity (low resolution).

Equation 7-34 then leads to the following formula for the spectral frequencies,  $\nu$ , of rotational lines:

$$\nu = \nu_0 + 2B_v J - 4D_v J^2 \quad (7-38)$$

where  $J$  is the rotational quantum number of the upper state involved in the transition. Except for the small correction term in  $D_v$ , it is seen that a rotational band consists of a number of equally spaced lines.

Figure 7-6 shows the structure of the infrared bands of atmospheric polyatomic molecules. Included are the V-R bands for two metal oxides.

### Strength of Bands

#### Electronic Bands

As in the case of atomic transitions, Equation 7-23 describes the spontaneous transition probability ( $\text{sec}^{-1}$ ) between an upper electronic state  $n$  and a lower one  $m$ . For molecules, however, the electric moment  $\vec{\mu}$  can be



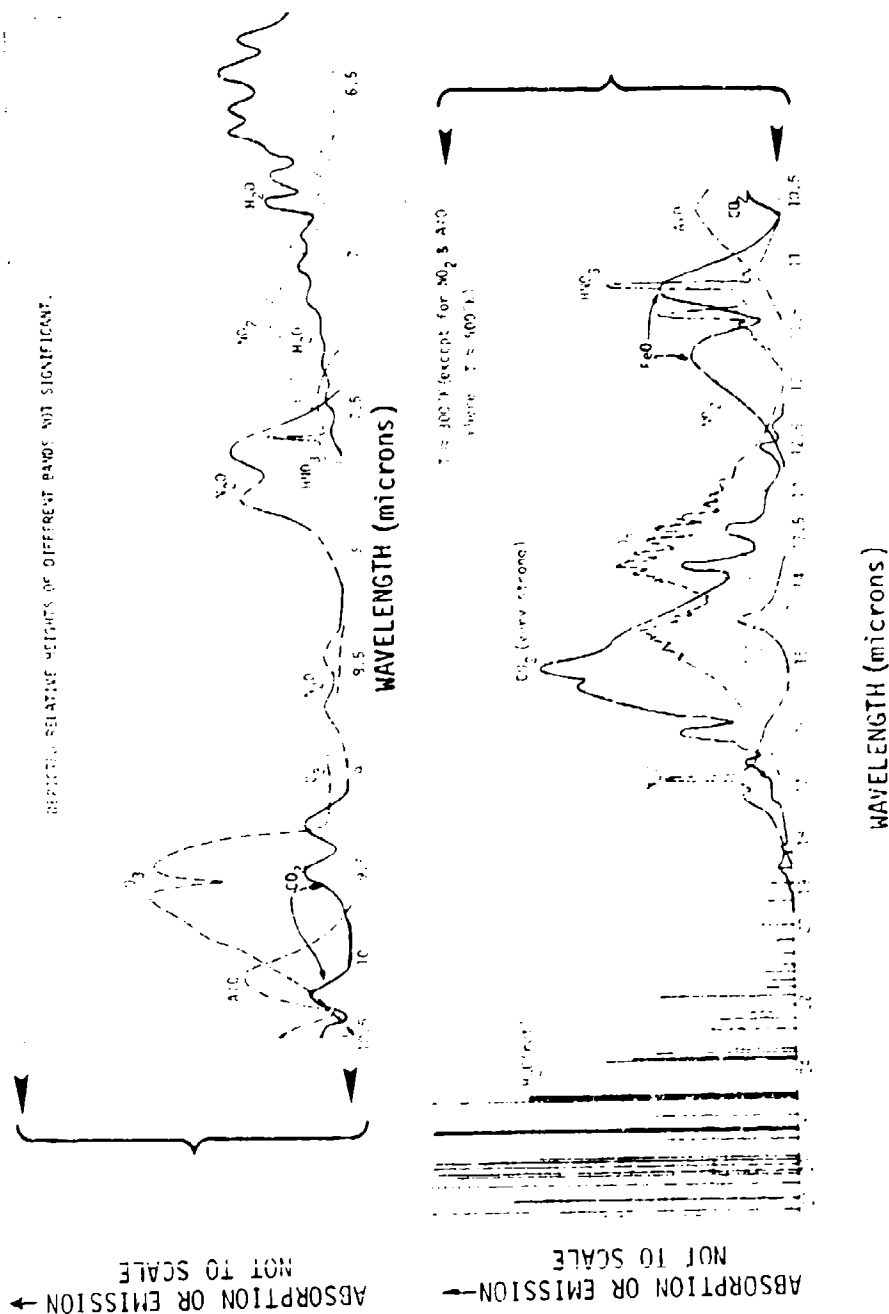


Figure 7-6. Structure of some V-R bands of atmospheric interest (from Ref. 7-31).

resolved into two parts, one depending on the electrons, the other depending on the nuclei:

$$\vec{p} = \vec{p}_e + \vec{p}_N$$

After averaging over the rotational motion, it can be shown (Reference 7-24) that for diatomic molecules the matrix element of  $\vec{p}$  between states  $nv'$  and  $mv''$  can be approximated (r-centroid approximation) by

$$|\vec{p}_{nv',mv''}|^2 = q_{v',v''} |\langle \vec{p}_e^{nm}(r) \rangle|^2 \quad (7-39)$$

where  $r$  is the internuclear separation and  $q_{v',v''}$ , the Franck-Condon factor, is given in terms of the so-called "overlap integral" by

$$q_{v',v''} = \left[ \int \psi_{v'} \psi_{v''} dr \right]^2 \quad (7-40)$$

The quantity  $|\langle \vec{p}_e^{nm}(r) \rangle|^2$  is the square of the average (over  $r$ ) of the matrix element between electronic states  $n$  and  $m$  and it is proportional to the electronic transition probability.  $\psi_{v'}$  denotes the vibrational part of the wave function (see Equation 7-19). It can be shown that the Franck-Condon factors have the property

$$\sum_{v'} q_{v',v''} = \sum_{v''} q_{v',v''} = 1 \quad (7-41)$$

and that each can be interpreted as the relative probability of a transition  $n \rightarrow m$  being accompanied by the vibrational change  $v' \rightarrow v''$ .

The energy emission rate is again determined by Equations 7-8 and 7-27 where the absorption oscillator strength is replaced by

$$f_{mv'',nv'} = \frac{8\pi^2 m_e}{3c^2 h} q_{v',v''} \frac{|\langle \vec{p}_e^{nm}(r) \rangle|^2}{R_m} \quad (7-42)$$

For strong electronic bands,  $f$ -values approaching unity are possible.

### Vibration-Rotation Bands

Equations 7-23, 7-25, and 7-27 can be used to describe the intensity of V-R bands if  $n$  and  $m$  are understood to refer to vibrational quantum numbers of a given electronic state. It can be shown (Reference 7-32) that when the electric dipole moment is expanded as

$$p = p_e + \left( \frac{\partial p}{\partial r} \right)_{r=r_e} (r - r_e) + \dots \quad (7-43)$$

then, approximately,

$$|p_{v+s,v}|^2 = \left( \frac{\partial p}{\partial r} \right)_{r=r_e}^2 \frac{r_e^2 B_e}{\omega_e} x_e^{s-1} \frac{(v+s)!}{s^2 v!} \quad (7-44)$$

Equations 7-25 and 7-44 then lead to a definition of the absorption oscillator strength for the fundamentals of V-R bands:

$$f_{v,v+1} = (v+1) f_{01} \quad (7-45)$$

where

$$f_{01} \approx \frac{8\pi^2 m c r_e^2 B_e}{3 e^2 h} \left( \frac{\partial p}{\partial r} \right)_{r=r_e}^2 \quad (7-46)$$

and, for the first overtone bands:

$$f_{v,v+2} = \frac{1}{2} (v+1)(v+2) f_{02} \quad (7-47)$$

where

$$f_{02} = x_e^2 f_{01} \quad (7-48)$$

These expressions can be considered as averages over all permitted rotational transitions of the V-R band.

Values of  $f_{01}$  for diatomic molecules are typically about  $10^{-8}$  and so are generally several orders of magnitude smaller than the  $f$ -numbers for allowed electronic transitions. The value of  $f_{01}$  can be related to an experimentally measured quantity  $S_0$ , the linear absorption coefficient,  $k_\nu$ , integrated over the V-R band at normal temperature and pressure (N.T.P.), in wavenumber units ( $\tilde{\nu}$  in  $\text{cm}^{-1}$ ),

$$S_0 = \int_{\tilde{\nu}} k_\nu d\tilde{\nu} \quad (\text{cm}^{-2}\text{atm}^{-1}) \quad (7-49)$$

It can be shown (Reference 7-52) that\*

$$f_{01} = \frac{mc^2}{hc^2 N_0} S_0 = 4.2 \times 10^{-8} S_0 \quad (7-50)$$

where  $N_0$  is Loschmidt's number ( $2.69 \times 10^{19}$  molecules  $\text{cm}^{-3}$ ). Similarly, for wavelengths  $\lambda_{\text{fundamental}} < 50\mu$ , the approximation

$$f_{02} \approx 4.2 \times 10^{-8} S_1' \quad (7-51)$$

holds, where  $S_1'$  is the linear absorption coefficient integrated over the first overtone band.\*\* From Equations 7-27 and 7-50 the useful result

\* More generally, it follows from Equations 7-11, 7-13, 7-21, and 7-27 that when the lower state is not the ground state,

$$A_{nm} = \frac{8\pi c}{F_m \nu_{nm}} \left( \frac{g_m}{g_n} \right) \left( \frac{S_0}{N_0} \right) = \frac{2.8}{F_m} \frac{g_m}{g_n} \frac{S_0}{\nu_{nm}}$$

$$f_{nm} = 4.2 \times 10^{-8} S_0 / F_m$$

where  $F_m$  is the fraction of molecules in the lower state at 296°K.

\*\* The quantity  $S_1'/N_0$  is almost a constant, independent of  $T$ , where  $N_0$  is the total species concentration. Similarly,  $S_2'/N_0$  is nearly independent of  $T$  when  $\lambda_{\text{fund}} < 11100/T_2$  microns.

$$A_{10} = 2.8 \frac{g_0}{g_1} S_0 / \lambda_\mu^2 \quad (7-52)$$

is also obtained, where  $\lambda_\mu$  is the fundamental wavelength in microns.

Table 7-9 shows the fundamental wavelengths for several species of atmospheric interest, together with measured values for  $S_0$ . Included are some metal oxides that may form following meteor- or bomb-debris deposition.

#### Pure Rotational Bands

For diatomic molecules (in  $\Sigma$  electronic states) the probability (sec<sup>-1</sup>) of a rotational transition can be found (Reference 7-53) from Equation 7-25 by making the replacement

$$\frac{\sum |\vec{p}_{n,m_i}|^2}{g_n} \rightarrow p_0^2 \frac{J}{2J+1} \quad (7-55)$$

where  $p_0$  is the permanent dipole moment of the molecule. When it is nonzero,  $p_0$  is of the order of  $10^{-18}$  esu.

For polyatomic molecules (and those diatomic molecules not in  $\Sigma$  electronic states), additional quantum numbers are involved and the formulas for the intensity are more complicated. For details see Reference 7-55.

Table 7-9. V-R band wavelengths (fundamentals) and absorption strengths for selected molecules.

SPECIES	BAND TYPE	$\lambda$ (microns)	$S_0$ ( $\text{cm}^{-2}\text{atm}^{-1}$ )	SPECIES	BAND TYPE	$\lambda$ (microns)	$S_0$ ( $\text{cm}^{-2}\text{atm}^{-1}$ )
CO <sub>2</sub>	$\nu_2$	15.0	240	N <sub>2</sub> O	$\nu_3$	4.5	1560
CO <sub>2</sub>	$\nu_3$	4.3	2500	NO	Fundamental	5.3	128
O <sub>3</sub>	$\nu_1$	9.0	10.4	NO <sup>+</sup>	Fundamental	4.3	90
O <sub>3</sub>	$\nu_2$	14.3	18	CO	Fundamental	4.7	237
O <sub>3</sub>	$\nu_3$	9.6	350	OH	Fundamental	2.8	480
NO <sub>2</sub>	$\nu_1$	7.6	900	FeO	Fundamental	11.5	450
NO <sub>2</sub>	$\nu_2$	13.3	552	MgO	Fundamental	12.9	
NO <sub>2</sub>	$\nu_3$	6.2	1430	LiO	Fundamental	13.4	
H <sub>2</sub> O	$\nu_1$	7.8	268	CuO	Fundamental	16.1	
N <sub>2</sub> O	$\nu_2$	17.0	37	UO	Fundamental	12.9	
				AlO	Fundamental	10.4	

#### 7.4 EXCITATION/DEEXCITATION AND EMISSION RATES

##### 7.4.1 ATOMS AND ATOMIC IONS

Excitation by electron impact is usually the most efficient mechanism. Even in atmospheric regions where the heavy ions (such as bomb-debris ions) are deposited, the excitation occurs primarily by electrons that have been heated by the ions. The species of primary interest are O, O<sup>+</sup>, N, and N<sup>+</sup>. Excitation of both the lower-lying metastable states and the higher-lying allowed states can occur.

##### Metastable States

Calculated cross sections,  $\sigma(E)$ , for electron excitation and deexcitation of the metastable states of O, O<sup>+</sup>, N, and N<sup>+</sup> have been reported by Henry, et al. (Reference 7-54). The excitation rate coefficients are then given by

$$k_{ex} = \sqrt{2/m} \int_w^{\infty} E^{1/2} \sigma(E) f(E) dE \quad (7-54)$$

where  $f(E)$  is the distribution function of electron energy (usually assumed to be Maxwellian) and  $w$  is the threshold energy. Use of the reported cross sections in Equation 7-54 leads to the results (Reference 7-35) shown in Figure 7-7.

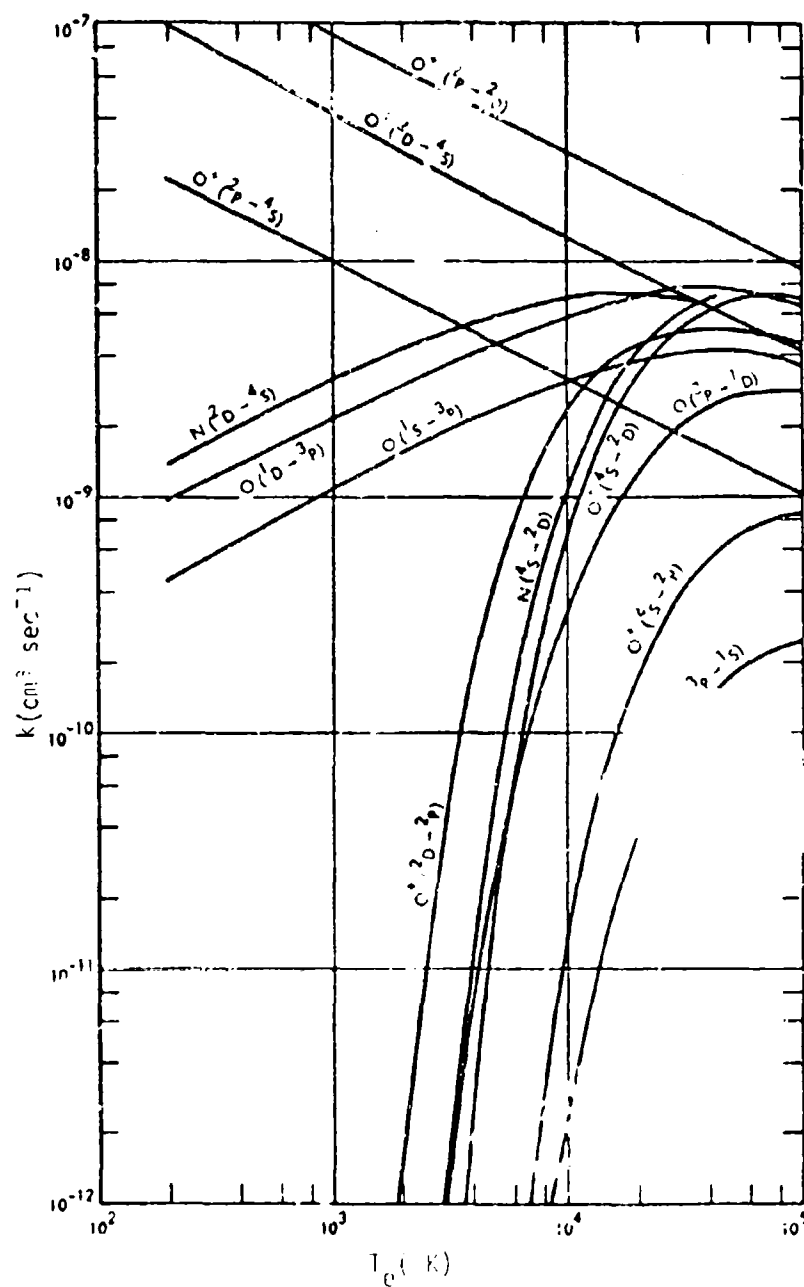
### Allowed States

Accurate calculations of the emitted power for neutral and singly ionized atoms of oxygen and nitrogen cannot presently be made because of insufficient data on excitation cross sections. A review of the current status of the subject of electron excitation of atomic states can be found in References 7-36 and 7-37. Where no specific data are available, the cross sections and rate coefficients for excitation of optically allowed states (i.e., those connected to the ground state by allowed radiative transitions) are usually based on Seaton's dipole approximation (Reference 7-38). The result is

$$k_{ex} = 1.57 \times 10^{-5} \frac{f}{T_c^{1/2} E_{ex}} \times 10^{-6.435 E_{ex}/T_c} \cdot Q(E_{ex}/T_c) \quad (7-55)$$

Here,  $f$  is the absorption oscillator strength for the transition,  $E_{ex}$  and  $T_c$  are the excitation energy and electron temperature, respectively, both in eV, and  $Q$  is a factor that ranges from unity for  $E_{ex}/T_c = 0.02$ , to 0.10 (atoms) and 0.22 (ions) for  $E_{ex}/T_c = 1$ . For excitation of other states (not directly accessible as permitted transitions from the ground state\*) no corresponding equation has been devised. Estimates of the visible power radiated per atom/ion as a function of electron temperature

\* Cross sections,  $\sigma(n'l' \leftarrow nl)$ , for electron excitation of forbidden transitions can be of the same order as those for optically allowed transitions when  $n'l' \neq nl$  (Reference 7-37).





have, nonetheless, been made (References 7-39, 7-40) but the results are not certain enough to warrant inclusion here.

#### 7.4.2 MOLECULES AND MOLECULAR IONS

Electron impact is the most common means for electronic excitation of molecules in a disturbed atmosphere. As mentioned earlier, cross sections for excitation of several different electronic states (both metastable and allowed) of air molecules have been measured in the laboratory and work is continuing. Data on the fluorescence efficiency of some bands, particularly for  $N_2$  and  $N_2^+$ , have also been obtained (Reference 7-41). By and large, however, the data are sufficiently incomplete to preclude, at this time, any detailed treatment of nonequilibrium optical radiation from molecular species. Instead, this section is devoted to the excitation and radiation of A-R bands in the infrared. Thermal emission (excitation by intermolecular collisions) is considered first, followed by non-thermal emission processes.

##### Thermal Emission

Thermal emission from molecules excited by collisions with other molecules occurs continually in the ambient atmosphere. In a nuclear environment it may be greatly enhanced in regions where the temperature is elevated (especially near fireballs).

##### Equilibrium Conditions (Boltzmann population of vibrational states)

In the harmonic oscillator approximation, the vibrational energy levels for a diatomic molecule are given by Equation 7-42. When the vibrational states are Boltzmann distributed, the number of molecules per unit volume  $N_v$  is then given in terms of the total number density,  $N$ , by the equation

$$N_v = N \frac{e^{-\epsilon_v/kT}}{\sum_{v=0}^{\infty} e^{-\epsilon_v/kT}}$$

Equations 7-8, 7-27, 7-45, and 7-56 can be combined to give the total band power per  $\text{cm}^3$  per steradian in the fundamental:

$$J_{\text{fund.}} = \sum_{v=0}^{\infty} J_{v+1,v} = \frac{2\pi N c^2 h}{m} \frac{f_{01} \sim^3}{(e^{hc\tilde{\nu}_0/kT} - 1)} \quad (7-57)$$

More generally, in terms of the integrated absorption coefficient  $S_0$ ,

$$\frac{J_{\text{fund.}}}{N} = \frac{4.4 \times 10^{-32} \tilde{\nu}_{10}}{(e^{1.438 \tilde{\nu}_{10}/T} - 1)} S_0 \text{ (watts molecule}^{-1} \text{ster}^{-1}) \quad (7-58)$$

where  $\tilde{\nu}_{10} = \nu_{10}/c = 1/\lambda_{10}$  is the wavenumber ( $\text{cm}^{-1}$ ) of the fundamental band. Similarly, for the first overtone band,

$$\begin{aligned} \frac{J_{\text{overtone}}}{N} &= \sum_{v=0}^{\infty} \frac{J_{v+2,v}}{N} \\ &= \frac{4.4 \times 10^{-32} \tilde{\nu}_{20}}{(e^{1.438 \tilde{\nu}_{20}/T} - 1)} S_0' \text{ (watts molecule}^{-1} \text{ster}^{-1}) \end{aligned} \quad (7-59)$$

where  $\tilde{\nu}_{20} = 2\nu_{10}$ .

Values of  $\tilde{\nu}_{10}$  and  $S_0$  for several bands of interest can be found from Table 7-9. Use of these values in Equation 7-58 then provides the total power per molecule in the fundamental band (summed over all rotational lines in the band). The spectral distribution of power within the band is a function of temperature and appears qualitatively like that shown in Figure 7-5. For diatomic molecules with no  $g$  branch, an approximate expression can be derived for the linear absorption coefficient of such bands (Reference 7-42):

$$k_{\nu} = \frac{\pi e^2 h N}{4 m c^2 B_e k T} \frac{(1 - e^{-h\nu/kT})}{Q} \sum_V f_{\nu\nu'} |\nu - \nu_{\nu'\nu}| e^{-E_V/kT} e^{-\frac{h(\nu - \nu_{\nu'\nu})^2}{4cB_e kT}} \quad (7-60)$$

Here  $Q$ , the partition function, is defined as

$$Q = \sum_{v=0}^{\infty} e^{-E_v/kT} \quad (7-61)$$

Equation 7-60 takes a particularly simple form in the harmonic oscillator approximation where only the transitions  $\nu' \rightarrow \nu'-1$  are allowed in emission,  $\nu_{\nu'\nu} \approx \nu_{10}$ , and  $E_v = h\nu_{10}(v+1/2)$ . Thus

$$k_{\nu} = \frac{\pi e^2 h N f_{01}}{4 m c^2 B_e k T} \frac{(1 - e^{-h\nu/kT})}{Q} e^{-h\nu_{10}/2kT} |\nu - \nu_{10}| \frac{e^{-\frac{h(\nu - \nu_{10})^2}{4cB_e kT}}}{[1 - e^{-h\nu_{10}/kT}]^2} \quad (7-62)$$

The spectral intensity in emission,  $I_{\nu}$ , can be found from Equation 7-60 by applying Kirchoff's law, Equation 7-14.

As noted above, the value of  $k_{\nu}/N$ , integrated over the fundamental band, is nearly independent of temperature. For sufficiently small values of  $kT$  the same is true for the first overtone band. Therefore, as the temperature is increased, the shape of a band in absorption broadens out with the peaks in the P and R branches diminishing so as to keep the area under them constant. If the Planck function  $B_e$  (Equation 7-15) does not change much over a band, similar remarks apply to the band in emission.

In general, the rotational structure of V-R bands is too complicated to be represented by simple equations such as (7-60) and (7-62). The distribution of rotational lines within bands is then often described statistically. A discussion of the various band models, applicable to polyatomic species, can be found in References 7-43 and 7-44.

### Nonequilibrium Conditions

Equations 7-58 and 7-59 are based on a Boltzmann distribution of vibrational states that requires

$$N_v = e^{-hv/kT} N_{v-1} \quad (7-63)$$

When effects due to collision limiting and earthshine radiation are included, however, the population distribution is modified (see Section 7.2.3). The steady state concentration,  $N_v$ , of molecules in vibrational state  $v$  can then be determined by equating the rate of population of the state by collisions and radiation (induced and spontaneous) to the rate of depopulation by the same processes. In the harmonic oscillator approximation, where the effective collision frequencies are given by (Reference 7-18):

$$\nu_{v,v-1}^i = \nu \nu_{v-1}^i \quad (7-64)$$

$$\nu_{v-1,v}^i = e^{-hv/kT} \nu_{v,v-1}^i \quad (7-65)$$

It is easily shown that, if  $\rho_v$  is the energy density of the radiation field, equation 7-63 should be replaced by

$$N_v = \left( \frac{e^{-hv/kT} \nu_{v,v-1}^i + (c^2/8\pi h\nu^3) \Lambda_{12} \rho_v}{\Lambda_{12} + 2\nu_{v,v-1}^i + (c^2/8\pi h\nu^3) \Lambda_{12} \rho_v} \right) N_{v-1} \quad (7-66)$$

Here,  $\Lambda_{12}$  is the spontaneous transition rate from the  $v = 1$  to the  $v = 0$  state. It can further be shown that the power emitted per molecule in the fundamental band is then obtained by multiplying Equation 7-58 by a

correction factor  $\delta$ , where\*

$$\delta = \frac{e^{-h\nu/kT} \nu'_{10} + (c^3/8\pi h \nu^3) A_{10} \rho_V}{A_{10} + \nu'_{10} (1 - e^{-h\nu/kT})} (e^{h\nu/kT} - 1) \quad (7-67)$$

Similarly, the power emitted in the first overtone band can be corrected, approximately, by multiplying Equation 7-59 by  $\delta^2$ .

Equation 7-67 can be evaluated for  $\delta$  if values for  $\nu'_{10}$ ,  $A_{10}$ , and  $\rho_V$  are assigned. The energy density of earthshine radiation above the surface of a flat earth can be defined as blackbody over  $2\pi$  steradians:

$$\rho_V = \frac{4\pi h \nu^3}{c^3} (e^{h\nu/kT_E} - 1)^{-1} \quad (7-68)$$

provided an approximate wavelength-dependent earth temperature,  $T_E$ , is assigned.  $T_E$  as a function of wavelength (at 100-km altitude), calculated from Anding's atmospheric absorption model (Reference 7-45), is shown in Figure 7-8. Values for the quenching frequencies,  $\nu'_{10}$ , are quite uncertain for most molecular bands of interest. For illustrative purposes, however, if values of  $\nu'_{10}$  equal to  $10^{-3}$  times the gas-kinetic collision frequency are assumed, and Equation 7-68 and Figure 7-8 are incorporated into Equation 7-67, the resulting variation of  $\delta$  with altitude is shown in Figure 7-9. It is seen that the enhanced emission due to earthshine excitation is especially prominent between about 70 and 110 km, particularly for the shorter wavelength infrared bands. In view of the uncertainties in the quenching frequencies, however, Figure 7-9 should be considered more as a qualitative indication than as a quantitative description of  $\delta$ .

---

\* The power,  $P$ , emitted per molecule due to earthshine scattering alone can be found from Equations 7-57 and 7-67 by taking the limit as  $\nu'_{10} \rightarrow 0$ . The result is

$$P_{\text{scatt.}} = 4\pi h \nu^3 \frac{2\pi c^3 f_0}{15} B'_{10}$$

where  $f_0 = 1/B'_{10} + 2c$ , and  $B'_{10}$  is given by Equation 7-15.

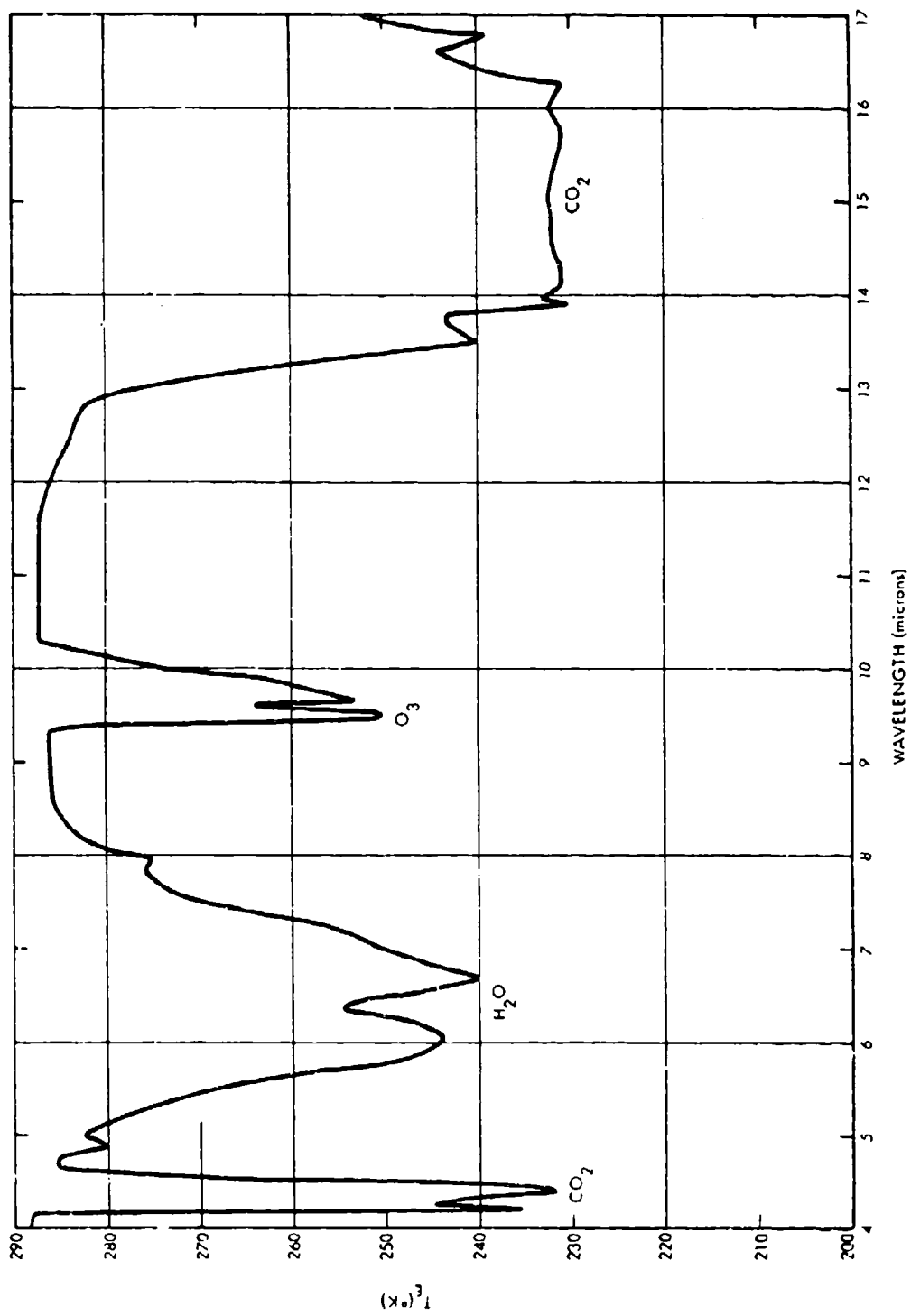


Figure 7-8. Equivalent temperature of earthshine as a function of wavelength.

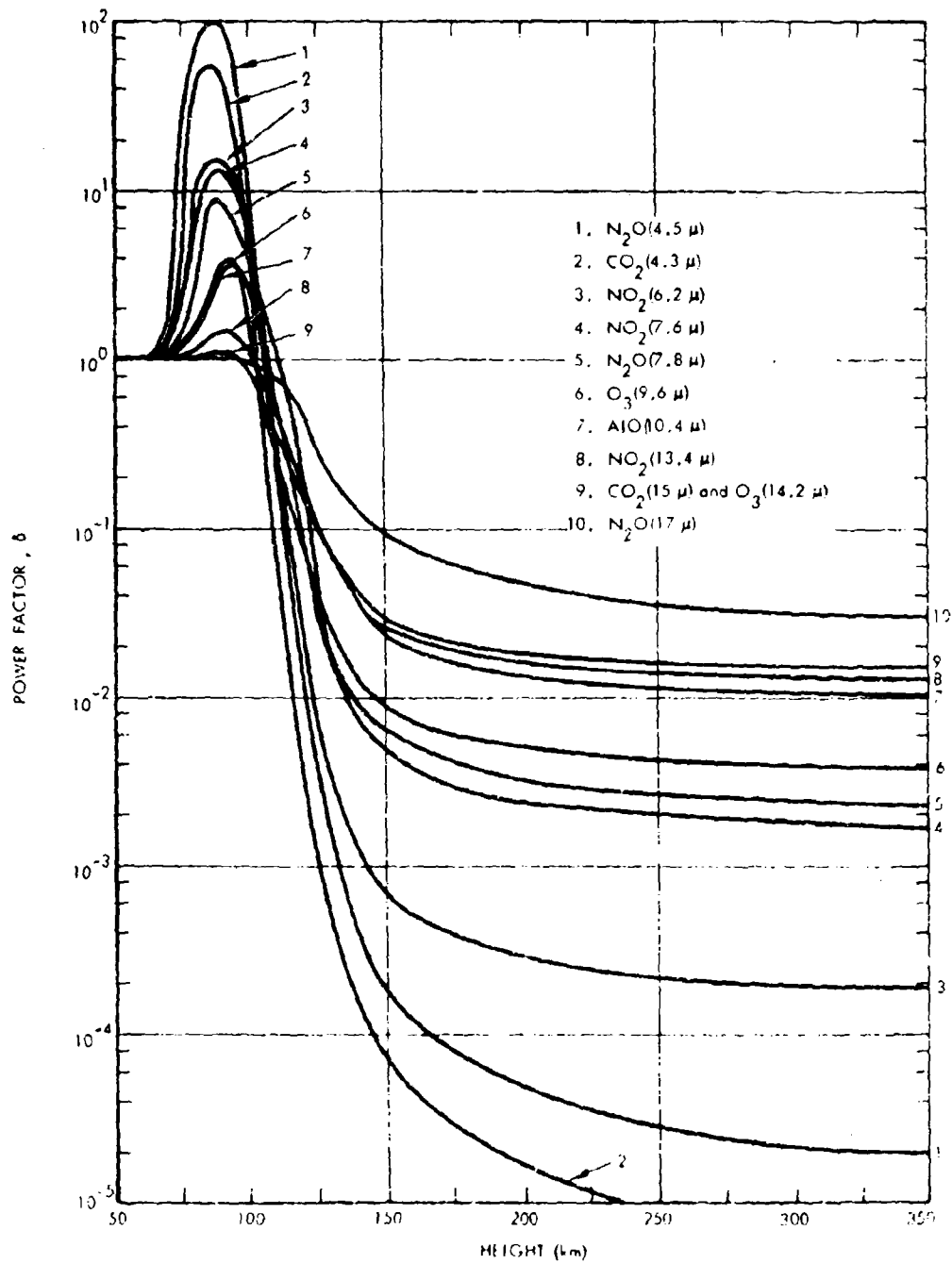


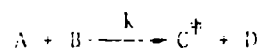
Figure 7-9. Power factor in "collision limited" radiation for the ambient atmosphere.

### Nonthermal Emission

Unlike thermal emission that requires an elevation in the temperature for its enhancement, the nonthermal emission processes considered below can be excited without an appreciable temperature rise. They may produce significant infrared radiation over large volumes of space, and for long periods of time.

### Chemiluminescence

For an arbitrary two-body reaction between species A and B that forms product species C and D such that C is vibrationally excited:



the volume rate of emission per steradian in the infrared V-R bands of molecule C is\*

$$J_{\text{chemi.}} = \frac{h\nu}{4\pi} \bar{\nu}_{\nu} k [A][B] \quad (7-69)$$

Here,  $k$  is the rate coefficient for the reaction and  $\bar{\nu}_{\nu}$  is the average number of photons of frequency  $\nu$  emitted per reaction. The spectral distribution of power is determined by  $\bar{\nu}_{\nu}$ .

Calculation of  $\bar{\nu}_{\nu}$  for any given reaction depends on knowing both the distribution of vibrational states immediately following the reaction and the quenching frequencies for each of the states. At the present time, neither of these is well known. In the absence of good data, calculations of  $\bar{\nu}_{\nu}$  are sometimes made by assuming that initially the vibrational states

\* For a three-body reaction, Equation 7-69 should be multiplied by  $[M]$ , the concentration of the third body, and  $k$  then refers to the rate coefficient for the three-body reaction.



are populated equally up to the maximum allowed by energy conservation. On this basis, one half of the available energy is allotted to vibrational motion. If  $v_{\max}$  is the vibrational quantum number for the highest state that can thus be populated, then in the absence of quenching, the value of  $\bar{\phi}$  for the fundamental band is approximately:

$$\bar{\phi}_{\text{fund.}}^0 \approx v_{\max}/2 \quad (7-70)$$

With quenching

$$\bar{\phi}_{\text{fund.}} \approx \bar{\phi}_{\text{fund.}}^0 \frac{A_{10}}{\lambda_{10} + v_{10}} \quad (7-71)$$

Some examples of reactions that may be chemiluminescent in a nuclear environment are shown in Table 7-10. Included in the table are values for  $\Delta E$ , the maximum energy available for excitation, as well as values for  $v_{\max}$ ,  $\bar{\phi}_{\text{fund.}}^0$ , and  $\lambda$ . It should be emphasized that the values for  $\bar{\phi}^0$  shown in Table 7-10 are based on an assumed distribution of vibrational states and are not experimentally confirmed values. Indeed, the only laboratory data presently available, that for the third reaction in Table 7-10, suggest a value for  $\bar{\phi}$  that is lower than the one shown by factors of about 5 to 10 (Reference 7-46).

The concentrations  $[A]$  and  $[B]$  appearing in Equation 7-69 will generally be functions of time. Determination of them usually entails the simultaneous solution of several first-order nonlinear differential equations describing the various chemical reactions that involve the species  $A$  and  $B$ . The rate coefficient,  $k$ , may also vary with time by virtue of its dependence on the temperature.

Table 7-10. Some chemiluminescent reactions of atmospheric interest.

REACTION	$\Delta E$ (ev)	$v_{\max}$	$\bar{\phi}_{\text{fund}}^0$	$\lambda_{\text{fundamental}}$ (microns)
$H+O_3 \rightarrow OH+O_2$	3.3	9	4.5	2.7
$N+O_3 \rightarrow NO+O_2$	5.5	> 30	> 15	5.3
$N(^4S)+O_2 \rightarrow NO+O(^3P)$	1.4	6	3	5.3
$N(^2D)+O_2 \rightarrow NO+O(^3P)$	3.8	18	9	5.3
$N(^2D)+O_2 \rightarrow NO+O(^1D)$	1.8	8	4	5.3
$O^+(^4S)+N_2 \rightarrow NO^++N(^4S)$	1.1	3	1.5	4.3
$N_2^++O \rightarrow NO^++N(^4S)$	3.1	11	5.5	4.3
$\rightarrow NO^++N(^2D)$	0.7	2	1	4.3
$N^++O_2 \rightarrow NO^++O(^3P)$	6.7	28	14	4.3
$\rightarrow NO^++O(^1D)$	4.7	18	9	4.3
$\rightarrow NO^++O(^1S)$	2.5	9	4.5	4.3
$NO+O+M \rightarrow NO_2+M$	3.1	(19,33,15)	(9.5,16,7.5)	(7.6,13.4,6.2)
$NO+O_2 \rightarrow NO_2+O$	2.1	(13,22,10)	(6.5,11,5)	(7.6,13.4,6.2)
$O+O+M \rightarrow O_2+M$	1.1	(7,12,9)	(3.5,6.4,5)	(9,14.3,9.6)

## Vibraluminescence

### CO<sub>2</sub> Vibraluminescence

Probably the most efficient vibraluminescent process in the atmosphere is Reaction 7-21 involving the transfer of vibrational energy from N<sub>2</sub> to CO<sub>2</sub>. Figure 7-10 shows the lowest vibrational energy level diagram for CO<sub>2</sub> and N<sub>2</sub> molecules. The energy of the  $v = 1$  state of N<sub>2</sub> is seen to differ from that of the (00<sup>+</sup>1) state of CO<sub>2</sub> by only 18 cm<sup>-1</sup>. After energy transfer to CO<sub>2</sub> has occurred, the (00<sup>+</sup>1) state of CO<sub>2</sub> can decay by radiation to the (00<sup>+</sup>0), (10<sup>+</sup>0), and (02<sup>+</sup>0) states with emission of bands at 4.3, 10.4, and 9.4μ, respectively. The corresponding transition probabilities are designated as A<sub>1</sub>, A<sub>2</sub>, and A<sub>3</sub>. Subsequent cascade from the (10<sup>+</sup>0) and (02<sup>+</sup>0) states lead to radiation at 13.8, 16.2, and 15μ with corresponding transition probabilities A<sub>6</sub>, A<sub>4</sub>, and A<sub>5</sub>. Values for these transition probabilities are shown in Table 7-11.

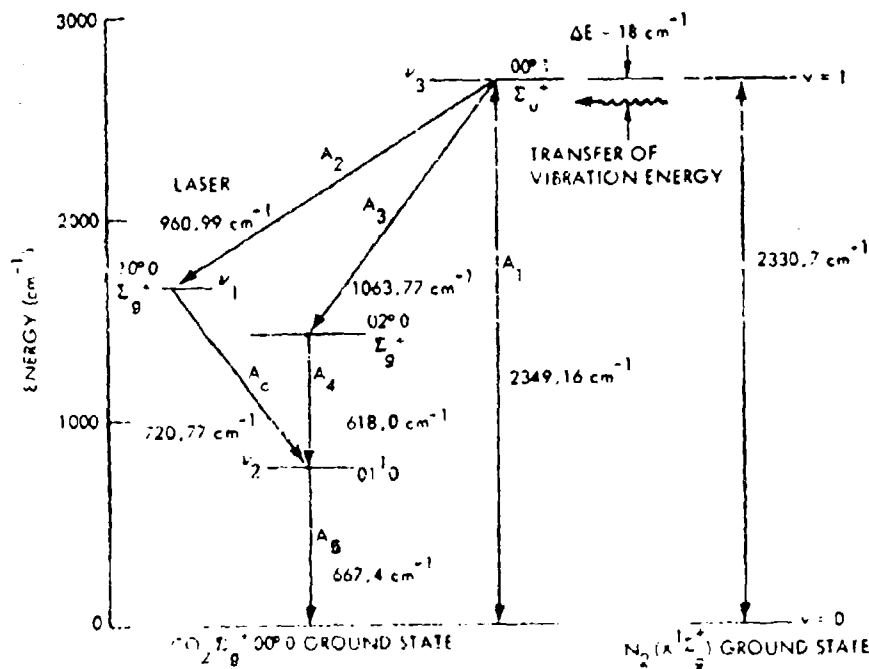


figure 7-10. Lower vibrational level scheme for CO<sub>2</sub> and N<sub>2</sub> molecules.

Table 7-11. Transition probabilities between some vibrational states of CO<sub>2</sub>

TRANSITION	A <sub>i</sub> (SEC <sup>-1</sup> )	λ (MICRONS)	REFERENCE
(00 <sup>0</sup> 1)-(00 <sup>0</sup> 0)	A <sub>1</sub> =390	4.3	7-47
(00 <sup>1</sup> 1)-(10 <sup>0</sup> 0)	A <sub>2</sub> =0.47	10.4	7-47
(00 <sup>1</sup> 1)-(02 <sup>0</sup> 0)	A <sub>3</sub> =0.70	9.4	7-47
(02 <sup>0</sup> 0)-(01 <sup>1</sup> 0)	A <sub>4</sub> =0.96	16.2	7-47
(01 <sup>1</sup> 0)-(00 <sup>0</sup> 0)	A <sub>5</sub> =1.5	15	7-48
(10 <sup>0</sup> 0)-(01 <sup>1</sup> 0)	A <sub>6</sub> =1.05	13.9	7-47

The power radiated in each of the bands can be found by applying the basic radiation formula (Equation 7-8). In the steady state, the concentration of CO<sub>2</sub> molecules in excited vibrational states is determined by equating the excitation rate of each state to the deexcitation rate, with proper allowance made for collisional quenching. In particular, if  $\nu_1$ ,  $\nu_2$ ,  $\nu_3$ , and  $\nu_4$  are the quenching frequencies for the (001), (010), (100), and (020) states, respectively, then

$$P_{00}(001) \approx \frac{I_0 I_{00} A_1 \nu_1}{A_1 + \nu_1} \quad (7-12)$$

$$P_{00}(010) = \left( \frac{\nu_2}{A_2 + \nu_2} \right) P_{00}(001) \quad (7-13)$$

$$P_{00}(100) = \left( \frac{\nu_3}{A_3 + \nu_3} + \frac{\nu_4}{A_4 + \nu_4} \right) \frac{I_{00} I_{00} A_1}{A_1 + \nu_1} \quad (7-14)$$

$$[\text{CO}_2(020)] = \left( \frac{A_3}{A_4 + v_4} \right) [\text{CO}_2(001)] \quad (7-75)$$

The fastest quenching process for the (001) state is the inverse to Reaction 7-22. Rates for this reaction, and those for quenching certain other states of  $\text{CO}_2$  including (010), can be found in References 7-45 and 7-46.

In the absence of any continuing mechanism for vibrational excitation of  $\text{N}_2$  molecules, the concentration  $[\text{N}_2(1)]$  will decay exponentially from its initial value.\* That is,

$$[\text{N}_2(1)] = [\text{N}_2(1)]_0 e^{-t/\tau_1} \quad (7-76)$$

where the time constant,  $\tau_1$ , is given by

$$\tau_1 = \frac{A_1 + A_2 + A_3 + v_4}{(A_1 + A_2 + A_3 + v_4) [\text{CO}_2]} \quad (7-77)$$

Equations 7-8 and 7-72 through 7-77 are sufficient to determine  $\text{CO}_2$  vibrationaluminescence once values for the quenching rates are provided.

#### Vibraluminescence Involving Other Species

The rate of energy transfer from  $\text{N}_2^+$  or  $\text{O}_2^+$  to infrared-active species of atmospheric interest other than  $\text{CO}_2$  has not been measured. The rates can be estimated, however, by applying the modified Rapp and Englander-Golden model (reference 7-26) that gives, for the probability of the exchange collision

$$A_{12}(1) + B_{12}(1) \rightarrow A_{12}(2) + B_{12}(2)$$

\* In a nuclear environment,  $\text{N}_2(1)$  is produced mainly by the prompt x-ray deposition.

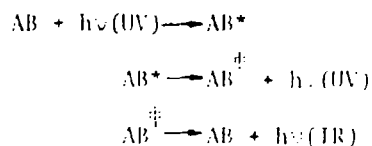
the expression

$$\langle p_{v_1 v_1'}^{v_2 v_2'} \rangle = \frac{512\pi^3 c u^2 L^3 E_d}{h^2} \left( \frac{2\pi kT}{3L} \right)^{1/2} U_{v_1 v_1'}^2 U_{v_2 v_2'}^2 \exp \left\{ -6 \left( \frac{\mu}{kT} \right)^{1/3} (\pi c L E_d)^{2/3} \right\} \quad (7-78)$$

Here,  $\mu$  is the reduced collision mass,  $L \approx 0.2\text{\AA}$  is the potential range parameter,  $U_{vv'}$  is the matrix element for the  $v$  to  $v'$  vibrational transition, and  $E_d$  is the energy defect in  $\text{cm}^{-1}$ . Some specific applications of Equation 7-78 can be found in Reference 7-20a.

### Solar-Induced Fluorescence

The infrared (IR) emission induced in a molecule AB by absorption of ultraviolet (UV) or visible light can be described by the processes:



As usual, the symbols  $*$  and  $\ddagger$  refer to electronic and vibrational excitation, respectively. The rate of IR-photon emission is

$$\dot{I}_i = \tau \dot{P} \quad (\text{photons sec}^{-1} \text{molecule}^{-1}) \quad (7-79)$$

where  $\dot{P}$  is the electronic excitation rate and  $\tau$  is the number of IR photons emitted per UV absorption. In terms of the Einstein B coefficient (see Equations 7-10 to 7-13),

$$\dot{P} = \frac{c_1}{4} \frac{B_{10}}{f} \frac{2\pi\nu}{c} \quad (7-80)$$

where  $\rho_{nm}$  is the energy density (ergs  $\text{cm}^{-3} \text{Hz}^{-1}$ ) of the radiation field. Equations 7-11, 7-27, and 7-80 then lead to the result

$$\dot{\xi} = \frac{\pi c^2}{mc} n \mathcal{F}_\nu f_{mn} \quad (7-81)$$

where  $\mathcal{F}_\nu = c\rho_\nu/h\nu$  is the photon flux (photons  $\text{cm}^{-2}\text{sec}^{-1}\text{Å}^{-1}$ ).

As an example, Table 7-12, based on Equation 7-81, shows the photon emission rate in the fundamental bands of  $\text{AlO}$  and  $\text{NO}$  arising from solar-induced fluorescence.  $n$  will normally be of the order of unity, so the last column in Table 7-12 is an estimate of  $\dot{\xi}$ . The power emitted per unit volume per steradian in the V-R bands is then given by

$$J_{\text{fluorescence}} = \frac{h\nu}{4\pi} \dot{\xi} [\text{AB}] \quad (7-82)$$

Further details, particularly with respect to the  $\text{AlO}$  and  $\text{NO}$  calculations, can be found in Reference 7-49.

Table 7-12. Photon (IR) emission rate per molecule from solar UV fluorescence.

MOLECULE	ABSORBING BAND SYSTEM	UV WAVE-LENGTH (Å)	$f_{X \rightarrow A}$	$\mathcal{F}_\nu$ (photons $\text{cm}^{-2} \text{sec}^{-1} \text{Å}^{-1}$ )	IR WAVE-LENGTH (microns)	$\dot{\xi}/n$ (IR photons $\text{sec}^{-1} \text{molecule}^{-1}$ )
$\text{AlO}$	$X^2\Sigma^+ \rightarrow A^2\Sigma$	4800	$1.7 \times 10^{-2}$	400	10.4	0.2
$\text{NO}$	$X^2\Pi \rightarrow A^2\Sigma$	2200	$\approx 7 \times 10^{-4}$	$\approx 0.3$	5.3	$\approx 6 \times 10^{-6}$

## REFERENCES

- 7- 1. Richtmyer, F. K., and E. H. Kennard, Introduction to Modern Physics, McGraw-Hill (1942).
- 7- 2. Panofsky, W. K. H. and M. Phillips, Classical Electricity and Magnetism, Addison-Wesley (1955).
- 7- 3. Pauling, L. and E. B. Wilson, Introduction to Quantum Mechanics, McGraw-Hill (1942).
- 7- 4. Cottrell, T. L. and J. C. McCoubrey, Molecular Energy Transfer in Gases, Butterworth, London (1961).
- 7- 5. Callear, A. B., Appl. Optics, Suppl. on Chem. Lasers, 145 (1965).
- 7- 6. Millikan, R. C. and D. R. White, "Systematics of Vibrational Relaxation," J. Chem. Phys. 39, 3209 (1963).
- 7- 7. Massey, H. S. W. and E. H. S. Burhop, Electronic and Ionic Impact Phenomena, Clarendon Press (1952).
- 7- 8. Stolarski, R. S. and A. E. S. Green, "Calculations of Auroral Intensities from Electron Impact," J. Geophys. Res. 72, 3967 (1967).
- 7- 9. Schulz, G. J. and J. T. Dowell, "Excitation of Vibrational and Electronic Levels in  $O_2$  by Electron Impact," Phys. Rev. 128, 174 (1962).
- 7-10. Schulz, G. J., "Vibrational Excitation of  $N_2$ , CO, and  $H_2$  by Electron Impact," Phys. Rev. 135, A988 (1964).
- 7-11. Hake, R. D. Jr., and A. V. Phelps, "Momentum-Transfer and Inelastic-Collision Cross Sections for Electrons in  $O_2$ , CO, and  $CO_2$ ," Phys. Rev. 158, 70 (1967).
- 7-12. Takayanagi, K., Prog. Theor. Phys. Suppl. No. 40, 216 (1967).
- 7-13. Kieffer, L. T., "Bibliography of Low-Energy Electron Collision Cross Section Data," NBS, Miscellaneous Publication 289, March 1967.



- 7-14. Borst, W. L., "Excitation of Several Important Metastable States of  $N_2$  by Electron Impact," *Phys. Rev. A.* 5, 648 (1972).
- 7-15. Seaton, M. J., Atomic and Molecular Processes (edited by D. R. Bates), Chap. 11, Academic Press (1962).
- 7-16. Mumma, M. J. and E. C. Zipf, "Dissociative Excitation of Vacuum Ultraviolet Emission Features by Electron Impact on Molecular Gases I.  $H_2$  and  $O_2$ ," *J. Chem. Phys.* 55, 1661 (1971).
- 7-17. Mumma, M. J. and E. C. Zipf, "Dissociative Excitation of Vacuum Ultraviolet Emission Features by Electron Impact on Molecular Gases II.  $N_2$ ," *J. Chem. Phys.* 55, 5582 (1971).
- 7-18. Herzfeld, K. F. and T. A. Litovitz, Absorption and Dispersion of Ultrasonic Waves, Academic Press (1959).
- 7-19. Gilmore, F. R., et al., "A Review of Atomic and Molecular Excitation Mechanisms in Non Equilibrium Gases up to 20000°K," *J. Quant. Spectrosc. Radiat. Transfer.* 9, 157 (1969).
- 7-20. Rapp, D. and P. Englander-Golden, "Resonant and Near-Resonant Vibrational-Vibrational Energy Transfer Between Molecules in Collisions," *J. Chem. Phys.* 40, 573 and 3120 (1964).
- 7-20a. Fisher, E. R. and R. H. Kummier, "Relaxation by Vibration-Vibration Exchange Processes, Part II: Binary Mixtures," R67SD46, Space Sciences Laboratory, General Electric Company, August 1967.
- 7-21. Hunten, D. M. and M. B. McElroy, "Quenching of Metastable States of Atomic and Molecular Oxygen and Nitrogen," *Rev. Geophys.* 4, 303 (1966).
- 7-22. MacKay, G. I. and R. E. March, "Collisional Deactivation Rates of Electronically Excited Molecular Ions II," *Canadian J. Chemistry* 50, 1 (1972).
- 7-23. Herzberg, G., Atomic Spectra and Atomic Structure, Dover Publications (1944).
- 7-24. Herzberg, G., Spectra of Diatomic Molecules, Van Nostrand-Reinhold Company (1950).
- 7-25. Herzberg, G., Infrared and Raman Spectra of Polyatomic Molecules, Van Nostrand-Reinhold Company (1945).
- 7-26. Herzberg, G., Electronic Spectra and Electronic Structure of Polyatomic Molecules, Van Nostrand-Reinhold Company (1966).

- 7-27. Chamberlain, J. W., Physics of the Aurora and Airglow, Academic Press (1961).
- 7-28. Wiese, W. L., et al., Atomic Transition Probabilities, Vol I, NSRDS-NBS4 - National Bureau of Standards 4, May 20, 1966.
- 7-29. Gilmore, F. R., "Potential Energy Curves for  $N_2$ , NO,  $O_2$ , and Corresponding Ions," RM-4034-PR, The Rand Corporation, June 1964.
- 7-30. Gilmore, F. R., "Basic Energy-Level and Equilibrium Data for Atmospheric Atoms and Molecules," RM-5201-ARPA, The Rand Corporation, March 1967.
- 7-31. Gilmore, F. R., Private Communication, 1971.
- 7-32. Penner, S. S., Quantitative Molecular Spectroscopy and Gas Emissivities, Addison-Wesley Publishing Company (1959).
- 7-33. Townes, C. H. and A. L. Schawlow, Microwave Spectroscopy, McGraw-Hill (1955).
- 7-34. Henry, R. J. W., et al., "Scattering of Electrons by C, N, O,  $N^+$ ,  $O^+$ , and  $O^{++}$ ," Phys. Rev. 178, 218 (1969).
- 7-35. McKee, J.W., et al., B1341
- 7-36. Moiseiwitch, B.L. and S.J. Smith, "Electron Excitation of Atoms," Rev. Mod. Phys. 40, 238 (1968).
- 7-37. Bely, O. and H. Van Regemorter, "Excitation and Ionization by Electron Impact," in Annual Review of Astronomy and Astrophysics, 8, 329 (1970).
- 7-38. Allen, C.W., Astrophysical Quantities, The Athlone Press, (1962).
- 7-39. Sappenfield, D., B2710.
- 7-40. Archer, E. H., "Electron Cooling and Excitation of Visible Radiation Induced by Collisions With N,  $N^+$ , and  $O^+$ ," DNA 2896 Mission Research Corporation, July 1972.
- 7-41. O'Neil and G. Davidson, "The Fluorescence of Air and Nitrogen Excited by Energetic Electrons," ASE-1602, AFCPL-67-0277, American Science and Engineering Inc., 1 Jan. 1968.

- 7-42. Penner, S. S. and L. D. Gray, "Approximate Infrared Emissivity Calculations for HCl at Elevated Temperatures," J. Opt. Soc. Am. 51, 460 (1961).
- 7-43. Plass, G. H., "Models for Spectral Band Absorption," J. Opt. Soc. Am. 48, 690 (1958).
- 7-44. Plass, G. N., "Useful Representations for Measurements of Spectral Band Absorption," J. Opt. Soc. Am. 50, 868 (1960).
- 7-45. Anding, D. C., "Band-Model Methods for Computing Atmospheric Slant-Path Molecular Absorption," NAVSOP-2499-1, The University of Michigan, Willow Run Laboratories, Feb. 1967.
- 7-46. Hushfar, F., et al., "Infrared Chemiluminescence of the Reaction  $N+O_2 \rightarrow NO+O$ ," App. Opt. 10, 1843 (1971).
- 7-47. Statz, H., et al., "Transition Probabilities Between Laser States in Carbon Dioxide," J. App. Phys. 37, 4278 (1966).
- 7-48. Ludwig, C. B., et al., "High Temperature Spectra of the 15- $\mu$  Band of  $CO_2$ ," General Dynamics GD/C-DBE65-024 (1965).
- 7-49. Holland, D.H., C. H. Humphrey, G. Gioumousis, M. Scheibe, D. R. Churchill, and L. M. Tannenwald, 82040.
- 7-50. Tolman, Richard C., The Principles of Statistical Mechanics, Oxford Uni. Press (1938).

CHAPTER 8

EQUILIBRIUM COMPOSITION OF AIR

William C. Hart

Dan H. Holland\*

Mission Research Corporation

August 1975

\* Now at New Millennium Associates, Santa Barbara, CA

## TABLE OF CONTENTS

	PAGE
8.0 INTRODUCTION	389
8.1 REFERENCES	395

## LIST OF FIGURES

Figure 8-1	The equilibrium composition of dry air for $T = 2000^{\circ}\text{K}$ .	390
Figure 8-2	The equilibrium composition of dry air for $T = 6000^{\circ}\text{K}$ .	391
Figure 8-3	The equilibrium composition of dry air for $T = 9000^{\circ}\text{K}$ .	392
Figure 8-4	The equilibrium composition of dry air for $T = 12000^{\circ}\text{K}$ .	393
Figure 8-5	The equilibrium composition of dry air for $T = 15000^{\circ}\text{K}$ .	394

## CHAPTER 8

### EQUILIBRIUM COMPOSITION OF AIR

#### 8.0 INTRODUCTION

The emphasis in this volume is on perturbations produced in air by various external agents, and the response of air to these perturbations. Nevertheless, it is convenient for many applications to have available the equilibrium composition of air in the absence of perturbations. The calculation of equilibrium properties is simple in principle but rather complicated in practice. As input data one requires knowledge of ionization potentials, dissociation energies, the configurations of the various atomic and molecular species, *etc.* The calculation then proceeds according to the well-known laws of statistical mechanics.

In this chapter we present only several curves showing the equilibrium composition of air as a function of density at a number of temperatures (Reference 8-1). For details as to input data and methods of calculation, the reader is referred to the reference works cited. Extensive tables have been prepared by Gilmore (References 8-2, 3, 4).

The reference density is  $\rho_0 = 1.29313 \times 10^{-3} \text{ gm/cm}^3$  in the following figures (Reference 8-1, Figures 11-9 to 11-13).

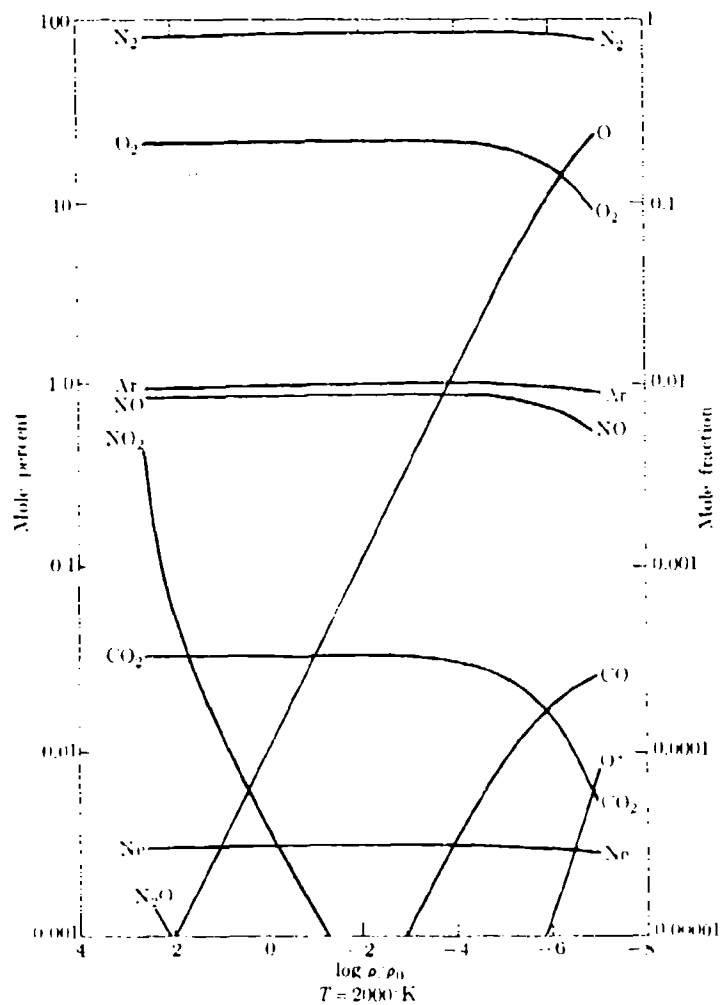


Figure 8-1. The equilibrium composition of dry air for  $T = 2000^{\circ}\text{K}$ .

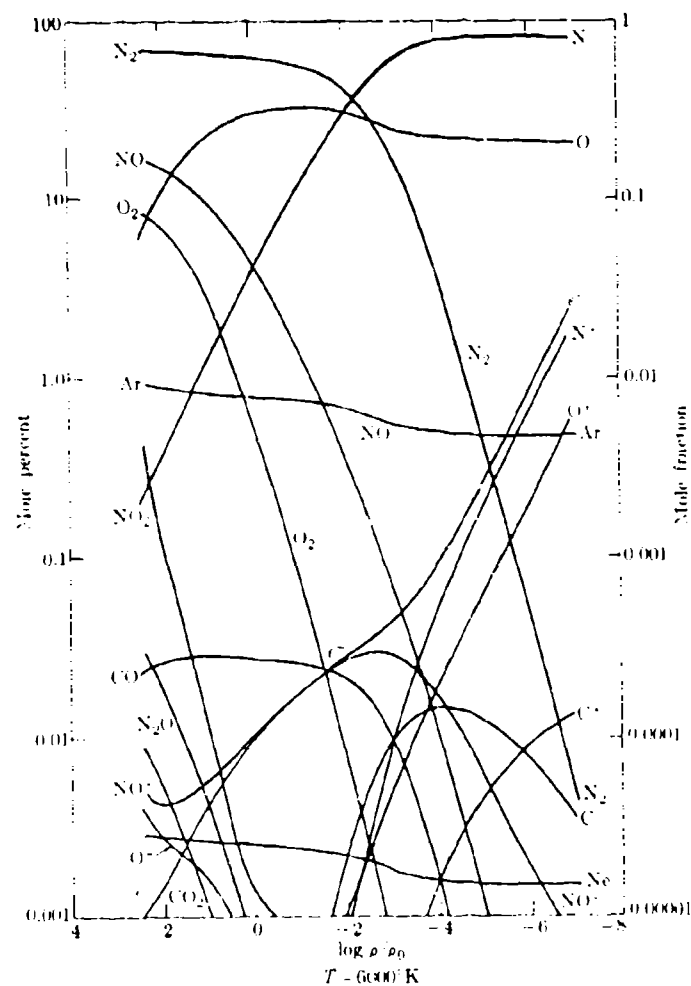


Figure 8-2. The equilibrium composition of dry air for  $T = 6000^{\circ}\text{K}$ .



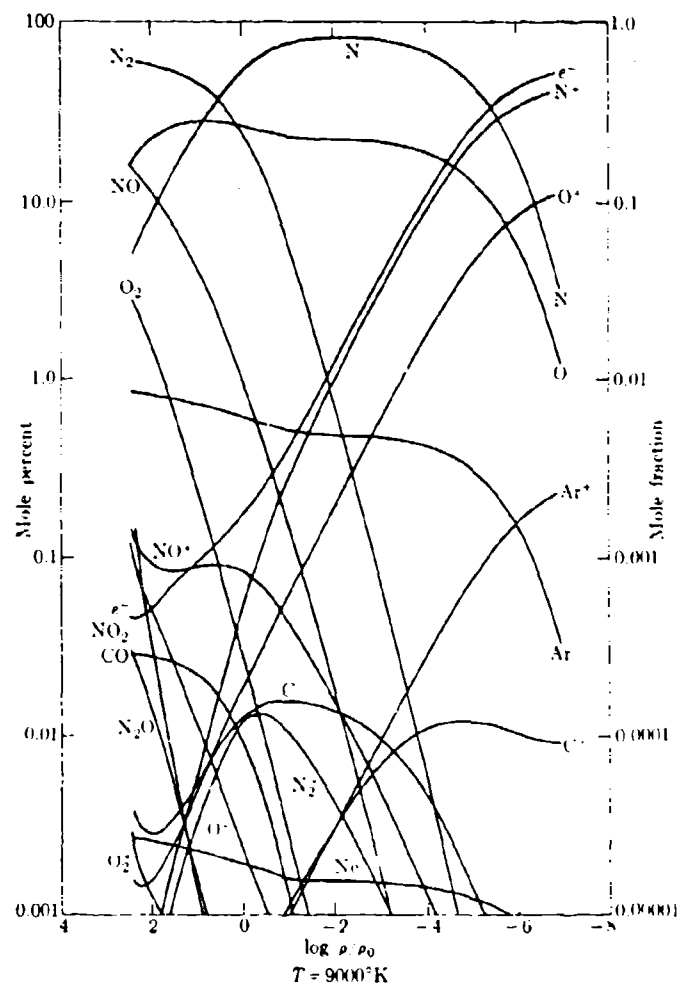


Figure 8-3. The equilibrium composition of dry air for  $T = 9000^\circ\text{K}$ .

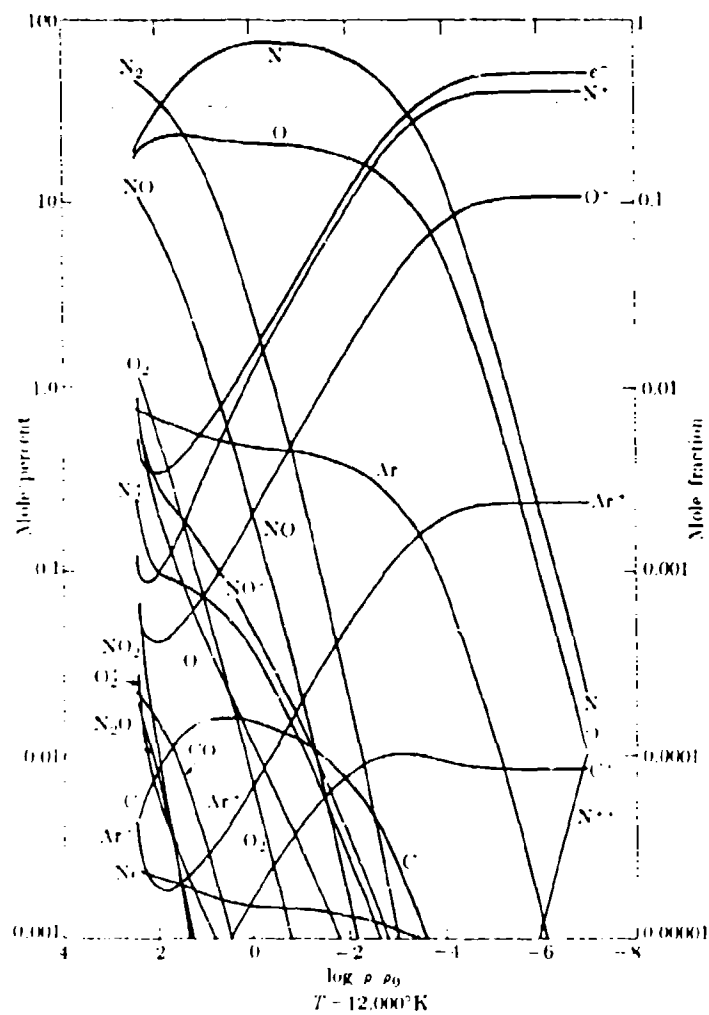
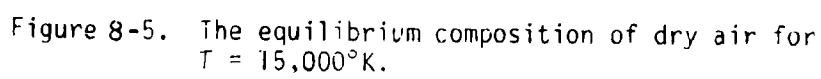


Figure 8-4. The equilibrium composition of dry air for  $T = 12,000^\circ\text{K}$ .



## 8.1 REFERENCES

- 8-1. Bond, T.W., K.M. Watson and J.A. Welch, Atomic Theory of Gas Dynamics, Addison Wesley Publishing Co. 1965.
- 8-2. Gilmore, F. R., Equilibrium Composition and Thermodynamic Properties of Air to 24,000°K, RM-1534 (Aug. 24 1955), The Rand Corporation, Santa Monica, Calif.
- 8-3. Gilmore, F.R., Additional Values for the Equilibrium Composition and Thermodynamic Properties of Air, The Rand Corporation, RM 2328, December 1959.
- 8-4. Gilmore, F.R., Thermal Radiation Phenomena, Vol. 1, The Equilibrium Thermodynamic Properties of High Temperature Air, Lockheed Research Laboratory, DASA 1917, May 1967.
- 8-5. Brush, S. R. Annotated Bibliography of Theories on Equation of State of High Temperature Gases, LRL, Livermore, Calif., UCRL 6473 and Supplements, July 1963.
- 8-6. Brush, S. R. High Pressure Equation of State Bibliography and Index 1925-1962, LRL, Livermore, Calif. UCRL 7160, January 1963.
- 8-7. Fuchs, K., G. J. Kynch, and R. Peirls, The Equation of State of Air at High Temperatures, British Dept. of Atomic Energy BDDA-16 Rept. MS 61 (Dec. 1942), available as PBL 87018, from the Office of Technical Services, U.S. Dept. of Commerce, Washington, D.C.
- 8-8. Bethe, H. A., The Specific Heat of Air up to 25,000°C, OSRD Report 369 (Feb. 9, 1942).
- 8-9. Hirschfelder, J.O. and J. L. Magee, Thermodynamic Properties of Air at High Temperatures, MDDC-590 (LADC-122) (Jan. 1, 1947), U.S. Atomic Energy Commission, Oak Ridge, Tenn.
- 8-10. Hirschfelder, J. O. and C. F. Curtiss, Thermodynamic Properties of Air II, Dept. of Chemistry, U. of Wisconsin (Naval Research Laboratory) Rept. CM-518 (1948).

- 8-11. Latter, R., Equation of State of Air on the Statistical Model, RM-1344-AEC (September 21, 1954), The Rand Corporation, Santa Monica, Calif.
- 8-12. Hilsenrath, J. and C. W. Beckett, Tables of Thermodynamic Properties of Argon-Free Air to 15,000°K, Arnold Engineering Development Center Report AEDC-TN-56-12, ASTIA Document No. AD-98974, September 1956, available as PB 131276, from the Office of Technical Services, U.S. Dept. of Commerce, Washington, D.C.
- 8-13. Logan, J. G., Jr., and C. E. Treanor, Thermodynamic Properties of Air from 3000°K to 10,000°K at Intervals of 100°K, Report No. BE-1007-A-3, Cornell Aeronautical Laboratory, Buffalo, New York (January 1957).
- 8-14. Predvoditelev, A. S., E. U. Stupochenko, E. U. Samuilov, I. P. Stanhanov, A. S. Pleshanov and I. B. Rozhdestvenskii, Tables of Thermodynamic Functions of Air for the Temperature Range 6000°-12,000°K and Pressure Range 0.001-1000 atm., Academy of Sciences USSR, also temperature range 12,000 - 20,000°K (1959) Infosearch Limited, London (1958).
- 8-15. Hilsenrath, J., M. Klein, Tables of Thermodynamic Properties of Air in Chemical Equilibrium Including Second Virial Corrections from 1500°K to 15,000°K, Arnold Eng. Dev. Center, U.S. Air Force, AEDC-TDR-63-161, August 1963; AEDC-TR-65-58, March 1965.
- 8-16. Stull, D. R. and H. Prophet, JANAF Thermochemical Tables, 2nd Edition, NSRDS-NBS37, July 1970.
- 8-17. Epstein, P. S., Textbook of Thermodynamics, J. Wiley and Sons, New York 1937.
- 8-18. White, W. B., S. M. Johnson and E. B. Dantzig, J. Chem. Phys. 28, 751, 1958.
- 8-19. Hochstim, A. and B. Adams, Progress in International Research on Thermodynamic and Transport Properties, Am. Soc. Mech. Eng., Academic Press, New York 1962, p. 228.

## CHAPTER 9

### THE BETA PATCH

Dan H. Holland \*

May 1975

\* Now at How Millennium Associates, Santa Barbara, CA

## TABLE OF CONTENTS

	<u>Page</u>
LIST OF FIGURES	399
9.1 INTRODUCTION	400
9.2 BETA ENERGY DEPOSITION	405
9.3 BETA PATCH ATTENUATION	412
9.4 A SIMPLE MODEL OF BETA PATCH ATTENUATION	416
9.5 DISCUSSION AND SUMMARY	430
REFERENCES	434

## LIST OF FIGURES

FIGURE	PAGE
9-1. Geometry of beta patch formation.	400
9-2. Energy loss of betas in air.	406
9-3. Comparison of energy deposition profiles calculated by Kownacki and Lowen.	413
9-4. Comparison of energy deposition profiles calculated by Lowen and Knapp.	414
9-5. Comparison of beta energy deposition profiles for dip angles of 30 and 90°.	415
9-6. Daytime beta patch attenuation.	417
9-7. Nighttime beta patch attenuation.	417
9-8. Calculated one-way attenuation through the beta patch (daytime).	426
9-9. The function $F$ .	428
9-10. Calculated one-way attenuation through the beta patch (nighttime).	429
9-11. The function $G$ .	431



## CHAPTER 9

### THE BETA PATCH

#### 9.1 Introduction

The beta patch is a layer of D-region ionization produced by delayed betas from radioactive fission fragments contained in high altitude ( $h \geq 100$  km) debris clouds. At such high altitudes scattering by air particles is negligible, and hence, the motion of the betas is strongly influenced by the geomagnetic field. The betas spiral down the field lines into the atmosphere, where they deposit their energy in ionizing collisions with air molecules, predominately in the 50-90 km altitude range. Thus the beta patch is just the projection along field lines onto the D-region of the debris cloud, as illustrated in Fig. 9-1. The radius of gyration of MeV betas in the geomagnetic field is of the order of 100 meters. Since typical debris distributions are tens or hundreds of kilometers in extent, the fact that the betas describe helical rather than straight line trajectories has little effect on the shape of the beta patch.

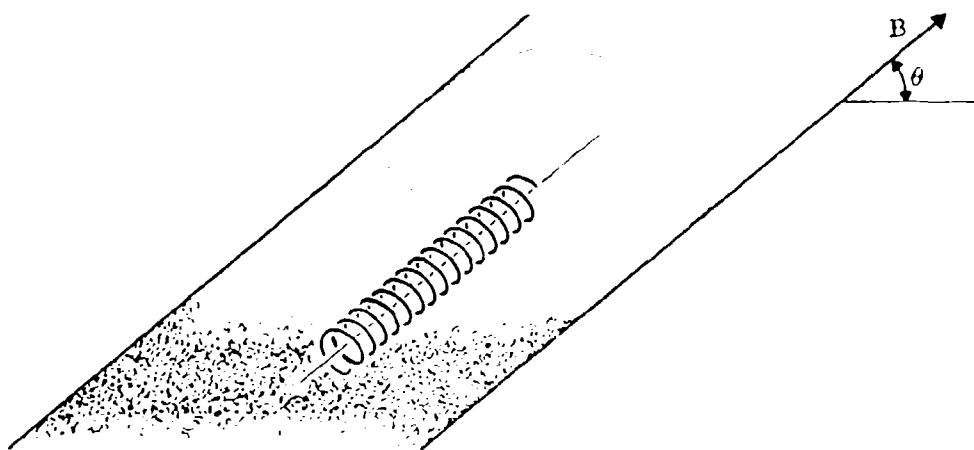


Figure 9-1. Geometry of Beta Patch Formation

If the debris lies on closed field lines, betas with an upward component of velocity parallel to the magnetic field follow the field to the magnetic conjugate region in the other hemisphere and form a beta patch there. Since the initial angular distribution of the betas is isotropic, the northern and southern beta patches are identical to the extent that the geomagnetic field is symmetric with respect to the equator. If the debris lies on open field lines, betas emitted upward along the field stream into the magnetotail and no beta patch is formed in the conjugate region west distant from the burst.

At low altitudes, below 30 km, the scattering of betas by air molecules dominates the magnetic forces and the field has little influence on the motion of the betas. At these altitudes the betas produce an ionized shell, the beta shell, surrounding the fireball/debris cloud. At still lower altitudes, the air density is so high that the betas are stopped and deposit their energy within the fireball/debris region to contribute to fireball blackout.

The importance of the beta patch lies in the large attenuation of radio and radar signals that propagate through the patch. For example, radio communications in the Pacific were severely disturbed for hours following the crash in 1966, and betas were probably responsible for this disturbance. The severity of the blackout produced by betas is much greater than that produced by a star surge, in spite of the fact that nearly equal quantities of energy are radiated in the two forms.

There are two reasons for the greater effectiveness of betas. The first is that the betas are guided by the geomagnetic field, and therefore deposit their energy over a smaller region where the energy flux is correspondingly higher. The second reason is that the gammas penetrate to lower altitudes, where the electrons they produce are quickly lost by attachment to oxygen molecules. The betas are deposited at higher altitudes, where the attachment rate is much lower, but where the collision frequency is still fairly high. Indeed the beta peak altitude is nearly optimum for producing radio attenuation.

The distribution with altitude of the energy deposited by a beta depends on its initial energy, the pitch angle of the helix along which it moves and the dip angle of the magnetic field. To find the total energy deposition profile for a given dip angle, it is necessary to sum over all pitch angles and over all energies in the fission beta spectrum. The spectrum varies with the time elapsed since fission, becoming softer and hence less penetrating with increasing time. The spectra of various fissile materials also differ, so the fraction of the yield contributed by the fission of various species must be known. In detailed calculations, variations with dip angle and beta spectrum must be taken into account. The results of such calculations are fairly insensitive to these factors, however, and in almost all cases practically all of the beta energy is deposited in the 50 to 90 km. altitude range.

The motion of charged particles in magnetic fields is discussed in Ch. 12.3.7. In a uniform field the pitch angle (i.e. the angle between the field and velocity vectors) of the helix described by the particle is constant, in the absence of collisions. If the field converges in the direction of

motion of the particle, however, the pitch angle increases, and conversely for a diverging field. The geomagnetic field converges with decreasing altitude. Hence, the pitch angle of the helix increases with decreasing altitude as an injected beta moves downward into the atmosphere. As a consequence of the increase in pitch angle, betas injected onto a given field line at a high altitude deposit their energy at higher altitudes than betas injected onto the same field line at a lower altitude.

From the standpoint of the ionization produced, the effect of the convergence of the geomagnetic field is negligible in most cases. The convergence of the field is important from the standpoint of trapping electrons into radiation belts, however. A small fraction of betas injected with pitch angles near 90 degrees have their pitch angles increased to 90 degrees because of the convergence of the field. At the point where this occurs, the beta is reflected, and now can its direction to now back upward along the field. If reflection occurs at a high enough altitude that scattering and energy loss are negligible, the beta is reflected repeatedly in the northern and southern hemispheres, and is trapped in a more or less stable orbit.

To the extent that convergence of the field can be neglected, betas of a given energy and pitch angle injected on the same field line produce the same energy deposition profile, regardless of the altitude of injection. If we assume accordingly that the ionization is independent of the altitude of injection, then the rate of ionization at a given point in the D-region is determined by the total rate of injection of betas into a magnetic flux tube of given cross-sectional area containing the point.

Since the spectrum and rate of radiation of betas by fission fragments are known, it is sufficient for ionization calculations to know the total number of fission fragments contained within a flux tube, or what is equivalent, the density per unit area of fission fragments on a horizontal plane when the entire debris distribution is projected parallel to the field onto the plane. This is an important simplification of the problem, since the distribution of fission fragments along the field lines need not be known for beta patch ionization and attenuation calculations. It has also the consequence that nothing about the longitudinal distribution of fission fragments along the field lines can be inferred from measurements of beta patch attenuation or ionization.

In the following sections of this chapter we present what might be called the basic theory of the beta patch. Various complications, such as changes in D-region chemistry, magnetic field perturbation, etc., are ignored here in the interests of simplicity. The detailed considerations involved in the basic model are discussed, and the results of machine calculations are summarized. For accurate results, these precise calculations are necessary. It is instructive, nevertheless, to perform crude analytical calculations also. These have the virtue of providing simple formulas for use in making rough estimates and they also expose the role played by various processes, thus enhancing our understanding of the nature of the phenomena occurring. Furthermore, in practical calculations great accuracy is seldom required because of the large uncertainties in debris distribution. An analytical model leading to simple

expressions that give results in good agreement with the machine calculations is discussed in Section 9-4.

## 9.2 Beta Energy Deposition

The average rate of energy loss per unit length by a fast electron is given by the Bethe-Bloch formula

$$-\frac{dE}{dx} = \frac{3\epsilon_0 N E^2 m c^2}{4 (E^2 - m^2 c^4)^{1/2}} \left\{ \ln \left[ \frac{(E - m c^2)^2 (E + m c^2)}{2 m c^2 I^2} \right] - \frac{m c^2 (2E - m c^2)}{E^2} \ln 2 + \frac{m^2 c^4}{E^2} + \frac{1}{8} \left( 1 - \frac{m c^2}{E} \right)^2 \right\} \quad (9-1)$$

where  $N$  is the density of atoms in the material being traversed,  $Z$  their mean atomic number,  $c$  the velocity of light, and  $m$  is the mass of the electron.  $E$  denotes the total relativistic energy of the electron

$$E = \frac{m c^2}{(1 - \frac{v^2}{c^2})^{1/2}} \quad (9-2)$$

so its kinetic energy is  $E - m c^2$ , with  $v$  denoting the velocity of the electron.

The quantity  $\epsilon_0$  in (9-1) is the Thomson cross section

$$\epsilon_0 = \frac{8\pi r_0^2}{3} = 6.57 \times 10^{-25} \quad (\text{cm}^2) \quad (9-3)$$

where  $r_0$  is the classical electron radius,  $2.80 \times 10^{-13}$  cm. Finally,  $I$  denotes the mean ionization potential of the atom, which we take to be 94 ev for air.  $\frac{dE}{dx}$  as calculated from (9-1) is shown in Fig. (9-1).

For all but very low energies, only the first term in the braces in (9-1) need be retained. Neglect of all the other terms leads to an error

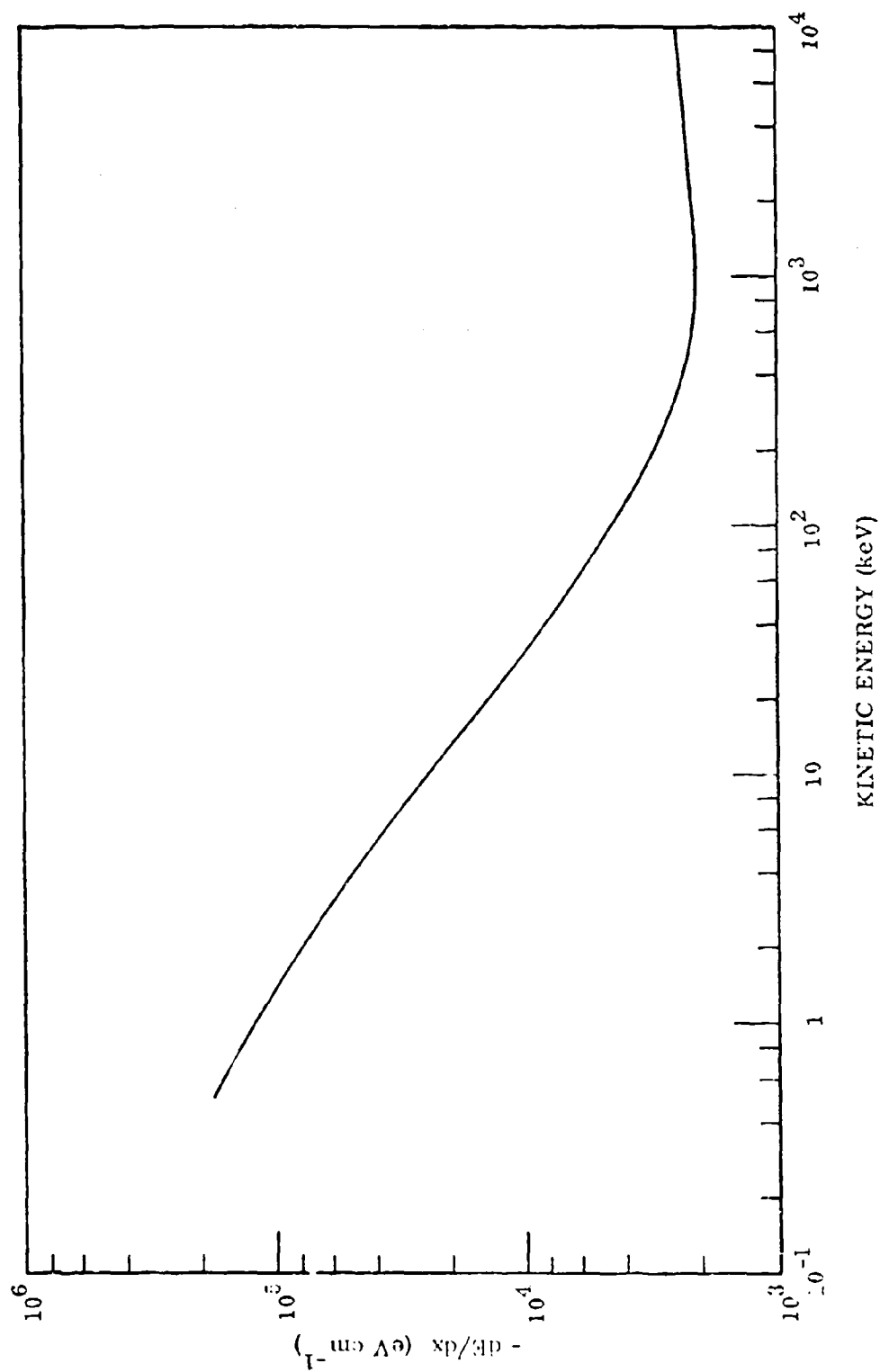


Fig. 9-2 Energy Loss of Betas in Air ( $1.29 \times 10^{-3} \text{ gm cm}^{-3}$ )

of but 5 percent for 5 KeV and only about 1 percent at 50 KeV. With this approximation, and taking  $Z = 7.2$  for air, we find

$$-\frac{dE}{dx} = 97.5 \frac{\rho}{\rho_0} \frac{E^2}{E^2 - m^2 c^4} \ln \left[ \frac{(E - mc^2)^2 (E + mc^2)}{2 mc^2 I^2} \right] \text{ (eV cm}^{-1}\text{)} \quad (9-4)$$

where  $\rho$  is the air density at the point of interest and  $\rho_0$  is the sea level atmospheric density, taken to be  $1.29 \times 10^{-3} \text{ gm cm}^{-3}$ .

As a beta progresses through the atmosphere its energy decreases. Because of the variation of atmospheric density with position, it is convenient to replace the length coordinate with a mass coordinate  $M$  given by

$$M = \int_{x_0}^x \rho(x) dx \quad (9-5)$$

We then have

$$\frac{dE}{dM} = \frac{1}{\rho} \frac{dE}{dx} \quad (9-6)$$

so that  $\frac{dE}{dM}$  depends only on the instantaneous energy of the beta and is independent of position and density. The mass traversed,  $M$ , and the instantaneous energy,  $E$ , are related to the initial energy,  $E_0$ , through the equation

$$M(E_0, E) = \int_E^{E_0} \frac{dE}{-dE/dM} \quad (9-7)$$

Equation (9-7) implicitly gives  $E$  as a function of  $E_0$  and  $M$ . In principle the expression can be inverted to obtain  $E$  as an explicit function of  $E_0$  and  $M$ , and the inversion can in fact be performed numerically.



Since  $\frac{dE}{dz}$  depends only on  $E$ , it follows that  $\frac{dE}{dz}$  is completely determined by knowledge of  $E_0$  and  $H$ , and can be regarded as a function of these variables.

The mass per unit area above altitude  $h$  is

$$\eta(h) = \int_h^{\infty} \rho(h') dh' = \rho(h) H(h) = \frac{p(h)}{g} \quad (9-8)$$

where  $\rho$ ,  $p$ , and  $H$  denote density, pressure and atmospheric scale height at altitude  $h$ , while  $g$  denotes the acceleration of gravity which is assumed to be constant over the altitude range of interest. The total mass actually traversed in arriving at altitude  $h$  by a beta entering the atmosphere from above and spiralling with constant pitch angle  $\phi$  down the field whose dip angle is  $\theta$  is

$$\mu(h, \phi) = \frac{\eta(h)}{\sin \theta \cos \phi} \quad (9-9)$$

The energy loss per unit length,  $\epsilon$ , measured along the axis of the cylinder is

$$\frac{dE}{ds} = \frac{1}{\cos \phi} \frac{dE}{dz} = \frac{\rho}{\cos \phi} \frac{dE}{dz} (E_0, \mu) \quad (9-10)$$

Now suppose that betas are being emitted isotropically from a plane source at a high enough altitude, say above 100 km, that the mass of air above the injection point is negligible. Let the number of betas emitted per unit area per unit time be  $H_0$ . We introduce the normalized energy distribution function  $f(E_0)$  such that

$$\int_{mc^2}^{\infty} f(E_0) dE_0 = 1 \quad (9-11)$$

Then the number of betas emitted per unit area per unit time per unit energy per steradian is  $\frac{N_B f(E_0)}{4\pi}$ . The corresponding flux per unit area normal to the field direction is increased by a factor  $(\sin \theta)^{-1}$ .

The rate of energy deposition per unit volume is obtained by multiplying this flux by  $\frac{dE}{ds}$  as given by (9-10) and integrating over the pitch angle and energy distributions.

$$\frac{dP}{dV}(h) = \frac{N_B \rho}{2 \sin \theta} \int_{E_{0 \min}(h)}^{\infty} dE_0 f(E_0) \int_0^{\varphi_{\max}} \left[ \frac{-dE}{ds}(E_0, \mu) \right] \frac{\sin \varphi d\varphi}{\cos \varphi} \quad (9-12)$$

The upper limit on the second integral,  $\varphi_{\max}$ , is the maximum pitch angle a beta with energy  $E_0$  can have and still penetrate to  $h$ , i.e., it is the pitch angle such that the mass traversed in reaching  $h$  is just equal to the range of a beta with energy  $E_0$ . From (9-9), therefore

$$\cos \varphi_{\max} = \frac{R(h)}{R(E_0) \sin \theta} \quad (9-13)$$

where  $R(E_0)$  is the range ( $\text{gm cm}^{-2}$ ) of a beta with energy  $E_0$ . Similarly, the lower limit on the first integral is the minimum energy the beta can have and still reach altitude  $h$ , i.e., the energy for which the range of the particle just equals the mass traversed as calculated from (9-9) with  $\varphi=0$ , so that

$$R(E_{\min}) = \frac{R(h)}{\sin \theta} \quad (9-14)$$

The expression (9-12) can be simplified somewhat by replacing  $\varphi$  as a variable of integration with  $\mu$ . The lower limit is then  $\mu_{\min}$ , the value

traversed when  $\varphi = 0$ , or

$$\mu_{\min} = \frac{\eta(h)}{\sin \theta} \quad (9-15)$$

The upper limit is the maximum mass a beta with energy  $E_0$  can penetrate, or  $\mu_{\max} = R(E_0)$ . Replacing  $\varphi$  with  $\mu$  by using (9-9), we find

$$\frac{dP(h)}{dV} = \frac{N_B \rho}{2 \sin \theta} \int_{E_{0 \min}}^{\infty} dE_0 f(E_0) \int_{\frac{\eta}{\sin \theta}}^{R(E_0)} \left[ \frac{dE}{dM} (E_0, \mu) \right] \frac{d\mu}{\mu} \quad (9-16)$$

Finally, we have for the rate of production of ionization

$$q = \frac{1}{W} \frac{dP}{dV} \quad (\text{electrons cm}^{-3} \text{ sec}^{-1}) \quad (9-17)$$

where  $W$  is the mean energy to form an ion pair

$$W = 33.9 \quad (\text{eV}) \quad (9-18)$$

for betas in air.

Equation (9-16) has been used by Kownacki<sup>(9-1)</sup> to calculate  $q$  for the beta spectrum of West<sup>(9-2,9-3)</sup>. Latter and Lelevier<sup>(9-4)</sup> have approximated (9-16) by assuming a monoenergetic source of beta and neglecting the variation of  $dE/dM$  with  $E$ . With these approximation,

$$f(E_0) = \delta(E_0 - \bar{E}) \quad (9-19)$$

$$\frac{dE}{dM} = - \frac{E}{R(\bar{E})} \quad (9-20)$$

and (9-16) becomes

$$\frac{dP}{dV} = \frac{N_B \rho (\bar{E} - mc^2)}{2 R(\bar{E}) \sin \theta} \ln \frac{R(\bar{E}) \sin \theta}{\eta(h)} \quad (9-21)$$

Knapp et al, in the Blackout Handbook (9-5), have approximated (9-16) by assuming a constant value of  $2 \text{ Mev cm}^2 \text{ gm}^{-1}$  for  $(-dE/dM)$  and taking  $f(E_0)$  to be

$$f(E_0) = \frac{1}{T} e^{-E_0/T} \quad (9-22)$$

where  $T = \bar{E} - mc^2$  is the kinetic energy. For  $dE/dM$  independent of energy and the exponential spectrum, (9-16) can be integrated analytically after a change in the order of integration. The result is

$$\frac{dP}{dV} = \frac{N_B \rho}{2 \sin \theta} \left( -\frac{dE}{dM} \right) E_1 \left[ \frac{(-dE/dM) T}{T \sin \theta} \right] \quad (9-23)$$

where  $E_1$  is the exponential integral

$$E_1(x) = \int_1^{\infty} \frac{e^{-xy}}{y} dy \quad (9-24)$$

In the derivation of (9-16) we have assumed that every beta follows a trajectory with constant pitch angle and loses energy at a well defined rate given by the Bethe-Bloch formula. As a consequence, the effects of range straggling from fluctuations in the rate of energy loss have been neglected, as well as the effects of elastic scattering. No calculations that include the effect of range straggling have been performed. The effects of multiple scattering have been taken into account by Lower et al, who have adapted the results of Spencer (9-6) to the present problem.

Multiple scattering introduces a random component into the motion of the betas. As a consequence, the actual distance traveled by a beta is greater than the geometrical displacement from its injection point. Therefore,

the energy deposition is greater near the injection point than the simple energy loss formula would predict, and is correspondingly lower near the end of the range of the beta. This has the effect of changing the  $\mu$  dependence of  $dE/dM$ . The calculation of Lowen et al. effectively replaces the Bethe-Bloch expression for the energy loss with an altered expression obtained from Spencer's results.

The results of the various calculations have been compared, and values of  $q$  computed from Lowen's formulation for various energy spectra and dip angles are also shown there. Typical comparisons are shown in Figs. 9-3 and 9-4, and the deposition profiles for a typical fission beta spectrum at dip angles of  $30^\circ$  and  $90^\circ$  are shown in Fig. 9-5. As is to be expected, Lowen's method tends to give larger production rates at high altitudes and lower production rates at lower altitudes. The differences are rather small however, and the effects of multiple scattering do not appear to be of great importance. Even the assumption that  $dE/dx$  is independent of energy does not introduce large errors, as seen from Fig. 9-4. The accuracy of this approximation, of course, stems from the slow variation of  $dE/dx$  in the energy range from a few hundred KeV to a few MeV, which includes the energies betas have during the time the bulk of their energy is being deposited.

### 9.3 Beta Patch Attenuation

Radio and radar attenuation through the beta patch have been calculated for various special cases by many workers, who have compared their results with experimental data. Rather than discuss all of these calculations,

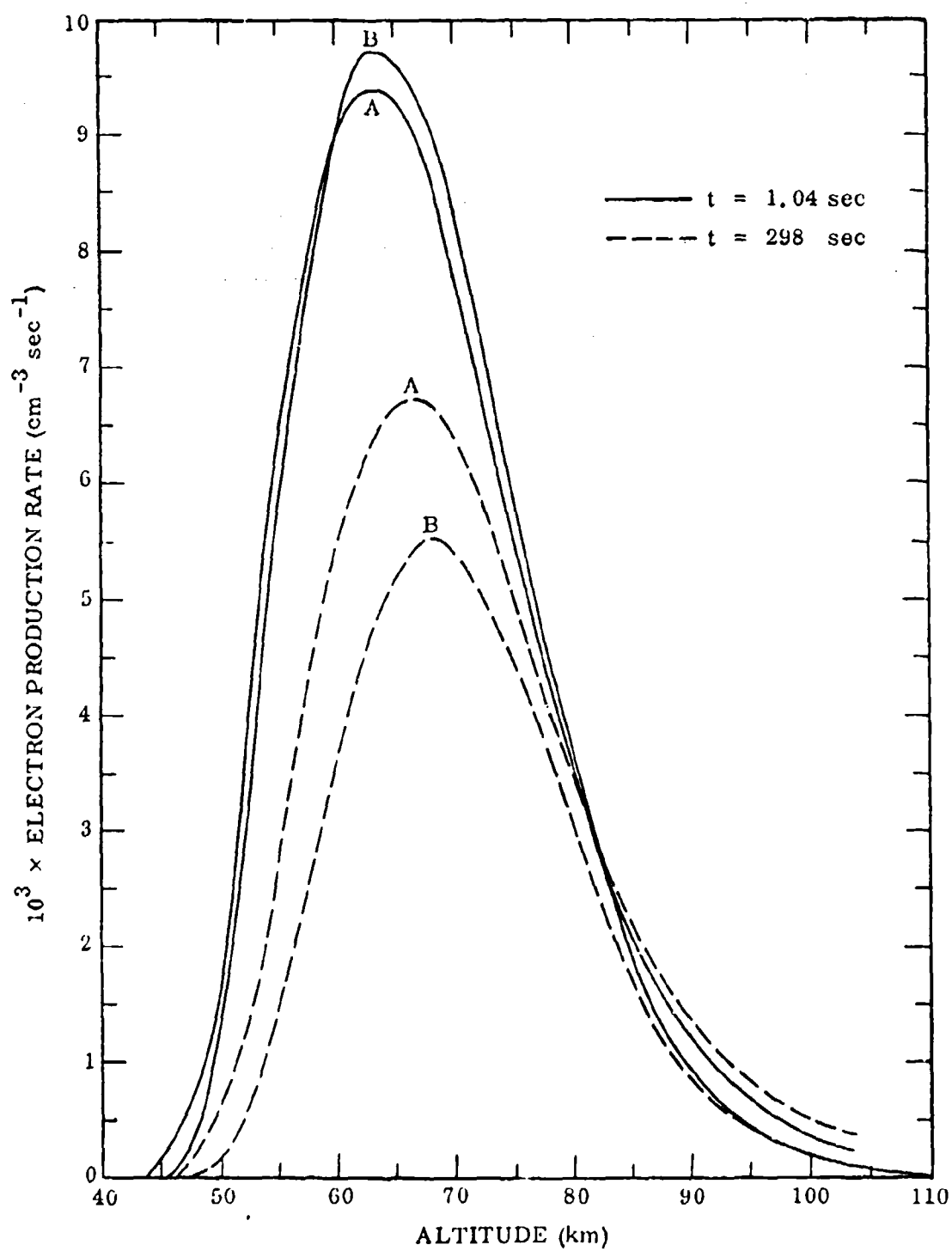


Fig. 9-3 Comparison of Energy Deposition Profiles Calculated by Kownacki (A) and Lowen (B)

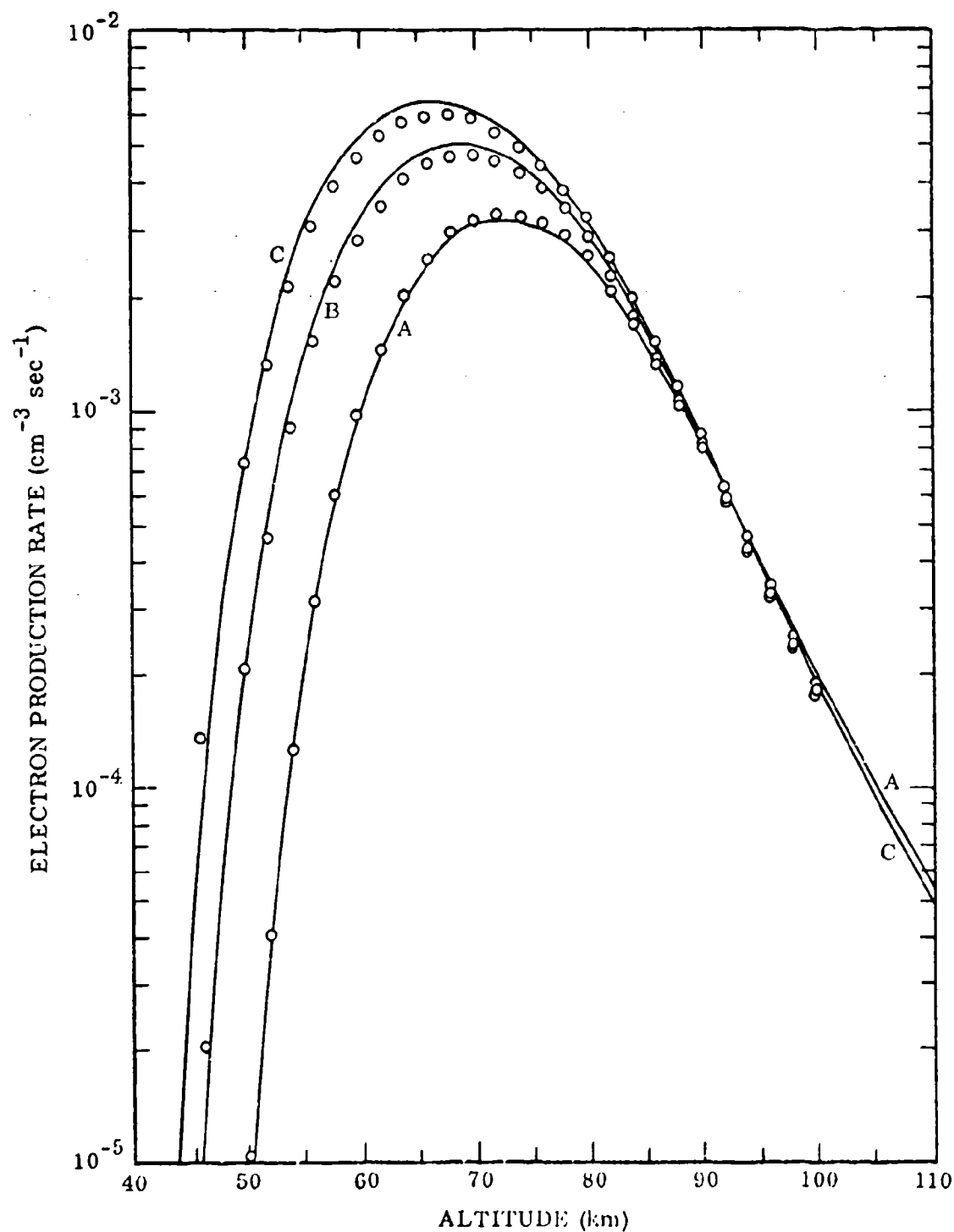


Fig. 9-4 Comparison of Energy Deposition Profiles Calculated by Lowen (Lines) and Knapp (Circled Points)

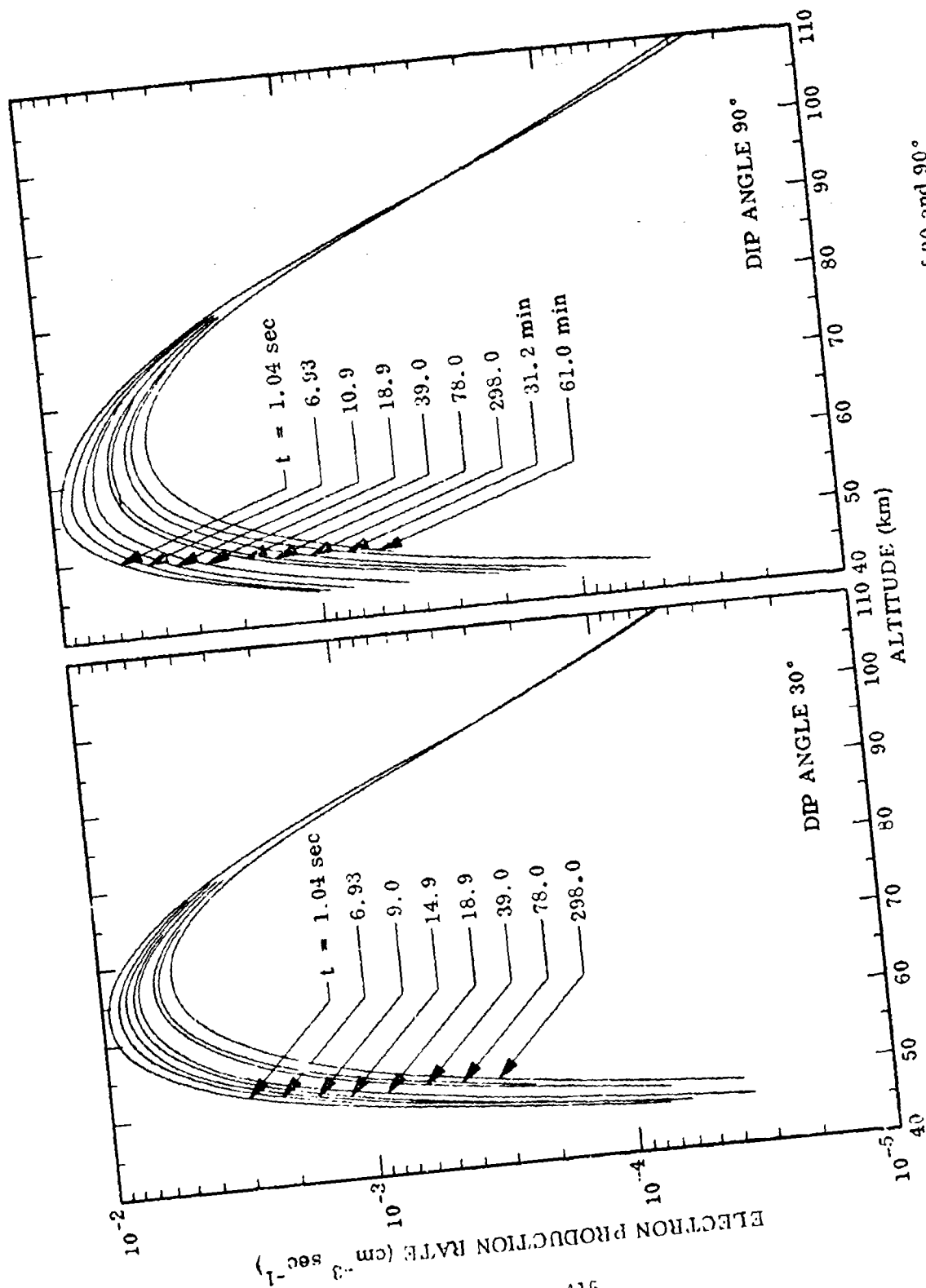


Fig. 9-5 Comparison of Beta Energy Deposition Profiles for Dip Angles of 30 and 90°



we confine our attention here to a particular parametric calculation, the results of which are applicable to a wide variety of special cases. We refer to the calculations of Knapp et al. for  $30^\circ$  dip angle and a wide range of both frequencies and beta intensities as given in the Blackout Handbook<sup>(9-5)</sup>.

The results of these calculations for daytime and nighttime are shown in Figs. (9-6) and (9-7). The calculations are based on the approximations for  $q$  discussed in the preceding section. Electron densities were found from these  $q$  values by solving the deionization equations in the lumped-parameter quasi-equilibrium approximation (see Ch. 5.2). Total path attenuations were then found by integrating the incremental attenuation coefficients along a vertical path through the ionosphere, according to the relationships given in Ch. 5.2. In spite of the many approximations, the results are believed to be accurate to within about a factor of two, and appear to agree with experimental data to within this accuracy.

#### 9.4 A Simple Model of Beta Patch Attenuation

A total of about six betas per fission are radiated, and about six percent of the total fission energy appears as beta kinetic energy. Assuming 200 MeV per fission, we find a mean beta energy of about 2 MeV. The number of betas radiated with energies greater than 6 MeV is very small, so the maximum effective beta energy is about 6 MeV. The range of a 2 MeV beta in air is about  $1 \text{ gm/cm}^2$  and the range for 6 MeV is about  $3 \text{ gm/cm}^2$ .

Betas that enter the atmosphere vertically will penetrate to an altitude such that the total mass of air above that altitude in a cylinder of  $1 \text{ cm}^2$  cross-section is equal to the range of the beta. The altitudes corresponding to 2 and 6 MeV are about 50 and 40 km, respectively. Thus for betas

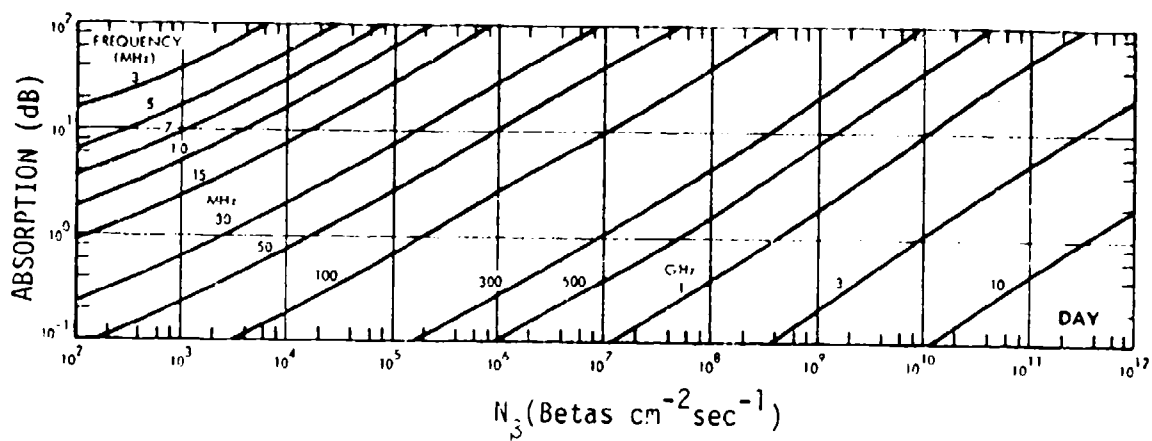


Figure 9-6. Daytime beta patch attenuation (Ref. 9-5).

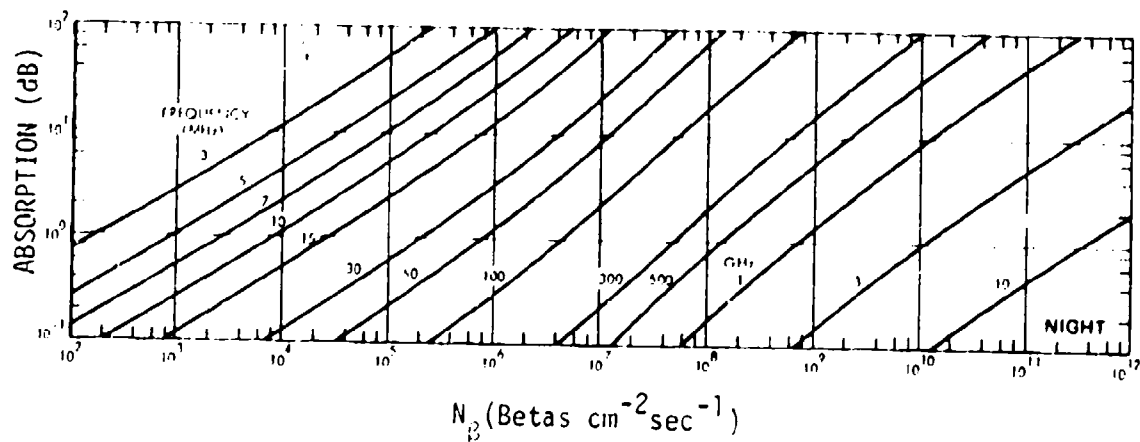


Figure 9-7. Nighttime beta patch attenuation (Ref. 9-5).

distributed in a fission spectrum and injected vertically downward into the atmosphere, we expect the maximum penetration to be about the 40 km altitude level, and the maximum energy deposition to be in the scale height above 50 km, with a peak in the middle of this region, or at about 53 km.

As already noted, the betas do not follow straight line trajectories, but instead spiral around magnetic field lines. The helical trajectories have two effects on the energy deposition profile. First, the energy loss per unit altitude traversed is increased by a factor of  $(\cos \phi)^{-1}$ , where  $\phi$  is the pitch angle and the vertical range is decreased correspondingly by a factor of  $\cos \phi$ . For an isotropic distribution, the mean value of  $\cos \phi$  is 0.5, so the mean vertical mass penetrated is decreased by a factor of two, and the peak in the energy deposition is shifted upward correspondingly. The result is to place the peak at an altitude of about 60 km.

The second effect of the pitch angle distribution is to increase the altitude range wherein the energy is deposited. Betas with small pitch angles give rise to a deposition profile peaking at low altitudes, while betas with the same energy but larger pitch angles give rise to a profile of the same shape but shifted to higher altitudes. Averaging over the pitch angle distribution produces a smeared-out profile about three scale heights thick, as compared with the thickness of about one scale height to be expected from a stream of betas having the same pitch angle.

The dip angle of the geomagnetic field also affects the variation with altitude of the deposition profile. If  $\delta$  is the dip angle, i.e., the angle between the geomagnetic field and the horizontal, then the energy loss per unit altitude traversed is increased by a factor  $(\sin \delta)^{-1}$  and the

vertical range correspondingly decreased by a factor  $\sin \theta$ . Thus the peak in the energy deposition profile for a dip angle of  $30^\circ$  will be about 5 km above that for the  $90^\circ$  dip angle case considered above, or at about 65 km.

The above estimates of the energy deposition profile are borne out both by detailed machine calculations and experimental data. In the examples of calculated deposition profiles for dip angles of  $90^\circ$  and  $30^\circ$  shown in Fig. (2-5), the peaks in the deposition profiles are seen to occur at about 60 and 65 km altitude, respectively. The full width of the curves at their half-maximum points is about 25 km or 3-4 scale heights.

To obtain an estimate of the attenuation of radio or radar signals propagated through the beta patch, we first note that most of the attenuation occurs in the 55-80 km altitude region. Above 80 km the air density and hence the collision frequency are so low that the contribution from higher altitudes is negligible, while below 55 km the free electrons produced by the betas are rapidly lost by attachment to  $O_2$  to form  $O_2^-$ .

Attachment is a three-body process, so the rate of attachment of electrons varies as the square of the air density. When attachment is the dominant electron loss process, the quasi-equilibrium electron density varies inversely as the rate of attachment, and hence inversely as the square of the air density. The attenuation per unit length is proportional to the product of electron density and collision frequency. The collisional frequency varies directly with air density, so the attenuation coefficient varies inversely as the air density. The electron density also varies directly with the electron production rate, which decreases rapidly with decreasing altitude below 55 km. At the same time the air density is increasing exponentially, so the attenuation coefficient

falls off rapidly below 55 km, and the contribution to attenuation from this region can generally be neglected.

As the basis for a simple calculation, we assume that all of the beta energy is deposited between 55 and 60 km, and that the electron production rate  $q$  is constant within this region. These approximations give a fairly accurate representation of the calculated profiles shown in Fig. (9-5). Within this region the deposition profiles for  $30^\circ$  and  $90^\circ$  dip angles agree to within about 50 per cent, so for the purposes of this simple calculation the variation with dip angle is ignored.

Assuming that 6 per cent of the fission yield appears as kinetic energy of delayed betas and that the radiated power varies with time as  $(1+t)^{-1.15}$ , we have for the beta power

$$P_\beta = \frac{9 \times 10^{-3} Y_f}{(1+t)^{1.15}} \quad (\text{energy sec}^{-1}) \quad (9-25)$$

where  $Y_f$  denotes the fission yield. Next we suppose that half of the energy is deposited in each of the conjugate beta patches, and that the projected debris distribution is uniform over a horizontal area of  $\pi R^2$ . Then the power deposited per unit volume per unit time in the deposition region is

$$\frac{dP_\beta}{dV} = \frac{P_\beta}{2\pi R^2 L} \quad (\text{energy time}^{-1} \text{ vol}^{-1}) \quad (9-26)$$

where  $L$  is the vertical thickness of the deposition region. The rate of production of free electrons is just  $dP_\beta/dV$  divided by the mean energy to form an ion pair, which we take to be 34 eV. Thus the electron production rate  $q$  is

$$q = \frac{4.4 \times 10^{13}}{R^2 (1+t)^{1.15}} Y_f \quad (\text{cm}^{-3} \text{ sec}^{-1}) \quad (9-27)$$

where  $Y_f$  denotes the fission yield in megatons,  $R$  the horizontal radius of the debris cloud in km,  $t$  the time after detonation in seconds, and we have taken  $L = 25$  km.

The simplest approximation for determining the electron density resulting from the ionization rate  $q$  is found by solving the lumped-parameter rate equations in the quasi-equilibrium approximation with the assumption of equal rate constants for electronic and ionic recombination. In this approximation we have

$$N_+ = \sqrt{q/\alpha} \quad (9-28)$$

$$N_e = \sqrt{q/\alpha} \frac{\gamma + \sqrt{\alpha q}}{\beta + \gamma + \sqrt{\alpha q}} \quad (9-29)$$

where  $\alpha$  denotes the recombination coefficient,  $\beta$  the electron attachment coefficient and  $\gamma$  the electron detachment coefficient. The solutions (9-28) & (9-29) are obtained by setting  $dN_+/dt = dN_e/dt = 0$ , and

$$\alpha_d = \alpha_1 = \alpha = \gamma \times 10^{-7} \text{ (cm}^3 \text{ sec}^{-1}) \quad (9-30)$$

The value of  $\gamma \times 10^{-7} \text{ cm}^3 \text{ sec}^{-1}$  has been shown by LeDevier<sup>11</sup> to give a best fit to experimental data when the assumption  $\alpha_d = \alpha_1 = \alpha$  is made.

The attenuation produced by the electrons is proportional to the product of the electron density and the ambient air density.

$$\frac{dA}{dh} = \frac{4.60 \times 10^4 N_e \text{ ev}}{(\text{ev})^2 + (h\nu)^2} \quad (\text{db km}^{-1}) \quad (9-31)$$

where  $N_e$  is the electron density ( $\text{cm}^{-3}$ ),  $\nu$  is the electron neutral

collisional frequency ( $\text{sec}^{-1}$ ),  $\omega$  is the angular frequency of the propagated wave ( $\text{rad sec}^{-1}$ ), and  $g$  and  $h$  are dimensionless constants of order unity. Electron-ion collisions have been neglected, an approximation which restricts the validity of the approximation to situations where the fractional ionization is below  $10^{-6}$  and hence where

$$\frac{y_T}{k^2 (1+t)^{1.15}} \sim 10^{-2}$$

We are interested in altitudes above 25 km. At 25 km,  $v = 3 \times 10^6 \text{ sec}^{-1}$  and is decreasing exponentially with increasing altitude. The  $t$  term in the denominator of (9-31) can therefore be neglected for frequencies of 10 MHz and above. For the conditions of interest  $k \approx 1$ , hence (9-31) can be written

$$\frac{dA}{dh} = \frac{1.17 \times 10^{-9} E_y}{r^2} \quad (\text{db km}^{-1}) \quad (9-32)$$

where  $r$  denotes the range in km. Substitution of (9-29) into (9-32) yields

$$\frac{dA}{dh} = \frac{1.17 \times 10^{-9} v}{r^2} \sqrt{\frac{75}{\pi}} \frac{v + \sqrt{v^2 + 4\alpha^2}}{\alpha + v + \sqrt{v^2 + 4\alpha^2}} \quad (9-33)$$

With our assumption that  $\alpha$  is constant in the 25 to 50 km altitude interval and negligible elsewhere, we have for the total attenuation through the lower path

$$A_B = \frac{1.17 \times 10^{-9}}{r^2} (\gamma + \sqrt{\alpha^2}) \sqrt{\frac{75}{\pi}} \frac{80}{2\pi} \frac{1}{\alpha + \gamma + \sqrt{\alpha^2}} \quad (9-34)$$

The collisional frequency in respect to the lower ionosphere is obtained as a function proportional to the square of the electron density  $N$ . If  $N = 10^{12}$ , we write

$$\gamma = 80 \quad (9-35)$$

$$\beta = b\rho^2 \quad (9-36)$$

and hence

$$\Lambda_\beta = \frac{1.17 \times 10^{-9}}{r^2} (\gamma + \sqrt{\alpha q}) \sqrt{q/\alpha} \approx \int_{55}^{80} \frac{\rho \, dh}{b\rho^2 + \gamma + \sqrt{\alpha q}} \quad (9-37)$$

Next we assume

$$\rho = \rho(55) e^{-z/H} \quad (9-38)$$

where  $H$  denotes the atmospheric scale height in km and  $z$  the altitude measured upward from 55 km. From (9-38)

$$\frac{d\rho}{dh} = -\frac{\rho}{H} \quad (9-39)$$

and hence can be written

$$\Lambda_\beta = \frac{1.17 \times 10^{-9}}{r^2} (\gamma + \sqrt{q/\alpha})^{1/2} \sqrt{q/\alpha} \frac{dH}{b^{1/2}} \frac{\rho(55)}{\rho(80)} \frac{b^{1/2} d\rho}{b\rho^2 + \gamma + \sqrt{\alpha q}} \quad (9-40)$$

The integration can be performed exactly with the result

$$\Lambda_\beta = \frac{1.17 \times 10^{-9}}{r^2} (\gamma + \sqrt{q/\alpha})^{1/2} \frac{v(h) - 1}{\beta^{1/2}(h)} \left\{ \tan^{-1} \frac{\beta^{1/2}(55)}{(\gamma + \sqrt{\alpha q})^{1/2}} - \tan^{-1} \frac{\beta^{1/2}(80)}{(\gamma + \sqrt{\alpha q})^{1/2}} \right\} \quad (9-41)$$

where  $v(h)$  and  $\beta^{1/2}(h)$  are evaluated at an arbitrary altitude, provided only that the same altitude is used for both  $v$  and  $\beta$ .

In keeping with our plan to perform a simple calculation that contains only the most essential features of the problem, we ignore all weapon-induced changes in D-region chemistry. Then the only effective detachment mechanisms are photodetachment by sunlight and by ambient atomic oxygen, so we assume



$$\gamma = \begin{cases} 2 \times 10^{-3} \text{ sec}^{-1} (\text{nighttime}) \\ 0.44 \text{ sec}^{-1} (\text{daytime}) \end{cases} \quad (9-42)$$

The nighttime value of  $2 \times 10^{-3}$  is taken from the Blackout Handbook as a value appropriate for the 75-80 km range where the small nighttime detachment rate has its only appreciable effect. The nighttime and daytime cases will be considered separately, attention first being given to the daytime case.

The attachment rates at 55 and 80 km are 20 and  $0.03 \text{ sec}^{-1}$ , respectively. During the daytime, when  $\gamma = 0.44$ ,  $\tan^{-1} \frac{\beta^{1/2}(55)}{(\gamma + \sqrt{\alpha q})^{1/2}}$  is larger than  $\tan^{-1} \frac{\beta^{1/2}(80)}{(\gamma + \sqrt{\alpha q})^{1/2}}$  by a factor ranging from about 6 for small values of  $\sqrt{\alpha q}$  to about 25 for large  $\sqrt{\alpha q}$ , and hence we neglect

$$\tan^{-1} \frac{\beta^{1/2}(80)}{(\gamma + \sqrt{\alpha q})^{1/2}} \quad \text{in (9-41) to obtain}$$

$$A_{\beta}^{\text{day}} \approx \frac{1.17 \times 10^3}{r^2} \sqrt{q/\alpha} \quad v(55) \equiv \frac{(\gamma + \sqrt{\alpha q})^{1/2}}{\beta^{1/2}(55)} \tan^{-1} \frac{\beta^{1/2}(55)}{(\gamma + \sqrt{\alpha q})^{1/2}} \quad (9-43)$$

where we have chosen to evaluate  $v(h)$  and  $\beta(h)$  at  $h = 55$  km.

For convenience we define the function

$$F(q, \gamma) = \frac{(\gamma + \sqrt{\alpha q})^{1/2}}{\beta^{1/2}(55)} \tan^{-1} \frac{\beta^{1/2}(55)}{(\gamma + \sqrt{\alpha q})^{1/2}} \quad (9-44)$$

Substitution of (9-27), (9-30), (9-42) and (9-44) into (9-43), with  $H = 7$  km and  $v(55) = 8 \times 10^7 \text{ sec}^{-1}$ , yields

$$A_{\beta}^{\text{day}} = \frac{2.2 \times 10^9}{r^2} F(q, \gamma) \left[ \frac{Y_F}{R^2 (1+t)^{1.15}} \right]^{1/2} \quad (\text{db}) \quad (9-45)$$

where  $Y_F$  denotes the fusion yield in MT,  $f$  the radar frequency in Hz,  $R$  the projected radius of the debris cloud in km, and  $t$  the time after burst in sec.

The values of one-way daytime attenuation through the beta patch calculated from (9-45) are shown by the solid curves in Fig. (9-8). No results are shown for  $\frac{Y_f}{R^2(1+t)^{1.15}} > 10^{-2}$ , because electron-ion collisions, which we have neglected, begin to become important for such large ionization rates. Also shown for comparison as dashed curves are the results of machine calculations given in the Blackout Handbook (9-5). The two sets of calculations are seen to give results that agree to within about thirty percent over a range of beta fluxes that spans ten order of magnitude. That the agreement is so very good is partly fortuitous, in view of some of the rather arbitrary choices of parameters made in deriving (9-45). Nevertheless, the possible choices for these parameters are sufficiently limited to preclude the possibility of changes by more than about a factor of three in the results, and so we can assert with confidence that the basic physics of beta patch formation is correctly contained in (9-45) and the assumptions made in its derivation.

A convenient approximation (9-45) can be found by noting that the function  $F(q, \gamma)$  is of quite limited variation for  $\gamma = 0.44$ . For  $\sqrt{\alpha q} \gg \beta(55)$ , the argument of the arctangent in (9-44) is small and the arctangent can be approximated by its argument, so that

$$\lim_{q \rightarrow \infty} F(q, \gamma) = 1 \quad (9-46)$$

For  $\sqrt{\alpha q} \ll \gamma = 0.44$ , the argument of the arctangent is approximately 6.8 and its value 1.42, and hence

$$\lim_{q \rightarrow 0} F(q, 0.44) = \frac{1.42}{6.8} = 0.21 \quad (9-47)$$

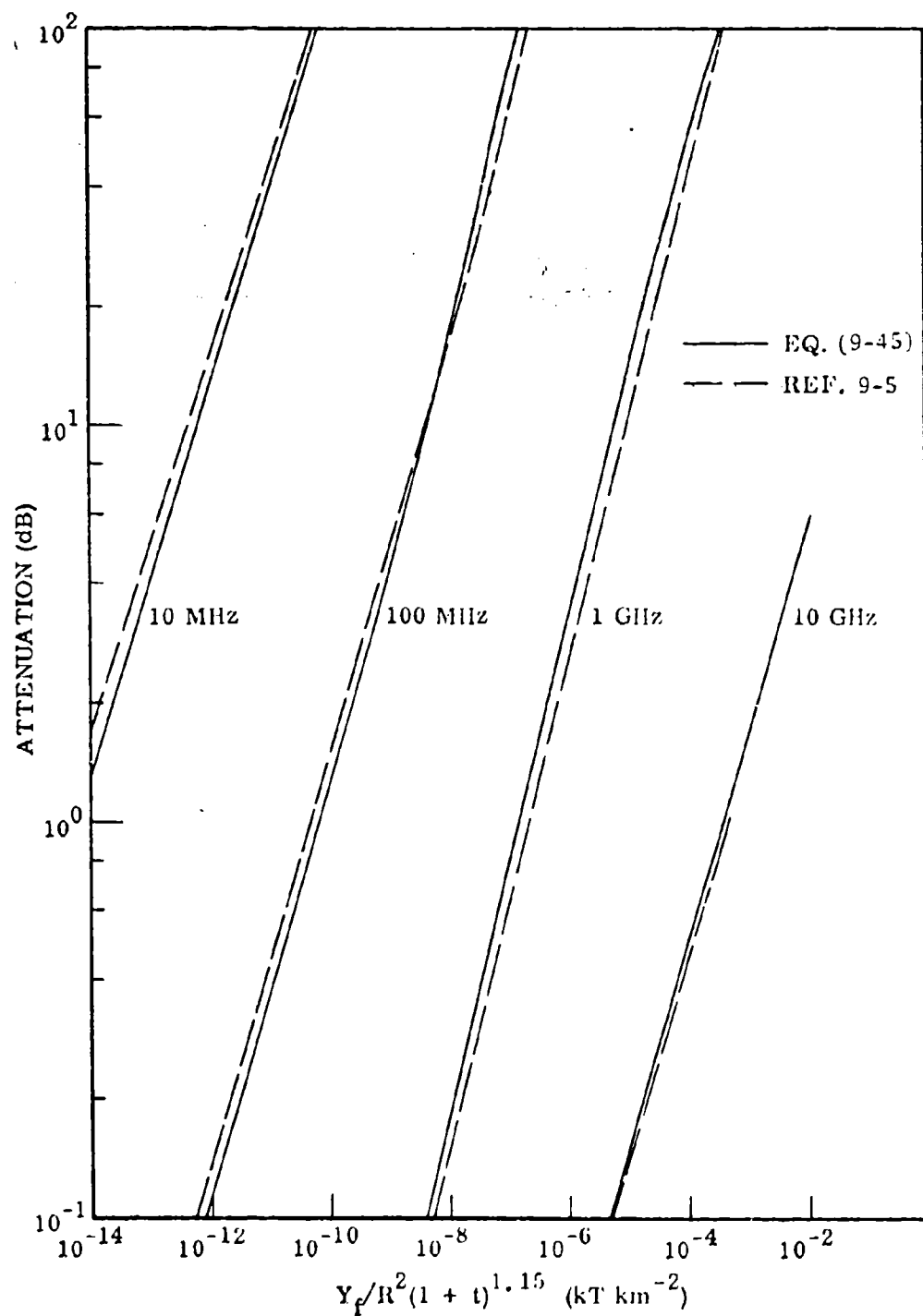


Fig. 9-8 Calculated One-Way Attenuation Through the Beta Patch (Daytime)

For intermediate values of  $q$ ,  $F$  varies monotonically between these limits as shown in Fig. (9-9). The small variation of  $F(q, 0.44)$  provides a convenient approximation without great loss of accuracy. If we use  $F(q, 0.44) = 0.5$  for all  $q$  in (9-21), the maximal error introduced is about a factor of two. Accordingly we write

$$A_{\beta}^{\text{day}} \approx \frac{2.6 \times 10^9}{r^2} \left[ \frac{Y_F}{R^2(1+t)^{1.15}} \right]^{1/2} \quad (9b) \quad (9-48)$$

As a formula suitable for approximate calculations in which errors by factors of two are unimportant.

To calculate the night time beta patch attenuation we return to Eq. (9-41). Because of the small night time attachment rate,

$\tan^{-1} \frac{b^{1/2}(80)}{(\gamma + \sqrt{2q})^{1/2}}$  is no longer negligible and must be kept. For convenience we define the function

$$G(q, \gamma) = \tan^{-1} \frac{b^{1/2}(80)}{(\gamma + \sqrt{2q})^{1/2}} = \tan^{-1} \frac{b^{1/2}(80)}{(\gamma + \sqrt{2q})^{1/2}} \quad (9-49)$$

Substitution of (9-27), (9-30), (9-42) and (9-49) into (9-41) yields

$$A_{\beta}^{\text{night}} = \frac{1.15 \times 10^9}{r^2} \left\{ 2 \times 10^{-3} + 9.55 \times 10^3 \left[ \frac{Y_F}{R^2(1+t)^{1.15}} \right]^{1/2} \right\}^{1/2} \left[ \frac{Y_F}{R^2(1+t)^{1.15}} \right]^{1/2} G(q, \gamma) \quad (9-50)$$

where as before the attenuation is one-way vertical expressed in db, and the units of  $r$ ,  $Y_F$ ,  $R$ , and  $t$  are km,  $W$ , km, and sec, respectively.

Attenuations calculated from (9-49) are compared with the results of machine calculations from the Element Ray Model in Fig. (9-10). While the

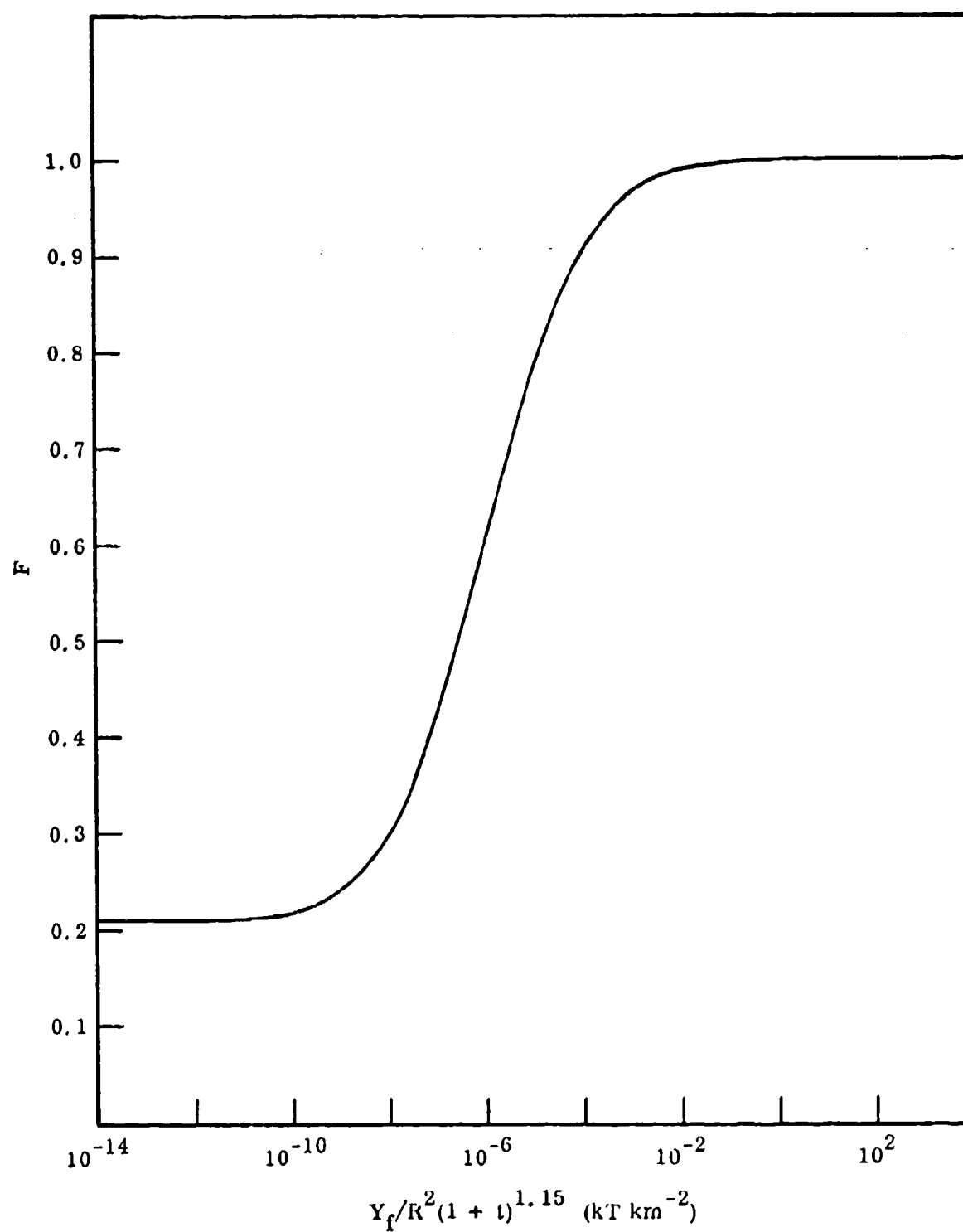


Fig. 9-9 The Function  $F$  [See Eq. (9.44)]

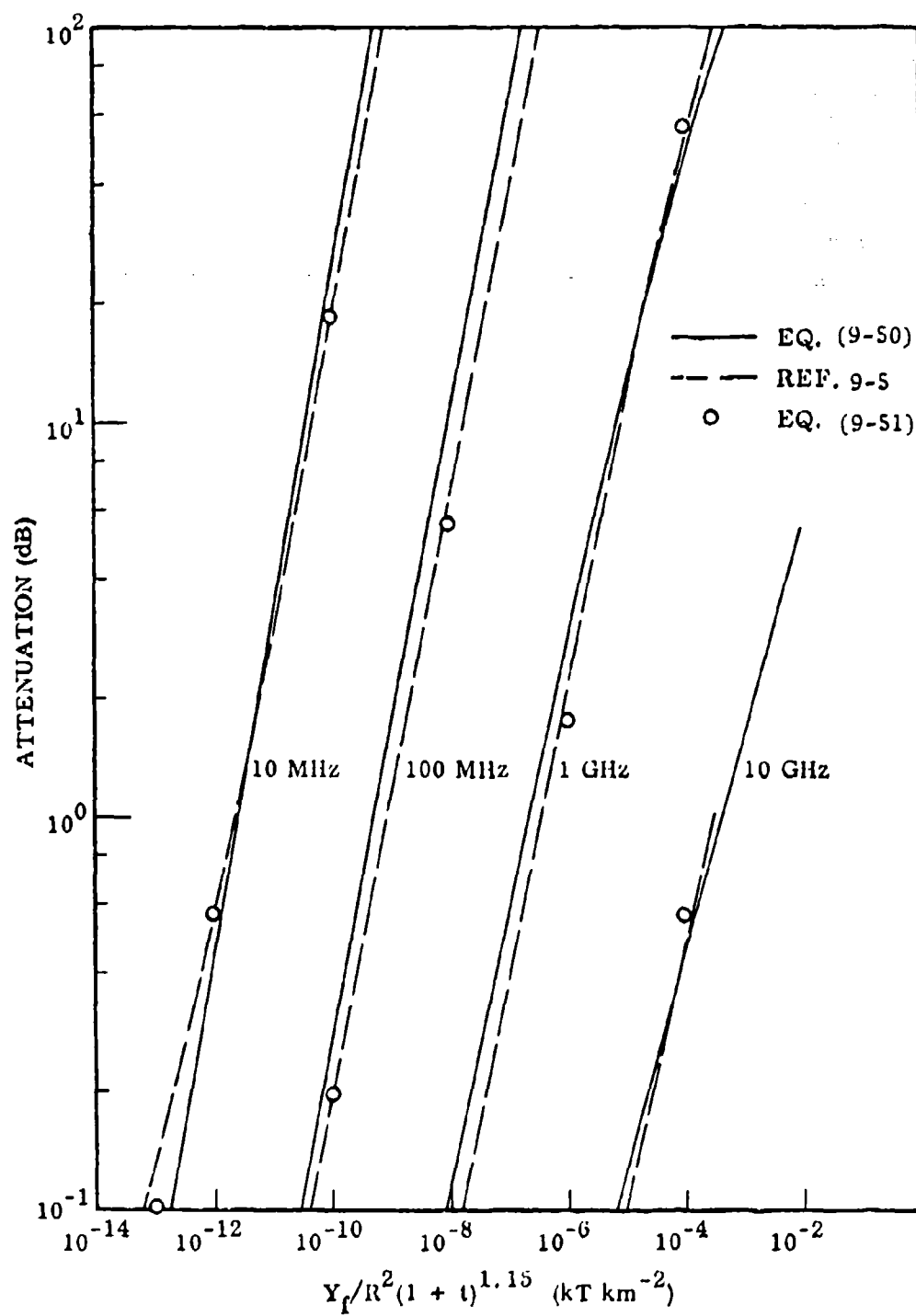


Fig. 9-10 Calculated One-Way Attenuation Through the Beta Patch (Nighttime)

agreement is not as close as that found for the daytime attenuation, it is still quite good and confirms our belief that the simple calculation contains correctly the most important elements of the problem.

For crude calculations (9-50) can be further approximated by noting that for  $\gamma = 2 \times 10^{-3}$ ,  $G(\alpha, \gamma)$  is of limited variation as shown in Fig. (9-11). We approximate  $G(\alpha, \gamma)$  over its entire range by 0.65. This value overestimates  $G(\alpha, \gamma)$  for both large and small values of  $\alpha$ , and underestimates it for intermediate values. The errors introduced at large and intermediate values of  $\alpha$  actually improve the agreement with the values from the Blackout Handbook. For small values of  $\alpha$ , we compensate for the overestimate and at the same time simplify the approximate expression still further by dropping the  $\gamma$  term in the first square root in (9-50). With these approximations we obtain

$$A_{\text{night}} \approx \frac{2.5 \times 10^{10}}{r^2} \left[ \frac{Y_f}{R^2(1+t)^{1.15}} \right]^{3/4} \quad (9-51)$$

Several points calculated from this expression are also shown in Fig. (9-10) where the improved agreement with the results from the Blackout Handbook is apparent.

## 9.5 Discussion and Summary

The good agreement of the approximate expression (9-48) with the results of machine calculations for daytime beta patch attenuation shows that daytime deionization in the beta patch is dominated by dissociative recombination. The variation of electron density, and hence of attenuation,

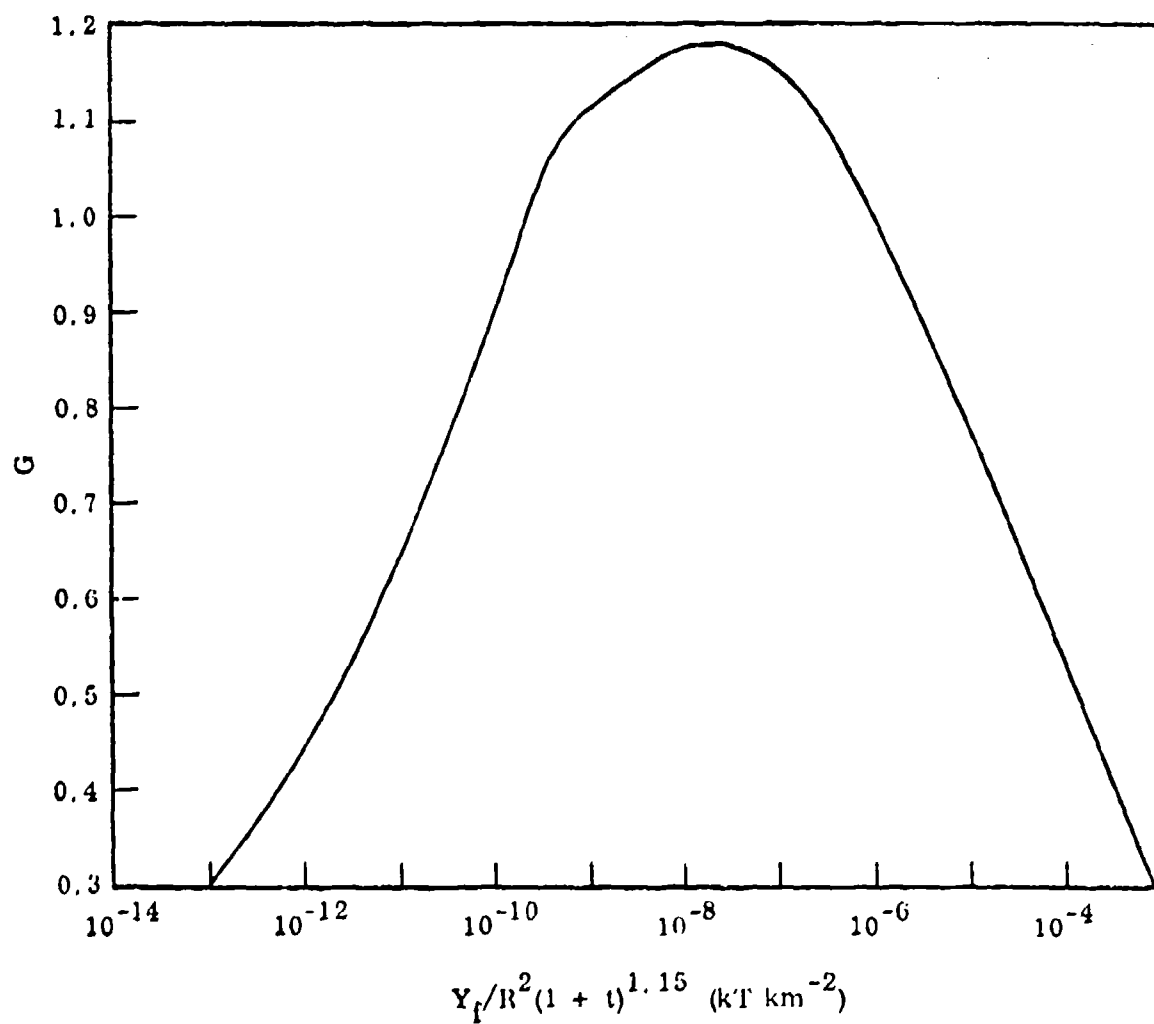


Fig. 1-11 The Function G [See Eq. (9.49)]



as the square root of the ionization rate is characteristic of electron loss by recombination. In fact, the attenuation given by (9-48) is just one half of that which would be obtained by neglecting attachment altogether. At lower ionization levels, of course, the importance of attachment is enhanced. Even at the lowest levels considered here, however, complete neglect of attachment leads to overestimation of the attenuation by only about a factor of five.

When attachment is the only operative electron loss mechanism, the electron density varies linearly with the production rate. The variation of the nighttime attenuation as the three-fourths power of the source strength in the approximation (9-51) indicates that both attachment and recombination influence the electron density under nighttime conditions. It follows that the attenuation can be increased by any mechanism that increases the rate of detachment of electrons from  $O_2^-$ . An increase in the detachment rate can be produced by changes in D-region chemistry, atmospheric heating, or photodetachment by fireball radiation.

Changes in D-region chemistry can be quite significant in a multiburst situation. The maximum effect of increased detachment is to render attachment negligible as an electron loss mechanism. If this occurs, the nighttime attenuation becomes approximately equal to the daytime value. The increase in attenuation would then be by about a factor of two or less at ionization levels important for frequencies of 1 GHz and above, but could be by an order of magnitude at ionization levels important for a few MHz.

In spite of its deficiencies, the basic theory presented in this chapter is adequate for most practical purposes because of the large uncertainties in the actual debris distribution at late times. The main interest in accurate calculations is not for making predictions, where lack of knowledge of the debris distribution makes the prediction semi-quantitative at best, but for the converse problem of inferring the debris distribution from attenuation measurements made during high altitude nuclear tests.

## REFERENCES

1. Kownacki, S., "Ionization of the Atmosphere Due to Beta Particles Emitted by Fission Products", in Journal of Geophysical Research, Vol. 68, pp 5461-5471 (1963).
2. West, H.I., Jr., L.G. Mann, and S.D. Bloom, Some Electron Spectra in the Radiation Belts in the Fall of 1962, Lawrence Radiation Lab., Livermore, Ca., UCRL 7659, April 1964. Also see Space Resesrch, Vol. 5, p. 423 (1965).
3. West, H.I., Jr., L.G. Mann, and S.D. Bloom, Spectra and Fluxes of Electrons Trapped in the Earths Magnetic Field Following Recent High Altitude Nuclear Bursts, Lawrence Radiation Lab., Livermore, Ca., UCRL 7309 Rev. I, April 1963.
4. Latter, R., and R.E. LeLevier, "Detection of Ionization Effects from Nuclear Explosions in Space", in Journal of Geophysical Research, Vol. 68, pp. 1643-1666 (1963).
5. Knapp, W.S., P.G. Fischer, and K. Schwartz, Aids for the Study of Electromagnetic Blackout, DASA2499 and DNA34994, General Electric/TEMPO, 1970 and 1975.
6. Spencer, L.V., Energy Dissipation by Fast Electrons, National Bureau of Standards (U.S.) Monograph 1, U.S. Government Printing Office, Washington DC, September 1959.

CHAPTER 10

ANALYTIC FLUID DYNAMICS

David H. Sowle  
Mission Research Corporation

May 1975

## TABLE OF CONTENTS

10.1	INTRODUCTION	439
10.2	IDEAL FLUID EQUATIONS	440
10.2.1	LAGRANGIAN FORMULATION	440
	Conservation of Mass	440
	Newton's Second Law	441
	Conservation of Energy	443
	Equation of State	443
	$\gamma$ -Law Gas	444
	Partial Solution: Initial Fireball Expansion	444
10.2.2	EULERIAN FORMULATION	447
	Continuity	449
	Momentum Equation	449
	Energy Equation	449
10.3	STATIC EQUILIBRIUM	450
10.3.1	MECHANICAL EQUILIBRIUM	450
	Water	450
	Air	450
10.3.2	STABILITY	452
10.3.3	FIRST BUOYANT FIREBALL RISE MODEL	455
10.4	STEADY FLOW	460
	Time Independent Eulerian Equations	460
	Gravitational Potential	460
	Enthalpy	461
	Streamlines	462
	Bernoulli's Equation	463

10.5	CIRCULATION	464
	Bjerknes' Theorem	464
	Kelvin's Theorem	465
	Vorticity	465
	Vortex	466
10.6	POTENTIAL FLOW	467
	Irrotational Flow	467
	Velocity Potential	467
	Confrontation with Reality	468
10.7	INCOMPRESSIBLE FLOW	470
	10.7.1 MOMENTUM EQUATION	470
	10.7.2 BERNOULLI'S EQUATION AND TIME DEPENDENT POTENTIAL	470
	General Equation	470
	10.7.3 INCOMPRESSIBLE POTENTIAL FLOW	471
	10.7.4 STAGNATION POINT	472
	10.7.5 DRAG	472
	10.7.6 STREAM FUNCTION	474
	10.7.7 MOVING SPHERE PROBLEM	476
	Energy and Impulse	478
	10.7.8 INITIAL RISE VELOCITY OF BUOYANT FIREBALLS	480
	Archimedes' Principle	480
	Impulse Equation	481
	10.7.9 SECOND BUOYANT FIREBALL RISE MODEL	482
	10.7.10 RAYLEIGH-TAYLOR INSTABILITY	485
	10.7.11 KELVIN-HELMHOLTZ INSTABILITY	488
10.8	REAL FLUID EFFECTS	491
	Basic Physics	492
	Diffusion	494
	Heat Conduction	495
	Viscosity	495

10.9	SOUND WAVES	497
	Wave Equation	497
	Characteristics	500
	Attenuation of Sound Waves	501
10.10	BALLISTIC FIREBALL RISE VELOCITY	504
10.11	SHOCKS	506
	Formation	506
	Limit on Slope	506
	Jump Conditions	507
	Irreversibility of Shocks	510
10.12	TURBULENCE	512
	Onset Criteria	513
	Fully Developed Steady Turbulence	514
	Decay of Turbulence	515
	Early Period	516
	Final Period	517
	REFERENCES	519

## ANALYTIC FLUID DYNAMICS

### 10.1 INTRODUCTION

Fluid dynamic problems susceptible to analytic solution rarely occur in applied physics. However, determination and ingenuity can always produce analytic solutions to crucial aspects of applied problems. Study of such partial solutions is necessary in order to gain an understanding of complex phenomena. Partial or approximate analytic solutions are also required as checks on more complete numerical solutions, which are well known to be prone to subtle error.

The following discussion develops fluid dynamic concepts and formalisms for those aspects most useful to an understanding of atmospheric and ionospheric nuclear explosions. Areas of inquiry to which an element of formalism may be applied are indicated, and illustrated by several partial solutions to nuclear explosion phenomena.



## 10.2 IDEAL FLUID EQUATIONS

An ideal fluid is one in which all quantities necessary for description are continuous differentiable variables. This implies that a volume element, however small, contains so many molecules that statistical deviations from the mean properties can be neglected and further that collisions among the molecules are so effective that molecules collide many times in traveling the width of the volume element. On the scale of most human experience molecules are in fact very numerous and their mean free path against collisions is very short, therefore the mathematical approximation of an ideal fluid is adequate to describe fluid behavior in regions of fairly smooth flow. Molecular effects, generally known as viscous effects are important in regions where fluid properties change abruptly; viscous effects are introduced in Section 8.

### 10.2.1 LAGRANGIAN FORMULATION

The simplest conceptual formulation of the equations of fluid dynamics is obtained by following the history of an element of fluid mass as it moves under local forces. This is the most common of the Lagrangian formulations. One may derive alternate Lagrangian formulations by following an "element" of momentum or energy but such formulations are rarely used and will not be discussed.

#### Conservation of Mass

If the vector  $\vec{r}_0$  represents the initial position of the fluid element and  $V_0$  the initial volume then the initial mass associated with a given fluid element is

$$M_0 = \rho_0 V_0$$

(10-1)

where  $\rho_0$  is initial density of the element. The mass clearly doesn't change as the element moves although the position,  $\vec{r}$ , volume,  $V$ , and density  $\rho$ , may change. Conservation of mass then implies

$$\frac{dM}{dt} = 0 \quad , \quad (10-2)$$

or

$$M = \rho V = M_0 = \rho_0 V_0 \quad (10-3)$$

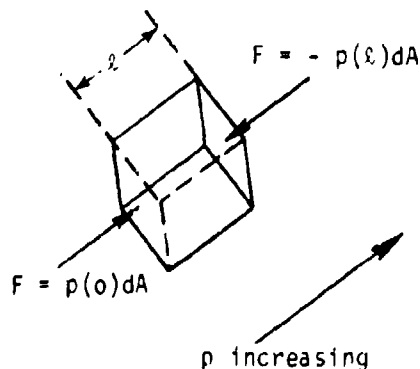
#### Newton's Second Law

Since the mass is constant, acceleration of the element  $\frac{d^2 \vec{r}}{dt^2}$ , may be written as

$$M_0 \frac{d^2 \vec{r}}{dt^2} = \vec{F} \quad , \quad (10-4)$$

where  $\vec{F}$  is the vector sum of all forces acting on the element. If the fluid has pressure,  $p$ , then the force acting on the element due to the surrounding fluid is just the sum of forces acting on each element of area of the volume.

The situation is illustrated in the sketch, for convenience let the volume be a cube with sides of area  $dA$  oriented along the direction in which the pressure is changing, that is, oriented along the gradient of the pressure. It is clear that the forces,  $p dA$ , acting transverse to the gradient cancel and the net force is



$$\begin{aligned}\vec{F} &= p(o)dA - p(l)dA = p(o)dA - \left( p(o)dA + \frac{\partial p}{\partial z} \vec{z}dA \right) \\ &= - \frac{\partial p}{\partial z} \vec{z}dA = - \frac{\partial \vec{p}}{\partial z} V\end{aligned}\quad (10-5)$$

It is also clear that a volume of any shape can be approximated to any desired degree of accuracy with a large number of cubes, so (10-5) is independent of the volume's shape. The traditional notation for the vector gradient is  $\nabla p$ ; in cartesian coordinates it can be evaluated as

$$\nabla p = \frac{\partial p}{\partial x} \hat{x} + \frac{\partial p}{\partial y} \hat{y} + \frac{\partial p}{\partial z} \hat{z} \quad (10-6)$$

where  $\hat{x}$  denotes a unit vector along the indicated coordinate. Thus force from internal pressure is

$$\vec{F} = -\nabla p V, \quad (10-7)$$

It is also possible to have a body force due to external causes, say gravitational acceleration,  $\vec{g}$ . Then Eq. (10-4) becomes

$$M_o \frac{d^2 \vec{r}}{dt^2} = - \nabla p V + M_o \vec{g} \quad (10-8)$$

Substituting Eq. (10-3) and canceling yields

$$\frac{d^2 \vec{r}}{dt^2} = - \frac{1}{\rho} \nabla p + \vec{g} \quad (10-9)$$

Eq. (10-9) is known as the force equation, or the momentum equation, since it expresses the conservation of momentum.

### Conservation of Energy

If the specific internal energy of the volume element is denoted by  $l$  (erg/gm) then the conservation of energy is expressed by the first law of thermodynamics as

$$M_0 \frac{dl}{dt} = -p \frac{dV}{dt} + \frac{dQ}{dt} \quad (10-10)$$

where  $\frac{dQ}{dt}$  is the net rate at which heat energy is being deposited in the volume element. Likely sources of heat are thermal conduction from other portions of the fluid or deposition/emission of radiation. For ideal fluids  $\frac{dQ}{dt}$  is taken to be zero. The condition  $dQ = 0$  defines adiabatic motion. Ideal fluids therefore undergo adiabatic or isentropic motion. From Eq. (10-3)

$$\frac{dV}{dt} = \frac{d}{dt} \left( \frac{4}{3} \pi R_0^3 \right) = M_0 \frac{d}{dt} \left( \frac{1}{\rho} \right) \quad (10-11)$$

Substituting Eq. (10-11) into (10-10), setting  $dQ = 0$ , and canceling the factors  $M_0$ , the equation of energy conservation is found to be

$$\frac{dl}{dt} = -\rho \frac{d}{dt} \left( \frac{1}{\rho} \right) \quad (10-12)$$

### Equation of State

Eqs. (10-5), (10-9), and (10-12) relate the four quantities,  $\vec{r}$ ,  $\rho$ ,  $p$ , and  $l$ . A fourth equation is needed to complete the system, in particular the equation of state which relates the thermodynamic properties  $\rho$ ,  $p$ , and  $l$ ,

$$p = p(\rho, l) \quad (10-13)$$

Frequently the equation of state is taken to be that of a polytropic gas,

$$p = (\gamma - 1)\rho I \quad , \quad \text{or equivalently, } p = \rho kT/m \quad (10-14)$$

with  $\gamma$  constant,  $k$  being Boltzmann's constant,  $T$  temperature, and  $m$  the mass of a molecule, although the form of Eq. (10-13) can be arbitrary provided it represents a realistic adiabatic fluid; for real fluids Eq. (10-13) is frequently tabular.

#### $\gamma$ -Law Gas

The combination of Eq. (10-14) and Eq. (10-12) provides useful simple relations for polytropic fluids. Substitute Eq. (10-14) into Eq. (10-12) and carry out the indicated differentiation to obtain

$$\frac{1}{I} \frac{dI}{dt} = (\gamma - 1) \frac{1}{\rho} \frac{d\rho}{dt} \quad (10-15)$$

Integration yields

$$I = I_0 (\rho/\rho_0)^{\gamma-1} \quad (10-16)$$

where subscript zero indicates initial value. Substitute Eq. (10-16) into Eq. (10-14) to obtain

$$p = p_0 (\rho/\rho_0)^{\gamma} \quad (10-17)$$

Eqs. (10-14), (10-16), and (10-17) are used interchangeably to represent a polytropic, or  $\gamma$ -law gas.

#### Partial Solution. Initial Fireball Expansion

Given a few facts and a great amount of bravery, one may find a useful approximation to initial fireball expansion using the formalism developed to this point. The required facts are:

- a. at very high temperature, radiation transports energy in air much more efficiently than fluid dynamic motion,<sup>1</sup>
- b. radiation transport is strongly temperature dependent, and
- c. the energy in a nuclear explosion is so high that radiation transport dominates material motion until air mass very large compared to bomb mass has been engulfed in the fireball.<sup>1</sup>

Facts a and c imply that a reasonable initial condition for fluid dynamic fireball motion is a sphere of radius  $R_0$  with initial density equal to ambient and initial velocity everywhere zero. Fact b implies that temperature can be taken to be constant throughout the fireball.

To obtain an approximate but useful description of initial expansion, assume the average pressure to act over a length comparable to the fireball radius,  $R$ , then Eq. (10-9) becomes

$$\frac{d^2 R}{dt^2} = -\frac{1}{\rho} \nabla p \sim -\frac{(p_a - p)}{\rho R} \quad (10-18)$$

where gravity has been neglected and  $p_a$  is ambient pressure. Use Eq. (10-17) to eliminate  $p$  in favor of  $\rho$ , then Eq. (10-3) to eliminate  $\rho$  in favor of  $R$  (using  $V = 4\pi R^3/3$ ), to reduce Eq. (10-18) to

$$\frac{d^2 R}{dt^2} = \frac{4\pi}{3M_0} \left[ p_0 R_0^5 / R^3 - p_a R^2 \right] \quad (10-19)$$

where  $p_0$  is initial value of fireball pressure. The left hand side may be manipulated to yield

$$\frac{d^2 R}{dt^2} = \frac{dv}{dt} = \frac{dR}{dt} \frac{dv}{dR} = v \frac{dv}{dR} = \frac{1}{2} \frac{d}{dR} v^2 \quad (10-20)$$

Substitute Eq. (10-20) into Eq. (10-19) and integrate to obtain

$$v = \left[ \frac{2}{\rho_a} \left\{ \frac{p_o}{2} \left( 1 - \frac{R_o^2}{R^2} \right) - \frac{p_a}{3} \left( \frac{R^3}{R_o^3} - 1 \right) \right\} \right]^{1/2} \quad (10-21)$$

where  $\rho_a$  is ambient air density.

Eq. (10-21) could possibly be integrated to obtain  $R$  vs  $t$  but is useful in its present form to obtain an estimate of the maximum size attained by a fireball on its first expansion. The velocity is brought to rest when the argument in the brackets is zero. If  $R \gg R_o$  one can neglect  $R_o^2/R^2$  compared to 1 and 1 compared to  $R^3/R_o^3$  to find

$$R_s \sim R_o \left( \frac{3}{2} p_o/p_a \right)^{1/3} \quad (10-22)$$

Typically, fireball air is reduced to atoms ( $m = \frac{1}{2} m_a$ ) and the temperature at which radiation ceases to transport energy efficiently might be 3000°K near the earth's surface, or 10,000°K near 100 km altitude. From Eq. (10-14)

$$\beta = p_o/p_a \sim 20 \text{ to } 60 \quad (10-23)$$

so

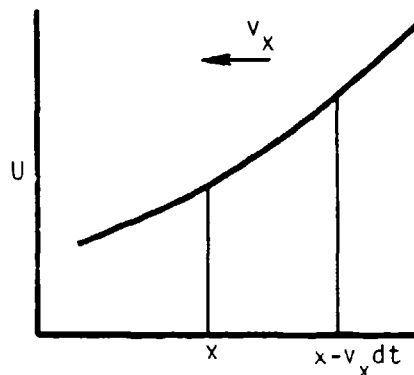
$$R_s/R_o \sim 3 \text{ to } 4 \quad (10-24)$$

The solution Eq. (10-21) represents oscillatory motion. It is very approximate at all times and not useful beyond the initial expansion because it neglects radial variations of the motion and entropy changing effects: blast, radiation, chemistry, etc.

However, several useful facts can be learned from it, including (1) one should expect some oscillation to occur, and (2) the radius at which pressure equilibrium is reached is likely to be around three times the radius at the end of the radiation transport phase.

### 10.2.2 EULERIAN FORMULATION

The Lagrangian equations of fluid dynamics were derived in a frame of reference moving with the local fluid velocity. The Eulerian formulation adopts a fixed frame of reference, in which the fluid and its associated quantities flow past the observer. To express equations in Eulerian form refer to the sketch indicating variation of some quantity of interest,  $U$ , along the  $x$ -axis.



Suppose the value of  $U$  at position  $x$  and time  $t$  is known. The value of  $U$  at  $x$  after an interval  $dt$  will be affected by material transport as well as temporal variation

$$U(x, t+dt) = U(x-v_x dt, t) + \frac{dU}{dt} dt, \quad (10-25)$$

where  $v_x$  is the  $x$ -component of velocity and the derivative  $\frac{dU}{dt}$  is taken in the frame moving with the fluid. Since  $dt$  is small it is irrelevant whether the time derivative is evaluated at  $x$  or  $x-v_x dt$ . If the time rate of change of  $U$  at a fixed point in space is denoted by the partial derivative  $\frac{\partial U}{\partial t}$  and spatial rate of change of  $U$  is denoted at fixed time as  $\frac{\partial U}{\partial x}$  then both sides of Eq. (10-25) can be expected to obtain

$$U(x, t) + \frac{\partial U}{\partial t} dt = U(x, t) - v_x \frac{\partial U}{\partial x} dt + \frac{dU}{dt} dt. \quad (10-26)$$

Solving for the derivative in the frame which moves with the fluid, the total derivative,  $\frac{dU}{dt}$ , in terms of partial derivatives, one obtains

$$\frac{dU}{dt} = \frac{\partial U}{\partial t} + v_x \frac{\partial U}{\partial x}. \quad (10-27)$$



Generalization of the above argument to three dimensions yields

$$\begin{aligned}\frac{dU}{dt} &= \frac{\partial U}{\partial t} + \left( v_x \frac{\partial U}{\partial x} + v_y \frac{\partial U}{\partial y} + v_z \frac{\partial U}{\partial z} \right) \\ &= \frac{\partial U}{\partial t} + \vec{v} \cdot \nabla U\end{aligned}\quad (10-28)$$

where the operator  $\vec{v} \cdot \nabla$  is defined by the expression in parentheses.

It is simpler to directly evaluate  $\frac{dV}{dt}$  rather than use Eq. (10-28). Let the volume be a rectangle bounded by  $x_0$  and  $x_1$ ,  $y_0$  and  $y_1$ , and  $z_0$  and  $z_1$ , then

$$\begin{aligned}\frac{dV}{dt} &= \frac{d}{dt} [(x_1 - x_0)(y_1 - y_0)(z_1 - z_0)] \\ &= \Delta x \Delta y [v_z(z_1) - v_z(z_0)] + \Delta x \Delta z [v_y(y_1) - v_y(y_0)] + \text{term in } v_x\end{aligned}\quad (10-29)$$

where  $\Delta x = x_1 - x_0$  etc. Since

$$v_z(z_1) - v_z(z_0) = v_z(z_0) + \frac{\partial v_z}{\partial z} \Delta z - v_z(z_0) = \frac{\partial v_z}{\partial z} \Delta z, \quad (10-30)$$

and similarly for the other terms, Eq. (10-29) reduces to

$$\frac{dV}{dt} = v \left( \frac{\partial v_x}{\partial x} + \frac{\partial v_y}{\partial y} + \frac{\partial v_z}{\partial z} \right) = \nabla \cdot \vec{v} \quad (10-31)$$

where the divergence  $\nabla \cdot$  is defined as the operator in parenthesis.

### Continuity

From Eq. (10-2),

$$\frac{dH}{dt} = \frac{d}{dt} (\rho V) = \rho \frac{dV}{dt} + V \frac{d\rho}{dt} = 0 \quad (10-32)$$

Use Eq. (10-31) to find

$$\frac{d\rho}{dt} = -\rho \nabla \cdot \vec{v} \quad (10-33)$$

then substitute Eq. (10-28) into Eq. (10-33) to find the equation of continuity

$$\frac{\partial \rho}{\partial t} + \nabla \cdot (\rho \vec{v}) = 0 \quad (10-34)$$

where we have used the vector identity

$$\nabla \cdot (\rho \vec{v}) = \vec{v} \cdot \nabla \rho + \rho \nabla \cdot \vec{v} \quad (10-35)$$

### Momentum Equation

Writing  $\vec{v} = \frac{d\vec{r}}{dt}$  and substituting Eq. (10-28) into (10-9) produces the momentum equation, also known as the force equation and as Euler's equation.

$$\frac{\partial \vec{v}}{\partial t} + \vec{v} \cdot \nabla \vec{v} = -\frac{1}{\rho} \vec{\nabla} p + \vec{g} \quad (10-36)$$

### Energy Equation

Substitution of Eq. (10-28) into (10-12) yields the energy equation

$$\frac{\partial H}{\partial t} + \vec{v} \cdot \nabla H = -p \frac{d}{dt} \left( \frac{1}{\rho} \right) \quad (10-37)$$

or, writing  $\frac{d}{dt} \left( \frac{1}{\rho} \right) = -\frac{1}{\rho^2} \frac{d\rho}{dt}$  and using Eq. (10-33)

$$\frac{\partial H}{\partial t} + \vec{v} \cdot \nabla H = -\frac{1}{\rho} \nabla \cdot \vec{v} \quad (10-38)$$

### 10.3 STATIC EQUILIBRIUM

#### 10.3.1 MECHANICAL EQUILIBRIUM

If a fluid is at rest in a uniform gravitational field (or at rest relative to any uniformly accelerating frame of reference) we can orient the coordinate system such that

$$\vec{g} = -g \hat{z} \quad (10-39)$$

Then Eq. (10-36) implies that under the condition of mechanical equilibrium (defined by the condition  $\vec{v} = \frac{\partial \vec{Y}}{\partial t} = 0$  everywhere)

$$\frac{\partial p}{\partial x} = \frac{\partial p}{\partial y} = 0 \quad \text{and} \quad \frac{\partial p}{\partial z} = -\rho g \quad (10-40)$$

Thus  $p$  is a function of  $z$  only.

#### Water

For a liquid such as water  $\rho$  can be regarded as independent of pressure to a first approximation, then integrate Eq. (10-40) to find

$$p = \rho_w g (z_s - z) + p_s \quad (10-41)$$

where  $\rho_w$  is density of water ( $\rho_w \approx 1 \text{ g/cm}^3$ ),  $z_s$  is surface altitude, and  $p_s$  is surface pressure, which must be equal to mean sea level air pressure ( $p_s \approx 10^6 \text{ dynes/cm}^2$ ). If the surface is to be static,

#### Air

In the case of a compressible fluid such as a gas we must appeal to the equation of state for a solution to Eq. (10-40).

For a gas such as air we may use Eq. (10-14) with  $\gamma = 7/5$  as long as the temperature is below a few thousand degrees, then Eq. (10-40) becomes

$$\frac{1}{p} \frac{\partial p}{\partial z} = - \frac{g}{(\gamma-1)I} \quad (10-42)$$

To proceed we must know  $I$  as a function of altitude or equivalently, the temperature,  $T$ , (via Eq. 10-14) as a function of altitude. Assume  $I$  to be linear with  $z$ ,

$$I = I_0 + \beta(z-z_0) \quad (10-43)$$

where  $\beta$  is some constant gradient and the subscript 0 labels reference values. Then Eq. (10-42) becomes

$$\frac{dp}{p} = - \frac{g dz}{(\gamma-1)[I_0 + \beta(z-z_0)]} \quad (10-44)$$

which can be integrated immediately to yield,

$$p = \begin{cases} p_0 [1 + \beta(z-z_0)/I_0]^{-\frac{\gamma}{\gamma-1}} & , \beta \neq 0 \\ p_0 e^{-z/H} & , \beta = 0 \end{cases} \quad (10-45)$$

where the scale height,  $H$ , is given by

$$H = (\gamma-1)I/g = kT/mg \quad (10-46)$$

using Eq. (10-14). Common usage denotes the combination  $kT/mg$  by scale height or local scale height even if  $\theta \neq 0$ . For rough calculations at altitudes below about 100 km it is adequate to assume  $T_0 \approx 220^\circ\text{K}(-53^\circ\text{C})$  and  $\theta = 0$  which yields  $H \approx 7$  km. If  $T$  is constant the system is not only in mechanical equilibrium but also in thermodynamic equilibrium. For more detailed considerations one must represent the atmosphere as composed of one or more segments using the more general solution Eq. (10-45) for  $\theta \neq 0$ .

### 10.3.2 STABILITY

The condition Eq. (10-40) is necessary for mechanical equilibrium but does not guarantee the equilibrium to be stable. Since in nature (as opposed to an ideal fluid) some fluctuations are always present we must find out whether the fluid equations will cause a departure from mechanical equilibrium to increase or be corrected. To be definite we will consider atmospheric stability but it should be noted that the following treatment is valid for any polytropic ( $\gamma$ -law) fluid in a uniformly accelerating frame.

A simple approach to the problem is to imagine some element of air to be gently displaced vertically from its equilibrium position, the remainder of the atmosphere being undisturbed. To simplify considerations further imagine the displacement velocity to be so low that the element of displaced air adjusts itself at all times to the pressure of its undisturbed surroundings.

Since we are concerned with an identifiable element we will choose the Lagrangian formulation. Specializing the momentum equation (10-9) to one-dimensional vertical motion and using Eq. (10-17), find the equation

$$\frac{d^2z}{dt^2} = -\frac{1}{\rho_0} \left( \frac{\rho_0}{p} \right)^{1/\gamma} \frac{\partial p}{\partial z} - g \quad (10-47)$$

The pressure is to be that appropriate to an atmosphere in mechanical equilibrium. From Eq. (10-45) we can evaluate the right hand side of Eq. (10-47) and find

$$\frac{d^2z}{dt^2} = g \left[ (1 + \bar{\theta}(z - z_0)/I_0)^{-1 + g/\gamma\bar{\theta}} - 1 \right] \quad (10-48)$$

Expanding Eq. (10-48) in a Taylor series for small displacements yields

$$\frac{d^2z}{dt^2} = - \left( \frac{g\bar{\theta}}{I_0} + \frac{g^2}{\gamma I_0} \right) (z - z_0) \quad (10-49)$$

The coefficient of  $(z - z_0)$  must be negative in order to accelerate the element back toward its initial position rather than farther away from it. This requires

$$\bar{\theta} > -g/\gamma \quad (10-50)$$

Using Eq. (10-14) to relate the gradient of specific internal energy to the temperature gradient we find for the atmosphere

$$\frac{dT}{dz} > - \frac{(1-\gamma)mg}{rk} \approx - 10^\circ/\text{km} \quad (10-51)$$

as the condition for stability. The temperature gradient corresponding to equality in Eq. (10-51) is known as the adiabatic gradient (or the adiabatic lapse rate) because any gentle displacement in such an atmosphere leaves the displaced air parcel in thermal, pressure, and density equilibrium with its surroundings.

If the temperature falls with increasing altitude faster than the adiabatic lapse rate the atmosphere is unstable against convective motion. That is, a

displaced air parcel will be accelerated to further displacement leading to convection. This case is exemplified by hot summer days when warm air rises in parcels from fields to form "thermals" (convection cells) which buzzards use to gain altitude without expenditure of energy and airline pilots know as a form of clear air turbulence; on moist days the larger cells form cumulus clouds. For many purposes a nuclear fireball may be regarded as an extremely intense convection cell.

If the temperature falls less rapidly than the adiabatic lapse rate the atmosphere is stable and Eq. (10-49) has simple harmonic motion as a solution

$$z = A \sin(\omega t + \phi) \quad , \quad (10-52)$$

where  $A$  is the amplitude of the motion and  $\phi$  is phase, both determined by initial conditions of the perturbation. Eq. (10-52) can be verified by substitution into Eq. (10-49). The angular frequency,  $\omega$ , is the natural frequency of oscillation of the atmosphere, known as the Brunt-Väisälä frequency

$$\omega_B = \sqrt{g \left( \frac{1}{H} \frac{dH}{dz} + \frac{g}{H^2} \right)} \quad , \quad (10-53)$$

found by substituting (10-52) into (10-49) and using (10-46) to define  $H$ .

Typically, the numerical value of the period of oscillation corresponding to  $\frac{dH}{dz} = 0$  in the atmosphere is

$$\tau_B = \frac{2\pi}{\omega_B} = 5 \text{ min.} \quad (10-54)$$

The above simplified treatment indicates continued oscillation, thus does not quite prove stability for lapse rates greater than adiabatic. We will follow convention at this point and appeal to the reader's intuition to believe that neglected effects; mixing with surrounding material energy transferred to surrounding material, and real fluid viscous effects; all tend to damp the oscillatory motion and thus produce stability. That such effects stabilize the motion can be shown easily although accurate quantitative evaluation is formidable. One approach to this problem is illustrated in the buoyant fireball rise model developed below.

### 10.3.3 FIRST BUOYANT FIREBALL RISE MODEL

A useful model of fireball rise for low-to-moderate yield or explosion altitude may be developed based on the idea of treating a fireball as an unstable convection cell.

In Section 10.2 the fireball was represented as a sphere of air which expands about a factor of 3 in radius before stopping. If the stopping radius,  $R_g$ , is small compared to a scale height then one can expect the fireball to reach approximate pressure equilibrium over its entire surface, with radius near  $R_g$ . This will be the case provided explosion yield or altitude is not too great.

To find the region of validity, let  $u_0$  be specific internal energy of air in the radiation fireball, then roughly

$$\frac{4}{3}\pi \rho_0 R_0^3 u_0 = W \quad (10-55)$$

where  $W$  is energy remaining in the fireball; allowing for thermal radiation and shock,  $W$  might be half the total explosion yield  $Y$ .



Substitution of  $p$  for  $I$  using Eq. (10-14), taking  $p_o/p_a$  to be 40 from Eq. (10-23), and interpreting  $Y$  in units of kilotons ( $= 4.2 \times 10^{19}$  erg), one finds

$$R_o(\text{km}) \approx 4 \times 10^{-3} (Y/\rho)^{1/3}, \quad (10-56)$$

where  $\rho$  is in  $\text{g/cm}^3$ .

Then, from Eq. (10-24)

$$R_s(\text{km}) \approx 3R_o = 1.2 \times 10^{-2} (Y/\rho)^{1/3}. \quad (10-57)$$

Using a value of 7 km for scale height, Eq. (10-57) shows that for yields near 1 kT the burst altitude must be well below 70 km, and for 1 MT the burst altitude must be well below 25 km for a pressure equilibrium fireball to form.

While such a fireball can be regarded as in pressure equilibrium, it is far from density or temperature equilibrium and therefore is not in mechanical equilibrium. It will be quite buoyant.

Once pressure equilibrium is attained, it can be assumed to hold throughout the rise, so one can treat the fireball as a Lagrangian convection cell with

$$p = p_a e^{-z/H}, \quad (10-58)$$

where  $p_a$  is ambient air pressure at the burst point and  $z$  is altitude above burst point.

Rising convection cells are known to mix with the surrounding air, causing entrained air to heat, become buoyant, and rise with the cell. Thus the cell gains mass according to

$$\frac{dM}{dz} = 4\pi \alpha R^2 \rho_a = 4\pi \alpha R^2 \rho_o e^{-z/H} \quad , \quad (10-59)$$

where Eq. (10-59) defines the entrainment coefficient,  $\alpha$ . To make the model tractable, assume  $\alpha = \text{constant}$ .

The volume changes by adiabatic expansion,  $\left. \frac{\partial V}{\partial z} \right|_s$ , and entrainment at constant pressure,  $\left. \frac{\partial V}{\partial z} \right|_p$ .

$$\frac{dV}{dz} = \left. \frac{\partial V}{\partial z} \right|_s + \left. \frac{\partial V}{\partial z} \right|_p \quad . \quad (10-60)$$

During most of the rise the fireball composition will be dominated by entrained air at near ambient temperatures so it is safe to assume the fireball gas constant to be equal to the gas constant of ambient air, then, using Eq. (10-59)

$$\left. \frac{\partial V}{\partial z} \right|_p = \frac{1}{\rho_a} \frac{dM}{dz} = 4\pi \alpha R^2 \quad . \quad (10-61)$$

The change at constant entropy is

$$\left. \frac{\partial V}{\partial z} \right|_s = \frac{d}{dz} \left[ V_o \left( \frac{p_o}{p} \right)^{\frac{1}{\gamma}} \right] = \frac{V}{\gamma H} \quad . \quad (10-62)$$

Substituting (10-61) and (10-62) into (10-60) yields

$$\frac{dV}{dz} = \frac{V}{\gamma H} + 4\pi \alpha R^2 \quad (10-63)$$

or

$$\frac{dR}{dz} = \frac{R}{3\gamma H} + \alpha \quad . \quad (10-64)$$

Since  $\alpha$  is assumed constant, Eq. (10-64) can be integrated to yield

$$\begin{aligned} R &= R_0 e^{\eta} [1+k(1-e^{-\eta})] \\ &\equiv R_0 e^{\eta} S(k, \eta) \end{aligned} \quad (10-65)$$

where

$$k \equiv 3 \gamma H / R_0 \quad \text{and} \quad \eta \equiv \alpha / 3 \gamma H \quad (10-66)$$

$\gamma$  is the gas constant and  $R_0$  is the initial pressure equilibrium fireball radius, from Eq. (10-22).

Now one can substitute Eq. (10-65) into (10-59) and find the mass

$$\begin{aligned} M &= M_0 \left\{ \frac{\rho}{\rho_0} + 3k \left[ \frac{(1+k)^2}{(3\gamma+2)} \left( 1 - e^{-(3\gamma+2)\eta} \right) \right. \right. \\ &\quad \left. \left. - \frac{2k(1+k)}{(3\gamma+1)} \left( 1 - e^{-(3\gamma+1)\eta} \right) + \frac{k^2}{3\gamma} \left( 1 - e^{-3\gamma\eta} \right) \right] \right\} \\ &\equiv M_0 Q(k, \eta) \end{aligned} \quad (10-67)$$

where  $M_0$  is the initial mass of displaced air.

The ratio of fireball density to ambient density can be found from Eq. (10-65) and (10-67) to be

$$\frac{\rho}{\rho_0} = e^{-5\eta+1} \frac{S^3(k, \eta)}{Q(k, \eta)} \quad (10-68)$$

Eq. (10-68) can be solved either iteratively or stepwise for some value of  $\rho/\rho_0$  taken to represent stabilization. A convenient choice is  $\rho/\rho_0 = 1$ , the neutral buoyancy condition.

The stabilization altitude is then

$$z_s = 3y \ln \quad . \quad (10-69)$$

It turns out that about as many calculations are required to solve Eq. (10-68) iteratively as are required to solve it by stepping at constant  $\Delta n$ , then interpolating for the condition  $\rho_a/\rho = 1$ . Stepwise solution has the great advantage that the constant  $k$  and the altitude advance  $\Delta z$  can be re-evaluated at each step, thus effectively removing the occasionally inadequate assumption, Eq. (10-58), of a purely exponential atmosphere.

To make use of this model, one must obtain at least one data point (yield, burst altitude and stabilization altitude) in order to empirically determine  $\alpha$  (typically  $.05 \leq \alpha \leq .1$ ). Then approximate stabilization altitude and final size may be obtained for other explosion conditions, keeping in mind the range of explosion altitudes found above for which the model is applicable.

## 10.4 STEADY FLOW

### Time Independent Eulerian Equations

Steady flow is defined to be flow where the fluid parameters are functions of space only and not time,

$$\frac{\partial \rho}{\partial t} = \frac{\partial v}{\partial t} = \frac{\partial I}{\partial t} = 0 \quad (10-70)$$

In this case the Eulerian equations are much simplified and become

$$\nabla \cdot (\rho \vec{v}) = 0 \quad , \quad (10-71)$$

$$\vec{v} \cdot \nabla \vec{v} = - \frac{1}{\rho} \nabla p + \vec{g} \quad , \quad (10-72)$$

$$\vec{v} \cdot \nabla I = \frac{p}{\rho} \nabla \cdot \vec{v} \quad . \quad (10-73)$$

Having eliminated time as a variable the equations look more tractable but we still cannot integrate any of them for a case of general interest and we would like to be able to do so.

Our attack will be to reduce the terms of Eq. (10-72) to integrable form, in particular we will attempt to write each term as the gradient of some quantity, making whatever assumptions are required as we proceed.

### Gravitational Potential

The easiest term to attack is  $\vec{g}$ . Define the gravitational potential

$$G \equiv -gz \quad , \quad (10-74)$$

then Eq. (10-72) becomes

$$\vec{v} \cdot \nabla \vec{v} = -\frac{1}{\rho} \nabla p + \nabla G \quad (10-75)$$

Now one term ( $\nabla G$ ) is directly integrable  $\left( \int_{z_0}^{z_1} \nabla G dz = G(z_1) - G(z_0) \right)$ .

### Enthalpy

We address the pressure term by introducing the thermodynamic variable enthalpy,

$$h = I + p/\rho \quad (10-76)$$

which is related to the other thermodynamic variables by

$$dh = T ds + \frac{1}{\rho} dp \quad (10-77)$$

where  $s$  is entropy. Since entropy doesn't change in adiabatic flow the first term in Eq. (10-77) is zero and one can write

$$\frac{1}{\rho} \nabla p = \nabla h \quad (10-78)$$

Substitute Eq. (10-78) into (10-75) to find

$$\vec{v} \cdot \nabla \vec{v} = \nabla (-h + G) \quad (10-79)$$

and only one term remains in a form not directly integrable. One can attempt to reduce the velocity term by substituting the vector identity

$$\vec{v} \cdot \nabla \vec{v} = \frac{1}{2} \nabla v^2 - \vec{v} \times (\nabla \times \vec{v}) \quad (10-80)$$

into Eq. (10-79) to obtain

$$\nabla(v^2/2 + W + G) = \vec{v} \times (\nabla \times \vec{v}) \quad (10-81)$$

where all of the integrable terms have been moved to the left hand side of the equation. We have apparently obtained an integrable term  $\left(\frac{1}{2} \nabla v^2\right)$  at the price of introducing the complex non-integrable term on the right of the equation.

### Streamlines

To continue we must introduce an additional restriction. Notice that the undesired term is the cross product of  $\vec{v}$  with a vector and therefore has no component in the direction of fluid motion (that is, no component along  $\vec{v}$ ). We therefore introduce the concept of lines which are everywhere tangent to the flow, streamlines, defined by

$$\frac{dx}{v_x} = \frac{dy}{v_y} = \frac{dz}{v_z} \quad (10-82)$$

Since the flow is steady a streamline defines the trajectory of a fluid particle.

### Bernoulli's Equation

If Eq. (10-81) is specialized to the case of motion along a streamline the gradient operator,  $\nabla$ , becomes the derivative with respect to distance along the streamline,  $\frac{d}{ds}$ , and the right hand side is zero since it has no component along a streamline. Then Eq. (10-81) becomes

$$\frac{d}{ds} \left( \frac{v^2}{2} + W + G \right) = 0, \quad (10-83)$$

which is immediately integrable. Doing so, followed by substitution for  $G$  and  $W$  from their definitions, Eqs. (10-74 and 10-76), yields Bernoulli's equation

$$\frac{v^2}{2} + \frac{1}{\rho} + p/\rho + gz = \text{constant} \quad (10-84)$$

It must be emphasized that Bernoulli's equation holds only if: (a) the flow is steady in time, (b) it is applied along a streamline, and (c) entropy is constant along a given streamline. In Section 11 a method for finding streamlines will be developed.

At this point we can understand some general characteristics.

Equation (10-84) is used to replace  $p$  and  $\rho$  in (10-81) for channels at altitudes which flow down from mountain ranges will produce high winds, high temperatures, though it is not always true that channels are likely to have high winds; the air is not always at zero, therefore has higher pressure than at the outer channel openings.

In order to develop a better understanding of the physical processes involved in the flow of air down a mountain range, it is necessary to consider the flow of air down a mountain range. The flow of air down a mountain range is a complex process involving many factors, including the geometry of the mountain range, the initial conditions of the air, and the physical properties of the air. The flow of air down a mountain range is a complex process involving many factors, including the geometry of the mountain range, the initial conditions of the air, and the physical properties of the air.

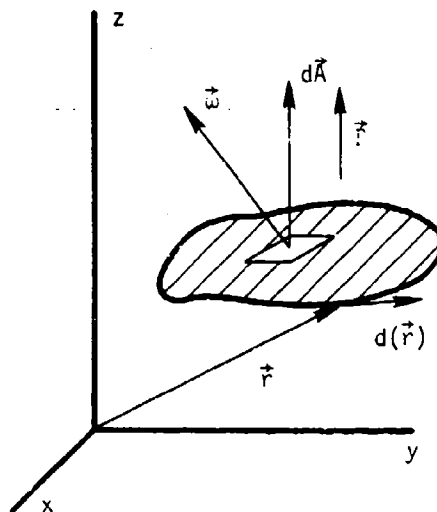


## 10.5 CIRCULATION

We introduce the concept of circulation of the fluid

$$\Gamma \equiv \oint \vec{v} \cdot d\vec{r} \quad (10-85)$$

where the position vector  $\vec{r}$  is to trace a closed loop in the fluid (see sketch). The direction of  $\vec{r}$  follows the right hand rule.



### Bjerknes' Theorem

Let all points on the locus of the loop be moving at the local fluid velocity, then

$$\frac{d}{dt} \Gamma = \frac{d}{dt} \oint \vec{v} \cdot d(\vec{r}) = \oint \frac{d\vec{v}}{dt} \cdot d\vec{r} + \oint \vec{v} \cdot d\left(\frac{d\vec{r}}{dt}\right) \quad (10-86)$$

where we have moved the time derivative through the space differential operator. The last term is just

$$\oint \vec{v} \cdot d\left(\frac{d\vec{r}}{dt}\right) = \oint \vec{v} \cdot d\vec{v} = \frac{1}{2} \oint d(v^2) = 0 \quad (10-87)$$

since the integral of a perfect differential around a closed loop is zero. Substituting from the momentum equation (10-9) for the total derivative  $\frac{d\vec{v}}{dt} = \frac{d^2\vec{r}}{dt^2}$  yields Bjerknes' theorem,

$$\frac{d\Gamma}{dt} = \oint \frac{d\vec{v}}{dt} \cdot d\vec{r} = - \oint \frac{1}{\rho} \nabla p \cdot d\vec{r} + \oint \frac{1}{\rho} \nabla \cdot \vec{v} d\vec{r} + \oint \frac{1}{\rho} \nabla \times \vec{v} \cdot d\vec{r} \quad (10-88)$$

Note that no assumptions were made in derivation of Bjerkne's theorem beyond Eq. (10-9) and the differentiability of  $\vec{v}$ ; in particular neither steady, incompressible, nor isentropic flow was assumed.

### Kelvin's Theorem

Now specialize to the case of isentropic flow where all fluid in the region containing the loop has the same value of entropy. Under this condition we can make the substitution of Eq. (10-78) into (10-88) to obtain Kelvin's theorem,

$$\frac{d\Gamma}{dt} = - \oint \frac{1}{\rho} \nabla p \cdot d\vec{r} = - \oint \nabla W \cdot d\vec{r} = 0 \quad (10-89)$$

By virtue of the differentiability of  $W$ , circulation contained within a loop moving with the material is constant in isentropic flow.

### Vorticity

Now define the vorticity

$$\vec{\zeta} = \nabla \times \vec{v} \quad (10-90)$$

and apply Stoke's theorem to Eq. (10-85) to find

$$\Gamma = \oint \vec{v} \cdot d\vec{r} = \int_A (\nabla \times \vec{v}) \cdot d\vec{A} = \int_A \vec{\zeta} \cdot d\vec{A} \quad (10-91)$$

where the relationship of  $\vec{r}$ ,  $d\vec{r}$ ,  $d\vec{A}$ , and  $\vec{\zeta}$  is illustrated in the sketch on the preceding page. We can make the loop as small as we wish and conclude that Kelvin's theorem implies that vorticity is constant along the path of any fluid element in isentropic flow. In the case of steady flow the path is a streamline but the conclusion so stated holds also for unsteady flow.

### Vortex

A vortex is defined as a mass of fluid which contains vorticity, therefore has non-zero circulation, and moves as a unit through the surrounding fluid. Examples of vortices include hurricanes, smoke rings, rising fireballs and atmospheric thermals. Wakes formed by fast moving objects also contain vortices. A number of problems involving vortex motion in incompressible fluids were worked out in the latter half of the nineteenth century, several are discussed in Reference 2. Unfortunately, Kelvin's theorem is almost the only theorem involving vorticity which is applicable to compressible fluids. The result is that while circulation and vortex motion are known to be very important to some nuclear weapons applications, there is very limited understanding of these quantities and their implications.

## 10.6 POTENTIAL FLOW

### Irrotational Flow

Kelvin's theorem is the tool required to allow a major simplification in the momentum equation, Eq. (10-9). For now we assume flow which is (a) isentropic, (b) has  $\omega = 0$  everywhere initially, and (c) has velocity everywhere differentiable in some region. Then Kelvin's theorem shows that  $\omega$  remains zero for all time within the region. Flow with  $\omega = 0$  is known as irrotational flow.

Now we can retrace the steps in Eqs. (10-74 through 10-81) without assuming steady flow to obtain

$$\frac{\partial \vec{v}}{\partial t} + \nabla(v^2/2 + w + G) = \vec{v} \times \vec{\omega} = 0 \quad (10-92)$$

### Velocity Potential

Any function whose curl (76) is zero can be represented by the gradient of a scalar potential, so we introduce the velocity potential by the equation

$$\vec{v} = \nabla \phi \quad (10-93)$$

Replacing  $\vec{v}$  by  $\nabla \phi$  in the partial time derivative of Eq. (10-92) yields

$$\nabla \left( \frac{\partial \phi}{\partial t} + v^2/2 + w + G \right) = 0 \quad (10-94)$$

Eq. (10-94) can be integrated directly to yield

$$\frac{\partial \phi}{\partial t} + v^2/2 + w + G = f(t) \quad (10-95)$$

where  $f(t)$  is a function of time only; in fact,  $f(t)$  can be absorbed into  $\phi$  and the right hand side of Eq. (10-95) set to zero. We have succeeded in reducing a second order partial differential equation to a first order ordinary differential equation.

### Confrontation with Reality

The potential flow technique is very useful although it does not approach the power implied by Eq. (10-95). The reason is that for many problems the apparently innocuous assumptions (a)-(c) fail and potential flow solutions bear only limited resemblance to reality. We show in Fig. 1-(a) the instantaneous potential flow solution for streamlines about a sphere moving

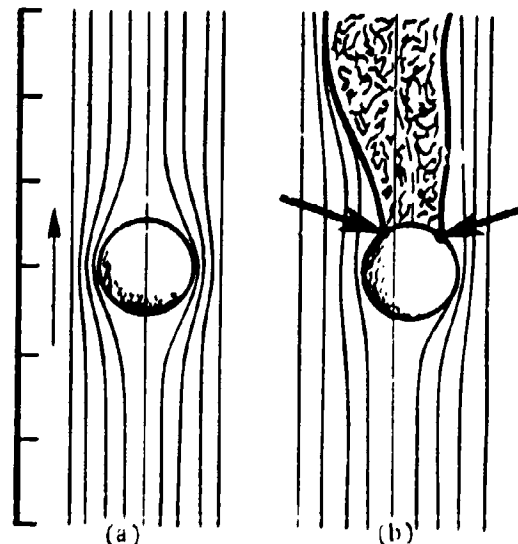


Figure 1. Comparison of potential flow to realistic flow.

through fluid. In (b) is shown a sketch of typical motion of a real sphere moving through a real fluid. The theoretical solution has the characteristics: (1) time steady, (2) no net forces act on the sphere due to the fluid, (3) motion is in a straight line, (4) all streamlines are smooth, and (5) flow is isentropic. The actual motion has the characteristics: (1') variable in time, (2') slowed down due to net resistive forces, (3') the motion traces a spiral, (4') motion is disordered in the wake indicated, and (5') non-isentropic in the wake.

The mathematical reconciliation of this disagreement is that interfaces which violate assumption (c) (discontinuous in  $\vec{v}$ ) can extend through the fluid provided they originate on a boundary, at which Kelvin's theorem doesn't hold. Any solid object represents such a boundary since an integration loop in Eq. (10-89) cannot penetrate the boundary.

The physicist looks at the matter somewhat differently. All real fluids are viscous to some extent. Therefore there is a boundary layer (however thin) around the object in which the Kelvin theorem is violated and vorticity is created. This vorticity separates from the body at the points indicated in the sketch by arrows and is carried away in the wake, gradually mixing with more fluid (without a true discontinuity in velocity anywhere). Thus the folk wisdom among most physicists regards this sort of fluid dynamic problem as a glaring counterexample to the seldom stated, but universally applied, metaphysical principle "small causes produce small effects".

Both the mathematician and physicist also point out that while a potential flow solution to a problem may exist it does not necessarily represent stable flow. Stability is frequently very difficult to analyze, even for small perturbations, and the experimental evidence indicates that some flows are stable against small perturbations but not against large perturbations.

Despite the crushing series of discrepancies listed above, potential flow is very useful for, even in case (b) in the sketch, the flow outside the body-wake boundary (most of the region) can be accurately represented by potential flow. Further, in many cases departures in behavior between experiment and theory are small on a percentage basis, thus potential flow can provide a first approximation. Still, those small departures for the sphere problem have caused spherical cannon balls to become museum curiosities.

Flow separation and wakes are not well understood at present. Laboratory evidence indicates that the separation of flow is influenced by both viscosity of the fluid and uniformity of the flow field, therefore it seems likely that separation, etc. would occur even for an ideal (non-viscous) fluid. We will develop the potential flow solution to the sphere problem in the following section because it is a useful approximation to air flow in the vicinity of a rising fireball, and touch upon viscosity and turbulent effects in later sections.

## 10.7 INCOMPRESSIBLE FLOW

Many problems arise, even for atmospheric motion, for which the density may be regarded as constant.

### 10.7.1 MOMENTUM EQUATION

If density is everywhere constant, it may be taken under the gradient in Euler's equation (10-36) and the momentum equation written as

$$\frac{\partial \vec{v}}{\partial t} + \vec{v} \cdot \nabla \vec{v} = - \nabla \left( \frac{p}{\rho_0} \right) + \vec{g} \quad (10-96)$$

### 10.7.2 BERNOULLI'S EQUATION AND TIME DEPENDENT POTENTIAL

In the case of constant  $\rho$ , the introduction of enthalpy is no longer necessary to develop Bernoulli's equation, which takes the simpler form

$$v^2/2 + p/\rho_0 - gz = \text{const.} \quad (10-97)$$

where  $\rho_0$  is the constant value of density.

Eq. (10-95) becomes

$$\frac{\partial}{\partial t} \left( \frac{v^2}{2} + p/\rho_0 - gz \right) = 0 \quad (10-98)$$

#### General Equation

The general flow problem can be reduced to two equations. If the enthalpy is no longer an interesting variable (if  $\rho$  is constant and constant,  $g$  is 1), becomes  $p/\rho_0$ , thus  $p$  is equivalent to  $h$ . If  $\rho$  is constant, Eq. (10-98) reduces to

$$\frac{\partial}{\partial t} \left( \frac{v^2}{2} + p/\rho_0 - gz \right) = 0 \quad (10-99)$$

We can replace the momentum equation (10-36) by an equation involving only velocity by taking the curl of Eq. (10-92)

$$\frac{\partial}{\partial t} (\nabla \times \vec{v}) = \nabla \times [\vec{v} \times (\nabla \times \vec{v})] \quad (10-100)$$

These two equations (10-99, 10-100) together with the boundary conditions define the problem. For surfaces the boundary condition is that the component of velocity normal to the surface be equal to the normal component of the surface velocity  $[v_n(\text{fluid}) = v_n(\text{surface})]$ .

### 10.7.3 INCOMPRESSIBLE POTENTIAL FLOW

If the flow is irrotational ( $\vec{\omega} = \nabla \times \vec{v} = 0$ ) then Eq. (10-100) is identically satisfied and when Eq. (10-93) is substituted into Eq. (10-99) we find that the potential satisfies Laplace's equation\*

$$\nabla^2 \phi = 0 \quad (10-101)$$

The boundary condition at surfaces now becomes the boundary condition that  $\frac{\partial \phi}{\partial n}$  (where  $n$  denotes the direction normal to the surface) be equal to the normal component of surface velocity  $\left[ \frac{\partial \phi}{\partial n} = v_n(\text{surface}) \right]$ .

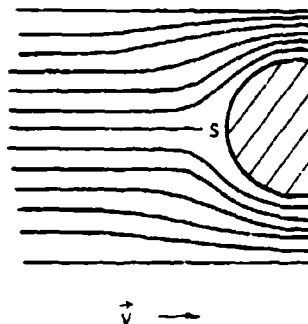
An important property of the velocity potential is that it depends only on velocities at the boundaries and not on acceleration. Time enters Eq. (10-101) only via the velocities at the boundaries. In this regard we point out that in Eq. (10-98) pressure is mathematically determined by acceleration via the term  $\frac{\partial^2 \phi}{\partial t^2}$ , a reversal of the physical interpretation.

\* Later introduced the velocity potential and found the form of Eq. (10-101) which it satisfies. Laplace's name is now associated with this generic form of equation.



#### 10.7.4 STAGNATION POINT

For a case in which gravity can be neglected Bernoulli's equation (10-97) shows that the highest pressure occurs at a stagnation point, where  $v = 0$ . This will occur along the line at which the flow separates to proceed along opposite sides of an obstruction, the point  $S$  in the sketch. If  $p_o$  is the pressure at infinite distance upstream and  $v_o$  is the speed of the object then the stagnation pressure is given by



$$p_s = p_o + \frac{1}{2} \rho_o v_o^2 \quad (10-102)$$

#### 10.7.5 DRAG

A short digression allows an intuitive understanding of turbulent drag to be gained at this point, even though turbulence hasn't yet been formally introduced into the discussion.

Eq. (10-102) allows us to write an expression for force opposing the motion of the object through the fluid

$$F_o = p_o A + \frac{1}{2} \rho_o v_o^2 f A \quad (10-103)$$

where  $A$  is the cross sectional area of the object and  $f$  is some factor smaller than unity which accounts for the fact that the average pressure over the forward portion of the object is less than the stagnation pressure.

Now, in potential flow the velocity approaches  $v_0$  everywhere at large distances so fast that the energy flux receding from the object is the same as that approaching the object (see moving sphere problem, Sec. 7.7), so no energy is lost. Therefore there can be no drag and the force on the rear of the object,  $F_r$ , which acts in the direction of motion, must be identical to  $F_o$ .

$$F_r = p_o A + \frac{1}{2} \rho_o v_o^2 f_r A = F_o \quad (10-104)$$

where we know  $p_o A$ , and  $\rho_o$  are the same values as in front.  $v_o$  must also be the same since there is a stagnation point in the rear, and therefore it must be true that

$$f_r = f_o ; \quad \text{potential flow.} \quad (10-105)$$

Now we accept the experimental fact, illustrated in Figure 1, that frequently motion behind the object is disordered. Observed random velocities at the rear are comparable to, but somewhat smaller than,  $v_o$  which is reasonable since it isn't likely that all of the motion can be randomized, say  $v_r = g v_o$ . We would also expect  $f_r$  to change somewhat but since  $f_r$  is in part determined by geometry it shouldn't be a strong function of velocity, thus the turbulent force at the rear should be

$$F_r' = p_o A + \frac{1}{2} \rho_o v_o^2 g^2 f_r A, \quad (10-106)$$

and the net drag force is

$$F_D = F_o - F_r' = \frac{1}{2} \rho_o v_o^2 A (f_o - g^2 f_r) = \frac{1}{2} \rho_o v_o^2 A C_D \quad (10-107)$$

with  $C_D = f_o - g^2 f_r$

where the drag coefficient,  $C_D$ , might be anticipated to have a value of the order of a few tenths ( $f_o$  and  $f_r$  should be a few tenths, and  $g \approx 1$  so  $C_D$

can't be very close to either one or zero) and  $C_D$  might be velocity and shape dependent, since the efficiency of randomization of energy may depend on both shape and velocity. These conclusions are all experimentally verified when the wake is well developed.

The form of Eq. (10-107) is standard for solid objects, with  $C_D$  being a measured quantity. It is presumed by many to be applicable to fireball motion as well although the value of  $C_D$  appropriate for the fireball case should not be anticipated to be the same as for solid objects. We now return to the incompressible potential flow problem.

#### 10.7.6 STREAM FUNCTION

If incompressible flow depends on only two coordinates, say  $x$  and  $y$ , we can define a stream function,  $\psi$ , which automatically satisfies Eq. (10-99) for either rotational or irrotational flow. Since Eq. (10-99) can be written

$$\nabla \cdot \vec{v} = \frac{\partial}{\partial x} v_x + \frac{\partial}{\partial y} v_y = 0, \quad (10-108)$$

we merely need to define  $\psi$  such that

$$v_x = \frac{\partial \psi}{\partial y} \text{ and } v_y = -\frac{\partial \psi}{\partial x} \quad (10-109)$$

to have Eq. (10-99) satisfied.

To find the equation which  $\psi$  must satisfy, substitute Eq. (10-109) into Eq. (10-100),

$$\frac{\partial}{\partial x} \left( \frac{\partial \psi}{\partial y} \right) - \frac{\partial}{\partial y} \left( \frac{\partial \psi}{\partial x} \right) = 0 \quad (10-110)$$

The form of Eq. (10-110) might lead one to believe that the stream function is more useful in expressing a solution efficiently than in obtaining a solution.

The equation of a streamline is found by substituting Eq. (10-109) into Eq. (10-82), which yields

$$\psi = \text{const.} \quad (10-111)$$

Thus the stream function allows a description of streamlines and both components of velocity (via Eq. 10-84) to be specified in a single scalar function.

In addition, problems may be formulated as problems in functions of a complex variable by combining  $\phi$  and  $\psi$  into a complex function

$$F(z) = \phi + i\psi, \quad (10-112)$$

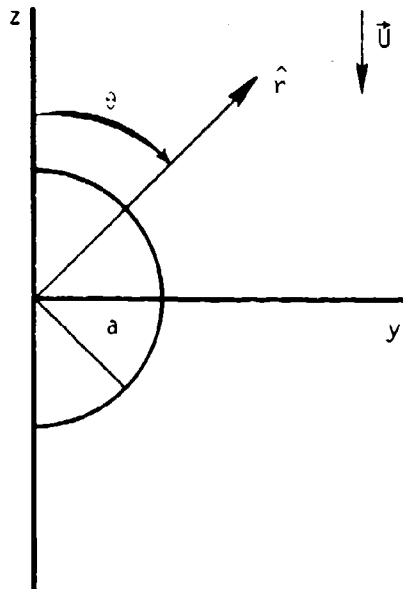
where

$$z = x + iy. \quad (10-113)$$

This formulation allows the powerful array of methods available in function theory to be applied to solution of incompressible potential flow past complex shapes.

### 10.7.7 MOVING SPHERE PROBLEM

The problem of a sphere moving through a fluid has special interest since it represents an approximation to a rising convection cell or fireball. Adopt a coordinate system at rest with respect to the sphere, which has radius  $a$ . Fluid streams by with velocities which approach  $-U\hat{z}$  at infinity in any direction, as indicated in the sketch.



In spherical polar coordinates the solution to Laplace's equation (10-101) can always be written

$$\phi = \sum_{n=-\infty}^{\infty} c_n P_n(\cos\theta) / r^{n+1} \quad , \quad (10-114)$$

where the  $c_n$ 's are constants and  $P_n(\cos\theta)$  are Legendre polynomials.

One boundary condition is that in the frame where the distant fluid is at rest, the laboratory frame, the mass flow out of the region must go to zero at large distances, that is,

$$\lim_{R \rightarrow \infty} \left[ 2\pi \int_0^\pi \rho \vec{v}_{LAB} R^2 \sin\theta d\theta \right] = 0 \quad (10-115)$$

which means

$$|\vec{v}_{LAB}| = |\vec{v} + U\hat{z}| = |\vec{v}_\perp + U\hat{z}| \sim r^{-3}$$

This boundary condition establishes

$$\begin{aligned} c_n &= 0, \quad n \leq -3 \\ c_{-2} &= -U \\ c_0 &= 0, \end{aligned} \quad (10-116)$$

and we can set  $c_{-1} = 0$  since it is only an additive constant ( $P_{-1} = 1$ ). The other boundary condition is that

$$\frac{\partial \phi}{\partial n} = \frac{\partial \phi}{\partial r} = 0 \text{ at } r = a, \text{ for all } \theta.$$

This boundary condition determines the remaining constants

$$\begin{aligned} c_1 &= -Ua^3/2 \\ c_n &= 0 \quad n \geq 2. \end{aligned} \quad (10-117)$$

Then

$$\phi = -Ur P_1(\cos\theta) \left(1 + \frac{a^3}{2r^3}\right) = -Ur \cos\theta \left(1 + \frac{a^3}{2r^3}\right). \quad (10-118)$$

The velocity components, in the frame of the moving sphere, are found from (10-93),

$$\begin{aligned} v_r &= \frac{\partial \phi}{\partial r} = -U \cos\theta (1 - a^3/r^3) \\ v_\theta &= \frac{1}{r} \frac{\partial \phi}{\partial \theta} = U \sin\theta \left(1 + \frac{a^3}{2r^3}\right). \end{aligned} \quad (10-119)$$

The stream function can be obtained from either component of velocity

$$\frac{\partial \psi}{\partial \theta} = -r^2 \sin \theta v_r \text{ or } \frac{\partial \psi}{\partial r} = r \sin \theta v_\theta \quad (10-120)$$

which yield

$$\psi = \frac{U r^2 \sin^2 \theta}{2} (1 - a^3/r^3) \quad (10-121)$$

Stream lines can now be specified by setting  $\psi$  to an arbitrary constant, then solving Eq. (10-121) for  $r(\theta)$ .

### Energy and Impulse

In discussions of moving sphere dynamics the kinetic energy and momentum associated with fluid exterior to the sphere must be taken into account. Expressions for these quantities are most conveniently found in the lab frame where

$$v_r = U \cos \theta a^3/r^3 \quad (10-122)$$

$$v_\theta = \frac{1}{2} U \sin \theta a^3/r^3 \quad (10-123)$$

If the fluid density outside the sphere is  $\rho$  then kinetic energy of fluid motion is obtained by direct integration,

$$\begin{aligned} E_f &= 2\pi \int_a^\infty r^2 dr \int_0^\pi \sin \theta d\theta \left[ \frac{1}{2} \rho (v_r^2 + v_\theta^2) \right] \\ &= \frac{1}{4} \left[ \frac{1}{3} - a^3/U^2 \right] = \frac{1}{4} M_f U^2 \end{aligned} \quad (10-124)$$

where  $M_f$  is the mass of displaced fluid.

Momentum of the exterior fluid is ill defined. The momentum integral corresponding to (10-124) results in a mathematical impasse, a radial integral

which diverges and an angular integral which is zero. The way around this impasse is to replace momentum by a quantity called impulse, which is dynamically equivalent to momentum. Impulse,  $P$ , is defined in terms of the force required to set the fluid in motion if the sphere starts from rest. Manipulation of (10-4) yields

$$\frac{dE}{dU} = F \frac{dz}{dU} \quad , \quad (10-125)$$

and the definition of impulse yields

$$\frac{dP}{dU} = F \frac{dt}{dU} = \frac{dE}{dU} \frac{dU}{dz} \frac{dz}{dU} = \frac{1}{U} \frac{dE}{dU} \quad , \quad (10-126)$$

where (10-125) was used along with  $U = \frac{dz}{dt}$ .

Differentiating (10-124) yields

$$\frac{dP}{dU} = \frac{1}{U} \frac{dE}{dU} = \frac{1}{2} M_f \quad (10-127)$$

Integrating yields the equation for impulse

$$P = \frac{1}{2} M_f U \quad (10-128)$$

where it must be borne in mind that  $M_f$  represents mass of displaced fluid.

As was stated in Section 6, if the sphere is a solid object a wake normally exists downstream within which a potential flow solution is not applicable. In the case of an object with a wake, one must use boundary conditions at the boundary of the wake to determine the coefficients of Legendre polynomials which describe motion outside the wake. Field data indicate the existence of a wake region for near-spherical vortices such as atmospheric thermals and fireballs as well. Unfortunately there is no reason to imagine



the wake associated with circulating fluid to be similar to that associated with a solid object. Very little quantitative information is available relative to "thermal" wakes.

#### 10.7.8 INITIAL RISE VELOCITY OF BUOYANT FIREBALLS

The "First Buoyant Fireball Rise Model" developed in 10.3.3 gave no information regarding time scale or velocity. Information developed in the moving sphere solution allows a partial solution for early rise velocity, accounting for buoyant forces only.

The impulse equation applied to the buoyant fireball after the end of the expansion stage is

$$\frac{d}{dt} P = F \quad (10-129)$$

where  $P$  is the total impulse of the system, comprised of a contribution from the buoyant sphere,  $\frac{4}{3} \pi \rho R^3 U$ , and the contribution (10-128) from the surrounding fluid, thus

$$\frac{4}{3} \pi \frac{d}{dt} \left[ \left( \rho + \frac{1}{2} \rho_a \right) R^3 U \right] = F \quad (10-130)$$

where  $\rho_a$  is ambient density.

#### Archimedes' Principle

The only force being considered here is buoyant force, which can be found from Archimedes' principle. Consider a thin vertical column of area  $dA$ , vertically spanning the fireball, located anywhere within the underdense region. The net force on the element consists of downward forces due to ambient pressure at the top and due to the element mass, plus an upward

force due to ambient pressure at the bottom

$$dF = dA (-p_t - g \rho a + p_B) \quad (10-131)$$

where  $a$  is the length of the vertical element. But

$$\rho a dA = dM \quad (10-132)$$

is the element mass, and the difference in ambient pressure is due to the mass of ambient air in a column

$$(p_B - p_t) dA = g \rho_a a dA = g dM_a \quad (10-133)$$

Integrated over the entire volume, Archimedes' principle states that buoyant force is that due to the mass discrepancy between the material occupying the volume and the displaced fluid; substitute (10-132) and (10-133) into (10-131),

$$F = \int dF = g \int (dM_a - dM) = g (M_a - M) \quad (10-134)$$

### Impulse Equation

Combination of (10-130) and (10-134) yields the impulse equation for a buoyant sphere

$$\frac{d}{dt} \left[ \left( c + \frac{1}{2} \rho_a \right) R^3 U \right] = g (\rho_a - \rho) R^3 \quad (10-135)$$

Equation (10-135) can be considerably simplified by noting that: (a) after expansion to pressure equilibrium,  $\frac{R}{R_s} \left( \frac{\rho_c}{\rho_s} \right)^{1/3} \ll 1$ , thus  $c$  can be neglected, and (b) prior to strong distortion of the spherical region no apparent forces exist to change  $R$  thus  $R$  can be taken as a constant equal to  $R_s$ .

Then (10-135) becomes

$$\frac{d}{dt} U = 2g \quad (10-136)$$

or, replacing  $\frac{d}{dt}$  by  $\frac{dz}{dt} \frac{d}{dz} = U \frac{d}{dz}$ ,

$$\frac{d}{dz} U^2 = 4g,$$

$$U = 2 \sqrt{gz} \quad (10-137)$$

Since the spherical bubble of low density air has no tensile strength at all and almost no inertia compared to the surrounding fluid, one would expect Eq. (10-137) to hold only until the fireball has risen the minimum distance which allows strong distortion, say  $R_g$ .

Then the initial buoyant rise velocity should be attained during a rise of about a fireball radius and would be expected to be about

$$U_0 \sim 2 \sqrt{gR_g} \quad (10-138)$$

Several effects have been neglected in deriving Eq. (10-138), including shock effects and initial expansion reaction (see Section 10.10) but for low yield (that is,  $R_g/H \ll 1$ ) Eq. (10-138) can be expected to be within a factor of about 2 of the correct result.

#### 10.7.9 SECOND BUOYANT FIREBALL RISE MODEL

Given one experimental fact and one brash assumption, we are now in a position to develop a dynamical approximate solution for the main phase of buoyant fireball rise. The experimental fact needed is that over a considerable extent of the rise, velocity is nearly constant for buoyant fireballs.

The required brash assumption involves the entrainment coefficient defined in Eq. (10-59). In References 3 and 4 a dimensional argument is presented for incompressible flow which yields

$$\alpha = \frac{g}{5} \frac{(c_a - 1)R}{U^2} \quad (10-139)$$

A fair amount of data supports this form when  $c_a$  is a constant, in which event  $\alpha$  turns out to be constant. We will assume  $\alpha$  to be given by (10-139) for the case of rising fireballs, despite the nonconstancy of  $c_a$  throughout the rise, and accept the consequent variability of  $\alpha$ .

Substitution of (10-139) into (10-59) yields

$$\frac{dM}{dz} = 4\pi R^2 \alpha = \frac{4\pi g}{5U^2} (c_a - 1)R^2 \quad (10-140)$$

Differentiate (10-140) with respect to  $z$  to obtain

$$\frac{d^2}{dz^2} M = \frac{g}{U^2} \frac{d}{dz} \left[ \frac{4}{5} (c_a - 1)R^2 \right] \quad (10-141)$$

Carrying out the differentiation of the RHS find

$$\frac{d}{dz} \left[ \frac{4}{5} (c_a - 1)R^2 \right] = -V_{c_a}/H + c_a \frac{dV}{dz} + \frac{dM}{dz} \quad (10-142)$$

Use (10-63) to evaluate  $\frac{dV}{dz}$  and (10-59) to evaluate  $\frac{dM}{dz}$  to find

$$\frac{d}{dz} \left[ \frac{4}{5} (c_a - 1)R^2 \right] = -\frac{(1-11)}{10} \frac{4}{5} \frac{g}{U^2} (c_a - 1)R^2 \quad (10-143)$$

Then (10-141) becomes

$$\frac{d^2}{dz^2} (\rho R^3) = - \frac{(\gamma-1)g}{\alpha H^2 H} \rho_a R^3 = - \frac{\omega_B^2}{U^2} \rho_a R^3, \quad (10-144)$$

where  $\omega_B$  is defined in (10-53).

During most of the rise  $\rho \approx \rho_a$ . With this assumption one can integrate (10-144) immediately to obtain

$$\rho R^3 = A \sin \left[ \frac{\omega_B}{U} z + \phi \right] \quad (10-145)$$

where the constants of integration,  $A$  and  $\phi$ , are evaluated by requiring  $\rho R^3 = \rho_0 R_s^3$  at  $z = 0$  and requiring (10-140) to hold at  $z = 0$ . These conditions yield

$$\phi = \tan^{-1} \left[ \frac{\omega_B U}{g(\rho_0/\rho_s - 1)} \right] \approx \frac{\omega_B \rho_s U}{g \rho_0}$$

and

$$A \approx \frac{g \rho_0 R_s^3}{\omega_B U} \quad (10-146)$$

where  $\rho_0$  represents ambient density at burst altitude and  $s$  indicates fireball quantities at pressure equilibrium radius. Using (10-138) for  $U$  one finds

$$\rho R^3 = \rho_0 R_s^2 \frac{\sqrt{g R_s}}{\omega_B} \sin \left[ \frac{\omega_B}{2 \sqrt{g R_s}} \left( z + \frac{4 R_s \rho_s}{\rho_0} \right) \right] \quad (10-147)$$

At some point the partial solution (10-147) must fail, surely by the time the entrainment coefficient,  $\alpha$ , goes to zero, or equivalently, the mass reaches a maximum. Since  $\alpha = 0$  is also the neutral buoyancy condition,

stabilization should be reached at or, since  $U$  is presumably still positive at that point if not constant, slightly above the point where mass ( $\rho R^3$ ) reaches a maximum. Neglecting the small phase factor, set the argument of the sin in Eq. (10-147) to  $\pi/2$  to obtain

$$z_S \approx \frac{\sqrt{gR_S}}{\omega_B} \quad (10-148)$$

and the time required is

$$\tau_S = \frac{z_S}{U} \approx \frac{\pi}{\omega_B} \approx 2.5 \text{ min}.$$

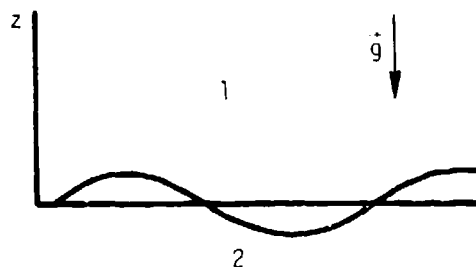
This partial solution indicates that time to stabilization is roughly independent of yield, and that rise distance,  $z_S$ , is very weakly dependent on yield. Since  $R_S \propto Y^{1/3}$ ,

$$z_S \propto Y^{1/6} \quad (10-149)$$

While this sort of partial solution has necessarily been grossly simplified in order to make a difficult problem tractable, the results do indicate reasonably the dependence of important parameters ( $U$ ,  $z$ ,  $M$ ,  $\tau_S$ ) and roughly their magnitudes.

#### 10.7.10 RAYLEIGH-TAYLOR INSTABILITY

A problem of interest, illustrated in the sketch, is the stability of an interface between fluids of different densities  $\rho_1$  and  $\rho_2$ , when the materials are subject to an acceleration perpendicular to the interface. As examples, the situation can represent an air-water interface in a gravitational field, or detonation products from an explosion being slowed down as they expand against shocked air.



Suppose for simplicity the interface is displaced by a small amount,  $z_I$ , from its equilibrium position at  $z = 0$ . Write the displacement as the real part of

$$z_I = a_0 e^{i(ky - \omega t)} \quad (10-150)$$

where  $k$  is real but  $\omega$  may be complex.

Any small displacement can be decomposed into sinusoidal components similar to Eq. (10-150), thus treating one will give an answer which can be generalized to any shape. To simplify further assume the fluids to be incompressible; the results will be semi-quantitatively correct even if this assumption be incorrect.

Solutions which satisfy Eq. (10-101) in the two regions and vanish as  $z \rightarrow \pm \infty$  are the real parts of

$$z_1 = c_1 e^{-kz + i(ky - \omega t)} \quad , \quad z_2 = c_2 e^{kz + i(ky - \omega t)} \quad (10-151)$$

As long as the perturbation is weak,  $kz \ll 1$ , we can take the  $z$  component of velocity as being perpendicular to the interface and equal to the interface velocity. Then the boundary condition which requires continuous normal velocity is

$$\frac{\partial z_1}{\partial z} = \frac{\partial z_2}{\partial z} \quad \text{at } z = 0 \quad \Rightarrow \quad -k c_1 = k c_2 e^{i(ky - \omega t)} \quad (10-152)$$

So

$$c_1 = -c_2 \quad \text{and} \quad c_2 = -c_1 \quad (10-153)$$

The pressure must also be continuous. Solve Eq. (10-98) for pressure to find

$$p_1 = p_2 = \rho_1 \frac{\partial \phi_1}{\partial t} + \rho_1 v_1^2/2 - \rho_1 gz = \rho_2 \frac{\partial \phi_2}{\partial t} + \rho_2 v_2^2/2 - \rho_2 gz \quad (10-154)$$

Eq. (10-154) can be simplified by noting that terms in  $v^2$  are negligible compared to other terms. Substituting from Eqs. (10-150, 151, 153) yields

$$\frac{\rho_1 \omega^2 a_0}{k} e^{-kz+i(ky-\omega t)} - \rho_1 g a_0 e^{i(ky-\omega t)} = - \frac{\rho_2 \omega^2 a_0}{k} e^{-kz+i(ky-\omega t)} - \rho_2 g a_0 e^{i(ky-\omega t)} \quad (10-155)$$

Cancelling common factors, setting  $z = 0$  and solving for  $\omega$  yields

$$\omega = \pm \sqrt{\frac{kg(\rho_2 - \rho_1)}{(\rho_2 + \rho_1)}} \quad (10-156)$$

The time dependence of the interface position is

$$z_1 = \exp \left\{ \pm i \sqrt{\frac{kg(\rho_2 - \rho_1)}{(\rho_2 + \rho_1)}} t \right\} \quad (10-157)$$

The amplitude of displacement oscillates if  $\rho_2 > \rho_1$ . On the other hand if  $\rho_2 < \rho_1$  the square root in Eq. (10-157) is imaginary and the amplitude will have one solution (the minus sign) which grows exponentially in time. Note that larger values of  $k$  (shorter wavelengths) grow fastest. This is known as the Rayleigh-Taylor instability. It causes relatively dense detonation

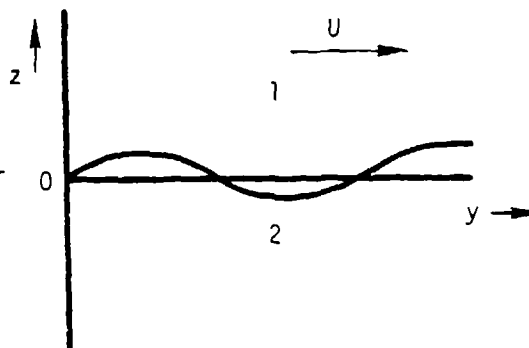


products to mix with air after an explosion. In addition, one should anticipate such instabilities in the region of the top of a rising underdense bubble, atmospheric thermal, or fireball.

Mechanisms analogous to Rayleigh-Taylor instabilities exist in plasma-magnetic interactions which cause high altitude nuclear fireballs and other plasmas to break up into geomagnetic field aligned "striations" (see Chap. 15).

#### 10.7.11 KELVIN-HELMHOLTZ INSTABILITY

Another problem of general interest concerns the fate of an interface between two fluids where a discontinuity occurs in the tangential component of velocity. In fact, the Rayleigh-Taylor problem just discussed provides one important example of such a situation, for the potentials of Eq. (10-151) produce a discontinuity in tangential velocity.



A more mundane example is furnished by wind blowing across the surface of water. We will again assume the fluids to be incompressible,  $|ka_1| \ll 1$ , and without loss of generality choose a coordinate system in which fluid 1 moves to the right with velocity  $U$  as indicated in the sketch. We again choose an initial perturbation of the form Eq. (10-150). Potentials which satisfy Laplace's equation (10-101) and the boundary conditions at large positive and negative  $z$  are:

$$\phi_1 = c_1 e^{-kz+i(ky-ct)} + Uy \quad \text{and} \quad \phi_2 = c_2 e^{kz+i(ky-ct)} \quad (10-158)$$

The components of velocity normal to the interface must be equal to each other and equal to the velocity of the interface. Neglecting terms of order  $|ka|$  we have

$$\frac{\partial \phi_2}{\partial y} = \frac{\partial z_I}{\partial t} \quad \text{and} \quad \frac{\partial \phi_1}{\partial y} - U \frac{\partial z_I}{\partial y} = \frac{\partial z_I}{\partial t} \quad (10-159)$$

where one must account for the contribution to  $v_n$  in fluid 1 due to the velocity  $U$  in the  $y$  direction, since  $U$  is not presumed small. Eqs. (10-159) allow the constants to be found

$$c_1 = i \left( \frac{\omega}{k} - U \right) a_0, \quad c_2 = i a_0 / k \quad (10-160)$$

In the unperturbed case Eq. (10-98) reduces to

$$p_1 + \frac{1}{2} \rho_1 U^2 = p_2 \quad (10-161)$$

Remembering this and substituting Eq. (10-158) into Eq. (10-98) with the values of the constants  $c_1$  and  $c_2$  just found yields

$$-\rho_2 \omega^2 / k = i \left( \frac{\omega}{k} - U \right) - \rho_1 U (-kU) \quad (10-162)$$

after cancellation of common factors and setting  $z = 0$ , as before. Solving for  $\omega$  yields

$$\omega = \frac{\rho_1 k U}{(\rho_1 + \rho_2)} \pm i k U \sqrt{\frac{\rho_1 \rho_2}{(\rho_1 + \rho_2)^2}} \quad (10-163)$$

The result, Eq. (10-163) indicates that sliding interfaces are always unstable, irrespective of the relative densities, or the value of  $U$ , or  $k$ . Had the effects of surface tension been included, instability would have been found for velocities  $U$  above a given value. Effects of viscosity (to be introduced in the following section) are not as clear, in general viscous forces seem to reduce the growth rate but do not produce stability. Viscous forces do, however, prevent the formation of a discontinuity in  $U$  or  $\rho$  at boundaries internal to a fluid. For boundaries where  $U$  and

$\rho$  vary continuously some unstable values of  $k$  always seem to occur, at least in those cases which have been worked out (Ref. 10-5), but the range of unstable  $k$  and the growth rate depend critically on the precise form of the assumed variation of  $\rho$  and of  $U$ . In cases worked out to date, the form of  $\rho$  and  $U$  variations have been chosen more for mathematical tractability than for physical reality.

Chapter 15.4.2 discusses the stabilizing effect of gravity on the Kelvin-Helmholtz instability. One can confidently expect the Kelvin-Helmholtz instability to aid in the mixing of expanding detonation products with air. It is also a candidate for producing mixing around the edge of rising fireballs, cumulus clouds, etc.

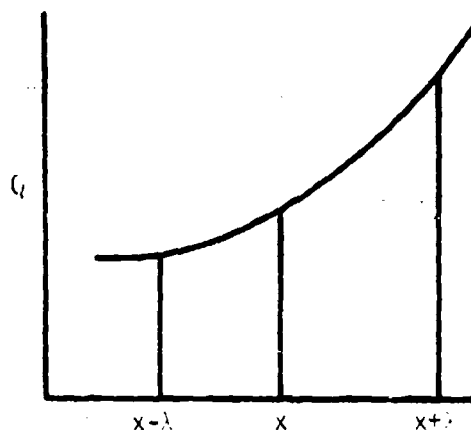
## 10.8 REAL FLUID EFFECTS

Real fluids are composed of discrete particles, atoms or molecules, which individually obey the laws of relativistic quantum mechanics. For most considerations (but not for superfluids, many astrophysical problems, and some nuclear weapons problems) it is a good approximation to neglect relativistic and quantum effects and treat each molecule as if it obeyed Newtonian mechanics.

Even so, each small volume element may contain a great number of particles with a variety of velocities and an irregular spatial distribution, far too many to tempt one to solve the equations of motion for each individual molecule. The ideal fluid approximation treats only the average of mass density, momentum density, and energy density, thus neglecting entirely the discrete nature of matter. The next stage of sophistication is to introduce effects on a molecular level, but treating only the average of quantities such as molecular interaction length (or mean free path), molecular speed, etc. In this way additional terms are introduced into the fluid equations which describe a first approximation to real fluids. A number of attempts at further sophistication have been devised and some are described in Chapter 12. The first, viscous fluid, approximation is conceptually straightforward but sufficiently complex mathematically that tensor notation rather than vector notation is necessary to allow the equations to be presented in a legible, albeit essentially intractable, form. Accordingly the discussion here will be limited to a physically sound but mathematically approximate derivation of the terms to be added to the equations of an ideal fluid, followed by treatment of some especially important effects which are straightforward.

### Basic Physics

Let  $Q$  be the mean value of any quantity associated with molecules and suppose  $Q$  varies with  $x$  as illustrated in the sketch. One may imagine  $Q$  to represent the mass density,  $\rho$ , of particles of a particular molecular species, the momentum density,  $\rho \vec{v}$ , or the internal energy density,  $\frac{1}{2} \rho v_T^2$ , where  $v_T$  is mean molecular velocity



of thermal motion. On the average, particles have the value of  $Q$  appropriate to their position,  $x$ . Random thermal motion causes about half of them to go toward positive  $x$  and half to go toward negative  $x$ . They go an average distance  $\lambda$  at velocity  $v_T$  before equilibrating via collisions at the new position. The flux of  $Q$  passing position  $x$  from lower values of  $x$  originates at  $x - \lambda$  and travels with velocity  $v_T$ .

$$F_- = Q(x-\lambda)v_T/2 \quad , \quad (10-164)$$

where the factor of 2 accounts for the fact that half the molecules at position  $x - \lambda$  will go in the opposite direction. The net flux past position  $x$  is the difference between  $F_-$  and a similar term due to material originating at  $x + \lambda$ ,

$$\begin{aligned} F &= F_- - F_+ = \frac{1}{2} v_T [Q(x-\lambda) - Q(x+\lambda)] \\ &= \frac{1}{2} v_T \left[ Q(x) - \lambda \frac{\partial Q}{\partial x} - \left( Q(x) + \lambda \frac{\partial Q}{\partial x} \right) \right] = - v_T \lambda \frac{\partial Q}{\partial x} \quad . \quad (10-165) \end{aligned}$$

Eq. (10-165) describes the flux of any interesting quantity down its gradient due to random molecular motion. The correct forms of  $v_T \lambda$  and accepted terminology for quantities of most general interest are given in Reference (10-6) and summarized in Table 1.

Table 1. Viscous Effects

Q	Name of Process	$V_T \lambda$ Coefficient	Form of Flux Term
Molecules	Diffusion	$D = \frac{3}{32n\sigma} \left( \frac{\pi kT(m_1+m_2)}{2m_1m_2} \right)^{1/2}$	$D \nabla \rho$
Momentum	Viscosity	$\eta = \frac{5}{64\sigma} \sqrt{\pi m kT}$	$(\eta \nabla) \vec{v}$
Energy	Conduction	$\kappa = \frac{75k}{256\sigma} \sqrt{\frac{\pi kT}{m}}$	$\kappa \nabla T$

All formulae in Table 1 are for molecules which are rigid spheres,  $D$  is for a binary mixture,  $k$  is Boltzman's constant,  $m$  is molecular mass, and  $T$  is temperature,  $\sigma$  is collision cross section, and  $n$  is total molecular density.

If one is interested in the building or depletion of the density  $Q$  in the vicinity of  $x$  imagine two surfaces located at  $x + dx/2$  and  $x - dx/2$ ; then the volume element of area  $dA$  and length  $dx$  around  $x$  at  $t + dt$  contains

$$Q(t+dt)dAdx = Q(t)dAdx + F(x-dx/2)dAdt - F(x+dx/2)dAdt \quad (10-166)$$

Expanding in Taylor series and cancelling the common factor  $dx$  yields

$$Q(t)dx + \left. \frac{\partial Q}{\partial t} \right|_m dt dx = Q(t)dx + F(x)dt - \frac{dx}{2} \frac{\partial F}{\partial x} dt - \left( F(x)dt + \frac{dx}{2} \frac{\partial F}{\partial x} dt \right) \quad (10-167)$$

where the designation  $\left|_m\right.$  implies that only molecular effects are being considered.

Cancelling, then substituting from Eq. (10-165) yields

$$\left. \frac{\partial Q}{\partial t} \right|_m = - \frac{\partial F}{\partial x} = \frac{\partial}{\partial x} \left( v_T \lambda \frac{\partial Q}{\partial x} \right) \quad (10-168)$$

We will now proceed to develop the Eulerian formulation of the fluid dynamic equations including viscous effects preparatory to applying them to some basic problems.

### Diffusion

To account for molecular effects in this approximation one needs to add the three-dimensional form of Eq. (10-168) to the equation of continuity (10-34) if the fluid is composed of molecules of different types (say a mixture of neutrons and air) to obtain the diffusion approximation,

$$\frac{\partial}{\partial t} \rho_i + \nabla \cdot (\rho_i \vec{v}) = \nabla \cdot (D \nabla \rho_i) \quad , \quad [\text{CONTINUITY}] \quad (10-169)$$

where subscript  $i$  labels the fluid constituent of interest; note the diffusion term is not necessary if only one species is present.

### Heat Conduction

The energy equation corresponding to Eq. (10-38) for real fluids is,

$$\frac{\partial I}{\partial t} + \vec{v} \cdot \nabla I = - \frac{p}{\rho} \nabla \cdot \vec{v} + \frac{1}{\rho} \nabla \cdot \kappa \nabla T \quad , \quad [\text{ENERGY}] \quad (10-170)$$

where  $\kappa$  is the coefficient of thermal conductivity and  $T$  is temperature. For a polytropic gas, from (10-14)

$$T = \frac{m}{k} (\gamma - 1) I \quad , \quad (10-171)$$

where  $m$  is the mass of an individual molecule and  $k$  is Boltzman's constant.

### Viscosity

In the case where the dynamic viscosity coefficient,  $\eta$ , is constant (not too bad an approximation normally) the momentum equation (10-36) can be written (Reference 10-7)

$$\left[ \frac{\partial \vec{v}}{\partial t} + (\vec{v} \cdot \nabla) \vec{v} \right] = - \nabla p + \rho \vec{g} + \rho \zeta \vec{v} + \frac{2}{3} \nabla (\vec{v} \cdot \vec{v}) + \nabla (\zeta \cdot \vec{v}) \quad [\text{MOMENTUM}] \quad (10-172)$$

where the second viscosity coefficient,  $\zeta$ , accounts for the temporal delay in reaching local equilibrium at the new value of  $\rho$  (from Eq. (10-35)  $\vec{v} \cdot \vec{v} = - \rho^{-1} dp/dt$ ). Frequently fluids equilibrate quickly compared to the characteristic time of the motion and  $\zeta$  is negligible; at any rate we will neglect  $\zeta$  in the following.

For incompressible flow, Eq. (10-172) reduces to

$$\frac{\partial \vec{v}}{\partial t} + (\vec{v} \cdot \nabla) \vec{v} = - \frac{1}{\rho} \nabla p + \vec{g} + \nabla^2 \vec{v} \quad , \quad [\text{MOMENTUM, INCOMPRESSIBLE}] \quad (10-173)$$



where  $\nu \equiv \eta/\rho$  is the kinematic viscosity.

For irrotational but compressible flow Eq. (10-172) reduces to

$$\frac{\partial \vec{v}}{\partial t} + (\vec{v} \cdot \nabla) \vec{v} = -\frac{1}{\rho} \nabla p + \vec{g} + \frac{4}{3} \nu \nabla (\nabla \cdot \vec{v}) \quad [\text{MOMENTUM, IRROTATIONAL}] \quad (10-174)$$

Since molecular forces will always cause fluid molecules immediately adjacent to a rigid boundary to adhere to the boundary, the boundary condition imposed in real fluids is that both normal and tangential components of the fluid velocity be zero relative to any rigid boundary, rather than merely the normal component of velocity as in an ideal fluid. The new boundary condition can alter the nature of the mathematical solution to a major degree and is a sufficient (but not always necessary) reason for the existence of wakes behind solid objects.

## 10.9 SOUND WAVES

### Wave Equation

The Eulerian equations of hydrodynamics can be made more tractable if the assumption is made that a weak isentropic disturbance exists. Write

$$p = p_0 + p', \quad \rho = \rho_0 + \rho', \quad I = I_0 + I' \quad , \quad (10-175)$$

where  $p_0$ ,  $\rho_0$ , and  $I_0$  are constant and assume the velocity  $\vec{u}$  is small. Substitution of Eq. (10-175) into Eqs. (10-34, 36, 38) and keeping only first order terms yields

$$\frac{\partial \rho'}{\partial t} + \rho_0 \nabla \cdot \vec{u} = 0 \quad (10-176)$$

$$\frac{\partial \vec{u}}{\partial t} + \frac{1}{\rho_0} \nabla p' = 0 \quad (10-177)$$

$$\frac{\partial I'}{\partial t} + \frac{p_0}{\rho_0} \nabla \cdot \vec{u} = 0 \quad , \quad (10-178)$$

where  $\vec{g}$  has been neglected as being uninteresting for present purposes. Since the flow is assumed isentropic we can write

$$\nabla p' = \left. \frac{\partial p}{\partial \rho} \right|_s \nabla \rho' = c^2 \nabla \rho' \quad (10-179)$$

where the quantity  $c$ , which will turn out to be the velocity of propagation, or sound speed, is defined as the square root of the rate of change of pressure with density at constant entropy,  $s$ .

$$c \equiv \sqrt{\left. \frac{\partial p}{\partial \rho} \right|_s} \quad (10-180)$$

For a polytropic gas, from Eq. (10-17) and (10-14)

$$c^2 = \frac{\gamma p}{\rho} = \frac{\gamma k T}{m} \quad (10-181)$$

The following treatment depends on compressibility of the medium; we might have assumed something other than entropy was conserved in the compression (say, temperature) and proceeded; only the value of  $c$  would change.

Substitution of Eq. (10-180) into Eq. (10-177) yields

$$\frac{\partial \vec{u}}{\partial t} + \frac{c^2}{\rho_0} \nabla \rho' = 0 \quad (10-182)$$

Now the pair, Eq. (10-176) and Eq. (10-182) involve only  $\vec{u}$  and  $\rho'$ . Differentiating Eq. (10-176) with respect to time yields

$$\frac{\partial^2 \rho'}{\partial t^2} + \rho_0 \nabla \cdot \frac{\partial \vec{u}}{\partial t} = 0 \quad (10-183)$$

Now substitute Eq. (10-182) for the term in  $\vec{u}$  to obtain

$$\frac{\partial^2 \rho'}{\partial t^2} - c^2 \nabla^2 \rho' = 0 \quad (10-184)$$

Eq. (10-184) is known as the wave equation. For plane symmetry in one dimension (no  $y$  or  $z$  dependence) it becomes

$$\frac{\partial^2 \rho'}{\partial t^2} - c^2 \frac{\partial^2 \rho'}{\partial x^2} = 0 \quad (10-185)$$

which has solutions, verifiable by substitution

$$\rho' = [f_1(x-ct) + f_2(x+ct)] \rho_0 \quad (10-186)$$

where  $f_1$  and  $f_2$  are arbitrary functions which are differentiable twice and small compared to 1.0. Integrating Eq. (10-179) shows that

$$p' = c^2 p' \quad (10-187)$$

where the integration constant must be zero to get back  $p_0$  when  $p' = p_0$ .

Substitution of Eq. (10-187) into Eq. (10-185) shows that the pressure perturbation also obeys the wave equation. To obtain the equation for  $u$  differentiate Eq. (10-182) with respect to time rather than Eq. (10-176), then substitute from Eq. (10-176) to find that  $\bar{u}$  obeys the same wave equation. From Eq. (10-187) and Eq. (10-186) we find

$$\begin{aligned} \frac{\partial u}{\partial t} &= - \frac{c^2}{\gamma} \frac{\partial p'}{\partial x} = - c^2 \frac{\partial}{\partial x} [f_1(x-ct) + f_2(x+ct)] \\ &= c \frac{\partial}{\partial x} [f_1(x-ct) - f_2(x+ct)] \end{aligned} \quad (10-188)$$

where the last step can be verified by carrying out the  $x$  and  $t$  differentiations. Then integrate Eq. (10-188) to obtain

$$u = c [f_1(x-ct) - f_2(x+ct)] \quad (10-189)$$

The internal energy is found from the equation of state

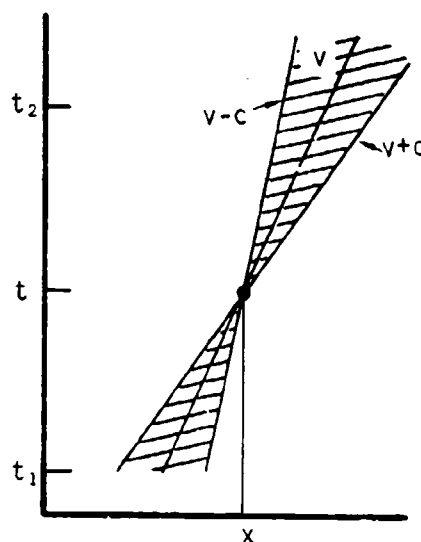
$$p' = \frac{1}{\gamma - 1} \left( \bar{p}' - \frac{\bar{p}'^2}{\bar{p}'} \right) = c^2 \bar{p}' \quad (10-190)$$

the Eqs. (10-186), (10-187), and (10-189) form a set which can be fit to any physically possible initial perturbation to find the solution functions  $f_1$  and  $f_2$ . Plane wave isentropic disturbances, or sound waves, in an

ideal compressible fluid can always be decomposed into two functions  $f_1$  and  $f_2$  which propagate at sound speed forward and backward and are unchanged in form.

### Characteristics

The results obtained above can immediately be generalized to the case where the fluid velocity is non-zero. If the fluid has velocity  $v$ , not necessarily small, then simply transform to the coordinate system moving with the fluid velocity  $v$  and find the disturbance to travel with velocity  $v \pm c$ . From the sketch it can be seen that a point at  $(x, t)$  can only be influenced by conditions existing at positions within the shaded region at prior times and can only influence conditions at positions in the shaded regions at subsequent times. Lines defined by the characteristic propagation velocities  $v \pm c$  are called characteristics of the motion. The concept of characteristics is particularly useful in supersonic flow problems where characteristics allow one to restrict attention to the limited region of space capable of influencing any point of interest.



Effects of non-linear terms in the ideal fluid equations have been neglected in the foregoing as well as real fluid, viscous effects. Viscous effects are important even in the linear approximation, therefore will be treated next.

### Attenuation of Sound Waves

To find the wave equation for a plane sound wave including viscous effects write the linearized form of Eq. (10-174) to obtain

$$\frac{\partial u}{\partial t} = -\frac{1}{\rho_0} \left[ \left. \frac{\partial p}{\partial \rho} \right|_s \frac{\partial \rho'}{\partial x} + \left. \frac{\partial p}{\partial s} \right|_p \frac{\partial s}{\partial x} \right] + \frac{4\nu}{3} \frac{\partial^2 u}{\partial x^2} \quad (10-191)$$

where the partial derivative with respect to entropy is necessary because viscous effects are irreversible, therefore the disturbance is no longer isentropic.

The entropy is found from its definition

$$ds \equiv \frac{\Delta I}{T} \quad (10-192)$$

where the symbol,  $\Delta$ , implies a differential irreversible change in  $I$ . From the equation of state, Eq. (10-14) and Eq. (10-192) we can evaluate

$$\left. \frac{\partial p}{\partial s} \right|_p = \left. \frac{\partial p}{\partial I} \right|_p \left. \frac{\partial I}{\partial s} \right|_p = (\gamma - 1)cT \quad (10-193)$$

The only irreversible heating term is that due to conduction in Eq. (10-170) therefore one can write the entropy from Eq. (10-192) as

$$s = \int dt \left( \frac{1}{T} \nabla \cdot \kappa \nabla T \right) \quad (10-194)$$

Now make a sequence of substitutions; replace  $T$  with  $I$  from Eq. (10-171) then, since only the perturbed portion of  $I$  has a gradient,

substitute  $I'$  for  $I$ , then use Eq. (10-190) to replace  $I'$  with  $\phi'$ , and obtain to first order

$$s = \frac{\kappa c^2}{\gamma \rho_0^2 I_0} \int dt \frac{\partial^2 \phi'}{\partial x^2} \quad (10-195)$$

Now substitute Eqs. (10-195), (10-193), and (10-180) into Eq. (10-191) to obtain

$$\frac{\partial u}{\partial t} + \frac{c^2}{\rho_0} \frac{\partial \phi'}{\partial x} = - \frac{c^2}{\rho_0} \frac{\partial}{\partial x} \int dt \frac{\partial^2 \phi'}{\partial x^2} + \frac{4}{3} \gamma \frac{\partial^2 u}{\partial x^2} \quad (10-196)$$

where

$$\xi = \frac{(\gamma-1)^2 \kappa m}{\gamma \rho_0 k} \quad (10-197)$$

Differentiate Eq. (10-196) with respect to time and differentiate Eq. (10-176) with respect to  $x$  as before to replace the second term on the left of Eq. (10-196) with a term in  $u$ , and obtain

$$\frac{\partial^2 u}{\partial t^2} - c^2 \frac{\partial^2 u}{\partial x^2} = - \xi \frac{c^2}{\rho_0} \frac{\partial^3 \phi'}{\partial x^3} + \frac{4}{3} \gamma \frac{\partial^3 u}{\partial x^2 \partial t} \quad (10-198)$$

In order to write Eq. (10-198) in terms of  $u$  only we note that to first order in  $\xi$  and  $\gamma$ ,  $\frac{c^2}{\rho_0} \frac{\partial \phi'}{\partial x} = - \frac{\partial u}{\partial t}$  from Eq. (10-196) so Eq. (10-198) can be written

$$\frac{\partial^2 u}{\partial t^2} - c^2 \frac{\partial^2 u}{\partial x^2} = \left( \xi + \frac{4}{3} \gamma \right) \frac{\partial^3 u}{\partial x^2 \partial t} \quad (10-199)$$

Now assume a traveling wave where

$$u = e^{i(kx - \omega t)} \quad (10-200)$$

where we may insist that  $\omega$  be real and search for an attenuation term in  $k$ . Substitute Eq. (10-200) into Eq. (10-199), carry out the indicated operations and cancel terms to obtain the dispersion relation

$$-\omega^2 + c^2 k^2 = i\omega k^2 \left( \zeta + \frac{4}{3}\nu \right) \quad (10-201)$$

Solving for  $k$

$$k = \frac{\omega}{\sqrt{c^2 - i\omega \left( \zeta + \frac{4}{3}\nu \right)}} \quad (10-202)$$

or, since the basic fluid equations are only meaningful if  $\left| \omega \left( \zeta + \frac{4}{3}\nu \right) \right| \ll 1$  (the wavelength is long compared to a molecular mean free path),

$$k = \frac{\omega}{c} + \frac{i\omega^2}{2c^3} \left( \zeta + \frac{4}{3}\nu \right) \quad (10-203)$$

Finally, the wave is attenuated according to

$$u = u_0 e^{-\frac{\omega^2}{2c^3} \left( \zeta + \frac{4}{3}\nu \right) x} + i \frac{\omega}{c} (x - ct) \quad (10-204)$$

We note that the case  $\nu = \zeta = 0$  reduces to a form equivalent to the ideal fluid solution, but that real sound waves are attenuated at a rate proportional to the square of their frequency. Thus a noise containing high frequencies such as thunder or an explosion is heard at long distances as a low pitched rumble.



## 10.10 BALLISTIC FIREBALL RISE VELOCITY

The buoyant convection cell models developed earlier are restricted to cases where  $R_s$  is much less than  $H$ . If  $R_s$  is much greater than  $H$  the fireball cannot approach pressure equilibrium over its entire surface and one must anticipate a very different type of behavior. Landshoff developed a simple partial solution for this important case which can now be presented.

Prior to expansion, pressure everywhere in the fireball is assumed to be some constant multiple of ambient pressure, given by (10-23),

$$p = \beta p_a e^{-z/H} \quad (10-205)$$

Initial acceleration at some point inside the fireball, obtained from (10-9) and (10-205), is entirely vertical since no horizontal gradients exist,

$$\frac{d^2 r}{dt^2} = \frac{dv}{dt} = -\frac{1}{\rho} \nabla p - g = \frac{\beta p_a}{H c_a} \quad (10-206)$$

But the ambient atmosphere is in hydrostatic equilibrium, so ambient pressure must hold all higher air against gravity

$$p_a = \int_0^\infty g \rho_a e^{-z/H} dz = g H \rho_a \quad (10-207)$$

Substitution of (10-207) into (10-206) yields

$$\frac{dv}{dt} = (\beta - 1) g \sim \beta g \quad (10-208)$$

In addition to its remarkable simplicity, Eq. (10-208) holds true for any point inside the fireball; all points within the fireball will be accelerated upward with the same constant value until a rarefaction wave from the expanding surface reaches them.

In particular, air at the explosion point will accelerate for a time

$$\tau = k_0/c, \quad (10-209)$$

where  $c$  is sound speed inside the fireball. After time  $\tau$  pressure, thus acceleration, will be much reduced. Then the final rise velocity of the central point, which will be near the average velocity of fireball material is

$$V_B = \beta g R_0/c. \quad (10-210)$$

From (10-14)

$$\beta = \frac{T_{m0}}{T_0} = \frac{kT_{m0}}{kT_0}. \quad (10-211)$$

Using (10-46) to replace ambient quantities by  $H$  and (10-181) to replace fireball quantities by  $c$ ,

$$\beta = \frac{c^2}{\gamma g H} \quad (10-212)$$

and

$$V_B = \frac{c}{\gamma} \frac{R_0}{H} \quad (10-213)$$

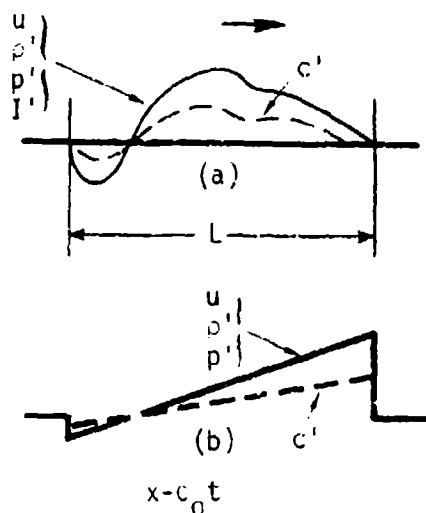
Clearly, when  $R_0 \geq H$ , the fireball will have risen so much during the time required to expand to  $R_0$  that ambient pressure will be too small to stop either expansion or rise. Such a fireball will follow a ballistic trajectory, freely expanding and effectively subject only to the force of gravity until it falls back into the atmosphere.

## 10.11 SHOCKS

### Formation

We have seen that in the linear, small perturbation, approximation a disturbance propagates at constant velocity,  $c$ , and is unchanged in form; and that in this same linear approximation viscosity effects cause the disturbance to decay. A general rigorous treatment of the full non-linear equations is beyond the current state of mathematical science. However, a plausible, approximate, discussion leads to correct conclusions regarding the major features of non-linear effects.

If an arbitrary but partly positive disturbance of length  $L$  propagates to the right as shown in (a) of the sketch, any of the properties,  $u$ ,  $\rho'$ ,  $p'$ ,  $I'$  have similar form, as indicated. Because the internal energy varies, sound speed will be perturbed by an amount  $c'$ . This means that the most extreme positive portions of the disturbance propagate faster than those with lesser values. After a time long compared to  $L/c'$  has passed, those portions of the disturbance which propagate fastest will be at the leading edge and those propagating slowest will trail. The shape of the disturbance must become similar to that illustrated in (b). The leading edge of the disturbance will form a discontinuity, known as a shock, trailing faster than sound speed in the unperturbed fluid. A similar argument shows that the leading edge of a rarefaction disturbance (all negative) must travel at sound speed and must spread.



### Limit on Slope

An order of magnitude estimate of the effect of viscosity can be obtained

from Eq. (10-174). Since  $u \sim cp'/\rho$ , from Eq. (10-189), we can approximate Eq. (10-174) for a plane case as

$$\frac{\partial u}{\partial t} + u \frac{\partial u}{\partial x} = \frac{Du}{Dt} = -c \frac{\partial u}{\partial x} + \frac{4}{3} \nu \frac{\partial^2 u}{\partial x^2} \quad (10-214)$$

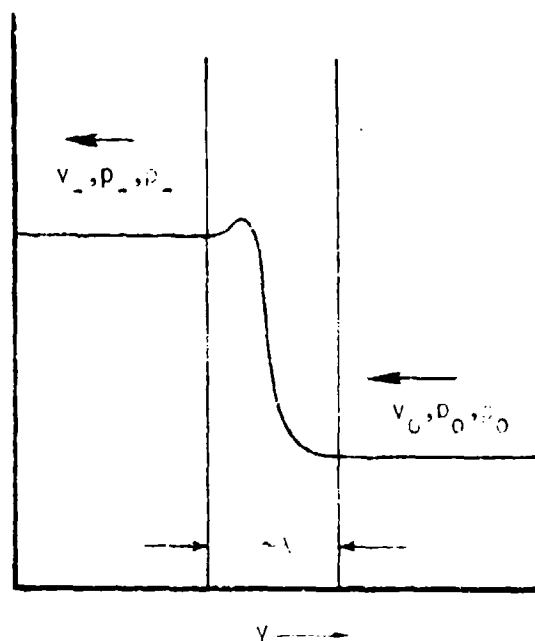
Clearly, the viscous forces (second term on right) dominate the pressure forces (first term on right) when

$$\frac{\partial u}{\partial x} \geq \frac{c}{\nu} u \approx \frac{u}{\lambda} \quad (10-215)$$

Thus we see that viscous forces will prevent the formation of gradients sharp compared to the molecular mean free path,  $\lambda$ . It is comforting to find the mathematical equations yielding the intuitive physical answer.

### Jump Conditions

The most important characteristics of shocks can be found by considering a segment of the shock front which is small compared to the scale of the disturbance but large compared to a molecular mean free path,  $\lambda$ . Furthermore we consider a time interval short compared to the time scale of development. Under such conditions it is possible to consider the shock to be plane and further to consider that conditions ahead and behind the shock are uniform. Without loss of generality, transform to a coordinate system moving at the current speed of the shock. In the moving frame all



quantities can be presumed to be constant with time, as shown in the sketch, and constant in space except for a transition region of thickness of order  $\lambda$ . The jump conditions, or Rankine-Hugoniot conditions, can be obtained by writing

down the Eulerian equations (10-169), (10-174), (10-170) in the frame which moves with shock velocity  $\zeta$ . Write  $y = x - \zeta t$ ,  $t = t$ ,  $u = v - \zeta$  where  $x, v$  are lab frame coordinates and  $y, u$  are coordinates in the moving frame.

then

$$\frac{\partial}{\partial x} = \frac{\partial y}{\partial x} \frac{\partial}{\partial y} = \frac{\partial}{\partial y}, \quad \frac{\partial}{\partial t} = \frac{\partial y}{\partial t} \frac{\partial}{\partial y} + \frac{\partial}{\partial t} = -\zeta \frac{\partial}{\partial y} \quad (10-216)$$

The equations become

$$0 = \frac{\partial \rho}{\partial t} + \frac{\partial}{\partial x}(\rho v) = -\zeta \frac{\partial \rho}{\partial y} + \frac{\partial}{\partial y} [\rho(u + \zeta)] = \frac{\partial}{\partial y} \rho u, \quad (10-217)$$

since we need no diffusion term. The momentum equation (10-174) reduces to

$$\rho u \frac{\partial u}{\partial y} = -\frac{\partial p}{\partial y} + \frac{4}{3} \eta \frac{\partial^2 u}{\partial y^2} \quad (10-218)$$

and the energy equation (10-170) becomes

$$\rho u \frac{\partial I}{\partial y} = -p \frac{\partial u}{\partial y} + \frac{\partial}{\partial y} \left( \kappa \frac{\partial I}{\partial y} \right) \quad (10-219)$$

The first jump condition can be immediately obtained from Eq. (10-217)

$$\rho_- u_- = \rho u = \rho_0 u_0 = \text{constant} \quad (10-220)$$

With this knowledge all combinations  $\rho u$  can be set to a constant. Then the momentum equation (10-218) can be integrated to obtain the second jump condition,

$$\rho_0 u_0 (u_- - u_0) = - (p_- - p_0) + \frac{4}{3} \eta \left( \left. \frac{\partial u}{\partial y} \right|_- - \left. \frac{\partial u}{\partial y} \right|_0 \right) = - (p_- - p_0) \quad (10-221)$$

The viscous term has no contribution because  $u$  is constant on both sides of the transition region. We rearrange Eq. (10-219) to obtain

$$\rho_o u_o \frac{\partial I}{\partial y} = - \frac{\partial}{\partial y} (pu) + u \frac{\partial p}{\partial y} + \frac{\partial}{\partial y} \left( \kappa \frac{\partial T}{\partial y} \right) \quad (10-222)$$

Now substitute from Eq. (10-218) for  $\frac{\partial p}{\partial y}$  to obtain an integrable equation

$$\rho_o u_o \frac{\partial I}{\partial y} = - \frac{\partial}{\partial y} (pu) - \frac{\rho_o u_o}{2} \frac{\partial}{\partial y} u^2 + \frac{4}{3} \eta \frac{\partial^2}{\partial y^2} u + \frac{\partial}{\partial y} \left( \kappa \frac{\partial T}{\partial y} \right) \quad (10-223)$$

or

$$\rho_o u_o (I_- - I_o) = - (p_- u_- - p_o u_o) - \frac{\rho_o u_o}{2} (u_-^2 - u_o^2) \quad , \quad (10-224)$$

where again the viscosity terms do not contribute outside of the transition region. Eqs. (10-220), (10-221), and (10-224) constitute the shock jump conditions which relate changes in fluid parameters across a shock. A common specialization can be written by assuming a polytropic equation of state, and transforming back to the lab frame by the substitution  $u = v - \xi$ . For  $v_o = 0$  the jump conditions reduce to

$$\frac{p_-}{p_o} = \frac{\gamma+1}{\gamma-1+2/M^2} \quad (10-225)$$

$$\frac{v_-}{\xi} = \frac{2}{(\gamma+1)} (1-1/M^2) \quad (10-226)$$

$$\frac{p_- - p_o}{p_o} = \frac{2\gamma}{(\gamma+1)} (M^2 - 1) \quad , \quad (10-227)$$

where subscript  $o$  refers to conditions ahead of the shock, subscript minus to conditions behind the shock and the Mach number,  $M$ , is defined as the ratio of shock speed to sound speed ahead of the shock

$$M \equiv \xi/c_0$$

(10-228)

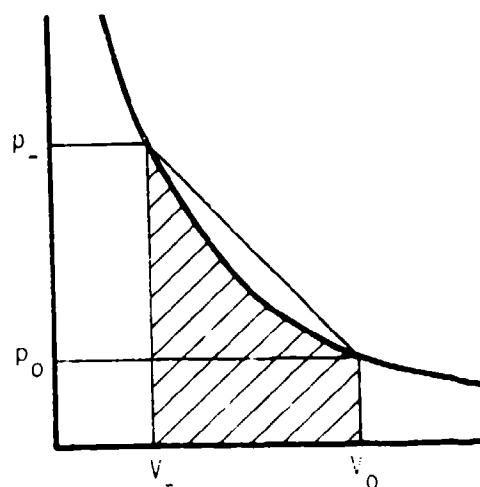
### Irreversibility of Shocks

An interesting feature of the derivation of the shock jump conditions is that the viscous terms, in  $\eta$  and  $\kappa$ , could have been dropped from the treatment and the ideal fluid equations used in the above derivations if only some sort of transition region were assumed, even a discontinuity would serve. This circumstance led to an interesting historical controversy since in fact the jump conditions were originally derived from the ideal fluid equations. The controversy stemmed from the fact that equations (10-220), (10-221), and (10-224) can be manipulated to show that

$$I_- - I_0 = \frac{(p_0 + p_-)}{2} \left( \frac{1}{\beta_0} - \frac{1}{\beta_-} \right) = \frac{(p_0 + p_-)}{2} (V_0 - V_-) \quad (10-229)$$

where  $V$  is specific volume (verify by substitution). It is easy to see that Eq. (10-229) yields a change in internal energy given by the integral under the straight line connecting points  $p_0, V_0$  to  $p_-, V_-$  in the sketch. On the other hand the ideal fluid equations describe only isentropic flow where

$$dI = -p dV$$



The shape of the adiabat,  $p$ - $V$  curve for every known real gas is concave upward as illustrated in the sketch, and the integral  $\int p dV$  will yield the smaller, cross hatched area indicated. Thus the jump conditions imply a greater change in internal energy than is consistent with isentropic flow, and shocks must be irreversible phenomena which cause an increase in entropy.

The experimental proof of the existence of shocks which obeyed the Rankine-Hugoniot jump conditions was taken as proof that the ideal fluid equations are incorrect. Of course it is true that the ideal fluid equations are in fact incorrect without the viscous terms. These terms provide the mechanism to cause entropy to increase in the transition region as well as a mechanism to determine the structure of the transition region.

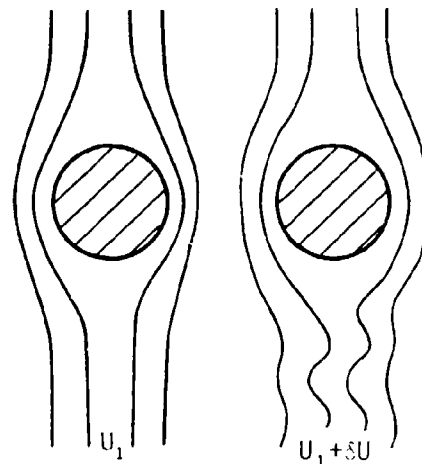


## 10.12 TURBULENCE

Flow is considered to be turbulent if erratic fluctuations of velocity occur whose magnitude is comparable to the mean velocity. Such flow is an important and frequent characteristic of real fluids. It is the most poorly understood of fluid dynamic phenomena.

There are two fundamental difficulties with the field of turbulence. The first difficulty is mathematical. Turbulent flow occurs where the smooth, or laminar solution to the fluid dynamic equations is unstable against perturbations, large or small. Mathematical analysis to determine the existence and degree of instability has been successfully carried out only for a few simple situations (see Section 7) for small perturbations; it is even more difficult for large perturbations. Thus in general one cannot even predict from first principles conditions under which turbulence will occur.

The second fundamental problem with turbulence is that the field includes a truly awe inspiring diversity of particular flow types. Frequently at the onset of turbulence the flow changes from symmetric laminar flow at, say, velocity  $U_1$ , to a quasi-periodic but still essentially smooth



flow with a single disturbance pattern overlayed on the laminar flow at slightly higher velocity,  $U_1 + \delta U$  as illustrated in the sketch. As velocity is increased the flow becomes more complicated until eventually fluctuations some distance behind the object appear to be random. The particular sequence of flow patterns and the conditions under which they appear differ with the geometry of the flow and, to a lesser extent,

with the viscosity of the fluid. Experimentally the patterns and their order of appearance also depend critically on the uniformity of the incident flow field, a very important consideration when one has no reliable theory. Thus one is faced with the task of describing flow fields which undergo all gradations from nearly laminar to nearly random with a different sequence of patterns for each different geometrical situation, and possibly each different experimental arrangement.

### Onset Criteria

Such insight as can be generally useful must necessarily be obtained without reference to details of the flow field. We know from the fluid dynamic equations that the only forces which tend to stabilize flow independent of the particular flow field are viscous forces. Viscous forces always convert kinetic energy into heat and therefore will generally tend to reduce velocity fluctuations. If one assumes the laminar flow field to be of unstable form then it is reasonable to suppose that inertial fluid forces must dominate viscous forces as a condition for significant instability to develop. For time steady flow this condition requires the second term on the left of Eq. (10-174) to be large compared to the viscosity term\*

$$|(\vec{v} \cdot \nabla) \vec{v}| \gg |\nu (\nabla^2 \vec{v})| \quad (10-251)$$

If the characteristic length of the flow is  $L$ , an order of magnitude estimate of Eq. (10-251) is

$$\frac{V^2}{L} \gg \nu \frac{V}{L^2} \quad (10-252)$$

\* For unsteady flow we obtain the same result by approximating

$$\frac{\partial \vec{v}}{\partial t} \sim \frac{V}{t} \sim \frac{V}{L} \sim \frac{V}{L} \sim \frac{V}{L}$$

or

$$R \equiv \frac{Lv}{\nu} \gg 1 \quad (10-253)$$

The ratio of inertial force to viscous force,  $R$ , is known as the Reynolds number. The above indicates that a necessary condition for the existence of turbulence is that the Reynolds number be large. Normally one uses a characteristic dimension of the object, say a radius, for  $L$  and the flow velocity for  $v$ . The value of  $R$  at which flow first becomes unstable for a particular geometry is known as the critical Reynolds number,  $R_{CR}$ . Typically  $R_{CR}$  is found experimentally to be between 10 and 100 for solid objects.

#### Fully Developed Steady Turbulence

Consider a situation where turbulence is fully developed. Turbulent eddies, defined loosely as regions over which the fluctuating component of velocity changes appreciably, should be present in all sizes throughout the region of interest. The largest eddies can be expected to have dimension comparable to (but probably smaller than) the dimension characterizing the flow field,  $L$ , and fluctuation velocities,  $u$ , comparable to but smaller than  $v$ . The energy per unit volume in the large eddies should be of order

$$E_L \sim \frac{1}{2} \rho (\overline{u})^2 \sim \rho v^2 \quad (10-254)$$

Small eddies, of dimension,  $\ell$ , might be expected to have fluctuations in velocity reduced by some power,  $p$ , of the ratio  $\ell/L$ , where  $p$  should not be too far from unity. The energy per unit volume in the small eddies then is of order

$$E_S = \frac{1}{2} \rho (\overline{u}_S)^2 \sim \rho v^2 (\ell/L)^{2p} \quad (10-255)$$

Thus if  $2p$  is positive and not too close to zero\* large eddies will contain more energy than small eddies.

On the other hand the rate of dissipation of energy by viscous forces is low for large eddies because their "local" Reynold's number is large

$$R_\lambda \sim \frac{\lambda v}{\nu} \quad (10-236)$$

Thus energy dissipation must occur in two stages, first the energy must be transferred from larger eddies to smaller eddies, then finally the smallest eddies must be dissipated by viscosity. Further, the rate of transfer of energy from larger eddies to smaller must be independent of viscous forces because, for the larger eddies, inertial forces dominate viscous forces. This rate of transfer of specific energy,  $\epsilon$ , can depend only on the eddy size and the characteristic velocity,  $v$ , in steady state. The simplest dimensionally correct combination is

$$\epsilon \sim v_\lambda^3 / \lambda \quad (10-237)$$

Equation (10-237) is no real help in estimating the overall rate of dissipation of energy via turbulence for a specific case since the available energy flux per gram is also of order  $v^3/L$ . One must obtain  $\epsilon$  experimentally or estimate it theoretically somehow.

However, given  $\epsilon$ , one can use Eq. (10-237) to determine the distribution of fluctuation velocity with eddy size

$$v_\lambda \sim (\epsilon \lambda)^{1/3} \quad (10-238)$$

This dependence of eddy velocity on size and energy dissipation rate is due to Kolmogorov.

\*  $p$  will shortly be found to be equal to  $1/3$ .

The smallest eddy, of size  $\ell_0$  can be expected to have a Reynold's number near unity, or

$$R_{\ell_0} \sim 1 \sim \frac{v_{\ell_0} \ell_0}{\nu} \sim \frac{\varepsilon^{1/3} \ell_0^{4/3}}{\nu}$$

then the smallest eddy, or inner scale size is

$$\ell_0 \sim \nu^{3/4} \varepsilon^{1/4} \quad (10-239)$$

The heirarchy of events then is (1) instabilities generate turbulence with most of the energy in large eddies, (2) rather mysterious ideal fluid instabilities cause the transfer of energy to smaller eddies at the rate  $\varepsilon$ , (3) the transfer to even smaller eddies continues until finally a size is reached at which viscosity is able to convert kinetic energy to heat at the rate  $\varepsilon$ .

### Decay of Turbulence

#### Early Period

Some rather loose arguments can be made for the temporal decay of uniform isotropic turbulence when it is strong enough that viscous forces are negligible. If it is assumed that angular momentum is conserved in the volume, a good assumption for truly homogeneous turbulence, and that the point to point velocity correlation

$$r(r) = \int \vec{v}(\vec{r}_1) \cdot \vec{v}(\vec{r}_2) d\vec{r}_1 d\vec{r}_2 \quad (10-240)$$

falls off faster than  $r^{-3}$ ,\* then Lighthill† has shown that the quantity

\* Not so obviously a good assumption.

$$v_L^2 \ell_L^5 = \text{constant}, \quad (10-241)$$

where  $v_L$  and  $\ell_L$  are the fluctuation velocity and scale size of the largest eddies, the so-called outer scale size.

Another relation can be obtained by requiring the energy to decay as  $t^{-1}$  (or writing  $\frac{\partial v^2}{\partial t} \sim -\frac{v^2}{t}$ ) and equating this decay to Eq. (10-237)

$$\frac{v_L^2}{t} \sim -\frac{v_L^3}{\ell_L} \quad \text{or} \quad v \sim \ell t \quad (10-242)$$

Eqs. (10-241) and (10-242) imply

$$v_L \sim t^{-5/7}, \quad (10-243)$$

and

$$\ell_L \sim t^{2/7}. \quad (10-244)$$

The outer scale size actually increases slowly as the turbulence dies out.

### Final Period

In the very late stages when viscosity forces become important even for the largest eddy we can use Eq. (10-174) to write

$$\frac{v}{t} \sim \frac{v}{\ell^2} \quad (10-245)$$

Combination of Eq. (10-245) with Eq. (10-241) shows

$$v \sim t^{-5/4},$$

(10-246)

in the final stage.

## REFERENCES

1. The Effects of Nuclear Weapons, S. Glasstone, Editor, U.S. Atomic Energy Commission, Revised Edition, February 1964.
2. Lamb, H. D. Hydrodynamics, 6th Ed., Cambridge U. Press, 1932.
3. Morton, B. R., G. S. Taylor, and J. S. Turner, "Turbulent Gravitational Convection from Maintained and Instantaneous Sources," Proc. Roy. Soc. A 234, p 171, 1956.
4. Turner, J. S., Buoyancy Effects in Fluids, Cambridge U. Press, 1973.
5. Chandrasekhar, S., Hydrodynamic and Hydromagnetic Stability, Oxford Press, 1961.
6. Chapman, Sidney and T. G. Cowling, The Mathematical Theory of Non-Uniform Gases, Cambridge University Press, 2nd Ed., 1958.
7. Landau, L. D., and E. M. Lifshitz, Fluid Mechanics, Pergamon Press, 1959.



CHAPTER 11  
NUMERICAL METHODS OF FLUID DYNAMICS

David H. Sowle  
Mission Research Corporation  
Thomas H. Johnson  
U.S. Air Force

May 1975

## TABLE OF CONTENTS

	<u>PAGE</u>
LIST OF FIGURES	523
11.1 INTRODUCTION	524
11.2 BASIC CONCEPTS	525
11.2.1 Numerical Approximation	525
11.2.2 Strong Disturbance	525
11.2.3 Eulerian Representation	526
11.2.4 Artificial Diffusion	526
11.2.5 Order and Truncation Error	534
11.2.6 Stability, Computer Time	534
11.2.7 Accuracy, Computer Capacity, Cost	536
11.2.8 Explicit-Implicit	537
11.2.9 Higher Order Techniques	538
11.2.10 Artificial Dispersion	539
11.2.11 Flux Corrective Techniques	542
11.2.12 Shocks: The von Neuman-Richtmeyer Method	543
11.3 TECHNIQUES	548
11.3.1 Impact of Several Dimensions	548
11.3.2 Lagrangian Hydrodynamics	548
11.3.3 Eulerian Equations in Advective Form-1D	550
Stability Analysis	552
Upstream-Downstream Scheme	554
Lax Scheme	555
Leap Frog Scheme	556
Lax-Wendroff Two-Step Scheme	557

11.3.4	Eulerian Equations in Advective Form-2D, 3D	558
	Leap Frog, Upstream-Downstream	558
	Time Split Lax-Wendroff	559
11.3.5	Eulerian Equations in Flux Divergence Form	560
11.3.6	Magnetohydrodynamics	562
11.3.7	Generalization to Two Fluids	563
11.3.8	Mixed Lagrangian-Eulerian Schemes	566
11.3.9	Boundary Conditions	566
	REFERENCES	568

#### ACKNOWLEDGEMENT

Numerical calculations illustrating the various difference schemes were carried out by Dennis E. Glenn.

## LIST OF FIGURES

<u>FIGURE</u>		<u>PAGE</u>
1	Numerical Diffusion.	527
2	Transport of a square wave with first and second order schemes.	540
3	Transport of a square wave with second order schemes damped.	542
4	Structure of a von Neumann-Richtmeyer shock.	547

## 11.1 INTRODUCTION

Despite over three hundred years of research in the field of calculus, only restricted classes of differential equations can be integrated analytically. Unfortunately, fluid dynamic equations do not fall into such a class. As a result, a diverse set of numerical methods, coded for computer application, have been devised to obtain approximate solutions to the fluid flow equations associated with nuclear explosions. Such techniques are known as "hydrodynamics" in the weapons effects community, or, if they include effects of magnetic forces, "magnetohydrodynamics", "hydromagnetics", or "MHD". If nonequilibrium air chemistry and simple radiation-deposition processes are included the resulting computer code (hydrocode) is also known as a "phenomenology" code. All such techniques are based upon numerical solution of the fluid equations; no qualitatively new feature is introduced by the addition of magnetic forces. The treatment of radiative processes and chemistry is purposely simplified to avoid introduction of serious numerical difficulties beyond those encountered in solution of the fluid equations.

This class of computer code was developed to furnish a predictive capability for atmospheric nuclear effects in the absence of test data. In this context phenomenology codes have been very successful in identifying important phenomena and in predicting gross features of explosions. In addition, phenomenology codes provide data for the most reliable quantitative prediction of system performance in a nuclear environment possible today, but their accuracy is ultimately limited by the accuracy to which the solution of the basic fluid equations is approximated.

The major objectives of this chapter will be to acquaint the reader with the basic characteristics of numerical solutions to the fluid dynamic equations and with their fundamental limitations. In the first portion of the chapter we will illustrate the essential features and limitations of such calculations by simple hydrodynamic examples. A set of useful difference techniques for hydrodynamics and magnetohydrodynamics is developed in the latter portion of the chapter, along with cursory discussions of some of the sophistications required to produce useful quantitative results.

## 11.2 BASIC CONCEPTS

### 11.2.1 NUMERICAL APPROXIMATION

The basic idea behind most numerical methods is to replace the correct differential equation, whose solution is unknown, with an approximate equation whose solution is known, and which is believed capable of representing the true equation over a short interval. If one can find such an approximation it is possible to estimate the desired function by solving repetitively a sequence of integrable equations, each solution in the sequence using results of the previous one as initial conditions. Modern scientific computers have been built to perform this type of repetitive sequence of operations rapidly and accurately and are the main tool of theoretical weapons effects research today.

### 11.2.2 STRONG DISTURBANCE

One of the requirements on atmospheric weapon effects hydrodynamics is that it must describe major disturbances of the atmosphere. This requirement implies that perturbation techniques and techniques such as have been developed for subsonic flow, weak shocks, and quasi-steady flow will not ordinarily be useful.

### 11.2.3 EULERIAN REPRESENTATION

Motion in the vertically stratified atmosphere caused by an initially near-spherical explosion requires at least two space dimensions for adequate description. The fluid usually contains strong shear layers and is frequently very convoluted. Numerical hydrodynamics, in two or three space dimensions, requires a more or less regular, rectilinear array of points (a grid) at which hydrodynamic quantities are assigned in order that valid estimates of spatial gradients may be obtained. To avoid severe distortion of the grid and consequent gross inaccuracy, the fluid must be allowed to flow through a grid fixed in space. The Eulerian formulation of fluid dynamics must be used—a fundamental choice.

### 11.2.4 ARTIFICIAL DIFFUSION

We proceed to illustrate a number of features fundamental to Eulerian hydrodynamics with a simple problem, but one chosen to place great stress on numerical Eulerian methods. Imagine we wish to calculate the one-dimensional motion of a body of fluid which initially has constant density  $\rho_0$  and is confined to some space interval. Let the initial pressure be zero everywhere, and suppose the fluid initially moves with velocity  $v$  in the positive  $x$  direction. Since no forces act, we know the material should move at constant velocity and maintain its shape, but it is instructive to see what an Eulerian hydrocode might predict. For convenience, we will choose our space grid with uniform spacing,

$$\Delta x = x_i - x_{i-1} \quad (11-1)$$

such that the interval  $x_1 - x_0$  has initial density  $\rho_0$  and all other intervals have zero density, see Figure 11-1(a). Take the time step

$$\Delta t = t^n - t^{n-1} = \text{const.} \quad (11-2)$$

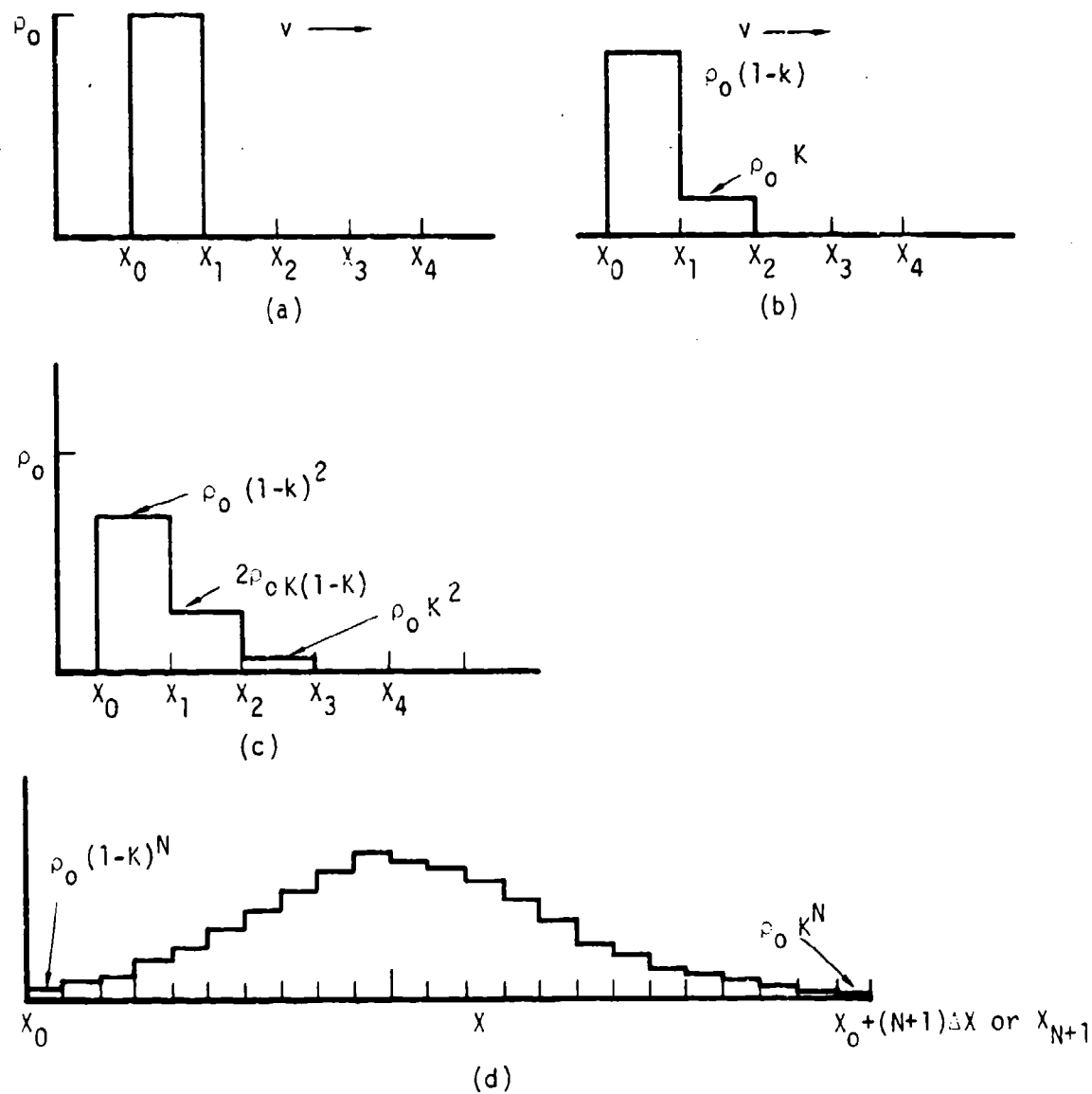


Figure 1. Numerical Diffusion. The distribution of material is illustrated for donor cell differencing. (a) initial, (b) after one cycle, (c) after two cycles, (d) after  $N$  cycles.



Since the density in a cell (grid interval,  $\Delta x$ ) must be regarded as uniform (we have no means of describing variations with scale finer than  $\Delta x$ ) we know the material transported per unit area in one cycle (interval  $\Delta t$ ) to the adjacent cell is

$$\Delta m = \rho_i(n) v \Delta t . \quad (11-3)$$

The decrease in density of cell  $i$  due to outflow is

$$\Delta \rho_i = - \Delta m / \Delta x = - \rho_i(n) v \Delta t / \Delta x \quad (11-4)$$

while the contribution to the density of cell  $i + 1$  is

$$\Delta \rho_{i+1} = + \rho_i(n) v \Delta t / \Delta x \quad (11-5)$$

The factor  $v \Delta t / \Delta x$  is the ratio of physical propagation velocity,  $v$ , to the maximum propagation velocity permitted by our scheme (one cell per cycle).

$$K = v \Delta t / \Delta x . \quad (11-6)$$

This ratio is known as the Courant number.

Figure 11-1 illustrates the solution obtained by this technique. It can be verified by induction that the general form for the density in the  $i^{\text{th}}$  cell after  $N$  cycles is

$$\rho_i(N) = \begin{cases} \rho_0 \frac{N!}{(N-i)! i!} (1-K)^{N-i} K^i , & i \leq N \\ 0 , & i > N \end{cases} \quad (11-7)$$

According to Eqs. (11-4) and (11-5), all material removed from a given cell is deposited in an adjacent cell, therefore one already knows that the scheme conserves mass, a desirable feature. As a further check, we note that Eq. (11-7) has the form of a binomial expansion, thus the total mass is given by

$$\begin{aligned} m &= \sum_{i=1}^N \rho_i \Delta x_i = \Delta x \rho_0 \sum_{i=1}^N \frac{N!}{(N-i)!i!} (1-K)^{N-i} K^i \\ &= \Delta x \rho_0 [(1-K)+K]^N = \Delta x \rho_0 \end{aligned} \quad (11-8)$$

as anticipated.

Since velocity is everywhere constant in this example, conservation of energy and momentum follow directly from conservation of mass, providing no new test of the scheme.

We can calculate the position of the center of mass

$$\langle x \rangle = \sum_{i=1}^N x_i \rho_i \Delta x_i / m = \Delta x \sum_{i=1}^N i \rho_0 \Delta x_i \quad (11-9)$$

by the trick of writing

$$iK^i = \lim_{\alpha \rightarrow 1} \left[ \frac{d}{d\alpha} (1-K)^\alpha \right] \quad (11-10)$$

then the quantity inside the summation looks similar to Eq. (11-8) and we find

$$\begin{aligned} \langle x \rangle &= \Delta x \lim_{\alpha \rightarrow 1} \left[ \frac{d}{d\alpha} \{ (1-K) + (K)^\alpha \} \right] \\ &= \Delta x \lim_{\alpha \rightarrow 1} [NK(1-K) + (1-K)^{N-1}] = NK\Delta x \end{aligned} \quad (11-11)$$

Substituting Eq. (11-6) for  $K$  and noting that  $t = N\tau$  we find the center of mass to be transported at velocity  $v$  as it should be,

$$\langle x \rangle = vt \quad (11-12)$$

So far we have seen that our simple scheme is capable of conserving mass and transporting material at the correct mean velocity, at least for this example. To make investigation of the integrity of shape of the material easier, we approximate Eq. (11-7) for large  $N$  and  $i$  by substituting the abbreviated form of Stirling's approximation for the factorials,

$$N! \approx (N/e)^N \quad (11-13)$$

yielding

$$\rho_1(N) \approx \frac{1}{N!} (1-K)^N \left[ \frac{(N-i) \left( \frac{K}{1-K} \right)^i}{\left( 1 - \frac{i}{N} \right)^N} \right] \quad (11-14)$$

Set the derivative of Eq. (11-14) with respect to  $i$  to zero to find the position of the maximum density,

$$i_{Mx} = N \quad (11-15)$$

or

$$x_{Mx} = i_{Mx} \tau = vN\tau = vt \quad (11-16)$$

The shape is correct insofar as the maximum density occurs at the proper position.

To investigate the integrity of the shape in the vicinity of the maximum we replace terms of the form  $Y^2$  with  $e^{p2nY}$  and expand the logarithm about  $Y_{MX} = \Delta X$  to find

$$Y = e^{-(X-vt)^2 / [2(1-K)v\Delta x]} \quad (11-17)$$

After successfully predicting mass conservation, mean motion, and position of maximum density, we are disappointed to find a shape very different from the correct square wave form.\* We have apparently found the solution to some problem other than we intended. In fact, Eq. (11-17) is similar in form to the solution of a diffusion equation with diffusion coefficient

$$D = (1-K)v\Delta x/2 \quad (11-18)$$

This unfortunate characteristic of the particular differencing scheme adopted ("donor cell" or "upstream" differencing) is inherent in all Eulerian hydrodynamics. One may reduce the effective value of the diffusion coefficient by a more sophisticated difference scheme but the effect (as witnessed to the particular form shown in Eq. (11-18)) cannot be eliminated. This effect is known as "artificial" or "numerical" diffusion and is the most important limitation to accuracy of weapons effects hydrocodes.

To investigate the nature of the artificial diffusion we obtain the result in a more rigorous but less practical manner by carrying out an analysis of the differential equation which we have attempted to solve. The equation for conservation of mass in one dimension is

\*In fairness, to the difference equation it should be pointed out that, had we chosen the more difficult and more interesting case of a steady object, we might have made the same mistake had we been much more sophisticated.

$$\frac{\partial \rho}{\partial t} = - \frac{\partial}{\partial x} (\rho v) \quad (11-19)$$

Our method of solution is equivalent to replacing this equation by an algebraic equation to be sequentially solved,\*

$$\frac{\rho_i^{n+1} - \rho_i^n}{t^{n+1} - t^n} = - \frac{\rho_i^n v_i^n - \rho_{i-1}^n v_{i-1}^n}{x_i - x_{i-1}} \quad (11-20)$$

Replacement of the differential equation whose solution is presumed to be unknown, Eq. (11-19), by the particular type of equation, with known solution, Eq. (11-20), illustrates the simplest general prescription for deriving a difference equation from a differential equation. We have replaced the differentials, "d", in Eq. (11-19) by finite increments, "Δ", assumed to be small, for example

$$\Delta \rho_i^n \equiv \rho_i^{n+1} - \rho_i^n \text{ replaces } \partial \rho; \text{ and } \Delta t^n \equiv t^{n+1} - t^n$$

replaces  $\partial t$ .

It is important to realize that almost all methods of numerical solution to differential equations are in essence this sort of retreat from calculus, in that the differential equation was originally derived by constructing a finite difference equation, then finding the limiting form as the differences go to zero. Our technique has prescribed a particular form, Eq. (11-20), of finite difference approximation to the equation of continuity, but has not been taken to the limit of infinitesimal differences. Careful scrutiny of Eq. (11-20) shows that we have approximated a quantity (the LHS)

---

\* Henceforth we adopt the standard terminology of representing the time cycle index,  $n$ , as a superscript and the space grid index,  $i$ , as a subscript.

which is "centered" at coordinates  $(x_i, t+\Delta t/2)$  as being equal to a quantity (the RHS) centered at coordinates  $(x_i-\Delta x/2, t)$ . One might expect such an approximation to cause inaccuracies for finite  $\Delta x, \Delta t$  and we now demonstrate this to be the cause of the numerical diffusion for this particular scheme.

We proceed now to solve Eq. (11-20) for  $\rho_i^{n+1}$ ,

$$\rho_i^{n+1} = \rho_i^n + \rho_{i-1}^n v \Delta t / \Delta x - \rho_i^n v \Delta t / \Delta x \quad (11-21)$$

where we have dropped the indices from  $v$  because  $v$  is constant.

Expand in Taylor series,

$$\rho_i^{n+1} = \rho_i^n + \frac{\partial \rho}{\partial t} \Delta t + \frac{1}{2} \frac{\partial^2 \rho}{\partial t^2} (\Delta t)^2 + \dots \quad (11-22)$$

and

$$\rho_{i-1}^n = \rho_i^n - \frac{\partial \rho}{\partial x} \Delta x + \frac{1}{2} \frac{\partial^2 \rho}{\partial x^2} (\Delta x)^2 + \dots \quad (11-23)$$

then substitute Eqs. (11-23) and (11-22) into Eq. (11-21) to obtain

$$\frac{\partial \rho}{\partial t} = -v \frac{\partial \rho}{\partial x} + \frac{v \Delta x}{2} \frac{\partial^2 \rho}{\partial x^2} - \frac{1}{2} \frac{\partial^2 \rho}{\partial t^2} (\Delta t)^2 \quad (11-24)$$

To express the last term as space derivatives we use the first term on the right to expand the time derivative twice; we find

$$\frac{\partial^2 \rho}{\partial t^2} = \frac{\partial}{\partial t} \left( \frac{\partial \rho}{\partial t} \right) = \frac{\partial}{\partial t} \left( -v \frac{\partial \rho}{\partial x} + \dots \right) = -v \frac{\partial}{\partial x} \left( \frac{\partial \rho}{\partial t} \right) - v^2 \frac{\partial^2 \rho}{\partial x^2} \quad (11-25)$$

Substituting into Eq. (11-24) yields

$$\frac{\partial p}{\partial t} = -v \frac{\partial p}{\partial x} + \frac{\Delta x v}{2} (1-K) \frac{\partial^2 p}{\partial x^2} \quad (11-26)$$

We find that our numerical approximation is yielding a solution to the correct equation through the first derivative but has introduced a spurious second order term into the differential equation, a diffusive term with the same diffusion coefficient as found in Eq. (11-18).

#### 11.2.5 ORDER AND TRUNCATION ERROR

By definition a finite difference approximation to a differential equation fails to go to the limit of zero interval. Therefore any difference equation, however sophisticated, must yield spurious derivatives of some order when expanded in Taylor series.

These spurious terms are known as truncation errors. The highest order derivative correctly represented by a difference scheme is known as the order of the scheme and the scheme is said to be truncated at that order. The donor cell technique illustrated above is truncated at first order and is therefore a first order difference scheme.

#### 11.2.6 STABILITY, COMPUTER TIME

The diffusion coefficient displayed in Eq. (11-26) has the important characteristic that it will be negative if the Courant number,  $Cr$ , is greater than 1, that is if

$$Cr = \frac{v \Delta t}{\Delta x} > 1 \quad (11-27)$$

A positive coefficient causes all perturbations, real or spurious, to be calculated quantities to grow out of control. This is illustrated in an example problem. Thus a positive diffusion coefficient amplifies numerical errors.

calculation in that incorrect perturbations tend to diminish as the problem progresses. Conversely, a negative diffusion coefficient causes perturbations to coalesce, therefore to grow, and makes the numerical solution unstable. The condition for the donor cell difference scheme to be stable numerically is that the Courant number be less than one for every cell in the mesh,

$$K_i = (|v_i| + c_i)\Delta t/\Delta x_i < 1, \quad \text{all } i \quad (11-28)$$

where we have written the condition for the general case, including variable  $\rho, v$ , and pressure,  $p$ . In Eq. (11-28),  $c_i$  represents the local propagation velocity for small disturbances, sound speed in hydrodynamics or Alfvén speed in MHD. Any hydrodynamic or magnetohydrodynamic difference scheme has a criterion similar to Eq. (11-28) to guarantee either stability or acceptable accuracy.\* This appears reasonable when one interprets the condition as a simple requirement that no more material be allowed to leave a cell in a single time step than was present in the cell initially; and the difference equation was originally justified on the basis that differences would be small. Higher order schemes generally have additional stability criteria.

The stability criterion usually is the factor which determines the amount of computer time required to solve a problem, since it controls the largest allowed time increment, as required by Eq. (11-28).

---

\* The distinction between stability and accuracy is not always recognized. This appears to be due to a theorem of Lax's which states that a stable scheme is convergent and vice versa (Ref. 11-1). Convergence guarantees that for sufficiently small interval, any accuracy may be obtained. Thus stability and accuracy tend to be regarded as equivalent. The operative distinction lies in the phrase "for sufficiently small interval", which may vary widely among differing schemes.



### 11.2.7 ACCURACY, COMPUTER CAPACITY, COST

Inspection of the diffusion coefficient in Eq. (11-26) reveals a technique whereby we can in principle increase accuracy to any desired extent. For a nontrivial case it is not possible to reduce  $D$  by choosing  $K \approx 1$  for more than the few cells with highest velocity ( $v$  is one of the quantities being calculated, and therefore is not within our control). However we can decrease  $D$  by decreasing the grid interval,  $\Delta x$ , and thus in principle increase accuracy to any desired degree.

For a problem with  $M$  space dimensions the number of required grid points,  $S$ , and therefore the amount of computer storage capacity required to represent a given volume of space increases with resolution,

$$S \propto \frac{1}{(\Delta)^M}, \quad (11-29)$$

where  $\Delta$  is the characteristic cell size in all  $M$  dimensions. Since the computer time required to advance one time step is proportional to the total number of grid points, and the criterion Eq. (11-28) requires finer time intervals for finer space intervals, the computer time,  $\$$ , required to carry a problem to a specified problem time (problem time is the value of  $t^n$ ) varies as

$$\$ \propto (\Delta)^{-(M+1)} \quad (11-30)$$

It is clear that one quickly reaches a practical resolution limit for two and three dimensional hydrodynamic problems. A typical new generation of scientific computer may have twice the storage, twice the speed, and cost 40 percent more per hour compared to the last generation. For two dimensional hydrocodes this will allow spatial resolution to be increased by a factor  $\sqrt{2}$ , about a 40 percent improvement, but at the price of a net increase of  $(\sqrt{2}-1) \approx 40$  percent in computer time and therefore an increase

of 100 percent in cost. For three dimensional problems we gain only about 26 percent in spatial resolution at the price of a 26 percent net increase in running time, thus a 75 percent increase in cost.

### 11.2.8 EXPLICIT - IMPLICIT

The self generated forces of fluid dynamics are of such a nature as to cause material to disperse. That is to say, if material is present in an isolated volume of space and contains momentum, then it moves on; if the material contains internal energy, the energy generates pressure which causes it to disperse. This generally dispersing characteristic is dictated by Newton's laws of mechanics and the second law of thermodynamics, and is reflected mathematically in the fluid equations by the time derivative of any basic quantity being negatively proportional to the quantity itself. The difference equation for a quantity, say  $\psi$ , will be of the form

$$\psi_i^{n+1} = \psi_i^n + (\text{terms not involving } \psi_i) - \alpha \psi_i \Delta t \quad (11-31)$$

where  $\alpha$  is positive. Inspection of Eq. (11-26) makes it clear that any scheme which evaluates the last term as explicitly proportional to  $\psi_i^n$ , (that is, any Explicit scheme) will be subject to a Courant condition to prevent  $\psi_i$  from changing sign during one cycle. That is, for any finite value of  $\alpha$ ,  $\psi_i^n$ , and the missing terms in Eq. (11-31), there exists a value of  $\Delta t$  large enough that  $\psi_i^{n+1}$  will change sign.

This constraint can be avoided by evaluating the last term in Eq. (11-31) in terms of the unknown quantity  $\psi_i^{n+1}$ , then finding a way to solve Eq. (11-31) for  $\psi_i^{n+1}$ . Clearly with this scheme the contribution of the term in  $\Delta t$  to the change in  $\psi$  goes to zero as  $\psi$  goes to zero, and thus cannot force  $\psi$  to change sign.

Rewrite Eq. (11-21) in these terms to obtain

$$\rho_i^{n+1} = \rho_i^n + \rho_{i-1}^{n+1} K - \rho_i^{n+1} K \quad (11-32)$$

If we expand in Taylor series as before we find Eq. (11-32) is an approximation to the solution of the differential equation

$$\frac{\partial \rho}{\partial t} = -v \frac{\partial \rho}{\partial x} + \frac{v \Delta x}{2} (1+K) \frac{\partial^2 \rho}{\partial x^2} \quad (11-33)$$

In an Implicit hydrodynamic scheme the diffusion coefficient is always positive and the scheme is always numerically stable against small perturbations; one sacrifices accuracy rather than stability if  $\Delta t$  is large. Implicit schemes of second order or greater require significantly more computer time per cycle than explicit schemes: the solution for point  $i$  at  $n+1$  will require simultaneous knowledge of both  $i+1$  and  $i-1$  at  $n+1$ . Thus a method of solving all cells simultaneously must be utilized and the gain in  $\Delta t$  must be extreme, especially in two or three dimensions, to justify an implicit technique. Implicit schemes are justified in cases where the Courant condition in an uninteresting portion of the grid causes a severe restriction on  $\Delta t$ .

### 11.2.9 HIGHER ORDER TECHNIQUES

Inspection of Eqs. (11-21) through (11-25) shows the origin of the artificial diffusion term to be the result of our choice of improperly centered space and time points for evaluation of derivatives. Had we evaluated our time derivative halfway between  $t^n$  and  $t^{n+1}$  and interpolated the flux, i.e., to the interface rather than approximating it at the mean value for the cell, we might have found a numerical approximation without the artificial diffusion term in Eq. (11-26). Such is indeed the case. Devising a method to approximate derivatives centered properly in space and time results in a scheme accurate through second order derivatives.

A large number of such schemes is possible, each resulting from a particular choice of method of approximation; for instance we could extrapolate conditions at  $t^{n+1/2}$  from  $t^n$  and  $t^{n-1}$ , or we could calculate a cycle with  $\Delta t/2$ , then use the results to advance quantities from  $t^n$  to  $t^{n+1}$ . Many such options are possible for both time and space coordinates. Any proper option chosen, followed faithfully, results in a scheme accurate through second order. The schemes run the gamut from unconditionally stable (as in the case of the implicit scheme above) through conditionally stable (as in the previous explicit scheme) to unconditionally unstable.

#### 11.2.10 ARTIFICIAL DISPERSION

It is clear that second order difference schemes are more accurate for small disturbances than first order schemes for given  $\Delta x, \Delta t$ . In weapons effects calculations accuracy for large disturbances is also required. Unfortunately all known second order schemes produce unacceptable errors for large perturbations such as a strong blast wave.

Second order schemes are dispersive. The added complexity introduced by a more sophisticated difference scheme allows a more complex result to be calculated, one in which components of a given disturbance, with different wave lengths, travel with different velocities, thus causing the disturbance to disperse. Figure 11-2 illustrates the results of numerical calculations of transport of an initially square density profile similar to the first example problem. In this case the region of nonzero density was initially 20 cells broad. The correct solution is shown and compared

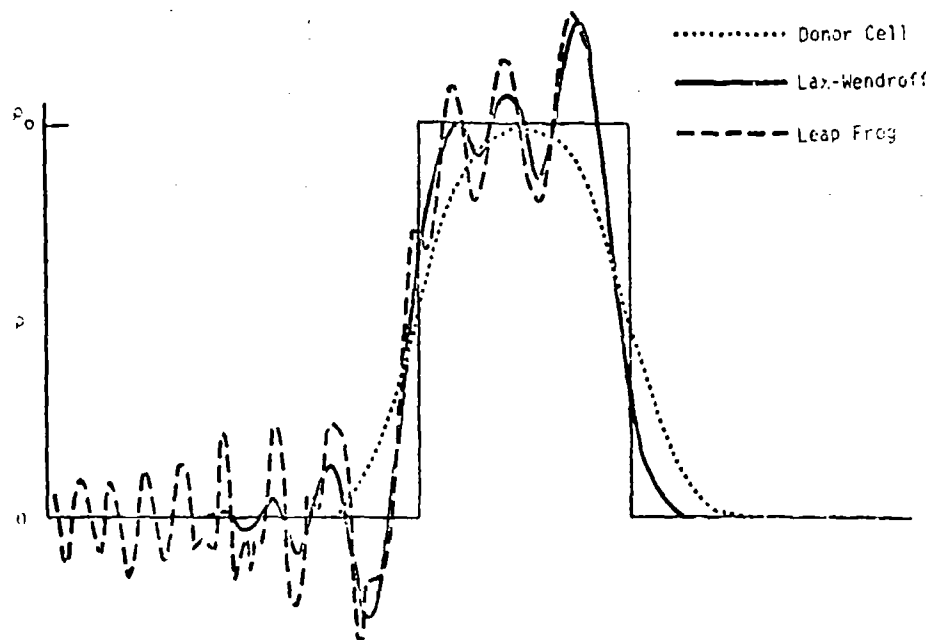


Figure 2. Transport of a square wave with first and second order schemes.

to numerical solutions with three methods, the first order donor cell method and two popular second order methods, the Lax-Wendroff technique, where

$$c_i^{n+1} = c_i^n - \frac{k}{2} \left( \frac{c_i^n}{i+1} - \frac{c_{i-1}^n}{i-1} \right) + \frac{1}{2} k^2 \left( \frac{c_i^n}{i+1} - 2 \frac{c_i^n}{i} + \frac{c_{i-1}^n}{i-1} \right), \quad (11-54)$$

and the Leap-Frog technique, where

$$c_i^{n+1} = c_i^{n-1} - k \left( \frac{c_i^n}{i+1} - \frac{c_{i-1}^n}{i-1} \right). \quad (11-55)$$

All three schemes were run with the Courant number,  $k = 0.2$ , while the disturbance traveled a distance equal to 1.75 times its initial width. It is clear that while the second order schemes are less diffusive than

the first order scheme for a strong disturbance (they produce a more narrow mean profile), their dispersive character produces results, such as negative values of mass and energy density, which are unacceptable for many applications.

The result of this circumstance is that an artificial term with diffusive characteristics must be re-introduced into the difference scheme to smooth results of second order methods, negating to a significant degree the increase in potential accuracy of the higher order difference scheme. The invention of diffusive terms designed to smooth the results in regions of space/time where necessary, while causing as little artificial diffusion as possible in regions where smoothing is not required, has become a well developed art.

Results of adding a simple diffusion-like term,

$$\Delta \rho = 0.05 \Delta x^2 (\rho_{i-1} - 2\rho_i + \rho_{i+1}) \quad (11-36)$$

to both second order schemes are illustrated in Figure 11-3. The problem is the same as illustrated in Figure 11-2 but now transported through a distance eight times the width of the initial disturbance. The second order schemes now yield indistinguishable results. The effective diffusion coefficient for either second order scheme is about half as large as for the first order scheme, as determined by full width at half maximum. In addition to introducing artificial diffusion into the second order schemes it is necessary to use machine logic to eliminate negative values of density, energy, etc.

The second order schemes are superior to first order schemes, but for strong disturbances, are clearly not a panacea. One has the feeling that third or fourth order schemes, while much more elaborate, will gain at most another factor of 2 in diffusion at the price of creating one or two new forms of numerical problem, but such schemes have not been tried.

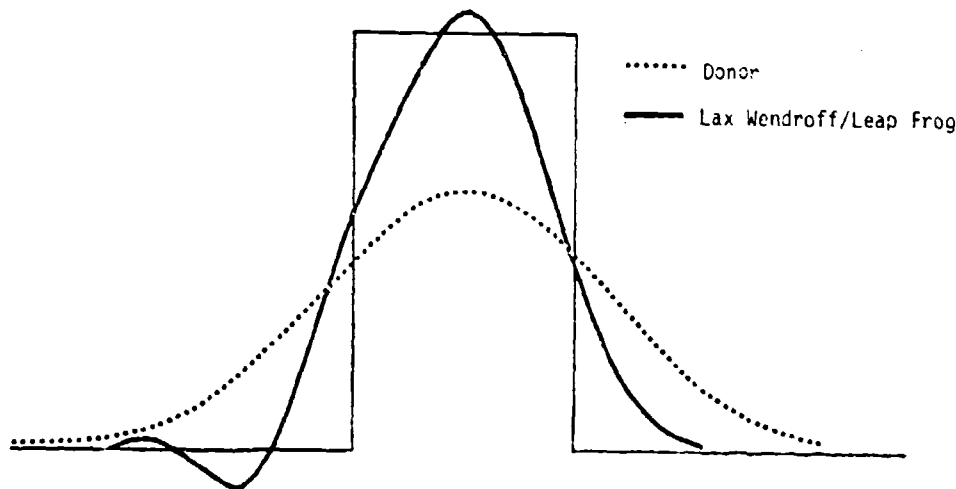


Figure 3. Transport of a square wave with second order schemes damped.

#### 11.2.11 FLUX CORRECTIVE TECHNIQUES

The most recent attempts to reduce artificial diffusion take the form of "direct intervention" or "machine analysis" rather than higher order numerical analysis. In oversimplified terms, these flux corrective techniques are complex logical-mathematical algorithms (an "algorithm" includes mathematical equations and, in addition, specifies the machine logic necessary to implement them) which attempt to detect conditions for which a gradient should be physically maintained, then force diffused material back into its proper position, thus "correcting" the flux. Such a technique has been demonstrated (Ref. 11-2) to maintain the shape of simple functions in one dimension.

Promising results have also been obtained for two-dimensional realistic problems but the algorithms tend to be designed with a limited class of problems in mind, their degree of generality has not yet been explored.

### 11.2.12 SHOCKS: THE VON NEUMANN-RICHTMEYER METHOD

In applications to atmospheric effects of strong explosions the inviscid form of the hydrodynamic equations (see Chapter 10) are normally differenced and solved numerically, the viscous terms (diffusion-viscosity-conduction) cannot be realistically included because they are generally many orders of magnitude smaller than the truncation error. This raises a problem in calculation of shocks, one of the dominant features of an explosion, since the inviscid equations, solved perfectly, conserve entropy whereas shocks do not (Chapter 10). In 1950 J. von Neumann and R. D. Richtmeyer (Ref. 11-3) invented a simple and elegant technique to handle numerical shocks which avoids the necessity of introducing special logic to calculate the jump conditions.

Preparatory to introducing the von Neumann-Richtmeyer method we will rederive the normal Rankine-Hugoniot jump conditions for a shock. These conditions can be taken as the definition of a shock; insofar as a numerical method correctly produces the jump conditions, the method is capable of treating problems involving shocks. In Chapter 10 it was pointed out that one may think of a small segment of a shock as being represented by a plane shock moving at constant velocity with uniform conditions ahead and behind. In a frame moving with the shock all partial time derivatives vanish and the inviscid hydrodynamic equations reduce to

$$\frac{\partial}{\partial x} (\rho v) = 0 \quad \text{(conservation of mass)} \quad (11-57)$$

$$\rho v \frac{\partial v}{\partial x} = - \frac{\partial p}{\partial x} \quad \text{(conservation of momentum)} \quad (11-58)$$

$$\rho v \frac{\partial}{\partial x} \left( e + \frac{v^2}{2} \right) = - p \frac{\partial}{\partial x} \left( \frac{1}{\rho} \right) \quad \text{(conservation of energy)} \quad (11-59)$$

and

$$p = p(\rho, e) \quad \text{(equation of state)} \quad (11-60)$$



where  $x(\text{cm})$  is the space coordinate relative to shock position,  $\rho(\text{g/cm}^3)$  is density,  $v(\text{cm/sec})$  is velocity relative to the shock front,  $p$  (dynes/cm<sup>2</sup>) is pressure, and  $I(\text{erg/g})$  is specific internal energy. The first jump condition can be obtained by integrating Eq. (11-37) from some reference point well removed from the shock, say  $x = +\infty$ , to an arbitrary point in the fluid. Thus

$$\rho v = \rho_0 v_0 \quad (11-41)$$

where subscript  $0$  indicates the value at the reference point. Since  $\rho v$  is constant, Eq. (11-38) can be integrated to obtain the second condition

$$\rho_0 v_0 (v - v_0) = - (p - p_0) \quad (11-42)$$

Now solve Eq. (11-41) for  $\rho^{-1}$  and substitute in Eq. (11-39) to obtain

$$\rho_0 v_0 \frac{\partial I}{\partial x} = - p \frac{\partial}{\partial x} v = - \frac{\partial}{\partial x} (p v) + v \frac{\partial p}{\partial x} \quad (11-43)$$

where the last step is an identity. Substitute from Eq. (11-38) for  $\frac{\partial p}{\partial x}$ , remembering that  $\rho v$  is constant, and integrate to obtain the third condition,

$$\rho_0 v_0 (I - I_0) = - (p v - p_0 v_0) - \frac{\rho_0 v_0}{2} (v^2 - v_0^2) \quad (11-44)$$

The above conditions, Eqs. (11-41), (11-42), and (11-44) are perfectly general solutions to plane inviscid hydrodynamics. To obtain the Rankine-Hugoniot conditions we simply: (1) assume all quantities are constant on both sides of the shock, and (2) evaluate the unsubscripted quantities on the opposite side from the subscripted quantities. We have seen in Chapter 10 that these jump conditions require an increase in entropy across the shock. However, it can be shown that Eqs. (11-37) through (11-40) cannot change entropy, therefore we have proven that inviscid hydrodynamic

is incapable of treating the shock problem. The mathematical solution to this dilemma lies in the fact that we nowhere made use of Eq. (11-40), the equation of state. We have the option of inventing an equation for  $I$  such that  $I$  is not a state variable, thus entropy can be increased. The von Neumann-Richtmeyer approach is mathematically equivalent to the just mentioned option but physically somewhat more realistic; a term is added to the pressure in Eqs. (11-58) and (11-59) but not in Eq. (11-40). We imagine adding a so-called "viscous pressure",  $q$ , to the hydrostatic pressure,  $p$ , to obtain

$$\frac{\partial}{\partial x} (\rho v) = 0 \quad (11-45)$$

$$\rho v \frac{\partial}{\partial x} \left( \frac{v}{2} \right) = - \frac{\partial}{\partial x} (p + q) \quad (11-46)$$

$$\frac{\partial I}{\partial x} = - (p + q) \frac{\partial}{\partial x} \left( \frac{1}{\rho} \right) \quad (11-47)$$

$$I = I(p, \rho) \quad (11-48)$$

It is easy to see that if we define  $P = p + q$ , the derivation of the jump conditions, Eqs. (11-41), (11-42), and (11-43) is unaltered provided only that

1.  $q$  is everywhere continuous,
- and
2.  $q$  goes to zero in regions distant from the shock.

But we must choose an equation for  $q$  which satisfies the additional condition:

3.  $q$  must produce a shock-like structure of thickness comparable to  $\lambda$ , in order that it can be numerically evaluated, and
4. numerical solution to Eqs. (11-45) - (11-48) must in fact yield the jump conditions.

The form suggested by von Neumann and Richtmeyer, as it is commonly implemented, is,

$$q = \begin{cases} a^2 \rho (\Delta x)^2 \left( \frac{\partial v}{\partial x} \right)^2, & \frac{\partial v}{\partial x} < 0 \quad (\text{compression}) \\ 0, & \frac{\partial v}{\partial x} > 0 \quad (\text{expansion}) \end{cases} \quad (11-49)$$

where  $a$  is a constant which can be adjusted to yield the shock thickness desired. We note that since  $q$  depends on velocity (and in fact is zero for expansions) the form Eq. (11-49) guarantees irreversibility and consequent increase of entropy for compressions.

Substitution of the form Eq. (11-49) into Eq. (11-46) and Eq. (11-47) and adoption of an ideal gas equation of state,

$$p = (\gamma - 1) \rho I \quad (11-50)$$

leads to a set of equations which can be solved for the case of an ideal shock. For a shock traveling to the right, the velocity of the shocked air relative to the shock front is

$$v = - \frac{\xi}{(\gamma + 1)} \left[ \gamma + \frac{1}{M^2} + \left( 1 - \frac{1}{M^2} \right) \sin \left( \sqrt{\frac{\gamma + 1}{2}} \frac{x}{a \Delta x} \right) \right], \quad |\sin| \leq 1 \quad (11-51)$$

or, in the lab frame

$$u = \xi \frac{(1 - 1/\gamma^2)}{(\gamma + 1)} \left[ 1 - \sin \left( \sqrt{\frac{\gamma + 1}{2}} \frac{x}{a \Delta x} \right) \right], \quad |\sin| \leq 1 \quad (11-52)$$

where  $\xi$  is the shock velocity and  $M = \xi/c_0$  is the Mach number. Eq. (11-51) can be verified by substitution, and given  $v$ , relations for  $\rho$ ,  $p$ , and  $I$  can be readily obtained from Eqs. (11-15), (11-46), and (11-50). The jump conditions are satisfied with zero gradient in all quantities when the argument of the sine is  $\pm \pi/2$ . Thus conditions (3) and (4) are satisfied as well as (1) and (2).

The ratio  $u/\xi$  is shown in Figure 11-4 for a medium strength shock,  $M = \sqrt{5}$ , in a gas with  $\gamma = 1.4$ . The number of cells over which the transition occurs scales directly with the coefficient  $a$ , and it appears from Figure 11-4 that the value  $a = 1$  (shock thickness ~3 cells) is as small as possible if one hopes to calculate changes in state due to the shock with reasonable accuracy. Thus,  $a = 1$  is the most common choice in practice.

The von Neumann-Richtmeyer method of treating shocks is one of the most successful innovations in numerical hydrodynamics. It can be shown (Ref. 11-1) that it will not cause any difference scheme to be unstable. However, one caution is in order. Use of this method precludes accurate calculation of such details as peak overpressure, peak temperature, etc. If one is interested in quantities which depend strongly on such details (e.g., radiation from a shock) special measures are necessary.

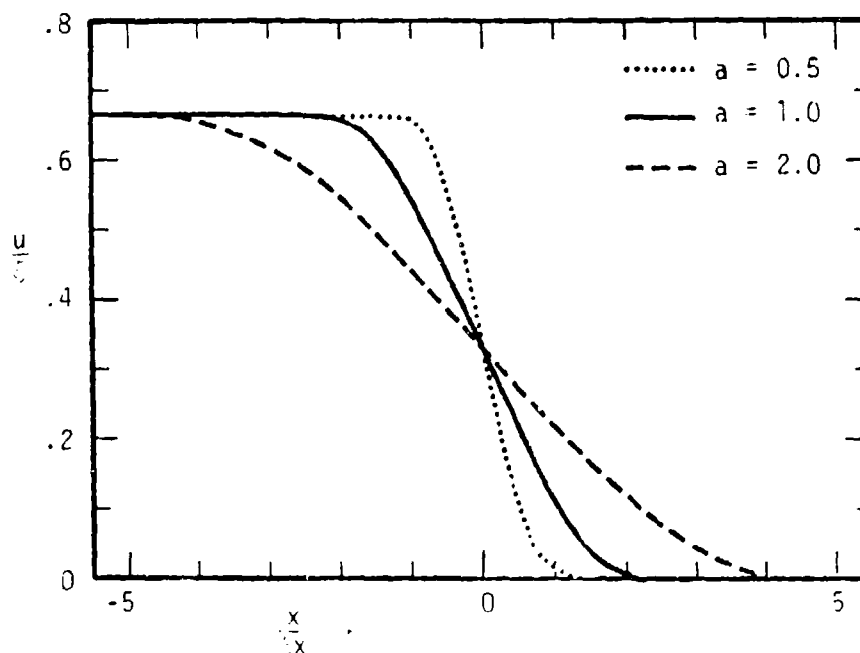


Figure 11-4. Structure of a von Neumann-Richtmeyer shock.

### 11.3 TECHNIQUES

#### 11.3.1 IMPACT OF SEVERAL DIMENSIONS

Fluid dynamic calculations require techniques appropriate to time dependent partial differential equations. In the normal case, fluid flow problems are formulated mathematically in three or four dimensions (one time dimension and two or three space dimensions). For this reason the powerful array of methods available for numerical solution of ordinary differential equations is inapplicable to fluid equations. Standard techniques for numerical solution of ordinary differential equations are truncated at fourth to sixth order, whereas we have seen that (for purely practical reasons) second order schemes represent the limit of the state of the art for hydrodynamic partial differential equations, nor is it clear that higher order schemes would greatly benefit weapons effects calculations.

#### 11.3.2 LAGRANGIAN HYDRODYNAMICS

The Lagrangian formulation of hydrodynamics is not diffusive. For this reason it is the preferred representation in situations where grid distortion does not introduce gross inaccuracies. Lagrangian hydrodynamics is almost universally applied to problems in one space dimension, rarely to problems in two or three space dimensions because of the effects of grid distortion mentioned in Sec. 11.2.3.

The Lagrangian formulation in one space dimension can be written

$$\frac{Dv}{Dt} = - \frac{\partial P}{\partial m} \quad (11-53)$$

$$\frac{Dx}{Dt} = v \quad (11-54)$$

$$\frac{D\rho}{Dt} = - \rho \frac{\partial v}{\partial x} \quad (11-55)$$

$$\frac{Dl}{Dt} = -p \frac{D}{Dt} \left( \frac{1}{\rho} \right) \quad (11-56)$$

$$p = p(\rho, l) \quad (11-57)$$

In these equations the total derivative  $\frac{D}{Dt}$  is evaluated in the frame of the moving fluid.  $R(\text{cm})$  is the current position of an element of fluid (the Eulerian coordinate) and  $r$  is the initial coordinate of the fluid element (the Lagrangian coordinate). If one reduces Eqs. (11-53 to 57) to difference equations in a straightforward manner, then staggers the time and space indices appropriately, an algorithm is obtained which appears to be accurate to second order (Ref. 11-1);

(1) Update velocities

$$v_i^{n+1/2} = v_i^{n-1/2} - \frac{\Delta t}{m_{j+1/2}} \left[ p_{i+1/2}^n - p_{i-1/2}^n \right] \quad (11-58)$$

(2) Update cell coordinates

$$R_j^{n+1} = R_j^n + \Delta t v_i^{n+1/2} \quad (11-59)$$

(3) Update cell densities

$$\rho_{i+1/2}^{n+1} = \frac{m_{i+1/2}}{(R_{i+1}^{n+1} - R_i^{n+1})} \quad (11-60)$$

(4) Update specific internal energies

$$l_{i+1/2}^{n+1} = l_{i+1/2}^n - p_{i+1/2}^{n+1/2} \left[ (1/\rho_{i+1/2}^{n+1}) - (1/\rho_{i+1/2}^n) \right] \quad (11-61)$$

(5) Update pressures

$$p_{i+1/2}^{n+1} = p \left( \rho_{i+1/2}^{n+1}, l_{i+1/2}^{n+1} \right) \quad (11-62)$$

Note the auxilliary quantity,  $m_{i+1/2} = \text{constant}$ .

The above algorithm would advance the quantities associated with a cell  $(v_i^{n+1/2}, R_i^n, \rho_{i+1/2}^n, I_{i+1/2}^n, m_{i+1/2})$  one step in time to second order accuracy were it not that  $p_i^{n+1/2}$  is unknown. There are two commonly used methods to resolve this dilemma:

- Sacrifice second order accuracy and use  $p_i^n$  in (4).
- Iterate on (4) and (5) to obtain  $p_i^{n+1/2}$ , normally only one iteration is carried out.

The entire scheme is explicit with stability criterion

$$\frac{c_{i+1/2}^n \Delta t}{R_{i+1}^n - R_i^n} < 1 \quad \text{all } i \quad (11-63)$$

where  $c$  is sound speed.

### 11.3.3 EULERIAN EQUATIONS IN ADVECTIVE FORM-1D

Preparatory to embarking on Eulerian difference schemes appropriate to several space dimensions we will develop the necessary technique in one space dimension. The hydrodynamic equations in Eulerian formulation can be written:

$$\frac{\partial \rho}{\partial t} + v \frac{\partial \rho}{\partial x} + \rho \frac{\partial v}{\partial x} = 0 \quad (11-64)$$

$$\frac{\partial v}{\partial t} + v \frac{\partial v}{\partial x} + \frac{1}{\rho} \frac{\partial p}{\partial x} = \frac{\partial v}{\partial t} + \frac{1}{\rho} \frac{\partial \rho}{\partial x} v \frac{\partial v}{\partial x} + v \frac{\partial v}{\partial x} + \frac{1}{\rho} \frac{\partial \rho}{\partial x} \frac{\partial v}{\partial x} = 0 \quad (11-65)$$

$$\frac{\partial p}{\partial t} + p \frac{\partial v}{\partial x} + v \frac{\partial p}{\partial x} = 0 \quad (11-66)$$

$$p = p(\rho, v) \quad (11-67)$$

where we have used the equation of state in Eq. (11-65) and arranged the terms in an unusual manner to facilitate replacement of the set of Eqs. (11-64 to 67) with the single vector equation\* in advective form;

$$\frac{\partial U}{\partial t} + A \frac{\partial U}{\partial x} = 0 \quad , \quad (11-68)$$

where the vector  $U$  and the matrix  $A$  are given by

$$U \equiv \begin{pmatrix} \rho \\ v \\ I \end{pmatrix} , \quad A \equiv \begin{pmatrix} v & p & 0 \\ \frac{1}{\rho} \frac{\partial p}{\partial v} \Big|_I & v & \frac{1}{\rho} \frac{\partial p}{\partial I} \Big|_p \\ 0 & p & v \end{pmatrix} \quad (11-69)$$

Substitution of Eq. (11-69) into (11-68) yields (11-64) to (11-66) directly.

With this formulation a valid difference scheme for  $U$  will generate difference equations for all of the quantities  $\rho, v, I$ ; a considerable increase in efficiency both in analysis and computer programming.

As a first attempt to form a difference equation with second order accuracy in space we may try,

$$U_i^{n+1} = U_i^n - \left( \frac{\Delta t}{2\Delta x} \right) A_i^n \left( U_{i+1}^n - U_{i-1}^n \right) \quad . \quad (11-70)$$

Having formulated a trial scheme, we need to know whether it is numerically stable or not.

\* The reader who shares the first author's aversion to matrices can safely think of  $U$  and  $A$  as simple functions; all of the following logic, conclusions, and equations will be valid.



### Stability Analysis

In practice, there are two methods of analyzing any given numerical scheme for stability. The first method has two steps, first carry out a "linear analysis" on an idealization of the intended difference scheme then second, try the real scheme to see if it actually is stable for interesting problems. The second method is simply to rely on intuition and try the scheme without analysis. The second method is most popular because: (a) linear analyses for many idealized schemes are available in the literature, (b) linear analysis of an actual scheme is prohibitively difficult due to complexities (examples:  $\Delta t^n$  and  $\Delta x_i$  are seldom constant, logic is introduced to prevent density and energy from going negative, or to correct flux; chemical, radiative, magnetic effects introduce complexities), and (c) linear analysis is valid only for weak perturbations, seldom an adequate description in weapons applications. Since weakly perturbed regions exist and are of interest even for strong explosions, a linear analysis for at least some portion of one's difference scheme is highly desirable, despite the limited validity of such an analysis.

To carry out a linear analysis we imagine a disturbance so weak that the matrix  $A$  in Eq. (11-69) can be approximated by one with constant coefficients so that Eq. (11-68) is linear in  $U$ . Now we assume a rigorous solution,  $U_i$ , to the linear form of Eq. (11-70) has been found and has been spatially Fourier analyzed. A particular component is,

$$U_{ik}^n = U_k^n W_k e^{i b x_i} \quad (11-71)$$

where  $U$  is time dependent,  $W$  is wave number dependent, and  $b = \sqrt{-1}$ .

We wish to know whether the amplitude of the time dependent factor,  $T$ , grows, decays, or is steady in time. If  $T$  grows in amplitude all perturbations, including errors, will be amplified and the scheme is unstable; if  $T$  decays, the scheme is stable.

Substitute Eq. (11-71) into (11-70) to obtain

$$T^{n+1} W_k e^{jkx_i} = T^n W_k e^{jkx_i} - \left( \frac{\Delta t}{2\Delta x} \right) A_1^n T^n W_k \left( e^{jkx_{i+1}} - e^{jkx_{i-1}} \right) \quad (11-72)$$

Multiply by  $W_k^{-1} e^{-jkx_i}$  to obtain

$$\begin{aligned} T^{n+1} &= T^n \left[ 1 - \left( \frac{\Delta t}{2\Delta x} \right) \left( W_k^{-1} A_1^n W_k \right) \left( e^{jk\Delta x} - e^{-jk\Delta x} \right) \right] \\ &= T^n \left[ 1 - j \left( \frac{\Delta t}{\Delta x} \right) \left( W_k^{-1} A_1^n W_k \right) \sin k\Delta x \right] \end{aligned} \quad (11-73)$$

Since each entry in  $W$  and  $A$  is a real number, the second quantity in the bracket is pure imaginary and we are guaranteed that

$$|T^{n+1}|/|T^n| = |1 - j(\text{real number})| > 1 \quad (11-74)$$

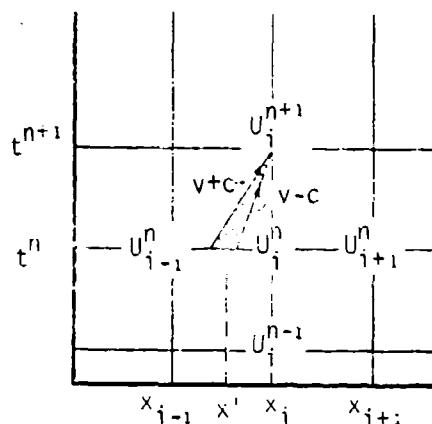
Therefore the magnitude of  $T$  grows in time and the trial difference scheme, Eq. (11-70), is unstable for all values of  $\Delta x, \Delta t$ , that is, it is unconditionally unstable.

the quantity

$$s = W^{-1} A_1^n W \quad (11-75)$$

is an eigenvalue of the matrix  $A_1^n$  and represents the characteristic propagation velocity of a disturbance at position  $i$ ;  $s$  is said to be a characteristic of Eq. (11-80). Typically,  $s$  is  $c$  for sound speed  $c$ .

The instability we have found can be made fairly plausible by reference to the sketch of  $x$ - $t$  space which illustrates the points in Eq. (11-70). The range of  $x$  which can influence  $U_i^{n+1}$  lies at the base of the cross hatched region bounded by the lines  $v+c$  and  $v-c$ . Any difference scheme must somehow interpolate  $x'$ , conditions in the vicinity of  $x'$ , and advance them.



It is fairly easy to imagine that Eq. (11-70) may have serious problems in this attempt (especially for subsonic flow) because it neglects conditions at one of the nearest points,  $U_i^n$ , when estimating  $x'$  and conditions nearby. The method is unstable because it uses different estimates of  $U_i^n$  in the two terms on the RHS of Eq. (11-70), the actual value and an average of the adjacent points. In the usual case these values are inconsistent and the definition of the partial derivative has, in a sense, broken down.

#### Upstream-Downstream Scheme

The sketch can provide inspiration for an altered scheme which is stable.

If we can decide which side of  $x_i$  provides the major influence on  $U_i^{n+1}$ , we can use  $U_i^n$  and either  $U_{i+1}^n$  or  $U_{i-1}^n$ , as appropriate, to approximate  $\frac{\partial U}{\partial x}$

$$U_i^{n+1} = \begin{cases} U_i^n + \frac{\Delta t}{\Delta x} s^+ (U_i^n - U_{i-1}^n) & \text{or} \\ U_i^n + \frac{\Delta t}{\Delta x} s^- (U_{i+1}^n - U_i^n) \end{cases} \quad (11-76)$$

This method is called the upstream-downstream, upstreaming, or donor cell differencing. Our first example, Section 11.2.4, was a simple application of this method. Normally it is adequate to test on the sign of the velocity at  $x_i$  to choose between the alternatives in Eq. (11-76).

Stability analysis applied to Eq. (11-71) yields stability provided the Courant condition is met;

$$K = \frac{\Delta t}{\Delta x} s_{\max} = (|v| + c)\Delta t/\Delta x < 1 \quad (11-77)$$

We have seen that this scheme is only first order accurate and relatively diffusive compared to second order schemes. However, it is very stable and was the first scheme successfully applied in atmospheric effects calculations (Ref. 11-11). From the first successful phenomenology code (1961) to the date of this writing (1975) most results used in the atmospheric effects community have been obtained with schemes similar to Eq. (11-76).

### Lax Scheme

A less obvious method to stabilize Eq. (11-70) and one which forms the foundation of an important second order scheme is the Lax scheme (Ref. 11-12).

We replace the  $U_i^n$  terms in Eq. (11-70) by an average of other  $U$ 's at  $n$ ,

$$U_i^{n+1} = \frac{1}{2} (U_{i+1}^n + U_{i-1}^n) - \left(\frac{\Delta t}{\Delta x}\right) A_i^n (U_{i+1}^n - U_{i-1}^n) \quad (11-78)$$

Analysis shows the Lax scheme to be stable provided

$$\frac{(|v| + c)\Delta t}{\Delta x} \leq 1 \quad (11-79)$$

as was the case for the upstream-downstream method.

The example in Section 11.2.4 leads us to anticipate that Eq. (11-78) will be strongly diffusive since it is not centered in time and uses no information from the point being advanced. Such is the case and the Lax scheme is not often used alone. It is often combined with the method next to be discussed to form a stable second order scheme.

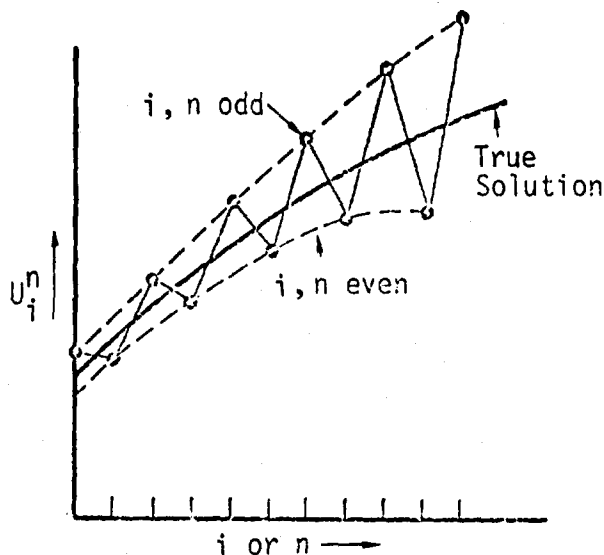
### Leap Frog Scheme

To find the Leap Frog scheme (Ref. 11-1) even more bravery must be exhibited than was required to generate the unsuccessful scheme (Eq. 11-70) where information at  $U_i^n$  was neglected in order to center the gradient in space. We now neglect all information at  $U_i^n$  to allow centering in both time and space in hopes of obtaining a scheme accurate to second order.

$$U_i^{n+1} = U_i^{n-1} - \left(\frac{\Delta t}{\Delta x}\right) A_i^n (U_{i+1}^n - U_{i-1}^n) \quad (11-80)$$

But now we are not dealing with any incompatible definitions of the same quantity. In this scheme there are two rather independent space-time grids, at even and odd values of  $n$  and  $i$ , which must be calculated simultaneously and which influence each other only through the gradient terms. The scheme turns out to be stable with the same stability condition as the Lax scheme. It has two serious drawbacks: (1) its use of information from two time cycles requires additional computer storage for given resolution, and (2) the calculations at even and odd values of  $n$  usually depart seriously from the correct answer, although their "average" remains second order accurate.

These incorrect solutions are known as computational modes and are illustrated in the sketch. One must either invent a method of obtaining the correct time average from two or three adjacent time cycles or prevent separation of the modes by introduction of some component of  $U_i^n$  into Equation (11-80) for  $U_i^{n+1}$  (e.g., replace  $U_i^{n-1}$  by  $.9U_i^{n-1} + .1U_i^n$ ), thereby sacrificing strict second order accuracy. Usually the latter is done.



### Lax-Wendroff Two-Step Scheme

Another scheme which is accurate to second order is obtained by taking half a time step using the Lax scheme (Ref. 11-11);

$$U_i^{n+1/2} = \frac{1}{2}(U_{i+1}^n + U_{i-1}^n) - \frac{\Delta t}{4\Delta x} A_i^n (U_{i+1}^n - U_{i-1}^n) \quad (11-81)$$

then the second half with the Leap Frog scheme

$$U_i^{n+1} = U_i^n - \frac{\Delta t}{2\Delta x} A_i^{n+1/2} (U_{i+1}^{n+1/2} - U_{i-1}^{n+1/2}) \quad (11-82)$$

The stability criterion for this Lax-Wendroff Two-Step scheme is

$$\frac{(|v| + c)\Delta t}{\Delta x} < \sqrt{2} \quad (11-83)$$

In one space dimension Eqs. (11-81) and (11-82) are normally combined into a single equation, the Lax-Wendroff One-Step, where we sacrifice time centering on  $\Delta$  and replace indices  $i \pm 2$  with  $i \pm 1$ ;

$$U_i^{n+1} = U_i^n - \frac{\Delta t}{4\Delta x} A^n (U_{i+1}^n - U_{i-1}^n) + \frac{1}{6} \left( \frac{\Delta t}{\Delta x} A^n \right)^2 (U_{i+1}^n - 2U_i^n + U_{i-1}^n) \quad (11-84)$$

Second order accuracy is not surprising since Eq. (11-84) is an approximation to the second order Taylor expansion of Eq. (11-68).

The Lax-Wendroff scheme requires less computer storage than does the Leap Frog scheme and does not, in principle, require sacrifice of second order accuracy since no problem similar to computational modes exists, although we have seen in Section 11.2.10 that in practice both second order schemes must introduce diffusion to counteract dispersion.

#### 11.3.4 EULERIAN EQUATIONS IN ADVECTIVE FORM-2D, 3D

##### Leap Frog, Upstream-Downstream

Write the general equation for two space dimensions as:

$$\frac{\partial U}{\partial t} + A \frac{\partial U}{\partial x} + B \frac{\partial U}{\partial y} = 0 \quad (11-85)$$

We can solve this first by generalizing the Leap Frog scheme Eq. (11-80) to

$$U_{ij}^{n+1} = U_{ij}^{n+1} - \left( \frac{\Delta t}{\Delta x} \right) A (U_{i+1,j}^n - U_{i-1,j}^n) - \left( \frac{\Delta t}{\Delta y} \right) B (U_{i,j+1}^n - U_{i,j-1}^n) \quad (11-86)$$

where the index  $j$  labels the  $y$  coordinate. Eq. (11-86) has Courant conditions on  $x$  and  $y$  which must be satisfied individually

$$\left| \frac{s_x \Delta t}{\Delta x} \right| < 1, \quad \left| \frac{s_y \Delta t}{\Delta y} \right| < 1 \quad (11-87)$$

The generalization to three space dimensions is just as straightforward.

The upstream-downstream method, Eq. (11-77), also generalizes directly to two and three dimensions.

Both the Leap Frog and upstream-downstream methods have the same strengths and weaknesses in two and three dimensions as they had in one dimension.

### Time Split Lax-Wendroff

Generalization of the Lax-Wendroff one-step method, Eq. (11-84) to two space dimensions is not direct since a second order Taylor expansion in two space dimensions requires a cross derivative of the form  $\frac{\partial^2}{\partial x \partial y}$ .

The cross term could be approximated directly but an alternative method is simpler to code in a computer. The concept is based on thinking of Eq. (11-84) as an operator equation

$$U^{n+1} = (I + X)U^n, \quad (11-88)$$

where the identity operator,  $I$ , produces the first term in Eq. (11-84) and the operator  $X$  produces the remainder of Eq. (11-84). The direct generalization to two space dimensions can be written as

$$U^{n+1} = (I + X + Y + \phi_{xy}^n) U^n. \quad (11-89)$$

where  $Y$  operates on the  $y$  coordinate as  $X$  does on the  $x$  coordinate, and  $\phi_{xy}$  produces the cross term. Rather than formulate Eq. (11-89) we create the Lax-Wendroff time split method by applying the process, Eq. (11-88) sequentially, first with  $X$  and second with  $Y$ ;

$$U' = (I + X)U^n, \text{ followed by}$$

$$U^{n+1} = (I + Y) U' = (I + Y)(I + X)U^n = (I + X + Y + YX)U^n \quad (11-84)$$



in hopes that  $YX$  will approximate  $\phi_{xy}$ .

This reduces the two dimensional difference equation to two sequential one dimensional difference equations by assuming advection along the  $x$  and  $y$  coordinates to occur independently. The general method of separate calculations for each space dimension is due to Marchuk and is known as the Marchuk method.

The Lax-Wendroff Time Split method turns out to be second order accurate, with stability criterion

$$\left( \frac{s_x^2 + s_y^2}{\Delta x^2 + \Delta y^2} \right) \Delta t^2 < 1 \quad (11-91)$$

### 11.3.5 EULERIAN EQUATIONS IN FLUX DIVERGENCE FORM

The above described techniques (upstream, Leap Frog, and Lax-Wendroff) or modifications thereto can be applied to realistic fluid dynamic (including MHD) problems and yield useful results. Since the numerical formulation is only approximate the basic conservation laws of mass, momentum, and energy are only approximately satisfied. A formulation of the hydrodynamic equations is available which assures precise obedience to the conservation laws, known as the flux divergence or conservative formulation. Define the vector,  $\vec{Q}$ , and the dyadic,  $\vec{F}$ .

$$\vec{Q} = \begin{pmatrix} \rho \\ \rho \vec{v} \\ \rho \left( I + \frac{1}{2} v^2 \right) \end{pmatrix} \quad \text{and} \quad \vec{F} \equiv \begin{pmatrix} \rho \vec{v} \\ \rho \vec{v} \vec{v} + p \\ \left( \rho I + p + \frac{1}{2} \rho v^2 \right) \vec{v} \end{pmatrix} \quad (11-92)$$

then it can be shown\* that the equation

$$\frac{\partial \vec{Q}}{\partial t} + \nabla \cdot \vec{F} = 0 \quad (11-93)$$

is equivalent to the hydrodynamic equations (11-64 to 11-66).

Flux divergent formulation of the difference schemes—upstreaming, Leap Frog, and Lax-Wendroff—can be derived from the previous equations by substitution of  $F$  for terms of the form  $AU$ . The conservation laws are satisfied within limits imposed only by finite computer word length because every term of the form  $\left(\frac{\Delta t}{\Delta x}\right) \vec{F}_i$  which is added to a given cell is subtracted from an adjacent cell.

The stability criteria for Eq. (11-93) are similar to the advective formulation<sup>†</sup>

$$\text{Upstream or Leap Frog: } \left| s_x \frac{\Delta t}{\Delta x} \right| < 1, \quad \left| s_y \frac{\Delta t}{\Delta x} \right| < 1$$

$$\text{Lax-Wendroff: } \frac{\left( s_x^2 + s_y^2 \right)}{\left( \Delta x^2 + \Delta y^2 \right)} \Delta t^2 < \frac{1}{2} \quad (11-94)$$

\* Derivation of the equations of hydrodynamics by substitution of Eq. (11-92) into (11-93) followed by manipulation is straightforward provided the reader substitutes (using the continuity eqn).

$\frac{\partial}{\partial t} \left( \frac{1}{2} \rho v^2 \right) = - \frac{1}{2} v^2 \nabla \cdot (\rho \vec{v}) + \rho \vec{v} \cdot \frac{\partial \vec{v}}{\partial t}$  in the energy equation; otherwise it can become exceptionally tedious.

For three dimensions add the third condition to Upstream and Leap Frog; replace 1/2 by 1/3 and include  $s_z$ ,  $\Delta z$ , for Lax-Wendroff.

### 11.3.6 MAGNETOHYDRODYNAMICS

In order to account for the interaction of conducting fluid with an externally imposed magnetic field one must include magnetic terms, presented in Chapter 12, to the momentum and energy equations and add equations for the magnetic induction vector,  $\vec{B}$ . These additional terms cause no conceptual or stability problems (Ref. 11-4); they are described in a clear and cursory manner in Reference 11-5.

A practical problem does arise. In addition to sound-like waves, one of the characteristic velocities of propagation for longitudinal waves in a hydro-magnetic fluid is

$$C_A \approx B/\sqrt{4\pi\rho} \quad , \quad (11-95)$$

and in addition, the tensile force associated with  $\vec{B}$  allows transverse Alfvén waves to propagate, also with velocity  $C_A$ .  $C_A$  is a physical velocity and therefore must be taken into account in the Courant condition. In regions of space where  $\rho$  is very small,  $C_A$  becomes very large and Eq. (11-95) can place a severe restriction on the allowable time step,  $\Delta t$ . Even more frustrating is the fact that typically the region of space where this occurs is in some corner of the grid where nothing of interest occurs throughout the calculation.

Several attacks have been made on this problem based on sacrificing accuracy in the uninteresting portion of space which limits  $\Delta t$ .

One scheme currently available for explicit difference schemes (Ref. 11-6) consists in specifying a maximum propagation velocity,  $V_M$ , then adding a so-called Boris density to the mass density in those terms involving  $\vec{B}$  forces on the fluid.

$$C_A^2 = 0 + R^2 / (4\pi V_M^2) \quad (11-96)$$

Substitution of Eq. (11-96) into (11-95) yields  $V_M$  as the limiting value of  $C_A$ .

An alternate approach is to formulate the difference equations implicitly (Ref. 11-7). Unfortunately no fully implicit formulation of the MHD equations in two and three space dimensions has yet been achieved so the problem of large  $C_A$  is only partially alleviated by this technique.

### 11.3.7 GENERALIZATION TO TWO FLUIDS

The magnetic forces act only on the ionized component of the air. These forces affect the neutral component only indirectly via collisional momentum exchange between the ionized and neutral material. Above 100 km altitude this momentum exchange becomes weak, and substantial relative velocities between ionized and neutral components may occur in regions where the ion number density is less than  $\sim 10^{16} \text{ cm}^{-3}$ . Thus, phenomenology codes for simulations above 100 km altitude usually carry two separate fluids to represent the ionized and neutral component.

The two fluid treatment suffers from the conceptual problem that in regions where the ion-neutral coupling is weak, the neutral-neutral coupling is even weaker (ion-neutral cross sections are greater than neutral-neutral cross sections), thus casting doubt on the validity of treating the neutrals as a fluid (see Chap. 12-4). The ideal treatment would be to simulate the neutrals with the Boltzmann equation in a four- to six-dimensional phase space; however, this is presently impossible even with the most sophisticated computer system. The two fluid equations do have the important properties of conserving mass, momentum, and energy.

therefore will not generate gross inaccuracies in most cases. They allow the independent motion of neutrals in the important regions of weak ionization, and the coupled magnetic-ion-neutral motion in regions of high ionization, to be correctly simulated, and thus represent a definite advance over any single fluid treatment.

Straightforward addition of quantities to the grid and terms in the equations of the chosen difference scheme can accomplish this important generalization with only one new problem arising. In cases where the momentum exchange length between fluids is short compared to a cell width a new, very restrictive, Courant-like condition threatens. Fortunately the two fluid interaction can be formulated in a way which avoids introduction of an additional stability criterion.

A simple approximation to the ion-neutral interaction terms can be written

$$\rho_1 \dot{\mathbf{v}}_1 = \rho_1 \rho_2 \chi (\mathbf{v}_2 - \mathbf{v}_1) + \mathbf{F}_1 \quad (11-97)$$

$$\rho_2 \dot{\mathbf{v}}_2 = -\rho_1 \rho_2 \chi (\mathbf{v}_2 - \mathbf{v}_1) + \mathbf{F}_2 \quad (11-98)$$

where subscript 1 refers to ionized fluid and subscript 2 refers to neutral fluid.  $\chi$  is a constant if the microscopic interaction is via polarization of the neutral by the ion; addition of other processes (principally charge exchange) complicates the following development only slightly. The  $\mathbf{F}$ 's represent all other forces, self pressure, magnetic forces, etc., taken constant over the time step. Define the mean velocity,

$$\langle \mathbf{v} \rangle = (\rho_1 \mathbf{v}_1 + \rho_2 \mathbf{v}_2) / (\rho_1 + \rho_2) \quad (11-99)$$

and the slip velocity,

$$v_s \equiv v_2 - v_1, \quad (11-100)$$

then Equations (11-97) and (11-98) become

$$\rho \langle \dot{v} \rangle = F_1 + F_2, \quad (11-101)$$

and

$$\dot{v}_s = -\rho \chi v_s + F_2/\rho_2 - F_1/\rho_1, \quad (11-102)$$

where  $\rho = \rho_1 + \rho_2$  is total density. Equation (11-101) is the single fluid force equation and is solved along with the other normal MHD equations, subject to the normal Courant condition.

Equation (11-102) can be integrated analytically to obtain

$$v_s^{n+1} = (F_2/\rho_2 - F_1/\rho_1)/(\rho \chi) + [v_s^n - (F_2/\rho_2 - F_1/\rho_1)/(\rho \chi)] \exp [-\rho \chi \Delta t], \quad (11-103)$$

which of course is accurate for any  $\Delta t$  over which  $\rho$  and the  $F$ 's can be considered constant, that is, first order accurate. The energy equation can be treated in a similar manner.

### 11.3.8 MIXED LAGRANGIAN-EULERIAN SCHEMES

A number of mixed Lagrangian-Eulerian schemes have been devised in an attempt to combine the advantages of the two treatments. Such schemes have made an important contribution to atmospheric effects and to other hydrodynamic applications. They are very diverse (reflecting diverse aims) and often very complex, but they do not represent any additional physical phenomena. The general approach of most mixed schemes is a Lagrangian step calculating fluxes of hydrodynamic quantities with respect to the fixed grid, followed by redefinition of the quantities in the fixed cells in terms of the fluxes (rather than a motion of the grid to follow the material flux). Philosophically, this amounts to a return to the highly intuitive donor-cell approach of straightforwardly calculating transported quantities. The interested reader is directed to Ref. 11-8 for a generalized attempt to reduce diffusion. Other, philosophically different and more successful, schemes have been developed for special purposes; see Ref. 11-9 for an attempt to reduce diffusion, optimized for the case of mostly radial explosions, and Ref. 11-10 for an attempt to reduce diffusion in reacting chemical species.

### 11.3.9 BOUNDARY CONDITIONS

Two types of boundaries are encountered in atmospheric effects work, reflective and transmissive.

The reflective boundary condition occurs: (1) at the axis when cylindrical coordinates are used for two space dimensional problems, (2) at a plane of symmetry in three space dimensional problems, and (3) occasionally to represent the surface of the earth. Reflective boundaries can be handled by treating density, internal energy, and parallel component of  $\vec{v}$  and  $\vec{B}$  as symmetric functions of the distance from the boundary, while the normal components of  $\vec{v}$  and  $\vec{B}$  are antisymmetric. In the case of cylindrical coordinates the behavior of the difference equations

must be investigated as the cylindrical radius approaches zero, and occasionally minor modifications are required, but in general reflective boundaries can be handled in a straightforward and satisfactory manner.

Transmittive boundaries occur on the top, sides (except for the axis or a symmetry plane), and normally at the bottom of the mesh, thus at most boundaries. No method of general validity exists for calculation of non-linear (e.g., strong disturbance) fluid flow through a transmittive boundary. The number of detailed treatments used for transmittive boundaries is nearly as large as the number of boundaries in existing computer codes, but the most popular method is to devise a scheme which assures approximately zero acceleration to be calculated at the boundary. This method is satisfactory in that it introduces no obvious gross errors into the calculation, although evaluation of the magnitude of potential errors is very difficult and usually not done.

One other method has been adopted to address the transmittive boundary problem for side boundaries in three space dimensions; transmittive boundaries are replaced with periodic boundaries, wherein one simply use conditions from the opposite side of the mesh to advance quantities near the boundary. This method has the advantages of simplicity and mathematical rigor but limits the maximum problem time to which physically meaningful results may be calculated to that time at which an effect of one of the "image" disturbances reaches the region of interest, a severe restriction on the utility of such a treatment.



## REFERENCES

1. Richtmeyer, R. D. and K. W. Morton, Difference Methods for Initial-Value Problems, John Wiley & Sons, 1967.
2. Boris, J. P., and D. L. Book, Flux-Corrected Transport I. SHASTA, A Fluid Transport Algorithm that Works, J. Comp. Phys. II, 38 (M73).
3. von Neumann, J. and R. D. Richtmeyer, J. Appl. Phys. Vol. 21, p 232, 1950.
4. Potter, D., Computational Physics, John Wiley & Sons, N.Y., 1973.
5. Methods in Computational Physics, Vol. 9 (S. Fernbach, M. Rotenberg and B. Alder, general editors), Academic Press, 1970.
6. Boris, J. P., A Physically Motivated Solution of the Alfven Problem, NRL Memo Report 2167, 1970.
7. Fajen, F. E., MICE, An Implicit Difference Scheme for MHD Calculations, DNA 2877Z, 1973.
8. Hirt, J. W., A. A. Amsden and J. L. Cook, An Arbitrary Lagrangian-Eulerian Computing Method for All Flow Speeds, J. Comp. Physics 14, 227-253, 1974.
9. Sappenfield, D., A Two-Dimensional Hydrodynamic Model for an Explosion in a Nonuniform Atmosphere, Los Alamos Report LA-4189-MS, 1969.
10. Sowle, D. H., P. G. Fischer and D. S. Sappenfield, An All-Altitude Air Burst Code Vol. 1: New Techniques, MRC-R-21, 1972.
11. Roache, Patrick J., Computational Fluid Dynamics, Hermosa Publishers, Albuquerque, N.M., 1972.

## CHAPTER 12

### PLASMA PHYSICS

Conrad L. Longmire

Ralph W. Kilb

April 1975

(Section 12.4.4 added December 1977)

Mission Research Corporation

## TABLE OF CONTENTS

	PAGE
12.1 INTRODUCTION	572
12.1.1 Definition of Plasma	572
12.1.2 Many Body Problems	574
12.1.3 Units	577
12.2 THERMAL EQUILIBRIUM	579
12.2.1 Response to a Perturbing Electrostatic Potential	579
12.2.2 Fluctuations in Charge Density	582
12.2.3 The Plasma Frequency	584
12.2.4 Collisions and the Plasma Parameter	589
12.2.5 Fourier Analysis of Collective Motions; Landau Damping	591
12.3 EQUATIONS OF PLASMA PHYSICS	593
12.3.1 The Boltzmann Equation	593
12.3.2 Maxwell's Equations	597
12.3.3 The Boltzmann - Maxwell Equations	598
12.3.4 Conservation Laws	599
12.3.5 Static Problems	602
12.3.6 Dynamic Problems	605
12.3.7 Adiabatic Particle Motions in Electromagnetic Fields	606

## TABLE OF CONTENTS (cont)

	<u>PAGE</u>
12.4    LARGE SCALE MOTIONS AND FLUID APPROXIMATIONS	607
12.4.1    Magnetohydrodynamics	607
12.4.2    The Approximation of Chew, Goldberger and Low	610
12.4.3    The Approximation of Longmire, Kilb and Crevier	612
12.4.4    Low- $\beta$ Plasmas Above 100 km Altitude	617
REFERENCES	624

## CHAPTER 12

### PLASMA PHYSICS

#### 12.1 INTRODUCTION

##### 12.1.1 DEFINITION OF PLASMA

A plasma may be loosely defined as a gas composed of charged particles. However, some qualifications need to be added to this simple statement, in order to convey fully the commonly accepted meaning of the term.

First, a plasma can also contain neutral atoms and molecules; in fact, it can be mostly neutral. A gas is called a plasma if it contains enough free charged particles to affect its properties of interest, for example, if its electrical conductivity becomes significant. Thus, the definition depends on the problem of interest. For most gases at room temperature the ionized fraction is negligible. At a few thousand degrees Kelvin it can be appreciable, and at temperatures above a few eV (electron-volts:  $1 \text{ eV} = 11,600^\circ\text{K}$ ) it approaches unity. However, high temperature is not always needed; a cold gas subjected to a burst of ionizing radiation will form a plasma until the free electrons and ions produced have had time to recombine to neutral atoms.

Second, it is conventional to call a collection of charged particles a plasma only if the particles interact appreciably with each other. A weak beam of electrons moving in given electromagnetic fields can be analyzed in terms of single particle mechanics. In an intense beam, fields made by the electrons themselves modify their motions. It may still be possible to predict the behavior of a plasma in terms of single particle mechanics, provided the fields include both those externally imposed and those generated by the collection of particles.

An atom or a molecule is a collection of charged particles that interact appreciably with each other, and as such could be regarded as the low temperature, quantum limit of plasmas with very few particles; however, nothing would be gained by such a viewpoint. The name plasma is usually reserved for more macroscopic systems. These systems can be quantum dominated, as in the case of free electrons in metals, charge carriers in semi-conductors, or any solid-density material at temperatures in the low eV region.

At lower densities and/or higher temperatures, classical mechanics gives a valid description of the motions of the particles. In this paper we shall restrict our attention to such classical plasmas. Note that even in classical plasmas, quantum effects enter in ionization, recombination, and other atomic processes; however, these effects can be separated from the problem of the motions of the particles.

Examples of natural classical plasmas include the ionosphere, the earth's radiation belts, the solar wind, and most stars. Plasmas are made in the laboratory by electric discharges of many sorts and by letting high intensity electron and laser beams interact with matter. Several types of electronic components are plasma devices, for example, klystrons, magnetrons, and vacuum tubes in general; these involve special plasmas in which charges of one sign, namely electrons, are dominant.

A nuclear explosion is a prolific source of plasma. The nuclear device itself is likely to be initially in a density range near solid. However, the temperature developed by the release of nuclear energy, either fission or fusion, is so high (in the keV range) that the plasma produced is approximately classical. For a nuclear burst in air, the air near the burst is ionized and heated by X rays and by the strong blast wave. As the altitude of the burst varies from sea level to high altitudes of 100 km or more, the density of the air plasma changes by factors of  $10^6$  or more, and there are corresponding changes in the scale and scope of plasma effects. At high

altitudes the geomagnetic field plays a significant role. For bursts underground or under water the scale and scope of plasma effects are reduced.

### 12.1.2 MANY BODY PROBLEMS

By definition, the general plasma problem is a many body problem. We cannot hope to solve its equations of motion exactly, given initial conditions, to find its behavior at later times. As a practical matter, we cannot even hope to state its initial condition in enough detail to warrant exact solution if the latter were possible. We have to be content with less detailed descriptions of the state of a plasma, and less accurate equations for predicting how the state changes with time.

A similar situation prevails, of course, in the statistical mechanics of, say, ordinary neutral gases. In that subject the state of a gas is specified by giving the average density and temperature (or average energy). In the extension of statistical mechanics to gas dynamics, these average quantities are allowed to be functions of position, and an average velocity is introduced, also a function of position. These averages cannot be defined at a point, but must be defined over volume elements which are large enough to contain many particles, but are nevertheless small compared with distances in which the average quantities vary appreciably. If such intermediate sized volume elements exist, then the equations of gas dynamics may predict with some accuracy the subsequent changes in density, temperature and velocity.

A further, less obvious requirement for the validity of the equations of gas dynamics involves the collision frequency and the collision mean free path. Namely, the distance and time scales of the variations in density, temperature and velocity, whose subsequent behavior is to be predicted, must be long compared with the collision mean free path and collision time, respectively. Otherwise, the variations will diffuse away in individual particle motions rather than by collective motions described adequately in terms of the average quantities. A gas of non-colliding particles will not exhibit

the simple and characteristic gas dynamic phenomenon of sound waves, for example. The collisions serve to retain local properties long enough for collective motions to develop.

In some plasmas the collision times and mean free paths are short enough to justify a gas dynamic approach. Then, for a cold plasma, it is necessary only to include the electromagnetic force on each volume element of the gas, and adjoin Maxwell's equations and Ohm's law to determine the fields and the current density. If the charged particles are hot, their pressure gradients modify Ohm's law, leading to thermoelectric effects. Magnetic forces on the charged particles can further complicate Ohm's law, resulting in the Hall effect, or tensor conductivity. While the complete set of equations for magnetogasdynamics (or magnetohydrodynamics, as it is more often called) is somewhat more formidable than for ordinary gas dynamics, the physical approach to the many body problem is the same.

It is important to realize, however, that there is a basic difference between collisions of charged particles with each other and collisions of neutral particles with neutral or charged particles, because of the long range of electromagnetic forces. Two neutral atoms, or a neutral atom and an ion, do not influence each other's motion at all unless they pass within a few Angstrom units from each other. The Coulomb force, however, falls off with distance  $r$  only as  $r^{-2}$ . Thus, the force  $dF$  on a given ion due to other ions lying in an element  $d\Omega$  of solid angle and in differential radius  $dr$  from the given ion is

$$dF = \frac{e^2}{r^2} N r^2 d\Omega dr$$

$$= e^2 N d\Omega dr.$$

(12-1)

(Here  $e$  is the charge of the ions and  $N$  is their average number density.) Thus, equal forces come from all radii. It is this long range property that



allows electromagnetic fields to reach macroscopic values. The macroscopic electromagnetic forces can be viewed as collisions between large numbers of charged particles at macroscopic distances. Now of course there is usually a lot of cancellation among the forces from distant charges, because they have different signs of charge and lie in different directions  $d\Omega$ . Nevertheless, plasma problems of interest often involve macroscopic fields. To handle such problems in the gasdynamic framework, one can divide the Coulomb collisions into distant and close collisions. The distant collisions are treated via the macroscopic fields, and the close collisions by the same techniques as in neutral gas dynamics. The dividing collision distance is the Debye length, which will be discussed below.

The discussion of collisions above focussed on electric forces. In a collision between two charged particles, there are also magnetic forces, but they are of the order  $(v/c)^2$  times the electric forces. Here  $v$  is the relative velocity and  $c$  is the velocity of light. Usually,  $(v/c)^2$  is a very small number, so that magnetic forces are negligible in binary (close) collisions. However, it often happens that for the distant collisions the magnetic forces are more important than electric forces. This occurs when the plasma is neutral on the average, so that distant electrical forces tend to cancel, but there is a net drift velocity of electrons with respect to (positive) ions, so that the magnetic forces do not cancel. Still, there are situations where the distant electric forces are significant, and we shall see such an example in Section 12.2.3.

The presence of a magnetic field leads to some localization of properties similar to the effect of a short collision mean free path. The motion of a charged particle in the plane perpendicular to the magnetic field is circular, the radius of the circle being the Larmor radius. Thus, charged particles cannot move freely across a magnetic field, and this provides the localization mentioned. Note, however, that the motion along the magnetic field is as if the particle were free: no localization is provided

in the direction parallel to the magnetic field. If in addition the collision mean free path is long, then we have a problem which is clearly beyond the scope of the methods of ordinary gas dynamics.

It is the problem of collisionless plasmas toward which most of the recent research in plasma physics has been directed, and that will occupy most of our attention in this Chapter. Our emphasis here will be on physical concepts, methods of calculation, and general results. We shall not have space to solve many problems in detail; the reader will have to refer to more extensive treatises for detailed discussion of a wider range of problems.

### 12.1.3 UNITS

We shall follow the almost universal convention in plasma physics in the use of cgs Gaussian units. The historical reason for this choice is probably the close association with atomic physics, and the relatively minor association with electrical engineering. It rarely occurs in plasma physics that one is called upon to read an ammeter or a voltmeter.

In the cgs Gaussian system, charges and electric fields are measured in electrostatic units (esu), while currents and magnetic fields are measured in electromagnetic units (emu). Maxwell's equations for the electric field  $\vec{E}$  and magnetic field  $\vec{B}$  are

$$\frac{1}{c} \frac{d\vec{B}}{dt} = -\nabla \times \vec{E}, \quad (12.1)$$

$$\frac{1}{c} \frac{d\vec{E}}{dt} = \nabla \times \vec{B} - 4\pi\vec{j}, \quad (12.2)$$

where  $c = 3 \times 10^{10}$  cm/sec is the velocity of light, and  $\vec{j}$  is the current density. The charge of an electron is

$$-e = -4.8 \times 10^{-10} \text{ esu.} \quad (12-4)$$

A density  $N$  of electrons (per  $\text{cm}^3$ ) moving with velocity  $\vec{v}$  makes charge density  $\rho$  and current density  $\vec{J}$

$$\rho = -Ne, \quad \vec{J} = -Ne \frac{\vec{v}}{c}. \quad (12-5)$$

The conservation of charge is expressed by

$$\frac{1}{c} \frac{\partial \rho}{\partial t} + \nabla \cdot \vec{J} = 0. \quad (12-6)$$

The electromagnetic (Lorentz) force  $\vec{F}$  on a moving electron is

$$\vec{F} = -e \left[ \vec{E} + \frac{\vec{v}}{c} \times \vec{B} \right] \text{ dynes.} \quad (12-7)$$

The energy density  $\epsilon_f$  in the electromagnetic field is

$$\epsilon_f = \frac{1}{8\pi} [E^2 + B^2] \text{ ergs/cm}^3. \quad (12-8)$$

We shall often express particle energies and temperatures in electron-volts.

The relation between eV and ergs is

$$1 \text{ eV} = 1.6 \times 10^{-12} \text{ erg.} \quad (12-9)$$

The relation of Gaussian units to MKS units is given by:

$$\begin{aligned} E: 1 \text{ esu} &= 3 \times 10^4 \text{ volts/meter.} \\ B: 1 \text{ emu (gauss)} &= 10^{-4} \text{ weber/m}^2. \\ \text{Current: } 1 \text{ emu (abamp)} &= 10 \text{ amps.} \\ \text{Voltage: } 1 \text{ esu (statvolt)} &= 300 \text{ volts.} \end{aligned} \quad (12-10)$$

We have written above only two of the usual four Maxwell equations. The other two are

$$\nabla \cdot \vec{B} = 0, \quad (12-11)$$

$$\nabla \cdot \vec{E} = 4\pi\rho. \quad (12-12)$$

These equations need to be used only as initial conditions, or in static problems. If they are satisfied initially, then Equations (12-2), (12-5) and (12-6) guarantee that they will always be satisfied.

## 12.2. THERMAL EQUILIBRIUM

We shall begin by discussing some aspects of plasmas at thermal equilibrium. We assume that the plasma is composed of electrons and one species of positive ions of charge  $+e$ ,  $-e$  being the electron charge. Let the average density of electrons be  $N$  electrons per unit volume. We shall assume that the plasma is neutral as a whole, so that the average ion density is  $N$ . Let the temperature of electrons and ions be  $T$  (energy units).

### 12.2.1 RESPONSE TO A PERTURBING ELECTROSTATIC POTENTIAL

Suppose we try to put an electrostatic potential into the plasma, say, by putting an electrode in the plasma and applying a voltage to it with respect to the plasma container. In order to keep the system at thermal equilibrium, the electrode will be imagined to be a perfect reflector of electrons and ions, i. e., the electrode is not a sink (or source) of either particles or energy. If the potential of the electrode is positive, it is obvious that electrons nearby will move close to it, and ions will move away from it. The excess of negative charge in the plasma near the electrode will reduce the potential seen by the remainder of the plasma.

To describe this effect quantitatively, let  $\phi(\vec{r})$  be the electrostatic potential function, which depends on the coordinate  $\vec{r}$ . Then at thermal equilibrium the density  $N_-$  of electrons will be given by the Boltzmann law

$$N_- = N \exp(e\phi/T), \quad (12-13)$$

and the density  $N_+$  of ions will be

$$N_+ = \frac{N}{2} \exp(-2e\phi/T). \quad (12-14)$$

We shall take  $\phi \rightarrow 0$  far from the electrode, in which limit

$$N_- \rightarrow N + 2N_+, \quad (12-15)$$

so that the plasma approaches neutrality. (Note that the total numbers of electrons and ions in the plasma are now not quite equal, so that a few electrons or ions had to be emitted or absorbed by the container wall, and a small shift in  $N$  might have occurred.) Poisson's equation (12-12) is then

$$\nabla^2 \phi = -4\pi Ne [\exp(e\phi/T) - \exp(-2e\phi/T)]. \quad (12-16)$$

This equation can be made dimensionless by letting

$$\begin{aligned} \phi &= e\phi/T, \\ \text{unit of length} &= \sqrt{\frac{T}{4\pi Ne^2}} = \lambda_D. \end{aligned} \quad (12-17)$$

In these units we find

$$\nabla^2 \phi = \left[ e^{\phi} - e^{-2\phi} \right], \quad (12-18)$$

where  $\psi^2$  is now to be expressed in terms of the scaled length. The character of the solutions of this equation can be understood in general without much difficulty, but we shall specialize to the case where  $\psi \ll 1$ , and assume a plane electrode. Then if  $x$  is the (scaled) distance from the electrode, we have approximately

$$\frac{\partial^2 \psi}{\partial x^2} \approx [1 + \psi - (1 - 2\psi)]$$

$$\approx (2+1)\psi \quad (12-19)$$

The solutions are

$$\psi = \psi_0 e^{\pm \sqrt{2+1} x} \quad (12-20)$$

In order to have  $\psi > 0$  deep in the plasma we choose the minus sign. Then in our original units the potential is

$$\psi = \psi_0 e^{-\sqrt{2+1} x / \lambda_D} \quad (12-21)$$

Thus, the potential penetrates the plasma only to distances of the order of  $\lambda_D$ . The solution to Equation (12-18) when  $\psi$  is not small compared with unity falls off even faster than the approximate results (12-21).

The unit of length  $\lambda_D$  is called the Debye length, and was originally introduced by Debye in a similar problem for electrolytes.

The arguments of this section are independent of the collision mean free path or the collision frequency. We have implicitly assumed, however, that some mechanism such as collisions, ultimately brings the plasma to thermal equilibrium.

### 12.2.2 FLUCTUATIONS IN CHARGE DENSITY

We consider a small spherical volume element of radius  $a$  in a much larger volume of plasma, and ask how large are the fluctuations in the number of electrons in the volume element. The average number of electrons in the element is

$$\bar{n} = \frac{4\pi}{3} a^3 N. \quad (12-22)$$

On the average, there will be the same amount of positive charge as negative charge. For simplicity we shall assume that the positive charges are fixed and do not fluctuate, although it would be easy to treat the complete problem.

If we neglect the electric forces, which tend to preserve neutrality, the rms variation  $\delta n$  of electrons would be, from purely random (Poissonian) statistics,

$$\delta n = \sqrt{\bar{n}}. \quad (12-23)$$

The electric potential energy associated with such an excess charge will tend to oppose the fluctuation. A lower limit to the potential energy  $\Delta V$  can be found by assuming that the excess charge lies near the outside of the sphere, so that

$$\Delta V = \frac{1}{2} \frac{(e\delta n)^2}{a} = \frac{1}{2} \frac{e^2 \bar{n}}{a}. \quad (12-24)$$

For an estimate we may guess that the actual distribution of charge is such as to multiply the potential energy by 2. Then from Equation (12-22)

$$\Delta V = \frac{1}{2} e^2 a^2 N. \quad (12-25)$$

According to the Boltzmann law, the probability of a configuration having potential energy  $\delta V$  is reduced by a factor  $\exp(-\delta V/T)$ . If  $\delta V$  is small compared with  $T$ , the potential energy will have little effect on the fluctuation; if  $\delta V$  is large compared with  $T$ , the potential energy will reduce the probability of the fluctuation. Thus, random statistics will apply if

$$\pi e^2 a^2 N \ll T,$$

i.e., if the radius of the volume element satisfies

$$a \ll \sqrt{\frac{T}{\pi N e^2}} = 2\lambda_D. \quad (12-26)$$

Thus, in volume elements with dimensions small compared with the Debye length, electric forces cause no shift of random statistics toward neutrality.

If  $a \gg \lambda_D$ , the effect of the potential will be large. We may estimate the mean fluctuation  $\delta n$  in a large volume by setting the potential energy equal to  $T$ ,

$$\frac{5}{4} \left( \frac{e \delta n}{a} \right)^2 = T, \quad (12-27)$$

or

$$\delta n = \sqrt{\frac{4Ta}{5e^2}}. \quad (12-28)$$

Thus,  $\delta n$  increases only as  $a^{1/2}$  for large volume, rather than as  $a^{3/2}$  as random statistics (Equation (12-25)) would indicate. In large volumes, the fluctuations depart less from neutrality, by a factor  $\lambda_D/a$ , than for random statistics.



### 12.2.3 THE PLASMA FREQUENCY

That large volume elements remain more electrically neutral than random statistics would imply is due, of course, to the fact that electrons are attracted towards a region having excess positive charge and repelled from a region with excess negative charge. The finite electron mass means that the time to neutralize an excess charge will also be finite, even in the absence of collisions. We shall investigate the dynamics of the neutralization here.

Suppose that we begin by displacing electrons from ions in some arbitrary way, and then holding them fixed for a time. The net charge density will lead to a static electric field  $\vec{E}_0$ , such that

$$\nabla \cdot \vec{E}_0 = 0. \quad (12-2b)$$

At some time, which we choose to be  $t = 0$ , we release the particles. Electrons and ions will begin to move in response to the electric field. The velocity  $\vec{v}$  of the electrons is determined by Newton's law (we assume  $\vec{B} = 0$ , at least initially).

$$\frac{d\vec{v}_e(\vec{r}, t)}{dt} = - \frac{e}{m} \vec{E}_0(\vec{r}, t), \quad (12-2c)$$

Because the ion mass  $M$  is so much larger than the electron mass  $m$ , the motion of ions will be negligible. The electric current density is given by Equation (12-2c), which on differentiation leads to

$$\begin{aligned} \frac{d\vec{J}}{dt} &= - \frac{N_e e}{M} \frac{d\vec{E}_0}{dt} = - \frac{N_e e}{M} \frac{d}{dt} \left( \frac{1}{N_e} \frac{d\vec{J}}{dt} \right) \\ &= - \frac{N_e e}{M} \left( \frac{1}{N_e} \frac{d^2 \vec{J}}{dt^2} + \frac{1}{N_e} \frac{d\vec{J}}{dt} \right). \end{aligned} \quad (12-3)$$

We shall restrict our attention to situations in which the variation of  $N$  is very small compared with the average of  $N$ . Since the variation in  $\vec{v}$  will turn out to be comparable with  $\vec{v}$  itself, the first term on the right in Equation (12-31) is negligible compared with the second. Thus, approximately

$$\frac{\partial \vec{J}}{\partial t} = -N \frac{e}{c} \frac{\partial \vec{v}}{\partial t} = \frac{Ne^2}{mc} \vec{r}. \quad (12-32)$$

Now take the time derivative of the Maxwell equation (12-3), and use (12-2) and (12-32), with the result

$$\frac{\partial^2 \vec{E}}{\partial t^2} = -c^2 \nabla(\nabla \cdot \vec{E}) + \omega_p^2 \vec{E}, \quad (12-33)$$

where we have defined the plasma frequency

$$\omega_p^2 = \frac{4\pi Ne^2}{m}. \quad (12-34)$$

The solution of Equation (12-33), with  $\vec{E} = \vec{E}_0$  at  $t = 0$ , is

$$\vec{E}(\vec{r}, t) = \vec{E}_0(\vec{r}) \cos \omega_p t. \quad (12-35)$$

Hence, we see, from Equation (12-29), that

$$\nabla \cdot \vec{E} = 0 \quad \text{at all times,} \quad (12-36)$$

that is, the electric field is "longitudinal" at all times and the magnetic field remains zero (from Equation (12-2)).

Equation (12-35) shows that the electric field simply oscillates in time, retaining its initial dependence on the spatial coordinate  $\vec{r}$ . The same is true of the charge density, which is proportional to  $\nabla \cdot \vec{E}$ .

If ion motions were included, it is easy to see that the only change in results would be to replace the electron mass in Equation (12-54) by the "reduced mass"  $m'$ ,

$$\frac{1}{m'} = \frac{1}{m} + \frac{1}{M}. \quad (12-57)$$

The analysis above neglects collisions. We may include collisions by assuming that electrons collide with ions or neutrals with frequency  $\nu$ , losing their directed velocity in each collision. Then Newton's law becomes

$$\frac{\partial \vec{v}}{\partial t} = - \frac{e}{m} \vec{E} - \nu \vec{v}, \quad (12-58)$$

and the equation for the current (12-52) becomes

$$\frac{\partial \vec{J}}{\partial t} + \nu \vec{J} = \frac{Ne^2}{mc} \vec{E}. \quad (12-59)$$

With Maxwell's equation (12-3) we obtain

$$\frac{\partial^2 \vec{E}}{\partial t^2} + \nu \frac{\partial \vec{E}}{\partial t} + \omega_p^2 \vec{E} = 0, \quad (12-60)$$

which replaces Equation (12-53) (again  $\nabla \times \vec{E} = 0$ ). The solution of this equation is of the type

$$\vec{E}(\vec{r}, t) = \vec{E}_0(\vec{r}) e^{-\nu t/2} \cos \omega_p' t. \quad (12-61)$$

Here the frequency of oscillation,  $\omega_p$ , is shifted by the collisions to a new value,  $\omega_p'$ ,

$$\omega_p' = \sqrt{\omega_p^2 - \frac{\nu^2}{4}}. \quad (12-62)$$

The oscillations are also damped by the collisions; thus, in the end the initial charge distribution will be neutralized and forgotten, the potential energy having been converted to heat.

We may think of fluctuations in a plasma as being produced by random motions of individual particles, but being opposed by the collective motions of all local electrons, i.e., the plasma oscillations. The plasma oscillations cannot neutralize fluctuations which are more rapid than  $\omega_p$ . The random fluctuations in a volume element with dimension  $a$  occur at frequencies of the order of  $v_t/a$ , where  $v_t$  is the thermal velocity of the electrons,

$$v_t = \sqrt{\frac{T}{m}}. \quad (12-43)$$

Thus, plasma oscillations can reduce fluctuations if

$$\frac{v_t}{a} > \omega_p, \quad (12-44)$$

or

$$\frac{1}{a} \sqrt{\frac{T}{m}} > \sqrt{\frac{4\pi N e^2}{m}},$$

or finally, if

$$a > \sqrt{\frac{T}{4\pi N e^2}} = \lambda_D. \quad (12-45)$$

This is the same conclusion we reached in Section 12.12.

Before closing this section, we shall note the relation of the above analysis to that for simple conductors. For a steady electric field, Equation (12-39) yields

$$\left( \frac{d^2 \phi}{dt^2} + \frac{4\pi N e^2}{m} \phi \right) = \frac{N e}{m c^2} \frac{d^2 \phi}{dt^2} \quad (12-46)$$

Thus the conductivity  $\sigma$  may be defined as

$$\sigma(\text{cm}^{-1}) = \frac{Ne^2}{mcv} = \frac{\omega_p^2}{4\pi cv} \quad (12-47)$$

The relation of the units of conductivity used here to MKS units is

$$\sigma(\text{cm}^{-1}) = 0.30 \sigma(\text{mho/meter}). \quad (12-48)$$

According to Equation (12-42), the plasma oscillation will disappear if (over-damping)

$$v > 2\omega_p, \quad (12-49)$$

or, from (12-47), if

$$\sigma < \frac{\omega_p}{8\pi c}. \quad (12-50)$$

It takes a poor conductor to fall into the overdamped class. In metallic copper,  $\omega_p \approx 1.8 \times 10^{15} \text{ sec}^{-1}$ , and  $\omega_p/8\pi c \approx 2.5 \times 10^6 \text{ cm}^{-1}$ , whereas  $\sigma \approx 10^9 \text{ cm}^{-1}$ ; thus, copper should and does exhibit plasma oscillations, as do most metals.

If the plasma oscillations are strongly overdamped, then the time dependence of the field from an initial charge distribution is

$$\vec{E}(\vec{r}, t) = \vec{E}_0(\vec{r}) e^{-\gamma t} \quad (12-51)$$

where

$$\gamma = \frac{1}{2} \left( \sqrt{\frac{1}{4} + \frac{\omega_p^2}{c^2}} + \frac{\omega_p^2}{c^2} \right)$$

The two solutions here are needed to accommodate arbitrary initial conditions, since Eq. 12-40 is second order. Choice of the plus sign gives a high relaxation rate  $\gamma \approx \nu$ ; this term in the general solution describes the adjustment of an arbitrary initial electron velocity to that which can be maintained by the electric force. Choice of the minus sign gives

$$\gamma \approx -\frac{\omega^2}{\nu} = 4\pi e^2 \quad , \quad (12-52)$$

and describes the later decay of the field and charge density. This is the relaxation rate quoted in many textbooks on electromagnetic theory, where the relation  $\vec{J} = \sigma \vec{E}$  is assumed. It is not valid in most metals, which are less than critically damped, so that Equation (12-41) should be used instead of (12-51).

#### 12.2.4 COLLISIONS AND THE PLASMA PARAMETER

In Sections 12.2.2 and 12.2.3 we showed that random statistics applies in volume elements with dimensions small compared with  $\lambda_D$ . This means that in collisions between a given particle and other particles within its Debye sphere, we may regard the positions of the other particles as being purely random or uncorrelated. On the other hand, for volume elements with dimensions large compared with  $\lambda_D$ , fluctuations from neutrality are reduced. This means that the Coulomb forces on a given particle from distant (greater than  $\lambda_D$ ) particles tend to cancel more perfectly than if the positions of these distant particles were random. The result of these facts is that, in accounting for the particulate (as opposed to continuum) aspect of a plasma, one needs to include scattering (a particulate effect) of a given particle only from particles within its Debye sphere, and the positions of these particles may be taken to be random. More distant particles affect the given particle only through the average, continuum fields they produce.

What is the number  $N_D$  of particles within a Debye sphere? Our derivation of the significance of  $\lambda_D$  assumed that  $N_D \gg 1$ . Otherwise, the statistical

formula (12-23) and our estimate of the potential energy in Sec. 12.2.2 are not correct, and it is not justified to assume that  $\vec{J}$  can be approximated by a smooth differentiable function as we implicitly assumed in Sec. 12.2.3. By direct calculation, we find

$$N_D = \frac{4\pi}{3} \lambda_D^3 N = \frac{1}{3\sqrt{4\pi}} \left[ \frac{T}{N^{1/3} e^2} \right]^{3/2}. \quad (12-53)$$

Since  $N^{1/3}$  is approximately the reciprocal of the mean distance between neighboring particles,  $N^{1/3} e^2$  is approximately the mean potential energy  $\bar{V}_n$  of the interaction between neighboring particles. Thus, the condition  $N_D \gg 1$  requires that the temperature  $T$  be large compared with  $\bar{V}_n$ .

If  $\lambda_D$  were equal to  $N^{-1/3}$  (which would give  $N_D = 4\pi/3$ ), use of the results of Secs. 12.2.2 and 12.2.3 (even though based on faulty arguments) would say that even the positions of neighboring particles are beginning to be correlated. The fact that this happens when  $T = \bar{V}_n$  is consistent. When  $N_D \gg 1$ , the fact that  $T \gg \bar{V}_n$  explains why neighboring particles are uncorrelated in position.

$N_D$  is called the plasma parameter. The statistical theory of particulate effects in plasmas is based on the assumption that

$$N_D \gg 1. \quad (12-54)$$

There is no well-developed theory for the case  $N_D \lesssim 1$ . We may expect that in such cases, neighboring ions and electrons would pair off, to form a neutral quasi-atom, since  $\lambda_D \sim \lambda_n$ . In fact, except for fairly dense plasmas ( $N > 10^{19} \text{ cm}^{-3}$ ), the temperature which gives  $N_D = 1$  is lower than the temperature needed to fully ionize the atoms; if the temperature is sufficient to ionize fully, then  $N_D$  will be greater than unity.

### 12.2.5 FOURIER ANALYSIS OF COLLECTIVE MOTIONS; LANDAU DAMPING

We showed in Section 2.3 that a perturbation in charge density, if imposed on the plasma and then released, will oscillate with the plasma frequency. For many purposes it is convenient to Fourier analyze the space and time dependence of such perturbations, i.e., to regard the total perturbation in the electrostatic potential to be made up of the sum of terms of the sort

$$\phi(\mathbf{r}, t) = A(\mathbf{k}) e^{i(\mathbf{k} \cdot \mathbf{r} - \omega t)}, \quad (12-55)$$

where  $A(\mathbf{k})$  is an amplitude that may depend on the wave vector  $\mathbf{k}$ . The results of Section 12.2.3 then indicates that

$$\omega = \omega_p, \text{ independent of } k. \quad (12-56)$$

The phase velocity  $v_\phi$  of these waves is

$$v_\phi = \frac{\omega}{k} = \frac{\omega_p}{k}, \quad (12-57)$$

which is an increasing function of wavelength. Strictly speaking, these waves do not propagate, since the group velocity  $v_g$  is

$$v_g = \frac{d\omega}{dk} = 0. \quad (12-58)$$

These results hold in a cold plasma. For finite electron temperature  $T$ , the electron pressure adds an additional restoring force to the electric field in opposing concentrations or rarefactions of electron density. In this case the frequency of oscillation can be shown to be (Ref. 12-1)

$$\omega^2 = \omega_p^2 + k^2 c_s^2, \quad (12-59)$$



where  $C_e$  is the speed of electron sound

$$C_e^2 = 3 \frac{T}{m} = 3 \overline{v_k^2} . \quad (12-60)$$

Here  $v_k$  is the component of the electron thermal velocity in the direction of  $\vec{k}$ . The factor 3 is the "ratio of specific heats" for a one-dimensional gas. For the dispersion relation (12-59) the group velocity does not vanish.

In a plasma at thermal equilibrium, each of the modes (12-55) can be expected to have, on the average, an amount of energy  $T$ , kinetic and potential. Energy is added or subtracted to the mode, in a random fashion, by interaction between the collective waves and individual electron motions, in their thermal deviations from the average collective motions. This interaction is strong for those waves for which the phase velocity is comparable with the electron thermal speed. In this case some electrons will see the electric field of the wave as having a frequency Doppler shifted almost to zero, and so can add or subtract large amounts of energy depending on whether an electron rides at such a phase as to be accelerated or decelerated by the wave electric field. For wavelengths much longer than the Debye length  $\lambda_D$  it can be seen from Equation (12-59) that the phase velocity  $\omega/k$  is much greater than the electron thermal speed, so that these waves interact only weakly. For wavelengths of the order of  $\lambda_D$ ,  $\omega/k$  is of the same order as the thermal speed, so that these waves interact strongly. A calculation of the rate of energy exchange shows that for wavelengths of the order of  $\lambda_D$ , the wave energy increases, if it is initially too low, and decreases, if it is initially too high, in a few periods of the plasma oscillation. At shorter wavelengths than  $\lambda_D$ , the "lifetime" of a collective wave is so short compared with its period that the collective wave concept is not useful.

The decay of energy in a collective wave due to interaction with individual particles, if the energy is initially far above the thermal level, is called Landau damping.

We may think of the wave amplitudes  $A(\vec{k})$  as representing certain degrees of freedom of the plasma, replacing some of the  $3N_T$  coordinates of the particles (here  $N_T$  is the total number of particles). The fraction of the total number of degrees of freedom that can be usefully thought of as collective waves is approximately  $1/N_D$ , the reciprocal of the plasma parameter. This fraction is usually small compared with unity.

### 12.3. EQUATIONS OF PLASMA PHYSICS

In this section we shall discuss the basic equations of plasma physics. We begin with the Boltzmann equation, which is the starting point for most plasma calculations.

#### 12.3.1 THE BOLTZMANN EQUATION

The Boltzmann equation governs the evolution in time  $t$  of the distribution function  $f(\vec{r}, \vec{v}, t)$  of particles in phase space, the six-dimensional space in which the independent variables are the position  $\vec{r}$  and the velocity  $\vec{v}$ . Thus we define a six-dimensional vector  $\vec{q}$  by

$$\vec{q} = (r_1, r_2, r_3, v_1, v_2, v_3), \quad (12-61)$$

where the subscripts 1,2,3 refer to a Cartesian coordinate system in ordinary space. A given particle is represented, in both position and velocity, by a point in phase space, which moves around as time elapses. A large number of particles can be described approximately by giving their density  $f$  in phase space.

The time derivative of  $\vec{q}$  for a given particle

$$\dot{\vec{q}} = (\dot{r}_1, \dot{r}_2, \dot{r}_3, \dot{v}_1, \dot{v}_2, \dot{v}_3) \quad (12-62)$$

is the six-dimensional velocity of the point in phase space representing that particle. Since  $\dot{\mathbf{r}}_1 = \mathbf{v}_1$ , etc., and since from Newton's law ( $m$  is the particle mass)

$$\dot{\mathbf{v}}_1 = \mathbf{F}_1/m, \text{ etc.}, \quad (12-63)$$

where  $\mathbf{F}_1, \mathbf{F}_2, \mathbf{F}_3$  are the components of the force field acting on the particles, we have

$$\dot{\mathbf{q}}_6 = (\mathbf{v}_1, \mathbf{v}_2, \mathbf{v}_3, \frac{\mathbf{F}_1}{m}, \frac{\mathbf{F}_2}{m}, \frac{\mathbf{F}_3}{m}). \quad (12-64)$$

We assume that the forces  $\mathbf{F}_1, \mathbf{F}_2$ , and  $\mathbf{F}_3$  are continuous functions of  $\vec{\mathbf{r}}$  and  $\vec{\mathbf{v}}$ , or  $\vec{\mathbf{q}}_6$ , and  $t$ . Then all the particles in a small volume element of phase space move with almost the same six-dimensional velocity. The flux of particles in phase space is therefore

$$\text{flux} = \dot{\mathbf{q}}_6 \cdot \mathbf{f}. \quad (12-65)$$

If there are sources and sinks of particles, with the net source represented by  $S(\vec{\mathbf{q}}_6, t)$ , then the conservation law of particles is expressed by the equation

$$\frac{\partial \mathbf{f}}{\partial t} + \dot{\mathbf{q}}_6 \cdot (\vec{\mathbf{q}}_6 \mathbf{f}) = S, \quad (12-66)$$

where  $\dot{\mathbf{q}}_6 \cdot$  is the six-dimensional divergence. In terms of three-space variables this equation is

$$\frac{\partial \mathbf{f}}{\partial t} + \vec{\nabla}_\mathbf{r} \cdot (\vec{\mathbf{v}} \mathbf{f}) + \frac{1}{m} \vec{\nabla}_\mathbf{v} \cdot (\vec{\mathbf{F}} \mathbf{f}) = S, \quad (12-67)$$

where  $\vec{\nabla}_\mathbf{r} \cdot$  and  $\vec{\nabla}_\mathbf{v} \cdot$  are the divergence with respect to  $\vec{\mathbf{r}}$  and  $\vec{\mathbf{v}}$  variables respectively, and we have used the result (12-64) of Newton's law. Now

$$\vec{r} \cdot \vec{v} = \frac{\partial v_1}{\partial r_1} + \frac{\partial v_2}{\partial r_2} + \frac{\partial v_3}{\partial r_3} = 0, \quad (12-68)$$

since the  $v_i$  and  $r_i$  are independent variables. Therefore

$$\frac{\partial f}{\partial t} + \vec{v} \cdot \nabla_r f + \frac{1}{m} \vec{F} \cdot \nabla_v f + \frac{1}{m} f \nabla_v \cdot \vec{F} = S. \quad (12-69)$$

For many force fields of practical interest

$$\nabla_v \cdot \vec{F} = 0; \quad (12-70)$$

in particular this is true for the force on particles of charge  $e$  by an electric field  $\vec{E}$  and a magnetic field  $\vec{B}$ , in which case

$$\vec{F} = e \left[ \vec{E} + \frac{\vec{v}}{c} \times \vec{B} \right]. \quad (12-71)$$

In such cases the equation for  $f$  is

$$\frac{\partial f}{\partial t} + \vec{v} \cdot \nabla_r f + \frac{1}{m} \vec{F} \cdot \nabla_v f = S. \quad (12-72)$$

Equation (12-70) is not true for a resistive force such as

$$\vec{F} = -k \vec{v}, \quad \nabla_v \cdot \vec{F} = -3k; \quad (12-73)$$

where  $k$  is a constant. In this case the form (12-69) would have to be retained.

The derivatives that occur on the left hand side of Equation (12-72) may be regarded as the total derivative

$$\frac{D}{Dt} = \frac{\partial}{\partial t} + \vec{r} \cdot \nabla_r + \frac{\dot{\vec{r}}}{m} \cdot \nabla_v \quad (12-74)$$

with respect to time moving along a particle trajectory, so that Equation (12-72) may be written

$$\frac{Df}{Dt} = S. \quad (12-73)$$

Thus, if there are no sources and sinks,  $f$  is constant as seen by a moving particle. This is the Liouville theorem.

Equation (12-72) contains more precise information than our derivation, in terms of a density of particles, would imply. For example, if  $f$  is initially a delta function which vanishes except at the position of some particle, and if  $S = 0$ , the form (12-73) shows that this delta function will move exactly as the particle does. Similarly, a collection of delta functions will move exactly as a collection of particles. Thus, Equation (12-72) or (12-73) can represent Newton's law exactly for a collection of particles. With this interpretation Equation (12-72) is properly called the Liouville equation.

We shall use Equation (12-72) with the interpretation that  $f$  is a continuous function representing the density of particles. In this interpretation,  $f$  does not contain information on the exact positions of particles, but only the number of particles in volume elements containing many particles. In this case we shall not be able to calculate the exact forces between neighboring particles, but only the forces that can be derived from the density function  $f$ . These include, for example, the electromagnetic force from the fields  $\vec{E}$  and  $\vec{B}$  that would result from a continuous distribution of charge and current implied by  $f$ . However, we can include the effect of collisions (forces) between neighboring particles in a statistical (rather than precise) way by putting into the source term  $S$  the average rate of scattering of particles into the velocity  $\vec{v}$  minus the average rate of scattering out of the velocity  $\vec{v}$ . With this interpretation Equation (12-72) or (12-73) is properly called the Boltzmann equation.

In the case of low density plasmas, the effect of collisions is often neglected, at least in first approximation. Since most plasmas contain at least two species, electrons and positive ions, separate density functions are introduced for each species, and the Boltzmann equation is written for each.

It is clear that if  $f(\vec{r}, \vec{v}, t_0)$  is given at time  $t_0$ , Equation (12-72) can be used to calculate  $\partial f / \partial t$ , so that we can find  $f(\vec{r}, \vec{v}, t_0 + \delta t)$  at a short time  $\delta t$  later. Repeating the process, we can find  $f$  at any later (or earlier) time. Thus given the initial value of  $f$ , Equation (12-72) determines  $f$  for all times.

The Boltzmann equation without the collision term is sometimes called the Vlasov equation.

### 12.3.2 MAXWELL'S EQUATIONS

The evolution in time of the electromagnetic fields  $\vec{E}$  and  $\vec{B}$  are governed by Maxwell's equations,

$$\frac{1}{c} \frac{\partial \vec{B}}{\partial t} = - \nabla \times \vec{E}, \quad (12-76)$$

$$\frac{1}{c} \frac{\partial \vec{E}}{\partial t} = \nabla \times \vec{B} - 4\pi \vec{J}, \quad (12-77)$$

where  $\vec{J}$  is the electric current density. It is clear that if  $\vec{E}$  and  $\vec{B}$  are given at some initial time and  $\vec{J}$  is given at all times, then these two equations will determine  $\vec{E}$  and  $\vec{B}$  at all times, by the same arguments as used above for the Boltzmann equation. The other two Maxwell equations,

$$\nabla \cdot \vec{B} = 0, \quad (12-78)$$

$$\nabla \cdot \vec{E} = 4\pi \rho, \quad (12-79)$$

where  $\rho$  is the charge density, are only initial conditions. If they are satisfied initially, then it can be shown from Equations (12-76) and (12-77) and from the conservation of charge,

$$\frac{1}{c} \frac{\partial \rho}{\partial t} + \nabla \cdot \vec{J} = 0, \quad (12-80)$$

that they will be automatically satisfied at all times. If  $\rho$ ,  $\vec{E}$  and  $\vec{B}$  vanish initially, Equations (12-78) and (12-79) are satisfied and it is not necessary to consider them further.

### 12.3.3 THE BOLTZMANN - MAXWELL EQUATIONS

We are ready now to collect a complete set of equations for the particles and fields. We write a Boltzmann equation for each species  $\alpha$  of particles,

$$\frac{\partial f_{\alpha}}{\partial t} + \vec{v} \cdot \nabla_{\vec{r}} f_{\alpha} + \frac{e_{\alpha}}{m_{\alpha}} \left[ \vec{E} + \frac{\vec{v}}{c} \times \vec{B} \right] \cdot \nabla_{\vec{v}} f_{\alpha} = S_{\alpha} \quad (12-81)$$

Here the source term  $S_{\alpha}$  can include scattering and production or loss of particles of species  $\alpha$  by ionization, deionization, or chemical reactions. Other force fields, e.g., gravitation, could be included if desired.

The charge and current densities contributed by the species  $\alpha$  are

$$\rho_{\alpha}(\vec{r}, t) = e_{\alpha} \int f_{\alpha}(\vec{r}, \vec{v}, t) d^3v \quad (12-82)$$

$$\vec{J}_{\alpha}(\vec{r}, t) = \frac{e_{\alpha}}{c} \int \vec{v} f_{\alpha}(\vec{r}, \vec{v}, t) d^3v \quad (12-83)$$

The total charge and current densities are

$$\rho = \sum_{\alpha} \rho_{\alpha}, \quad \vec{J} = \sum_{\alpha} \vec{J}_{\alpha} \quad (12-84)$$

We now add Maxwell's Equations (12-76)-(12-79) and the set of equations is complete. The conservation of charge follows from Equations (12-81) provided the sources of charge for all species sum to zero, as we shall see in the next section.

#### 12.3 4 CONSERVATION LAWS

We now integrate the Boltzmann equation for the species  $\alpha$  over velocity space, for a given coordinate  $\vec{r}$  and time  $t$ . For purposes of this integration, it is more convenient to use the form (12-67) than (12-81). The integral over velocity of the term  $\vec{\nabla}_v \cdot (\vec{F}f)$  vanishes, since it can be transformed by Gauss' theorem into an integral over a surface in velocity space at arbitrarily large velocity where, in order for the kinetic energy density to be finite, it must approach zero faster than  $v^{-5}$ . Thus the integration gives

$$\frac{\partial}{\partial t} [\int f d^3v] + \vec{\nabla}_r \cdot [\int \vec{v} f d^3v] = \int S d^3v. \quad (12-85)$$

Here we have dropped the subscript indicating species, for brevity. Now the density  $N$  of particles in coordinate space is

$$N(\vec{r}, t) = \int f d^3v, \quad (12-86)$$

and the mean particle velocity  $\vec{V}$  is

$$\vec{V}(\vec{r}, t) = [\int \vec{v} f d^3v] / N(\vec{r}, t), \quad (12-87)$$

so that Equation (12-85) is

$$\frac{\partial N}{\partial t} + \vec{\nabla} \cdot [N \vec{V}] = \int S d^3v. \quad (12-88)$$



Since  $N \vec{V}$  is the flux of particles in coordinate space, this equation would express the conservation of particles if the right hand side vanished. We have included in  $S_\alpha$  two types of terms. First, it includes sources minus sinks, and the integral of these over velocity space is the net source in coordinate space, which properly appears on the right of the conservation law. Second, we have included collision terms. Since these terms give the rate of scattering of particles from one velocity to another at the same point  $\vec{r}$  of coordinate space, their integral over velocity space vanishes. Thus, Equation (12-88) indeed expresses the conservation of particles, or on multiplying by the charge  $e_\alpha$  it expresses the conservation of charge.

Note that if the net source and  $\vec{V}$  were known, Equation (12-88) could be used to calculate the time development of  $N$ . However, we need an equation for  $\vec{V}$ . Such an equation can be obtained by multiplying Equation (12-67) by  $mv_i$  ( $v_i$  is a Cartesian component of  $\vec{v}$ ) and integrating over velocity space. The result is

$$\frac{\partial}{\partial t} [N m V_i] + \sum_j \frac{\partial}{\partial x_j} [m \int v_i v_j f d^3v] - \int F_j f d^3v = m \int v_j S d^3v. \quad (12-89)$$

The term  $N m V_i$  is the momentum density in coordinate space. The term

$$P_{ij} = m \int v_i v_j f d^3v \quad (12-90)$$

is the momentum flow tensor, or stress tensor, of the particles; it is the flux of the  $i$ 'th component of momentum in the  $j$ 'th direction. Its divergence gives the outflow of the  $i$ 'th component of momentum per unit volume. The term involving the force  $F_j$ , for the Lorentz force (12-71), is

$$\int F_i f d^3v = \rho E_i + (\vec{J} \times \vec{B})_i. \quad (12-91)$$

Thus this term is the electromagnetic force per unit volume. The term involving  $S$  is the net source of momentum per unit volume from the particle source, plus momentum given to the species  $\alpha$  by other species in collisions. Collisions between particles of species  $\alpha$  with others of the same species give no momentum source since collisions conserve momentum. The sum of the collisional source of momentum over all species vanishes for the same reason. Thus, we see that Equation (12-89) expresses the conservation of momentum.

Equations (12-88) and (12-89) would determine both  $N$  and  $\vec{V}$  if  $P_{ij}$  were known. It is clear that taking higher velocity moments of the Boltzmann equation will never lead to a sufficient set of equations to determine the unknowns that appear in them, unless we make some arbitrary assumption about the higher moments. Such an assumption might be that the velocity distribution is Maxwellian about the average velocity  $\vec{V}(r,t)$ ; this assumption leads to the approximation called magnetohydrodynamics. In order to justify it, the collision time and mean free path must be small compared to times and distances in which  $N$  and  $\vec{V}$  change appreciably.

Taking the moments, however, does display the conservation laws in coordinate space. There is one more conservation law, that of energy, which is obtained by multiplying Equation (12-67) by  $\frac{mv^2}{2}$  and integrating over velocity space. The result is

$$\frac{d}{dt} \left[ \frac{m}{2} \int v^2 f d^3v \right] + \nabla \cdot \left[ \frac{m}{2} \int v^2 \vec{v} f d^3v \right] = e \vec{E} \cdot \vec{E} + \int \frac{mv^2}{2} S d^3v \quad (12-92)$$

The first bracket is the energy density, the second is the energy flux,  $e \vec{E} \cdot \vec{E}$  is the energy given to the particles by the fields, and the term on the right is the net source of energy per unit volume. Again, collisions

between particles of the same species produce no net change in energy; different species can transfer energy from one to another. The sum of the energies of all species and the energy in the electromagnetic fields is constant.

Other moments do not lead to additional quantities that are conserved over the entire system of particles and fields. It was to be expected that the conservation of particles, momentum, and energy could be derived from the Boltzmann equation, since the Boltzmann equation was derived by combining the conservation of particles in phase space with Newton's law of motion. We repeat that the coordinate space conservation laws are insufficient to determine the solution of plasma problems in general; for this purpose we must return to the Boltzmann equation.

### 12.3.5 STATIC PROBLEMS

Some simplifications occur in static problems. We must first define what we mean by a static problem. Let us put some plasma into a container, and impose externally some static electric and magnetic fields, and wait for equilibrium to occur; that might give us a static solution.

If the container is ordinary solid material, any plasma particle striking the wall will usually either stick in the wall or be neutralized. The only practical exception to this rule is in the case of vapors of alkali metals (e.g., Cesium), which have low ionization potentials and can be kept partially ionized in a box of Tungsten, say, at a few thousand degrees Kelvin.

The ideal container for plasma is a gravitational potential well, which neither cools nor absorbs the plasma particles. The stars are natural examples.

The question obviously arises as to whether electric or magnetic fields can contain plasma. Electric potentials attract only charges of one sign. But, for example, a focused beam of energetic electrons can hold a number of positive ions near its focal point. However, this method of holding plasma has not yet become of practical importance. A great deal of attention has been directed towards the possibility that magnetic fields may be used to contain plasma. We know, for example, that a few charged particles can be kept orbiting almost indefinitely in a suitably designed cyclotron magnetic field. Furthermore, charges of both sign are contained, so that we could hold a lot of plasma without encountering the space charge repulsion that would arise with charges of only one sign.

Magnetic confinement works by having the magnetic force  $\vec{J} \times \vec{B}$  in opposition to the plasma pressure. The current density  $\vec{J}$  arises essentially from the fact that positive and negative charges gyrate in opposite directions. Collisions between positive and negative particles tend to destroy their relative velocity, reducing  $\vec{J}$ . The final result of many collisions is that the charged particles diffuse across the magnetic field in the direction their pressure gradient would have them go. In equilibrium, the plasma pressure will rest on the container walls, and not on the magnetic field. This does not define an interesting static problem.

However, collisions occur relatively slowly in high temperature, low density plasmas. Thus, it is interesting to examine the possibility of static solutions when collision effects are ignored. We shall assume a very simple situation in which there are no sources or sinks of particles, the plasma is neutral and there is no electric field, the magnetic field  $\vec{B}$  is always in the direction of the Cartesian coordinate  $z$ , and its magnitude  $B_z$  and the distribution function  $f$  depend only on the coordinate  $x$ . The  $x$  component of Equation (12-89) becomes in this case

$$\frac{\partial}{\partial x} [m \int v_x^2 f d^3v] - J_y B_z = 0. \quad (12-93)$$

The square bracket here is the pressure  $P_{xx}$  due to "thermal" velocity  $v_x$  in the  $x$  direction. The Maxwell equation (12-77) in this case becomes

$$J_y = - \frac{1}{4\pi} \frac{\partial}{\partial x} B_z. \quad (12-94)$$

Thus, Equation (12-93) can be written

$$\frac{\partial}{\partial x} (P_{xx} + \frac{1}{8\pi} B_z^2) = 0. \quad (12-95)$$

The term  $B_z^2/8\pi$  may be called the magnetic pressure, so that the condition for a static solution is that the sum of particle pressure and magnetic pressure be constant. Similar equations apply in more complicated situations, but particle and magnetic pressures are tensors (stress tensors).

These equations are necessary conditions for stress balance, or to have a static solution if collisions are neglected. They do not, however, tell us what the distribution function  $f$  must be. For example, if we are to have a current  $J_y$ , there must be a net velocity in the  $y$  direction, but Equation (12-95) gives no information on this point. Again we see that the conservation laws do not contain all the information that may be needed. To get more information we must return to the static Boltzmann equation.

Solving even the static Boltzmann equation without collisions is difficult to impossible in general, since the term involving the force  $(\vec{E}f$  in Equation 12-67) is nonlinear. However, if we are willing to assume plane or axial symmetry, some solutions can be constructed, using the fact that the static, collisionless Boltzmann equation is satisfied if  $f$  is an arbitrary function of the particle constants of motion. One constant of motion is the energy  $w = \frac{1}{2} m v^2 + e\phi$ , where  $\phi$  is the electrostatic

potential. Depending on the symmetry, the canonical momenta  $p_i = m v_i + e A_i / c$ , where  $\vec{A}$  is the magnetic vector potential, or their angular counterparts, may be constants of motion. After choosing  $f$  to be some function of  $w$  and  $p_i$ , one can integrate  $f$  over velocity and find the charge and current densities  $\rho$  and  $\vec{J}$ , which will now depend on  $\phi$  and  $\vec{A}$ . Then if we can solve Poisson's and Ampere's equations

$$\nabla^2 \phi = -4\pi \rho(\phi, \vec{A}), \quad \nabla \cdot (\nabla \times \vec{A}) = 4\pi \vec{J}(\phi, \vec{A}), \quad (12-96)$$

we will have consistent solutions for  $f$  and the fields. Examples of this technique are given in Reference 12-2.

#### 12.3.6 DYNAMIC PROBLEMS

The only useful time dependent solutions to the Boltzmann equation that have been found are those in which  $f$  and the fields deviate only slightly from static solutions. Thus, one writes

$$f = f_0 + f_1, \quad \vec{E} = \vec{E}_0 + \vec{E}_1, \quad \vec{B} = \vec{B}_0 + \vec{B}_1, \quad (12-97)$$

where  $f_0$ ,  $\vec{E}_0$  (often = 0), and  $\vec{B}_0$  satisfy the static equations, and  $f_1$ ,  $\vec{E}_1$ , and  $\vec{B}_1$  are assumed to be small. On substituting into the Boltzmann equation, terms involving only  $f_0$ ,  $\vec{E}_0$ , and  $\vec{B}_0$  cancel each other. Then dropping the quadratically small terms  $\vec{E}_1 f_1$  and  $\vec{B}_1 f_1$ , we obtain linear equations for  $f_1$ ,  $\vec{E}_1$ , and  $\vec{B}_1$ ; these involve  $f_0$ ,  $\vec{E}_0$ , and  $\vec{B}_0$ , but the latter are known functions.

The linearized Boltzmann equation is usually solved by Fourier analysis of the spatial dependence, similar to our treatment in Sec. 12.2.5. Then, for example, with an assumed initial perturbation of the static solution, one can find how the perturbation develops in time. In some cases the perturbation oscillates in time, and we say we have found a type of plasma

wave. In other cases the perturbation may grow exponentially in time, and we say that we have found an instability. Situations in which plasma is confined by a magnetic field usually tend to be unstable for some type of perturbation. Many examples of such perturbation calculations are given in Reference 12-2. The effect of collisions can also be treated in the perturbation analysis.

The nonlinear interaction of the perturbations with themselves can also be treated in a statistical way. This is the "quasilinear" theory, which is described in Reference 12-2.

### 12.3.7 ADIABATIC PARTICLE MOTIONS IN ELECTROMAGNETIC FIELDS

A good deal of insight into the behavior of plasmas can be gained by understanding how particles move in electromagnetic fields that vary slowly in time and space, that is, slowly compared with the Larmor period in time and compared with the Larmor radius in space. In a constant magnetic field a charged particle follows a helical path about a central field line, or "guiding center". In a slowly varying magnetic field the guiding center stays on the same ~~field~~ line, but the orbital kinetic energy  $w_{\perp}$  varies proportionally to the magnitude  $B$ . Hence  $w_{\perp}/B$  (which is the magnetic dipole moment of the orbiting particle) is approximately constant, i.e., is an adiabatic invariant. Thus, as a particle in a static magnetic field enters a region of increased  $B$ , its parallel energy  $w_{\parallel}$  must decrease as  $w_{\perp}$  increases; this is the magnetic "mirror" effect, i.e., the particle is repelled by the region of increased  $B$ .

In crossed electric and magnetic fields, the guiding center "drifts" with velocity

$$\dot{\mathbf{r}}_D = c \nabla \times \mathbf{E} / B^2, \quad (12-98)$$

which is the condition that the electric and magnetic forces cancel on the average. Gradients of the magnetic field components cause other drifts of the guiding center, and a time-varying electric field causes the plasma to polarize. These effects are easy to derive, and are discussed in Reference 12-4.

## 12.4 LARGE SCALE MOTIONS AND FLUID APPROXIMATIONS

Problems involving large scale motions of plasmas—for example, the explosion of a plasma in a magnetic field—cannot of course be treated by perturbation techniques. In principle, such problems can be treated by solving the Boltzmann equation. In practice, however, the six independent space and velocity variables plus time make both analytical and computer solutions quite hopeless. Even if we assume axial symmetry in space, we have two space variables, three velocity variables, and time. As a result, various fluid approximations are commonly used in treating such problems.

Fluid approximations exist at four levels, with several possible variations of each. We shall describe the four levels briefly.

### 12.4.1 MAGNETOHYDRODYNAMICS

The simplest approximation is to take the equations of gas dynamics and add electrical conductivity. These equations are essentially the conservation laws of Section 12.3.1. The first equation expresses the conservation of mass,

$$\frac{\partial \rho}{\partial t} + \nabla \cdot \rho \vec{V} = 0. \quad (12-99)$$

Here  $\rho$  is the mass density (not the charge density) and  $\vec{V}$  is the fluid velocity. The second equation expresses the conservation of momentum, or Newton's law,

$$\rho \left[ \frac{\partial \vec{V}}{\partial t} + \vec{V} \cdot \nabla \vec{V} \right] = - \nabla p + \vec{J} \times \vec{B}. \quad (12-100)$$

Here  $p$  is the fluid pressure, which is related to the particle stress tensor (12-98) in the following way: If one assumes that the velocity distribution function in Equation (12-96) is Maxwellian at temperature  $T$  about an average velocity  $\vec{V}$ , then



$$P_{ij} = \rho V_i V_j + \delta_{ij} P, \quad (12-101)$$

where  $\delta_{ij}$  is the diagonal unit tensor and

$$P = NT. \quad (12-102)$$

This is the ideal gas equation of state. When this evaluation of  $P_{ij}$  is used in Equation (12-89), Equation (12-100) results, after Equation 12-99 is used to eliminate  $\partial(Nm)/\partial t = \partial\rho/\partial t$ .

Since the role of Equation (12-100) is to determine  $\vec{V}$ , we need an equation for  $\vec{J}$ . A common choice is Ohm's law for a moving medium,

$$\vec{J} = \sigma[\vec{E} + \frac{1}{c} \vec{V} \times \vec{B}]. \quad (12-103)$$

The square bracket here is the electric field in a frame moving with the fluid (we assume  $V \ll c$ ). The factor  $\sigma$  is the electrical conductivity, or reciprocal of the resistivity. Equation (12-103) says that the electric force on the charge carriers (usually assumed to be electrons) is balanced by the resistive drag they experience in moving relative to the rest of the fluid. Sometimes the pressure gradient of electrons is added to this force balance; thermoelectric effects are thereby included. The inertia of the electrons is commonly ignored, which means that electron plasma oscillations are not included. A term  $\sigma \vec{J} \times \vec{B}/cN$  has also been ignored in Equation (12-103); its inclusion would yield Hall effects.

Equation (12-100) contains no electric force on the fluid. It is usually assumed that the electrical conductivity is high enough that collections of charge are negligible.

Maxwell's equations are included to determine  $\vec{E}$  and  $\vec{B}$ . Commonly the displacement current ( $\partial\vec{E}/\partial t$ ) is neglected in Equation (12-77), which becomes

$$\vec{J} = \frac{1}{4\pi} \nabla \times \vec{B} \quad (12-104)$$

This equation is used to eliminate  $\vec{J}$  from Equation (12-100), and is also used in Equation (12-103) so that  $\vec{E}$  can be found in terms of  $\vec{V}$  and  $\vec{B}$ .

$$\vec{E} = -\frac{1}{c} \vec{V} \times \vec{B} + \frac{1}{4\pi c} \nabla \times \vec{B} \quad (12-105)$$

This result for  $\vec{E}$  is then used in Equation (12-76), giving the equation for  $\vec{B}$ ,

$$\frac{1}{c} \frac{\partial \vec{B}}{\partial t} = \frac{1}{c} \nabla \times (\vec{V} \times \vec{B}) - \nabla \times \left( \frac{1}{4\pi c} \nabla \times \vec{B} \right) \quad (12-106)$$

With Equation (12-104), the magnetic force term can be written

$$\vec{J} \times \vec{B} = -\frac{1}{4\pi} \nabla (\vec{B} \cdot \vec{B}), \quad (12-107)$$

which latter form can be written as the divergence of the magnetic stress tensor; however, there is no particular advantage in using the tensor form.

Often it is assumed that the conductivity is so high that the last terms in each of Equations (12-105) and (12-106) can be dropped. From the resulting form of Equation (12-106) it can then be shown that the  $\vec{B}$  lines can be regarded as moving with the fluid at each point.

The last conservation law, that of energy, is taken in various forms. Sometimes the flow is assumed to be adiabatic, so that

$$\frac{P}{P_0} = \left( \frac{\rho}{\rho_0} \right)^\gamma$$

is used in place of the equation of state (12-102); here  $P_0$  and  $\rho_0$  are the initial pressure and density of a given parcel of fluid, and  $\gamma$  is usually taken to be 5/3. Sometimes the full energy equation, with heat conduction, is used.

From our earlier discussion it is clear that the equations of magnetohydrodynamics will be valid only if collision times and mean free paths are small compared with times and distances in which plasma properties change appreciably.

Sometimes it is assumed that a plasma and a neutral fluid occupy the same volume, and that the two fluids have different motions with a collisional coupling term causing an interaction between them. Further discussions of the two fluid equations are given in Section 12.4.4. Strictly speaking, the use of magnetohydrodynamics for the plasma in this case is inconsistent, since the collisions that validate magnetohydrodynamics would lock the two fluids together. On the other hand, for rarefied plasma where collisions would not be so effective, the equations of magnetohydrodynamics fail to account for the free flow of ionized particles along the magnetic field lines, or of neutral particles across field lines as well as along them.

#### 12.4.2 THE APPROXIMATION OF CHEW, GOLDBERGER AND LOW

The chief deficiency of the magnetohydrodynamic approximation for plasmas in which collisions are a weak effect lies in the restrictions imposed by the assumption that the velocity distribution is spherically symmetric about the average velocity  $\bar{V}$ . This implies a rapid sharing of kinetic energies associated with motions parallel and perpendicular to the magnetic field. While the Larmor motion around the guiding center guarantees approximately equal kinetic energies associated with the two components of velocity normal to the field, there is no a priori relation between these and the parallel kinetic energy. The plasma model in which particles are visualized as revolving rapidly about their guiding center with arbitrary perpendicular and parallel velocities leads to the following evaluation of the particle stress tensor of Equation (12-90), in a Cartesian coordinate system in which the  $z$  axis is locally parallel to the magnetic field:

$$(P_{ij}) = m \begin{pmatrix} V_1^2 & V_1 V_2 & V_1 V_3 \\ V_2 V_1 & V_2^2 & V_2 V_3 \\ V_3 V_1 & V_3 V_2 & V_3^2 \end{pmatrix} + \begin{pmatrix} p & 0 & 0 \\ 0 & p_1 & 0 \\ 0 & 0 & p_1 \end{pmatrix}. \quad (12-108)$$

Here the first tensor on the right gives the momentum flow (or stress) connected with the average velocity of all the particles at the given space point, averaged over longer periods, and the second tensor (the pressure tensor) gives the contribution due to deviations from the average,

$$p = n \int (v_1 V_1)^2 f d^3v, \\ p_1 = n \int (v_1 - V_1)^2 f d^3v = n \int (v_1 - V_1)^2 f d^3v. \quad (12-109)$$

Since the direction of the magnetic field may vary in space, it is useful to express the pressure tensor in a fixed three-dimensional coordinate system. If  $\hat{b}(x, y, z)$  is a unit vector field which is everywhere parallel to the  $\vec{B}$  field, we can write the pressure tensor as

$$P_{ij} = P \delta_{ij} + (P_1 - P) b_i b_j. \quad (12-110)$$

It is easy to see that this tensor takes the form of that in Equation (12-108) if  $\vec{b}$  is parallel to the  $x$  axis.

Now, to derive, and to apply, the above-mentioned set of equations by using this definition of the pressure tensor in the conservation laws, the conservation of mass, momentum, and energy, let us consider the conservation of momentum tensor.

$$\frac{d}{dt} \int \left( \frac{1}{2} \rho \vec{v} \cdot \vec{v} \right) dV = \int \left( \rho \vec{v} \cdot \vec{v} \right) dV = \int \left( \rho \vec{v} \cdot \vec{v} \right) dV = \int \left( \rho \vec{v} \cdot \vec{v} \right) dV. \quad (12-111)$$

The first two terms following  $\vec{J} \times \vec{B}$  here combine to indicate that the gradient of  $p_{\perp}$  acts only in the perpendicular direction and that of  $p_{\parallel}$  only in the parallel direction. The last term has a simple interpretation in terms of centrifugal and magnetic mirror forces on charged particles in curving and diverging field lines respectively.

CGL also derived the general energy conservation equations which govern the time variation of  $p_{\perp}$  and  $p_{\parallel}$ . The thermal conduction terms in these equations have to be specified by other means, since they involve higher (third) velocity moments of the Boltzmann equation, as in Equation (12-92). A common approximation is to assume that the pressures obey an adiabatic law, with  $\gamma = 2$  (two dimensional gas) for  $p_{\perp}$  and  $\gamma = 3$  (one dimensional gas) for  $p_{\parallel}$ .

The treatment of Maxwell's equations in the CGL approximation is basically the same as in the magnetohydrodynamic approximation.

While the CGL approximation contains more plasma physics than the magnetohydrodynamic approximation, it still does not adequately account for the streaming of energetic particles along field lines. This effect is treated as parallel heat conduction, which means that energetic ions flowing into a region of cold plasma are assumed to share their parallel energy with that of the cold plasma. Thus, parallel energy diffuses, rather than streams, as it should.

#### 12.4.3 THE APPROXIMATION OF LONGMIRE, KILB AND CREVIER

Since the motion of particles parallel to the magnetic field is essentially as free particles, it is clear that no fluid approximation can adequately describe the parallel particle motion. The Boltzmann equation provides a thorough description of the motion of free particles. It was proposed by Longmire, Kilb and Crevier (LKC, to be published) therefore, that in taking

the velocity moments of the Boltzmann equation, one should integrate only over the two components of the velocity that are perpendicular to  $\vec{B}$ , leaving the parallel velocity in Boltzmann form. Thus, instead of getting the spatial particle density

$$N(\vec{r}, t) = \int f(\vec{r}, \vec{v}, t) d^3v, \quad (12-112)$$

LEE obtain

$$N(\vec{r}, v_{\parallel}, t) = \int f(\vec{r}, \vec{v}, t) d^2v_{\perp}. \quad (12-113)$$

The function  $N$ , which is called the pseudodensity, is still a distribution function in the parallel velocity. When integrated over  $v_{\parallel}$ , it yields  $N(\vec{r}, t)$ .

In the general case,  $N$  depends on four space and velocity variables and time, which are probably too many to be manageable analytically or with present computers. However, for problems with axial symmetry, there will be three variables plus time, as in three dimensional hydrodynamics. Present computers can handle such problems. Accordingly, LEE worked out the relevant moments of the Boltzmann equation for the case of axial symmetry.

Taking into account the rapid Larmor motion of particles about their guiding centers on a magnetic field line (which may be moving), it is clear that the Boltzmann distribution function will be approximately of the form

$$f = f(\vec{r}, (\vec{r} - \vec{V}_E)^2, v_{\parallel}, t), \quad (12-114)$$

where  $\vec{V}_E$  is the average perpendicular velocity of particles near space point  $\vec{r}$ , independent of the parallel velocity.

$$\int \vec{v} f(\vec{r}, (\vec{r} - \vec{V}_E)^2, v_{\parallel}, t) d^2v_{\perp} = \vec{V}_E f(\vec{r}, t), \quad (12-115)$$

Thus  $\vec{V}_\perp$  is a fluid velocity in the perpendicular direction. On the other hand, since particles with different  $v_\parallel$  may have different amounts of Larmor kinetic energy, the perpendicular pressure may depend on  $v_\parallel$ .

$$\int \frac{1}{2} m (v_\perp - V_\perp)^2 f d^2 v_\perp = \mathcal{P}_\perp(\vec{r}, v_\parallel, t). \quad (12-116)$$

Thus, we call  $\mathcal{P}_\perp$  a pseudopressure, because it still depends on  $v_\parallel$ . Since we shall not need the parallel pressure, we shall henceforth drop the subscript  $\perp$  and use simply  $\mathcal{P}$ .

Equations for  $\mathcal{E}$ ,  $\vec{V}_\perp$  and  $\mathcal{P}$  are obtained by taking the appropriate velocity moments of the Boltzmann equation. The perpendicular velocity integrals are facilitated by writing

$$d^2 v_\perp = d(\vec{v} \cdot \vec{b} - u) d^3 v, \quad (12-117)$$

where  $u$  is the  $\chi$ -function and  $\vec{b}$  is a unit vector parallel to  $\vec{k}$ . Integration with this factor picks out the value  $u$  for the parallel velocity. In doing the integrals of those terms in the Boltzmann equation that contain spatial gradients, one must remember that  $\vec{b}$  depends on the spatial coordinate.

For the case of axial symmetry in which the  $\vec{B}$  lines lie in the  $(r, z)$  planes of the usual cylindrical coordinate system, we obtain the equation for  $\mathcal{E}$ ,

$$\frac{\partial \mathcal{E}}{\partial t} + \nabla_\parallel (\mathcal{E} \vec{V}_\parallel + \mathcal{P} \vec{V}_\parallel) + \nabla_\perp \cdot (\mathcal{E} \vec{V}_\perp + \mathcal{P} \vec{V}_\perp) + \nabla_\parallel (\mathcal{P} \vec{V}_\parallel + \mathcal{E} \vec{V}_\parallel) + \nabla_\perp \cdot (\mathcal{P} \vec{V}_\perp + \mathcal{E} \vec{V}_\perp) = 0. \quad (12-118)$$

Here  $E_{\parallel}$  is the parallel part of any force field, e.g., gravitational, acting on the particle. The similarity of this equation with a Boltzmann equation for a gas having only one velocity variable  $u$  should be apparent. Comparing with Equation (12-67), we see that  $f$  is replaced by  $\bar{f}$ , and that there is a partial time derivative, a spatial divergence, and a divergence with respect to the velocity variables, here only one. Thus, the quantity in brackets operated on by  $\partial/\partial u$  must represent the product of  $\bar{f}$  by the effective parallel force acting on the parallel motion. The various terms in this bracket can, in fact, be interpreted in terms of forces acting in the parallel direction. The first term is the magnetic mirror force associated with diverging field lines. The next two terms represent a Coriolis type force associated with  $\bar{V}_{\perp}$  and a  $\hat{b}$  direction rotating either in time  $(\partial\hat{b}/\partial t)$  or as the particle moves along the field line  $(u(\hat{b} \cdot \nabla)\hat{b})$ . The next term is a centrifugal force arising when the flow lines of  $\bar{V}_{\perp}$  are curved. The last term  $E_{\parallel}$  is self evident.

The equation for  $\bar{V}_{\perp}$  obtained by LKC is exactly equivalent to the CGL Equation (12-11) provided we use the relation

$$\bar{V} \times \bar{V}_{\perp} = \bar{V} \hat{b}, \quad (12-119)$$

where  $\bar{V}_{\perp}$  is the average parallel velocity,

$$\bar{V}_{\perp} = \frac{1}{N} \int u \bar{f} du, \quad (12-120)$$

The CGL pressures, in terms of the LKC variables, are

$$p_{\perp} = \int \bar{f} u^2 du, \quad p_{\parallel} = m \int (u \bar{V}_{\perp})^2 \bar{f} du, \quad (12-121)$$



The equation for  $\mathcal{E}$  obtained by LEC is

$$\begin{aligned} \frac{\partial \mathcal{E}}{\partial t} + \nabla \cdot [(\vec{V}_i + u\vec{b})\mathcal{E}] = & - \mathcal{E}[u\vec{v} \cdot \vec{b} + \vec{v} \cdot \vec{V}_i + \vec{V}_i \cdot (\vec{b} \cdot \vec{v})\vec{b}] \\ & - \frac{\partial}{\partial u} \left[ \frac{\mathcal{E}^2}{m_i} \vec{v} \cdot \vec{b} + \mathcal{E} \left( \vec{V}_i \cdot \frac{\partial \vec{b}}{\partial t} + u\vec{V}_i \cdot (\vec{b} \cdot \vec{v})\vec{b} \right. \right. \\ & \left. \left. + \vec{V}_i \cdot (\vec{V}_i \cdot \vec{v})\vec{b} + \frac{E}{m} \right) \right]. \end{aligned} \quad (12-122)$$

This equation is Boltzmann-like, in that it still contains the velocity variable  $u$ . Its terms are capable of interpretation as energy flow or as work done by various forces.

The LEC equations account for the free streaming of ions along field lines. It should be realized that in any fluid approximation, including this one, the effect of those plasma instabilities which cannot be described in terms of the approximation used must be invoked artificially in the fluid equations. These instabilities may affect especially the transport coefficients, such as the diffusion across magnetic field lines of particles (resistivity), momentum (viscosity), and energy (heat conduction). In addition, they may act to isotropize the pressure tensor. While a great deal of work has been done on instabilities, it cannot yet be said that criteria for their existence or their ultimate effects are well in hand. Such criteria and effects, as may be proposed, could be coupled into the LEC equations.

#### 12.4.4 LOW- $\beta$ PLASMAS ABOVE 100 KM ALTITUDE

In the normal ionospheric E and F-layers the ion-electron pressure  $P$  is much less than the magnetic pressure  $B^2/8\pi$ . The ratio  $8\pi P/B^2$  is often referred to as the plasma- $\beta$ . Such low- $\beta$  plasmas also occur after a few minutes subsequent to high altitude nuclear bursts and for barium cloud releases in the ionosphere. Under these conditions it is not possible energetically to cause substantial distortions of the magnetic field. Thus  $\partial \vec{B}/\partial t$  is very small, and as a consequence of Maxwell's Equation (12-2), the electric field must be primarily electrostatic. Experience with numerical computations shows that it is very difficult to accurately solve the magneto-hydrodynamic Equations (12-100) through (12-107) when the plasma- $\beta$  is small. One must recast these equations to obtain a more viable procedure for finding a solution (Ref. 12-4).

A key point is that currents will be induced in the high altitude plasma as it moves about in response to the applied forces such as gravity, neutral winds, pressure gradients, etc. The effect of these currents is to average the applied forces along each field line via  $\vec{J} \times \vec{B}$  forces such that essentially all of the electrons in a given magnetic flux tube will  $\vec{E} \times \vec{B}$  drift together to another field-aligned flux tube. Because only a negligibly small space-charge is needed to set up the spatially varying electrostatic field  $\vec{E}$  that causes the  $\vec{E} \times \vec{B}$  drift of the plasma, it is crucial that the current density  $\vec{J}$  be essentially divergence-free, i.e., that:

$$\nabla \cdot \vec{J} = 0 \quad (12-125)$$

To employ this equation we must express  $\vec{J}$  in terms of the electric field and the forces acting on the plasma. For the conditions discussed in this subsection, the ion-electron plasma is collisional because the plasma evolves on a time scale of minutes and the expected plasma temperature-density parameters are in the range of less than 0.1 eV at  $10^4 \text{ cm}^{-3}$  to

less than 2 eV at  $10^9 \text{ cm}^{-3}$ . On the other hand, above 100 km altitude, collisions with neutrals are insufficient to provide tight coupling with the neutral fluid. Thus we must employ a multi-fluid description, with the neutrals, the ions, and the electrons obeying the following momentum conservation equations:

$$\frac{\partial(\rho_o \vec{V}_o)}{\partial t} + \nabla \cdot (\rho_o \vec{V}_o \vec{V}_o) = -\nabla P_o + \rho_o \vec{g} - \nu_{io} \rho_i (\vec{V}_o - \vec{V}_i) - \nu_{eo} \rho_e (\vec{V}_o - \vec{V}_e) \quad (12-124)$$

$$\begin{aligned} \frac{\partial(\rho_i \vec{V}_i)}{\partial t} + \nabla \cdot (\rho_i \vec{V}_i \vec{V}_i) = & -\nabla P_i + \rho_i \vec{g} + eN_i (\vec{E} + \vec{V}_i \times \vec{B}/c) \\ & + \nu_{io} \rho_i (\vec{V}_o - \vec{V}_i) - \nu_{ei} \rho_e (\vec{V}_i - \vec{V}_e) \end{aligned} \quad (12-125)$$

$$\begin{aligned} \frac{\partial(\rho_e \vec{V}_e)}{\partial t} + \nabla \cdot (\rho_e \vec{V}_e \vec{V}_e) = & -\nabla P_e + \rho_e \vec{g} - eN_e (\vec{E} + \vec{V}_e \times \vec{B}/c) \\ & + \nu_{eo} \rho_e (\vec{V}_o - \vec{V}_e) + \nu_{ei} \rho_e (\vec{V}_i - \vec{V}_e) \end{aligned} \quad (12-126)$$

The subscripts o, i, and e respectively indicate neutral, ion, and electron fluid parameters. The ion-neutral, electron-neutral, and electron-ion collision frequencies are denoted by  $\nu_{io}$ ,  $\nu_{eo}$ , and  $\nu_{ei}$ . Detailed calculations of these collision frequencies for nuclear burst conditions are given in Ref. 12-5; approximate values are indicated in the glossary of Chapter 13 of this compendium.

The terms involving  $\nu_{io}$ ,  $\nu_{eo}$ , and  $\nu_{ei}$  in the three above equations account for momentum transfer between the three fluids via collisions. In Equation (12-124), the last term is negligible compared to the others. The usual magnetohydrodynamic equation is obtained by adding Equations (12-125) and (12-126). Neglecting some small terms, this yields:

$$\frac{\partial(\rho_i \vec{V}_i)}{\partial t} + \nabla \cdot (\rho_i \vec{V}_i \vec{V}_i) = -\nabla(P_i + P_e) + \rho_i \vec{g} + \vec{J} \times \vec{B} + v_{i0} \rho_i (\vec{V}_e - \vec{V}_i) \quad (12-127)$$

Equations (12-124) and (12-127), together with (12-106) and (12-107), are referred to as the two-fluid MHD equations.

Returning now to the problem of obtaining a suitable expression for  $\vec{J}$ , we will solve Equations (12-125) and (12-126) for  $\vec{V}_i$  and  $\vec{V}_e$  and then find  $\vec{J}$  from

$$\vec{J} = \frac{eN}{c} (\vec{V}_i - \vec{V}_e) \quad (12-128)$$

To solve those two equations for the transverse-to- $\vec{B}$  velocity components  $\vec{V}_{i\perp}$  and  $\vec{V}_{e\perp}$  we introduce the auxiliary notation:

$$\vec{A}_i = \nabla P_i - \rho_i \vec{g} + \frac{\partial(\rho_i \vec{V}_i)}{\partial t} + \nabla \cdot (\rho_i \vec{V}_i \vec{V}_i) \quad (12-129)$$

$$\vec{A}_e = \nabla P_e - \rho_e \vec{g} + \frac{\partial(\rho_e \vec{V}_e)}{\partial t} + \nabla \cdot (\rho_e \vec{V}_e \vec{V}_e) \quad (12-130)$$

$$\gamma_{i0} = \nu_{i0}/\Omega_i; \quad \gamma_{e0} = \nu_{e0}/\Omega_e; \quad \gamma_{ei} = \nu_{ei}/\Omega_e \quad (12-131)$$

$$d = (1 + \gamma_{i0}^2)(1 + \gamma_{e0}^2) + \gamma_{ei}(\gamma_{i0} + \gamma_{e0}) [2 + \gamma_{i0}\gamma_{e0} + \gamma_{ei}(\gamma_{i0} + \gamma_{e0})] \quad (12-132)$$

where the  $\gamma$ 's are the ratios of the collision frequencies to the appropriate gyro-frequency. These  $\gamma$ 's are all positive numbers. For nuclear burst conditions,  $\gamma_{i0}$  and  $\gamma_{e0}$  are less than unity above about 75 km and 150 km altitude respectively, and they are nearly proportional to the neutral fluid density. At any particular point the ratio  $\gamma_{e0}/\gamma_{i0}$  is small and about equal to  $1/2$  so that  $\gamma_{ei}$  is proportional to  $N_e$  and

outside fireballs the  $\eta_{ei}$  is generally smaller than  $\eta_{eo}$  at altitudes below 200 km. Above 300 km altitude, or inside fireballs,  $\eta_{ei}$  is usually larger than  $\eta_{eo}$  and may also be larger than  $\eta_{io}$ . At altitudes above about 150 km  $d$  is approximately unity because  $\eta_{io}$ ,  $\eta_{eo}$ , and  $\eta_{ei}$  are generally small at high altitudes.

The exact solutions for  $\vec{V}_{i\perp}$  and  $\vec{V}_{e\perp}$  are obtained by inverting a  $4 \times 4$  matrix, with the result that

$$\begin{aligned} \vec{V}_{i\perp} d = & \left[ 1 + \eta_{eo}^2 + \eta_{ei}(\eta_{io} + \eta_{eo}) \right] \frac{c}{B} (\vec{E}_{\perp} + \frac{1}{cN} \vec{A}_{e\perp}) \times \vec{b} \\ & + \left[ \eta_{io}(1 + \eta_{eo}^2) + \eta_{ei}\eta_{eo}(\eta_{io} + \eta_{eo}) \right] \left[ \frac{c}{B} (\vec{E}_{\perp} + \frac{1}{cN} \vec{A}_{e\perp}) + \vec{V}_o \times \vec{b} \right] \\ & + \left[ \eta_{io}^2(1 + \eta_{eo}^2) + \eta_{ei}(\eta_{io} + \eta_{eo})[1 + 2\eta_{io}\eta_{eo} + \eta_{ei}(\eta_{io} + \eta_{eo})] \right] \vec{V}_{o\perp} \\ & - \left[ \eta_{io}(1 + \eta_{eo}^2) + \eta_{ei}[1 + \eta_{eo}^2 + 2\eta_{io}\eta_{eo} + \eta_{ei}(\eta_{io} + \eta_{eo})] \right] \frac{c}{cNB} (\vec{A}_i + \vec{A}_e)_{\perp} \\ & + \left[ 1 + \eta_{eo}^2 + 2\eta_{eo}\eta_{ei} \right] \frac{c}{cNB} \vec{b} \times (\vec{A}_i + \vec{A}_e) \end{aligned} \quad (12-133)$$

$$\begin{aligned} \vec{V}_{e\perp} d = & \left[ 1 + \eta_{io}^2 + \eta_{ei}(\eta_{io} + \eta_{eo}) \right] \frac{c}{B} (\vec{E}_{\perp} + \frac{1}{cN} \vec{A}_{e\perp}) \times \vec{b} \\ & - \left[ \eta_{eo}(1 + \eta_{io}^2) + \eta_{ei}\eta_{io}(\eta_{io} + \eta_{eo}) \right] \left[ \frac{c}{B} (\vec{E}_{\perp} + \frac{1}{cN} \vec{A}_{e\perp}) + \vec{V}_o \times \vec{b} \right] \\ & + \left[ \eta_{eo}^2(1 + \eta_{io}^2) + \eta_{ei}(\eta_{io} + \eta_{eo})[1 + 2\eta_{io}\eta_{eo} + \eta_{ei}(\eta_{io} + \eta_{eo})] \right] \vec{V}_{o\perp} \\ & - \eta_{ei} \left[ 1 + \eta_{io}\eta_{eo} + \eta_{ei}(\eta_{io} + \eta_{eo}) \right] \frac{c}{cNB} (\vec{A}_i + \vec{A}_e)_{\perp} \\ & - \eta_{ei}(\eta_{io} - \eta_{eo}) \frac{c}{cNB} \vec{b} \times (\vec{A}_i + \vec{A}_e) \end{aligned} \quad (12-134)$$

Using these expressions for  $\vec{V}_{i\perp}$  and  $\vec{V}_{e\perp}$  in Equation (12-128), we obtain:

$$\begin{aligned} \frac{e\vec{J}_{\perp}}{cN} = & -(\eta_{i0}^2 - \eta_{e0}^2) \left[ \frac{c}{B} (\vec{E}_{\perp} + \frac{1}{cN} \vec{A}_{e\perp}) \times \vec{b} - \vec{V}_{o\perp} \right] \\ & + (\eta_{i0} + \eta_{e0}) \left[ 1 + \eta_{i0}\eta_{e0} + \eta_{ei}(\eta_{i0} + \eta_{e0}) \right] \left[ \frac{c}{B} (\vec{E}_{\perp} + \frac{1}{cN} \vec{A}_{e\perp}) + \vec{V}_o \times \vec{b} \right] \\ & - \left[ \eta_{i0}(1 + \eta_{e0}^2) + \eta_{ei}\eta_{e0}(\eta_{i0} + \eta_{e0}) \right] \frac{c}{cNB} (\vec{A}_1 + \vec{A}_e)_{\perp} \\ & + \left[ 1 + \eta_{e0}^2 + \eta_{ei}(\eta_{i0} + \eta_{e0}) \right] \frac{c}{cNB} \vec{b} \times (\vec{A}_1 + \vec{A}_e) \end{aligned} \quad (12-135)$$

Equations (12-125) and (12-126) may also be solved for the parallel-to- $\vec{b}$  current density  $\vec{J}_{\parallel}$ :

$$\frac{c}{cN} \left[ \eta_{e0} + \eta_{ei} \left( 1 + \frac{\eta_{e0}}{\eta_{i0}} \right) \right] \vec{J}_{\parallel} = \left( 1 + \frac{\eta_{e0}}{\eta_{i0}} \right) \frac{c}{B} (\vec{E}_{\parallel} + \frac{1}{cN} \vec{A}_{e\parallel}) - \frac{\eta_{e0}}{\eta_{i0}} \frac{c}{cNB} (\vec{A}_1 + \vec{A}_e)_{\parallel} \quad (12-136)$$

No approximations have been made in deriving Equations (12-133)-(12-136) from the MHD Equations (12-125) and (12-126) except the negligible one that  $N_i = N_e = N$ . In particular, the  $\vec{E}$  fields appearing in these equations could be inductive as well as electrostatic.

In applications to low- $\beta$  plasmas above 100 km altitude, the above exact equations are simplified by assuming that the  $\vec{E}$  field is electrostatic and by ignoring all but the  $\nabla P_e$  term in Equation (12-130) for  $\vec{A}_e$ . Ignoring the spatial variation of the electron temperature  $T_e$ , one may then introduce a potential function  $\phi$  such that:

$$-\nabla\phi = \vec{E} + \frac{1}{c} \frac{d\vec{A}}{dt} \quad (12-137)$$

Furthermore, terms in Equation (12-135) involving  $n_{eo}$  or  $n_{ej}$  are dropped, and in Equation (12-136) terms involving the ratio  $n_{eo}/n_{io}$  are dropped. The resultant approximate equation for the current density  $\vec{J}$  is:

$$\begin{aligned} \vec{J} = & - \frac{eN}{R(n_{ei} + n_{eo})} \nabla_{\parallel} \psi - \frac{n_{io}}{1 + n_{io}^2} \frac{eN}{B} \left[ \vec{\nabla}_{\perp} \psi + n_{io} \vec{b} \cdot \vec{\nabla}_{\perp} \psi \right] \\ & + \frac{n_{io}}{1 + n_{io}^2} \frac{eN}{c} \left[ \vec{\nabla}_0 \cdot \vec{b} + n_{io} \vec{\nabla}_{0\perp} \right] - \frac{n_{io}}{1 + n_{io}^2} \frac{1}{B} \left[ \vec{\nabla}_{\perp} p + n_{io} \vec{b} \cdot \vec{\nabla}_{\perp} p \right] \\ & + \frac{1}{1 + n_{io}^2} \frac{1}{B} \vec{b} \cdot \left[ \vec{A} + n_{io} \vec{R}_{\perp} + n_{io} \vec{\nabla}_{\perp} \right] \end{aligned} \quad (12-138)$$

where  $P$  is the total ion-electron pressure  $= P_i + P_e$ . The coefficient of  $\nabla_{\parallel} \psi$  is referred to as the parallel-to- $\vec{b}$  conductivity, while the coefficients of  $\vec{\nabla}_{\perp} \psi$  and  $\vec{b} \cdot \vec{\nabla}_{\perp} \psi$  are referred to as the Pedersen and Hall conductivities, respectively. Above 150 km altitude, the parallel conductivity is usually much larger than the Pedersen or Hall conductivities, so  $\nabla_{\parallel} \psi$  must be much smaller than  $\nabla_{\perp} \psi$  in order that  $\vec{J}_{\parallel}$  and  $\vec{J}_{\perp}$  have about the same magnitude and will be required approximately by  $\vec{J} \cdot \vec{b} = 0$ . Thus, for large-scale phenomena the potential variation along the field line will usually be much less than that across the field lines. Often one employs an "equipotential" assumption along the field line to simplify the first differential equation further.

A differential equation for the magnetic potential can then be obtained by substituting  $\vec{J}$  from Equation (12-138) into Equation (12-134). It is important to remember the difference of  $\vec{b}$  to be used; it should be noted that the difference of  $\vec{b}$  to be used in the first term of Equation (12-138) will generally be small, even though the magnitude of the term may be large. The difference of this term is due to the tendency of a field line to curve and is not important in this case since the magnitude of the term is small when the field

lines are curved. It is convenient to replace this term by making use of the mathematical identity:

$$\begin{aligned} \frac{1}{1+\eta_{i0}^2} \frac{1}{B} \vec{b} \times \nabla P &\equiv - \nabla \times \left[ \frac{P \vec{b}}{B^2 (1+\eta_{i0}^2)} \right] + \frac{2P}{(1+\eta_{i0}^2) B} \vec{b} \times [(\vec{b} \cdot \nabla) \vec{b}] \\ &+ \frac{2\eta_{i0}^2 P \vec{b} \times \nabla \eta_{i0}}{(1+\eta_{i0}^2)^2 B} + \frac{\beta \vec{J}_{\parallel} - 2\vec{J}_{\perp}}{2(1+\eta_{i0}^2)} \end{aligned} \quad (12-139)$$

The first term on the r.h.s. of this equation is the "magnetization" current. It is divergence-free so it will not contribute to the  $\nabla \cdot \vec{J}$  equation and therefore will not contribute to the differential equation for  $\psi$ . The second term yields the magnetic field curvature effect. The last two terms can be neglected in low- $\beta$  plasmas. The effect of this substitution is to replace the  $\nabla P$  force by the magnetic field curvature force  $2P(\vec{b} \cdot \nabla) \vec{b}$  in the last bracket of Equation (12-138). The resultant differential equation for  $\psi$  is then

$$\begin{aligned} \nabla \cdot \left[ \frac{eN}{B(c_1 + \eta_{e0})} \nabla_{\parallel} \psi \right] &+ \nabla \cdot \left[ \frac{\eta_{i0}}{1+\eta_{i0}^2} \frac{eN}{B} (\nabla_{\perp}^2 \psi + \eta_{i0} \vec{b} \times \nabla_{\perp} \psi) \right] \\ &= \nabla \cdot \left[ \frac{1}{1+\eta_{i0}^2} \frac{\vec{b}}{B} - (2P(\vec{b} \cdot \nabla) \vec{b} - \rho_i \nabla_{i0} \vec{V}_{o\perp} - \rho_i \vec{k}_{\perp} + \rho_i \vec{V}_{i\perp}) \right] \\ &- \nabla \cdot \left[ \frac{\eta_{i0}}{1+\eta_{i0}^2} \frac{1}{B} (\nabla_{\perp}^2 P - \rho_i \nabla_{i0} \vec{V}_{o\perp} - \rho_i \vec{k}_{\perp} + \rho_i \vec{V}_{i\perp}) \right] \end{aligned} \quad (12-140)$$

For cases wherein the "equipotential" assumption is reasonable, one integrates this equation along the length of the field lines. Assuming that  $\vec{J}_{\parallel}$  is zero at the end points, the integral of the first term on the left side of Equation (12-140) is zero. In the second term the field-line integrals of the coefficients  $eN_{i0}/(1+\eta_{i0}^2)B$  and  $eN_{i0}^2/(1+\eta_{i0}^2)B$  yield the Pedersen and Hall conductances  $\Sigma_P$  and  $\Sigma_H$ , respectively.



## REFERENCES

- 12-1. Longmire, C.L., Elementary Plasma Physics, Interscience, New York, 1963.
- 12-2. Krall, N.A., and A.W. Trivelpiece, Principles of Plasma Physics, McGraw-Hill, New York, 1973.
- 12-3. Chew, G.F., M.L. Goldberger, and F.E. Low, "The Boltzmann Equation and the One-Fluid Hydromagnetic Equations in the Absence of Particle Collisions", Proc. Roy. Soc., A256, 112 (1956).
- 12-4. Haerendel, G., R. Lüst, and E. Rieger, "Motion of Artificial Ion Clouds in the Upper Atmosphere", in Planet. Space Sci., Vol. 15, pp 1-18 (1967).
- 12-5. Stoeckly, R.E., R.W. Stagat, and R.W. Kilb, Collisional Momentum and Energy Transfer Rates for Two-Fluid Nuclear-Burst Simulations, DNA 3827T, Mission Research Corporation, July 1975.

CHAPTER 13  
STRIATION FORMATION

Ralph W. Kilb

Sections 13.1 to 13.4, May 1972

Sections 13.5 to 13.7, December 1977

Mission Research Corporation

## TABLE OF CONTENTS

	<u>PAGE</u>
LIST OF ILLUSTRATIONS	627
13.1 INTRODUCTION	628
13.2 BASIC EQUATIONS	638
13.3 THE ENERGY METHOD FOR EXAMINING STABILITY	640
13.3.1 Rayleigh-Taylor Gravitational Instability	645
13.3.2 Plasma Supported by Magnetic Field	650
13.3.3 Plasma in a Curved Magnetic Field	652
13.4 NORMAL MODE ANALYSIS	656
13.4.1 Deceleration Instability with Gravity	656
13.4.2 Kelvin-Helmholtz Shear Instability	658
13.4.3 Ion-Neutral Slip Instability (Gradient Drift, $E \times B$ )	661
13.4.4 Viscous, Resistive, and Diffusive Effects	665
13.4.5 The Effect of Coupling the Neutral and Ionized Fluids	668
13.5 FIELD-LINE AVERAGED INSTABILITIES	671
13.5.1 Basic Equations for Low- $\beta$ Plasmas	672
13.5.2 Linearized Equations for Low- $\beta$ Plasmas	677
13.5.3 Collisional-Drift Instability (Drift-Dissipative)	683
13.6 RECOMMENDED DISPERSION RELATIONS	689
13.6.1 Perturbation Growth During Blast Wave Expansion	689
13.6.2 Perturbation Growth During Intermediate Time	690
13.6.3 Late-Time Striation Growth	691
13.7 NON-LINEAR STRIATION EVOLUTION	695
13.8 GLOSSARY OF SYMBOLS	700
REFERENCES	704

## LIST OF TABLES

Table 1. Simplified instability growth rates	636
--	-----

## LIST OF ILLUSTRATIONS

<u>Figure</u>	<u>Page</u>
13-1 Late time high-altitude striations.	623
13-2 Redwood barium release after 10 minutes.	630
13-3 Redwood barium release after 23 minutes.	630
13-4 Large amplitude flow in thin Hele-Shaw cell.	631
13-5 Inverted beaker example of Rayleigh-Taylor gravitational instability.	632
13-6 Typical unstable displacements $\delta(r)$ .	646
13-7 Growth rate as a function of wavelength for stratified medium with unstable region of height D.	649
13-8 Equilibrium configuration for plasma supported by a magnetic field.	649
13-9 Simple z-pinch. Unstable, radius of curvature of field lines points out of plasma.	651
13-10 Mirror configuration. Unstable, radius of curvature of field lines points out of plasma near centerplane.	653
13-11 Cusped configuration. Stable, radius of curvature of field lines points into plasma.	653
13-12 Line integral path for determining the growth rate when $\lambda \rightarrow 0$ .	655
13-13 Shear instability when two layers have horizontal counterflow.	656
13-14 Ion-neutral slip instability in the frame of the ion cloud.	662
13-15 Nonlinear vorticity equation in two-dimensional geometry.	696

### 13.1 INTRODUCTION

Above about 150 km altitude the earth's magnetic field has a dominant effect on an ionized plasma. Bursts which occur above the D-layer will rise rapidly and will contain large amounts of ionized plasma. When the plasma rises above 150 km altitude it will be affected by the magnetic field. High altitude barium releases form  $Ba^+$  plasmas that also are affected by the magnetic field. Instabilities will cause the plasma to break up into long filaments aligned with the magnetic field lines. Fig. 13-1 shows a photograph taken by W. Chesnut of high altitude striations. The striations generally extend several hundred kilometers along the magnetic field lines and have a variety of widths. Roughly speaking, one may describe striations as long rods of relatively high electron density imbedded in a background of lower density.

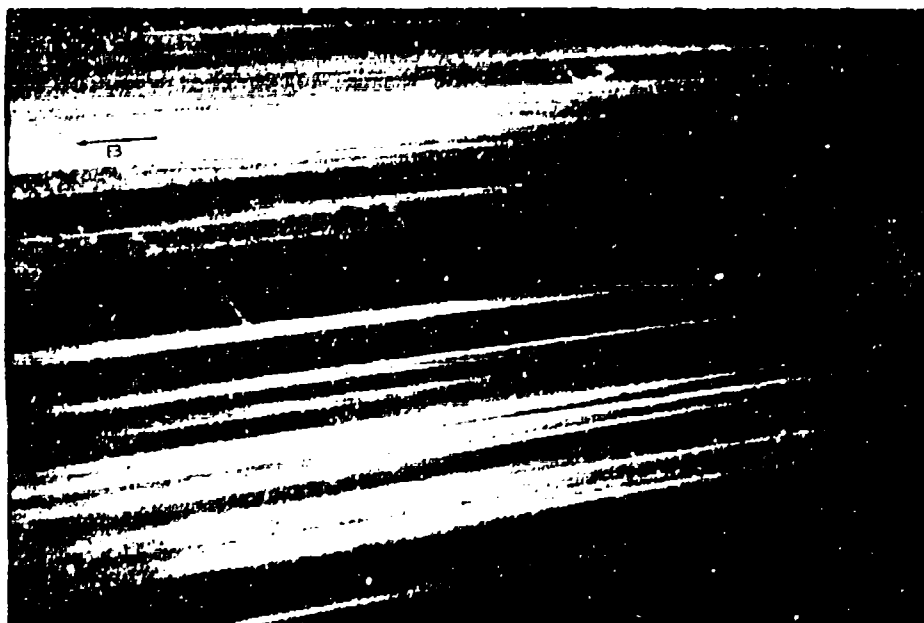


Figure 13-1. Late time high altitude striations.

These striated regions, which fill a large sector of the sky, can degrade electromagnetic signals that cross the striations or produce unusual HF and VHF propagation modes. They produce scintillations in the amplitude and phase of communication signals and also in the amplitude, range, and direction of radar returns. Because the striations generally emit more optical and infra-red radiation than the background, optical scanning systems may produce false target signals when scanning across a striation that approximately fills the field of view. It is therefore important that the formation and structure of striations be understood so that communication, radar, and optical system effects can be determined.

Striations have also been observed in barium cloud releases above 150 km altitude. The barium atoms from the release expand rapidly and are photoionized to  $Ba^+$  ions by the sun's radiation. The initially spherical barium plasma of about 10 km diameter is then acted upon by ambient electric fields, neutral winds, and the earth's magnetic field. The plasma expands freely along the field lines, but cannot easily expand in the transverse directions. Its cross section transverse to the field becomes distorted by the neutral wind blowing through the plasma. After a few minutes the "backside" of the plasma, out of which the neutral wind is blowing, develops a steep electron density gradient. Some minutes later sheet-like distortions develop on the "backside" that eventually break up into filaments of plasma aligned with the magnetic field. Fig. 13-2 shows the Redwood release at 10 min when steepening of the "backside" has occurred, and Fig. 13-3 shows the same release at 25.5 min when thin sheets and rods have been drawn out of the plasma. W. P. Boquist kindly supplied these prints. In these figures the magnetic field lines are nearly perpendicular to the page, so one is viewing the thin sheets and rods nearly "end-on" along their long axis. A side-on view of the striated portion would be similar to Fig. 13-1. This particular instability is often referred to as the ion-neutral slip, gradient-drift, or Simon E2B instability (Linson and Workman, Ref. 13-8; and Simon, Ref. 13-30.)

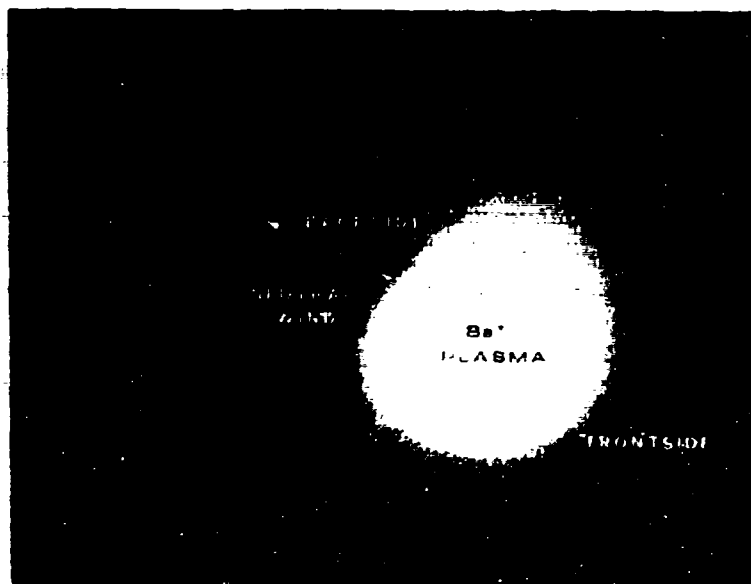


Figure 13-2. Redwood barium release after 10 minutes. The electron density gradients have steepened on the "backside", but no striations have formed yet.



Figure 13-3. Redwood barium release after 23 minutes. The magnetic field lines are nearly perpendicular to the plane of the paper, so the striated sheets and rods are seen nearly "end-on".

J.A. Thomson (Ref. 13-1) has developed a hydrodynamic analog of the above instability in a Hele-Shaw cell. In this experiment, a heavier fluid initially overlies a lighter fluid in a wide, thin cell made of two vertical close-spaced glass plates. The gravitational force in conjunction with strong viscous forces in the fluid arising from the close spacing of the plates yield a mathematical set of equations analogous to those of the ion-neutral slip instability. The development of instabilities in the Hele-Shaw cell should therefore simulate the development of striation cross sections formed in barium releases. Fig. 13-4 shows the large amplitude unstable motion that develops in the Hele-Shaw cell. The large protuberances in Fig. 13-4 are similar to those seen in Fig. 13-3 for barium releases. The Hele-Shaw cell instabilities are also analogous to "water-tonguing" instabilities observed in oil fields when water pressure (a heavy fluid) is used to push oil (a light fluid) toward the wells through porous sand layers which act as a resistive medium.

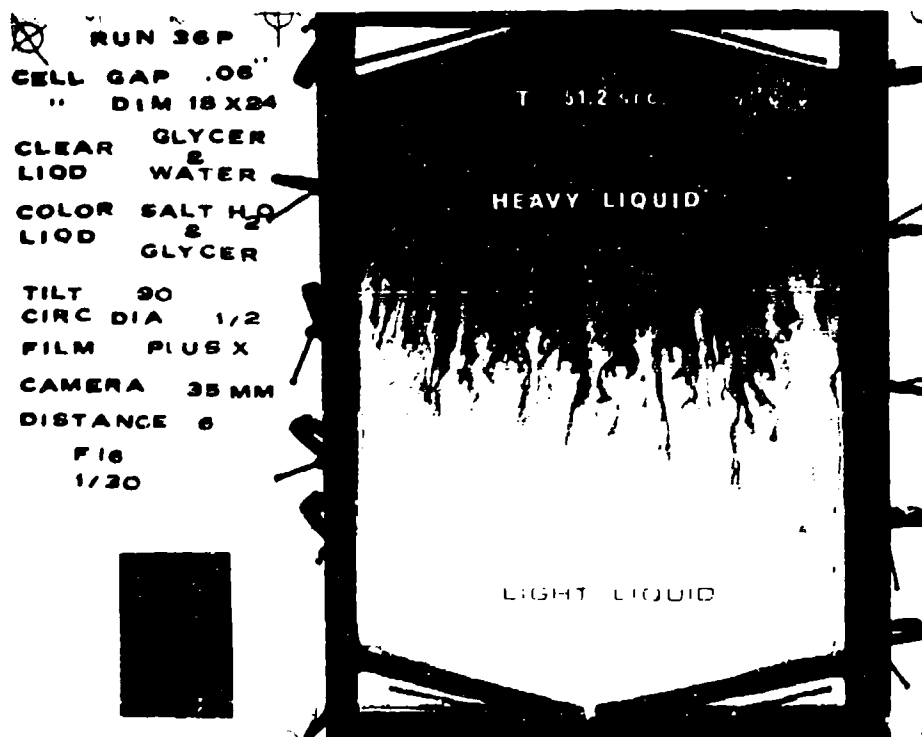


Figure 13-4. Large amplitude flow in thin Hele-Shaw cell.



The attempt to contain, accelerate, or decelerate a plasma in various experimental devices often leads to a very rapid breakup of the plasma into field-aligned striations. For example, a hot plasma contained by a simple magnetic mirror field of two coils soon breaks up into filaments that migrate outward from the coils' axis. The cause of the instability in these cases is often related to the curvature of the magnetic field lines acting on the plasma.

In principle one should solve the magnetohydrodynamic equations in three dimensions, either analytically or numerically, and thereby discover whether the plasma motion or containment is stable. In practice, this generally is not feasible. Often, however, one can obtain an approximate analytical or numerical solution if one assumes some degree of symmetry, such as axial or planar symmetry, thus reducing the problem to one or two dimensional motion. Generally, the motion proves stable with the reduced dimensionality. One may then ask whether re-introduction of three dimensions would lead to unstable breakup of the plasma. This question can be answered by doing a perturbation analysis which allows motion in the previously suppressed dimensions. If the small perturbations grow in time, the plasma is unstable and can ultimately be expected to break up into striations.

The simplest example of an instability is the Rayleigh-Taylor gravitational instability. Suppose that water is held up in an inverted beaker by air pressure as shown in Fig. 13-5a. A stable configuration can be achieved if a stiff frictionless piston separates the water from the air below it, because this imposes a one-dimensionality on the problem that satisfies the equilibrium condition

$$0 = - \frac{\partial P}{\partial z} - \rho g$$

where  $z$  is the vertical coordinate,  $P(z)$  is the pressure in the water or air, and  $\rho(z)$  is the density.

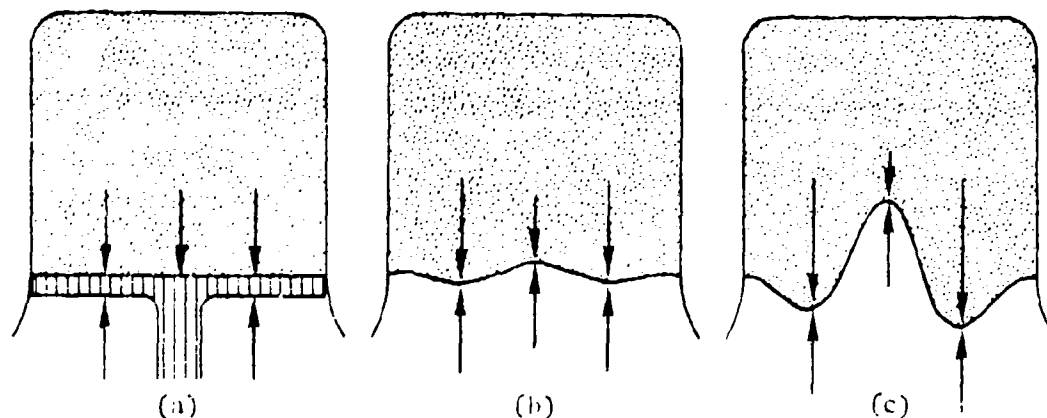


Figure 13-5. Inverted beaker example of Rayleigh-Taylor gravitational instability.

Because of the stiff piston, the only allowed air-water interface displacements in configuration 13-5a are those that move the whole interface either upward or downward. Such one-dimensional vertical displacements simply introduce stable oscillations about the equilibrium configuration.

If the piston were removed, however, the above one-dimensional equilibrium would still be satisfied, but small two- or three-dimensional ripples could now develop as shown in Fig. 13-5b. Such a ripple would be unstable because there is more water pushing down on the trough than on the crest. Consequently the ripple grows, as in Fig. 13-5c, and the water falls out of the beaker with a complex three-dimensional motion.

This process generally occurs whenever a light fluid supports a heavy

fluid. For highly conducting plasmas the magnetic field pressure often acts like a massless fluid pressure, so certain magnetic field-plasma configurations will have instabilities analogous to the Rayleigh-Taylor instabilities. The unstable protuberances will, however, be mostly transverse to the field lines, with relatively smooth variation along the field lines. Otherwise the field lines would become twisted by the growing instability, and such twisting would be energetically unfavorable.

In the present chapter we present a fairly detailed description of how one performs a perturbation analysis for a given self-consistent set of plasma parameters. The analysis determines whether the plasma is stable or unstable, and if unstable, the growth rate of the perturbation as a function of wavelength and plasma parameters.

The formation of striations in an unstable plasma is symptomatic of its drive toward a state of lower potential energy. For an initially quiescent plasma, it is possible to derive an energy principle. In Section 13-3 we show how the energy principle can be used to determine stability for certain plasma problems. Used in conjunction with Rayleigh's principle, one may also find the perturbation growth rate. We consider in detail the Rayleigh-Taylor gravitational instability (13.3.2), a plasma supported by a magnetic field (13.3.3), and the effect of magnetic field curvature (13.3.4).

For ionospheric phenomena, the scale of the plasma parameter variation is generally very large. Thus, the perturbation wavelength will often be small compared with the scale of plasma variation. In this case one may assume simple sinusoidal perturbations which convert the linearized differential equations to sets of algebraic equations. Solution of these equations then yields a dispersion relation relating the growth rate of the perturbation to the plasma parameters and the wavelength. This technique is applied to the gravitational-deceleration instability (13.4.1), the Kelvin-Helmholtz shear instability

(13.4.2), and the ion-neutral slip (or gradient-drift, Simon  $\vec{E} \times \vec{B}$ ) instability (13.4.3). In Section 13.4.4 we show that the dissipative effects of viscosity, diffusivity, and resistivity lead to reduced growth rates at short wavelengths. In Section 13.4.5 we show how the striations of the ion-electron plasma gradually couple with striations of the neutral fluid as the coupling coefficient between the two fluids becomes large.

In low- $\beta$  plasmas (where  $\beta$  is the ratio of plasma pressure over magnetic pressure), current loops can be generated that cause an averaging of the various forces acting along a field line. The differential equation describing field-line-averaged striation growth is derived in Section 13.5.2. Section 13.5.3 gives a simplified description of the collisional-drift instability which is a result of plasma pressure gradients; since almost any plasma is likely to have some pressure gradients, this instability is also referred to as a type of "universal" instability. The collisional-drift instability is peculiar in that it requires a perturbation parallel to the field line, as well as transverse to it, for unstable growth. In contrast, the other fluid instabilities discussed above are usually quenched when the perturbation has a significant parallel-to- $B$  dependence.

Table 1 summarizes the various processes and gives simplified growth rates for each instability acting separately. In practice, these instabilities will act simultaneously and so one requires a dispersion relation combining these results. For low- $\beta$  plasmas, a suitable expression combining most of these instabilities (except the collisional-drift and Kelvin-Helmholtz), and including the damping effects of diffusion, viscosity, and chemistry is provided in Section 13.6.3 (see Equation 13-141).

To determine system effects, it is important to have a reasonable description of the distribution of striation sizes, the electron density variation within a striation, and the power-spectral-density of the electron density fluctuations. In recent years much effort has gone into the computation of non-linear

Table 1. Simplified instability growth rates (if the perturbation  $\gamma \propto 1/r^2$ , except for shear flow).

See Glossary of Symbols at the end of this chapter on page 200.		
Instability Name	Growth Rate $\gamma$ (sec <sup>-1</sup> )	Cause and Comments
<b>Gravitational Force</b>		
Payleigh-Taylor	$\sqrt{g - g_{eff}}$	Unstable if $g$ points out of high density region.
<b>Deceleration</b>		
Rayleigh-Taylor	$\sqrt{g - g_{eff}}$	Unstable if $g$ points into high density region.
<b>Sonn E-B</b>		
Gradient Drift	$-(\vec{E}_0 \cdot \nabla_{\perp})_1 - \frac{1}{2} \nabla_{\perp}^2 \phi$	Drive force of neutral wind acting on ions. Unstable if neutral wind blows out of high density plasma.
Ion-Neutral Slip		Plasma pressure in conjunction with curved field. Unstable if radius of curvature of field line points out of high density plasma.
<b>Field Curvature</b>		
	$\frac{1}{2} \frac{(\nabla_{\perp}^2 \phi)^2}{H_1} (\vec{b} \cdot \nabla_{\perp}) - \frac{1}{2} \nabla_{\perp}^2 \phi$	Plasma pressure in conjunction with electron collisions. Requires $\omega \gg \Omega_e R$ and $\frac{1}{2} \nabla_{\perp}^2 \phi \gg \Omega_e R$
<b>Collisional-Drift</b>		
Drift Dissipative	$0.15 \frac{(\nabla_{\perp}^2 \phi)^2}{H_1} \left( \frac{1}{H_1} \frac{1}{\nabla_{\perp}^2 \phi} \right)$	
universal type		$\frac{1}{2} \nabla_{\perp}^2 \phi \gg \frac{4 R}{(\nabla_{\perp}^2 \phi)^2} \left( \frac{1}{H_1} \frac{1}{\nabla_{\perp}^2 \phi} \right)$ where
<b>Relative Kinetic Energy of Shear Flow</b>		
	$\frac{1}{2} \frac{(\nabla_{\perp}^2 \phi)^2}{H_1} \left( \frac{1}{H_1} \frac{1}{\nabla_{\perp}^2 \phi} \right)$	For zero radius (where $\vec{b} \cdot \nabla_{\perp} = 1$ )
<b>Relative Kinetic Energy of Shear Flow</b>		
More		It is assumed to be much greater than the distance $D$ across which the fluid velocity changes from $V_d$ to $V_p$ .

striation evolution to determine these properties. Section 13.7 gives a short review of some recent results. No definite answers can as yet be given for these important non-linear striation properties. Hopefully further analysis and numerical simulation will yield definitive results in the next few years.

The instabilities discussed here are based on an analysis of the usual magnetohydrodynamic equations and are presently believed to be the dominant cause of striations after nuclear bursts. The reader should be aware, however, that there exist in the literature an almost endless variety of other types of instabilities. Generally these are based on finer descriptions of the plasma; for example, the use of the Vlasov equation and associated microinstabilities, etc. These topics will not be discussed here.

## 13.2 BASIC EQUATIONS

We consider striation formation in plasmas with temperatures of about 0.1 eV, velocities of about  $10^5$  cm/sec, and number densities in the range of  $10^5$  to  $10^{15}$  cm $^{-3}$ . Such plasmas will generally have a substantial neutral component, and there may be significant slip between the neutral and ionized components at sufficiently low densities. Thus we shall model the plasma as consisting of a neutral fluid and an ionized fluid, with collisional coupling tying them together. We also take into account the effect of resistivity and viscosity because these retard the growth of small wavelength striations.

The equations of mass, momentum, and energy conservation are:  
(See Glossary, p. 700, for definition of symbols)

### 1. Mass Conservation

$$\frac{\partial \rho_0}{\partial t} + \nabla \cdot (\rho_0 \vec{V}_0) = 0 \quad (15-1)$$

$$\frac{\partial \rho_1}{\partial t} + \nabla \cdot (\rho_1 \vec{V}_1) = 0 \quad (15-2)$$

### 2. Momentum Conservation

$$\rho_0 \frac{\partial \vec{V}_0}{\partial t} + \rho_0 \vec{V}_0 \cdot \nabla \vec{V}_0 = -\nabla P_0 + \rho_0 \vec{g} + s \rho_1 \rho_0 (\vec{V}_0 - \vec{V}_1) + \mu_0 \nabla^2 \vec{V}_0 - m N_e v_{e0} (\vec{V}_0 - \vec{V}_e) \quad (15-3)$$

$$\rho_1 \frac{\partial \vec{V}_1}{\partial t} + \rho_1 \vec{V}_1 \cdot \nabla \vec{V}_1 = -\nabla P_1 + \vec{J} \times \vec{B} + \rho_1 \vec{g} + s \rho_1 \rho_0 (\vec{V}_0 - \vec{V}_1) + \mu_1 \nabla^2 \vec{V}_1 + m N_e v_{e0} (\vec{V}_0 - \vec{V}_e) \quad (15-4)$$

### 3. Energy Conservation

$$\frac{d}{dt} \left[ \frac{P_0}{\rho_0} \right] = \frac{\gamma-1}{\rho_0 \gamma} \left[ \frac{M_1}{M_0 + M_1} s \rho_1 \rho_0 (\vec{V}_0 - \vec{V}_1)^2 + \nabla \cdot (\alpha_0 \nabla T_0) \right] \quad (15-5)$$

$$\frac{d}{dt} \left[ \frac{P_1}{\rho_1} \right] = \frac{\gamma-1}{\rho_1 \gamma} \left[ \frac{M_0}{M_0 + M_1} s \rho_1 \rho_0 (\vec{V}_0 - \vec{V}_1)^2 + \frac{m v_{e0} c^2}{2 N_e} \vec{J}^2 + m N_e v_{e0} (\vec{V}_0 - \vec{V}_e)^2 + \nabla \cdot (\alpha_1 \nabla T_1) \right] \quad (15-6)$$

### 4. Maxwell's Equations

$$\nabla \cdot \vec{B} = 0 \quad (15-7)$$

$$\nabla \times \vec{B} = 4\pi \vec{J}, \quad (13-8)$$

$$\frac{\partial \vec{B}}{\partial t} = -c \nabla \times \vec{E} \quad (13-9)$$

where we have neglected the displacement term  $\partial \vec{E} / \partial t$  in Eq. 13-8.

To find  $\nabla \times \vec{E}$ , we consider the momentum conservation of the electrons:

$$m \vec{\dot{V}}_e = -\frac{1}{N_e} \nabla P_e - e \left( \vec{E} + \frac{\vec{V}_1 \times \vec{B}}{c} \right) + \frac{\vec{J} \times \vec{B}}{N_e} + m \vec{g} + \frac{mc}{e N_e} (v_{e1} + v_{e0}) \vec{J} + m v_{e0} (\vec{V}_0 - \vec{V}_1) \quad (13-10)$$

where we have used the relation

$$\vec{V}_e = \vec{V}_1 - \frac{c}{4\pi N_e} \vec{J} \quad (13-11)$$

We now need to evaluate the curl of Eq. 13-10. We ignore the electron inertial term, and assume that the electron density gradient is parallel to the pressure gradient so  $\nabla \times (\nabla P_e / N_e) \approx 0$ . Addition of Eqs. 13-3 and 13-4 yields (if we neglect the viscous terms):

$$\rho_0 \vec{\dot{V}}_0 + \rho_1 \vec{\dot{V}}_1 = -\nabla (P_0 + P_1) + \vec{J} \times \vec{B} + (\rho_0 + \rho_1) \vec{g} \quad (13-12)$$

so  $\nabla \times (\vec{J} \times \vec{B} / N_e)$  often tends to be small and is traditionally neglected. Consequently, the substitution of  $\nabla \times \vec{E}$  found from Eq. 13-10 into Eq. 13-9 yields:

$$\frac{\partial \vec{B}}{\partial t} \approx \nabla \times [\vec{V}_1 \times \vec{B} - \eta \vec{J}] \quad (13-13)$$

Our basic set of equations are then Eqs. 13-1 through 13-8 and Eq. 13-13. In most cases we may simplify Eqs. 13-3 and 13-4 somewhat by dropping the relatively small  $m N_e v_{e0} (\vec{V}_0 - \vec{V}_1)$  electron-neutral collisional term. We will also neglect collisional heating effects and heat conduction by dropping the right-hand sides of Eqs. 13-5 and 13-6. Actually, viscous heating has already been ignored in Eqs. 13-5 and 13-6.



### 13.3 THE ENERGY METHOD FOR EXAMINING STABILITY

An energy principle can be derived for examining the stability of various equilibrium configurations when the plasma can be modeled as a single fluid without dissipative processes (Ref. 13-2, 13-3, 13-4). In this case the constant total energy of the system can be represented as the sum of potential and kinetic energy. The potential energy must be either a maximum or minimum with respect to various possible displacements of the plasma and fields from the equilibrium configuration. If all possible displacements raise the potential energy, the configuration is stable, since kinetic energy cannot be negative; if some displacements reduce the potential energy, the configuration is unstable to those displacements.

The equilibrium parameters of the plasma obey:

$$\vec{V} = 0 \quad (13-14)$$

$$0 = -\nabla P + \vec{J} \times \vec{B} + \rho \vec{g} \quad (13-15)$$

$$\nabla \times \vec{B} = 4\pi \vec{J} \quad (13-16)$$

$$\nabla \times \vec{E} = 0 \quad (13-17)$$

If the ion-neutral collision time is long compared to the instability growth time, the pressure  $P$  and related density  $\rho$  should be that of the ion-electron fluid alone. On the other hand, if the collision time is short one should use the combined  $P \equiv P_1 + P_2$  and  $\rho \equiv \rho_1 + \rho_2$ .

In order to use the energy principle we must calculate the changes in  $\vec{E}$  and  $P$  associated with various displacements of the plasma. This is most easily done for small displacements from equilibrium. Thus we obtain the linearized equations by assuming small perturbed values  $\vec{V}'$ ,  $\vec{E}'$ ,  $\vec{J} + \vec{J}'$ ,  $\vec{B} + \vec{B}'$ , etc., and retaining only first order terms in the small quantities. Momentum balance is then given by:

$$\rho \frac{\partial \vec{V}'}{\partial t} = -\nabla P' + \vec{J} \times \vec{B}' + \vec{J}' \times \vec{B} + \rho \vec{g} \quad (13-18)$$

The partial derivative with respect to time yields

$$\rho \frac{\partial^2 \vec{V}'}{\partial t^2} = -\nabla \frac{\partial P'}{\partial t} + \vec{J} \times \frac{\partial \vec{B}'}{\partial t} + \frac{\partial \vec{J}'}{\partial t} \times \vec{B} + \vec{g} \frac{\partial \rho'}{\partial t} \quad (13-19)$$

From mass and energy conservation we have to first order

$$\frac{\partial \rho'}{\partial t} = -\nabla \cdot (\rho \vec{V}') \quad (13-20)$$

$$\frac{\partial P'}{\partial t} = \frac{dP'}{dt} - \vec{V}' \cdot \nabla P = -\gamma P \nabla \cdot \vec{V}' - \vec{V}' \cdot \nabla P \quad (13-21)$$

and, defining a new quantity  $\vec{Q}$ , we have from Faraday's law

$$\frac{\partial \vec{B}'}{\partial t} = -c \nabla \times \vec{E}' = \nabla \times (\vec{V}' \times \vec{B}) \equiv \vec{Q}(\vec{V}') \quad (13-22)$$

Note that  $\vec{Q}$  is a linear function of the perturbed velocity  $\vec{V}'$ .

The partial time derivative of Ampere's law yields

$$\frac{\partial \vec{J}'}{\partial t} = \frac{1}{4\pi} \nabla \times \frac{\partial \vec{B}'}{\partial t} = \frac{1}{4\pi} \nabla \times \vec{Q} \quad (13-23)$$

Substitution of Eqs. 13-20 through 13-23 into Eq. 13-19 yields:

$$\rho \frac{\partial^2 \vec{V}'}{\partial t^2} = \gamma \nabla (P \nabla \cdot \vec{V}') + \nabla (\vec{V}' \cdot \nabla P) - \vec{g} \nabla \cdot (\rho \vec{V}') + \vec{J} \times \vec{Q}(\vec{V}') - \vec{B} \times \nabla \times \vec{Q}(\vec{V}') / 4\pi \quad (13-24)$$

We may define a displacement vector  $\vec{\xi}(\vec{r}, t)$  that is related to the perturbed velocity  $\vec{V}'(\vec{r}, t)$  by:

$$\frac{\partial \vec{\xi}}{\partial t} = \vec{V}'(\vec{r}, t) \quad (13-25)$$

To first order in small quantities,  $\vec{\xi}(\vec{r}, t)$  is the displacement of an element of the plasma from its equilibrium position. Substitution into Eq. 13-24, and a partial integration with respect to time yields

$$\rho \frac{\partial^2 \vec{\xi}}{\partial t^2} = \vec{F}(\vec{\xi}) \quad , \quad (13-26)$$

where the operator  $\vec{F}$  is defined by

$$\vec{F}(\vec{\xi}) = \gamma \nabla (\nabla \cdot \vec{\xi}) + \nabla (\vec{\xi} \cdot \nabla P) - \vec{g} \nabla \cdot (\rho \vec{\xi}) + \vec{J} \times \vec{Q}(\vec{\xi}) - \vec{B} \times \nabla \times \vec{Q}(\vec{\xi}) / 4\pi \quad (13-27)$$

and

$$\vec{Q}(\vec{\xi}) = \nabla \times (\vec{\xi} \times \vec{B}) = \vec{B}'(\vec{r}, t) \quad (13-28)$$

The quantity  $\vec{F}(\vec{\xi})$  is the unbalanced force resulting from the displacement. An important property of the operator  $\vec{F}$  is that it is self-adjoint (Ref. 2). Eq. 13-26 together with appropriate boundary conditions determines  $\vec{\xi}(\vec{r}, t)$ . Because Eq. 13-26 is linear in  $\vec{\xi}$ , we may look for solutions which are periodic in time,

$$\vec{\xi}(\vec{r}, t) = \vec{\xi}(\vec{r}) e^{i\omega t} \quad (13-29)$$

Then Eq. 13-26 becomes

$$\alpha^2 \rho \vec{\xi} = \vec{F}(\vec{\xi}) \quad (13-30)$$

This is an eigenvalue equation. It has solutions  $\vec{\xi}_n(\vec{r})$  that satisfy the boundary conditions ( $\vec{\xi}_n$  vanishes at infinity; matching of fields at plasma vacuum interfaces; etc.) only for certain values  $\alpha_n^2$  of  $\alpha^2$ . Because  $\vec{F}$  is self-adjoint, the  $\alpha_n^2$  are all real, and the  $\alpha_n$  are purely real or purely imaginary. If any of the  $\alpha_n^2$  are positive, the corresponding mode can grow exponentially with time and the system is unstable.

Thus, one way to show instability is to find modes with positive eigenvalues  $\alpha_n^2$ . This can be done for certain plasma problems, but it sometimes proves easier to use the following energy principle. Define the kinetic energy of the perturbed motion

$$T = \frac{1}{2} \int \rho \left( \frac{\partial \vec{\xi}}{\partial t} \right)^2 d^3r \quad (13-31)$$

The time rate of change of  $T$  is:

$$\frac{dT}{dt} = \int \rho \frac{\partial \vec{\xi}}{\partial t} \cdot \frac{\partial^2 \vec{\xi}}{\partial t^2} d^3r = \int \frac{\partial \vec{\xi}}{\partial t} \cdot \vec{F}(\vec{\xi}) d^3r \quad (13-32)$$

and because  $\vec{F}$  is self-adjoint we can write

$$\int \frac{\partial \vec{\xi}}{\partial t} \cdot \vec{F}(\vec{\xi}) d^3r = \int \vec{\xi} \cdot \vec{F}\left(\frac{\partial \vec{\xi}}{\partial t}\right) d^3r = \frac{1}{2} \frac{d}{dt} \int \vec{\xi} \cdot \vec{F}(\vec{\xi}) d^3r \quad (13-33)$$

Defining the potential energy  $V$

$$V \equiv - \frac{1}{2} \int \vec{\xi} \cdot \vec{F}(\vec{\xi}) d^3r \quad (13-34)$$

we can then write Eq. 13-32 as

$$\frac{d}{dt} (T+V) = 0 \quad (13-35)$$

so the total energy  $T+V$  of the system remains constant during the plasma displacement  $\vec{\xi}(\vec{r}, t)$

Thus the plasma is unstable if displacements  $\vec{\xi}(\vec{r}, t)$  exist that make  $V < 0$ , because then the kinetic energy  $T$  must become non-zero. Furthermore, an estimate of the growth rate  $\gamma$  may be obtained from Rayleigh's principle. Substitution of Eq. 13-29 into 13-31 and use of  $T + V = 0$  during the displacement leads to:

$$\omega^2 = -2V / \int \rho \xi^2 d^3r \quad (13-36)$$

In fact, extremizing the function  $T+V$  with respect to the variational parameter  $\vec{\xi}$  yields Eq. 13-30.

To actually use the energy principle, we must substitute Eq. 13-27 into 13-31 and evaluate  $V$  for various trial  $\vec{\xi}(\vec{r})$ . Thus

$$\begin{aligned} 2V &= \int_{\text{plasma}} \left[ -\frac{1}{2} (\nabla \cdot \vec{P})^2 + \frac{1}{2} (\nabla \cdot \vec{P})^2 + \frac{1}{2} (\nabla \cdot \vec{P})^2 - \vec{J} \times \vec{Q} + \frac{1}{2} \frac{\vec{J} \cdot \vec{Q}}{V_0} \right] d^3r \\ &= \int_{\text{plasma}} \left[ \frac{1}{2} (\nabla \cdot \vec{P})^2 + \frac{1}{2} (\nabla \cdot \vec{P})^2 + \frac{1}{2} (\nabla \cdot \vec{P})^2 + \frac{1}{2} (\nabla \cdot \vec{P})^2 + \frac{1}{2} (\nabla \cdot \vec{P})^2 + \frac{1}{2} (\nabla \cdot \vec{P})^2 \right] d^3r \\ &= \int_{\text{surface}} \left[ \frac{1}{2} \frac{\vec{B} \cdot \vec{Q}}{V_0} - \frac{1}{2} \frac{\vec{B} \cdot \vec{Q}}{V_0} + \frac{1}{2} \frac{\vec{B} \cdot \vec{Q}}{V_0} \right] d^3r \end{aligned} \quad (13-37)$$

where we have used Gauss' theorem on the first and last terms in the initial equation after substituting

$$\vec{\xi} \cdot \vec{B} \times \nabla \times \vec{Q} = \nabla \cdot [\vec{Q} \times (\vec{\xi} \times \vec{B})] + Q^2 \quad (15-38)$$

The volume integral in Eq. 13-37 is over the extent of the plasma, and the surface integral is over the plasma surface that has area elements  $d\vec{S}$  pointing outward from the plasma. If the plasma is of infinite extent, the surface integral may be dropped because  $\vec{\xi}$  approaches zero at large  $\vec{r}$ . If, however, the plasma is bounded by a vacuum magnetic field as in some plasma confinement devices, then the surface integral can be important. For further discussion of the surface term, the reader is referred to Rose and Clark (Ref. 13-3). The surface term is not important in the cases we analyze below.

The  $\gamma P (\nabla \cdot \vec{\xi})^2 + (\nabla \cdot \vec{\xi}) (\vec{\xi} \cdot \nabla P)$  term in the volume integral of Eq. 13-37 accounts for changes in the internal energy of the plasma and work done in the expansion of fluid against fluid pressure. The  $(\vec{\xi} \cdot \vec{g}) \nabla \cdot (\rho \vec{\xi})$  term gives the change in gravitational potential energy, and  $Q^2/4\pi - \vec{\xi} \cdot \vec{J} \times \vec{Q}$  relates to changes in the magnetic field energy.

Because instability is indicated when  $V < 0$  the  $\gamma P (\nabla \cdot \vec{\xi})^2$  and  $Q^2/4\pi$  terms in Eq. 13-37 are stabilizing. Thus we expect the unstable displacements to have relatively small divergence  $\nabla \cdot \vec{\xi}$  and small changes in the local magnetic field  $\vec{Q}$ . Except in special cases, however, one cannot generally expect that  $\nabla \cdot \vec{\xi} = 0$  and  $\vec{Q} = 0$ , because these restrictions on the displacements  $\vec{\xi}(\vec{r})$  could exclude instabilities associated with the other terms in Eq. 13-37.

We now proceed to apply the energy principle to several stability problems.

### 13.3.1 RAYLEIGH-TAYLOR GRAVITATIONAL INSTABILITY

Let us first consider the relatively simple problem of the stability of a stratified medium in a gravitational field. It is well known (Ref. 13-5) that unstable flow occurs if the temperature falls sufficiently fast with increasing height. Thus water heated from below in a teapot ( $\partial T/\partial z < 0$ ) develops unstable convection cells, whereas atmospheric basins with temperature inversions ( $\partial T/\partial z > 0$ ) are stable and remain stratified, as previously discussed in Chapter 10, Section 10.7.10. The energy principle derived above also applies to the case of a simple fluid. In this case we drop the  $\vec{\xi} \cdot \vec{J} \times \vec{Q}$  and  $Q^2/4\pi$  terms in the potential energy given in Eq. 13-37. Let  $\vec{g} = (0, 0, -g)$  in a cartesian coordinate system. Then the initial equilibrium must satisfy

$$0 = -\frac{\partial P}{\partial z} - \rho g \quad (13-39)$$

Here  $P = \rho \kappa T/M$ , where  $M$  is the molecular mass of the gas and  $\kappa$  is Boltzmann's constant. The density  $\rho(z)$  and temperature  $T(z)$  may both be functions of height. Substituting into Eq. 13-39 yields

$$\frac{\partial \rho}{\partial z} = -\frac{Mg\rho}{\kappa T} - \frac{\rho}{T} \frac{\partial T}{\partial z} \quad (13-40)$$

Thus an initial equilibrium exists for a wide range of arbitrarily chosen  $\partial \rho/\partial z$ , as long as one chooses a corresponding temperature profile  $T(z)$  satisfying Eq. 13-40. The question is then whether a particular profile  $\rho(z)$  is unstable to small displacements  $\vec{\xi}(\vec{r})$ .

Figure 13-6 shows a typical displacement field one might expect if the stratified region between  $z_0$  and  $z_1$  were unstable, while the regions below  $z_0$  and above  $z_1$  were stable. These displacements have a large  $\nabla \cdot \vec{\xi}$ , but relatively small  $\nabla \times \vec{\xi}$ . In the unstable region the flow is mainly in the vertical direction, with a sinusoidal  $y$ -dependence  $e^{iky}$  of wavelength  $\lambda$  and wave vector  $k = 2\pi/\lambda$ . In the stable region above  $z_1$  we must have  $\nabla \cdot \vec{\xi} \approx 0$ , match the  $\xi_z$  of the unstable region at  $z = z_1$ , and have  $\vec{\xi}(\vec{r})$

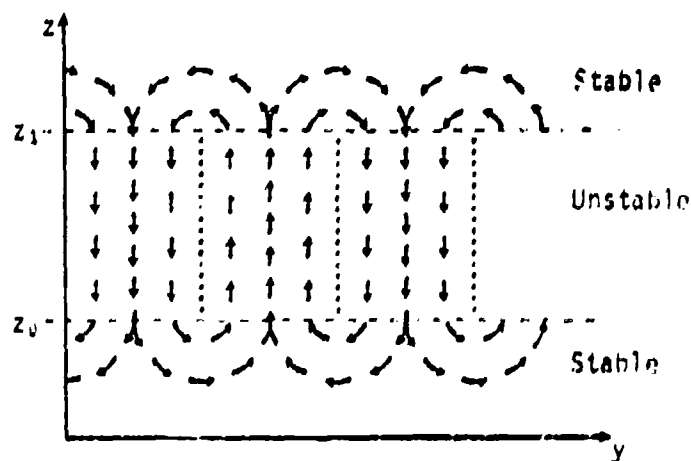


Figure 13-6. Typical unstable displacements  $\xi(\vec{r})$ .

vanish as  $z \rightarrow z_1$ . In the stable region below  $z_0$  we again must have  $\nabla \cdot \xi = 0$ , match the  $\xi_y$  of the unstable region at  $z = z_0$ , and have  $\xi_z(\vec{r})$  vanish as  $z \rightarrow -\infty$ .

We can obtain an estimate of  $\gamma \cdot \vec{r}$  from Eq. 13-37 by minimizing  $V$  with respect to  $\gamma \cdot \vec{r}$ , because this will yield the maximum growth rate  $\alpha$  according to Eq. 13-36. Substitution of Eq. 13-39 into 13-37 yields

$$2V = \int \left[ \frac{1}{2} \rho (\gamma \cdot \vec{r})^2 + \frac{1}{2} \mu (\nabla \cdot \vec{r})^2 + \frac{1}{2} \frac{\partial^2}{\partial z^2} (\gamma \cdot \vec{r})^2 \right] d\vec{r} \quad (13-40)$$

We now minimize the integrand with respect to  $\gamma \cdot \vec{r}$  and find:

$$\gamma \cdot \vec{r} = \frac{1}{\rho} \left( \frac{\partial}{\partial z} \right)^2 \xi_z = \frac{1}{\rho} \left( \frac{\partial}{\partial z} \right)^2 \xi_z \quad (13-41)$$

which then yields

$$\begin{aligned} \Delta V = & \int \left[ -\frac{\rho' g^2}{\gamma \kappa T} - \alpha \frac{\partial \rho}{\partial z} \right] \xi_z^2 d^3 r \\ & + \int \left[ \left(1 - \frac{1}{\gamma}\right) \frac{\rho M g^2}{\kappa T} + \frac{\mu \rho}{T} \frac{\partial T}{\partial z} \right] \xi_z^2 d^3 r \end{aligned} \quad (13-43)$$

where we have used Eq. 13-40.

Because  $V$  must be negative for unstable growth, it is clear from Eq. 13-43 that the unstable regions are those where

$$\frac{\partial \rho}{\partial z} > -\frac{\rho M g}{\gamma \kappa T} \approx -\frac{\rho}{15 \times 10^5 \text{ cm}} \quad (13-44)$$

or, equivalently

$$-\frac{\partial T}{\partial z} > \gamma \frac{1}{\gamma - 1} \frac{M g}{T} \approx 10^{-4} \text{ (}^\circ \text{K/cm)} \quad (13-45)$$

Consequently, positive density gradients (or sufficiently negative temperature gradients) produce instability. Because of our non-zero choice of  $\gamma \cdot \xi_z$  in Eq. 13-42, uniform densities or even those with negative density gradients greater than  $-\rho M g / \gamma \kappa T$  are also weakly unstable. Meteorologists refer to  $-\partial T / \partial z$  as the atmospheric lapse rate, and to  $(\gamma - 1) M g / \mu$  as the adiabatic lapse rate. Thus, Eq. 13-45 shows that the atmosphere is unstable if the temperature decreases with altitude more rapidly than the adiabatic lapse rate of  $10^4 \text{ K/km}$  (Ref. 13-10 or Chapter 10.7.10).

The relative magnitudes of  $\nabla \cdot \xi_z$  and  $\nabla \cdot \xi_r$  are important in instability theory and can be estimated by noting that  $\xi_z \approx 1, \xi_r e^{i \mathbf{k} \cdot \mathbf{r}}$ . Thus  $|\nabla \cdot \xi_z| \approx k \xi_z$  and

$$\frac{|\nabla \cdot \xi_z|}{|\nabla \cdot \xi_r|} \approx \frac{M g}{\gamma \kappa T} \approx \frac{1}{20 \times 15 \times 10^5 \text{ cm}} \quad (13-46)$$

Wavelengths shorter than  $10^5 \text{ cm}$  will therefore have negligible  $\nabla \cdot \xi_z$  compared to  $\nabla \cdot \xi_r$ .

To estimate the growth rate  $\alpha$  we must evaluate the integrals in Eqs. 13-36 and 13-43. Let us assume that the density is constant below  $z = z_0$  and above  $z = z_1$  with respective values  $\rho_0$  and  $\rho_1$ , and that  $\rho(z)$  varies linearly from  $\rho_0$  to  $\rho_1$  in the region  $z_0 < z < z_1$ . An appropriate  $\xi_z(\mathbf{r})$  with  $\nabla \cdot \xi_z \approx 0$  and matching  $\xi_z$  at the boundaries  $z_0$  and  $z_1$  is:



$$\vec{\xi}(\vec{r}) = \begin{cases} (0, \xi \sin ky e^{-k(z-z_1)}, \xi \cos ky e^{-k(z-z_1)}) & \text{for } z > z_1 \\ (0, 0, \xi \cos ky) & \text{for } z_0 < z < z_1 \\ (0, -\xi \sin ky e^{k(z-z_0)}, \xi \cos ky e^{k(z-z_0)}) & \text{for } z < z_0 \end{cases} \quad (13-47)$$

Evaluation of the integrals from  $z = -\infty$  to  $z = +\infty$ , over a wavelength  $\lambda$  in the  $y$ -direction, and over an arbitrary  $\delta x$  yields:

$$-2V = \pi g(\rho_1 - \rho_0) \xi^2 / k \quad (13-48)$$

$$\int \rho \xi^2 d^3 r = (\rho_1 + \rho_0) (\lambda + \pi D) \xi^2 / 2k \quad (13-49)$$

where  $D = z_1 - z_0$ , and we have ignored the  $\rho M g^2 / \gamma k T$  term in Eq. 13-43. The growth rate is then obtained from Eq. 13-36

$$\alpha = \sqrt{\frac{2\pi g(\rho_1 - \rho_0)}{(\rho_1 + \rho_0)(\lambda + \pi D)}} \quad (13-50)$$

Note that for wavelengths small compared to the height of the unstable region ( $\lambda \ll \pi D$ ), the growth rate is nearly constant. At long wavelengths ( $\lambda \gg \pi D$ ), however, the growth rate decreases as  $1/\sqrt{\lambda}$ . This wavelength dependence tends to appear in other types of instabilities. It is a result of the inertia  $(\rho_1 + \rho_0) \lambda \xi^2 / 2k$  of the mass flowing in the stable regions above  $z_1$  and below  $z_0$ . This inertia dominates the inertia  $(\rho_1 + \rho_0) \pi D^2 \xi^2 / 2k$  of the unstable region if  $\lambda \gg \pi D$ , thus yielding  $\alpha \approx 1/\sqrt{\lambda}$ .

Figure 13-7 shows the variation of the growth rate with wavelength. We shall see later that viscous effects suppress the growth rates at very small wavelengths. The basic cause of the instability is that when  $\partial \rho / \partial z > 0$ , the fluid can achieve a lower state of gravitational potential energy by following the flow field  $\vec{\xi}(\vec{r})$ . We have shown in a rather roundabout manner that a layer of heavy fluid atop a light fluid, e.g., water on top of oil, will be unstable and will break up into smaller components that fall downward with a corresponding rise of components of the light fluid.

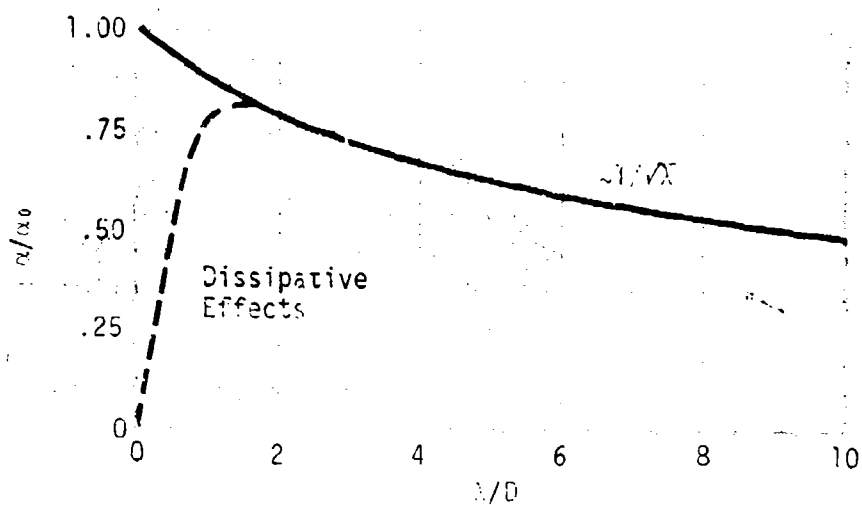


Figure 13-7. Growth rate as a function of wavelength for stratified medium with unstable region of height  $D$ .

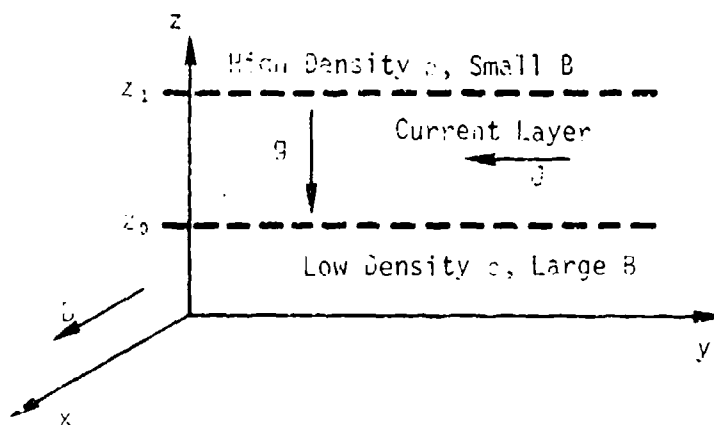


Figure 13-8. Equilibrium configuration for plasma supported by a magnetic field.  $D = z_1 - z_0$ .

### 13.3.2 PLASMA SUPPORTED BY MAGNETIC FIELD

We now consider a plasma supported by a magnetic field against gravity. This situation occurs when one attempts to levitate a conducting fluid or plasma with a magnetic field. It might also be relevant to very high-altitude Barium clouds released at the magnetic equator that sink under the force of gravity. This problem is analogous to that of the gravitational instability, with the magnetic field acting like a massless fluid trying to support the plasma.

Figure 13-8 shows the assumed configuration. We assume that the plasma has a large extent in the x- and y-direction, so the plasma density  $\rho(z)$  is a function of height  $z$  alone. The magnetic field  $(B(z), 0, 0)$  has only an x-component, and the current  $(0, -J(z), 0)$  flows only in the negative y-direction. We assume some sort of return current path is available elsewhere so polarization in the y-direction will not occur. The equilibrium equations 13-15 and 13-16 are then

$$0 = -\frac{\partial P}{\partial z} + JB - \rho g \quad (13-51)$$

$$\frac{\partial B}{\partial z} = -4\pi J \quad (13-52)$$

For the displacement  $\vec{\xi}(\vec{r})$  we assume  $[0, \xi_y(y, z), \xi_z(y, z)]$ . No dependence on the x-coordinate is assumed because this would bend the magnetic field lines. Such bending of the initially straight field lines would increase the magnetic field energy and thereby quench the growth of such displacements. Evaluating the perturbed magnetic field  $\vec{Q}$  by Eq. 13-28 yields

$$\vec{Q} = \nabla \times (\vec{\xi} \times \vec{B}) = \vec{B} \cdot \nabla \vec{\xi} - \vec{\xi} \cdot \nabla \vec{B} - \vec{B} \nabla \cdot \vec{\xi} = 4\pi J \xi_z \hat{i}_x - \vec{B} \nabla \cdot \vec{\xi} \quad (13-53)$$

so the perturbed field is parallel to the equilibrium field. Thus

$$Q^2/4\pi = 4\pi J^2 \xi_z^2 - 2JB \xi_z \nabla \cdot \vec{\xi} + (\nabla \cdot \vec{\xi})^2 B^2/4\pi \quad (13-54)$$

$$\vec{J} \times \vec{Q} \cdot \vec{\xi} = 4\pi J^2 \xi_z^2 - JB \xi_z \nabla \cdot \vec{\xi} \quad (13-55)$$

and the change in magnetic energy is

$$Q^2/4\pi \cdot \vec{J} \cdot \vec{Q} \cdot \vec{z} = -B^2 V \cdot \vec{z} + (V \cdot \vec{z})^2 B^2/4\pi \quad (13-56)$$

This change in magnetic energy will be positive and quench the instability unless  $V \cdot \vec{z}$  is small. Substitution into Eq. 13-37 now yields

$$2V = \int \left[ \left( \gamma P + \frac{B^2}{4\pi} \right) (V \cdot \vec{z})^2 - 2\alpha g \vec{z} \cdot V \cdot \vec{z} - g \frac{\partial \rho}{\partial z} z^2 \right] d^3 r \quad (13-57)$$

where we have used the equilibrium condition 13-51.

Note the striking similarity of Eqs. 13-41 and 13-57. The only change is that the magnetic field pressure  $B^2/8\pi$  is added, with an effective  $\gamma$  of 2, to  $\gamma P$ . Minimizing  $V$  w.r.t. to  $V \cdot \vec{z}$  yields

$$V \cdot \vec{z} = \frac{g \frac{\partial \rho}{\partial z}}{\gamma P + B^2/4\pi} \approx \frac{g \frac{\partial \rho}{\partial z}}{10^{16} \text{ cm}} \quad (13-58)$$

where we have used a barium cloud of  $\rho \approx 10^{-11} \text{ gm/cm}^3$  in the earth's equatorial field of  $B = 0.3$  gauss as a numerical example. Thus for wavelengths less than a few kilometers,  $V \cdot \vec{z}$  is again small compared to  $V \cdot \vec{z}$ , and the terms in Eq. 13-57 involving  $(V \cdot \vec{z})^2$  are usually negligible compared to  $-g \frac{\partial \rho}{\partial z} z^2$ . Just as in the pure gravitational case, the unstable regions of the plasma are where  $\partial \rho / \partial z > 0$ , so the bottom region of the plasma is unstable while the top region with  $\partial \rho / \partial z < 0$  is stable.

The growth rate  $\alpha$  can be estimated just as in the preceding section, and for a layer of thickness  $l$  across which the density increases from  $\rho_0$  to  $\rho_1$  we find the same wavelength dependence as shown in Fig. 13-6 and Fig. 13-7. We will show later that resistive as well as viscous effects can quench the growth rate at small  $\alpha$  when a magnetic field supports the plasma. As in the previous example, the source of the instability is the decrease in gravitational potential energy as the plasma falls.

### 13.3.3 PLASMA IN A CURVED MAGNETIC FIELD

Suppose one attempts to confine a plasma by a magnetic field. In practical cases this almost always requires a magnetic configuration with regions of curved field lines. Examples are: (1) a simple z-pinch, where the plasma is confined by the magnetic field of a current flowing inside it; (2) a magnetic mirror, where confinement is on the axis between two field coils with parallel currents; and (3) a cusp geometry, where confinement is on the axis between the two field coils with opposed currents. Figures 13-9, 13-10, and 13-11 show typical configurations. We will find that plasma regions where the radius of curvature of the field line points away from the dense plasma are unstable, whereas regions where the curvature vector points into the plasma are stable.

The cause of the instability is the tension along the curved field lines. When the curvature vector points outward from the plasma, the tension is relieved somewhat and the magnetic energy is lowered by interchanging tubes of plasma containing the same amount of magnetic flux. In the z-pinch this interchange is called the sausage instability, while the topologically similar interchange in the mirror field configuration is called the flute instability. The same kind of interchange in the cusp geometry leads to an increase in magnetic energy, so the cusp configuration is stable.

Let us analyze in detail a plasma of large extent that has a local region where the field lines have curvature  $R$  and where  $VP$  is large compared to  $P/R$ . Topologically, this local region is similar to a portion of that shown in Fig. 13-9(c), with  $r \approx R$  and  $\delta\phi \ll 1$ . We therefore employ a  $(r, \phi, z)$  coordinate system with origin at the center of curvature of the field lines penetrating the local region of interest. Thus  $\vec{B} = (0, B(r), 0)$ ,  $\vec{J} = (0, 0, J(r))$ , and  $\nabla P = (dP/dr, 0, 0)$ . The most unstable perturbations will be those that do not cause further bending of the field lines so  $\vec{\xi}(\vec{r})$  should not be a function of the  $\phi$ -coordinate. An appropriate displacement vector is

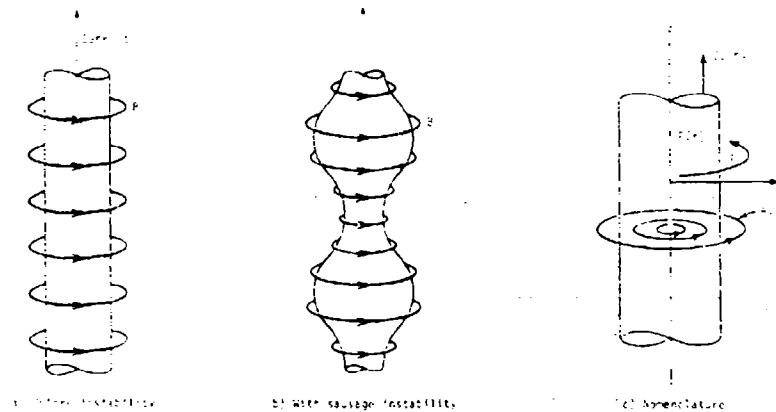


Figure 13-9. Simple z-pinch. Unstable, radius of curvature of field lines points out of plasma.

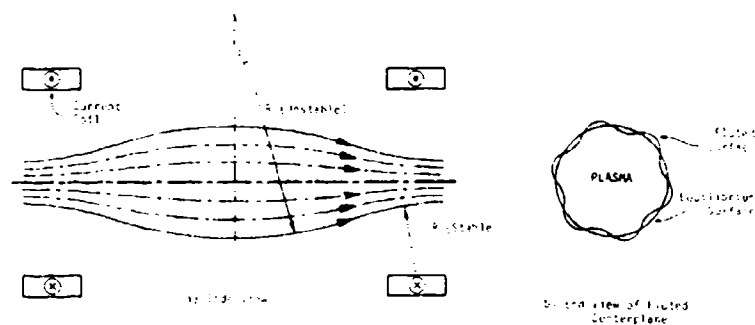


Figure 13-10. Mirror configuration. Unstable, radius of curvature of field lines points out of plasma near center-plane.

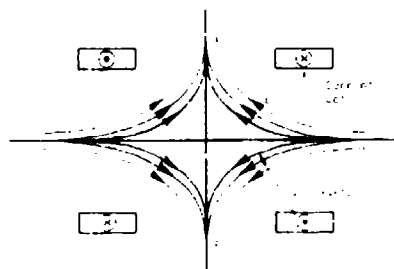


Figure 13-11. Cusped configuration. Stable, radius of curvature of field lines points into plasma.

$\xi = (\xi_r(r, z), 0, \xi_z(r, z))$  with a predominately sinusoidal  $e^{ikz}$  dependence. The equilibrium equations 13-15 and 13-16 become

$$0 = -\frac{\partial P}{\partial r} - JB = -\frac{\partial}{\partial r}\left(P + \frac{B^2}{8\pi}\right) - \frac{B^2}{4\pi r} \quad (13-59)$$

$$J = \frac{1}{4\pi r} \frac{\partial rB}{\partial r} \quad (13-60)$$

The perturbed magnetic field  $\vec{Q}$  is found from the dyadics (Ref. 13-61)

$$\nabla \vec{B} = \frac{\partial B}{\partial r} \hat{r}_1 \hat{r}_1 - \frac{B}{r} \hat{r}_1 \hat{r}_1, \quad (13-61)$$

$$\nabla \vec{\xi} = \frac{\partial \xi_r}{\partial r} \hat{r}_1 \hat{r}_1 + \frac{\xi_r}{r} \hat{r}_1 \hat{r}_1 + \frac{\partial \xi_z}{\partial z} \hat{r}_1 \hat{r}_1 + \frac{\partial \xi_z}{\partial r} \hat{r}_1 \hat{r}_1 + \frac{\partial \xi_z}{\partial z} \hat{r}_1 \hat{r}_1, \quad (13-62)$$

$$\vec{Q} = \nabla \cdot (\vec{\xi} \times \vec{B}) = \vec{B} \cdot \nabla \vec{\xi} - \vec{\xi} \cdot \nabla \vec{B} - \vec{B} \nabla \cdot \vec{\xi} = \hat{r}_1 \left[ \xi_z \left( \frac{\partial B}{\partial r} - 4\pi J \right) - B \nabla \cdot \vec{\xi} \right] \quad (13-63)$$

Note that  $\vec{Q}$  is parallel to the unperturbed  $\vec{B}$ , which was assumed to be along  $\hat{r}_1$ . Evaluation of  $2V$  by Eq. 13-57 and use of the equilibrium condition 13-59 yields

$$2V = \int \left[ \left( \gamma P + \frac{B^2}{4\pi} \right) (\nabla \cdot \vec{\xi})^2 - \frac{B^2 \xi_r}{4\pi r} \nabla \cdot \vec{\xi} + \frac{\xi_z^2}{r} \left( \frac{B^2}{4\pi} - 2JB \right) \right] d^3r \quad (13-64)$$

If we now blithely assume that  $\nabla \cdot \vec{\xi} = 0$ , then we would gain the impression from Eq. 13-64 that low beta plasmas, with  $B^2/r \gg 2JB$ , are always stable. This is incorrect. To find the correct criterion we must minimize the integrand in 13-64 w.r.t.  $\nabla \cdot \vec{\xi}$ , yielding

$$\nabla \cdot \vec{\xi} = \frac{B^2 \xi_r}{2\pi r} \left/ \left( \gamma P + \frac{B^2}{4\pi} \right) \right. \quad (13-65)$$

Thus in a low beta plasma  $\nabla \cdot \vec{\xi} \approx 2/r$  and therefore the change in magnetic energy  $Q^2/4\pi - \vec{B} \cdot \vec{Q} \approx 0$ . Substitution of Eq. 13-65 into 13-64 and use of 13-59 yields:

$$2V = \int \xi_r^2 \left[ \frac{1}{r} \frac{1}{4\pi} \frac{B^2}{(1 + \frac{B^2}{4\pi P})} + \frac{1}{r} \frac{B^2}{4\pi} \right] d^3r \quad (13-66)$$

The plasma will therefore be unstable in those regions where the pressure decreases sufficiently fast as one goes outward along the radius of

curvature, say  $\partial P / \partial r \approx -2\gamma P / r$ . One may obtain an approximate  $2V$  for a plasma with varying radii of curvature  $\vec{R}(\vec{r})$  by rewriting 13-66 as

$$2V = \int \xi_{\parallel}^2 \left[ \frac{4\gamma P B^2}{R (4\pi\gamma P + B^2)} + \frac{2\vec{R} \cdot \nabla P}{R^2} \right] d^3r \quad (13-67)$$

where  $\xi_{\parallel}$  is the component of  $\vec{\xi}(\vec{r})$  along  $\vec{R}(\vec{r})$ . In addition to being a function of the coordinates transverse to the  $\vec{B}$  field,  $\xi_{\parallel}$  will generally also depend on the coordinate parallel to  $\vec{B}$ . This dependence on the parallel coordinate must be weak, however, because new terms will appear in 13-63 which can change the criterion 13-67. Broadly speaking, the unstable displacements  $\vec{\xi}(\vec{r})$  will be those which are relatively large where  $\vec{R} \cdot \nabla P < 0$  and which gradually taper off where  $\vec{R} \cdot \nabla P > 0$ . To get an estimate of the instability growth rate, consider a plasma with a region where  $\vec{R} \cdot \nabla P \approx -P/R^2$  over a distance  $D \ll R$  along the radius of curvature. According to Eq. 13-65,  $\nabla^2 \xi$  will be negligible compared to  $\nabla^2 \xi$  if  $D \ll 4\pi^2 R (\gamma P + B^2/4\pi) / B^2$ . In this case we may approximate  $\vec{\xi}(\vec{r})$  with the displacement shown in Fig. 13-6 and Eq. 13-17, replacing  $z$  by the coordinate along the radius of curvature  $\hat{R}$  and replacing  $y$  by the coordinate perpendicular to both  $\vec{B}$  and  $\hat{R}$ . On integration of pressure drop  $\Delta P$  along a wavelength we find:

$$-2V = -\pi \int_0^D 2B\hat{R} \cdot \nabla P \xi^2 d\hat{R} \quad (13-68)$$

while the inertial term is the same as in Eq. 13-24. The growth rate for perturbations localized in the unstable region is therefore

$$\gamma = \sqrt{\frac{4\pi B^2 \hat{R} \cdot \nabla P}{P(1 + \gamma^2/4\pi)(1 + 4\pi)}} \quad (13-69)$$

For the simple pinch and the central region of the mirror geometry,  $\hat{R} \cdot \nabla P$  and the plasma confinement are stable. For the cusp geometry,  $\hat{R} \cdot \nabla P$  is unstable and the plasma is stable. A more detailed analysis of these geometries that include the finite size of the plasma, see Sec. 13-4 and 13-5, and the discussion of Thompson (Ref. 13-10).



### 13.4 NORMAL MODE ANALYSIS

An alternative method of finding the growth rates of striations is to linearize the equations of motion and then find growing solutions directly. This proves very difficult in small experimental devices where the equilibrium plasma properties often change substantially over a striation wavelength. For atmospheric and nuclear weapon phenomena, however, the scale of the unperturbed plasma variation is often large compared to the striation wavelengths. In this case the linearized differential equations can be reduced to more tractable algebraic equations. One may also take into account the dissipative effects of viscosity, resistivity, and diffusivity.

#### 13.4.1 DECELERATION INSTABILITY WITH GRAVITY

Let us consider an unperturbed plasma that has large regions in which deceleration or acceleration is occurring. We consider the relatively simple case wherein the magnetic field lines are straight, and allow a gravitational force to act on the plasma. We assume that the unperturbed  $\vec{V} \cdot \vec{W}$  and similar linearized terms are negligible; these shear terms lead to the Kelvin-Helmholtz instability discussed below. We also ignore dissipative effects here.

The unperturbed plasma satisfies

$$\rho \dot{\vec{V}} = -\nabla \left( p + \frac{B^2}{8\pi} \right) + \rho \vec{g} \quad (13-70)$$

As usual, we assume that the most unstable perturbation will not bend the magnetic field lines. We employ a cartesian coordinate system  $(x, y, z)$  and let the unperturbed  $\vec{B} = [B(y), 0, 0]$ . The displacements  $\vec{\xi}(x, y, z)$  are then functions of  $y$  and  $z$  and with  $\vec{\xi} = (\xi_x, \xi_y, \xi_z)$  and are assumed to have an exponential time dependence  $e^{i\omega t}$ .

The linearized equations of motion are

$$\alpha^2 \rho \vec{\xi} = -\nabla(P' + \vec{B} \cdot \vec{B}' / 4\pi) - \rho'(\vec{V} - \vec{g}) = \nabla \left[ \left( \gamma P + \frac{B^2}{4\pi} \right) \vec{\xi} - \rho \vec{\xi} \cdot (\vec{V} - \vec{g}) \right] - \rho'(\vec{V} - \vec{g}) \quad (13-71)$$

where we have used  $P' = -\gamma P \nabla \cdot \vec{\xi} - \vec{\xi} \cdot \nabla P$ ,  $\vec{B}' = -\vec{\xi} \cdot \nabla \vec{B} - \vec{B} \nabla \cdot \vec{\xi}$ , and employed Eq. 13-70. We now consider wavelengths that are small compared to the unstable plasma regions ( $\lambda \ll \pi D$ ). In these regions  $\vec{\xi}(\vec{r}) \approx \vec{\xi} \exp(i\vec{k} \cdot \vec{r})$  where  $\vec{\xi}$  and  $\vec{k}$  are both constant vectors, and the displacements outside the unstable region (e.g.,  $z > z_1$  and  $z < z_0$  in Fig. 13-6) do not strongly influence the growth rate.

A solution to Eq. 13-71 is then obtained by choosing  $\vec{\xi}$  parallel to  $(\vec{V} - \vec{g})$ , and choosing  $\nabla \cdot \vec{\xi} = \rho \vec{\xi} \cdot (\vec{V} - \vec{g}) / (\gamma P + B^2 / 4\pi)$ . Because  $\rho' = -\nabla \cdot (\rho \vec{\xi})$ , we then find the approximate growth rate  $\alpha$  for  $\lambda \ll \pi D$

$$\alpha^2 \rho = (\vec{V} - \vec{g}) \cdot \nabla \rho + \frac{\rho^2 (\vec{V} - \vec{g})^2}{\gamma P + B^2 / 4\pi} \quad (13-72)$$

where the last term is usually negligible. Note that  $-\vec{V}$  acts as a pseudo-gravitational acceleration  $\vec{g}$ , which is a result of their symmetrical appearance in Eqs. 13-70 and 13-71. Thus the unstable regions of the plasma are those where the density increases in direction of the vector  $(\vec{V} - \vec{g})$ . This criterion is analogous to that of the Rayleigh-Taylor gravitational instability (Eq. 13-50) in the limit of  $\lambda \ll \pi D$ .

When the wavelength is much longer than the height of the unstable region ( $\lambda \gg \pi D$ ), an approximate growth rate may be obtained by integrating Eq. 13-71 over the closed path shown in Fig. 13-12 employing the approximate  $\vec{\xi}(\vec{r})$  given in Eq. 13-47. The line integral of  $\alpha^2 \rho \vec{\xi}$  yields

$$\oint \alpha^2 \rho \vec{\xi} \cdot d\vec{r} \approx \alpha^2 \left[ \frac{2\rho_1 L}{k} + \frac{2\rho_0 L}{k} + \frac{2D L (\rho_1 + \rho_0)}{\pi} \right] \quad (13-73)$$

In the line integral of the r.h.s. of 13-71, the gradient term does not contribute, and

$$\oint \rho'(\vec{V} - \vec{g}) \cdot d\vec{r} = \oint \rho \vec{\xi} \cdot (\vec{V} - \vec{g}) \cdot d\vec{r} = 2 \int_0^L \left( \frac{\partial \rho}{\partial z} (\vec{V} - \vec{g}) \cdot \vec{e}_z \right) dz \quad (13-74)$$

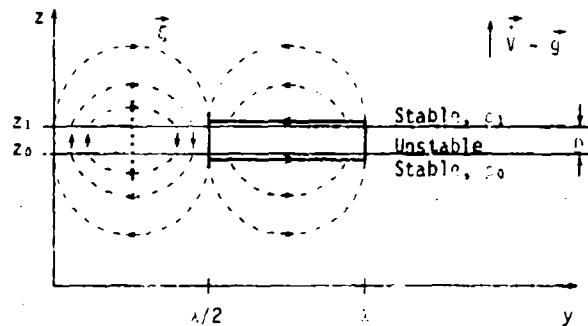


Figure 13-12. Line integral path (solid heavy line) for determining the growth rate when  $\lambda \gg \pi D$ . Dashed curves indicate perturbation flow lines.

Equating 13-73 and 13-74 yields the growth rate

$$\alpha = \sqrt{\frac{2\pi(\rho_1 - \rho_0)(\vec{V} - \vec{g}) \cdot \hat{i}_z}{(\rho_1 + \rho_0)(\lambda + \pi D)}} \quad (13-75)$$

where  $\hat{i}_z$  is a unit vector along the density gradient  $\nabla \rho$ . Note that Eq. 13-75 is similar to 13-50, and even reduces to the dominant first term of 13-72 in the limit of  $\lambda \ll \pi D$ .

#### 13.4.2 KELVIN-HELMHOLTZ SHEAR INSTABILITY

The simplest example of a shear instability occurs when a stratified medium in a gravitational field has layers moving with different horizontal velocities  $\vec{V} = (0, V(z), 0)$  as shown in Fig. 13-13.

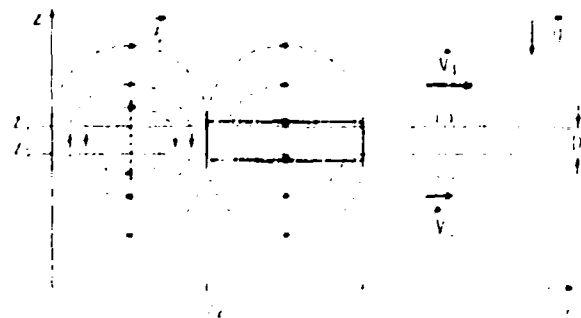


Figure 13-13. Shear instability when two layers have horizontal counter flow.

Suppose we have two layers with densities  $\rho_0$  and  $\rho_1$ . Let  $\rho_0 > \rho_1$ , so the configuration would be stable against the Rayleigh-Taylor gravitational instability discussed in Section 13.3.1. If the upper layer is now given a relative velocity with respect to the lower one, then there is a source of kinetic energy that can overcome the stabilizing effect of  $\partial\rho/\partial z < 0$ . An example of the shear instability is the generation of waves by strong winds blowing over the surface of the ocean (see Chapter 10.7.11).

A qualitative estimate of the relative velocity needed for instability can be obtained by supposing that two equal neighboring volumes at  $z$  and  $z+\delta z$  are interchanged (Ref. 13-5). The change in gravitational energy per unit volume is

$$\delta W = -g(\rho_1 - \rho_0)\delta z, \quad (13-76)$$

Before interchange, the momentum of the two volumes was  $\rho_1 V_1 + \rho_0 V_0$ . We determine a mean velocity  $V$  after interchange by conserving momentum, so  $(\rho_1 + \rho_0)V = \rho_1 V_1 + \rho_0 V_0$ . The change in kinetic energy is therefore

$$\frac{1}{2} \rho_0 V_0^2 + \frac{1}{2} \rho_1 V_1^2 - \frac{1}{2} (\rho_0 + \rho_1) V^2 = \frac{1}{2} \frac{\rho_0 \rho_1}{\rho_1 + \rho_0} (V_1 - V_0)^2 \quad (13-77)$$

Instability is therefore energetically possible if

$$\frac{1}{2} \frac{\rho_0 \rho_1}{\rho_1 + \rho_0} (V_1 - V_0)^2 > -g(\rho_1 - \rho_0)\delta z = g(\rho_0 - \rho_1) \frac{\lambda}{4\pi} \quad (13-78)$$

where for a perturbation of wavelength  $\lambda$  we estimate that the associated  $\delta z \approx \lambda/4\pi$ . Thus for a given relative velocity  $(V_1 - V_0)$  of the layers, instability is always energetically possible for sufficiently small wavelengths  $\lambda$ . However, a restriction on  $\lambda$  is that it be greater than  $4\pi h$ , where  $h$  is the thickness of the transition layer (see Ref. 13-5, Section 104, for a detailed example when  $\rho_1 = 0$ ).

Let us consider the two layer shear instability in detail for  $\lambda \gg \pi D$  and with straight magnetic field lines  $\vec{B} = [B(z), 0, 0]$  transverse to  $\vec{V}$ . The unperturbed plasma must satisfy

$$\rho \vec{V} \cdot \nabla \vec{V} = -\nabla \left( P + \frac{B^2}{8\pi} \right) + \rho \vec{g} \quad (13-79)$$

where in our case  $\vec{V} \cdot \nabla \vec{V} = 0$  because  $\vec{V} = (0, V(z), 0)$ . The linearized equations are (assuming  $\xi(\vec{r}) = \xi \exp(i\vec{k} \cdot \vec{r} + i\omega t)$ ):

$$\alpha \rho (\alpha + i\vec{V} \cdot \vec{k}) \xi + \alpha \rho \frac{\partial V}{\partial z} \xi_1 \hat{y} = -\nabla \left( P' + \frac{\vec{B} \cdot \vec{B}'}{4\pi} \right) + \rho' \vec{g} \quad (13-80)$$

$$(1 + i\vec{V} \cdot \vec{k}/\alpha) \rho' = -\nabla \cdot (\rho \xi) \quad (13-81)$$

We shall not need  $P'$  and  $\vec{B}'$  explicitly. In the limit that  $\lambda \gg D$ , we must require that the vertical displacements  $\delta z$  be the same at the surface interface  $z = z_0$  to  $z = z_1$ . Because  $\partial \delta z / \partial t + \vec{V} \cdot \nabla \delta z = V'_1$ , this yields  $\delta z = \xi_1 / (1 + i\vec{V} \cdot \vec{k}/\alpha)$ , and  $\xi_1$  must be chosen so that  $\delta z$  is continuous across the interface (Ref. 13-5). An approximate divergence-free choice for  $\xi(\vec{r})$  with constant  $\vec{V}_1$  and  $\vec{V}_0$  is then:

$$\xi(\vec{r}) = \begin{cases} \left[ 0, (1 + ikV_1/\alpha) \xi_1 \sin ky, e^{-k(z-z_1)}, (1 + ikV_1/\alpha) \xi_1 \cos ky, e^{-k(z-z_1)} \right], & z > z_1 \\ [0, 0, (1 + ikV/\alpha) \xi_1 \cos ky] & \text{for } z_0 < z < z_1 \\ \left[ 0, -(1 + ikV_0/\alpha) \xi_1 \sin ky, e^{k(z-z_0)}, (1 + ikV_0/\alpha) \xi_1 \cos ky, e^{k(z-z_0)} \right], & z < z_0 \end{cases} \quad (13-82)$$

We now perform a line integral of Eq. 13-80 around the path indicated in Fig. 13-13. This yields

$$\frac{1}{\alpha} (1 + ikV_1/\alpha) P' + \frac{1}{\alpha} (1 + ikV_0/\alpha) P' + \alpha (1 + ikV/\alpha) P' + \alpha (1 + ikV_1/\alpha) P' = 0 \quad (13-83)$$

where we have neglected the contribution of the term  $\rho' \vec{g} \cdot \vec{r}$  to the integral. We now also assume long wavelength such that  $kD \ll 1$  and so, therefore

$$kD \ll 1$$

neglect the  $\langle \rho \rangle (\alpha + ikV)^2$  term. Solution of Eq. 13-83 for the growth rate  $\alpha$  yields:

$$\alpha = \frac{-ik(\rho_1 V_1 + \rho_0 V_0) \pm \sqrt{\rho_1 \rho_0 k^2 (V_0 - V_1)^2 - (\rho_0 + \rho_1)(\rho_0 - \rho_1)gk}}{\rho_0 + \rho_1} \quad (13-84)$$

Thus there are growing unstable waves when the wavelengths  $\lambda = 2\pi/k$  are short enough so that the quantity under the radical is positive. The maximum unstable wavelength for a given  $(V_0 - V_1)$  is obtained by setting the radical to zero, and this yields the criterion derived in Eq. 13-78 above.

For the shear instability, the growth rate  $\alpha$  generally has an imaginary component  $-ik(\rho_1 V_1 + \rho_0 V_0)/(\rho_0 + \rho_1)$ . This means that the unstably growing wave moves along the interface with a velocity equal to the mass weighted velocities of the two layers.

Note that the growth rate does not depend on the transverse magnetic field. However, a magnetic field with components parallel to  $\vec{V}_1 - \vec{V}_0$  would reduce the growth rate (Ref. 13-5).

### 13.4.3 ION-NEUTRAL SLIP INSTABILITY (GRADIENT DRIFT, E-B)

When  $Ba^+$  ion clouds are generated at altitudes above 150 km, they drift at velocities of ~50 meters/sec. in response to the ambient winds and electric fields. Because of the relatively low collision rate between ions and neutrals at these high altitudes, the ion cloud moves relative to the ambient neutral fluid. The "back side" of the cloud, i.e., the side out of which the neutrals are streaming, develops a relatively steep density gradient  $\nabla n$  after a few minutes. Field aligned striations then appear in this back side region of large  $\nabla n$  (see Figs. 13-2 and 13-3).

This particular problem was first analyzed by Tinson and Workman (Ref. 13-6). The instability is often referred to as the "Simon ExB" or the "gradient drift" instability. Viewed from a coordinate frame fixed in the ion cloud, the source of the instability is the kinetic energy of

the neutral fluid flowing out of the ion cloud. Essentially, the outward flow of neutrals drags along chunks of the high density plasma to form sheets of striations as a result of ion-neutral collisions. The ion-neutral collision frequency is given by  $\nu_{in} = s\rho_0$ .

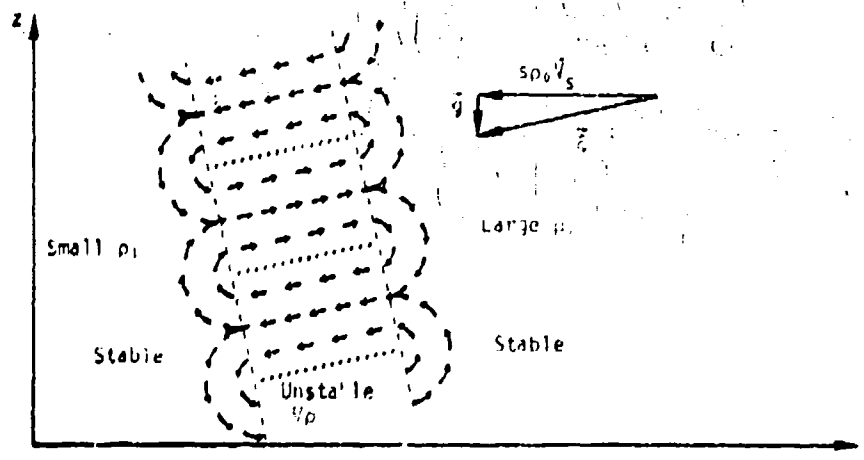


Figure 13-14. Ion-neutral slip instability in the frame of the ion cloud.

Let us consider an ion cloud that is moving with uniform velocity  $\hat{V}_1$  in a background neutral fluid moving with  $\hat{V}_0$ . We assume the energy of the ion cloud is small compared to  $B^2/8\pi$  so the field lines remain straight ( $\hat{B} = [B(y,z), 0, 0]$  in a cartesian coordinate system). We consider instability wavelengths small compared to the width of the unstable layer and take  $\tilde{\zeta}(\vec{r}, t) = \tilde{\zeta} \exp(i\vec{k} \cdot \vec{r} + \omega t)$ . In a frame fixed with the earth, the perturbations will move with the ion cloud, so the growth rate will have an imaginary component  $\omega = \omega_r - iV_1 \cdot \vec{k}$ . We now transform to the frame moving with the ion cloud  $\vec{r}' = \vec{r} - \hat{V}_1 t$ . In the cloud frame the growth rate is purely real ( $\omega_r$ ), and the ion-neutral slip velocity is  $\hat{V}_s = \hat{V}_0 - \hat{V}_1$  as shown in Fig. 13-14. The unperturbed plasma must satisfy

$$0 = -\left(P_1 + \frac{P_1^2}{8\pi}\right) \cdot \nabla \hat{B} \cdot \nabla \hat{V}_s \quad (13-85)$$

We assume  $\rho_0 \gg \rho_1$  so the neutral fluid perturbations may be ignored. The linearized equations in the ion cloud frame are then

$$\alpha_1^2 \rho_1 \vec{\xi} = -\nabla \left( P_1 + \frac{\vec{B} \cdot \vec{B}'}{4\pi} \right) + \rho_1' (\vec{g} + s \rho_0 \vec{V}_s) - \alpha_1 s \rho_1 \rho_0 \vec{\xi} \quad (13-86)$$

$$\rho_1' = -\nabla \cdot (\rho_1 \vec{\xi}) \quad (13-87)$$

$$P_1' = -\gamma P_1 \nabla \cdot \vec{\xi} - \vec{\xi} \cdot \nabla P_1 \quad (13-88)$$

$$\vec{B}' = -\vec{\xi} \cdot \nabla \vec{B} - \vec{B} \nabla \cdot \vec{\xi} \quad (13-89)$$

where in Eq. 13-89 we have assumed  $\vec{\xi}(\vec{r}) = [0, \xi_y(y, z), \xi_z(y, z)]$  so the field lines will not be bent by the perturbation. Substitution of the last three equations into 13-86 and use of 13-85 yields

$$(\alpha_1^2 + \alpha_1 s \rho_0) \rho_1 \vec{\xi} = \rho_1' (s \rho_0 \vec{V}_s + \vec{g}) + \nabla \left[ \rho_1 \vec{\xi} \cdot (s \rho_0 \vec{V}_s + \vec{g}) + \left( \gamma P + \frac{B^2}{4\pi} \right) \nabla \cdot \vec{\xi} \right] \quad (13-90)$$

For wavelengths small compared to the width of the unstable region, an approximate solution of Eq. 13-90 for  $\vec{\xi}(\vec{r})$  is obtained by choosing  $\nabla \cdot \vec{\xi} = \rho_1 \vec{\xi} \cdot (s \rho_0 \vec{V}_s + \vec{g}) / (\gamma P + B^2/4\pi)$  and letting  $\vec{\xi}$  be parallel to the vector  $(s \rho_0 \vec{V}_s + \vec{g})$ . The first two terms of Eq. 13-90, with use of 13-87, then yield the dispersion relation

$$(\alpha_1^2 + \alpha_1 s \rho_0) = -(s \rho_0 \vec{V}_s + \vec{g}) \cdot \nabla \ln \rho_1 + \frac{B^2 (s \rho_0 \vec{V}_s + \vec{g})^2}{\gamma P + B^2/4\pi} \quad (13-91)$$

where the last term is usually negligible. When  $s \rho_0$  is negligible, this gives the small wavelength limit for the gravitational instability discussed in sections 13.3.1 and 13.3.2. When  $s \rho_0$  is dominant, as in barium clouds, the real part of the growth rate is approximately

$$\gamma_r = \left( \vec{V}_s \cdot \frac{\vec{g}}{g} + \frac{\vec{g} \cdot \vec{g}}{g^2} \right) \cdot \Delta n_1 \quad (13-92)$$



Thus the plasma cloud is unstable in those regions where the density gradient  $\nabla\rho_1$  decreases in the direction of  $(\vec{V}_0 - \vec{V}_1 + \vec{g}/s\rho_0)$ .

Because  $\vec{g}/s\rho_0$  is usually small compared to  $\vec{V}_0 - \vec{V}_1$ , the "back side" of the cloud is unstable, whereas the "front side" remains stable and smooth. Typical parameters at 200 km altitude are a horizontal  $\vec{V}_1$  of about  $5 \times 10^3$  cm/sec,  $\rho_0 \approx 2 \times 10^{-13}$  gm/cm<sup>3</sup>,  $s \approx 0.25 \times 10^{13}$  cm<sup>2</sup>/gm/sec, and cloud density changes on a scale of  $10^4 - 10^5$  cm. The perturbations will therefore grow in the direction

$$\vec{\xi} \propto \vec{V}_1 + \vec{g}/s\rho_0 = -5000\hat{i}_y - 2000\hat{i}_z, \quad (13-93)$$

i.e., in an approximately horizontal direction with a downward component, and the growth rate on the "back side" of the cloud is

$$\alpha_1 \approx 0.5 \text{ to } 0.05 \text{ sec}^{-1} \quad (13-94)$$

so the e-folding time of the perturbation is only a few seconds when the cloud has a steep gradient. The above analysis does not account for the observed delay in striation formation of several minutes while the back side of the cloud is steepening. This may be due to diffusive effects discussed in the next section or to the convection of plasma out of the region of unstable striation growth as the  $Ba^+$  cloud distorts in its steepening process. It could also involve dissipative currents running along the field lines to the lower ionosphere. (See Section 13.5.2 below.)

#### 13.4.4 VISCOUS, RESISTIVE, AND DIFFUSIVE EFFECTS

The dissipative effects of viscosity, resistivity, and diffusivity reduce the growth rate  $\alpha$  at small wavelengths. In certain cases, very short wavelength perturbations become stable when dissipative effects are taken into account, so that perturbations grow only above a minimum critical wavelength  $\lambda_c$ . These dissipative effects may also be involved in the delayed appearance time of striations until the plasma parameters exceed some threshold values; e.g., as in barium cloud releases, but present understanding of striations does not allow us to be certain of this.

Viscosity is taken into account by including the  $\mu \nabla^2 \vec{V}'$  term in the linearized momentum equation. Because  $\vec{V}' \sim \alpha \vec{\xi} \exp(i\vec{k} \cdot \vec{r} + \alpha t)$ , the viscous term  $-\alpha \mu k^2 \vec{\xi}$  should be added to the r.h.s. of Eqs. 13-71, 13-80, and 13-86. For example, the dispersion relation 13-72 for the gravitational-deceleration instability then becomes

$$\alpha^2 \rho = (\vec{V} - \vec{g}) \cdot \nabla \rho + \frac{\rho^2 (\vec{V} - \vec{g})^2}{\gamma P + B^2/4\pi} - \alpha \mu k^2 \quad (13-95)$$

In the limit of small wavelength ( $k = 2\pi/\lambda \rightarrow \infty$ ), the unstable root of 13-95 is approximately

$$\lim_{\lambda \rightarrow 0} \alpha \sim \frac{\lambda^2}{4\pi^2 \mu} \left[ (\vec{V} - \vec{g}) \cdot \nabla \rho + \frac{\rho^2 (\vec{V} - \vec{g})^2}{\gamma P + B^2/4\pi} \right] \quad (13-96)$$

Consequently, as indicated by the dashed curve in Fig. 13-7, the growth rate becomes small at short wavelengths rather than approaching the constant value suggested by the dissipation-free analysis (Eq. 13-73).

Resistive effects are obtained when the linearized  $\alpha B'$  term in Eq. 13-13 is retained in computing the perturbed magnetic field  $\vec{B}'$ . Because

$4\pi\vec{J}' = \nabla \times \vec{B}'$ , and using  $\nabla \times (\eta \nabla \times \vec{B}') \approx \eta k^2 \vec{B}'$  one finds

$$\begin{aligned} (1 + \eta k^2 / 4\pi\alpha) \vec{B}' &= \nabla \times (\vec{\xi} \times \vec{B}) \\ &= \hat{i}_\phi \left[ \xi_r \left( \frac{2B}{R} - 4\pi J \right) - B \nabla \cdot \vec{\xi} \right] \end{aligned} \quad (13-97)$$

where in the last step we have assumed a curved magnetic field configuration as in Section 13.3.3. The equilibrium equations 13-59 and 13-60 for a plasma confined by a curved magnetic field still hold. The linearized momentum balance equation is:

$$\begin{aligned} \alpha^2 \rho \vec{\xi} &= - \left( \rho' + \frac{\vec{B} \cdot \vec{B}'}{4\pi} \right) + \frac{\vec{B} \cdot \nabla \vec{B}'}{4\pi} + \frac{\vec{B}' \cdot \nabla \vec{B}}{4\pi} \\ &= \nabla \left\{ \gamma P \nabla \cdot \vec{\xi} + \xi_r \frac{\partial P}{\partial r} - \frac{B}{4\pi(1 + \eta k^2 / 4\pi\alpha)} \left[ \xi_r \left( \frac{2B}{R} - 4\pi J \right) - B \nabla \cdot \vec{\xi} \right] \right\} \\ &\quad - \frac{\hat{i}_r B}{2\pi r (1 + \eta k^2 / 4\pi\alpha)} \left[ \xi_r \left( \frac{2B}{R} - 4\pi J \right) - B \nabla \cdot \vec{\xi} \right] \end{aligned} \quad (13-98)$$

When the perturbation wavelength is small compared to the width of the unstable region, an approximate solution is obtained by choosing  $\nabla \cdot \vec{\xi}$  so that the term  $\nabla \{ \dots \}$  in Eq. 13-98 vanishes, and by letting  $\vec{\xi}$  be parallel to  $\hat{i}_r$ . As noted in Section 13.3.3, in the case of field curvature it is important to have a good approximation for  $\nabla \cdot \vec{\xi}$  in order to get the correct dispersion relation for low beta plasmas. Substitution of  $\nabla \cdot \vec{\xi}$  into the last term of Eq. 13-98 then yields the dispersion relation

$$\alpha^2 \rho = \frac{2JB}{R(1 + \eta k^2 / 4\pi\alpha)} = - \frac{1}{(1 + \eta k^2 / 4\pi\alpha)} \left( \frac{2}{R} \frac{\partial P}{\partial r} \right) \quad (13-99)$$

where we have retained only the dominant term and have used the equilibrium condition 13-59.

As in the case of viscosity, the unstable root of Eq. 13-99 becomes

proportional to  $\lambda^2$  at small wavelengths, so resistive effects also lead to a reduced growth rate as shown by the dashed curve in Fig. 13-7.

In addition to resistive diffusion of magnetic flux, electron-ion and electron-neutral collisions also lead to a diffusive spreading of the plasma. In fact, these two processes are simply two different aspects of the same dissipative process. Collisions yield a contribution to  $\nabla \cdot \vec{\xi}$  that is especially large at small wavelengths. Rather than attempting to compute this contribution directly from the linearized equations 13-1 to 13-13, it proves easier to replace 13-2 by

$$\frac{\partial \rho}{\partial t} + \nabla \cdot (\rho \vec{V}) = D_1 \nabla^2 \rho \quad (13-100)$$

where  $\vec{V}$  now does not include the transverse diffusive velocity, and  $D_1$  is the diffusion coefficient transverse to a magnetic field. The value of  $D_1$  may depend on the particular plasma configuration and boundary conditions. As a typical example, we employ the value given by Gurevich and Tsedilina (Eq. 1.20 of Ref. 13-9):

$$D_1 = \frac{\kappa(T_i + T_e)}{M_1} \cdot \frac{v_{ei} + v_{eo}}{\Omega_e \Omega_i + v_{io}(v_{ei} + v_{eo})} \quad (13-101)$$

where  $\Omega_e$  and  $\Omega_i$  are the electron and ion gyrofrequencies. For plasmas above 100 km altitude,  $v_{io}(v_{ei} + v_{eo})$  is negligible compared to  $\Omega_e \Omega_i$ .

Linearization of Eq. 13-100 and use of  $\nabla^2 \rho' \approx -k^2 \rho'$  yields

$$(1 + k^2 D_1 / \alpha) \rho' = -\nabla \cdot (\rho \vec{\xi}) \quad (13-102)$$

Except in cases involving magnetic field curvature, we may now ignore the relatively small non-diffusive  $\nabla \cdot \vec{\xi}$ . For example, use of the above  $\rho'$  in Eq. 13-71 for the Rayleigh-Taylor gravitational or

deceleration instability now leads to the dispersion relation

$$\alpha^2 \rho = \frac{(\vec{V} - \vec{g}) \cdot \nabla \rho}{1 + k^2 D_L / \alpha} \quad (13-103)$$

As in the case of viscous and resistive effects, the unstable root of Eq. 13-103 varies as  $\lambda^2$  in the limit of small wavelengths, so the growth rate again is quenched when  $\lambda \rightarrow 0$  as indicated in Fig. 13-7.

If we also include viscous effects in addition to resistive and diffusive effects, then the term  $-\alpha \mu k^2$  should be added to the dispersion relations 13-99 and 13-103. The resultant dispersion relations then show that unstable perturbations, i.e., those with positive growth rates  $\alpha$ , exist only for wavelengths longer than some critical minimum wavelength  $\lambda_c$ . At the critical wavelength the growth rate is zero. For example, in the Rayleigh-Taylor instability we add  $-\alpha \mu k^2$  to Eq. 13-103, set  $\alpha$  to zero, and find the critical wave number.

$$k_c^4 = \frac{(\vec{V} - \vec{g}) \cdot \nabla \rho}{\mu D_L} \quad (13-104)$$

Unstable growth occurs only for wavelengths  $\lambda$  larger than  $2\pi/k_c$ .

Note that in order to find a minimum critical wavelength we had to take into account: (1) that the perturbation wavelength is small compared to the width of the unstable region; (2) resistive-diffusive effects; and (3) viscous effects.

#### 13.4.5 THE EFFECT OF COUPLING THE NEUTRAL AND IONIZED FLUIDS

In Section 13.4.3 we analyzed the ion-neutral slip instability wherein a strong neutral wind streamed through the plasma cloud and collisional coupling was weak so the neutral fluid was only negligibly perturbed. We now wish to examine a case of stronger coupling such that the neutral fluid is perturbed by the instability.

The simplest example is that of the Rayleigh-Taylor gravitational instability of a partially ionized gas supported by straight magnetic field lines. We assume there is no ion-neutral streaming in the equilibrium configuration, so the unperturbed neutral and plasma fluids obey

$$0 = -\nabla P_0 + \rho_0 \vec{g} \quad (13-105)$$

$$0 = -\nabla(P_1 + B^2/8\pi) + \rho_1 \vec{g} \quad (13-106)$$

Linearization of the momentum balance equations 13.3 and 13.4, and choice of  $\nabla \cdot \vec{\xi}_0$  and  $\nabla \cdot \vec{\xi}_1$  so that the gradient terms become zero, leads to the following equations for the perturbed displacements  $\vec{\xi}_0$  and  $\vec{\xi}_1$  of the neutral and plasma fluids:

$$\rho_0 \alpha^2 \vec{\xi}_0 = \frac{\rho_0 \vec{g} \vec{\xi}_0 \cdot \nabla P_0}{\gamma P_0} - \vec{g} \vec{\xi}_0 \cdot \nabla \rho_0 - s \rho_1 \rho_0 \alpha (\vec{\xi}_0 - \vec{\xi}_1) \quad (13-107)$$

$$\rho_1 \alpha^2 \vec{\xi}_1 = \frac{\rho_1 \vec{g} \vec{\xi}_1 \cdot \nabla (P_1 + B^2/8\pi)}{\gamma P_1 + B^2/4\pi} - \vec{g} \vec{\xi}_1 \cdot \nabla \rho_1 + s \rho_1 \rho_0 \alpha (\vec{\xi}_0 - \vec{\xi}_1) \quad (13-108)$$

A solution to these equations is obtained if  $\vec{\xi}_0$  and  $\vec{\xi}_1$  are taken parallel to  $\vec{g}$ . We therefore let  $\vec{\xi}_0 = a_0 \vec{g}$  and  $\vec{\xi}_1 = a_1 \vec{g}$ , and use the equilibrium conditions 13-105 and 13-106 to eliminate  $\nabla P_0$  and  $\nabla(P_1 + B^2/8\pi)$ . This yields two equations for the unknown  $a_0$  and  $a_1$ :

$$\rho_0 \alpha^2 a_0 = \frac{\rho_0^2 g^2}{\gamma P_0} a_0 - \vec{g} \cdot \nabla \rho_0 a_0 - s \rho_1 \rho_0 \alpha (a_0 - a_1) \quad (13-109)$$

$$\rho_1 \alpha^2 a_1 = \frac{\rho_1^2 g^2}{\gamma P_1 + B^2/4\pi} a_1 - \vec{g} \cdot \nabla \rho_1 a_1 + s \rho_1 \rho_0 \alpha (a_0 - a_1) \quad (13-110)$$

The dispersion relation is now obtained by setting the determinant of the coefficients of  $a_0$  and  $a_1$  in Eqs. 13-109 and 13-110 to zero. This yields the quartic in  $\alpha$ :

$$\begin{aligned}
& \rho_1 \rho_0 \alpha^4 + s \rho_1 \rho_0 (\rho_1 + \rho_0) \alpha^3 + \left[ \left( \vec{g} \cdot \nabla \rho_0 - \frac{\rho_0^2 g^2}{\gamma P_0} \right) \rho_1 + \left( \vec{g} \cdot \nabla \rho_1 - \frac{\rho_1^2 g^2}{\gamma P_1 + B^2/4\pi} \right) \rho_0 \right] \alpha^2 \\
& + \left[ \vec{g} \cdot \nabla (\rho_0 + \rho_1) - \frac{\rho_0^2 g^2}{\gamma P_0} - \frac{\rho_1^2 g^2}{\gamma P_1 + B^2/4\pi} \right] s \rho_1 \rho_0 \alpha \\
& + \left( \vec{g} \cdot \nabla \rho_1 - \frac{\rho_1^2 g^2}{\gamma P_1 + B^2/4\pi} \right) \left( \vec{g} \cdot \nabla \rho_0 - \frac{\rho_0^2 g^2}{\gamma P_0} \right) = 0
\end{aligned} \tag{13-111}$$

In the limit of no coupling ( $s \rightarrow 0$ ), the cubic and linear terms in  $\alpha$  become zero, and the remaining terms have the solutions

$$\rho_0 \alpha^2 = -\vec{g} \cdot \nabla \rho_0 + \rho_0^2 g^2 / \gamma P_0 \tag{13-112}$$

$$\rho_1 \alpha^2 = -\vec{g} \cdot \nabla \rho_1 + \frac{\rho_1^2 g^2}{\gamma P_1 + B^2/4\pi} \tag{13-113}$$

Thus when there is no coupling, the neutral fluid and plasma fluid act completely independently, as one might expect, and individually obey the Rayleigh-Taylor instability criterion.

In the limit of very strong coupling ( $s \rightarrow \infty$ ), the cubic and linear terms of 13-111 become dominant, and the unstable growth rate is:

$$(\rho_1 + \rho_0) \alpha^2 = -\vec{g} \cdot \nabla (\rho_1 + \rho_0) + \frac{\rho_0^2 g^2}{\gamma P_0} + \frac{\rho_1^2 g^2}{\gamma P_1 + B^2/4\pi} \tag{13-114}$$

Thus for very strong coupling, the fluids act essentially like a single fluid of density  $\rho_1 + \rho_0$ . There are slight differences from a single fluid behavior in the last two terms which arise from the non-zero values of  $\nabla \cdot \vec{\xi}_0$  and  $\nabla \cdot \vec{\xi}_1$ , but these terms are usually negligible compared to  $\vec{g} \cdot \nabla (\rho_1 + \rho_0)$ .

For intermediate values of the coupling constant  $s$ , the quartic dispersion relation 13-111 must be solved numerically. Furthermore, if the initial equilibrium configuration has zero-order ion-neutral slip and curved magnetic field lines, or if diffusive and viscous effects are also taken into account, then further terms must be added to equations 13-107 and 13-106 that lead to an even more complex dispersion

relation than 13-111. The algebraic procedures involved are straightforward but tax one's patience.

### 13.5 FIELD-LINE AVERAGED INSTABILITIES

In low- $\beta$  plasmas (where  $\beta \equiv 8\pi P_1/B^2$ ) the  $\vec{J} \times \vec{B}$  force in the momentum conservation equation 13-4 is usually comparable to the other applied forces on the plasma. Currents are generated in the plasma which will field-line-average these applied forces so that the low- $\beta$  plasma attempts to drift as a unit from one field-aligned flux tube to another. It is crucial that these currents flow in closed loops (i.e., that  $\nabla \cdot \vec{J} = 0$ ) because otherwise erroneously large electrostatic  $\vec{E}$  fields would be calculated.

For low- $\beta$  plasmas it is better to recast the MHD equations 13-4 and 13-10 to get an explicit equation for  $\vec{J}$  in terms of the electric field and the various applied forces (see Chapter 12.4.4). In the instability analysis we also note that the electric field is primarily electrostatic because there is not sufficient energy available to distort the magnetic field, so according to Eq. 13-9 the curl of  $\vec{E}$  must be negligible.

To account for transverse-to-B plasma diffusion it turns out to be much easier to employ electron number conservation rather than ion number conservation, even though  $N_i = N_e$  within the plasma. Transverse diffusion can then be accounted for by retaining the electron collision terms in the equation for  $\vec{v}_{e\perp}$ , but the electron collision terms in the exact equation for  $\vec{J}$  may be ignored. (If one chose to use ion number conservation, then electron collision terms in both  $\vec{v}_{i\perp}$  and  $\vec{J}$  would have to be retained to get correct diffusive results. This turns out to lead to much more laborious algebra.)



To simplify the analysis, we shall ignore the spatial variation of the ion and electron temperature. Temperature gradients are not believed to be an important source of unstable growth in the ionosphere. We shall, however, include viscous effects and Finite-Larmor-Radius (FLR) effects in order to analyze correctly instabilities on a scale of 10-100 meters wherein these effects have a stabilizing influence.

Another simplification is the omission of Hall terms in the equation for  $\vec{J}$ . This will restrict our perturbation analysis of striation growth to altitudes above  $\sim 150$  km. The full significance of the Hall terms is not understood at this time.

### 13.5.1 BASIC EQUATIONS FOR LOW- $\beta$ PLASMAS

Having assumed an electrostatic  $\vec{E}$  field and a spatially independent electron temperature, we may now employ a potential function  $\psi$  such that (see Chapter 12.4.4):

$$-\nabla\psi = \vec{E} + \frac{\kappa T_e}{e} \nabla \ln N \quad (13-115)$$

We introduce the notation:

$$\eta_{io} \equiv v_{io}/\Omega_i; \quad \eta_{ii} = v_{ii}/\Omega_i; \quad \eta_{ei} = v_{ei}/\Omega_e; \quad \eta_{eo} = v_{eo}/\Omega_e \quad (13-116)$$

$$d \equiv 1 + \eta_{io}^2; \quad \sigma_{||} = eN/B(\eta_{ei} + \eta_{eo}) = e^2 N/mc(v_{ei} + v_{eo})$$

The basic equations we must analyze are:  $\nabla \cdot \vec{J} = 0$ , where for a low- $\beta$ , high altitude plasma (see Eqs. 12-138 and 12-139 of Chapter 12)

$$\begin{aligned} \vec{J} = & -\nabla \times (\vec{P}\vec{B}/B^2 d) - \sigma_{||} \vec{E}_{||} - \frac{eN}{Bd} \eta_{io} \nabla_{\perp} \psi - \frac{\eta_{io}}{Bd} \nabla_{\perp} p \\ & - \frac{1}{Bd} \vec{b} \times \left[ \rho v_{io} \vec{V}_{o\perp} + \rho \vec{g}_{\perp} - \rho \vec{V}_{i\perp} - 2\vec{P}\vec{b} \cdot \nabla \vec{b} + \mu \nabla_{\perp}^2 \vec{V}_{i\perp} + \vec{b} \times \nabla_{\perp} (Nf) \cdot \nabla_{\perp} \vec{V}_{i\perp} \right] \end{aligned} \quad (13-117)$$

$$\vec{V}_{e\perp} = \frac{c}{B} \vec{b} \times \nabla_{\perp} \psi + \frac{en_{eo}}{B} \nabla_{\perp} \psi - \frac{cr_{ei}}{eNB} \nabla_{\perp} P \quad (13-118)$$

$$\begin{aligned} \frac{\partial N}{\partial t} &= -\nabla \cdot (N\vec{V}_{e\perp} + N\vec{V}_{e\parallel}) + q - K_T N^2 - K_O N_O N \\ &= -\vec{V}_{e\perp} \cdot \nabla N - N\vec{V}_{e\perp} \cdot \nabla + \nabla \cdot \left( \frac{c}{B} \vec{b} \times \nabla_{\perp} \psi - N\vec{V}_{e\parallel} \right) + q - K_T N^2 - K_O N_O N \end{aligned} \quad (13-119)$$

$$\vec{V}_{i\perp} \approx \frac{c}{B} \vec{b} \times \nabla_{\perp} \psi + \frac{c}{eNB} \vec{b} \times \nabla_{\perp} P \quad (13-120)$$

where  $P$  is the plasma pressure ( $P_i + P_e$ ) and  $n$  is the ion mass density.

The first term in Eq. 13-117 is due to the "magnetization" of the plasma. It is divergence-free and therefore will not contribute to the equation for  $\nabla \cdot \vec{J} = 0$ . It is convenient in the following perturbation analysis to define an auxiliary current density  $\vec{J}_2$  which omits this term, i.e.,

$$\begin{aligned} \vec{J}_2 &\equiv \vec{J} + \nabla \times (P\vec{b}/B^2 d) \\ &= -\sigma_{\parallel} \nabla_{\parallel} \psi - \frac{en}{Bd} n_{i0} \nabla_{\perp} \psi - \frac{n_{i0}}{Bd} \nabla_{\perp} P \\ &\quad - \frac{1}{Bd} \vec{b} \times [\sigma_{\parallel} \nabla_{i0} \vec{V}_{O\perp} + \sigma_{\parallel} \vec{g}_{\perp} - \sigma_{\parallel} \vec{V}_{i\perp} - 2P\vec{b} \cdot \nabla \vec{b} + \sigma_{\parallel}^2 \vec{V}_{i\perp} + \vec{b} \times \nabla_{\perp} (N\vec{V}_{i\perp})] \end{aligned} \quad (13-121)$$

The  $\sigma_{\parallel} \nabla_{\parallel} \psi$  term in Eq. 13-121 and 13-117 accounts for the parallel-to-B conductivity in the plasma, and the  $(en_{i0} \nabla_{\perp} \psi/Bd)$  term accounts for the Pedersen conductivity. The term  $(n_{i0}/Bd) \nabla_{\perp} P$  is required to account for diffusive decay due to electron-neutral collisions, and also allows "image" striation growth. The terms inside the square bracket of the last line of Eq. 13-121 and 13-117 are the various forces acting on the plasma. Instabilities can be driven by the neutral wind force  $(\sigma_{\parallel} \nabla_{i0} \vec{V}_{O\perp})$ , the gravitational force  $(\sigma_{\parallel} \vec{g}_{\perp})$ , the inertial force  $(-\sigma_{\parallel} \vec{V}_{i\perp})$ , and the magnetic curvature force  $(-2P\vec{b} \cdot \nabla \vec{b})$ . The last two terms in Eq. 13-121 and 13-117 are approximate viscous and finite-Larmor-Radius (FLR) forces, where

$$\eta \approx \frac{0.105 N e T_e n_{ii}}{n_{ii} (1 + 0.146 n_{ii}^2)} \quad \frac{\text{gr}}{\text{cm} \cdot \text{sec}} \quad (13-122)$$

$$N e \approx \frac{N e T_e}{2 n_{ii} (1 + n_{ii}^2)} \quad \frac{\text{gr}}{\text{cm} \cdot \text{sec}} \quad (13-123)$$

The equation for  $\eta$  has been chosen to fit the limiting values of  $\eta$  at large and small values of  $n_{ii}$  (see Spitzer, Ref. 13-11, Eqs. 3-54 and 3-55). Because  $n_{ii}$  is usually small in a low- $\beta$  plasma,  $N e$  is usually larger than  $\eta$ , so FLR forces may dominate viscous forces. Actually, the viscous and FLR forces are much more complex than indicated in Eq. 13-117 and 13-121. Somewhat more accurate expressions are (Ref. 13-5, 13-7, 13-12, and 13-13):

$$\text{Viscous Force} \approx n \nabla_{\perp}^2 \vec{V}_{\perp} + (\vec{V}_{\perp} \cdot \nabla) \cdot \vec{T}_{\perp} \vec{V}_{\perp} - (\vec{b} \cdot \nabla \vec{b}) \cdot \vec{T}_{\perp} (\vec{V}_{\perp} \cdot \nabla) + \frac{1}{5} \nabla_{\perp}^2 \vec{V}_{\perp} \cdot \vec{V}_{\perp}$$

$$\text{FLR Force} \approx [\vec{b} \cdot \nabla_{\perp} (N e)] \cdot \vec{V}_{\perp} \vec{V}_{\perp} + N e \nabla_{\perp}^2 (\vec{V}_{\perp} \cdot \vec{b}) + \vec{T}_{\perp} (N e) \cdot \vec{V}_{\perp} \cdot \vec{b} \quad (13-124)$$

The complete expressions for these forces would require additional terms involving  $\vec{V}_{\perp}$  and  $\vec{V}_{\parallel}$ , but it is customary to ignore such terms in low- $\beta$  plasmas. For our perturbation analysis we retain only the first term of each of the above two equations because we assume that the unperturbed ion velocity gradients  $\nabla \vec{V}_{\perp}$  are negligible; if these  $\nabla \vec{V}_{\perp}$  were substantial the other terms in Eqs. 13-124 could drive instabilities. Usually, however, reliable values for the unperturbed  $\nabla \vec{V}_{\perp}$  are not known, so we omit these terms to reduce the algebraic complexity.

Eq. 13-118 for the transverse-to-B electron velocity  $\vec{V}_{\perp}$  is a minor simplification of the exact form shown in Eq. 12-134 of Chapter 12. The leading term  $(c \vec{b} \cdot \nabla / B)$  of Eq. 13-118 is often referred to as the  $\mathbf{E} \times \mathbf{B}$  drift velocity. Actually, it also includes electron drift due to the

electron pressure gradient, as indicated by Eq. 13-115. Because of the high conductivity along the field lines, the potential  $\phi$  tends to vary only slightly along  $\vec{B}$ , as compared to its variation transverse-to- $\vec{B}$ . Thus  $\phi$  is nearly an equipotential along the field lines, and so this  $\vec{E} \times \vec{B}$  drift velocity tends to transport the electrons from one field-aligned flux tube to another.

The  $en_{e0} \nabla_{\perp}^2 \phi / B$  term in Eq. 13-118 (in conjunction with the  $n_{i0} \nabla_{\perp}^2 \phi / B d$  term in Eq. 13-117) allows plasma diffusion across field lines due to electron-neutral collisions. The  $en_{e0} \nabla_{\parallel}^2 \phi / c N$  term in Eq. 13-118 accounts for plasma diffusion due to electron-ion collisions. Usually these last two terms in Eq. 13-118 are quite small compared to the leading  $\vec{E} \times \vec{B}$  drift term, but these two small terms yield the divergent velocity that characterizes diffusively spreading flow.

Eqs. 13-117 and 13-118 replace the ion and electron momentum conservation Eqs. 13-1 and 13-10 in this lower plasma perturbation analysis. The ion mass conservation Eq. 13-1 is replaced by the electron number conservation Eq. 13-119. The latter also includes the effects of solar photoionization and chemistry. Using Eq. 13-11, the second line of Eq. 13-119 employs the transverse-to- $\vec{B}$  electron velocity  $\vec{V}_{e\perp}$  and the parallel-to- $\vec{B}$  ion velocity  $\vec{V}_{i\parallel}$  because we shall find it convenient to do our perturbation analysis in a reference frame moving with the unperturbed transverse-to- $\vec{B}$  electron velocity and the unperturbed parallel-to- $\vec{B}$  ion velocity. Thus we will define our convective time derivative to be  $\frac{d}{dt} = \frac{\partial}{\partial t} + \vec{V}_{e\perp} \cdot \nabla_{\perp} + \vec{V}_{i\parallel} \cdot \nabla_{\parallel}$ .

$$\frac{d}{dt} n_e = -\nabla_{\perp} \cdot \vec{V}_{e\perp} - \nabla_{\parallel} \cdot \vec{V}_{i\parallel} \quad (13-119)$$

The reason for this particular choice is that the unperturbed  $\vec{V}_{e\perp}$  term is completely independent of distance along the field line because of the nearly constant potential and magnetic field. Thus  $\vec{V}_{e\perp} \cdot \nabla_{\perp}$  will only contribute when the

field line if  $\nabla \cdot \vec{J}_\perp$  is non-zero along  $\vec{B}$ . On the other hand, non-zero  $\nabla \cdot \vec{J}_\parallel$  along the field lines is accounted for mainly by variation of  $\vec{V}_{e\parallel}$  along  $\vec{B}$ , so it proves more astute to use  $\vec{V}_{i\parallel}$  in Eq. 13-125. This procedure minimizes the following algebra.

The  $q$  in Eq. 13-119 is the electron-ion production rate due to solar photoionization. During the daytime, the maximum production rate occurs at about 120-180 km altitude with  $q_{\max} \approx 10^3$ - $10^4$  electrons/cm<sup>3</sup>sec. (Ref. 13-14, Section 17.4.1). Above about 180 km altitude in an undisturbed atmosphere,  $q$  decreases nearly exponentially with altitude because of the decreasing air density. In the following perturbation analysis we shall compute the ratio  $N'/N$  of the perturbed electron density  $N'$  to the unperturbed density  $N$ . As will be shown below, the photo-production  $q$  causes the ratio  $N'/N$  to decrease in time because of the increase of  $N$  by photoionization.

The  $K_r N^2$  term in Eq. 13-119 accounts for chemical decay of ionization via collisional-radiative reactions such as  $O^+ + e \rightarrow O + h\nu$ . The rate coefficient  $K_r$  is in the range of  $10^{-12}$  to  $10^{-11}$  cm<sup>3</sup>/sec (Ref. 13-15, page 24-5). This term causes noticeable decay of the ratio  $N'/N$  when the electron density is above  $10^8$  cm<sup>-3</sup>.

The  $K_{O,N_2} N$  term in Eq. 13-119 accounts for ion-molecule reactions with subsequent rapid dissociative recombination: e.g.,  $O^+ + N_2 \rightarrow NO^+ + N$  followed by  $NO^+ + e \rightarrow N + O$ . It turns out that the ratio  $N'/N$  is not affected by this reaction chain because  $N'$  and  $N$  decrease similarly with time.

To perform the perturbation analysis of Eqs. 13-117 to 13-119, we must have an expression for the transverse-to- $B$  ion velocity  $\vec{V}_{i\perp}$ . Eq. 13-120 is a very crude approximation to the exact expression given by Eq. 12-153 of Chapter 12. The simple form of Eq. 13-120 will suffice here because we are

using a good approximation for  $\vec{J}$  in Eq. 13-117. We shall also need an expression for the perturbed ion acceleration  $\vec{V}_{1\perp}'$ , which will be discussed below.

### 13.5.2. LINEARIZED EQUATIONS FOR LOW- $\beta$ PLASMAS

We now obtain the linearized form of Eqs. 13-118 to 13-121 by the following replacement in those equations:  $\phi \rightarrow \phi'$ ,  $N \rightarrow N+N'$ ,  $c \rightarrow c+M_1 N'$ ,  $P \rightarrow P+P'$ ,  $\vec{V}_{e\perp} \rightarrow \vec{V}_{e\perp} + \vec{V}_{e\perp}'$ ,  $\vec{V}_{i\perp} \rightarrow \vec{V}_{i\perp}'$ ,  $\vec{V}_{1\perp} \rightarrow \vec{V}_{1\perp} + \vec{V}_{1\perp}'$ , and  $\vec{J}_2 \rightarrow \vec{J}_2 + \vec{J}_2'$ . Note that we have assumed that the unperturbed ion velocity gradients  $\nabla \vec{V}_{i\perp}$  are negligible. We also assume that the ion-electron temperature is not perturbed, so  $P' = \kappa(T_i + T_e)N'$ .

Assuming that the perturbed quantities are small and retaining only first order terms in these small quantities, we find the linearized equation for  $\vec{J}_2'$ :

$$\vec{J}_{2\parallel}' = -\sigma_{\parallel} \nabla_{\parallel} \phi' \quad (13-126)$$

$$\begin{aligned} \vec{J}_{2\perp}' &= \frac{N'}{N} \vec{J}_{2\perp} + \frac{N'}{N} \frac{\eta_{10}}{Bd} \nabla_{\perp} P - \frac{eN}{Bd} \eta_{10} \nabla_{\perp} \phi' - \frac{\eta_{10}}{Bd} \nabla_{\perp} P' \\ &\quad + \frac{1}{Bd} \vec{b} \times \left[ \vec{V}_{1\perp}' - \mu^2 \nabla_{\perp}^2 \vec{V}_{1\perp}' - \vec{b} \times \nabla_{\perp} (Nf) \cdot \nabla_{\perp} \vec{V}_{1\perp}' \right] \\ &= -\frac{N'}{NBd} \vec{b} \times \left[ \eta_{10} (\vec{V}_0 - \vec{V}_e)_{\perp} + \vec{b} \nabla_{\perp}^2 \vec{V}_{1\perp}' - 2P \vec{b} \cdot \nabla_{\perp} \vec{b} \right] - \frac{eN\eta_{10}}{Bd} \left[ \nabla_{\perp} \phi' + \frac{1}{eN} \nabla_{\perp} P' \right] \\ &\quad + \frac{1}{Bd} \vec{b} \times \left[ \nabla \left( \frac{d\vec{V}_{1\perp}'}{dt} + \frac{c}{eN} \vec{J}_{1\perp} \cdot \nabla_{\perp} \vec{V}_{1\perp}' \right) - \mu^2 \nabla_{\perp}^2 \vec{V}_{1\perp}' - \vec{b} \times \nabla_{\perp} (Nf) \cdot \nabla_{\perp} \vec{V}_{1\perp}' \right] \quad (13-127) \end{aligned}$$

We have employed Eq. 13-121 to eliminate  $\vec{J}_{2\perp}$  in the above equation, and used  $\vec{V}_{1\perp} = -(c/B)\vec{b} \cdot \nabla_{\perp} \vec{V}_{e\perp}$  to eliminate the unperturbed  $\vec{V}_{1\perp}$  in Eq. 13-121. It is noteworthy that this results in the appearance of the unperturbed electron-neutral slip velocity  $(\vec{V}_0 - \vec{V}_e)_{\perp}$  rather than the usual ion-neutral slip

velocity  $(\vec{V}_0 - \vec{V}_1)_\perp$  in the second form of Eq. 13-127. The distinction between these two slip velocities at this stage of the analysis is probably academic, however, because in actual applications at high altitudes one cannot accurately distinguish between them.

To replace the perturbed ion acceleration  $\ddot{\vec{V}}_{1\perp}$  appearing in the first form of Eq. 13-127, we have employed:

$$\begin{aligned}\ddot{\vec{V}}_{1\perp} &= \frac{d\dot{\vec{V}}_{1\perp}}{dt} + \vec{V}_1 \cdot \nabla \dot{\vec{V}}_{1\perp} + \vec{V}_1 \cdot \nabla \dot{\vec{V}}_{1\perp} \\ &= \frac{d\dot{\vec{V}}_{1\perp}}{dt} + (\vec{V}_{e\perp} + \frac{c}{eN} \vec{J}_\perp + \vec{V}_{1\perp}) \cdot \nabla \dot{\vec{V}}_{1\perp} + \vec{V}_1 \cdot \nabla \dot{\vec{V}}_{1\perp} \\ &= \frac{d\dot{\vec{V}}_{1\perp}}{dt} + \frac{c}{eN} \vec{J}_\perp \cdot \nabla \dot{\vec{V}}_{1\perp} + \vec{V}_1 \cdot \nabla \dot{\vec{V}}_{1\perp}\end{aligned}\quad (13-128)$$

where we have used Eq. 13-11 to obtain the second line, and Eq. 13-125 to obtain the third line of Eq. 13-128. We shall drop the  $\vec{V}_1 \cdot \nabla \dot{\vec{V}}_{1\perp}$  term, however, on the supposition that the unperturbed  $\dot{\vec{V}}_{1\perp}$  is negligible.

We shall see later that it is the  $(c/eN) \vec{J}_\perp \cdot \nabla \dot{\vec{V}}_{1\perp}$  term in Eq. 13-127 that drives the collisional-drift instability discussed below. For the unperturbed  $\vec{J}_\perp$  here, we require only the crude approximation of the "magnetization" term, i.e.,  $\vec{J}_\perp = (\vec{b} \cdot \nabla P)/B$ , so:

$$\frac{c}{eN} \vec{J}_\perp \cdot \nabla \dot{\vec{V}}_{1\perp} = \frac{1}{B} \vec{b} \cdot \nabla P \cdot \nabla \dot{\vec{V}}_{1\perp} \quad (13-129)$$

Thus the unperturbed pressure gradient is the driving force of the collisional-drift instability. Note that this term is similar to the very first term, i.e., the FLR term in Eq. 13-127 where we substituted  $\vec{V}_1$  by  $\vec{V}_1 \cdot \nabla$  and used Eq. 13-125 to replace  $\vec{V}_1$ . In fact the FLR term cancels about 75% of Eq. 13-129, thereby exerting a stabilizing effect.

To eliminate  $\vec{V}'_{1\perp}$  from Eq. 13-127 we use the linearized version of the approximate Eq. 13-126:

$$\vec{V}'_{1\perp} \approx \frac{c}{B} \vec{b} \times \nabla_{\perp} \psi' + \frac{c}{eNB} \vec{b} \times \nabla_{\perp} p' \quad (13-130)$$

At this point we assume that all perturbed plasma parameters have a spatial dependence in the transverse-to-B coordinates of the form  $\exp(i\vec{k}_{\perp} \cdot \vec{r}_{\perp})$ , so we can replace the operator  $\nabla_{\perp}$  by  $i\vec{k}_{\perp}$  wherever it operates on a perturbed quantity in Eqs. 13-127 and 13-130. The resultant  $\vec{J}'_{2\perp}$  is:

$$\begin{aligned} \vec{J}'_{2\perp} = & -\frac{N'}{kBd} \vec{b} \times \left[ \tau_{10} (\vec{V}_0 - \vec{V}_c)_{\perp} + \rho \vec{s}_{\perp} - e \vec{V}'_{1\perp} - 2p\vec{b} \cdot \vec{\nabla} \vec{b} \right] \\ & - i\vec{k}_{\perp} \frac{eN}{Bd} \left\{ \tau_{10} + \frac{e\omega k_{\perp}^2}{eNB} - \frac{ic\vec{b} \times \nabla_{\perp} (Nf) \cdot \vec{k}_{\perp}}{eNB} + \frac{ic\vec{J}_{\perp} \cdot \vec{k}_{\perp}}{eN\Omega_1} \right\} \left( \psi' + \frac{p'}{eN} \right) \\ & + \frac{1}{\Omega_1} \frac{d}{dt} \left( \psi' + \frac{p'}{eN} \right) \end{aligned} \quad (13-131)$$

Two basically different vectors appear here. The first line of Eq. 13-131 is a vector rotated  $90^\circ$  with respect to the sum of the driving forces of plasma-neutral slip, gravity, inert  $\rho$ , and magnetic curvature. The second part of Eq. 13-131 is a vector along  $\vec{k}_{\perp}$ . To complete our analysis we must choose a direction for  $\vec{k}_{\perp}$ . I believe the correct choice is to align  $\vec{k}_{\perp}$  with the vector direction of the first line in Eq. 13-131, because otherwise there would be a component of the perturbed  $\vec{J}'_{2\perp}$  along the  $\vec{k}_{\perp} \times \vec{b}$  direction which would not be properly taken into account in the linearized equation  $\nabla \cdot \vec{J}' = 0$ , i.e., in  $-\nabla \cdot \vec{J}'_{\parallel} = \nabla \cdot \vec{J}'_{\perp} = i\vec{k}_{\perp} \cdot \vec{J}'_{\perp}$ . Since according to Eq. 13-118 the perturbed plasma moves primarily in the direction  $\vec{b} \times \nabla_{\perp} p' = i\vec{b} \times \vec{k}_{\perp} p'$ , the above choice for the  $\vec{k}_{\perp}$  direction means that the perturbed plasma will move in the direction of the sum of the driving forces, which is intuitively reasonable. The reader should be aware, however, that other authors have occasionally suggested that one should rotate the  $\vec{k}_{\perp}$



direction until maximum perturbation growth is achieved. I believe this is erroneous in this linearized analysis because it would allow perturbed  $\vec{J}_\perp$  to flow in the  $\vec{k}_\perp \times \vec{b}$  direction which do not have any obvious way of closing off to form closed current loops.

The linearized form of Eq. 13-118 is

$$\vec{V}_{e\perp}' = \frac{c}{B} \vec{b} \times \nabla_\perp \phi' + \frac{c\eta_{eo}}{B} \nabla_\perp \phi' - \frac{c\eta_{ei}}{eN} \nabla_\perp \phi' \quad (13-132)$$

We also need an expression for  $d(N'/N)/dt$ , employing Eq. 13-125 as the definition of the convective time derivative. Note that

$$\frac{d}{dt} \left( \frac{N'}{N} \right) = \frac{1}{N} \frac{dN'}{dt} - \frac{N'}{N^2} \frac{dN}{dt} \quad (13-133)$$

From Eq. 13-119 we find:

$$\begin{aligned} \frac{dN}{dt} &\equiv \frac{\partial N}{\partial t} + \vec{V}_{e\perp}' \cdot \nabla N + \vec{V}_{i\parallel}' \cdot \nabla N \\ &= -N \vec{\nabla} \cdot \vec{V}_{e\perp}' + \frac{c}{B} \nabla \cdot \vec{J}_\parallel' - N \vec{\nabla} \cdot \vec{V}_{i\parallel}' + q - K_F N^2 - K_O N_O N \end{aligned} \quad (13-134)$$

From the linearized form of Eq. 13-119 we obtain:

$$\begin{aligned} \frac{dN'}{dt} &= -\vec{V}_{e\perp}' \cdot \nabla N - N \vec{\nabla} \cdot \vec{V}_{e\perp}' - N \vec{\nabla} \cdot \vec{V}_{e\perp}' + \frac{c}{B} \nabla \cdot \vec{J}_\parallel' - N \vec{\nabla} \cdot \vec{V}_{i\parallel}' - \nabla \cdot (N \vec{V}_{i\parallel}') \\ &= -2K_F N N' - K_O N_O N' \end{aligned} \quad (13-135)$$

Substitution of Eqs. 13-134 and 13-135 into 13-133 yields

$$\frac{d}{dt} \left( \frac{N'}{N} \right) = - \vec{V}'_{\perp} \cdot \nabla \ln N - \vec{V}'_{\perp} \cdot \vec{V}'_{\perp} - \frac{c}{cN} \nabla \cdot \vec{J}'_{\parallel} - \frac{cN'}{cN^2} \nabla \cdot \vec{J}'_{\parallel} - \frac{1}{N} \nabla \cdot (N \vec{V}'_{\parallel}) - K_R N' - q \frac{N'}{N^2} \quad (13-136)$$

We will make the reasonable assumption that  $\vec{V}'_{\parallel}$  is negligible, although this is not completely obvious. We now eliminate  $\vec{V}'_{\perp}$  and  $\vec{J}'_{\parallel}$  from the above equation by using Eqs. 13-152 and 13-126. Replacing  $\vec{V}_{\perp}$  by  $i\vec{k}_{\perp}$  and using  $\vec{J}'_{\parallel} = \kappa(T_1 + T_e) N'$ , we obtain

$$\frac{d}{dt} \left( \frac{N'}{N} \right) = - \frac{1}{N} \left[ \frac{c}{B} \vec{k}_{\perp} \cdot \nabla \ln N - \frac{c}{cN} \nabla \cdot (\sigma_{\parallel} \vec{V}_{\parallel} \varphi') - \frac{cN'}{cN^2} \nabla \cdot \vec{J}'_{\parallel} \right] - \frac{K_R^2 c \kappa (T_1 + T_e) \mu_0 c i}{cB} \frac{N'}{N} + \frac{K_R^2 c \kappa \phi'}{B} - \left( K_R N + \frac{q}{N} \right) \frac{N'}{N} \quad (13-137)$$

There are two unknown perturbation functions here:  $N'/N$  and  $\varphi'$ . The other quantities are to be obtained from the unperturbed plasma parameters. A second equation is obtained from  $\nabla \cdot \vec{J}'_{\perp} = 0$ , i.e., from  $-\nabla \cdot \vec{J}'_{\parallel} = i\vec{k}_{\perp} \cdot \vec{J}'_{\perp}$ . Using Eqs. 13-126 and 13-131 this yields:

$$\begin{aligned} \nabla \cdot \vec{J}'_{\perp} = & \frac{1}{N} \left[ \frac{1}{B} \vec{k}_{\perp} \cdot \left[ \omega_{j0} (\vec{V}'_{\perp} - \vec{V}'_{\parallel} \vec{b}) + \vec{k}_{\perp} \cdot \vec{V}'_{\perp} - \omega_{j0} \vec{V}'_{\perp} - 2p\vec{k}_{\perp} \cdot \vec{V}'_{\perp} \right] \right. \\ & \left. + \frac{1}{B} \left[ \frac{1}{\omega_{j0}} + \frac{c k_{\perp}^2}{cNB} - \frac{1}{cNB} \frac{1}{\omega_{j0}} + \frac{1}{cN} \frac{1}{\omega_{j0}} \right] \left( \varphi' + \frac{\kappa(T_1 + T_e) N'}{cN} \right) \right. \\ & \left. + \frac{1}{cN} \frac{d}{dt} + \frac{\kappa(T_1 + T_e)}{cN} \frac{d}{dt} \left( \frac{N'}{N} \right) \right] \end{aligned} \quad (13-138)$$

where  $\omega_{j0} = \omega_{j0} + \frac{1}{2} \omega_{j0}^2$ . Eqs. 13-137 and 13-138 are the final equations that determine the linearized striation growth. To solve them, one must specify the initial value of  $N'/N$  along the field line and specify the boundary condition for  $\varphi'$  at the two ends of the field line. In Eq. 13-138, the perturbation  $\vec{J}'_{\perp}$  may be approximated by the "magnetization" current density  $\vec{J}'_{\perp} = \vec{k}_{\perp} \times \vec{b} [P/B]$ .

A perennial problem in perturbation analysis is the question of the initial value of the perturbation. There appears to be no logical answer. In practice, employment of an initial  $N'/N$  of about  $10^{-3}$ - $10^{-2}$  along the entire field line yields reasonable results.

The correct boundary conditions for  $N'$  is obtained by noting that  $N'_\parallel$  must be zero at the two ends of the field line; otherwise, spurious buildup of space-charge on the field line would be implied, thereby negating the whole analysis of  $\nabla \cdot \vec{J}' = 0$ . From Eq. 13-126, the correct boundary condition is that  $\nabla_\parallel N' = 0$  at the two ends of the field line.

Let us review the significance of the terms in Eq. 13-137 and 13-138. The first term in Eq. 13-137 is a result of incompressible  $E \times B$  drift in a plasma with an unperturbed density gradient  $\nabla_\perp nN$ . If  $\nabla_\perp nN$  were zero along the whole length of the field line, no perturbation growth could occur. The second term in Eq. 13-137 arises from  $\nabla \cdot \vec{J}'_\parallel$ ; it is usually small compared to the other terms except near the foot of the field line where it may cause "image" striations. The magnitude of  $N'$  in these "image" striations is usually small compared to the maximum  $N'$  along the field line because any buildup of  $N'$  at the striation foot via  $\nabla \cdot \vec{J}'_\parallel$  means a corresponding depletion of  $N'$  at another position along the field line. The third term in Eq. 13-137 is usually ignored because reliable values for the unperturbed  $\nabla \cdot \vec{J}'_\parallel$  are generally not available; however, it appears that this term would normally be negligible anyway.

The terms in the second line of Eq. 13-137 retard striation growth. The term involving  $\nu_{ei}$  accounts for diffusive decay due to electron-ion collisions. The term involving  $\nu_{eo}$  accounts for diffusive decay via electron-neutral collisions (to get this effect one must retain the term  $\nu_{eo} \cdot (T_i + T_e) N' / cN$  in the second line of Eq. 13-138). Note that diffusive decay is more rapid if  $k_\perp^2$  is large, i.e., at small wave lengths.

The last term in Eq. 13-157 accounts for decay of the striation amplitude  $N'/N$  due to collisional-radiative recombination and solar photoionization. The lack of strong striation growth in the normal daytime ionosphere may be a result of the stabilizing effect of the  $qN'/N^2$  term.

In the first line of Eq. 13-158, the terms inside the bracket are the driving forces of the ion-neutral slip (or gradient-drift, or  $E \times B$  instability), the gravitational instability, the Rayleigh-Taylor inertial instability, and the magnetic field curvature instability. Note that in accordance with the discussion following Eq. 13-131, the  $\vec{k}_\perp \times \vec{B}$  vector direction should be aligned with the direction of the vector sum inside this bracket.

The  $\eta_{ij}$  term in the second line of Eq. 13-158 accounts for the ion-neutral collisional drag retardation. The viscous retardation is given by the  $c_1 k_\perp^2 / cNB$  term, and like the diffusion terms in Eq. 15-157, viscous effects are more important at small perturbation wavelengths that have the large  $k_\perp^2$  values. The term involving  $\gamma_\perp(Nf)$  is from the FLR effect; it usually yields a stabilizing effect. Note that when one is assessing the relative stabilizing influence of viscous and FLR effects, one must compare  $k_\perp$  to the magnitude of the unperturbed  $\gamma_\perp(Nf)$ .

the  $\vec{J}_\perp \cdot \vec{E}_\perp$  term in Eq. 13-158 drives the collisional-drift instability, which will be discussed in greater detail below. The  $dI'/dt$  and  $d(N'N)/dt$  terms in Eq. 13-158 arise from the drag effect of ion inertia; these terms are important at extremely high altitudes (where there is negligible air density so that the  $\eta_{ij}$  term in the second line of 13-158 vanishes).

### 13.5.3. COLLISIONAL-DRIFT INSTABILITY (SPHER-DISSIPATIVE)

Radar back scatter from the ionospheric E-layer indicates plasma density fluctuations on the 300-1000 Hz of orders. It has been suggested (e.g.,

Ref. 13-16) that the collisional drift instability is a possible source of these fine scale fluctuations. S. R. Goldman (Ref. 13-17) has suggested that this instability may cause fine scale striations under certain restricted conditions. This particular instability is the result of transverse-to-B pressure gradients. Because one generally assumes that temperature gradients are not important, this means that any transverse-to-B density gradients will drive the drift instability. Because some density gradients are bound to occur in a plasma, this instability is also referred to as a "universal" instability. The drift instability may also occur in the absence of collisions as a result of "inverse Landau damping" (Ref. 13-18, Section 8.16.2; Ref. 13-19); this collisionless version of the drift instability will not be analyzed here because it requires the use of the Vlasov equation. T.H. Johnson has suggested that the collisionless drift instability may be relevant to striations.

The collisional-drift instability is included in the general analysis given in Section 13.5.2. Let us re-examine this instability in its most simple form in the absence of any diffusive, viscous, FLR, or chemistry effects. We omit all driving forces of unstable growth except the plasma pressure gradient  $\nabla p$ . Perturbed ion inertial effects must be retained, however, to obtain this instability. A finite  $\sigma_{||}$  must be employed, but  $\eta_{i0}$  will be set to zero. Thus, the equations that must be analyzed are the following simplified versions of Eqs. 13-118 through 13-121:

$$\vec{J}_2 \equiv \vec{J} + \nabla \times (P\vec{B}/B^2) = -\sigma_{||} \nabla_{||} \psi + \frac{e}{B} \vec{b} \times \vec{V}_{i\perp} \quad (13-139)$$

$$\vec{V}_{i\perp} \approx \frac{c}{B} \vec{b} \times \nabla_{\perp} \psi + \frac{c}{enB} \vec{b} \times \nabla_{\perp} p \quad (13-140)$$

$$\vec{V}_{e\perp} = \frac{c}{B} \vec{b} \times \nabla_{\perp} \psi \quad (13-141)$$

$$\frac{\partial N}{\partial t} = -\vec{V}_{e\perp} \cdot \nabla N - N \vec{V}_{e\perp} \cdot \vec{\nabla} + \nabla \cdot \left( \frac{c}{e} \vec{J}_{||} - N \vec{V}_{i||} \right) \quad (13-142)$$

where  $\nabla\psi$  is given by Eq. 13-115. Linearization of Eq. 13-139 yields simplified versions of Eqs. 13-126 and 13-127:

$$\vec{J}'_{2\parallel} = -\sigma_{\parallel}\nabla_{\parallel}\psi' \quad (13-143)$$

$$\vec{J}'_{2\perp} = \frac{\rho}{B} \vec{b} \times \left( \frac{d\vec{V}'_{1\perp}}{dt} + \frac{c}{eN} \vec{J}'_{\perp} \cdot \nabla_{\perp} \vec{V}'_{1\perp} \right) \quad (13-144)$$

where we are using the unusual definition of the convective derivative  $d/dt$  given by Eq. 13-125, and have employed Eq. 13-128 to replace the perturbed ion acceleration  $\vec{V}'_{1\perp}$ . Eliminating  $\vec{V}'_{1\perp}$  by means of Eq. 13-130 and replacing the operator  $\nabla_{\perp}$  by  $i\vec{k}_{\perp}$  wherever it operates on a perturbed quantity, Eq. 13-144 yields a simplified version of Eq. 13-131:

$$\vec{J}'_{2\perp} = -i\vec{k}_{\perp} \frac{eN}{B\Omega_i} \left[ \frac{ic\vec{J}'_{\perp} \cdot \vec{k}_{\perp}}{eN} \left( \psi' + \frac{P'}{eN} \right) + \frac{d}{dt} \left( \psi' + \frac{P'}{eN} \right) \right] \quad (13-145)$$

The  $\nabla_{\perp}P$  driving force of the collisional drift instability appears in this equation via the unperturbed  $\vec{J}'_{\perp}$ , which is given by the "magnetization" current density. Assuming a spatially uniform  $T_i$  and  $T_e$ , this  $\vec{J}'_{\perp}$  is:

$$\vec{J}'_{\perp} = \vec{b} \times \nabla_{\perp} P/B = \frac{\kappa(T_i + T_e)}{B} \vec{b} \times \nabla_{\perp} N \quad (13-146)$$

Using Eqs. 13-143 and 13-145 in  $\nabla \cdot \vec{J}' = 0$  (i.e.,  $-\nabla \cdot \vec{J}'_{\parallel} = i\vec{k}_{\perp} \cdot \vec{J}'_{\perp}$ ) yields

$$\begin{aligned} \nabla \cdot (\sigma_{\parallel} \nabla_{\parallel} \psi') &= \frac{eNk_{\perp}^2}{B\Omega_i} \left[ \frac{ic\vec{J}'_{\perp} \cdot \vec{k}_{\perp}}{eN} \left( \psi' + \frac{\kappa(T_i + T_e)}{e} \frac{N'}{N} \right) \right. \\ &\quad \left. + \frac{d\psi'}{dt} + \frac{\kappa(T_i + T_e)}{e} \frac{d}{dt} \left( \frac{N'}{N} \right) \right] \end{aligned} \quad (13-147)$$

Linearization of Eqs. 13-141 and 13-142 yields

$$\frac{d}{dt} \left( \frac{N'}{N} \right) = -i\psi' \frac{c}{B} \vec{b} \times \vec{k}_{\perp} \cdot \nabla_{\perp} N - \frac{c}{eN} \nabla \cdot (\sigma_{\parallel} \nabla_{\parallel} \psi') \quad (13-148)$$

Solution of Eqs. 13-147 and 13-148 yields the two unknown perturbation functions  $\psi'$  and  $N'/N$ . These two equations are simplified versions of the more general Eqs. 13-138 and 13-137. To avoid spurious buildup of space charge on the field line, the boundary condition  $\nabla_{\parallel} \psi' = 0$  (i.e.,  $J'_{\parallel} = 0$ ) must be applied at each end of the field line when solving Eq. 13-147.

To obtain an algebraic dispersion relation, we make the further assumptions that the spatial variation along the field line has the form  $\exp(ik_{\parallel} z_{\parallel})$  and that the time variation is  $\exp(\omega t)$ . Thus  $\psi'$  has the functional form

$$\psi'(\vec{r}_{\perp}, z_{\parallel}, t) = \psi'_0 \exp(i\vec{k}_{\perp} \cdot \vec{r}_{\perp} + ik_{\parallel} z_{\parallel} + \omega t) \quad (13-149)$$

where  $\psi'_0$  is an arbitrary constant. A similar form is employed for  $N'/N$ . With this functional form, Eqs. 13-147 and 13-148 reduce to the algebraic equations

$$-k_{\parallel}^2 \psi'_0 = \frac{eNk_{\perp}^2}{B\epsilon_1} \left[ \frac{ic\vec{J}_{\perp} \cdot \vec{k}_{\perp}}{eN} + \frac{c(T_1 + T_e)}{e} \frac{N'}{N} \right] \quad (13-150)$$

$$\omega \frac{N'}{N} = -i\omega' \frac{c}{B} \vec{b} \cdot \vec{k}_{\perp} \cdot \nabla_{\parallel} N + \frac{c}{eN} k_{\parallel}^2 \psi'_0 \quad (13-151)$$

Using Eq. 13-151 to eliminate  $N'/N$  in Eq. 13-150, one obtains the quadratic dispersion relation

$$0 = \omega^2 + \left[ \frac{c\epsilon_1 k_{\parallel}^2}{eNk_{\perp}^2} + \frac{ic}{eN} \vec{J}_{\perp} \cdot \vec{k}_{\perp} + \frac{c(T_1 + T_e)}{e} \left( \frac{c}{eN} k_{\parallel}^2 \psi'_0 - i \frac{c}{B} \vec{b} \cdot \vec{k}_{\perp} \cdot \nabla_{\parallel} N \right) \right] + \frac{ic}{eN} \vec{J}_{\perp} \cdot \vec{k}_{\perp} - \frac{c(T_1 + T_e)}{e} \left( \frac{c}{eN} k_{\parallel}^2 \psi'_0 - i \frac{c}{B} \vec{b} \cdot \vec{k}_{\perp} \cdot \nabla_{\parallel} N \right) \quad (13-152)$$

Using Eq. 13-146 to replace  $\vec{J}_{\perp} \cdot \vec{k}_{\perp}$ , the growing root of Eq. 13-152 is given by

$$\alpha = -\frac{1}{2} \left( \frac{\Omega_i B}{e N k_{\perp}^2} + \frac{c K (T_i + T_e)}{e^2 N} \right) \sigma_{\parallel} k_{\parallel}^2 + i \frac{c K (T_i + T_e)}{e B} \vec{b} \times \vec{k}_{\perp} \cdot \nabla \ell n N$$

$$+ \frac{1}{2} \left[ \left( \frac{\Omega_i B}{e N k_{\perp}^2} + \frac{c K (T_i + T_e)}{e^2 N} \right)^2 \sigma_{\parallel}^2 k_{\parallel}^4 - \frac{4 i c K (T_i + T_e)}{e B} \vec{b} \times \vec{k}_{\perp} \cdot \nabla \ell n N \frac{\Omega_i B \sigma_{\parallel} k_{\parallel}^2}{e N k_{\perp}^2} \right]^{1/2}$$
(13-153)

Unstable growth occurs if  $\alpha$  has a positive real part,  $\alpha_r$ . An unusual feature of the collisional-drift instability is that no unstable growth occurs unless  $k_{\parallel}$  is finite, i.e., the perturbation must vary along the field line. Study of Eq. 13-153 shows that at small values of  $k_{\parallel}$  the real part of  $\alpha$  is proportional to  $k_{\parallel}$ , whereas at large values of  $k_{\parallel}$  the real part is proportional to  $1/k_{\parallel}^2$ . Thus there is some intermediate value,  $k_{\parallel}^*$ , at which the growth rate attains a maximum value,  $\alpha_r^*$ ; these are given by

$$k_{\parallel}^* = \sqrt{\frac{k_{\perp}^2 c N K (T_i + T_e) |\vec{b} \times \vec{k}_{\perp} \cdot \nabla \ell n N|}{\sigma_{\parallel} \Omega_i B^2 [1 + k_{\perp}^2 K (T_i + T_e) / M_i \Omega_i^2]}} \quad (13-154)$$

$$\alpha_r^* = \frac{0.3 K (T_i + T_e) |\vec{b} \times \vec{k}_{\perp} \cdot \nabla \ell n N|}{M_i \Omega_i [1 + k_{\perp}^2 K (T_i + T_e) / M_i \Omega_i^2]} \quad \text{if } k_{\parallel} = k_{\parallel}^* \quad (13-155)$$

This growth rate  $\alpha_r^*$  is a function of the magnitude and direction of  $\vec{k}_{\perp}$ . The growth rate is maximized when  $\vec{k}_{\perp}$  is orthogonal to  $\vec{V}_{\perp} N$ ; this is intuitively reasonable because the perturbation  $\vec{E} \times \vec{B}$  drift is then in direction of  $\vec{V}_{\perp} N$ , i.e., in direction of the driving force  $\vec{V}_{\perp} P$ . The growth rate  $\alpha_r^*$  is proportional to  $k_{\perp}$  at small  $k_{\perp}$  values, and proportional to  $1/k_{\perp}$  at large  $k_{\perp}$  values. The growth rate attains a maximum  $\alpha_r^{**}$  at an intermediate value  $k_{\perp}^{**}$ :



$$k_{\perp}^{**} = \sqrt{M_i \Omega_i^2 / \kappa (T_i + T_e)} \quad (13-156)$$

$$k_{\parallel}^{**} = \sqrt{\frac{eN \frac{1}{2} \nabla_{\perp} \ell n N}{4\sigma_{\parallel} B} \left( \frac{M_i \Omega_i^2}{\kappa (T_i + T_e)} \right)^{1/2}} = \sqrt{\frac{(v_{ei} + v_{eo}) \frac{1}{2} \nabla_{\perp} \ell n N}{4\Omega_e} \left( \frac{M_i \Omega_i^2}{\kappa (T_i + T_e)} \right)^{1/2}} \quad (13-157)$$

$$\alpha_r^{**} = 0.15 \frac{1}{2} \nabla_{\perp} \ell n N \sqrt{\frac{\kappa (T_i + T_e)}{M_i}} \quad \text{if } k_{\perp} = k_{\perp}^{**} \text{ and } k_{\parallel} = k_{\parallel}^{**} \quad (13-158)$$

The growth rate  $\alpha_r^{**}$  is the maximum possible growth rate that can be extracted from the simple collisional-drift instability dispersion relation given by Eq. 13-152. When  $T_e \approx T_i$ , note that the transverse-to-B perturbation wavelength (given by  $\lambda_{\perp}^{**} \equiv 2\pi/k_{\perp}^{**}$ ) of this fastest growing mode is about  $2\pi R_g$ , where  $R_g$  is the thermal ion gyro radius ( $R_g \equiv \sqrt{2\kappa T_i / M_i \Omega_i^2}$ ). For oxygen ions in a 0.3 gauss field with  $(T_i + T_e) \approx 0.2$  eV one finds  $\lambda_{\perp}^{**} \approx 38$  meters, which is comparable to the observed fluctuation size in the equatorial F-layer.

There is a certain amount of mystique in the literature associated with the choice of the  $k_{\parallel}$  value to be used in Eq. 13-153. Often it is recommended that  $k_{\parallel} \approx 2\pi/z_{\parallel}$ , where  $z_{\parallel}$  is the length along the field line over which the unperturbed plasma parameters are approximately constant. E.g., Goldman (Reference 13-17) used  $z_{\parallel} \approx 100$  km, whereas Hudson and Kennel have a more intricate recommendation (Ref. 13-16, Eq. 5). It seems reasonable to me to employ 13-158 if  $2\pi/k_{\parallel}^{**} \leq z_{\parallel}$ . It must be noted that Eq. 13-153 will yield a smaller growth rate than the  $\alpha_r^{**}$  of Eq. 13-158 if the chosen  $k_{\parallel}$  deviates from the  $k_{\parallel}^{**}$  value given by Eq. 13-157. Thus the choice of  $k_{\parallel}$  to be employed in Eq. 13-153 is quite critical in determining the growth rate.

It would probably be best to avoid the whole problem of choosing  $k_{\parallel}$  by solving Eqs. 13-147 and 13-148 numerically with the boundary condition that  $V_{\parallel} = 0$  at the ends of the field line. I am not aware of any studies

of this type, however. For realistic comparisons with ionospheric data, one should of course employ the more general Eqs. 13-137 and 13-138 that include the stabilizing effects of diffusion, viscosity, FLR, and ion-neutral collisions.

### 13.6 RECOMMENDED DISPERSION RELATIONS

In analyzing density perturbation growth after high-altitude nuclear bursts, it is useful to consider three different time regimes. The first covers the initial blast wave expansion during the first few hundred milliseconds. The second time regime spans from  $\sim 0.5$  seconds to  $\sim 100$  seconds during which the fireball accelerates upward and expands horizontally; during this time the plasma- $\beta$  is still high and the geomagnetic field is quite distorted. The third time regime is subsequent to  $\sim 100$  seconds when the fireball plasma- $\beta$  has become less than unity, so the magnetic field has relaxed back to nearly its geomagnetic configuration.

#### 13.6.1 Perturbation Growth During Blast Wave Expansion

During the initial blast wave expansion the Rayleigh-Taylor deceleration instability is the dominant cause of density perturbations. During this early phase the plasma pressure is much greater than  $B^2/8\pi$  so the magnetic field exerts only a negligible force compared to the hydrodynamic forces. The perturbation growth rate is then given by a simplified version of Eq. 13-72:

$$\alpha = \sqrt{\vec{V} \cdot \nabla \ell_{np}} \quad (13-159)$$

In a simple spherical blast wave expansion,  $\vec{V}$  is directed radially inward behind the shock front whereas  $\nabla \ell_{np}$  is directed radially outward (Ref. 13-20). Thus, a simple blast wave is stable to density perturbation behind the shock front.

For bursts below  $\sim 200$  km altitude, however, the hot plasma behind the shock front radiates very rapidly. This depletes its internal energy and causes a density compression which may allow  $\nabla n_p$  to be directed radially inward in some regions behind the shock front. Eq. 13-159 predicts those regions will be unstable.

In practice, it proves very difficult to get accurate density profiles from simulations during the initial blast wave expansion. Without accurate unperturbed  $\nabla n_0$ , one cannot make reliable predictions of the growth rate via Eq. 13-159. Nevertheless, it is clear that unstable zones do appear inside the blast wave, and the non-linear evolution of these perturbations may persist to later times. These three-dimensional density-fluctuations can be particularly important to some optical sensing systems. These 3-D fluctuations may in some cases (at least in low yield bursts) persist long enough to eventually expand along the magnetic field lines and thereby cause late-time striations.

#### 13.6.2 Perturbation Growth During Intermediate Times

During the intermediate time span from  $\sim 0.5$  sec to  $\sim 100$  sec when the plasma- $\beta$  is high ( $\beta \equiv 8\pi P/B^2$ ), the ion-electron fluid and neutral fluid tend to be strongly coupled. Thus one needs an intricate dispersion relation of the type discussed in Section 13.4.5. The actual dispersion relation would be more complex than Eq. 13-111 because the effects of curved magnetic field lines, deceleration, ion-neutral slip, diffusion, resistivity, and viscosity must be treated simultaneously.

During this time span it is possible to get reliable values for the unperturbed plasma parameters from simulations. Our results indicate that for large yield bursts, the perturbation amplification is relatively modest. In view of the very intricate nature of the complete

dispersion relation and the resultant weak perturbation growth, it seems reasonable to ignore perturbation growth during this intermediate time span when the plasma- $\beta$  is greater than unity.

### 13.6.3. Late-Time Striation Growth

Computations of striation growth subsequent to large yield high altitude bursts indicate that most of the perturbation growth occurs after the plasma- $\beta$  drops below unity. It is the leakage of neutral fluid out of the fireball plasma that seems to be the predominant cause of striation growth via the ion-neutral slip instability. At these late times field-line-averaging can be an important effect, especially when one segment along the field-line is locally unstable and an adjoining segment is locally stable; this situation tends to occur in the "heave" region far from the fireball.

At the time of this writing (Dec. 1977), the relevance of the collisional-drift instability to striations has not been fully explored. Thus we propose to ignore this type instability to obtain the following simplified versions of Eqs. 13-137 and 13-138:

$$\frac{d}{dt} \left( \frac{N'}{N} \right) = -i\psi' \frac{c}{B} \vec{b} \times \vec{k}_\perp \cdot \nabla \mathcal{E} n N - \frac{c}{eN} \nabla \cdot (\sigma_{\parallel} \nabla_{\parallel} \psi') \\ - \frac{k_\perp^2 c k (T_i + T_e) \eta_{ei}}{eB} \frac{N'}{N} + \frac{k_\perp^2 c \eta_{eo} \psi'}{B} - \left( K_r N + \frac{q}{N} \right) \frac{N'}{N} \quad (13-160)$$

$$\nabla \cdot (\sigma_{\parallel} \nabla_{\parallel} \psi') = i \frac{N'}{N} \frac{\vec{b} \times \vec{k}_\perp}{B(1+n_{i0}^2)} \cdot \left[ \rho v_{i0} (\vec{V}_0 - \vec{V}_e)_\perp + \rho \vec{g}_\perp - \rho \vec{V}_{i\perp} - 2P \vec{b} \cdot \nabla \vec{b} \right] \\ + \frac{eNk_\perp^2}{B(1+n_{i0}^2)} \left[ \eta_{i0} \psi' + \frac{ck_\perp^2}{eNB} \psi' + \frac{1}{N_i} \frac{d\psi'}{dt} + \frac{\eta_{i0} k (T_i + T_e)}{e} \frac{N'}{N} \right] \quad (13-161)$$

Here we have omitted FLR effects, and assumed that the perturbed ion velocity and acceleration are given approximately by  $c\vec{E}' \times \vec{B}/B^2$  and  $c(d\vec{E}'/dt) \times \vec{B}/B^2$ , respectively, rather than by the more accurate expressions of Eq. 13-128 and 13-130.

As discussed in Section 13.5.2, the  $\vec{b} \times \vec{k}_\perp$  vector direction should be aligned with the direction of the driving forces of the instability, i.e., along  $[\rho v_{i0}(\vec{V}_0 - \vec{V}_e)_\perp + c\vec{g}_\perp - c\vec{V}_{i1} - 2P\vec{b} \cdot \nabla \vec{b}]$ .

Integration of Eqs. 13-160 and 13-161 is a straightforward numerical procedure. Often, however, one is interested in computing a "local" growth rate which ignores field-line-averaging of striation growth. The dispersion relation for the local growth rate,  $\alpha$ , is obtained from the differential equations 13-160 and 13-161 by assuming a time-dependence  $e^{i\alpha t}$  and setting  $\nabla \cdot (\sigma_{ii} \nabla \phi')$  to zero. This yields two algebraic equations

$$\alpha \frac{N'}{N} = \left[ \frac{k_\perp^2 c n_{e0}}{B} - i \frac{c}{B} \vec{b} \times \vec{k}_\perp \cdot \nabla \phi' N \right] \cdot \left[ \frac{k_\perp^2 c k (T_i + T_e) n_{ei}}{cB} + k_r N + \frac{q}{N} \right] \frac{N'}{N} \quad (13-162)$$

$$0 = i \frac{N'}{N} \frac{\vec{b} \times \vec{k}_\perp}{B(1+n_{i0}^2)} \cdot \left[ \rho v_{i0}(\vec{V}_0 - \vec{V}_e)_\perp + c\vec{g}_\perp - c\vec{V}_{i1} - 2P\vec{b} \cdot \nabla \vec{b} \right] + \frac{cNk_\perp^2}{B(1+n_{i0}^2)} \left[ \left( n_{i0} + \frac{cNk_\perp^2}{cNB} + \frac{1}{n_i} \right) \cdot \left( \frac{r_{i0} c (T_i + T_e)}{c} \frac{N'}{N} \right) \right] \quad (13-163)$$

Solving Eq. 13-162 for  $\alpha'$  and using this to eliminate  $\alpha'$  in Eq. 13-163 yields the dispersion relation. Dropping the imaginary terms in the resultant dispersion relation and simplifying some minor terms yields:

$$(c + k_\perp^2 n_{i1} + k_r N + \frac{q}{N}) \left( n_{i0} + \frac{1}{n_i} k_\perp^2 \right) = - \left[ v_{i0}(\vec{V}_0 - \vec{V}_e)_\perp + \vec{g}_\perp - \vec{V}_{i1} - \frac{2c(T_i + T_e)}{M_i} \vec{b} \cdot \nabla \vec{b} \right] \cdot \nabla \phi' \quad (13-164)$$

This relatively simple quadratic dispersion relation for the growth rate  $\alpha$  encompasses the effects of the ion-neutral slip, gravitational, deceleration, and curved field line instabilities. It also includes the damping effects of viscosity, diffusion, and chemistry. The coefficient  $D_{\perp}$  is the standard transverse-to-B diffusion coefficient

$$D_{\perp} = \frac{ck(T_i + T_e)}{eB} \frac{v_{ei} + v_{eo}}{\Omega_e} \quad (13-165)$$

In this "local" approximation, the amplitude fluctuation  $N'/N$  of a particular moving plasma element at time  $t$  is related to the initial amplitude  $(N'/N)_0$  by:

$$\frac{N'}{N} = \left( \frac{N'}{N} \right)_0 \exp \left[ \int_0^t \alpha dt \right] \quad (13-166)$$

The  $\alpha(t)$  required here is obtained from Eq. 13-164, using the unperturbed plasma parameters at the successive locations of the moving plasma element. Initial amplitudes of  $10^{-3}$  to  $10^{-2}$  appear to yield reasonable results.

A critical wavenumber  $k_c$  can be obtained from Eq. 13-164 by setting  $\alpha = 0$  in it, and solving for the resultant  $k_{\perp}^2$ . Unstable growth occurs only for wavelengths larger than  $\lambda_c = 2\pi/k_c$ .

Plasma plumes rising along the geomagnetic field lines will attain very large velocities ( $V_{i||} \approx 5$  km/sec) parallel to the field lines. Due to the curvature of the geomagnetic dipole field there will be a centrifugal acceleration associated with the  $V_{i||}$ . Technically, this acceleration is a part of  $\vec{V}_{i\perp}$ , and it is given by

$$\vec{V}_{i\perp} = V_{i||}^2 \vec{b} \cdot \nabla \vec{b} + \text{other terms} \quad (13-167)$$

In low- $B$  plasmas the other terms in this equation are usually negligible. Using a geocentric dipole approximation for the earth's geomagnetic field, the curvature of the dipole field lines at a point  $(r, \theta, \phi)$  is

$$\vec{b} \cdot \nabla \vec{b} = - \frac{3(1+\cos^2\theta)\sin\theta}{r(1+3\cos^2\theta)^{3/2}} \vec{e}_\phi \times \vec{b} \quad (13-168)$$

where  $r$  is the distance from the center of the earth,  $\theta$  is the geomagnetic colatitude, and  $\vec{e}_\phi$  is a unit vector in the geomagnetic eastward direction. For rapidly moving hot plasmas high in the magnetosphere, the last two terms in Equation 13-164 can partially counterbalance or even exceed the transverse-to- $B$  gravitational acceleration  $\vec{g}_\perp$ .

We recommend Eq. 13-164 as the most useful single dispersion relation for late-time striation growth. It does not include the collisional-drift instability discussed in Section 13.5.3. One may, however, be misled by the local nature of the dispersion relation 13-164 when the stable and unstable segments along a particular field line can mutually cancel each other by field-line-averaging effects. W.R. Wortman has shown that this cancellation is particularly likely to happen when the field-line-integral of the electron density,  $\int N dz_\parallel$ , is independent of the transverse-to- $B$  coordinates, i.e., when there is the same electron content on all field lines. In such cases one must numerically integrate Eqs. 13-160 and 13-161 to obtain reliable prediction of striation growth. This seems to be particularly important in the normal ionosphere and in the heave region far outside the fireball-plume. The fireball-plume volume, on the other hand, appears to be described fairly reliably by the "local" dispersion relation Eq. 13-164 and the Lagrangian-type integral of Eq. 13-166.

### 13.7 NON-LINEAR STRIATION EVOLUTION

The above procedures allow a reasonably valid prediction of where and when striations will appear in a plasma. In system applications, however, one must in addition have a fairly detailed description of the nature of the striations. For example, for communication system evaluations it is necessary to have the power-spectral density of the electron density fluctuations.

A great amount of effort has been applied in recent years to compute the non-linear evolution of striations (Refs. 13-21 to 13-25). These computations have proved to be unusually onerous because of the difficulty of obtaining accurate electrostatic potential solutions and of the special need to suppress numerical diffusion on an Eulerian computational grid with limited spatial resolution.

Fig. 13-15 shows a recently computed one-level, two-dimensional, non-linear evolution of striations by McDonald, Ossakow, Zalesak, and Zabusky<sup>(13-26)</sup>. The purpose of these computations was to determine the effect of diffusion on striation splintering. To concentrate on this aspect of striation evolution, a very simple set of equations and geometry was employed. A vertical B-field of 0.5 gauss was used. A uniform height-independent neutral wind ( $\vec{V}_0 = 100$  m/sec) and a constant ion-neutral collision frequency ( $\nu_{i0} = 0.08 \nu_i$ ) was assumed. Hall terms, gravity, pressure, and inertial forces were ignored, so the field-line integrated version of Eq. 12-140 of Chapter 12 was reduced to:

$$\frac{d}{dt} \left( \frac{1}{\mu_0} \nabla_{\perp} \cdot \vec{E} \right) = \frac{B}{c} \nabla_0 \cdot \vec{b} \cdot \nabla_{\perp} E_P \quad (13-169)$$

where  $E_P$  is the Pedersen conductance  $\int dz_{\parallel} e N \eta_{i0} / (1 + \eta_{i0}^2) B$ , which in this case is simply proportional to  $N(x, y, t)$  because of the assumed constant value of  $\eta_{i0} = \nu_{i0} / \omega_{ci}$ . Thus  $E_P$  can be replaced by  $N$  in Eq. 13-169.



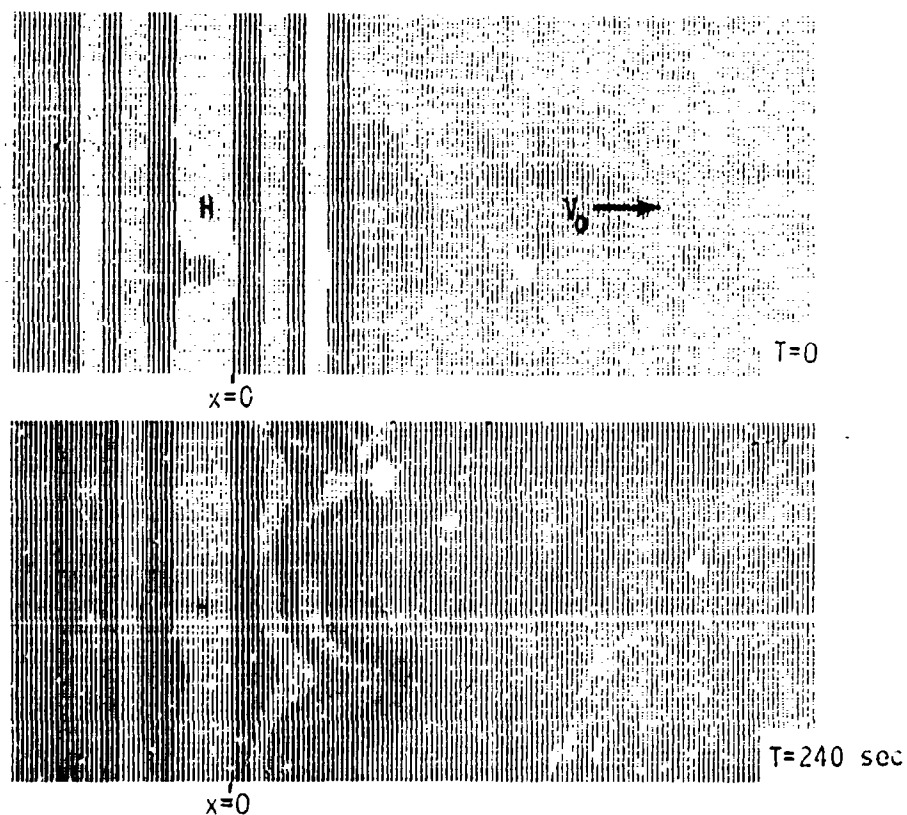


Figure 13-15. Nonlinear striation evolution in two-dimensional geometry. Contours of constant  $N$  are boundaries between light and dark areas. A maximum  $N/N_b$  of 11.32 relative to the background  $N_b$  occurs in the lightest band (labeled H). The magnetic field is out of the plane of the paper. A neutral wind  $\vec{V}_0$  of 100 m/sec is blowing in the positive  $x$ -direction. The  $x$ -extent is 49.9 km and the  $y$  extent is 12.4 km; the finite difference grid was  $162 \times 42$  points, and doubly periodic boundary conditions were used. The grid was shifted along the  $x$ -axis during the computation to keep the striations near the center of the grid; the  $x=0$  position indicates the original right-side location of the highest density  $N/N_b$  band.



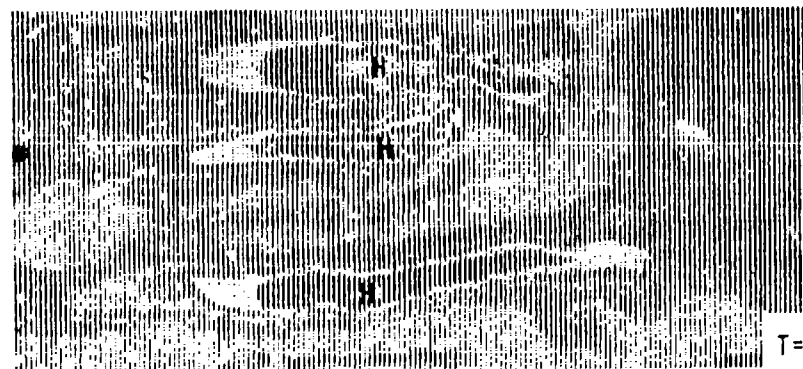
T=360 sec

x=0



T=480 sec

x=0



T=720 sec

x=0

Figure 13-15 (continued)

Electron number conservation was simplified to

$$\frac{\partial N}{\partial t} = - \nabla \cdot (\vec{V}_{\perp} N) + D_{\perp} \nabla_{\perp}^2 N \quad (13-170)$$

where  $D_{\perp}$  is the transverse-to-B diffusion coefficient, and  $\vec{V}_{\perp}$  is the  $E \times B$  drift velocity

$$\vec{V}_{\perp} = \frac{c}{B} \hat{b} \times \nabla_{\perp} \psi \quad (13-171)$$

No motion parallel-to-B was allowed, thus reducing the problem to two-dimensional motion in the x-y plane transverse-to-B. The unperturbed density profile was of the form

$$N = N_0 \{1 + 10 \exp[-(x/8\text{km})^2]\} \quad (13-172)$$

and initial random density perturbations of 3% amplitude were imposed. The resultant initial configuration is shown in the top panel of Fig. 13-15. Doubly periodic boundary conditions were used, so the configurations shown in Fig. 13-15 repeat infinitely in both the x- and y- directions.

If absolutely no density perturbations had been imposed on the unperturbed  $N$  of Eq. 13-172, the  $N(x,y)$  configuration would not change because  $\vec{J} \times \hat{b}$  forces associated with currents flowing in the y-direction would perfectly balance the neutral wind forces exerted on the plasma. As a result of the initial random density perturbations, however, striations are drawn out of the plasma by the neutral wind. These perturbations become quite non-linear by 240 sec, and evolve in a very complex manner by 720 sec as shown in Fig. 13-15.

McDonald points out that the above simplified set of equations has only three dimensional parameters: (1) the wind velocity  $V_0$  (cm/sec); (2) the diffusion coefficient  $D_{\perp}$  (cm<sup>2</sup>/sec); and (3) a typical density gradient length  $L = 1/(\nabla_{\perp} N)$  (cm). From these three parameters one can form a dimensionless ratio  $R$ :

$$R \equiv \frac{V_o L}{D_{\perp}} \quad (13-173)$$

McDonald points out that this is analogous to the dimensionless Reynolds number  $R_o \equiv VL/\nu$  which determines the transition from laminar to turbulent flow in hydrodynamics. He therefore proposes that Eq. 13-173 may be a key parameter for the striation bifurcation process. For the computed results displayed in Fig. 13-15, the ratio  $R$  was held constant at the value 800 by continuously adjusting the employed  $D_{\perp}$  value as the mean gradient length  $L$  of the evolving plasma decreased from 8.22 km to 1.21 km during the course of the computation.

When the computations were repeated with a sequence of other  $R$  values, it was found that in cases with  $R > 400$  the striations tended to bifurcate, whereas in cases with  $R < 400$  striations did not bifurcate to smaller sizes. Thus, McDonald proposes that the smallest striation length scale may be given approximately by:

$$L_{\min} \approx \frac{400 D_{\perp}}{V_o} \quad (13-174)$$

Further work on this interesting topic is underway.

### 13.8 GLOSSARY OF SYMBOLS FOR CHAPTER 13.

$\alpha$  = growth rate of the perturbation  $e^{\alpha t}$  ( $\text{sec}^{-1}$ )

$\alpha_r$  = real part of growth rate ( $\text{sec}^{-1}$ )

$\vec{B}$  = magnetic field vector (gauss)

$\vec{b} = \vec{B}/B$  = unit vector along field

$\vec{b} \cdot \nabla \vec{b}$  = field curvature vector ( $\text{cm}^{-1}$ )

$\beta$  = plasma beta =  $8\pi(P_i + P_e)/B^2$

$c$  = speed of light  $\approx 3 \times 10^{10} \text{ cm/sec}$

$d = 1 + \eta_{i0}^2$

$d/dt$  = convective time derivative defined by Eq. 13-125

$D = z_1 - z_0$  = thickness of density transition layer. See Fig. 13-12.

$D_{\perp}$  = transverse-to-B diffusion coef. =  $\frac{ck(T_i + T_e)}{cB} \frac{(v_{ei} + v_{eo})}{\Omega_e}$   
 $= \frac{4.9 \times 10^{-4} (T_i + T_e)}{B^2} \left[ \frac{43.7 N_i}{T_e^{3/2}} + 2.03 \times 10^{-10} T_e^{0.64} N_o \right] \frac{\text{cm}^2}{\text{sec}}$

$e$  = electron charge =  $4.8 \times 10^{-10}$  esu

$\vec{E}$  = electric field strength in esu (statvolt/cm)

$\eta$  = resistivity in emu =  $\frac{mc^2}{e^2 N_e} (v_{ei} + v_{eo})$

$$\approx \left[ \frac{1.55 \times 10^{14}}{T_e^{3/2}} + 722 \left( \frac{N_o}{N_e} \right) T_e^{0.64} \right] \text{cm}^2/\text{sec}$$

(Note that  $\vec{E}_{\text{resistive}} = \eta \vec{J}/c$  in our unit system)

$\eta_{ei} = v_{ei}/\Omega_e$ ;  $\eta_{eo} = v_{eo}/\Omega_e$ ;  $\eta_{i0} = v_{i0}/N_i$ ;  $\eta_{ji} = v_{ji}/N_j$

$f$  = finite-Larmor-radius factor =  $\frac{kT_i}{2\Omega_i (1 + v_{i1}^2/c^2)}$   $\frac{\text{gm cm}^2}{\text{sec}}$

$g$  = gravitational acceleration  $\approx 981/(r/r_{\text{earth}})^2$  cm/sec<sup>2</sup>

$\gamma$  = specific heat ratio. About 5/3 for atoms or 7/5 for molecules

$\vec{J} = eN_e(\vec{V}_i - \vec{V}_e)/c$  = current density in emu (abamp/cm<sup>2</sup>)

$\vec{J}_2 \equiv \vec{J} + \nabla \times (\vec{P}\vec{B}/B^2d)$ , see Eq. 13-121

$\vec{k}$  = perturbation wave vector ( $k = 2\pi/\lambda$ )

$k_c$  = critical wave number at which  $\alpha = 0$ .

$K_r$  = collisional radiative recombination coef.  $\approx 10^{-12}$  to  $10^{-11}$  cm<sup>3</sup>/sec

$K_o$  = ion-molecule reaction rate  $\approx 10^{-12}$  to  $10^{-10}$  cm<sup>3</sup>/sec

$\kappa$  = Boltzmann's constant =  $1.38 \times 10^{-16}$  erg/deg

$\mathcal{K}_o$  = neutral fluid thermal conductivity (Hirschfelder, Curtiss, Bird)

$$= \frac{25 \kappa N_o}{32(\gamma-1)(N_o \sigma_{oo} + N_i \sigma_{oi})} \sqrt{\frac{\pi \kappa T_o}{M_o}} \approx \frac{450 \sqrt{T_o}}{(1+4N_i/N_o)} \frac{\text{ergs}}{\text{deg cm sec}}$$

where  $\sigma_{oo} \approx 13 \times 10^{-16}$  cm<sup>2</sup> and  $\sigma_{oi} \approx 4\sigma_{oo}$

$\mathcal{K}_{1,\parallel}$  = electron thermal conductivity parallel to magnetic field (Spitzer)

$$\approx 0.4 \times 0.225 \times 20 \left(\frac{2}{\pi}\right)^{3/2} \frac{\kappa (\kappa T_e)^{5/2}}{m^{1/2} e^4 (1+v_{eo}/v_{ei}) \ell n \Lambda} \frac{\text{ergs}}{\text{deg cm sec}}$$

$\mathcal{K}_{1,\perp}$  = ion thermal conductivity perpendicular to magnetic field

$$= \frac{8(\pi M_i \kappa)^{1/2} N_i \ell^2 e^2 c^2 \ell n \Lambda}{3B^2 T_i^{1/2}} \frac{1}{1+v_{i\perp}^2/\Omega_i^2} \frac{\text{ergs}}{\text{deg cm sec}}$$

$\lambda$  = wavelength of perturbation (cm);  $\lambda = 2\pi/k$ ,  $\lambda_{\perp} = 2\pi/k_{\perp}$ ,  $\lambda_{\parallel} = 2\pi/k_{\parallel}$ ,  $\lambda_c = 2\pi/k_c$

$m$  = mass of electrons =  $9.1 \times 10^{-28}$  gms

$M_i$  or  $M_1$  = mass of ions =  $16 \times 1.66 \times 10^{-24}$  gms for  $O^+$

$M_o$  = mass of neutral atoms or molecules  $\approx 20 \times 1.66 \times 10^{-24}$  gms for air

$\eta_o$  = neutral fluid viscosity coefficient (Hirschfelder, Curtiss, and Bird)

$$= \frac{5\eta_o}{16(N_o \sigma_{oo} + N_i \sigma_{oi})} \sqrt{\frac{\pi \kappa T_o}{M_o}} \approx \frac{2 \times 10^{-5} T_o^{1/2}}{1+4N_i/N_o} \frac{\text{gm}}{\text{cm sec}}$$

$\mu_i$  = ion viscosity coefficient (Spitzer)

$$\approx \frac{0.205 N_i \kappa T_i \nu_{ii}}{\Omega_i^2 (1 + 0.146 \nu_{ii}^2 / \Omega_i^2)} = \frac{2.6 \times 10^{-23} N_i^2}{B^2 \sqrt{T_i} [1 + 4.5 \times 10^{-8} N_i^2 / T_i^3 B^2]} \frac{\text{gm}}{\text{cm sec}} \quad \text{for } O^+$$

$N = N_i = N_e$  = number density of ions or electrons ( $\text{cm}^{-3}$ )

$N_0$  = number density of neutral atoms or molecules ( $\text{cm}^{-3}$ )

$\nu_{ei}$  = electron-ion collision frequency (Longmire or Spitzer)

$$= \frac{4}{3} \left( \frac{2\pi}{m} \right)^{1/2} \frac{e^4 Z^2 N_i \ell n \Lambda}{(\kappa T_e)^{3/2}} \approx \frac{43.7 N_i}{T_e^{3/2}} \text{ sec}^{-1}$$

$\nu_{eo}$  = electron-neutral collision frequency (Eq. 5-31 of Ref. 13-27)

$$\approx 2.03 \times 10^{-10} T_e^{0.64} N_0 \text{ sec}^{-1} \quad \text{if } 100^\circ \text{K} < T_e < 100,000^\circ \text{K}$$

$\nu_{io}$  = ion-neutral collision frequency =  $s \rho_0$  (see  $s$  below)

$\nu_{ii}$  = ion-ion collision frequency (Spitzer)

$$= \frac{8 \times 0.714 \pi e^4 Z^4 N_i \ell n \Lambda}{M_i^{1/2} (3 \kappa T_i)^{3/2}} \approx \frac{N_i}{3 T_i^{3/2}} \text{ sec}^{-1} \quad \text{for } O^+$$

$\Omega_i$  = ion gyro frequency =  $eB/M_i c = 602B$  rad/sec for  $O^+$

$\Omega_e$  = electron gyro frequency =  $eB/mc = 1.76 \times 10^7 B$  rad/sec

$P_i, P_e$  = ion pressure, electron pressure ( $\text{ergs/cm}^3$ )

$P_0, P_i$  = neutral fluid pressure, ion-electron pressure ( $P_i + P_e$ )

$\Phi$  = potential function (see Eq. 13-115)

$q$  = solar photoionization rate ( $\text{electrons/cm}^3 \text{sec}$ )

$\vec{Q}$  = function defined in Eqs. 13-22 and 13-28

$\vec{R}$  = radius of curvature of field lines ( $\vec{R}/R^2 \equiv -\vec{b} \cdot \nabla \vec{b}$ )

$$R_g = \sqrt{\frac{\kappa(T_i + T_e)}{M_i \Omega_i^2}} = \text{ion thermal gyro radius (if } T_e = T_i)$$

$\rho_0$  = neutral fluid mass density ( $\text{gm/cm}^3$ ); also density of lower stratum

$\rho_1$  = ion-electron mass density ( $\text{gm/cm}^3$ ); also density of upper stratum

$\rho_i, \rho_e$  = mass densities of ions and electrons (gm/cm<sup>3</sup>)

$s$  = ion-neutral coupling constant =  $\langle \sigma V \rangle / (M_o + M_i)$

$$\approx \begin{cases} 2.5 \times 10^{13} \text{ cm}^3/\text{gm sec} & \text{for air ions} \\ 0.25 \times 10^{13} \text{ cm}^3/\text{gm sec} & \text{for Ba}^+ \text{ in air} \end{cases}$$

$\sigma_{||}$  = parallel-to-B conductivity =  $c/\eta$

$$= \frac{e^2 N_e}{mc(\nu_{ei} + \nu_{eo})} = \frac{e N_e}{B(\eta_{ei} + \eta_{eo})} \quad (\text{cm}^{-1})$$

$T_o, T_i$  = temperature of neutral fluid, and ion-electron fluid (°K)

$T_i, T_e$  = temperature of ions and electrons (°K)

$\vec{V}_o$  = velocity of neutral fluid; also velocity of lower stratum (cm/sec)

$\vec{V}_i$  = velocity of ion-electron fluid; also velocity of upper stratum

$\vec{V}_i, \vec{V}_e$  = velocity of ion and electron fluids (cm/sec)

$\vec{V}_s = (\vec{V}_o - \vec{V}_i)_\perp$  = ion-neutral slip velocity transverse-to-B

$\vec{V}$  = acceleration of fluid (cm/sec<sup>2</sup>)  $\equiv \partial \vec{V} / \partial t + \vec{V} \cdot \nabla \vec{V}$

$\vec{\xi} = \vec{\xi}(\vec{r}, t)$  = perturbation displacement vector (see Eq. 13-25).

$Z$  = charge state of ions = 1



## REFERENCES

- 13-1. Thomson, J. A., A Hydrodynamic Analog of Ionospheric Plasma Releases, PD 71-013, Physical Dynamics, Inc., October 1971.
- 13-2. Bernstein, I., E. Frieman, M. Kruskal, and R. Kulsrud, Proc. Roy. Soc. London A244, 17 (1958).
- 13-3. Rose, D. J. and M. Clark, Jr., Plasmas and Controlled Fusion, John Wiley & Sons, New York (1961).
- 13-4. Longmire, C. L., Elementary Plasma Physics, John Wiley & Sons, New York (1963).
- 13-5. Chandrasekhar, S., Hydrodynamic and Hydromagnetic Stability, Oxford University Press, London (1961).
- 13-6. Morse, P. M. and H. Feshbach, Methods of Theoretical Physics, McGraw-Hill Book Co., New York (1953).
- 13-7. Thompson, W. B., An Introduction to Plasma Physics, Second (Revised) Edition, Addison-Wesley, London (1964).
- 13-8. Linson, L. M., and J. B. Workman, "Formation of Striations in Ionospheric Plasma Clouds," J. of Geophysical Research (Space Physics), Vol. 75, pp. 3211-3219, 1970.
- 13-9. Gurevich, A. V., and E. E. Tsedilina, "Motion and Spreading of Inhomogeneities in a Plasma," Soviet Physics Uspekhi, Vol. 10, pp. 214-236 (1967).
- 13-10. Beer, Tom, Atmospheric Waves, John Wiley & Sons, New York (1974).
- 13-11. Spitzer, Jr., L., Physics of Fully Ionized Gases, Second Revised Edition, Interscience Publishers, New York, 1962.
- 13-12. Chapman, S., and T. G. Cowling, The Mathematical Theory of Non-Uniform Gases, Cambridge, 1960, p. 338.
- 13-13. Roberts, K. V., and J. B. Taylor, "Magnetohydrodynamic Equations for Finite Larmor Radius," in Physical Review Letters, Volume 8, pp. 197-198 (1962).

- 13-14. Banks, P. M., and G. Kockarts, Aeronomy, Part A and Part B, Academic Press, New York 1973.
- 13-15. DNA Reaction Rate Handbook, Second Edition, DNA 1948H, DASIAC (General Electric-TEMPO) 1972.
- 13-16. Hudson, M. K., and C. F. Kennel, "Linear Theory of Equatorial Spread F" in Journal of Geophysical Research, Volume 80, pp 4581-4590 (1975).
- 13-17. Goldman, S. R., Plasma Physics Mechanisms Relevant to Striation Structuring and Decay, DNA 4245T, JAYCOR, Feb. 1977.
- 13-18. Krall, H. A., and A. W. Trivelpiece, Principles of Plasma Physics, McGraw-Hill, New York, 1973.
- 13-19. Krall, H. A., "Drift Waves" in Advances in Plasma Physics, Volume 1, pp 153-199, Interscience Publishers, 1968.
- 13-20. Sedov, L. I., Similarity and Dimensional Methods in Mechanics, Academic Press (1959); Chapter IV, Section II.
- 13-21. Zabusky, N. J., J. H. Doles III, and F. W. Perkins, "Deformation and Striation of Plasma Clouds in the Ionosphere: 2. Numerical Simulation of a Nonlinear Two-dimensional Model," Journal of Geophysical Research, Vol. 78, pp 711-724 (1973).
- 13-22. Lloyd, K. H., and G. Haerendel, "Numerical Modeling of the Drift and Deformation of Ionospheric Plasma Clouds and Their Interaction with Other Layers of the Ionosphere," Journal of Geophysical Research, Vol. 78, pp 7389-7415 (1973).
- 13-23. Scannapieco, A. J., S. L. Ossakow, S. R. Goldman, and J. M. Pierre, "Plasma Cloud Late Time Striation Spectra," Journal of Geophysical Research, Vol. 81, pp 6037-6045 (1976).
- 13-24. Scannapieco, A. J., and S. L. Ossakow, "Nonlinear Equatorial Spread-F," Geophysical Research Letters, Vol. 3, p 451 (1976).
- 13-25. Doles III, J.H., and N.J. Zabusky, and F.W. Perkins, "Deformation and Striation of Plasma Clouds in the Ionosphere: 3. Numerical Simulations of a Multilevel Model with Recombination Chemistry," Journal of Geophysical Research, Vol. 81, pp 5987-6004 (1976).
- 13-26. McDonald, B. E., S. L. Ossakow, S. T. Zalesak, and N. J. Zabusky, "Determination of Minimum Scale Size in Plasma Cloud Striations," to be published in Proceedings of the 2nd Symposium on the Effect of the Ionosphere on Space Systems and Communications, Naval Research Laboratory, January 24-26, 1978.

- 13-27. Stoeckly, R. E., R. W. Stagat, and R. W. Kilb, Collisional Momentum and Energy Transfer Rates for Two-Fluid Nuclear-Burst Simulations, DNA 332/T, Mission Research Corporation, July 1975.
- 13-28. Kruskal, M., and N. Schwarzschild, "Some Instabilities of a Completely Ionized Plasma," Proceedings of the Royal Society, Vol. A223, 348-360 (1954).
- 13-29. Rosenbluth, M. N., and C. L. Longmire, "Stability of Plasmas Confined by Magnetic Fields," Annals of Physics, Vol. 1, 120. (1957).
- 13-30. Simon, A., "Instability of Partially Ionized Plasma in Crossed Electric and Magnetic Fields," The Physics of Fluids, Vol. 6, 382-388 (1963).
- 13-31. Kadomtsev, B. B., Plasma Turbulence, Academic Press, New York (1965).
- 13-32. Haerendel, G, R. Lüst, E. Rieger, "Motion of Artificial Ion Clouds in the Upper Atmosphere," Planetary Space Science, Vol. 15, pp 1-18 (1967).
- 13-33. Simon, A., "Growth and Stability of Artificial Ion Clouds in the Ionosphere," J. Geophysical Research, Vol. 75, 6287-6294 (1970).
- 13-34. Longmire, C. L., On the Motion of Artificial Ion Clouds, LANC-N-11, Los Alamos Nuclear Corporation, September 1970.
- 13-35. Thomson, J. A. L., "Quasi-steady Motions of Weakly Ionized Inhomogeneous Plasma Clouds in a Strong Magnetic Field," in Volume 3 (Theoretical Considerations) of Project Secede: 1970 Summer Study Proceedings, RADC TR-70-216, Stanford Research Institute, September 1970.
- 13-36. Volk, H. J., and G. Haerendel, "Striations in Ionospheric Ion Clouds," J. Geophysical Research, Vol. 76, 4541-4559 (1971).
- 13-37. Simon, A., and A. M. Sleeper, "Barium Cloud Growth in a Highly-Conducting Medium," J. Geophysical Research, Vol. 77, 2353-2358 (1972).
- 13-38. Perkins, F. W., R. J. Zabusky, J. H. Doles III, "Deformation and Striation of Plasma Clouds in the Ionosphere," Journal of Geophysical Research, Vol. 78, pp 697-709 (1973).
- 13-39. Perkins, F., "Spread F and Ionospheric Currents," Journal of Geophysical Research, Vol. 78, pp 218-226 (1973).

- 10-40. Sniou, J. A., and A. Simon, "Barium Cloud Growth and Striation in a Conducting Background," Journal of Geophysical Research, Vol. 79, pp 1895-1902 (1974).
- 13-41. Goldman, S. R., S. L. Ossakow, and D. L. Book, "On the Nonlinear Motion of a Small Barium Cloud in the Ionosphere," Journal of Geophysical Research, Vol. 79, pp. 1471-1477, (1974).
- 13-42. Scannapieco, A. J., S. L. Ossakow, D. L. Book, B. E. McDonald and S. R. Goldman, "Conductivity Ratio Effects on the Drift and Deformation of F-Region Barium Clouds Coupled to the F-Region Ionosphere," Journal of Geophysical Research, Vol. 79, pp. 2913-2918 (1974).
- 13-43. Ott, F., and P. L. Farley, "The k-Spectrum of Ionospheric Irregularities," Journal of Geophysical Research, Vol. 79, pp 2469-2472, (1974).
- 13-44. Eognien, T. D., and J. Heinstock, "Theory of the Nonlinear Spectrum of the Gradient Drift Instability in the Equatorial Electrojet," Journal of Geophysical Research, Vol. 79, pp. 4733-4746 (1974).
- 13-45. Perkins, F. W., and J. M. Bales III, "Velocity Shear and the ExB Instability," Journal of Geophysical Research, Vol. 80, pp 211-214 (1975).
- 13-46. Goldman, S. R., A. J. Scannapieco, L. Baker, and S. L. Ossakow, "Coupled Barium Cloud-Ionosphere Systems, 4. Striation Penetration into an Inhomogeneous Ionosphere," NRL Memo Rep. 3083, Naval Research Laboratory, Washington, D. C. July 1975.
- 13-47. Francis, S. H., and F. W. Perkins, "Peculiarities of Striation Scale Sizes for Plasma Clouds in the Ionosphere," Journal of Geophysical Research, Vol. 80, pp 3111-3120 (1975).
- 13-48. Ossakow, S. L., A. J. Scannapieco, S. R. Goldman, D. L. Book and B. E. McDonald, "Theoretical and Numerical Studies of Ionospheric Inhomogeneities Produced by Plasma Clouds", in Effect of the Ionosphere on Space Systems and Communications, edited by S. M. Goldman, U. S. Government Printing Office, Washington, D. C., (1975), pp. 117-122.
- 13-49. Hudson, R. A., and J. T. Farley, "The Collisional Perturbation in a Partly-Ionized Plasma," Journal of Plasma Physics, Vol. 14, pp 135-147, (1975).

## CHAPTER 14

### PROPAGATION OF ELECTROMAGNETIC WAVES

John Ise, Jr.

General Research Corporation

August 1973

(Section 14.6 added February 1978)

## TABLE OF CONTENTS

	<u>PAGE</u>
14.1 INTRODUCTION	710
14.2 PROPAGATION OF ELECTROMAGNETIC WAVES THROUGH FREE SPACE	716
14.2.1 Energy Propagation	716
14.2.2 Free Space Solutions of Maxwell's Equations	718
14.2.3 The Radiation Zone - Plane Waves	720
14.3 THE CONSTITUTIVE RELATIONS IN A MAGNETO-PLASMA	726
14.3.1 The Permittivity Tensor	726
14.3.2 Complex Permittivity in a "Cold" Plasma	728
14.3.3 Validity Criteria	732
14.4 PROPAGATION OF ELECTROMAGNETIC WAVES IN PLASMAS	738
14.4.1 Isotropic Homogeneous Plasma	738
14.4.2 Homogeneous Magnetoactive Plasmas	741
14.4.3 Inhomogeneous Plasmas	743
14.5 SUMMARY	751
14.6 ADDENDUM: SATELLITE COMMUNICATIONS	754
14.6.1 Introduction	754
14.6.2 The Effect of Gaussian Irregularities	756
14.6.3 The Effect of More Realistic Irregularities	762
REFERENCES	765

## 14.1 INTRODUCTION

In this chapter we shall consider the propagation of radio and radar waves under typical conditions, i. e., when propagation paths traverse the earth's atmosphere, including the ionosphere and regions that have been disturbed by nuclear detonations. The propagation medium can affect the signals by decreasing their magnitude, by increasing the effective noise level, and by distorting the signal in various ways. We shall derive numerical expressions for the magnitude of each of these effects.

The propagation of electromagnetic (EM) waves is governed by Maxwell's equations. These describe both the propagation of the wave and its interaction with the medium through which it is propagating. Before presenting a detailed discussion of Maxwell's equations and their solutions, however, a simplified introduction for those totally unfamiliar with the subject appears to be desirable. The simplest example of an EM wave is a plane-polarized plane wave propagating in free space. In this case the wave comprises two components: an electric field and a magnetic field. The fields are mutually perpendicular and both are perpendicular to the direction of propagation. The magnitudes of the fields vary both in space and time, but the direction, which they are perpendicular to everywhere the wave is, that is the direction of the wave propagation, is everywhere the same. The magnitudes and direction of the fields in a plane wave are everywhere the same on any plane perpendicular to the direction of propagation, that is the surface of the wave plane wave.

In the following sections it is shown that for propagation in a vacuum the electric field satisfies the wave equation

$$\nabla^2 \vec{E} - \frac{1}{c^2} \frac{\partial^2 \vec{E}}{\partial t^2} = 0 \quad (11-1)$$

Since the wave is a plane wave, the only variation with space must be with the coordinate parallel to the direction of propagation, which we take to be the  $z$  axis. Furthermore, since the wave is plane-polarized the direction of  $\vec{E}$  is everywhere the same, and this direction is perpendicular to the  $z$  axis. We are free to call this the  $x$  direction, so  $\vec{E} = E(z,t)\hat{e}_x$  where  $\hat{e}_x$  is a unit vector in the  $x$  direction. Since  $\hat{e}_x$  varies neither with space nor with time, it drops out of Eq. 11-1 and we have:

$$\frac{\partial^2 E}{\partial z^2} - \frac{1}{c^2} \frac{\partial^2 E}{\partial t^2} = 0 \quad (11-2)$$

Thus, we have replaced the vector equation (11-1) by the scalar equation (11-2), a procedure not possible in general, as will be shown in following sections. Similar remarks apply to the magnetic field, but  $\vec{B}$  is in the  $y$  direction, since it must be perpendicular to both  $\vec{E}$  and the direction of propagation. Thus,  $\vec{B} = B(z,t)\hat{e}_y$ , and  $B$  is also a solution of Eq. 11-2.

It is quite apparent that any function of the form  $E = E_0 f(\omega t - kz)$ , where  $E_0$  is constant, is a solution of Eq. 11-2 since  $\frac{\partial^2 E}{\partial z^2} = -k^2 E$  and  $\frac{\partial^2 E}{\partial t^2} = -\omega^2 E$ , where  $f''$  denotes the second derivative of  $f$  with respect to its argument. In particular, there exist monochromatic solutions:

$$E = E_0 e^{-i(\omega t - kz)} \quad (11-3)$$

where  $\omega = 2\pi\nu$  and

$$k = \frac{\omega}{c} = \frac{2\pi}{\lambda} \quad (11-4)$$



In these equations  $\omega$  is the angular frequency of the wave ( $\text{rad sec}^{-1}$ ),  $\lambda$  is the wavelength, and  $k$  is called the "propagation constant." The negative sign in the exponent in 14-3 defines a wave traveling in the positive  $z$  direction, while the positive sign defines a wave traveling in the negative  $z$  direction.

Now suppose that a wave such as that defined in 14-3 is propagating, not in *vacuo*, but through an ionized plasma instead. Its propagation characteristics will be altered as a consequence of the interaction between the EM field and the charged particles in the plasma. To get an idea of the effects of this interaction, we shall study the following simple model:

- 1) The positive ions are infinitely massive, and hence are unaffected by the EM wave.
- 2) The much less massive electrons move under the influence of the electric field. We assume the electrons move freely for one mean free path, and then are scattered. The scattering destroys the correlation between the direction of motion of the electrons and the direction of the electric field, and thus has the effect of a damping force. Heating of the plasma by the field is neglected, however.
- 3) No external macroscopic magnetic fields are present.
- 4) The motion of the electrons is nonrelativistic, so their interaction with the  $B$  component of the EM wave can be neglected.

The damping force referred to above is the time rate of change due to collisions of the velocity induced by the electric field. Since each collision is assumed to destroy completely the coherence of the motion, this force is just the momentum of an electron divided by the time between collisions. We define the effective collision frequency  $\nu$  to be:

$$\nu_{\text{eff}} = \tau^{-1} = \bar{\nu}/\lambda_c \quad (14-5)$$

where  $\lambda_c$  is the collision mean free path and  $\bar{\nu}$  is the mean of the absolute value of the thermal velocity. Then the drag force  $F_D$  is

$$F_D = -m\dot{x}\nu_{\text{eff}} \quad (14-6)$$

where  $m$  is the mass of the electron and the dot denotes differentiation with respect to time of the field-induced displacement  $x$  of the electron. We now have for the equation of motion of the electron

$$m\ddot{x} + \nu_{\text{eff}}m\dot{x} = -eE = -eE_0 e^{i(kz - \omega t)} \quad (14-7)$$

This equation is readily solved to yield the steady state solution

$$x = \frac{e(\omega - i\nu_{\text{eff}})}{m\omega(\omega^2 + \nu_{\text{eff}}^2)} E \quad (14-8)$$

The polarization density  $p$  is

$$p = -N_e ex = -N_e \frac{e^2(\omega - i\nu_{\text{eff}})}{m\omega(\omega^2 + \nu_{\text{eff}}^2)} E = \alpha E \quad (14-9)$$

where  $\alpha$  is by definition the polarizability of the medium and  $N_e$  is the electron number density.

It is shown in many texts on electricity and magnetism, e.g., Ref. 14-1, that the index of refraction  $n$  is related to the polarizability through the equation

$$n = (1 + 4\pi\alpha)^{1/2} \quad (14-10)$$

Hence,

$$n = \left[ 1 - \frac{4\pi N_e e^2 (\omega - i\nu_{\text{eff}})}{m\omega(\omega^2 + \nu_{\text{eff}}^2)} \right]^{1/2} = \left[ 1 - \frac{p^2 (\omega - i\nu_{\text{eff}})}{\omega(\omega^2 + \nu_{\text{eff}}^2)} \right]^{1/2} \quad (14-11)$$

where we have introduced the plasma frequency  $\omega_p$  defined by

$$\omega_p^2 = \frac{4\pi N e^2}{m} \quad (14-12)$$

In the presence of a refractive medium, the dispersion relation, Eq. 14-4, is replaced by the generalized version

$$k = \frac{n\omega}{c} \quad (14-13)$$

If we define  $k_0 = \omega/c$ , then Eq. 14-13 can be written  $k = nk_0$ . The plane wave solutions 14-3 are rewritten accordingly to read

$$E = E_0 e^{-i(\omega t + nk_0 z)} \quad (14-14)$$

The meaning of the plasma frequency is made clear by considering Eqs. 14-11 and 14-14 in the limit where  $\nu_{\text{eff}} \ll \omega$ . In this case,  $n = (1 - \omega_p^2/\omega^2)^{1/2}$ . If  $\omega > \omega_p$ ,  $n$  is real and the polarization of the dielectric produces a phase shift of the wave relative to the phase of a wave propagating in vacuum. If  $\omega < \omega_p$ ,  $n$  is pure imaginary and any wave traversing the medium will be damped exponentially. Since we have assumed  $\nu_{\text{eff}} = 0$ , there are no losses in the medium. Hence the case  $\nu_{\text{eff}} \ll \omega < \omega_p$  corresponds to total reflection of an incoming wave at the interface between the plasma and the ambient medium.

Likewise, a transmitter imbedded in a plasma with  $\omega_p > \omega$  will have difficulty transmitting a signal. The signal falls off as  $e^{-|n|k_0 z}$ , so the amplitude is small for  $z \gg \lambda_0/2|n|$ , where  $\lambda_0$  is the free-space wavelength, i. e.,  $\lambda_0 = 2\pi/k_0$ . If the dimensions of the plasma are very large compared with  $\lambda_0/2|n|$ , very little energy can be radiated to the outside world.

We wish to stress the fact that the exponential damping in the case  $\nu_{\text{eff}} \ll \omega < \omega_p$  does not imply that energy is being absorbed by the plasma. Rather, the energy is being diverted or returned to its source. This

manifests itself as reflection in the case of a wave incident on the plasma, and as an impedance mismatch in the case of an antenna imbedded in the plasma.

When  $\nu_{eff} \neq 0$ ,  $n$  is either pure real or pure imaginary, depending on whether  $\omega > \omega_p$  or  $\omega < \omega_p$ , as discussed above. When the role of  $\nu_{eff}$  cannot be neglected,  $n$  is complex. To see the significance of this, suppose that  $|\nu_p^2/\omega^2 - i\nu_{eff}/\omega(\omega^2 - \nu_{eff}^2)| \ll 1$ . Then the square root in Eq. 14-11 can be expanded to yield

$$n \approx 1 - \frac{i}{2} \left[ \frac{\nu_p^2/\omega^2 - i\nu_{eff}/\omega(\omega^2 - \nu_{eff}^2)}{1 - \nu_{eff}^2/\omega^2} \right] \quad (14-15)$$

In this expression the term proportional to  $\nu_p^2/\omega^2$  in the numerator describes a change in the real part of the index of refraction, and leads to such effects as reflection, refraction, and phase shifts. The imaginary part, proportional to  $\nu_{eff}$ , describes true absorption of energy by the plasma. In this case a wave can traverse the plasma, but its amplitude decreases exponentially as it does so. We note that for a given value of  $\omega$ , the absorption term increases monotonically with increasing  $\nu_{eff}$ , rises to a maximum for  $\nu_{eff} = \omega$ , and decreases thereafter, approaching a variation as  $\nu_{eff}^{-1}$  for  $\nu_{eff} \gg \omega$ .

In the preceding paragraphs we have attempted to outline the effects on EM propagation of the presence of a plasma. The discussion should be considered a qualitative one, however, and any quantitative results are in order. Rather than listing a list of facts, we now turn to a detailed, rigorous discussion of the effects based on Maxwell's equations.

The chapter is organized into five main sections. In the first section we discuss in detail the propagation of electromagnetic waves. In the second section we will Maxwell's equations and give, as examples, of their solutions in the constant density approximation, which is nearly always valid for

the waves of interest. The second section discusses the general constitutive equations connecting the various field vectors in an ionized magnetoplasma, and gives a brief review of those plasma parameters relevant to the formulation of these constitutive equations. The third section is concerned with the propagation of plane waves in uniform "cold" magnetoplasmas (spatial dispersion negligible) with a short discussion of more general cases. The fourth section deals with wave propagation in nonuniform plasmas, and the final section quantifies the various propagation effects for typical systems.

## 14.2 PROPAGATION OF ELECTROMAGNETIC WAVES THROUGH FREE SPACE

### 14.2.1 ENERGY PROPAGATION

The basic equations governing the vacuum propagation of the vectorial electromagnetic fields are the Maxwell equations which (in Gaussian units) are (e.g. Refs. 14-1 through 14-4)

$$\left. \begin{aligned} \vec{\nabla} \times \vec{E} &= -\frac{1}{c} \frac{\partial \vec{B}}{\partial t} \equiv -\frac{1}{c} \vec{B} \\ \vec{\nabla} \times \vec{H} &= \frac{1}{c} \frac{\partial \vec{D}}{\partial t} + 4\pi \vec{j} \\ \vec{\nabla} \cdot \vec{D} &= 4\pi \rho \\ \vec{\nabla} \cdot \vec{B} &= 0 \end{aligned} \right\} \quad (14-16)$$

In uniform media these may be supplemented by the usual constitutive relations

$$\vec{D} = \epsilon \vec{E} = \vec{E} + 4\pi \vec{p} \quad \vec{B} = \mu \vec{H} \quad \vec{j} = \sigma \vec{E} \quad (14-17)$$

$\vec{p}$  is the polarization density induced by the field and we have assumed no external current sources or convective currents are present. In *vacuo*,  $\vec{j} = \vec{p} = 0$ , and in our units  $\epsilon = \mu = 1$ . We nevertheless carry the quantities  $\epsilon$  and  $\mu$  formally in our equations, for generalization in the next section.

The transmission of energy by an electromagnetic wave may be understood by considering the Poynting vector  $\vec{P}$ , defined by

$$\vec{P} \equiv \frac{c}{4\pi} (\vec{E} \times \vec{H}) . \quad (14-18)$$

From the first two Eqs. of 14-16

$$\vec{\nabla} \cdot \vec{P} \equiv \frac{c}{4\pi} (\vec{H} \cdot \vec{\nabla} \times \vec{E} - \vec{E} \cdot \vec{\nabla} \times \vec{H}) = - \frac{1}{4\pi} (\vec{E} \cdot \vec{\nabla} \times \vec{H} + \vec{H} \cdot \vec{\nabla} \times \vec{E}) - c\vec{E} \cdot \vec{j} \quad (14-19)$$

We note that the energy densities stored in the electric and magnetic fields are  $\frac{\vec{E} \cdot \vec{D}}{8\pi}$  and  $\frac{\vec{H} \cdot \vec{B}}{8\pi}$ , respectively, so the various terms on the right hand side of Eq. 14-19 can be identified as the rates of change of these densities together with a term describing ohmic heating losses. Taking the volume integral of Eq. 14-19 and applying the divergence theorem, we find

$$- \frac{\partial}{\partial t} \int d\vec{x} \left( \frac{\vec{B} \cdot \vec{H} + \vec{D} \cdot \vec{E}}{8\pi} \right) = c \int \vec{E} \cdot \vec{j} d\vec{x} + \int \vec{P} \cdot d\vec{S} \quad (14-20)$$

where the first integral on the right is over a volume and the second is over a surface that bounds it. The left side of Eq. 14-20 is the rate of decrease of the sum of the electric and magnetic field energies while the first term on the right represents the work done by the electric forces per unit time on the moving charges which constitute the current  $\vec{j}$  (in Gaussian units the dimensions of  $\vec{j}$  are abamp/cm<sup>2</sup>, while  $\vec{E}$  is measured in esu). The last term will fail to vanish, for an arbitrarily large enclosing surface  $S$ , only for fields  $\vec{E}$  and  $\vec{H}$  which fall off no faster than  $1/r$  at large distances, and for such "radiation" fields the vector  $\vec{P}$  thus can be considered to represent the rate of flow of electromagnetic field energy per unit area across a given surface. As is well known, this representation is not unique, since it also holds if  $\vec{P}$  is replaced by any other vector differing from  $\vec{P}$  by the curl of an arbitrary vector function of the space coordinates.

## 14.2.2 FREE SPACE SOLUTIONS OF MAXWELL'S EQUATIONS

Although Maxwell's equations intermingle the various components of the vectors  $\vec{E}$  and  $\vec{H}$ , as pointed out earlier, a scalar equation for each rectangular field component can be derived by eliminating all the other components from Maxwell's equations. Thus assuming  $\mu = \text{constant}$ , applying the curl operator to the second Eq. 14-16, and using the first equation plus the vector identity  $\vec{\nabla} \times (\vec{\nabla} \times \vec{H}) = \vec{\nabla} (\vec{\nabla} \cdot \vec{H}) - \nabla^2 \vec{H} = -\nabla^2 \vec{H}$ , we obtain

$$\left( \nabla^2 - \frac{\epsilon \mu}{c^2} \frac{\partial^2}{\partial t^2} \right) \vec{H} = -4\pi \vec{\nabla} \times \vec{J} \quad (14-21)$$

with a similar equation for the components of  $\vec{E}$ . (The solutions for the individual field components  $\vec{E}$  and  $\vec{H}$  from these equations are not, of course, independently specifiable because of their coupling through Maxwell's equations.)

The significance of the wave velocity  $v = c/\sqrt{\epsilon\mu}$  is immediately apparent from Eq. 14-21 and the right hand side of the equation represents the sources of the fields. We now introduce two other quantities that will prove useful in obtaining general solutions of the Maxwell equations. The first, the vector potential  $\vec{A}$ , takes account of the fourth relation (Eq. 14-16), by letting

$$\vec{B} = \vec{\nabla} \times \vec{A} \quad (14-22)$$

Eq. 14-22 and the first relation of Eq. 14-16 are likewise satisfied by defining the scalar potential  $\phi$  by

$$\vec{E} = -\vec{\nabla} \phi - \frac{1}{c} \frac{\partial \vec{A}}{\partial t} \quad (14-23)$$

From Eqs. 14-22 and 14-23 and the second of Eqs. 14-16, we obtain

$$\vec{\nabla} \cdot \vec{A} + \frac{1}{c^2} \frac{\partial^2 \phi}{\partial t^2} = \vec{\nabla} \cdot \left( \vec{\nabla} \times \vec{A} + \frac{1}{c} \frac{\partial \vec{A}}{\partial t} \right) = -4\pi \vec{\nabla} \cdot \vec{J} \quad (14-24)$$

Since Eq. 14-22 still leaves the vector potential  $\vec{A}$  undefined to within the gradient of some arbitrary function, this latter function may be fixed by setting the term in brackets in Eq. 14-24 equal to zero. This Lorentz condition assures a relativistically covariant relation between the scalar and vector potentials, (i.e., makes  $\vec{A}, \phi$  a four vector) and makes both satisfy the same type of wave equation as that obeyed by  $\vec{E}$  and  $\vec{H}$ , Eq. 14-21. Thus the Lorentz condition, together with 14-23, transforms the third relation of Eq. 14-10 into

$$\nabla^2 \phi - \frac{1}{v^2} \ddot{\phi} = - \frac{4\pi q}{\epsilon} \quad (14-25)$$

The above equations 14-21, 14-24, and 14-25 are all of the same form

$$\square u(\vec{x}, t) - \frac{1}{v^2} \ddot{u} = -g(\vec{x}, t) \quad (14-26)$$

where  $\square$  is the d'Alembertian operator,  $\nabla^2 - \frac{1}{v^2} \frac{\partial^2}{\partial t^2}$ . The solution of this equation (e.g., Refs. 14.1-14.3) is easily shown, by analogy to Poisson's equation, to be

$$u(\vec{x}, t) = \frac{1}{4\pi} \int \frac{g(\vec{x}', t - |\vec{x}' - \vec{x}|/v)}{|\vec{x}' - \vec{x}|} d\vec{x}' \quad (14-27)$$

where the retarded time  $t - |\vec{x}' - \vec{x}|/v$  defines the time at which the time varying currents and charges (analogous, in Eqs. 14-21, 14-24, and 14-25, to the function  $g$  in the integrand of Eq. 14-27) are introduced into the integration.

Thus the solutions for the vector and scalar potentials  $\vec{A}$  and  $\phi$ , from which the field vectors  $\vec{E}$  and  $\vec{H}$  are derived immediately in Eqs. 14-22 and 14-23, are

$$\vec{A}(\vec{x}, t) = \frac{1}{4\pi} \int \frac{\vec{j}(\vec{x}', t - |\vec{x}' - \vec{x}|/v)}{|\vec{x}' - \vec{x}|} d\vec{x}' \quad (14-28)$$



$$\phi(\vec{x}, t) = \frac{1}{c} \int d\vec{x}' \frac{[\rho(\vec{x}')] }{|\vec{x} - \vec{x}'|} \quad (14-29)$$

where the square brackets [ ] indicate that the variables within the brackets are to be evaluated at the retarded time  $t - |\vec{x} - \vec{x}'|/c$ . These equations then give the formal solution to Maxwell's equations as an integral over the region containing currents and charges, the integrals at each source point  $\vec{x}'$  being evaluated at an earlier time corresponding to light travel time, at velocity  $c$ , to the field point  $\vec{x}$ . These "retarded" potentials may be understood in terms of information-collecting spheres, concentric about the field point  $\vec{x}$ , converging radially with velocity  $c$ , and sampling each source point  $\vec{x}'$  at a time earlier than the time of interest by an amount  $|\vec{x} - \vec{x}'|/c$ , the time necessary for the sphere through  $\vec{x}'$  to converge on the field point  $\vec{x}$ .

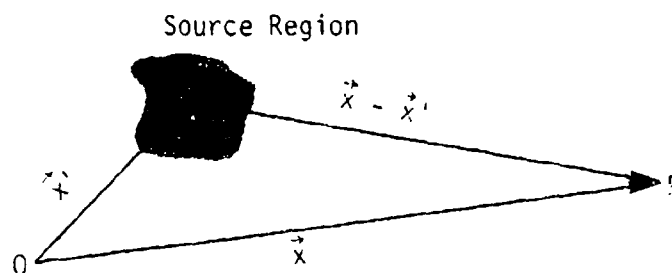


Figure 14.1 Geometry of field point (P), origin (O) and source region.

### 14.2.3 THE RADIATION ZONE - PLANE WAVES

For any distribution of charges and currents we can make a Fourier analysis over time and consider each Fourier component separately. Thus we assume, for a radiation pulse finite in time,

$$\vec{A}(\vec{x}, t) = \int d\omega \vec{A}_\omega(\vec{x}) e^{-i\omega t} \quad (14-30)$$

where the Fourier component  $\vec{A}_\omega$  is found by taking the Fourier transform of Eq. 14-28 (for details see Ref. 14-6, p. 1362).

$$\vec{A}_\omega(\vec{x}) = \mu \int \vec{j}_\omega(\vec{x}') \frac{e^{ikr}}{r} d\vec{x}', \quad (14-31)$$

where  $r = |\vec{x} - \vec{x}'|$ . The corresponding Fourier component of the magnetic field,  $\vec{B}_\omega$ , is, from Eq. 14-22

$$\vec{B}_\omega(\vec{x}) = \nabla \times \int \vec{j}_\omega(\vec{x}') \frac{e^{ikr}}{r} d\vec{x}' \quad (14-32)$$

where it must be remembered that the operator  $\vec{\nabla}$  operates on the field coordinates  $\vec{x}$ .

Since  $\vec{x}$  only occurs in expressions involving  $|\vec{x} - \vec{x}'|$ ,  $\vec{\nabla}$  can be replaced by  $\vec{\nabla}'$  and taken inside the integral, although of course it does not operate on  $\vec{j}_\omega(\vec{x}')$ . Thus we can write

$$\begin{aligned} \vec{B}_\omega &= -\mu \int \vec{j}_\omega(\vec{x}') \cdot \vec{\nabla}' \left( \frac{e^{ikr}}{r} \right) d\vec{x}' \\ &= -\mu \left\{ \int \frac{\vec{j}_\omega(\vec{x}') \cdot \vec{r}}{r^3} e^{ikr} d\vec{x}' - ik \int \frac{\vec{j}_\omega(\vec{x}') \cdot \vec{r}}{r^2} e^{ikr} d\vec{x}' \right\} \end{aligned} \quad (14-33)$$

The first term is merely the retarded form of the static field, and falls off as  $r^{-2}$ . This term, which dominates close to the source distribution of  $\vec{j}$ , is called the "induction field," but from the arguments cited after Eq. 14-20 this term contributes nothing to the energy radiated. The radiated energy must originate in the last term (and the corresponding term for  $\vec{E}$ ), which falls off as  $r^{-1}$ , and is called the "radiation field." The reconstitution of the various Fourier components  $\vec{B}_\omega$  then gives

$$\begin{aligned}\vec{B}(\vec{x}, t) &= \int d\omega \vec{B}_\omega(\vec{x}) e^{-i\omega t} \\ &= \mu \int \left( \frac{[\dot{\vec{j}}] \times \vec{r}}{r^3} + \frac{1}{c} \frac{[\vec{j}] \times \vec{r}}{r^2} \right) d\vec{x}',\end{aligned}\quad (14-34)$$

$$\text{where } [\dot{\vec{j}}(\vec{x}')] = \int -i\omega \vec{j}_\omega(\vec{x}') e^{i(kr - \omega t)} d\omega \quad (14-35)$$

is the time derivative of the current at the retarded time.

The Fourier component of the electric field may be computed from Eq. 14-23 in exactly the same manner (e.g., Ref. 14-1, p. 247), and contains three terms

$$\begin{aligned}\vec{E}_\omega(\vec{x}) &= \frac{1}{\epsilon} \int \frac{\rho_\omega \vec{r}}{r^3} e^{ikr} d\vec{x}' + \frac{1}{\epsilon} \int [(\vec{j}_\omega \cdot \vec{r}) \vec{r} - \vec{r} \times (\vec{j}_\omega \times \vec{r})] \frac{e^{ikr}}{r^4} d\vec{x}' \\ &\quad + \frac{ik}{\epsilon} \int [\vec{r} \times (\vec{j}_\omega \times \vec{r})] \frac{e^{ikr}}{r^3} d\vec{x}'\end{aligned}\quad (14-36)$$

where the first term is simply the retarded Coulomb field, the second is the induction field and the last term the true radiation field. The Fourier components  $[\rho_\omega]$  and  $[\vec{j}_\omega]$  are related by the continuity equation for charge conservation

$$\vec{\nabla} \cdot \vec{j}_\omega - ik\rho_\omega = 0 \quad (14-37)$$

Two fundamental properties of the radiation field in isotropic media appear immediately from Eq. 14-35 and Eq. 14-36, namely

1. the electric field, the magnetic field and the radius vector  $\vec{r}$  form an orthogonal triad of mutually perpendicular vectors, and in view of the definition Eq. 14-18 of the Poynting vector, the energy flow is outward from the source region along the radius vector  $\vec{r}$ .
2. the field amplitudes both fall off as  $r^{-1}$ . If the source dimensions are of order  $d \ll \lambda = 2\pi v/\omega$ , as is often the

case for communications antennas, there are three spatial regions of interest:

the near (static) zone	$d \ll r \ll \lambda$
the induction zone	$d \ll r \sim \lambda$
the radiation zone	$d \ll \lambda \ll r$

The fields have very different properties in these three regions, as seen from Eq. 14-36.

On the other hand, if  $d \gg \lambda$ , which is typical of radar antennas, conditions are quite different. One may properly ask the distance  $r$  from the source distribution to which it is necessary to go before the radiation field (the last term in Eq. 14-33 and 14-36) becomes a good approximation to the total field. Expansion of the integrand in the terms of Eq. 14-36 in powers of  $r^{-1}$  leads to three conditions  $kr \gg 1$ ,  $d \ll r$ , and  $kd^2 \ll r$ . The first two are obvious, that the distance be large compared to both the wavelength and the linear dimensions of the source. The third, perhaps less obvious, states that for source regions larger than a wavelength, the "Rayleigh distance"  $kd^2 = 2\pi d^2/\lambda$  is the factor that determines the range beyond which the radiation field is a good approximation to the total field. The significance of this Rayleigh distance is clear for a radar antenna, since it is the distance along the antenna axis at which the center and edge are out of phase by 0.5 radian. For typical radars

wavelength	$3 \text{ cm} < \lambda < 100 \text{ cm}$
linear size	$d \lesssim 3 \times 10^3 \text{ cm}$
beam width	$\lambda/d \gtrsim .01 \text{ rad}$
Rayleigh distance	$kd^2 \lesssim 20 \text{ km}$

We may therefore consider, for the purposes of this chapter, that typical distances are always in the radiation or wave zone, and we turn now to a discussion of plane wave propagation in isotropic media.

We may assume, without loss of generality, that

$$\left. \begin{aligned} \vec{E}(\mathbf{x}, t) &= \hat{e}_1 E_0 e^{i(\vec{k} \cdot \vec{x} - \omega t)} \\ \vec{B}(\mathbf{x}, t) &= \hat{e}_2 B_0 e^{i(\vec{k} \cdot \vec{x} - \omega t)} \end{aligned} \right\} \quad (14-38)$$

where  $\hat{e}_1$  and  $\hat{e}_2$  are two constant unit vectors and  $E_0$ ,  $B_0$  are complex amplitudes constant in space and time. In the absence of charges and currents, i.e., far from any source regions, both  $\rho$  and  $\vec{j}$  are zero, and the vanishing of the divergence of  $\vec{E}$  and  $\vec{B}$  (from Eqs. 14-16) demands that

$$\hat{e}_1 \cdot \vec{k} = \hat{e}_2 \cdot \vec{k} = 0 \quad (14-39)$$

so that, as already noted,  $\vec{E}$  and  $\vec{B}$  are both perpendicular to the direction of propagation  $\vec{k}$ . Substitution of Eq. 14-38 into the first relation Eq. 14-10 gives

$$i[(\vec{k} \times \hat{e}_1)E_0 - \frac{\omega}{c} \hat{e}_2 B_0] e^{i(\vec{k} \cdot \vec{x} - \omega t)} = 0 \quad (14-40)$$

which has the solution

$$\hat{e}_2 = \frac{\vec{k} \times \hat{e}_1}{k} \quad (14-41)$$

$$B_0 = \sqrt{\mu\epsilon} E_0 \quad (14-42)$$

so that  $(\hat{e}_1, \hat{e}_2, \vec{k})$  form a set of orthogonal vectors and  $\vec{E}$  and  $\vec{B}$  are in phase and in constant ratio for isotropic media.

Clearly the wave described by Eq. 14-38 is plane polarized with electric polarization vector  $\hat{e}_1$ . A general state of polarization is described by a linear combination of two such waves with polarization vectors  $\hat{e}_1$  and  $\hat{e}_1'$ , where  $\hat{e}_1 \perp \hat{e}_1'$ , and amplitudes  $\vec{E}_0$  and  $\vec{E}_0'$ . These latter quantities, being complex numbers, allow the possibility of a phase difference between the two waves. Thus a general solution for a plane wave propagating in the direction  $\vec{k}$  is

$$\vec{E}(\vec{x}, t) = (\hat{e}_1 \vec{E}_0 + \hat{e}_1' \vec{E}_0') e^{i(\vec{k} \cdot \vec{x} - \omega t)} \quad (14-43)$$

If  $\vec{E}_0$  and  $\vec{E}_0'$  have the same phase, Eq. 14-43 represents a linearly polarized wave, with polarization vector at angle  $\theta = \tan^{-1} (E_0'/E_0)$  relative to  $\hat{e}_1$  and magnitude  $E = \sqrt{|E_0|^2 + |E_0'|^2}$ . If  $E_0$  and  $E_0'$  have different phases, the wave is elliptically polarized; if they are out of phase by  $90^\circ$  and have the same magnitude, the wave is circularly polarized.

Up to this point we have discussed plane-wave monochromatic solutions in the far-field, or radiation zone, which are valid for almost all of the configurations of interest. However, even in the most sharply tuned radar transmitter there is a finite, though usually small, fractional spread of frequencies. (Recall that the Fourier analysis of a wave train leads to the very simple result that the frequency spread is about the reciprocal of the time duration of the pulse, thus the finite time duration will itself lead to a finite frequency spread.) The basic Maxwell equations are linear, so that in principle the linear superposition of solutions with different frequencies may be made in a straightforward manner. However, there are several subtleties that may present themselves in treating propagation through plasmas, and we shall discuss these in more detail in Section 14.4. In brief,

1. In dispersive media like plasmas, the permittivity is a function of the electromagnetic wave frequency, so that different components of the wave travel with different speeds and change phase with respect to one another (at a given point in space). This changes the pulse shape.
2. The group velocity, or energy flow velocity, may differ greatly from the phase velocity.
3. Different frequency components may be attenuated quite differently.
4. In inhomogeneous plasmas, the different frequency components may not even follow the same geometrical path,

so that linear superposition at a given point becomes quite complicated.

### 14.3 THE CONSTITUTIVE RELATIONS IN A MAGNETO-PLASMA

#### 14.3.1 THE PERMITTIVITY TENSOR

The chief plasma regions of interest are the D-, E-, and F-regions, where (under normal or weapon-induced conditions) typical electron densities of interest are from  $10^3 \text{ cm}^{-3}$  to  $10^{12} \text{ cm}^{-3}$ , and neutral densities range from about  $10^9 \text{ cm}^{-3}$  to  $10^{15} \text{ cm}^{-3}$  or so. Typical plasma temperatures, at times of interest for radar propagation, are from a few hundred degrees to perhaps 1 eV. The field Eqs. 14-16 are written in terms of average values of the field vectors, averages in the statistical ensemble sense. Averaging over "physically infinitesimal" volumes is only valid if fluctuations in the number of particles in the volume are small. Fortunately, because of the very small ratio of the interparticle separations to the wavelength, conventional macroscopic (continuum) electrodynamics is valid. In Eqs. 14-16 then, the fields  $\vec{E}$  and  $\vec{B}$  are the statistical averages of the microfields, and all the plasma properties are expressed in the form of the constitutive relation between  $\vec{D}$  and  $\vec{E}$ .

The most general linear relationship between these vectors is

$$D_i(\vec{x}, t) = \int_{-\infty}^t dt' \int d\vec{x}' \hat{\epsilon}_{ij}(t, t', \vec{x}, \vec{x}') E_j(\vec{x}', t') \quad (14-44)$$

where  $i, j$  are tensor indices 1 through 3 and the repeated index  $j$  denotes a sum over  $j$ . The limits on the time integral involve only the principle of causality. For homogeneous, non-time varying media,

$$D_i(\vec{x}, t) = \int_{-\infty}^t dt' \int d\vec{x}' \hat{\epsilon}_{ij}(t - t', \vec{x} - \vec{x}') E_j(\vec{x}', t') \quad (14-45)$$

The kernel  $\hat{\epsilon}_{ij}$  can be interpreted as the displacement produced by a delta-function electric field  $\vec{E}$ . Note that the form of Eq. 14-45

implies the following general properties of the plasma.

1. Frequency Dispersion. If the electromagnetic field frequency is sufficiently low, so that induced polarization is established essentially instantaneously,  $\vec{D}$  at time  $t$  depends on  $\vec{E}$  at the same instant. For sufficiently high frequency,  $\vec{D}(t)$  will depend on the behavior of  $\vec{E}$  at previous times.
2. Spatial Dispersion. If the frequency is high enough, or the refractive index sufficiently large, the wavelength in the plasma may become comparable to various microscopic characteristic lengths, such as the inter-ionic spacing, or the Debye length (to be defined below). This leads to non-local dependence of  $\vec{D}$  on  $\vec{E}$ . This non-local relationship may also result from a field effect transmitted to distant points by thermal motion of electrons. In the literature, spatially non-dispersive plasmas (with which we shall be almost exclusively concerned) are often called "cold plasmas," and spatially dispersive plasmas are called warm.
3. Anisotropy. A plasma may be anisotropic due to spatial dispersion, in which case the propagation vector  $\vec{k}$  provides a natural axis of symmetry. Similarly, even in spatially non-dispersive media, anisotropy can be produced by the presence of a steady magnetic field.

We shall consider these three general properties at greater length below, when we make numerical estimates of their effect.

From the definition of the displacement  $\vec{D}$  (cf. Eq. 14-17)

$$\frac{\partial \vec{D}}{\partial t} = \frac{\partial \vec{E}}{\partial t} + 4\pi c \vec{j}' = \frac{\partial \vec{E}}{\partial t} + 4\pi \frac{\partial \vec{p}}{\partial t} \quad (14-16)$$

where  $\vec{j}'$  is the displacement current associated with the varying polarization  $\vec{p}$  (see, e.g., Ref. 14-1). For monochromatic waves of angular frequency  $\omega$ , this becomes



$$\vec{D} = \vec{E} + \frac{4\pi i}{k} \vec{j}, \quad (14-47)$$

Taking the Fourier transform of Eq. 14-45, we find

$$\vec{D}(\omega, \vec{k}) = \epsilon'_{ij}(\omega, \vec{k}) E_j(\omega, \vec{k}) \quad (14-48)$$

where

$$\begin{aligned} E_i(\vec{x}, t) &= \int d\omega \int d\vec{k} E_i(\omega, \vec{k}) e^{i(\vec{k} \cdot \vec{x} - \omega t)} \\ \epsilon'_{ij}(\omega, \vec{k}) &= \int_0^\infty d\tau \int d\vec{R} e^{-i(\vec{k} \cdot \vec{R} - \omega\tau)} \hat{\epsilon}_{ij}(\tau, \vec{R}) \end{aligned} \quad (14-49)$$

$\tau$  and  $\vec{R}$  being defined respectively, as  $t - t'$ ,  $\vec{x} - \vec{x}'$ . The tensor  $\epsilon'_{ij}(\omega, \vec{k})$  is the complex permittivity tensor, and may be separated into Hermitian and anti-Hermitian components

$$\epsilon'_{ij}(\omega, \vec{k}) = \epsilon_{ij}(\omega, \vec{k}) + i \frac{4\pi}{k} \sigma_{ij}(\omega, \vec{k}) \quad (14-50)$$

where  $\epsilon_{ij}$  and  $\sigma_{ij}$  are both Hermitian. In "cold" plasmas without spatial dispersion

$$\epsilon'_{ij}(\omega, \vec{k}) = \epsilon'_{ij}(\omega) = \epsilon_{ij}(\omega) + i \frac{4\pi}{k} \sigma_{ij}(\omega) \quad (14-51)$$

In this case there is no need to take spatial Fourier components. Furthermore, in the absence of an external magnetic field, where complete local isotropy exists, the tensors  $\epsilon_{ij}(\omega)$  and  $\sigma_{ij}(\omega)$  in Eq. 14-51 become scalar quantities  $\epsilon(\omega)$  and  $\sigma(\omega)$ , the permittivity and conductivity, respectively.

### 14.3.2 COMPLEX PERMITTIVITY OF A "COLD" PLASMA

These quantities are determined by the motions of the electrons (and, to a much lesser extent, the ions) in the applied electromagnetic field. The usual elementary derivations such as that in the introduction, of the expressions for  $\epsilon$  and  $\sigma$  begin by considering the equation of motion of an electron under the combined influences of the applied field and

collisions with molecules and ions. Considering only billiard-ball collisions with molecules for simplicity (this assumption will be relaxed later), one may ascribe an effective collision cross-section  $\pi a^2$  to each molecule, so that the effective collision frequency  $\nu_{\text{eff}}$  is  $\pi a^2 N \bar{v}$ ,  $N$  being the molecular concentration and  $\bar{v}$  some mean electron velocity. The mean change in momentum of the electron per second, due to collisions, is thus  $-m \nu_{\text{eff}} \dot{\vec{r}}$ , and the equation of motion of the electron is

$$m \ddot{\vec{r}} + m \nu_{\text{eff}} \dot{\vec{r}} = -e \vec{E}_0 e^{-i\omega t} \quad (14-52)$$

whose steady state solution is

$$\dot{\vec{r}} = \frac{e \vec{E}}{m \omega (\omega + i \nu_{\text{eff}})} \quad (14-53)$$

The induced polarization due to  $N$  electrons  $\text{cm}^{-3}$  is thus

$$\vec{p} = -Ne \dot{\vec{r}} = (e' - 1) \vec{E} / 4\pi \quad (14-54)$$

so that

$$e' = 1 - \frac{4\pi N e^2}{m \omega (\omega + i \nu_{\text{eff}})} = 1 - \frac{\omega_p^2 (\omega - i \nu_{\text{eff}})}{\omega (\omega^2 + \nu_{\text{eff}}^2)} \quad (14-55)$$

and comparison with Eq. 14-51 gives for the permittivity  $\epsilon$  and conductivity  $\sigma$

$$\begin{aligned} \epsilon &= 1 - \frac{4\pi N e^2}{m (\omega^2 + \nu_{\text{eff}}^2)} \\ \sigma &= \frac{N e^2 \nu_{\text{eff}}}{m c (\omega^2 + \nu_{\text{eff}}^2)} \end{aligned} \quad (14-56)$$

where the effective collision frequency  $\nu_{\text{eff}}$  is still to be accurately defined, particularly for the case of electron-ion collisions, where the forces that transfer energy from electrons to ions (and are thus responsible for the finite conductivity) are long-range.

To find general expressions for  $\nu_{\text{eff}}$ , and thus  $\epsilon$  and  $\sigma$  in weak and strong fields, the Boltzmann equation must be invoked (e.g., Refs. 14-8 - 10 and Chapter 12). The state of the gas is defined by the distribution function  $f(\vec{x}, \vec{v}, t)$ , whereby the mean number of particles  $dN$  in the volume element  $d\vec{x}$  and velocity interval  $d\vec{v}$  is  $dN = f d\vec{x} d\vec{v}$ . The Boltzmann equation from which  $f$  is to be found is

$$\frac{\partial f}{\partial t} + \vec{v} \cdot \vec{\nabla} f - \frac{e}{m} (\vec{E} + \frac{\vec{v}}{c} \times \vec{B}) \cdot \vec{\nabla}_v f = S \quad (14-57)$$

where  $\vec{\nabla} f$  is the usual vector gradient and

$$\vec{\nabla}_v f = \frac{\partial f}{\partial v_x} \hat{e}_x + \frac{\partial f}{\partial v_y} \hat{e}_y + \frac{\partial f}{\partial v_z} \hat{e}_z \quad (14-58)$$

$S$ , the collision integral, represents the change in  $f$  due to particle collisions at a fixed point in space and time, and may also include terms due to ionization, inelastic scattering, etc. In equilibrium and without external fields  $\vec{E}$  and  $\vec{H}$ , the distribution function  $f$  is Maxwellian.

$$f = f_0(v) = N \left( \frac{m}{2\pi kT} \right)^{3/2} e^{-mv^2/2kT} \quad (14-59)$$

If we write the distribution function  $f$ , for an isotropic plasma, as

$$f = f_0 + \frac{\vec{v} \cdot \vec{f}_1(v)}{v} \quad (14-60)$$

where the non-symmetrical part  $\vec{f}_1$  is regarded as a small perturbation, then Eq. 14-57 becomes (e.g., Ref. 14-11)

$$\frac{\partial \vec{f}_1}{\partial t} - \frac{e\vec{E}}{m} \frac{\partial f_0}{\partial v} + \nu(v) \vec{f}_1 = 0 \quad (14-61)$$

the last term being an approximate linearized version of the collision term  $S$ . In arriving at this expression we have assumed that  $v$ ,  $E$ ,  $H$  and  $f_1$  are all small, and have retained only the lowest order terms in the small quantities. With  $\vec{E} = \vec{E}_0 e^{-i\omega t}$  we seek a solution in the form  $\vec{f}_1 = \vec{f}_1 e^{-i\omega t}$ . This gives immediately

$$\vec{f}_1 = \frac{e\vec{E}\partial f_0/\partial v}{m[v(v)-i\omega]} \quad (14-62)$$

The total current density  $\vec{j}'$  due to the induced charge motion is

$$\begin{aligned} \vec{j}' &= -\frac{e}{c} \int \vec{v} f d\vec{v} = -\frac{4\pi e}{3c} \int_0^\infty \vec{f}_1 v^3 dv \\ &= \frac{8e^2 N \vec{E}}{3\sqrt{\pi} mc} \left\{ \int_0^\infty \frac{v(u) u^4 e^{-u^2} du}{\omega^2 + v^2(u)} + i\omega \int_0^\infty \frac{u^4 e^{-u^2} du}{\omega^2 + v^2(u)} \right\} \end{aligned} \quad (14-63)$$

where we have used Eqs. 14-59, 14-62, introduced the dummy variable  $u = v \sqrt{m/2kT}$  and integrated in spherical polar coordinates with the polar axis along  $\vec{f}_1$ . Since

$$\vec{j}' = \left( \sigma + i\omega \frac{\epsilon - 1}{4\pi c} \right) \vec{E} = i\omega \frac{\epsilon' - 1}{4\pi c} \vec{E} \quad (14-64)$$

we may equate 14-63 and 14-64 to find  $\sigma$  and  $\epsilon$ , expressed now in terms of integrals over the velocity dependent collision frequency.

It is possible to define an effective collision frequency  $\nu_{eff}$ , as in 14-56, but unless  $\nu(v)$  is independent of the velocity,  $\nu_{eff}$  as defined in 14-56 must be regarded as a function of the frequency  $\omega$ , and is different in the expressions for  $\epsilon$  and  $\sigma$ . In the limiting case of high frequencies, where  $\omega \gg \nu_{eff}$ , Eqs. 14-63 and 14-64 give

$$\nu_{eff} = \frac{8}{3\sqrt{\pi}} \int_0^\infty v(u) u^4 e^{-u^2} du = \frac{2}{3\sqrt{2\pi}} \left( \frac{m}{kT} \right)^{5/2} \int_0^\infty v(v) v^4 e^{-mv^2/2kT} dv \quad (14-65)$$

The velocity-dependent collision frequency, with either neutral molecules (subscript m) or ions (subscript i) is given in terms of the transport cross sections  $q_{m,i}(v)$  for elastic collisions of electrons with molecules and ions through the usual relations

$$\nu_{m,i}(v) = q_{m,i}(v) v N_{m,i} \quad (14-66)$$

where  $N_{m,i}$  are respectively the number densities of molecules and ions.

Using the measured linear energy dependence (Ref. 14-11) of the electron scattering cross section from air molecules we are led to the following expression for the effective electron-neutral collision frequency

$$\nu_{\text{eff}, m} = 1.7 \times 10^{11} \frac{N_m}{2.7 \times 10^{19}} \cdot \frac{T}{300} \quad (14-67)$$

so that at atmospheric pressure  $\nu_{\text{eff}} = 1.7 \times 10^{11} \text{ sec}^{-1}$ .

For electron-ion collisions the Rutherford scattering cross section

$$q_i(v) = 2\pi \left( \frac{e^2}{mv^2} \right)^2 \ln(1 + p_m^2 m^2 v^4 / e^4) \quad (14-68)$$

is used in Eq. 14-66 to compute  $\nu_i(v)$ . In this case  $p_m$  is the maximum impact parameter (corresponding to the minimum angle of deflection) and is determined by the screening of the Coulomb field of a given ion by the field of other electrons and ions surrounding that ion, which screening prevents the logarithmic term in 14-68 from diverging. The Debye length  $D$ , a characteristic distance within which the charges in a plasma collect around a given charge and screen its field, is given by (e.g., Ref. 14-8),

$$D = \left( \frac{kT}{4\pi e^2 N} \right)^{1/2} = 6.9 \sqrt{\frac{T}{N}} \text{ (cm)} \quad (14-69)$$

where  $T$  is expressed in degrees K and  $N$  in  $\text{cm}^{-3}$ . Using this value of  $D$  for  $p_m$  in 14-68 and integrating Eq. 14-66 over a Maxwell distribution leads to the following value for  $\nu_{\text{eff}, i}$

$$\nu_{\text{eff}, i} = \pi \frac{e^4}{(kT)^2} \frac{[N_i]}{[V]} \ln \left( 0.47 \frac{kT}{e^2 N_i^{1/3}} \right) = \frac{5.5 N_i}{T^{3/2}} \ln \left( 280 \frac{T}{N_i^{1/3}} \right) \quad (14-70)$$

### 14.3.3 VALIDITY CRITERIA

At this point we have derived those properties of partially ionized plasmas that are necessary to compute electromagnetic wave propagation therein. We have made, explicitly or implicitly, however, a number of

simplifying approximations and assumptions which it is well to point out. A fuller discussion of these points is given in Refs. 14-10 and 14-12.

First, we note that spatial dispersion arises from the fact that the displacement at a point is determined not only by the electric field at that point, but also at neighboring points within the Debye length. The criterion for neglect of spatial dispersion (the cold plasma limit) is thus  $kD \ll 1$ ,  $k$  being the wave number. For frequencies of usual interest,  $\lambda \gg 3$  cm and with plasma temperatures and densities of normal interest this condition is well satisfied.

Second, the effective field in the plasma has been taken as the mean macroscopic field. The proof of this contention, usually assumed without proof as obvious, is quite complicated and treated in some detail in Ref. 14-10.

Third, we have applied classical theory to the interaction of electrons and ions with the radiation field. Heitler (Ref. 14-13) has shown that in the scattering of electromagnetic radiation by free electrons, quantum corrections are of the order of  $\hbar\omega/mc^2$ , entirely negligible even for optical frequencies. Since the refractive index is entirely determined by light scattering, and is equal to  $\sqrt{\epsilon}$  in the absence of collisions, Eq. 14-56 is exact and the same as that obtained (Ref. 14-14) by the quantum theory of dispersion.

Similarly in treating absorption resulting from collisions as an inverse process, electron bremsstrahlung, the probabilities of the direct and inverse processes being connected by Einstein's famous relation (i.e., Ref. 14-14) classical theory is applicable here if the radiation quantum energy is much less than the electron kinetic energy, which again is always the case for the plasmas and frequencies of interest.

One further assumption regarding our classical treatment of the plasma gas has been that the plasma is non-degenerate. The condition for this to obtain is that the energy  $kT$  should be greater than the temperature  $T_d$  of degeneracy, given by

$$kT_d \sim \hbar^2 N^{2/3} / m \quad (14-71)$$

The physical significance of  $T_d$  is that at this temperature the energy  $kT_d$  is equal to the zero-point energy  $\hbar^2 / mr^2 = \hbar^2 N^{2/3} / m$  which pertains to the localization of electrons in a volume  $r^3 \sim 1/N$ . Even for  $N \sim 10^{15} \text{ cm}^{-3}$ ,  $T_d \sim 10^{-1} \text{ }^\circ\text{K}$ , so that classical statistics are always valid.

Fourth, the assumption that the plasma permeability  $\mu$  is equal to unity is clearly applicable only to plasmas in thermodynamic equilibrium, since non-equilibrium states may possess diamagnetic susceptibilities that are quite appreciable. For an equilibrium non-degenerate electron gas the susceptibility  $\chi$  is (e.g., Ref. 14-15, p. 456)

$$\chi = \frac{\mu-1}{4\pi} = \frac{2}{3} \left( \frac{e\hbar}{2mc} \right)^2 \frac{N}{kT} \quad (14-72)$$

and even for  $N \sim 10^{15} \text{ cm}^{-3}$  and  $T \sim 300 \text{ }^\circ\text{K}$ ,  $\chi \sim 10^{-12}$  so that  $\mu$  is essentially unity.

Fifth, we have already mentioned, in our discussion of the Boltzmann equation, that the electric field must be small enough that the equilibrium distribution function  $f_0$  is not thereby affected. It is easy to solve for the average energy gained by an electron (over the Maxwellian  $3/2 kT$ ) by equating the energy gained by the electrons from the electric field to the energy lost by electrons to heavy particles by collisions. The former energy is from Eq. 14-53

$$u = -e\vec{r} \cdot \vec{E} = \frac{e^2 E^2}{m(v_{\text{eff}}^2 - i\omega)} \quad (14-73)$$

with a time average of

$$\bar{u} = e^2 E_0^2 v_{\text{eff}} / 2m(\omega^2 + v_{\text{eff}}^2) \quad (14-74)$$

The energy  $\bar{u}_1$ , transmitted per unit time by the electrons to heavy particles is

$$\bar{u}_1 = \delta \left( \frac{1}{2} m \bar{v}^2 - \frac{3}{2} kT \right) v_{\text{eff}} \quad (14-75)$$

where  $\delta$  is the fractional energy lost by the electron per collision  $\sim 2 m/M$ .

The criterion that the field be weak is clearly that the mean additional kinetic energy per electron be small relative to the thermal energy, or

$$\frac{1}{2} m \bar{v}^2 - \frac{3}{2} kT \ll \frac{3}{2} kT \quad (14-76)$$

Using Eqs. 14-74 and 14-75, we find

$$E \ll E_p = \left[ \frac{3(mkT)\delta(\omega^2 + v_{\text{eff}}^2)}{e^2} \right]^{1/2} \quad (14-77)$$

where  $E_p$  is the so-called plasma field. The magnitude of the plasma field is

$$E_p = 1.3 \times 10^{-12} \left( \delta T(\omega^2 + v_{\text{eff}}^2)^{1/2} \right) \frac{\text{dynes}}{\text{esu}} = 4 \times 10^{-8} \left( \delta T(\omega^2 + v_{\text{eff}}^2)^{1/2} \right) \frac{\text{volts}}{\text{meter}} \quad (14-78)$$

With typical ionospheric temperatures  $\sim 10^3$  °K and  $\delta \sim (1-10) \times 10^{-4}$  for collisions with both molecules and ions (Ref. 14-10) one sees that non-linearity can occur in fields that are comparable to those from powerful radio transmitters. A discussion of experiments to investigate ionospheric heating by absorption of radio-frequency waves is given in Ref. 14-16. For microwave frequencies the plasma field, being proportional to the radar frequency, is much higher and our weak-field approximation is quite reasonable.



The sixth approximation lies in possible quantum mechanical corrections to Rutherford's scattering law, Eq. 14-68. The validity of classical mechanics for an electron moving in a Coulomb field depends on the wavelength of the electron,  $h/mv$ , being small compared to the distance of closest approach  $2ze^2/mv^2$  of the electron to the nucleus of charge  $ze$ . This gives the following condition for the electron velocity and corresponding plasma temperature, in order that classical theory be valid (we assume  $z = 1$ )

$$v \ll 3 \times 10^8 \text{ cm/sec}, \quad T \sim \frac{mv^2}{3k} \ll 3 \times 10^5 \text{ }^\circ\text{K} \quad (14-79)$$

which is seen to be everywhere valid.

The seventh restriction relates to the assumption, implicit in the derivation of the Boltzmann equation, that the collision time is short compared to the radar wave period, so that the field is constant during the collision. For collisions with neutral particles, this is always satisfied since the collision time is about equal to the molecular radius  $\sim 10^{-8}$  cm divided by the thermal velocity  $\sim 10^7$  cm/sec, or  $10^{-15}$  sec. For Coulomb collisions, on the other hand, the appropriate distance is the Debye length. In this case the condition for validity is that  $\omega/2\pi \ll \bar{v}/D$ , or from Eqs. 14-12 and 14-69

$$\frac{4\pi Ne^2}{m\omega^2} \equiv \frac{\omega_p^2}{\omega^2} \gg 1 \quad (14-80)$$

where  $\omega_p$  is the "plasma frequency" for which the permittivity  $\epsilon$  vanishes, from 14-56 in the limit that  $\omega \gg v_{\text{eff}}$ . Thus for purely ionic collisions, the condition (14-80) holds only for frequencies for which  $\epsilon < 0$ , and for those more interesting cases when  $\epsilon \gtrsim 0$ , the theory breaks down. This is only the case, of course, when ion collisions play the dominant part (as compared to collisions with neutrals), and even in this case the restriction implied by Eq. 14-80 is mostly academic. The reason is that the maximum impact parameter  $p_m$  (set equal to the Debye length  $D$ ) enters only in a logarithmic term in Eq. 14-68, and the exact value used for

$p_m$  is relatively unimportant. (The error resulting from equating  $p_m$  and  $D$  may be very important in very rarefied media such as interstellar plasmas--in this case  $p_m$  must be set equal to the distance traveled by an electron in one period of the radar wave; a fuller discussion of this point is found in Ref. 14-10.)

The eighth approximation is the neglect of all microprocesses except elastic scattering in the Boltzmann equation, whereas in fact such processes as inelastic collisions, excitation, ionization, attachment and detachment, recombination, dissociation, etc., might be expected to have an effect on the electron distribution function  $f$ . The inclusion of such effects is straightforward but lengthy (e.g., Refs. 14-8, 14-10, 14-12). Suffice it to say that our assumption of a Maxwellian electron distribution function in the ionosphere, and even in the solar corona, is a good approximation to reality. The phenomenon of "runaway" electrons is not relevant to ionospheric plasmas, in the absence of external fields.

The ninth approximation was made in Eq. 14-54 when we neglected the effects of the heavy ions on the polarizability, and hence on  $\epsilon$ . Because of the inverse mass dependence in Eq. 14-54, it is clear that unless the ion number density exceeds that of the electrons by a factor of the ionic mass relative to the electron mass ( $\sim 10^4$ ), the ion contribution to the polarizability is negligible. This can occur only at very low altitudes, because of the rapid decrease in electron attachment with increasing altitude. For microwave radars operating under normal tropospheric and ionospheric electron densities, ions may be safely neglected. They may, however, have important effects on VLF propagation.

The tenth approximation lies in the neglect of electron-electron collisions in the Boltzmann equation, although the collision cross section of electrons with electrons is of the same order as for singly charged ions. This may be shown (e.g., Ref. 14-8) to introduce no substantive error, when  $v_{eff} \gg v_{th}$  because from conservation of momentum, electron-electron

collisions cannot in themselves change the mean electron current. Electron-electron collisions are important, however, in the opposite limit of low frequencies, when  $\omega \ll \nu_{\text{eff}}$ , and it may be shown (Ref. 14-17) that the conductivity is reduced by a factor 1.73 for equal electron and ion densities when collisions between electrons are taken into account.

The last assumption we shall touch on is the purely numerical one of assuming the radar frequency large compared to the collision frequency in Eq. 14-65. This is almost always the case in practice at the frequencies and atmospheric densities of interest. Still, for low frequencies ( $\lesssim 10^5 \text{ sec}^{-1}$ ), low altitudes, or high electron densities, the opposite situation may obtain, and in this case we may write, formally

$$\left. \begin{aligned} \epsilon &= 1 - K_E \frac{4\pi N_e^2}{m(\omega^2 + \nu_{\text{eff}}^2)} \\ \sigma &= K_\sigma \frac{Ne^2 \nu_{\text{eff}}}{mc(\omega^2 + \nu_{\text{eff}}^2)} \end{aligned} \right\} \quad (14-81)$$

where  $\nu_{\text{eff}}$  is the effective collision frequency of Eq. 14-56 valid for high frequencies, and  $K_E$ ,  $K_\sigma$  are functions of  $\omega/\nu_{\text{eff}}$ . By definition  $K_E$  and  $K_\sigma \rightarrow 1$  as  $\omega/\nu_{\text{eff}} \rightarrow \infty$ , and for intermediate values of  $\omega/\nu_{\text{eff}}$  these factors give the deviation of  $\epsilon$  and  $\sigma$  from the formulae obtained from the elementary theory. These factors, for collisions of electrons with both neutrals and ions, vary by no more than a factor of two for all values of  $\omega/\nu_{\text{eff}}$ , and we shall henceforth use the approximations in Eqs. 14-67 and 14-70 for all values of  $\omega$  and  $\nu_{\text{eff}}$ .

## 14.4 PROPAGATION OF ELECTROMAGNETIC WAVES IN PLASMAS

### 14.4.1 ISOTROPIC HOMOGENEOUS PLASMA

We treat first the simplest case of transverse plane electromagnetic waves in an isotropic homogeneous plasma, characterized by  $\mu = 1$  and a constant effective collision frequency, so that Eqs. 14-56, 14-67, and

14-70 obtain. In exact analogue with the previous derivation of Eq. 14-21, one obtains from the first two Eqs. 14-16 the following equation for the components of  $\vec{E}$ , for a time variation  $e^{-i\omega t}$

$$\nabla^2 \vec{E} - \nabla(\nabla \cdot \vec{E}) + \frac{\omega^2}{c^2} \epsilon'(\omega) \vec{E} = 0 \quad (14-82)$$

For transverse waves, where  $\text{div } \vec{E} = 0$ , we may write

$$\vec{E} = \vec{E}_0 e^{i(\vec{k} \cdot \vec{r} - \omega t)} \quad (14-83)$$

and we obtain the dispersion relation

$$k^2 = \left( \frac{\omega^2}{c^2} \right) \epsilon'(\omega) \quad (14-84)$$

For homogeneous plane waves, for which the planes of equal phase and amplitude coincide, the vector  $\vec{k}$  may be written in the form

$$\vec{k} = \left( \frac{\omega}{c} \right) (n + i\kappa) \frac{\vec{k}}{k} \quad (14-85)$$

and if the z-direction be chosen as the direction of propagation, we may write the field (14-83) in the form

$$\vec{E} = \vec{E}_0 e^{\pm i\omega z/c} e^{i\omega(\pm \frac{nz}{c} - t)} \quad (14-86)$$

where by 14-81, 14-84, and 14-85

$$(n + i\kappa)^2 = \epsilon' = \epsilon + \frac{14\pi\sigma c}{\omega} \quad (14-87)$$

The upper and lower signs in the exponentials of Eq. 14-86 correspond to wave propagation in the positive and negative z-directions, respectively. The quantities  $n$  and  $\kappa$  are the indices of refraction and absorption. The wavelength  $\lambda$  in the medium is seen from Eq. 14-86 to be

$$\lambda = \lambda_0 / n \quad (14-88)$$

where  $\lambda_0 = 2\pi c/\omega$  is the wavelength in *vacuo*. The phase velocity  $v_p$  in the medium is

$$v_p = c/n. \quad (14-89)$$

The absorption index  $\kappa$  has the following significance: over a distance  $\lambda_0/2\pi\kappa$  the wave amplitude changes by a factor  $e$ . According to Eq. 14-87

$$\epsilon = n^2 - \kappa^2 \quad \text{and} \quad 2n\kappa = + \frac{4\pi c\sigma}{\omega} \quad (14-90)$$

from which

$$\left. \begin{aligned} n^2 &= \epsilon/2 + \sqrt{(\epsilon/2)^2 + \left(\frac{2\pi c\sigma}{\omega}\right)^2} \\ \kappa^2 &= -\epsilon/2 + \sqrt{(\epsilon/2)^2 + \left(\frac{2\pi c\sigma}{\omega}\right)^2} \end{aligned} \right\} \quad (14-91)$$

$n$  and  $\kappa$  being positive by definition, so that the positive sign must be taken for the square root.

When  $\sigma = 0$ , there is no absorption of energy from the wave, since  $\sigma E^2$  is the Joule heating. There still may be damping, however, even with  $\sigma = 0$ . Thus Eq. 14-86 has the form of pure traveling waves when  $\epsilon > 0$ , and  $n = \sqrt{\epsilon}$ ,  $\kappa = 0$ , so that no damping exists. When  $\epsilon < 0$ , however,  $n = 0$ ,  $\kappa = \sqrt{-\epsilon}$  and the solution (Eq. 14-86) is damped. This damping means that traveling waves cannot propagate in the medium, i. e., a wave incident on a medium with  $\epsilon < 0$  is completely reflected.

For finite conductivity,  $\sigma \neq 0$ , and Eq. 14-91 applies. For the usual case applicable to electron densities and frequencies of interest, the imaginary part of the permittivity is small compared to the real part, so that

$$|\epsilon| \gg \frac{4\pi c\sigma}{\omega} \quad (14-92)$$

and when  $\epsilon > 0$ , Eq. 14-91 becomes

$$\left. \begin{aligned} n \approx \sqrt{\epsilon} &= \left[ 1 - \frac{\omega_p^2}{(\omega^2 + \nu_{\text{eff}}^2)} \right]^{1/2} \\ \kappa \approx \frac{2\pi\sigma c}{\omega} / \sqrt{\epsilon} &= \frac{\omega_p^2 \nu_{\text{eff}}}{2\omega(\omega^2 + \nu_{\text{eff}}^2)} \left[ 1 - \frac{\omega_p^2}{(\omega^2 + \nu_{\text{eff}}^2)} \right]^{-1/2} \end{aligned} \right\} \quad (14-93)$$

These, together with Eq. 14-67 (or 14-70) for the collision frequency  $\nu_{\text{eff}}$ , completely define the absorption  $\kappa$  and refractive index  $n$  of an isotropic plasma.

#### 14.4.2 HOMOGENEOUS MAGNETOACTIVE PLASMAS

A plasma in a magnetic field  $\vec{B}_0$  is anisotropic and its electromagnetic properties may be described by a frequency-dependent complex permittivity tensor

$$\epsilon'_{ij} = \epsilon_{ij} + i \frac{4\pi\sigma_{ij}}{\omega}, \quad j'_i = \sigma_{ij} E_j, \quad D_i = \epsilon'_{ij} E_j \quad (14-94)$$

where the usual summation rule applies to repeated subscripts. The magnetic field effects would be expected to relate to the relative magnitudes of the gyro-frequency  $\omega_B$ , the collision frequency  $\nu_{\text{eff}}$ , and the radar frequency  $\omega$ , where

$$\omega_B = \frac{eB_0}{mc} \quad (14-95)$$

is a few megahertz in the Earth's field of 0.2 - 0.5 gauss. As in Eq. 14-52 we write the equation of motion of an electron as

$$m\ddot{\vec{r}} + m\nu_{\text{eff}}\dot{\vec{r}} = -e\vec{E}_0 e^{-i\omega t} - \frac{e\dot{\vec{r}}}{c} \times \vec{B}_0 \quad (14-96)$$

The steady state solution of this apparently simple equation is straightforward but fraught with algebraic complexity. If the direction of the

magnetic field is chosen for simplicity as the z-axis, the components of the permittivity tensor  $\epsilon'_{ij}$  may be shown to be (Ref. 14-18)

$$\left. \begin{aligned} \epsilon'_{xx} &= \epsilon'_{yy} = 1 - \frac{1}{2} \omega_p^2 \left( \frac{1}{\omega(\omega - \omega_B) + i\nu_{\text{eff}}\omega} + \frac{1}{\omega(\omega + \omega_B) + i\nu_{\text{eff}}\omega} \right) \\ \epsilon'_{xy} &= -\epsilon'_{yx} = -i \frac{\omega_p^2 \omega_B}{\omega(\omega + \omega_B + i\nu_{\text{eff}}) (\omega - \omega_B + i\nu_{\text{eff}})} \\ \epsilon'_{zz} &= 1 - \frac{\omega_p^2}{(\omega^2 + i\omega\nu_{\text{eff}})} \\ \epsilon'_{xz} &= \epsilon'_{zx} = \epsilon'_{yz} = \epsilon'_{zy} = 0 \end{aligned} \right\} (14-97)$$

Comparison with Eq. 14-55 establishes the significance of the magnetic field. Its effect is the replacement of  $\omega^2$  by  $\omega(\omega \pm \omega_B)$  in the denominator of the first two Eqs. 14-97. In a magnetoactive medium  $\vec{D}$  and  $\vec{E}$  are in general not parallel: along  $\vec{B}$ ,  $D_z = \epsilon_{zz} E_z$ , but  $D_x \pm iD_y = (\epsilon_{xx} \pm i\epsilon_{xy}) (E_x \pm iE_y)$ . Since from Eq. 14-97 (when  $\nu_{\text{eff}} = 0$ )

$$\epsilon_{xx} \pm i\epsilon_{xy} = 1 - \frac{\omega_p^2}{\omega(\omega \pm \omega_B)}, \quad (14-98)$$

which is real, it follows that in the x-y plane the vector  $\vec{D}$  is proportional to  $\vec{E}$  for a field  $\vec{E}$  of constant magnitude rotating clockwise or anti-clockwise. Thus, for longitudinal propagation of a wave along the field-direction there are two normal waves, corresponding to opposite circular polarizations, each of which has its own characteristic phase velocity.

The general case of arbitrary angle between the magnetic field and the direction of propagation becomes quite complicated, and is treated in great detail in Ref. 14-18. Fortunately, at most frequencies of interest, the frequency  $\omega$  is so much greater than the gyrofrequency  $\omega_B$  that magnetoactive effects may be neglected, and Eq. 14-93 will be taken as a suitable approximation.

#### 14.4.3 INHOMOGENEOUS PLASMAS

we now discuss the more realistic case corresponding to propagation under actual conditions when the plasma is inhomogeneous, as in the natural ionosphere and in the atmosphere disturbed by ionizing radiation. We obtain fundamentally different limits when the scale distance over which appreciable changes in plasma properties occur is large or small compared to the wavelength.

We consider for simplicity normal incidence of transverse waves into a medium in which all variation of plasma properties is in the  $z$ -direction, and the boundary is located at  $z_0$ . In this case 14-82 becomes

$$\frac{d^2 E}{dz^2} + \frac{\omega^2}{c^2} \epsilon'(z) E = 0 \quad (14-99)$$

where  $E$  stands for either  $E_x$  or  $E_y$ . The component  $E_z$  is taken to be zero. This equation is immediately recognized as the wave equation and many results from acoustics and quantum mechanics are of direct relevance. In particular, if the plasma properties change slowly enough, the approximations of geometrical optics, whose analogue in quantum mechanics is the WKB method (Ref. 14-19), may be used. This method consists in seeking a solution to Eq. 14-99 in the form

$$E(z) = E_0(z) e^{-i\omega\phi(z)/c} \quad (14-100)$$

where  $E_0(z)$  and  $\phi(z)$  are slowly varying functions of  $z$  to be determined. Substituting Eq. 14-100 into 14-99 and equating to zero the terms of each order in  $\omega/c$  leads to a general solution of the form (e.g., Ref. 14-19).

$$E(z) = \frac{C_+}{[\epsilon'(z)]^{1/4}} \exp \left[ \frac{i\omega}{c} \int_{z_0^+}^z \sqrt{\epsilon'(z)} dz \right] + \frac{C_-}{[\epsilon'(z)]^{1/4}} \exp \left[ - \frac{i\omega}{c} \int_{z_0^-}^z \sqrt{\epsilon'(z)} dz \right] \quad (14-101)$$



where  $C_{\pm}$  and  $z_0^{\pm}$  are constants. The conditions for validity of this solution are (with  $\sqrt{\epsilon'} = n + i\kappa$ )

$$\frac{\lambda_0 \sqrt{n'^2 + \kappa'^2}}{2\pi(n^2 + \kappa^2)} \ll 1, \quad \text{and} \quad \frac{\lambda_0 \sqrt{n''^2 + \kappa''^2}}{2\pi \sqrt{n^2 + \kappa^2} \sqrt{n'^2 + \kappa'^2}} \ll 1 \quad (14-102)$$

where  $n' = dn/dz$ ,  $n'' = d^2n/dz^2$ , etc. When absorption is absent, this becomes

$$\frac{\lambda_0}{2\pi} \frac{|dn/dz|}{n^2} \ll 1, \quad \frac{\lambda_0}{2\pi} \frac{|d^2n/dz^2|}{n \frac{dn}{dz}} \ll 1 \quad (14-102a)$$

where the first condition states that the fractional variation in medium properties in one wavelength is small. It is violated in two cases: if the gradient of  $n$  is steep enough, or if the refractive index  $n$  is sufficiently small.

The Eq. 14-101 consists of two completely independent solutions in the geometrical optics approximation, as in a homogeneous medium, so that reflection of waves can occur only in regions where geometrical optics is not valid, *i.e.*, when  $dn/dz$  is large, or  $n$  is small. We have already noted that waves do not propagate when the refractive index is negative--in the absence of absorption waves are completely reflected from a region where  $n = 0$ , provided the electron density continues to increase ( $n$  becoming more negative) over a distance large compared to  $\lambda_0/2\pi$  beyond the point where  $\epsilon = n^2 = 0$ . This total reflection is analogous to total internal reflection in optics, and explains the complete ionospheric reflection of radio waves even at vertical incidence. For a wave incident from medium 1 (free space) onto a boundary with medium 2, Snell's law gives total internal reflection for angles of incidence  $\theta_1 \geq \sin^{-1}(n_2/n_1)$ , if  $n_1 > n_2$ . For normal incidence ( $\theta_1 = 0$ ) total internal reflection can occur only when  $n_2 = 0$ , which is possible in a plasma (the absence of a sharp boundary is not important in this case).

When absorption is present, reflection is never total, except for the pathological case of an infinitely sharp gradient between free space and an infinite electron density. Reference 14-18 gives solutions for the reflection from various electron density contours between two regions, such as linear, parabolic, exponential, etc. For an exponential gradient where  $d$  is the e-folding distance of the electron density, the power reflection coefficient  $R$  is given by

$$R = \exp \left[ \frac{-4\omega d}{c} \tan^{-1} \left( \frac{v_{\text{eff}}}{\omega} \right) \right] \quad (14-103)$$

if the collision frequency  $v_{\text{eff}}$  is independent of electron density as at low altitudes (Eq. 14-67). Ref. 14-20 extends this calculation to the case where the collision frequency is proportional to the electron density, which is the case at high altitudes (Eq. 14-70), when the electron-neutral collision frequency (Eq. 14-67) is small compared to the electron-ion values (Eq. 14-70).

For values of electron density and density gradients in the normal ionosphere, and even in most situations following nuclear detonations, the geometrical (or ray) optics approximation is valid and we may confidently trace propagation paths using successive applications of Snell's law for contiguous differential path elements. The relevant vector differential equation is (Ref. 14-4)

$$\frac{d}{ds} \left( n \frac{d\vec{r}}{ds} \right) = \vec{\nabla} n \quad (14-104)$$

$\vec{r}$  being the position vector of a point on the ray path (from any arbitrary origin) and  $s$  the length of the ray measured from a fixed point on it.

Not only is ray optics valid for the geometrical progression of any individual ray, but the intensity of a ray bundle may also be found by applying ray optics to all the rays in the bundle and following the changes in cross-sectional area, as long as conditions (Eq. 14-102) are fulfilled. Although this process sounds simple in theory, it can become

quite complex mathematically, and various simplifications have evolved for treating propagation of electromagnetic waves under different ionospheric conditions corresponding to the validity of Eq. 14-102.

We derived Eq. 14-102 on the basis of a one-dimensional variation of material properties, and hence of the field. This is almost always a good approximation in the normal ionosphere, since the variation of electron density with altitude usually outweighs any horizontal gradients. However, there are cases, discussed below in connection with propagation through cylindrically symmetric regions of ionization, where the wavefront becomes rippled, and at some point crossing of two neighboring rays can occur. At such foci, geometric-optic approximations for intensity break down, and similarly on caustic surfaces (usually envelopes of trajectories of neighboring rays), the wave-character of the propagation must be considered (e.g., Ref. 14-2, pp. 439-452).

Most previous workers analyzed propagation through high-altitude ionization in terms of a statistical ensemble of scatterers, usually aligned preferentially along the Earth's magnetic field, in terms of the "thin phase screen" approximation (e.g., Refs. 14-21 to 14-23). This approximation is a linearized version of ray optics in which it is assumed that refractive effects are so weak that the rays are essentially straight lines, being bent slightly at the scattering region. Subsequent propagation of the wave, after passing through the phase screen, then proceeds according to standard Kirchhoff diffraction theory. These papers were primarily concerned with the propagation of radio waves, of much lower frequency than microwave radars. Nevertheless there are cases when the mathematical techniques are quite relevant to radar propagation as well. Thus, it has been observed that high-altitude barium releases tend to form ionized striations along the earth's magnetic field, and similar structure has been noticed in high-altitude nuclear detonations (Ref. 14-24).

Reference 14-25 gives a summary and comparison of three principal techniques of treating propagation through such striated media, the Born

approximation, the eikonal or geometrical optics approximation, and the thin-screen approximation. The range of validity of the Born approximation is shown to be exceeded for all interesting plasma densities, and the thin-screen approximation is shown to be, in almost all cases, a sufficiently good approximation to the eikonal approximation. We restrict our remaining comments to the thin-screen method, the mathematical techniques of which have been worked out in great detail in Refs. 14-2, 21-26.

As an example of the thin-screen approximation we present an heuristic derivation of its predictions for the case of a radar observing a target at range  $R$  through a region of depth  $L$  (along the radar beam) filled with clumps of ionization of characteristic size  $a$  and separated by a mean distance  $b$  ( $R \gg L \gg b \gg a \gg \lambda$ ). We may consider these radially symmetrical ionized clumps to be extended along the field lines, like auroral striations or streamers, and consider only effects in a plane normal to the field lines. Almost independent of the exact form of the radial distribution of electron density  $n_e$  within each ionization clump, or striation, calculations for specific cases have led to the conclusion that the rms angular deflection  $\theta_1$  of a ray passing through the striation is

$$\theta_1 \sim n_c / n_{cr} \quad (14-105)$$

where  $n_{cr}$  is that value of electron density for which the plasma frequency  $\omega_p$  (cf. Eq. 14-80) is equal to the radar angular frequency  $\omega \equiv 2\pi f$ ,

$$n_{cr} = 1.24 \times 10^{-9} f^2 \equiv mc^2 / 4\pi e \quad (14-106)$$

In this approximation, the ray proceeds through the thin screen by a random walk process, being as likely at each encounter with a striation to be scattered either right or left. Hence if  $N_s$  is the mean number of striations encountered by a ray in traversing a length  $L$ , given by  $N_s \sim 2La/\pi b^2$ , the rms overall spreading  $\theta_{rms}$  of the beam on emergence is

$$\theta_{\text{rms}} = \frac{n_e}{n_{\text{cr}}} \sqrt{N_s} = \frac{n_e}{n_{\text{cr}}} \left( \frac{2La}{\pi b^2} \right)^{1/2} \quad (14-107)$$

(The average value,  $\bar{\theta}$  is of course zero.) The total phase shift,  $\phi$ , on the average, is

$$\bar{\delta\phi} = -ka \frac{n_e}{n_{\text{cr}}} N_s \quad (14-108)$$

and the rms value is

$$\delta\phi_{\text{rms}} = ka \frac{n_e}{n_{\text{cr}}} \sqrt{N_s} \quad (14-109)$$

This means that the initially plane wavefront (we assume the radar effectively at infinity) is now wrinkled upon emergence from the thin-screen region. The correlation length of the phase fluctuations perpendicular to the beam is of the order of  $a$ , for  $b > a$ , independent of how many striations there may be. A plot of the local wave normal direction (taken as zero for the initial direction) against distance normal to the direction of propagation will show a series of wiggles, of mean spacing  $a$  between successive zero-crossings, and of mean amplitude  $\theta_{\text{rms}}$ .

The subsequent development of this wrinkled wavefront proceeds according to standard Kirchhoff-Huyghens diffraction theory and, if the target is at a sufficient distance, leads to the possibility of multiple images, which are seen to be the "glint points," along the wavefront, for a series of straight lines drawn from the target. The number  $N_i$  of these images is easily seen to be about

$$N_i = 1 + \frac{\theta_{\text{rms}} R}{a} \quad (14-110)$$

where  $R$  is the distance from the striated region to the target and only that fraction of these images within the linear field-of-view of the beam will ordinarily be visible. The intensity of the various images

is in general reduced inversely as  $N_1$ , and in addition there are large fluctuations about this average value (cf. Ref. 14-25).

At this point we have derived all the formulae necessary to account for absorption and refraction of monochromatic radar waves in plasmas, homogeneous and otherwise, when the variation in plasma properties is small in a wavelength. In addition, for the case of a one-dimensional variation of plasma properties we have discussed the question of energy reflection from gradients sharp compared to a wavelength. The last remaining issue is that of reflection, or scattering, from turbulent irregularities of scale size less than or comparable to a radar wavelength.

Radar backscatter, or clutter, from such media is discussed in Refs. 14-27 and 14-28. Relevant examples for BMD radars are backscatter from turbulent reentry wakes, from possible turbulent irregularities in and around fireballs at low and intermediate altitudes, and from E- and F-region structured ionization such as field aligned striations in which spatial structure of the order of a radar wavelength exists. We shall here merely sketch the derivation of the relevant equations, referring to Refs. 14-27 and 14-28 for details. The starting point is Eq. 11-82 which together with  $\vec{\nabla} \cdot \epsilon^i \vec{E} = \vec{\nabla} \cdot n^2 \vec{E} = 0$  may be written as

$$\nabla^2 \vec{E} + k^2 n^2 \vec{E} + 2\vec{\nabla}(\vec{E} \cdot \vec{\nabla} \log n) = 0 \quad (14-111)$$

Assuming small local fluctuations  $\delta n(r)$  in the refractive index  $n$ , we may write  $n = \bar{n} + \delta n$ , where  $\bar{n}$  is the mean value, which for underdense plasmas we may set equal to unity. Expanding the electric field  $\vec{E}$  in a similar way, we write  $\vec{E} = \vec{E}_0 + \vec{E}_1$ , where  $E_1$  is of order  $\delta n$ , compared to  $E_0$ . This leads to two equations, one for  $E_0$ , which we may take as the incident plane wave, and the other for  $E_1$ , which is seen to be the amplitude of the electric vector of the scattered wave. The latter equation is

$$\nabla^2 \vec{E}_1 + k^2 \vec{E}_1 = -2k^2 \delta n \vec{E}_0 - 2\vec{\nabla}(\vec{E}_0 \cdot \vec{\nabla} \delta n) \quad (14-112)$$

which is of the form (14-26). The solution of this equation, after some algebra, may be shown to be

$$E_1(\vec{r}) = \frac{k^2 e^{ikr}}{2\pi r} \vec{E}_0 \int_V \delta n(\vec{r}') e^{i(\vec{k} - k\vec{m}) \cdot \vec{r}'} d\vec{r}' \quad (14-113)$$

where  $\vec{m}$  is a unit vector from the origin (chosen within the scattering volume  $V$ ) to the observation point. With a similar expression for the scattered magnetic field component  $\vec{B}_1$ , the Poynting vector for scattered energy may be computed and averaged over the volume, and one finally obtains for the radar cross-section per unit volume of the medium, at a radar frequency  $\omega = ck$ ,

$$q(k) = k^4 (\delta\epsilon)^2 \int d\vec{r} \rho(\vec{r}) \exp(2i\vec{k} \cdot \vec{r}) \quad (14-114)$$

where  $\rho(\vec{r})$  is the normalized autocorrelation function describing the rate of variation of the dielectric constant fluctuations. The value of  $\rho(0)$  is unity, and  $\rho$  falls off with increasing  $\vec{r}$  in some manner depending on the shape and scale size of the fluctuations. The integral is called the spectral density function of the fluctuations,  $\Phi(2k)$ .

Neglecting absorption, so that  $\delta\epsilon$  is real, we may use Eq. 14-56 to evaluate  $\delta\epsilon$ , and we find that

$$q(k) = \left( \frac{4\pi e^2}{mc^2} \right)^2 \delta n_e^2 \Phi(2k) \quad (14-115)$$

where  $\delta n_e$  is that fluctuation in electron density that produces a fluctuation  $\delta\epsilon$  (or  $\delta n$ ) at the radar frequency. Note that the frequency dependence of the backscatter cross-sections per unit volume thus depends only on the spectrum of the fluctuations, through  $\Phi(2k)$ . From the definition of  $\Phi(2k)$  the radar signals automatically search out the spatial components of electron density fluctuations which equal half the radar wavelength, for the case of  $180^\circ$  backscatter that we are considering.

i.e., the radar measures those fluctuations which satisfy the Bragg interference conditions.

For a discussion of the solution for various forms of the autocorrelation function  $\rho(\vec{r})$ , isotropic (exponential, Gaussian, etc.) and anisotropic, as in field-aligned ionization, which is generally taken as elongated along the field-lines compared to the transverse dimensions, Refs. 14-27 and 14-28 should be consulted.

#### 14.5 SUMMARY

We list below a summary of the relevant equations and spatial regions of importance. The plasma properties necessary to describe the propagation of monochromatic radar beams are the indices of refraction  $n$  and absorption  $\kappa$ , given by Eq. 14-93. These latter are expressed in terms of the plasma frequency  $\omega_p$ , where  $\omega_p^2 = 4\pi N e^2 / m$ .

#### Energy Absorption

To a very good approximation, Eq. 14-81 may be expressed as

$$\text{Absorption (db/km)} = \frac{4.6 \times 10^4 N \nu_{\text{eff}}}{\nu_{\text{eff}}^2 + \omega^2} \quad (14-116)$$

The effective collision frequency  $\nu_{\text{eff}}$  is the sum of that due to neutrals (Eq. 14-67) and ions (Eq. 14-70), where below the D-region usually only the electron-neutral value is important, and ionic collisions dominate in the ionosphere.

#### Refraction

Tropospheric refraction can occur at extremely low look angles (cf. Ch. 1) but refraction is otherwise a purely ionospheric phenomenon. Subject to Eqs. 14-102 demanding small fractional changes in electron density over a wavelength, ray optics (Eq. 14-104) may be used to trace the



propagation path. The index of refraction  $n$  in the ionosphere (Eq. 14-93) may be written in terms of the critical electron density  $n_{cr}$  corresponding to the radar frequency (Eq. 14-106), provided  $\nu_{off} \ll \omega$

$$n = \sqrt{1 - \frac{n_e}{n_{cr}}} \approx 1 - \frac{n_e}{2n_{cr}} \quad (14-117)$$

### Multipath and Scattering

These effects have been discussed in terms of wave-front crinkling in passing through a high-altitude ensemble of electron inhomogeneities, and the subsequent convergence of several parts of this crinkled wave-front onto a target, by Huygen's principle. For a particular geometrical arrangement of these ionization regions (mean density  $n_e$ , size  $a$ , mean spacing  $b$ , and extent  $L$  along the radar beam) a beam divergence  $\theta_{rms}$  due to multiple refraction of rays occurs, where

$$\theta_{rms} \sim \frac{n_e}{n_{cr}} \left( \frac{2La}{\pi b^2} \right)^{1/2} \quad (14-107)$$

This beam divergence in itself produces an effective energy attenuation at the target, and in addition there will be  $N_i$  multiple images,  $N_i$  being given by Eq. 14-110.

Nuclear multipath is also possible at low altitudes, but in order to bend a ray significantly without prohibitive attenuation the electron gradients must be very large indeed. (Compare Eq. 14-103 on the reflectivity at normal incidence of an exponential electron density gradient.)

### Backscatter (Clutter)

Radar reflections can occur from electron density gradients sharp compared to a wavelength. Eq. 14-103 gives the reflectivity from a one-dimensional exponential gradient ( $d$  being the e-folding distance).

This equation may be written, at low altitudes where  $\nu_{eff} < \omega$ , as

$$\text{Reflectivity (db loss)} = 6f_{\text{GHz}}^2 d_{\text{cm}} \quad (14-118)$$

where the "reflectivity" is expressed in terms of the two-way db path loss.

Reflection from underdense turbulent gradients is expressed in terms of the autocorrelation function  $\rho(r)$  describing the rate of variation of electron density variations, by Eq. 14-115 .

### Dispersion

Real radar waves have a finite bandwidth, and the various frequency components have different indices of refraction in a plasma, by Eq. 14-93. This dispersion leads to several effects, the principal one being pulse stretching. This latter is easily calculable. In traversing a distance  $L$  of plasma of mean electron density  $n_e$ , a pulse of center frequency  $f_o$  experiences a time delay

$$\Delta T = \frac{L}{c} (n - 1) = \frac{n_e L}{750 f_o^2} \quad (14-119)$$

where we have assumed  $n_e \ll n_{cr}$  (Eq. 14-117). In addition, there will be a difference  $\delta\Delta T$  in delay for the upper and lower frequencies in the bandwidth  $BW(s^{-1})$ , given by

$$\delta\Delta T = \Delta T \cdot \frac{2BW}{f_o} \quad (14-120)$$

This pulse stretching may be accompanied by severe pulse distortion, particularly as the different frequency components may not even travel the same path, as we assumed above. The treatment of a wide band pulse traveling through a strongly dispersive medium is currently the subject of intensive investigation, and has not yet been solved. Further discussion of these points is found in Refs. 14-5, 14-10, and 14-18.

## 14.6 ADDENDUM: SATELLITE COMMUNICATIONS

### 14.6.1 INTRODUCTION

In the five years since the main body of this chapter was written, a rapidly growing interest in satellite communications has manifested itself (*e.g.*, Refs. 14-29 through 14-32), in contrast to the emphasis on radar propagation in this chapter. Although most satellite communications links also operate in the same frequency range used by radars, so that the equations governing electromagnetic propagation remain unchanged, there are enough differences in some of the system parameters that different propagation effects need emphasis. We give below a very abridged discussion of some of the major areas of active research in this area and refer the reader to the references for further details.

The previous discussion of propagation through ionospheric striations was based entirely on Gaussian irregularities and the thin phase screen approximation. With suitable modifications to take account of the fact that the striated region may be of considerable extent along the propagation direction (*i.e.*, the use of multiple separated thin phase screens) this technique is still applicable (Ref. 14-33). Furthermore, nearly all results obtained by more complex mathematical methods are much more easily visualized on the basis of the early thin screen analyses (*e.g.*, Refs. 14-21 through 14-23). For this reason we omit all discussion of other approximate solutions such as the Born, Rytov or Markov approximations and refer the reader to Refs. 14-28 and 14-30 through 14-34 for information on those methods.

For radars the principal effects of ionospheric striations are angular scintillation that degrades tracking accuracy, and amplitude scintillation that degrades the single-pulse detection range (Ref. 14-35). Phase coherence in the signal may be degraded as well, but the effects are negligibly small over the short duration of most radar pulses. (These

phase fluctuations do however set a limit to the coherent integration of many pulses, as discussed in Ref. 14-36, which impacts on the performance of synthetic-aperture radars such as SEASAR (Ref. 14-37)). However, for most BMD radars the only effect of the phase fluctuations is through the amplitude and angle scintillations produced between the thin screen and the radar.

For most satellite communications links angular errors are of considerably less importance, since in general tracking is not a problem, due to the comparatively smaller antennas and consequently larger beams. (The effects of antenna size on scintillation characteristics are discussed in Ref. 14-38 and more fully in Ref. 14-39. These effects are quite simply explicable in terms of the thin screen approximation, as discussed below.) For many communication systems, only amplitude scintillation is important\*. This signal fading is caused by the relative motion of the ground-satellite communication link and the striations which lie across the propagation path.

The assumption of a Gaussian auto-correlation function for electron-density fluctuations within the scattering medium formed the basis for the early thin-screen analyses, and is equivalent to assuming that the striations form a random distribution of Gaussian rods aligned along the magnetic field, with two different characteristic dimensions along and perpendicular to the magnetic field. This particular function, chosen for ease of mathematical treatment, was chosen before *in-situ* measurements and simultaneous observations at various frequencies were made (e.g., Ref. 14-40). The power spectrum of ionospheric electron density fluctuations now is felt to be much better represented by a power-law spectrum than the previously assumed Gaussian spectrum.

---

\* Direct effects of phase scintillations on coherent signal processors are discussed in Ref. 14-45.

Nevertheless, the early thin-screen analyses afford a powerful and intuitive geometrical way of understanding many details of the diffraction process, and the principal differences in using a power-law spectrum are reflected in the frequency—and distance—variations of such parameters as the scintillation index, cross-correlation of inphase and quadrature components, and statistics of deep fades. We therefore return to the previous thinscreen analysis based on a collection of single size Gaussian striations, derive the relevant equations for bit-error probability of a communications channel, and finally turn to the differences produced by a more realistic medium.

#### 14.6.2 THE EFFECT OF GAUSSIAN IRREGULARITIES

It is easy to show that in a medium consisting of a collection of randomly located single size Gaussian striations whose radial variation of electron density  $n_e$  in a plane normal to the magnetic field is

$$n_e = n_0 e^{-r^2/a^2}, \quad (14-121)$$

the auto-correlation function  $B(X)$  is given by

$$B(X) = \langle n_e(\vec{r}) n_e(\vec{r} + \vec{X}) \rangle = \frac{\pi}{2} n_0^2 a^2 \Sigma e^{-X^2/2a^2}. \quad (14-122)$$

Here  $\Sigma$  is the areal density of striation axes (e.g.,  $\Sigma \approx 0.1/a^2$ ).  $B(X)$  is the *in-situ* autocorrelation of the electron density fluctuations. The rms deviation of these fluctuations is given by  $\sqrt{B(0)}$ . The *in-situ* power-spectrum of these fluctuations is the Fourier transform of the autocorrelation function, which also happens to be Gaussian:

$$\begin{aligned} N(q) &\equiv \frac{1}{2\pi} \int_{-\infty}^{\infty} e^{iqX} B(X) dX \\ &= \sqrt{\frac{\pi}{8}} n_0^2 a^3 \Sigma e^{-q^2 a^2/2} \end{aligned} \quad (123)$$

The phase screen power-spectrum  $\Phi(q)$  caused by these electron density fluctuations after emergence of the wave from a screen of thickness  $L$  is related to  $N(q)$  by (see Reference 14-41)

$$\Phi(q) = \frac{\sqrt{2\pi} e^4 \lambda^2 a L}{m^2 c^4} N(q) = \frac{\pi}{2} \frac{e^4 \lambda^2 n_o^2 a^4 \Sigma L}{m^2 c^4} e^{-q^2 a^2 / 2} \quad (14-124)$$

and the auto-correlation of the phase in the direction normal to the propagation direction  $Z$  is

$$\begin{aligned} R(X) &= \int_{-\infty}^{\infty} e^{-iqX} \Phi(q) dq \\ &= \pi \sqrt{\frac{\pi}{2}} \frac{e^4 \lambda^2 n_o^2 a^3 \Sigma L}{m^2 c^4} e^{-X^2 / 2a^2} \end{aligned} \quad (14-125)$$

Here we have assumed that the rods were infinitely long in the field direction  $y$ , for geometric simplicity. Note that the shape of the phase auto-correlation function is independent of the screen thickness  $L$ , *i.e.*, no matter how many Gaussian rods are sprinkled along the propagation direction, the mean de-correlation distance of the phase fluctuations remains constant at  $\sqrt{2}a$ . (The rms phase deviation,  $\phi_o \equiv \sqrt{R(0)}$ , of course increases with  $L$ .) Thus the phase front upon emergence from the screen is rippled with a mean wavelength about the size "a" of the Gaussian striations, and a mean ripple amplitude  $\phi_o$ . The intensity fluctuations then build up by standard diffraction theory as the wave proceeds onward, and a very useful geometrical plot of the scintillation index as a function of the wavelength  $\lambda$ , distance  $Z$  from the screen, size "a" and  $\phi_o$  was first given by Singleton (Reference 14-42), reproduced here in Figure 14-2.

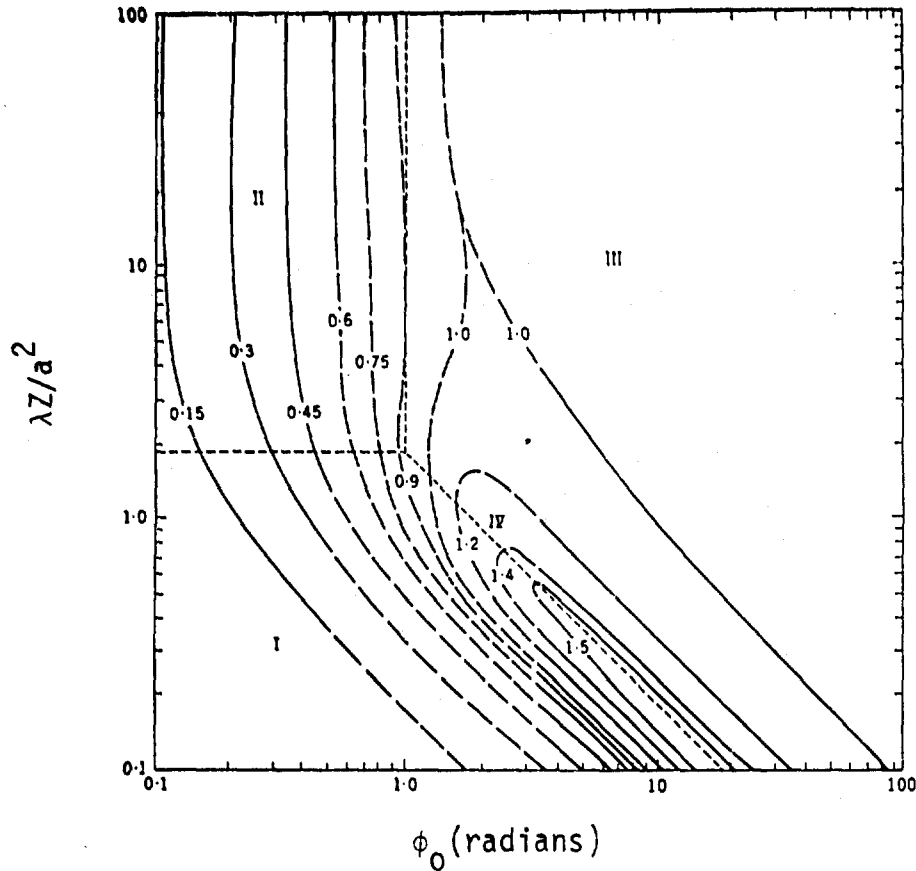


Figure 14.2. Curves of constant Scintillation Index  $S_4$  on a plot of  $\lambda Z/a^2$  vs  $\phi_0$ . The broken lines correspond to an exact solution; the full lines to an approximation. (Source: Reference 14-42).

The Scintillation Index  $S_4$  whose contour lines are shown is defined by

$$S_4 = \left[ \langle E^4 \rangle - \langle E^2 \rangle^2 \right]^{1/2} / \langle E^2 \rangle \quad (14-126)$$

$E$  being the magnitude of the (complex) electric field strength.

We note that for strong scintillation (taken as  $\phi_0 \geq 1$  radian) a focusing effect takes place which produces a peak in  $S_4$  near  $\lambda Z/a^2 = \pi/\sqrt{3}\phi_0$ , at which distance  $S_4$  can actually exceed unity. Mercier (Ref. 14-22) had earlier shown that as  $Z \rightarrow \infty$  the even-order moments of  $E$  coincided with

those of a Rice-distribution of amplitudes, *i.e.*, the distribution of the amplitude of a constant signal plus in-phase and quadrature Gaussian noise. Mercier was able to derive various approximate analytic expressions in the limit  $Z \rightarrow \infty$ , and for  $\phi_0^2 \leq 10 \text{ rad}^2$ . This focusing phenomena is a characteristic of the assumption of single-size Gaussian irregularities. For a power law spectrum (for which the irregularity size "a" is meaningless) scintillations are determined by irregularities with sizes comparable to the Fresnel dimensions  $\sqrt{\lambda Z}$ . It can easily be shown (*e.g.*, Ref. 14-23) that the focusing distance (for Gaussian striations) is equal to the radius of curvature of the wavefront at the screen.

A very useful way of visualizing the development of intensity scintillations as the rippled wavefront progresses beyond the phase screen was given by Sachs (Ref. 14-43). On the basis of the Kirchhoff diffraction integral he developed the connection with geometrical optics by interpreting the intensity at any field point as the sum of all the Huygens wavelets emanating from the "glint points" of the wavefront, *i.e.*, those points of local perpendicularity to a radius vector from the field point. By considering the intensity of each of these image points in terms of the local radius of curvature of the wave front, and adding all the image rays with proper consideration of their phase, he was able to derive the distribution of intensities  $P(E, E_0, \phi_0)$ . Here  $E$  is the observed amplitude,  $E_0$  is the amplitude of the wave upon entering the phase screen and  $\phi_0$  is the rms phase deviation, which determines the scintillation index  $S_4$  as shown in Figure 14-2. For additional analyses, see Reference 14-46.

The effect of fading on a digital communication system is now easily written down. A digital information signal is composed of a sequence of symbols (*cf.* Ref. 14-31), each symbol being transmitted as a sequence of elements. The Probability of Element Error  $P_e$ , or Bit Error Probability, is defined as the probability that the receiver assumes any element other



than the one transmitted. This may be shown to be related only to the signal-to-noise ratio on the link, which is proportional to the square of the amplitude  $E$ . Thus in the presence of fading the probability of element error is

$$P_e(E_o, \phi_o) = \int_0^{\infty} dE P_e(E) P(E, E_o, \phi_o) \quad (14-127)$$

For a particular type of modulation and detection, the DPSK (differentially coherent detection of phase-shift-keying), and for the Rician intensity statistics appropriate to a Gaussian auto-correlation function,  $P_e$  is shown as a function of the vacuum signal-to-noise ratio (proportional to  $E_o^2$ ) in Figure 14-3 for various values of the parameter  $S_4$ , which is related to  $\phi_o$  by (cf Reference 14-23).

$$S_4^2 = 1 - e^{-2\phi_o^2} \quad \text{for large } Z > a^2/\lambda \quad (14-128)$$

For most communication systems a value of  $P_e \leq 10^{-5}$  is essential: larger values produce intolerably high error rates. From Fig. 14-3 it is seen that in an unstriated medium the "vacuum" signal-to-noise ratio must be at least 10.3 dB in order to insure  $P_e \leq 10^{-5}$ . And for values of  $\phi_o > 1$  radian (which thus predict  $S_4$  values near unity) the signal-to-noise value must be some 48 dB! Thus the impact of the striated medium is immediately obvious. The situation is much the same for other types of modulation and detection of the communication channel.

This analysis was based on the assumption of a Gaussian autocorrelation function, which produces Rician intensity statistics, at distances large enough that the intensity variations have fully developed, which from Figure 14-2 is seen to be  $Z > a^2/\lambda$ . From Equation 14-125 it is apparent that  $\phi_o$  (which equals  $\sqrt{R(0)}$ ) is proportional to the radar

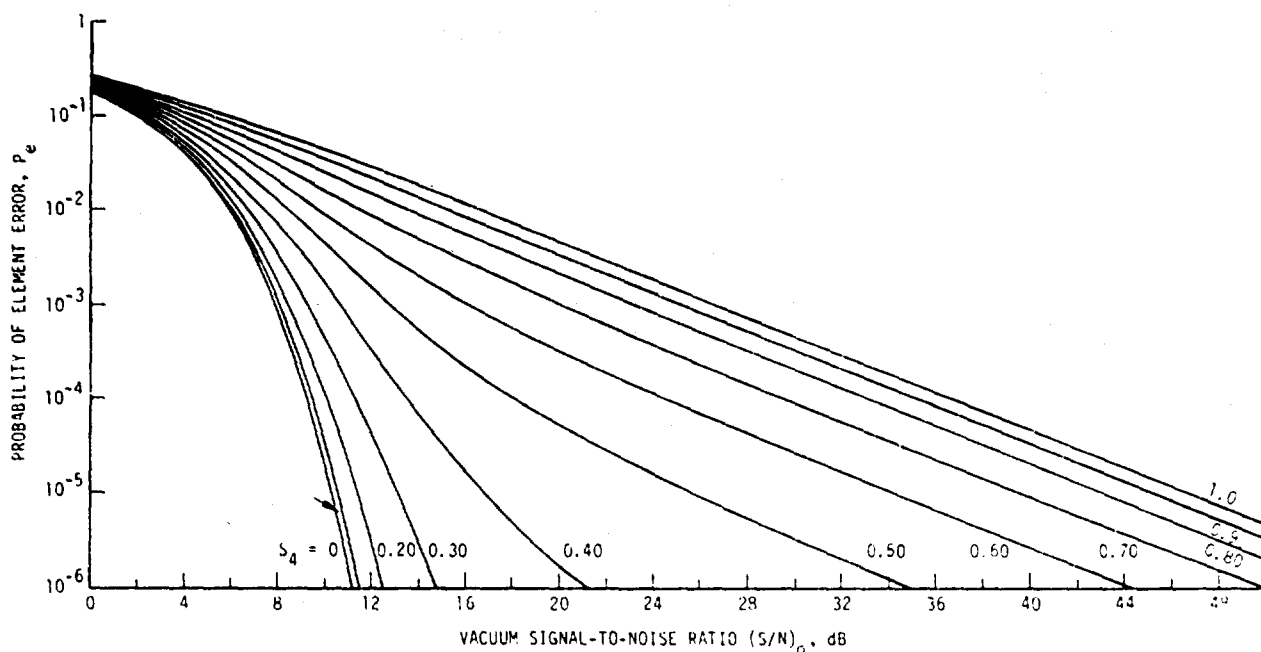


Figure 14-3. Probability of element error on one link of a binary DPSK communication system (source: Ref. 14-35).

wavelength  $\lambda$ . From Fig. 14-2 it is seen that this variation of  $\phi_0$  with  $\lambda$  corresponds to straight lines of slope +1. In the far-field the variation of scintillation index with wavelength is linear for  $\phi_0 < 1$  radian; in the near-field ( $2\lambda/a^2 < 1$ ),  $S_4 \propto \lambda^2$ . Since more recent ionospheric experiments have indicated that a power-law is a better descriptor for the spatial irregularity power spectrum than a Gaussian (which implies a single size "a" of Gaussoid irregularities, as we have seen) it is not surprising that this simple variation of the scintillation index with wavelength has not been verified.

### 14.6.3 THE EFFECT OF MORE REALISTIC IRREGULARITIES

Qualitatively the impact of a spectrum of fluctuation scale sizes can be seen from the ray-optics analogy discussed by Sachs. He ascribed the field amplitude at any point  $X$  to the sum of the individual intensities from the "glint points" of the wave front, which on the average were separated by a distance  $a$  for the Gaussian striations. With a spectrum of scale sizes there may be expected to be substantially more small-scale ripples and thus glint points contributing to the total amplitude at  $X$ , but each contributing a smaller amplitude. A detailed numerical study of how these secondary wavelets contribute to the total amplitude at  $X$  is given in Ref. 14-44 where the Fast Fourier Transform is applied to the angular spectrum of plane waves making up the rippled wavefront. The numerical comparison of intensity build up with distance from a Gaussian screen and one characterized by a Kolmogorov power spectrum is given in that paper. No significant qualitative differences were found in this comparison, particularly in the distribution of intensities, although some softening of the transition from near- to far-field was seen for the Kolmogorov spectrum, reflecting the larger range of "focal lengths" present, and the spatial scale of the intensity ripples was considerably less for the Kolmogorov spectrum, as would be expected due to the small ripples.

For the Gaussian phase screen the spatial scale of the intensity fluctuations is merely  $a/\phi_0$  at large  $Z$ . This may be easily derived by noting that two sources separated in angle by  $\theta$  give a fringe pattern  $\lambda/\sin\theta \sim \lambda/\theta$ . From Sachs' treatment by glint points, the rms angular bending is

$$\theta = \frac{\lambda}{2\pi} \frac{d\phi}{dx} = \frac{\lambda}{2\pi} \frac{2\pi\phi_0}{a}, \quad (14-129)$$

since the average distance to decorrelate the phase by  $2\pi\phi_0$  is simply  $a$ . This gives the result  $a/\phi_0$  immediately.

We note at this point a tacit assumption relating to the antenna size, which has resulted in some confusion and improper inference in the past. It has been fairly widely accepted (*e.g.*, Ref. 14-38) that when the antenna size becomes larger than the intensity fluctuation scale size  $a/\phi_0$ , as may easily happen for  $a \approx 200$  meters and  $\phi_0 \gg 1$ , the intensity variations average out over the antenna and no scintillations will be seen. This is in general not true, because the scale size of the fringe pattern is intimately tied to the size of the aperture measuring it. For specificity, consider that the scintillation is caused by a lateral drift of the striations across the satellite-ground receiver line-of-sight. If the striations are considered to be "frozen" in their pattern with respect to each other, the scintillations in intensity are caused by the drifting in at one side of the beam and out at the other of image sources which are the glint points of the wavefront at the receiver position. The instantaneous amplitude measured by the antenna depends on the number of these image sources in the beam, their individual amplitudes, and their relative phases. It is true that any two image sources separated by an angle greater than the beam angle  $\alpha = \lambda/D$ , where  $D$  is the antenna diameter, cannot both be visible to the antenna. Replacing  $\theta$  in the previous expression  $\lambda/\theta$  for fringe spacing by this value  $\alpha$  then gives  $D$ , the antenna diameter, as the minimum fringe spacing visible to this antenna. Thus the antenna, acting as an angular filter to exclude image separations greater than  $\alpha$ , may also be thought of as a spatial filter for fringes smaller than the antenna size. This is by no means equivalent to saying that there will be no scintillations visible as the screen drifts by overhead, *i.e.*, some deep fades may still occur whenever those images currently in the beam happen to interfere destructively.

In summary, a size spectrum of electron density fluctuations changes the intensity fluctuation scale size and its variation with distance, but does not produce qualitative differences in the distribution of intensities and

hence (from Eq. 14-127) the bit error probability. The change in scale size can be important, because as the line-of-sight sweeps through the striated medium, the fading time will be reduced over that of the single size Gaussian striations; also, the lateral decorrelation distances on the ground between two separated receivers (as in a spatial diversity scheme) may be reduced. A discussion of various diversity and coding alleviation techniques is given in Ref. 14-31.

## REFERENCES

- 14-1. Panofsky, W. K. H., and Melba Phillips, Classical Electricity and Magnetism, Addison Wesley, 1962.
- 14-2. Bremmer, H., "Propagation of Electromagnetic Waves," Encyclopedia of Physics, Vol. 16, Springer-Verlag, 1958.
- 14-3. Stratton, J. A., Electromagnetic Theory, McGraw-Hill, 1941.
- 14-4. Born, M., and E. Wolf, Principles of Optics, 2nd Ed., Pergamon, 1964.
- 14-5. Jackson, J. D., Classical Electrodynamics, Wiley & Sons, 1962.
- 14-6. Morse, P. M. & H. Feshbach, Methods of Theoretical Physics, Vol. 2, McGraw-Hill, 1953.
- 14-7. Clemmow, P. C., and J. P. Dougherty, Electrodynamics of Particles and Plasmas, Addison Wesley, 1969.
- 14-8. Spitzer, Lyman Jr., Physics of Fully Ionized Gases, 2nd Ed., Interscience, 1962.
- 14-9. Chapman, S., and T. G. Cowling, The Mathematical Theory of Non-Uniform Gases, 3rd Ed., Cambridge, 1968.
- 14-10. Ginzberg, V. L., The Propagation of Electromagnetic Waves in Plasmas, Pergamon, 1970.
- 14-11. Phelps, A. V., J. Appl. Phys. 31, 1723 (1960).
- 14-12. Allis, W. P., "Motions of Ions and Electrons," Encyclopedia of Physics, Vol. 21, S. Flugge, ed. Springer-Verlag (1956).
- 14-13. W. Heitler, Quantum Theory of Radiation, 3rd Ed., Clarendon Press, Oxford, 1954.
- 14-14. Grandy, W. T., Jr., Introduction to Electrodynamics and Radiation, Academic Press, 1970.

- 14-15. Joos, G., Theoretical Physics, 2nd Ed., Blackie & Sons, 1951.
- 14-16. Utlaut, W. F., et al., Science 174, 4006 (1971), "Intense RF Ionospheric Modification."
- 14-17. Landshoff, R., Phys. Rev. 76, 904, (1949); 82, 442 (1951).
- 14-18. Budden, K. G., Radio Waves in the Ionosphere, Cambridge Press 1961.
- 14-19. Schiff, L.I., Quantum Mechanics (3rd ed.) McGraw-Hill, New York, 1968.
- 14-20. Redmond, P. J., Radar Reflection Coefficients From a Plasma Gradient, General Research Corporation RM-1545
- 14-21. Booker, H. G., et al., "Diffraction From an Irregular Screen with Application to Ionospheric Problems," Phil. Trans. Roy. Soc. A 242, 579 (1950).
- 14-22. Mercier, R.P., "Diffraction by a Screen Causing Large Random Phase Fluctuations," Proc. Cambridge Phil. Soc. 58, 382-400 (1962).
- 14-23. Salpeter, E., "Interplanetary Scintillations," Astrophysical Journal, 147, 433 (1966).
- 14-24. Haerendel, G. and R. Lüst, "Artificial Plasma Clouds in Space," Sci. Amer. 80, November 1968.
- 14-25. Redmond, P., private communication, DNA-2952F, June, 1972.
- 14-26. Stavroudis, O. N., The Optics of Rays, Wavefronts, and Caustics, Academic Press 1972.
- 14-27. Booker, H. G. and W. E. Gordon, "A Theory of Radio Scattering in the Troposphere," Proc. Inst. Radio Eng. 38, 401, (1950).
- 14-28. Tatarski, V. I., Wave Propagation in a Turbulent Medium, McGraw-Hill, 1961.

- 14-29. Effects of the Ionosphere on Space Systems and Communication: Symposium Proc. Jan 20-22, 1975, J.M. Goodman, Editor, Naval Research Laboratory.
- 14-30. Crane, R.K., "Ionospheric Scintillation", Proc. IEEE, 65, 180, 1977.
- 14-31. Pritchard, W.L., "Satellite Communication—An Overview of the Problems and Programs", Proc. IEEE, 65, 294, 1977.
- 14-32. Effects on the Ionosphere on Space and Terrestrial Systems: Symposium Proc. Jan 24-26, 1978, J.M. Goodman, Editor, Naval Research Laboratory.
- 14-33. Bramley, E.N., "The Accuracy of Computing Ionospheric Radio-Wave Scintillation by the Thin-Phase-Screen Approximation," J. Atm. and Terr. Phys., 39, 367, 1977.
- 14-34. Fante, Ronald L., "Electromagnetic Beam Propagation in Turbulent Media", Proc. IEEE, 63, 1669, 1975.
- 14-35. VanBlaricum G., and H. Ostrowsky, Ionospheric Modification: Its Effects on Radar and Satellite Detection Systems, General Research Corporation RM-1911, October 1974.
- 14-36. Rino, C.L., et al., The Ionospheric Limitation to Coherent Integration in Transionospheric Radars, Paper A-8 of Ref. 14-32.
- 14-37. Brown, W.D., Effects of the Ionosphere on the Performance of the SEASAR Synthetic-Aperture Radar, Paper 1-13 in Ref. 14-32.
- 14-38. Briggs, B.H., "Brief Review of Scintillation Studies," Radio Science 1, 1163, 1966.
- 14-39. Knepp, Dennis L., "Antenna Aperture Effects on Measurements of Propagation Through Turbulence", p. 292 of Ref. 14-29 or IEEE Trans. Antenna Propagat., 23, 682-687, 1975.
- 14-40. Rino, C.L., et al., Amplitude and Phase Scintillation as Measured by the DNA Wideband Satellite, Paper I-2 of Ref. 14-32.



- 14-41. Taur, Roger, "Ionospheric Scintillation at Frequencies Above 1 GHz", Comstat Technical Review 4, 461, 1974.
- 14-42. Singleton, D.G., "Saturation and Focusing Effects in Radio-Star and Satellite Scintillations", J. Atm. and Terr. Phys., 32, 187, 1970.
- 14-43. Sachs, D., Propagation Effects of Large Phase Variations in a Striated Plasma, DNA 3852T, Science Applications Inc., November 1975.
- 14-44. Buckley, R., "Diffraction by a Random Phase-Changing-Screen: A Numerical Experiment," J. Atm. and Terr. Phys., 37, 143, 1975.
- 14-45. Ostrowsky, H., et al., The RCSCOE Manual, Vol. 20—Satellite Communication Model, DNA 3964F-20, General Research Corporation, January 1977.
- 14-46. Uscinski, B.J., The Elements of Wave Propagation in Random Media, McGraw-Hill Co., 1977.

## DISTRIBUTION LIST

### DEPARTMENT OF DEFENSE

Assistant Secretary of Defense  
Comm. Cmd. Cont. & Intell.

ATTN: M. Epstein  
ATTN: J. Babcock

Assistant to the Secretary of Defense  
Atomic Energy

ATTN: Executive Assistant

Command & Control Technical Center

ATTN: C-312, R. Mason  
3 cy ATTN: C-650

Defense Advanced Rsch. Proj. Agency

ATTN: TIO  
ATTN: STO, S. Zakanycz

Defense Communications Agency

ATTN: Code 480  
ATTN: Code 810, J. Barna  
ATTN: Code 101B  
ATTN: Code 205

Defense Communications Engineer Center

ATTN: Code R410, J. McLean  
ATTN: Code R820  
ATTN: Code R720, J. Worthington  
ATTN: Code R123

Defense Documentation Center

12 cy ATTN: DD

Defense Intelligence Agency

ATTN: DB, A Wise  
ATTN: DT-187, K. Morton  
ATTN: DT-5  
ATTN: DT-1B  
ATTN: HQ-TR, J. Stewart  
ATTN: DC-7D, W. Wittig  
ATTN: DB-4C, E. O'Farrell  
ATTN: RDS-3A

Defense Nuclear Agency

ATTN: DDST  
ATTN: RAEV, H. Fitz. Jr.  
ATTN: RATN  
ATTN: SPAS  
15 cy ATTN: TITL  
15 cy ATTN: RAAE  
4 cy ATTN: STVL

Field Command

Defense Nuclear Agency

ATTN: FCPR

Field Command

Defense Nuclear Agency

ATTN: FCPRL

Interservice Nuclear Weapons School

ATTN: TIV

Joint Chiefs of Staff

ATTN: J 3, WMMCCS Evaluation Office

### DEPARTMENT OF DEFENSE (Continued)

Joint Strat. Tgt. Planning Staff  
ATTN: JLTW-2

National Security Agency

ATTN: W32, O. Bartlett  
ATTN: B3, F. Leonard  
ATTN: R52, J. Skillman

NATO School (SHAPE)

ATTN: U.S. Documents Officer

Under Secy. of Def. for Rsch. & Engrg.

ATTN: Strategic & Space Systems (OS)

WMMCCS System Engineering Org.

ATTN: R. Crawford  
3 cy ATTN: T. Neighbors

Electromagnetic Compatibility Analysis Center

2 cy ATTN: CCA

### DEPARTMENT OF THE ARMY

Atmospheric Sciences Laboratory

U.S. Army Electronics Research & Development Command

ATTN: DELAS-EO-ME, H. Ballard  
ATTN: DELAS-EO, F. Niles  
ATTN: DELAS-AS, H. Holt  
ATTN: DELAS-EO-MO, R. Olsen

SMD Advanced Technology Center

Huntsville Office

Department of the Army

ATTN: ATC-O, W. Davies  
ATTN: ATC-I, M. Capps  
ATTN: ATC-O, L. Hayes  
ATTN: ATC-R, W. Dickerson  
ATTN: ATC-R, D. Russ

BMD Systems Command

Department of the Army

ATTN: BMDSC-HW, R. DeKalb  
ATTN: BMDSC-AOLIB  
2 cy ATTN: BMDSC-HW

Deputy Chief of Staff for Rsch. Dev. & Acq.

Department of the Army

ATTN: DAMA-CSS-N  
ATTN: DAMA-WSZ-C  
ATTN: DAMA-CSZ-C

Electronics Tech. & Devices Lab.

U.S. Army Electronics Research & Development Command

ATTN: DELET-R, S. Kronenberg  
ATTN: DELET-ER, H. Bomke  
ATTN: DELET-IR, E. Hunter

Harry Diamond Laboratories

Department of the Army

ATTN: DELHD-I-TL  
ATTN: DELHD-N-RB, R. Williams  
ATTN: DELHD-N-P, F. Wizenitz  
2 cy ATTN: DELHD-N-P

DEPARTMENT OF THE ARMY (Continued)

U.S. Army Ballistic Research Labs.  
ATTN: Technical Library  
ATTN: J. Mester  
ATTN: ORDAR-BLP, J. Heimerl

U.S. Army Combat Surv. & Target Acq. Lab.  
ATTN: C. Markow  
ATTN: DELCS-K

U.S. Army Comm-Elec Engrg. Instal. Agency  
ATTN: CCC-EMEO, W. Nair  
ATTN: CCC-EMEO-PED, G. Lane  
ATTN: CLL-CED, CCO, W. Neuendorf

U.S. Army Communications Command  
ATTN: CC-OPS-WR, H. Wilson  
ATTN: Technical Library

U.S. Army Foreign Science & Tech. Ctr.  
2 cy ATTN: DRXST-SD

U.S. Army Materiel Dev. & Readiness Cmd.  
ATTN: DRCLDC, J. Bender

U.S. Army Missile Intelligence Agency  
ATTN: J. Gamble

U.S. Army Communications R & D Command  
2 cy ATTN: DRDCO-COM-RY, W. Kesselman

U.S. Army Missile R & D Command  
2 cy ATTN: Redstone Scientific Info. Center

U.S. Army Nuclear & Chemical Agency  
ATTN: Library  
ATTN: MONA-WE, J. Berberet  
ATTN: MONA-WE, F. Thompson

U.S. Army Research Office  
2 cy ATTN: DRXRO-ZC, R. Mace

U.S. Army Satellite Comm. Agency  
ATTN: DRCPM-SC

U.S. Army TRADOC Systems Analysis Activity  
ATTN: ATAA-TDC, J. Hesse  
ATTN: ATAA-TCC, F. Payan, Jr.  
ATTN: ATAA-PL

Deputy Chief of Staff for Operations and Plans  
Department of the Army  
ATTN: DAMO-TZC, P. Kenny  
ATTN: DAMO-TCW

White Sands Missile Range  
Department of the Army  
ATTN: STEWS-TE-ANL, L. Flores

U.S. Army Communications Systems Agency  
ATTN: CCM-CCS-A

U.S. Military Academy  
2 cy ATTN: T. Johnson

U.S. Army Signal School  
2 cy ATTN: ATSN-CD

DEPARTMENT OF THE NAVY

Naval Electronic Systems Command  
ATTN: PME 117-T  
ATTN: Code 5011  
ATTN: NAVELEX 3101, T. Hughes  
ATTN: PME 117

Naval Intelligence Support Ctr.  
ATTN: NISC-50  
ATTN: Document Control

Naval Ocean Systems Center  
ATTN: Code 5321, I. Rothmuller  
ATTN: Code 5324, W. Moler  
ATTN: M. Paulson  
ATTN: Code 532, J. Richter  
ATTN: Code 5322, H. Hughes  
ATTN: Code 8151, C. Baggett  
ATTN: Code 532  
ATTN: Code 532, R. Pappert  
ATTN: Code 532, J. Bickie

Naval Postgraduate School  
ATTN: Code 1424

Naval Research Laboratory  
ATTN: Code 6780, S. Ossakow  
ATTN: Code 7555  
ATTN: Code 7551  
ATTN: Code 6780, J. Fedder  
ATTN: Code 6780, P. Palmadesso  
ATTN: Code 6700, T. Coffey  
ATTN: Code 7500, HG. Comm. Dir., B. Wald  
ATTN: Code 6730, E. McClean  
ATTN: Code 2627  
ATTN: Code 6709, W. Ali  
ATTN: Code 6701, J. Brown  
ATTN: Code 7175, J. Johnson  
ATTN: Code 7122, D. McNutt  
ATTN: Code 6780, D. Strobel  
ATTN: Code 7580  
ATTN: Code 6707, J. Davis

Naval Space Surveillance System  
ATTN: J. Burton

Naval Surface Weapons Center  
ATTN: Code F-14, R. Butler

Office of Naval Research  
ATTN: Code 420  
ATTN: Code 465  
ATTN: Code 421

Naval Air Development Center  
ATTN: Code 6091

Office of the Chief of Naval Operations  
ATTN: OP 941  
ATTN: OP 604

Strategic Systems Project Office  
Department of the Navy  
ATTN: NSP-2141  
ATTN: NSSP-2722, F. Wimberly  
ATTN: NSSP-2722, M. Meserole  
ATTN: NSP 43

DEPARTMENT OF THE NAVY (Continued)

Naval Surface Weapons Center  
White Oak Laboratory  
ATTN: Code R42, C. Infonsino  
ATTN: Code F31  
ATTN: Code X211

DEPARTMENT OF THE AIR FORCE

Aerospace Defense Command  
ATTN: DC, Mr. Long

Aerospace Defense Command  
ATTN: XPDQ  
ATTN: XP

Air Force Avionics Laboratory, AFSC  
ATTN: AAU, A. Johnson  
ATTN: AAD

Air Force Geophysics Laboratory, AFSC  
ATTN: PHP, J. Aarons  
ATTN: LKO, P. Huffman  
ATTN: OPR-1, J. Ulwick  
ATTN: LNB, K. Champion  
ATTN: LKB, R. Narcisi  
ATTN: OPR, P. Murphy  
ATTN: OPP, A. Stair  
ATTN: OPR, H. Gardiner  
ATTN: OPR, J. Kennealy  
ATTN: PHI, J. Buchau  
ATTN: PHP, J. Mullen

Air Force Systems Command  
ATTN: DLXP  
ATTN: DLTW  
ATTN: DLAE  
ATTN: Technical Library  
ATTN: SDR  
ATTN: DLS

Air Force Technical Applications Center  
ATTN: TFR, C. McNeely  
ATTN: Technical Library  
ATTN: TF  
ATTN: TFE, J. Van Workum  
ATTN: TD  
ATTN: TFS, M. Schneider  
ATTN: TN

Air Force Weapons Laboratory, AFSC  
ATTN: DYC, J. Frasier  
ATTN: CA  
ATTN: DYC  
ATTN: DE, C. Needham  
ATTN: SUL  
ATTN: DYC, J. Barry  
ATTN: DYC, J. Kamm  
ATTN: DYT, M. Fry  
2 cy ATTN: DED, G. Ganong

Assistant Chief of Staff  
Intelligence  
Department of the Air Force  
ATTN: INED

Electronic Systems Division, AFSC  
ATTN: YSEA  
ATTN: BCKC, L. Clark  
ATTN: XRW, J. Bead

DEPARTMENT OF THE AIR FORCE (Continued)

Deputy Chief of Staff  
Operations Plans and Readiness  
Department of the Air Force  
ATTN: AFXOKCD  
ATTN: AFXOXFD

Deputy Chief of Staff  
Research, Development, & Acq.  
Department of the Air Force  
ATTN: AFRDSS  
ATTN: AFRDSP  
3 cy ATTN: AFRDQ

Deputy Chief of Staff  
Programs & Analyses  
Department of the Air Force  
ATTN: PACSC, W. Adams  
ATTN: PACSC, R. Paul

Foreign Technology Division, AFSC  
ATTN: NIIS, Library  
ATTN: TQTD, B. Ballard  
ATTN: SDED, A. Oakes

Air Logistics Command  
Department of the Air Force  
ATTN: MM, R. Blackburn

Rome Air Development Center, AFSC  
ATTN: OCS, V. Coyne  
ATTN: TSLD  
ATTN: OCSA, J. Simons

Rome Air Development Center, AFSC  
2 cy ATTN: EEP

Space & Missile Systems Organization  
Air Force Systems Command  
ATTN: CS, P. Sivgals

Space & Missile Systems Organization  
Air Force Systems Command  
3 cy ATTN: WE

Space & Missile Systems Organization  
Air Force Systems Command  
ATTN: DYS

Space & Missile Systems Organization  
Air Force Systems Command  
ATTN: MNX  
ATTN: MNHL, S. Kennedy  
ATTN: MNWH, M. Baron

Space & Missile Systems Organization  
Air Force Systems Command  
ATTN: RSP

Space & Missile Systems Organization  
Air Force Systems Command  
ATTN: SKA, C. Rightmyer  
ATTN: SKA, M. Clavin

Space & Missile Systems Organization  
Air Force Systems Command  
ATTN: SZJ  
ATTN: SZJ, L. Kelley  
ATTN: SZJ, L. Doan  
ATTN: SZOE, H. Hayden

DEPARTMENT OF THE AIR FORCE (Continued)

Strategic Air Command  
Department of the Air Force  
ATTN: XPFS, B. Stephan  
ATTN: XPFS, R. Lewis  
2 cy ATTN: DCX, Chief Scientist  
ATTN: OOKSN  
ATTN: NRT  
ATTN: XPFS  
ATTN: ADWATE, B. Bauer

DEPARTMENT OF ENERGY

Department of Energy  
Albuquerque Operations Office  
ATTN: D. Sherwood

Department of Energy  
ATTN: A. Labowitz  
ATTN: Classified Library

Department of Energy  
ATTN: Office of Military Applications (RD&T)

OTHER GOVERNMENT AGENCIES

Central Intelligence Agency  
ATTN: NED/OSI-2648 Hqs.  
ATTN: OSI/PSTD, Rm. 5, F 19

Department of Commerce  
National Bureau of Standards  
ATTN: A. Phelps

Department of Commerce  
National Bureau of Standards  
ATTN: J. DeVoe  
ATTN: R. Moore  
ATTN: M. Krauss  
ATTN: K. Kessler  
ATTN: S. Abramowitz

Department of Commerce  
National Oceanic & Atmospheric Admin.  
Environmental Research Laboratories  
ATTN: D. Williams  
ATTN: Aeronomy Lab. G. Reid  
ATTN: F. Fehsenfeld  
ATTN: R. Grubb  
3 cy ATTN: E. Ferguson

Department of Transportation  
Office of the Secretary  
ATTN: R. Doherty  
ATTN: R. Lewis  
ATTN: S. Coronitti

Institute for Telecommunications Sciences  
National Telecommunications & Info. Admin.  
ATTN: W. Utlaut  
ATTN: D. Crombie  
ATTN: L. Berry  
ATTN: G. Falcon  
ATTN: A. Jean

NASA  
Langley Research Center  
ATTN: C. Schneider

OTHER GOVERNMENT AGENCIES (Continued)

NASA  
Goddard Space Flight Center  
ATTN: J. Siry  
ATTN: A. Tompkin  
ATTN: Technical Library  
3 cy ATTN: A. Aiken

NASA  
George C. Marshall Space Flight Center  
ATTN: W. Roberts  
ATTN: H. Stone  
ATTN: W. Oran  
ATTN: C. Balcher  
ATTN: J. Watts

NASA  
ATTN: P. Kurzhals  
ATTN: J. Haughey  
ATTN: A. Schardt  
ATTN: D. Dement  
ATTN: D. Cauffman

NASA  
Ames Research Center  
ATTN: R. Whitten

NASA  
Wallops Flight Center  
ATTN: J. Gray

DEPARTMENT OF DEFENSE CONTRACTORS

Aero-Chem Research Labs., Inc.  
ATTN: A. Fontijn

Aerodyne Research, Inc.  
ATTN: M. Camac  
ATTN: F. Bien

Aerogjet Electro-Systems Co.  
Div. of Aerogjet-General Corp.  
ATTN: J. Graham

Aerospace Corp.  
ATTN: W. Grabowsky  
ATTN: V. Josephson  
ATTN: T. Widhosh  
ATTN: A. Morse  
ATTN: S. Cohen  
ATTN: D. Olsen  
ATTN: T. Salmi  
ATTN: S. Bower  
ATTN: R. McNeal  
ATTN: T. Taylor  
ATTN: F. Morse  
ATTN: R. Slaughter  
ATTN: I. Garfunkel  
ATTN: G. Anderson  
ATTN: H. Mayer  
ATTN: N. Stockwell  
ATTN: J. Carter  
ATTN: J. Reinheimer  
ATTN: R. Rawcliffe  
ATTN: Library

Analytical Systems Engineering Corp.  
ATTN: Radio Sciences

DEPARTMENT OF DEFENSE CONTRACTORS (Continued)

Argonne National Laboratory  
ATTN: Library Svcs. Rpts. Sec.

Avco Everett Research Lab., Inc.  
ATTN: C. Von Rosenberg, Jr.  
ATTN: Technical Library  
ATTN: AS30

Battelle Memorial Institute  
ATTN: R. Thatcher  
ATTN: STOIAC  
ATTN: H. Lamuth

Aeronautical Research Associates of Princeton, Inc.  
ATTN: H. Pergament

Berkeley Research Associates, Inc.  
ATTN: J. Workman

Boeing Company  
ATTN: D. Murray  
ATTN: G. Hall  
ATTN: G. Keister  
ATTN: S. Tashird  
ATTN: J. Kenney  
ATTN: W. Cooley  
ATTN: R. Scheppe  
ATTN: V. Jones

Boston College  
2 cy ATTN: Chairman, Dept. of Physics  
2 cy ATTN: D. McFadden

Boston College  
Space Data Analysis Lab.  
ATTN: E. Hegblom  
ATTN: W. Grieder

BDM Corp.  
ATTN: L. Jacobs  
ATTN: W. Sweeney  
ATTN: J. Braddock  
ATTN: Library

Brown Engineering Company, Inc.  
ATTN: G. Harney  
ATTN: J. Beaupre  
ATTN: R. Deliberis  
ATTN: J. Cato  
ATTN: M. Passino

University of California at Riverside  
ATTN: J. Pitts, Jr.  
ATTN: A. Lloyd

University of California at San Diego  
ATTN: H. Booker

California Institute of Technology  
Jet Propulsion Lab.  
ATTN: J. Ajello

University of California  
ATTN: H. Johnston  
ATTN: F. Mozer  
ATTN: H. Strauss  
ATTN: W. Miller

DEPARTMENT OF DEFENSE CONTRACTORS (Continued)

Calspan Corp.  
ATTN: M. Dunn  
ATTN: J. Grace  
ATTN: C. Treanor  
ATTN: W. Wurster

Charles Stark Draper Lab., Inc.  
ATTN: D. Cox  
ATTN: J. Gilmore

University of Colorado  
Office of Contracts and Grants  
ATTN: C. Lineberger, JILA  
ATTN: G. Lawrence, LASP  
ATTN: J. Pearce, LASP

Columbia University  
ATTN: H. Foley

Columbia University  
La Mont Doherty Geological Observatory-Torrey Cliff  
ATTN: R. Phelan

Computer Sciences Corp.  
ATTN: J. Spoor  
ATTN: C. Nail  
ATTN: H. Blank

Comsat Labs.  
ATTN: G. Hyde  
ATTN: R. Taur

Concord Sciences  
ATTN: E. Sutton

Cornell University  
Department of Electrical Engineering  
ATTN: D. Farley, Jr.  
ATTN: M. Kelly

University of Denver  
Colorado Seminary  
Denver Research Institute  
ATTN: D. Murcrav

University of Denver  
Space Science Lab.  
ATTN: B. Van Zyl

EG&G, Inc.  
Los Alamos Division  
ATTN: J. Breedlove  
ATTN: J. Fu  
ATTN: J. Walker  
ATTN: D. Wright

Electrospace Systems, Inc.  
ATTN: P. Phillips  
ATTN: H. Logston

Environmental Psch. Inst. of Michigan  
ATTN: IRIA Library

ESL, Inc.  
ATTN: J. Marshall  
ATTN: C. Prettie  
ATTN: J. Roberts

DEPARTMENT OF DEFENSE CONTRACTORS (Continued)

Ford Aerospace & Communications Corp.  
ATTN: J. Mattingley

General Electric Co.  
Space Division  
ATTN: F. Alyea  
ATTN: J. Burns  
ATTN: M. Bortner  
ATTN: P. Zavitsanos  
ATTN: R. Edsall  
ATTN: T. Baurer

General Electric Co.  
Re-Entry & Environmental Systems Div.  
ATTN: R. Edsall

General Electric Co.  
ATTN: G. Millman  
ATTN: F. Reibert

General Electric Company-TEMPO  
Center for Advanced Studies  
ATTN: T. Stevens  
ATTN: W. McNamara  
ATTN: V. Stull  
ATTN: W. Knapp  
ATTN: M. Stanton  
ATTN: D. Chandler  
ATTN: J. Jordano  
2 cy ATTN: B. Gambill/B. Berkowitz  
5 cy ATTN: DASIAC

General Electric Tech. Services Co., Inc.  
ATTN: G. Millman

General Research Corp.  
ATTN: J. Ise, Jr.  
ATTN: J. Garbarino

Geophysical Institute  
ATTN: T. Davis  
ATTN: B. Watkins  
ATTN: Technical Library  
ATTN: J. Wagner  
3 cy ATTN: N. Brown

GTE Sylvania, Inc.  
Electronics Systems Grp-Eastern Div.  
ATTN: M. Cross  
ATTN: E. Motchok  
ATTN: A. Murphy

HSS, Inc.  
ATTN: D. Hansen

IBM Corp.  
Federal Systems Division  
ATTN: F. Ricci  
ATTN: C. Johnson

University of Illinois  
ATTN: K. Yeh

Information Science, Inc.  
ATTN: W. Dudziak

International Tel. & Telegraph Corp.  
ATTN: Technical Library  
ATTN: G. Wetmore

DEPARTMENT OF DEFENSE CONTRACTORS (Continued)

Institute for Defense Analyses  
ATTN: H. Wolfhard  
ATTN: J. Bengston  
ATTN: J. Aein  
ATTN: E. Bauer

Jamieson Science & Engineering  
ATTN: J. Jamieson

JAYCOR  
ATTN: S. Goldman

Johns Hopkins University  
Applied Physics Lab.  
ATTN: T. Evans  
ATTN: T. Potemra  
ATTN: J. Newland  
ATTN: Document Librarian  
ATTN: P. Komiske

Kaman Sciences Corp.  
ATTN: F. Foxwell  
ATTN: N. Beauchamp  
ATTN: P. Tracy  
ATTN: D. Perio  
ATTN: T. Meagher

Lawrence Livermore Laboratory  
University of California  
ATTN: L-96, T. Donich  
ATTN: L-262, W. Duewer  
ATTN: Technical Information Dept. Library  
ATTN: L-262, D. Wuebbles  
ATTN: A. Kaufman  
ATTN: A. O'Dell  
ATTN: L-31, R. Hager  
ATTN: L-48, E. Woodward  
ATTN: L-325, G. Haugan  
ATTN: L-71, J. Chang  
ATTN: L-389, R. Ott

Linkabit Corp.  
ATTN: I. Jacobs

Litton Systems, Inc.  
AMECOM Division  
ATTN: R. Grasty

Lockheed Missiles & Space Co., Inc.  
ATTN: Dept. 6012  
ATTN: D. Churchill

Lockheed Missiles and Space Co., Inc.  
ATTN: J. Cladis  
ATTN: J. Reagan  
ATTN: T. James  
ATTN: M. Walt  
ATTN: J. Kumer  
ATTN: W. Imhof  
ATTN: R. Jonsson  
ATTN: R. Au  
ATTN: R. Sears  
ATTN: B. McCormac

University of Lowell  
Center for Atmospheric Research  
ATTN: G. Boett

DEPARTMENT OF DEFENSE CONTRACTORS (Continued)

Los Alamos Scientific Laboratory

ATTN: H. Argo  
ATTN: E. Jones  
ATTN: R. Carlos  
ATTN: J. Malik  
ATTN: J. Wolcott  
ATTN: D. Westervelt  
ATTN: G. Barasch  
ATTN: R. Taschek  
ATTN: G. Davis  
ATTN: Librarian  
ATTN: M. Pongratz  
ATTN: J. Zinn  
ATTN: R. Jeffries  
ATTN: P. Keaton  
ATTN: H. Hoerlin

University of Lowell Rsch. Foundation  
ATTN: K. Bibl

M.I.T. Lincoln Lab.

ATTN: L. Loughlin  
ATTN: J. Evans  
ATTN: D. Towle

Martin Marietta Corp.  
ATTN: R. Heffner

McDonnell Douglas Corp.

ATTN: J. Moule  
ATTN: G. Mroz  
ATTN: N. Harris  
ATTN: Technical Library Services  
ATTN: R. Halprin  
ATTN: W. Olson

University of Minnesota  
ATTN: J. Winkler

Mission Research Corp.

ATTN: W. Crevier  
ATTN: W. Schlueter  
ATTN: F. Fajen  
ATTN: S. Gutsche  
ATTN: P. Fischer  
ATTN: M. Scheibe  
ATTN: R. Kilb  
ATTN: R. Hendrick  
ATTN: C. Longmire  
ATTN: D. Archer  
ATTN: D. Sappenfield  
ATTN: R. Bogusch  
ATTN: D. Holland  
ATTN: W. Hart  
ATTN: F. Guigliand  
ATTN: A. Michalett  
ATTN: C. Humphrey  
ATTN: T. Johnson

5 cy ATTN: Technical Library  
50 cy ATTN: D. Sowle

Mitre Corp.

ATTN: C. Callahan  
ATTN: A. Kymmel  
ATTN: G. Harding

Pacific-Sierra Research Corp.  
ATTN: E. Field, Jr.

DEPARTMENT OF DEFENSE CONTRACTORS (Continued)

Mitre Corp.

ATTN: M. Horrocks  
ATTN: J. Wheeler  
ATTN: W. Hall  
ATTN: W. Foster

National Academy of Sciences  
National Materials Advisory Board  
ATTN: J. Sievers  
2 cy ATTN: E. Dyer

Pennsylvania State University  
Ionosphere Research Lab.  
ATTN: Ionospheric Research Lab.

Photometrics, Inc.  
ATTN: I. Kofsky

Physical Dynamics, Inc.  
ATTN: A. Thompson

Physical Dynamics, Inc.  
ATTN: E. Fremouw

Physical Science Lab.  
ATTN: W. Berning

Physical Sciences, Inc.  
ATTN: K. Wray  
ATTN: G. Caledonia  
ATTN: R. Taylor

Physics International Co.  
ATTN: Technical Library

University of Pittsburgh  
Cathedral of Learning  
ATTN: W. Fite  
ATTN: F. Kaufman  
ATTN: M. Biondi

Princeton University  
Forrestal Campus Library  
ATTN: Library

R & D Associates

ATTN: H. Ory  
ATTN: A. Latter  
ATTN: R. Turco  
ATTN: W. Karzas  
ATTN: R. Lindgren  
ATTN: W. Wright, Jr.  
ATTN: C. MacDonald  
ATTN: R. Lelevier  
ATTN: B. Gabbard  
ATTN: R. Latter  
ATTN: D. Dee  
ATTN: C. Griefinger  
3 cy ATTN: F. Gilmore

R & D Associates

ATTN: H. Mitchell  
ATTN: J. Rosenoren

Roger Manasse  
ATTN: R. Manasse

Ravtheon Co.  
ATTN: G. Thome



DEPARTMENT OF DEFENSE CONTRACTORS (Continued)

Rand Corp.

ATTN: C. Crain  
ATTN: E. Bedrozian

Riverside Research Institute

ATTN: V. Trapani

Sandia Laboratories

Livermore Laboratory

ATTN: R. Murphey  
ATTN: T. Cook

Sandia Laboratories

ATTN: W. Brown  
ATTN: C. Williams  
ATTN: D. Thornbrough  
ATTN: Space Project Div.  
ATTN: 3141  
ATTN: T. Wright  
ATTN: R. Glasser  
ATTN: D. Dahlgren  
ATTN: M. Kramm  
ATTN: C. Mehl  
ATTN: L. Anderson

Science Applications, Inc.

ATTN: D. Hamlin  
ATTN: C. Smith  
ATTN: R. Lee  
ATTN: J. McDougall  
ATTN: L. Linson  
ATTN: E. Straker  
ATTN: D. Sachs

Science Applications, Inc.

ATTN: J. Dishon

Science Applications, Inc.

ATTN: D. Divis  
ATTN: W. Mendes

Science Applications, Inc.

ATTN: J. Cockayne  
ATTN: M. Knasel  
ATTN: M. McDonnell

Space Data Corp.

ATTN: E. Allen

SRI International

ATTN: C. Hulbert  
ATTN: F. Perkins

Stewart Radiance Laboratory

ATTN: R. Huppi

DEPARTMENT OF DEFENSE CONTRACTORS (Continued)

SRI International

ATTN: R. Hake, Jr.  
ATTN: G. Price  
ATTN: W. Jaye  
ATTN: V. Gonzales  
ATTN: M. Baron  
ATTN: R. Livingston  
ATTN: W. Chesnut  
ATTN: D. McDaniels  
ATTN: J. Depp  
ATTN: G. Smith  
ATTN: D. Neilson  
ATTN: C. Rino  
ATTN: G. Carpenter  
ATTN: P. Leonard  
ATTN: A. Burns  
ATTN: R. Leadabrand

Technology International Corp.

ATTN: W. Doquist

TRI-COM, Inc.

ATTN: D. Murray

TRW Defense & Space Sys. Group

ATTN: R. Plebuch  
ATTN: S. Altschuler  
ATTN: D. Dee

Utah State University

Contract/Grant Office

ATTN: K. Baker  
ATTN: L. Jensen

Visidyne, Inc.

ATTN: H. Smith  
ATTN: W. Reidy  
ATTN: T. Dennes  
ATTN: J. Carpenter  
ATTN: C. Humphrey

Wayne State University

ATTN: R. Kummier

Wayne State University

Department of Physics

ATTN: W. Kauppila

Yale University

ATTN: Engineering Department